Physics of Atomic Nuclei, Vol. 64, No. 7, 2001, pp. 1157–1164. From Yadernaya Fizika, Vol. 64, No. 7, 2001, pp. 1235–1241.

Proceedings of the International Conference "Nuclear Structure and Related Topics"

Shifted Identical Bands: A New Phenomenon*

E. F. Jones[1], P. M. Gore, J. H. Hamilton[**], A. V. Ramayya, A. P. de Lima[1], R. S. Dodder, J. Kormicki, J. K. Hwang, C. J. Beyer, X. Q. Zhang, S. J. Zhu[2,3], G. M. Ter-Akopian[3,4], Yu. Ts. Oganessian[4], A. V. Daniel[4], J. O. Rasmussen[5], I. Y. Lee[5], J. D. Cole[6], M. W. Drigert[6], and W.-C. Ma[7] and the GANDS95 Collaboration

Department of Physics and Astronomy, Vanderbilt University, Nashville, USA

Received October 25, 2000

Abstract—The levels in ^{162}Gd were identified in spontaneous fission studies. Its transition energies are remarkably similar to those in ^{160}Gd. From that work, an analysis of yrast bands in even–even proton to neutron-rich Ba to Pb nuclei led to the discovery of a new phenomenon, shifted identical bands (SIB). SIBs are yrast bands in neighboring nuclei (a, b) with moments of inertia which are identical when shifted by a constant amount κ, so $J_{1a}(1 + \kappa) = J_{1b}$, from 2^+ to 8^+ and higher to 16^+. Out of over 700 comparisons, 55 SIBs were found from stable to the most neutron-rich Ce–W nuclei with $|\bar{\kappa}|$ between 1.5% and 13%, where the spread in κ is less than $\pm 1\%$, and only four identical bands ($\bar{\kappa} \cong 0$). As examples, we found for ^{158}Sm–^{160}Gd, $\bar{\kappa} = (-3.2^{+0.1}_{-0.2})\%$ (where the $\pm$ is the total spread in κ from -3.1 to -3.4); ^{156}Nd–^{160}Gd, $(-10.6^{+0.4}_{-0.2})\%$; ^{158}Sm–^{160}Sm, $(3.4^{+0.5}_{-0.3})\%$. The J_1 values were fitted to a variable moment of inertia model with parameters J_0 and C whose values correlate with the SIB J_1 values. The SIBs are not correlated either with deformation or with the N_pN_n product of the IBA model. © *2001 MAIK "Nauka/Interperiodica".*

1. INTRODUCTION

The discovery of identical bands (IB) in both superdeformed and normal deformed bands was a major highlight of nuclear structure research in the 1990s [1]. Bands in two neighboring nuclei with essentially equal transition energies and moments of inertia for every spin state in the band are classified as identical bands. As noted [1], IBs test our theoretical understanding of large amplitude collective motion, demanding more precise microscopic approaches to calculating moments of inertia. Almost all IBs involve even–even and even–odd neighbors in proton-rich nuclei [1]. A series of nearly "IBs" was reported for the α chain ^{156}Dy to ^{172}W compared to ^{180}Os [2]. There, energy similarities were somewhat correlated with N_pN_n. Two IBs have been reported in neutron-rich nuclei, $^{98,\,100}$Sr and $^{108-110}$Ru [3].

While investigating the structure of neutron-rich nuclei in prompt γ–γ–γ coincidence studies in the spontaneous fission of ^{252}Cf, we discovered a new phenomenon, which we call shifted identical bands (SIB). We identified levels in ^{160}Sm and ^{162}Gd [3, 4] and new high spin states in the heavy partners in neutron-rich Ba to Gd nuclei [3]. The new ^{162}Gd yrast transition energies were so similar to ^{160}Gd that this initiated a comparison of the moments of inertia of neighboring even–even nuclei in the $A = 140$–162 region. We classified shifted identical bands as occurring when two yrast cascades in nuclei separated by two to eight nucleons have their transition energies and moments of inertia become identical when E_γ and J_1 for one nucleus are shifted by a constant amount with less than $\pm 1\%$ total spread in the constant κ, where $J_{1a}(1 + \kappa) = J_{1b}$ for every state from 2^+ to 8^+ and higher to 16^+. We extended this analysis to even–even nuclei from Ba to Pb, from proton- to neutron-rich nuclei, and to some excited superdeformed bands. The SIBs are grouped in stable to the most neutron-rich Sm to Yb nuclei known, while SIBs are not seen in their lighter mass nuclei nor in Ba, Ce, or Os nuclei, except

*This article was submitted by the authors in English.

[1)]Department of Physics, University of Coimbra, Portugal.
[2)]Department of Physics, Tsinghua University, Beijing, China.
[3)]Joint Institute for Heavy Ion Research, Oak Ridge, USA.
[4)]Flerov Laboratory for Nuclear Reactions, JINR, Dubna, Russia.
[5)]Lawrence Berkeley National Laboratory, Berkeley, USA.
[6)]Idaho National Engineering and Environmental Laboratory, Idaho Falls, USA.
[7)]Department of Physics, Mississippi State University, USA.
[**]e-mail: j.h.hamilton@vanderbilt.edu

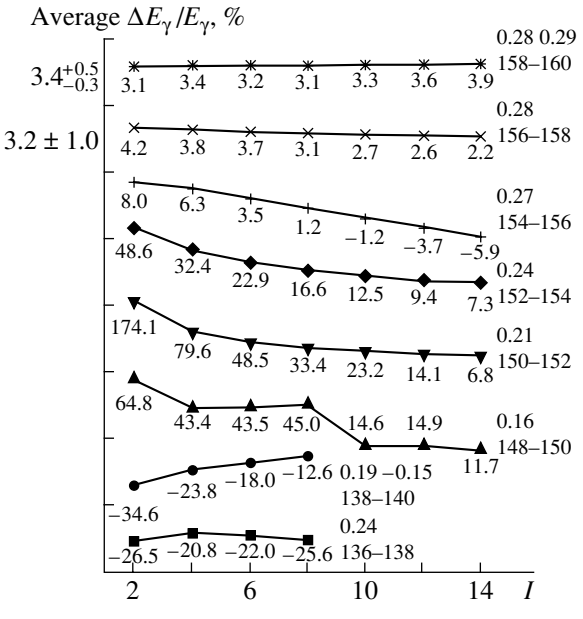

Fig. 1. Percentage differences in transition energies for isotopes of Sm ($Z = 62$), separated by $2n$. Theoretical β_2 deformations are given for each nucleus.

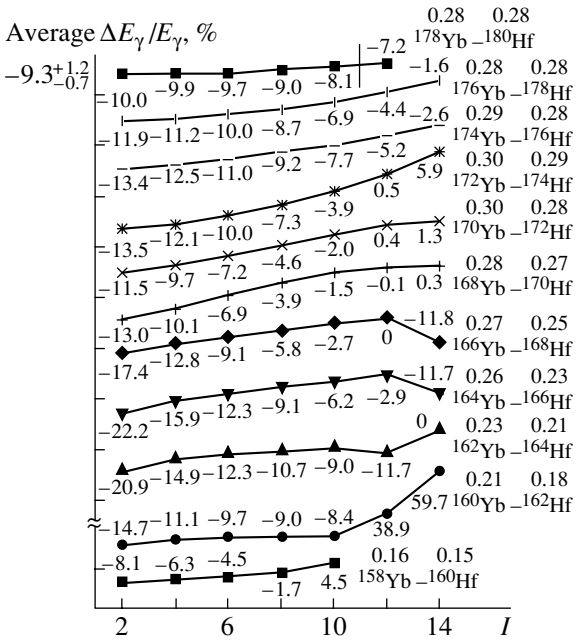

Fig. 2. Percentage differences in transition energies for $^{158–178}$Yb and $^{160–180}$Hf, separated by $2p$. Theoretical β_2 deformations are given. The experimental values show the same peaking effect as the theoretical values.

for ^{152}Ce. Some SIBs are seen in the Pt–Pb very neutron deficient nuclei for 4^+ to 14^+ states. This new phenomenon of SIBs provides new challenges for microscopic theories.

2. PROCEDURE

In our analysis, the percentage differences in transition energies E_γ between corresponding pairs of levels in two neighboring nuclei were calculated as

$$\frac{\Delta E_\gamma}{E_\gamma} = \frac{E_{\gamma_{\text{nuclide } a}} - E_{\gamma_{\text{nuclide } b}}}{E_{\gamma_{\text{nuclide } b}}} = \kappa$$
$$= -\frac{\Delta J_1}{J_1} = -\frac{J_{1_{\text{nuclide } a}} - J_{1_{\text{nuclide } b}}}{J_{1_{\text{nuclide } a}}},$$

where nuclide b is the heavier mass nuclide. J_1 is the kinematic moment of inertia, so $E_{\gamma a} = (1+\kappa)E_{\gamma b}$ and $J_{1a}(1+\kappa) = J_{1b}$. We define an identical band as one in which $\Delta E_\gamma/E_\gamma$ remains constant within $\pm 1\%$ of zero, and a shifted identical band as one that is constant within $\pm 1\%$ of a $\bar{\kappa} \geq 1\%$. For the SIBs observed, the absolute value of $\bar{\kappa}$ falls between one and thirteen percent. We calculated the experimental J_1 values and did variable moment of inertia fits to these data. We also calculated $\Delta J_2/J_2$.

In the variable-moment-of-inertia (VMI) model [5], J_1 is allowed to vary as a function of two parameters: J_0, the ground-state moment of inertia, and C, the restoring force constant that measures the hardness of a nucleus to stretching (the smaller C, the softer the nucleus). In the VMI model, assuming no component along the symmetry axis, J_1 is

$$J_{1\text{th}} = \frac{1}{6}\left(2J_0\right.$$

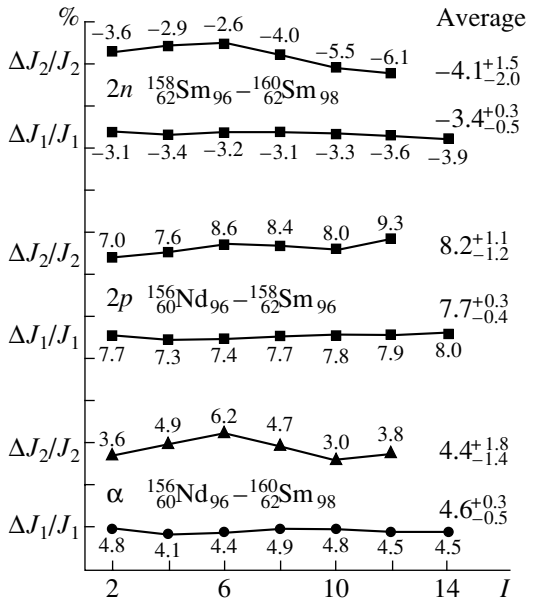

Fig. 3. Percent differences in the kinematic and dynamic moments of inertia for the comparisons $^{158–160}$Sm, ^{156}Nd–^{158}Sm, and ^{156}Nd–^{160}Sm.

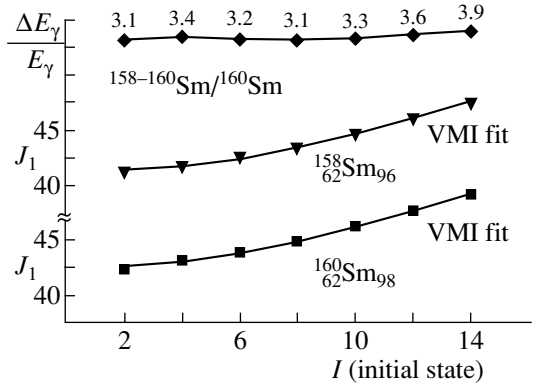

Fig. 4. VMI fits and $\Delta E_\gamma/E_\gamma$ for 2^+ to 14^+. For $2n$ separation, $\Delta E_\gamma/E_\gamma$ and $\Delta J_{1\mathrm{th}}/J_{1\mathrm{th}}$ (in %) are $3.4^{+0.5}_{-0.3}$ and -3.4 ± 0.3, where the "+" and "−" values give the total spread. J_0 (in $\hbar^2$/MeV), C (in MeV$^3/\hbar^4$), $\sqrt{\overline{(J_{1\mathrm{th}} - J_{1\mathrm{exp}})^2}}$ (in $\hbar^2$/MeV) are 41.5, 5.63×10^{-3}, 0.147 and 42.8, 4.86×10^{-3}, 0.131 for ^{158}Sm and ^{160}Sm, respectively.

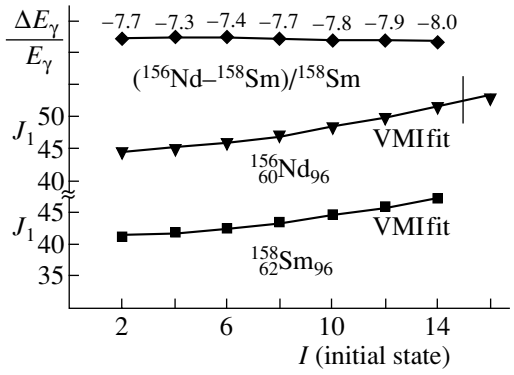

Fig. 5. VMI fits and $\Delta E_\gamma/E_\gamma$ for 2^+ to 14^+. For $2p$ separation, $\Delta E_\gamma/E_\gamma$ and $\Delta J_{1\mathrm{th}}/J_{1\mathrm{th}}$ (in %) are $-7.7^{+0.4}_{-0.3}$ and $7.6^{+0.2}_{-0.1}$, where the "+" and "−" values give the total spread. J_0 (in $\hbar^2$/MeV), C (in MeV$^3/\hbar^4$), $\sqrt{\overline{(J_{1\mathrm{th}} - J_{1\mathrm{exp}})^2}}$ (in $\hbar^2$/MeV) are 44.8, 4.21×10^{-3}, 0.127 and 41.5, 5.63×10^{-3}, 0.147 for ^{156}Nd and ^{158}Sm, respectively.

$$+\left(\frac{54x}{C} + 8J_0^3 - 6\sqrt{\frac{3x(27x + 8CJ_0^3)}{C^2}}\right)^{1/3}$$

$$+\left(\frac{54x}{C} + 8J_0^3 + 6\sqrt{\frac{3x(27x + 8CJ_0^3)}{C^2}}\right)^{1/3}\Bigg),$$

where $x = I(I+1)$. Values of J_0 and C were adjusted to obtain a least squares fit for the $J_{1\mathrm{th}}$ values vs. the $J_{1\mathrm{exp}}$ values at each spin. The root-mean-squares of the differences between the $J_{1\mathrm{th}}$ and $J_{1\mathrm{exp}}$ values were calculated along with $\Delta J_{1\mathrm{th}}/J_{1\mathrm{th}}$ for each point.

3. RESULTS

As a test of our approach, we investigated two superdeformed bands in superdeformed double magic (at high spins) ^{192}Hg and its neighbor ^{194}Hg, which have "one of the most spectacular examples of IBs" [1]. The SD-1−SD-1 and SD-1−SD-3 bands of $^{192,\,194}$Hg were compared, including VMI fits to the experimental J_1 data. The average $\Delta E_\gamma/E_\gamma$ values from 14^+ to 46^+ and average $\Delta J_2/J_2$ values from 12^+ to 44^+ are $(1.0 \pm 0.2)\%$ and $(-1.3^{+1.6}_{-1.8})\%$ for the two SD-1 bands and are $(-0.1^{+0.3}_{-0.9})\%$ and $(-0.1^{+2.2}_{-2.4})\%$ for the SD-1−SD-3 bands. The J_1, J_2 shifts are correlated with the difference in J_0, 0.9% and 0.2%, respectively, between the two pairs of bands in ^{192}Hg and ^{194}Hg. In the first case, one has a small SIB and in the second case the "spectacular" IB. Note that $\Delta J_2/J_2$ values have a greater spread than $\Delta J_1/J_1$. Superdeformed nuclei are thought of as being very hard, and the SD-1 bands of $^{192,\,194}$Hg have large

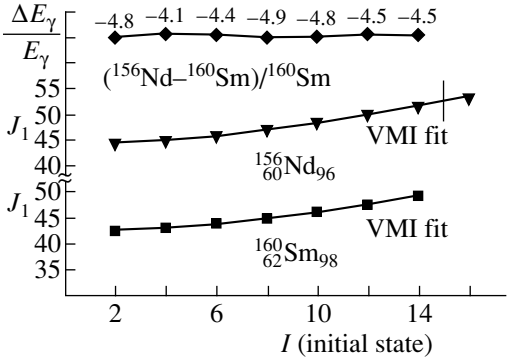

Fig. 6. VMI fits and $\Delta E_\gamma/E_\gamma$ for 2^+ to 14^+. For 1α separation, $\Delta E_\gamma/E_\gamma$ and $\Delta J_{1\mathrm{th}}/J_{1\mathrm{th}}$ (in %) are $-4.6^{+0.5}_{-0.3}$ and 4.58 ± 0.02, where the "+" and "−" values give the total spread. J_0 (in $\hbar^2$/MeV), C (in MeV$^3/\hbar^4$), $\sqrt{\overline{(J_{1\mathrm{th}} - J_{1\mathrm{exp}})^2}}$ (in $\hbar^2$/MeV) are 44.8, 4.21×10^{-3}, 0.127 and 42.8, 4.86×10^{-3}, 0.131 for ^{156}Nd and ^{160}Sm, respectively.

$C = 4.62$, 4.46 MeV$^3/\hbar^4$, respectively. It is surprising that even larger values of C are found for a number of SIB bands. Values of C are nearly equal for shifted identical bands, as they are for $^{192,\,194}$Hg.

The values of $\Delta E_\gamma/E_\gamma$ were calculated for the following even−even nuclei separated by $2n$, $2p$, α, $4n$, $4p$, $\alpha + 2n$, $\alpha + 2p$, 2α, and $2n$−$2p$: $^{126-148}$Ba, $^{128-152}$Ce, $^{128-156}$Nd, $^{132-160}$Sm, $^{138-162}$Gd, $^{148-166}$Dy, $^{150-170}$Er, $^{154-178}$Yb, $^{160-184}$Hf, $^{164-186}$W, $^{170-192}$Os, $^{176-184}$Pt, $^{178-186}$Hg, $^{186-188}$Pb, and the $1p$, $1n$, $1n$−$1p$ cases involving $^{177-185}$Au, $^{178-186}$Hg, and $^{183-187}$Tl nuclei.

In essentially all cases, as the neutron number in-

creases for a given Z, there is a progression from very uncorrelated yrast transition energies (where there are no SIBs) to strongly correlated energies, which we have termed shifted identical bands, in the most neutron-rich nuclei known, as illustrated in Figs. 1, 2. Examples of $\Delta J_1/J_1$ and $\Delta J_2/J_2$ are shown in Fig. 3. The VMI model was used to obtain fits to the above isotopes. Both identical and shifted identical bands were found among the comparisons of these isotopes. Identical bands were found to occur where $J_{0a} \sim J_{0b}$ and large $C_a \sim C_b$, and shifted identical bands were found in comparisons with large $C_a \sim C_b$ but the J_0's were different. Note that SIBs only occurred for large C values, corresponding to hard nuclei with small stretching. For example, ^{134}Sm and ^{136}Sm are soft nuclei (both with $C = 2.23 \times 10^{-3}$ MeV$^3/\hbar^4$), and these yrast bands are not SIBs (see Fig. 1). The SIB in $^{158-160}$Sm has $C = 5.63 \times 10^{-3}$ and 4.86×10^{-3} MeV$^3/\hbar^4$, respectively (see Fig. 4), with $E_\gamma(^{158}\mathrm{Sm}) = (1.034)E_\gamma(^{160}\mathrm{Sm})$ for every transition from the 2^+ to the 14^+ state, and a spread of only 1.031 to 1.039. Theoretical values of J_1 for each point have $\Delta J_{1\mathrm{th}}/J_{1\mathrm{th}}$ values with con-

Table 1. $\Delta E_\gamma/E_\gamma$ for examples of SIB and IB in ground-state yrast bands

$2n$ separation in yrast bands			
Z/N	pair	$I_{\max}$	$\Delta E_\gamma/E_\gamma, \%$
62/94–96	$^{156-158}$Sm	14	3.2 ± 1.0
62/96–98	$^{158-160}$Sm	14	$3.4^{+0.5}_{-0.3}$
64/96–98	$^{160-162}$Gd	10	$5.3^{+1.0}_{-0.9}$
66/96–98	$^{162-164}$Dy	14	$9.1^{+0.8}_{-0.6}$
66/98–100	$^{164-166}$Dy	8	$-5.0^{+0.8}_{-1.2}$
68/96–98	$^{164-166}$Er	12	$12.8^{+0.8}_{-0.7}$
68/100–102	$^{168-170}$Er	12	1.5 ± 0.7
70/102–104	$^{172-174}$Yb	14	$2.6^{+0.4}_{-0.3}$
70 /104–106	$^{174-176}$Yb	12	$-6.5^{+1.3}_{-0.4}$
		10	-6.7 ± 0.2
70/106–108	$^{176-178}$Yb	8	$-2.6^{+0.4}_{-0.8}$
72/104–106	$^{176-178}$Hf	12	$-5.4^{+0.9}_{-0.6}$
72/108–110	$^{180-182}$Hf	8	-3.7 ± 0.9

Table 2. $\Delta E_\gamma/E_\gamma$ for examples of SIB and IB in ground-state yrast bands

1α separation in yrast bands			
Z/N	pair	$I_{\max}$	$\Delta E_\gamma/E_\gamma, \%$
60–62/94–96	^{154}Nd–^{158}Sm	10	$-4.0^{+1.4}_{-1.6}$
60–62/96–98	^{156}Nd–^{160}Sm	14	$-4.6^{+0.5}_{-0.3}$
62–64/94–96	^{156}Sm–^{160}Gd	10	$0.1^{+0.7*}_{-0.6}$
62–64/96–98	^{158}Sm–^{162}Gd	10	$1.9^{+1.1}_{-0.9}$
		8	$1.6^{+0.7}_{-0.6}$
64–66/94–96	^{158}Gd–^{162}Dy	12	$-1.8^{+0.4}_{-0.2}$
64–66/96–98	^{160}Gd–^{164}Dy	8	$3.0^{+1.0}_{-0.4}$
64–66/98–100	^{162}Gd–^{166}Dy	8	$-6.9^{+1.0}_{-0.9}$
66–68/94–96	^{160}Dy–^{164}Er	10	-5.7 ± 0.7
66–68/98–100	^{164}Dy–^{168}Er	8	$-8.8^{+0.8}_{-1.0}$
68–70/94–96	^{162}Er–^{166}Yb	12	$-0.4^{+0.4*}_{-1.0}$
68–70/98–102	^{166}Er–^{170}Yb	8	$-5.1^{+0.7}_{-1.1}$
68–70/100–102	^{168}Er–^{172}Yb	14	$1.9^{+0.9}_{-0.6}$
70–72/94–96	^{164}Yb–^{168}Hf	8	$0.5^{+0.9*}_{-1.0}$

* Identical bands.

Table 3. $\Delta E_\gamma/E_\gamma$ for examples of SIB and IB in ground-state yrast bands

$2p$ separation in yrast bands			
Z/N	pair	$I_{\max}$	$\Delta E_\gamma/E_\gamma, \%$
60–62/94	^{154}Nd–^{156}Sm	10	$-7.0^{+0.7}_{-1.0}$
60–62/96	^{156}Nd–^{158}Sm	14	$-7.7^{+0.4}_{-0.3}$
62–64/90	^{152}Sm–^{154}Gd	14	$-1.5^{+0.6}_{-0.4}$
62–64/94	^{156}Sm–^{158}Gd	10	$-3.6^{+1.2}_{-1.0}$
		8	$-3.9^{+0.9}_{-0.7}$
62–64/96	^{158}Sm–^{160}Gd	10	$-3.2^{+0.1}_{-0.2}$
62–64/98	^{160}Sm–^{162}Gd	10	$-1.3^{+1.1}_{-0.8}$
64–66/98	^{162}Gd–^{164}Dy	14	$-1.5^{+1.0}_{-0.7}$
		10	-1.8 ± 0.4
66–68/100	^{166}Dy–^{168}Er	12	-3.9 ± 0.3
68–70/102	^{170}Er–^{172}Yb	12	$0.3 \pm 0.5^*$
70–72/108	^{178}Yb–^{180}Hf	10	$-9.3^{+1.2}_{-0.7}$
		8	$-9.7^{+0.7}_{-0.3}$
72–74/112	^{184}Hf–^{186}W	8	$-11.4^{+0.6}_{-1.0}$

* Identical bands.

Table 4. $\Delta E_\gamma/E_\gamma$ for examples of SIB and IB in ground-state yrast bands

Z/N	pair	$I_{\max}$	$\Delta E_\gamma/E_\gamma, \%$
$4p$ separation in yrast bands			
60–64/94	^{154}Nd–^{158}Gd	12	$-10.3^{+0.7}_{-0.3}$
		10	-10.4 ± 0.2
60–64/96	^{156}Nd–^{160}Gd	10	$-10.6^{+0.4}_{-0.2}$
62–66/96	^{158}Sm–^{162}Dy	8	$-8.8^{+1.2}_{-0.7}$
62–66/98	^{160}Sm–^{164}Dy	8	$-3.3^{+0.7}_{-0.5}$
$4n$ separation in yrast bands			
62/94–98	$^{156-160}$Sm	14	$6.6^{+0.9}_{-0.6}$
64/94–98	$^{158-162}$Gd	10	$9.4^{+0.9}_{-1.1}$
		8	$9.6^{+0.7}_{-1.0}$
70/102–106	$^{172-176}$Yb	12	$-4.0^{+1.0}_{-0.5}$
		10	$-4.2^{+0.2}_{-0.3}$
70/104–108	$^{174-178}$Yb	8	$-9.2^{+0.3}_{-0.5}$
72/106–110	$^{178-182}$Hf	8	$-5.4^{+0.7}_{-1.1}$

Table 5. Location by Z and N of SIBs from 2^+ to 8^+ and higher (underlining indicates the most neutron rich isotope whose levels are known to 8^+)

SIB for ranges 2^+ to 8^+, 10^+, 12^+, or 14^+									
Neutron number N \ Atomic number Z	58	60	62	64	66	68	70	72	74
90			X	X					
92		X		X		X			
94	X	X	X	X	X				
96		X	X	X	X	X			
98			X	X	X	X		X	
100					X	X	X		
102						X	X		
104						X	X	X	
106							X	X	
108							X	X	
110								X	
112								X	X

siderably smaller errors since they are averaged over all points. Examples of $2p$ and α separation SIBs are given in Figs. 5 and 6. Nearly the same constancy found in $\Delta J_1/J_1$ is also found in $\Delta J_2/J_2$, where J_2 is the dynamical moment of inertia, as seen in Fig. 3. The $\Delta J_2/J_2$ spreads are larger than those of $\Delta J_1/J_1$ for SIB, as for superdeformed bands. Surprisingly, the SIB J_2 spreads are often smaller (Fig. 3) than the J_2 spreads for SD bands. So, when shifted, SIBs are more identical than the "most spectacular" IBs.

Tables 1–4 show the IB and SIB that start at 2^+ for the $2n$, α, $2p$, $4n$, $4p$ separations. No IB or SIB occur for any combination with Ba or Os nuclei. Out of over 700 comparisons in Ba–Os nuclei, 55 cases of SIBs that begin at the 2^+ state were found and all involve stable to the most neutron-rich known nuclei with $N = 90$–112 (Table 5). As Z increases, the SIBs move up in N to the most neutron-rich nuclei. There are marked differences in magnitude (factors up to 9) and sign of κ for neighboring pairs for $2n$, $2p$, and α separations. Only 4 IBs were found in the over 700 comparisons. All β_2 values for SIBs nuclei range from 0.23–0.30 theoretically and are somewhat larger up to 0.35 experimentally, corresponding to well-deformed nuclei. In proton-rich W, Pt, Hg, and Pb nuclei, there are SIB and IB starting at 4^+ or 6^+, which are not considered in this paper. Their 2^+ and sometimes 4^+ states are perturbed by shape coexistence [6]. There are only four ground-state identical bands seen in e–e Ba to Pb, so SIBs are a different phenomenon.

We observed 55 cases of ground-state SIB: one case in ^{152}Ce; 9 in $^{152-156}$Nd; 20 in $^{152-160}$Sm; 21 in $^{154-162}$Gd; 18 in $^{160-166}$Dy; 14 in $^{160,\,164-170}$Er; 17 in $^{170-178}$Yb; 9 in $^{168,\,176-184}$Hf; and one in ^{186}W (note there is double counting since each of the 55 cases involves a pair of isotopes). Eighty-two percent of SIBs occur in the stable to most neutron-rich well-deformed Sm to Yb nuclei. However, there are other nearby nuclei with equally large deformations that do not exhibit SIBs. We also note that the $2p$ SIBs cluster in Sm and Gd (11 of 22), the $2n$ SIBs are nearly uniformly spread from Sm to Hf, and the α SIBs are clustered in Gd to Er (13 of 20), somewhat

Table 6. Examples of $\Delta E_\gamma/E_\gamma$ values for comparisons of ground-state yrast bands in nuclei with identical N_pN_n values (a, b, c, d indicate the same $(N_pN_n)(N'_pN'_n)$)

Type	Pair	$(N_pN_n)(N'_pN'_n)$	Range	$\Delta E_\gamma/E_\gamma, \%$
4α	^{156}Dy–^{172}W	(16, 8)(8, 16)	2–14	$7.8^{+4.1}_{-3.3}$
3α	^{158}Dy–^{170}Hf	(16, 10)(10, 16)	2–14	$1.0^{+2.5}_{-2.9}$
2α	^{160}Dy–^{168}Yb	(16, 12)(12, 16)^a	2–14	$0.5^{+1.9}_{-1.6}$
2α	^{160}Er–^{168}Hf	(14, 10)(10, 14)^b	2–12	$1.5^{+0.4}_{-0.5}$
α	^{162}Dy–^{166}Er	(16, 14)(14, 16)^c	2– 8	$0.8^{+1.0}_{-0.7}$
α	^{162}Er–^{166}Yb	(14, 12)(12, 14)^d	2–12	$-0.4^{+0.4}_{-1.0}$
$4p$	^{152}Gd–^{156}Er	(14, 6)(14, 6)	2–12	$-11.8^{+11.7}_{-6.2}$
$4p$	^{154}Gd–^{158}Er	(14, 8)(14, 8)	2–12	$-21.2^{+11.2}_{-14.8}$
$4p$	^{156}Gd–^{160}Er	(14, 10)(14, 10)^b	2–12	$-20.1^{+7.9}_{-9.2}$
$4p$	^{158}Gd–^{162}Er	(14, 12)(14, 12)^d	2–12	$-15.8^{+7.6}_{-6.3}$
$4p$	^{160}Gd–^{164}Er	(14, 14)(14, 14)	2–10	$-14.8^{+3.5}_{-2.8}$
$4p$	^{162}Gd–^{166}Er	(14, 16)(14, 16)^c	2–10	$-8.9^{+2.8}_{-1.6}$
$8p$	^{158}Sm–^{166}Yb	(12, 14)(12, 14)^d	2–12	$-21.3^{+8.9}_{-7.6}$
$8p$	^{160}Sm–^{168}Yb	(12, 16)(12, 16)^a	2–12	$-13.8^{+8.2}_{-5.7}$
$8p$–$4n$	^{156}Gd–^{168}Hf	(14, 10)(10, 14)^b	2–14	$-19.0^{+8.2}_{-9.3}$
$6p$–$2n$	^{158}Sm–^{162}Er	(12, 14)(12, 14)^d	2–12	$-20.9^{+9.6}_{-7.6}$
$6p + 2n$	^{158}Gd–^{166}Yb	(14, 12)(12, 14)^d	2–12	$-16.2^{+6.8}_{-6.1}$
$4p$–$4n$	^{160}Sm–^{160}Dy	(12, 16)(16, 12)^a	2–12	$-14.0^{+6.3}_{-4.3}$
$2p$–$2n$	^{158}Sm–^{158}Gd	(12, 14)(14, 12)^d	2–12	$-6.2^{+2.9}_{-2.2}$
$2p$–$2n$	^{162}Gd–^{162}Dy	(14, 16)(16, 14)^c	2–10	$-10.1^{+0.8}_{-0.8}$

correlated with the $2p$ cases. Since the results to some degree cluster around neutron midshell, where the saturation of collectivity is expected, one could expect that saturation may play a role. Clearly there is no correlation with $A^{5/3}$, for example, for ^{158}Sm–^{160}Sm, $\bar{\kappa} = 3.4$ and for ^{158}Sm–^{160}Gd, $\bar{\kappa} = -3.2$, so adding $2p$ gives the opposite sign to adding $2n$ and has the opposite change in E_γ, J_1. More importantly, there is no correlation with deformation. For example, look at the two $^{158-160}$Gd–$^{162-164}$Dy α cases of SIB where $\bar{\kappa} = -1.8$ and $+3.0$, respectively. The experimental β_2 for Gd are 0.348 and 0.353, and for Dy are 0.341 and 0.348, respectively. The Gd deformations are larger in both cases, and so one expects their transition energies to be smaller. This is consistent with the first case but exactly opposite in the latter case. As another example, the $2p$ chain of Yb to Hf is shown in Fig. 2. Note that the deformations peak at midshell around $N = 102$ but no IB or SIB are seen there. The only SIB is in the most neutron-rich nuclei known with $N = 108$ and lower deformation.

Table 7. $\Delta E_\gamma/E_\gamma$ values for 1α separated SIBs compared with $\Delta E_\gamma/E_\gamma$ values of their associated $2n$ and $2p$ comparisons (a line over a component indicates the average is taken over a spread of values with two examples)

1α pair	$\Delta E_\gamma/E_\gamma$, %	$2n+2p$	$2p+2n$
$^{154}_{60}$Nd–$^{158}_{62}$Sm	$-4.0^{+1.4}_{-1.6}$	2.6 −7.7	−7.0 +3.2
^{156}Nd–^{160}Sm	$-4.6^{+0.5}_{-0.3}$	Unknown	−7.7 +3.4
$^{156}_{62}$Sm–$^{160}_{64}$Gd	$0.1^{+0.7}_{-0.6}$	3.2 −3.2	−3.6 +3.9
^{158}Sm–^{162}Gd	$1.9^{+1.1}_{-0.9}$	3.4 −1.3	−3.2 +5.3
$^{158}_{64}$Gd–$^{162}_{66}$Dy	$-1.8^{+0.4}_{-0.2}$	$\overline{3.9}^{+1.7}_{-2.0}$ $-\overline{5.4}^{+1.8}_{-1.2}$	$-\overline{6.3}^{+2.9}_{-2.1}$ $+\overline{4.9}^{+2.7}_{-3.1}$
^{160}Gd–^{164}Dy	$3.4^{+1.4}_{-0.8}$	5.3 −1.5	$-\overline{5.4}$ +9.1
^{162}Gd–^{166}Dy	$-6.9^{+1.0}_{-0.9}$	Unknown	−1.5 −5.1
$^{160}_{66}$Dy–$^{164}_{68}$Er	-5.7 ± 0.7	$\overline{4.9}$ $-\overline{10.1}$	$-\overline{11.8}$ $+\overline{7.1}$
^{164}Dy–^{168}Er	$-8.8^{+0.8}_{-1.0}$	−5.0 −3.9	$\overline{-7.8}$ $-\overline{1.0}$
$^{162}_{68}$Er–$^{166}_{70}$Yb	$-0.4^{+0.4}_{-1.0}$	$\overline{5.8}^{+5.8}_{-6.2}$ $-\overline{5.8}\pm$ 4.9	$-\overline{9.1}^{+6.6}_{-8.2}$ $+\overline{10.0}^{+10.5}_{-8.8}$
^{168}Er–^{172}Yb	$1.9^{+0.9}_{-0.6}$	1.5 +0.3	$-\overline{1.8}$ $+\overline{3.9}$

Thus, collectivity and saturation of collectivity are not correlated with SIB occurrence.

Now look at the N_pN_n scheme suggested earlier [2], where N_pN_n are the smaller number of particles or holes from magic numbers. First the "identical bands in widely dispersed nuclei" noted earlier [2] in ^{156}Dy to ^{172}W α chain compared to ^{180}Os do have relatively small average κ's but their spreads in κ are large, $0.2^{+6.1}_{-5.4}$, $-0.2^{+7.2}_{-4.7}$, $-0.5^{+7.1}_{-6.2}$, $-1.6^{+6.9}_{-4.7}$, and $-7.1^{+4.2}_{-2.3}$, respectively. So, they are not really identical in the usual sense. In Table 6 are shown the six pairs with the same $(N_pN_n)(N'_pN'_n)$ values noted earlier [2], ^{156}Dy–^{172}W, ^{160}Er–^{168}Hf, ^{158}Dy–^{170}Hf, ^{162}Er–^{166}Yb, ^{160}Dy–^{168}Yb, and ^{162}Dy–^{166}Er along with eight other such cases, and six of eight Gd–Er cases, which form a long chain of identical N_pN_n nuclei that go from spherical ^{148}Gd–^{152}Er to well-deformed ^{162}Gd–^{166}Er. As seen in Table 6, in the earlier noted six cases [2] there is one SIB and two IBs but with the exception of an SIB in ^{162}Gd–^{162}Dy, all the others have large $\bar{\kappa}$ with large spreads, including all the Gd–Er chain with two cases left out. Note (Table 6) four of the earlier six cases [2] have multiple other same N_pN_n pairs all with large $\bar{\kappa}$ and large spreads. N_pN_n for the SIB nuclei go from 80 to 288 but many others in this range are not SIBs. The absence of SIBs in many cases and of any consistency for equal N_pN_n nuclei suggests the global collective features tracked by N_pN_n cannot account for the observed SIBs.

Finally, the SIBs for α, $\alpha+2n$, $\alpha+2p$, $4n$, $4p$, and $2n$–$2p$ separations have the following differences: For Nd to Dy SIBs, their $\Delta E_\gamma/E_\gamma$ are obtained by adding, including sign, the $2n$ and $2p$ values even when the $2n$ and $2p$ values are different in magnitude and sign (see Table 7). For Er, Yb, and Hf nuclei, the SIBs for α separation are the result of combining $2n$ and $2p$ neighboring nuclei with no SIB where the $\Delta E_\gamma/E_\gamma$ change in $2n$ is in the opposite direction so as to cancel the $2p$ non-SIB variation. For example, in ^{160}Dy–^{164}Er, from 2^+ to 10^+, $\Delta E_\gamma/E_\gamma$ for 1α is (-5.7 ± 0.7)%, but over the same range $\Delta E_\gamma/E_\gamma$ for ^{160}Dy–^{162}Er goes from -14.9% to -8.7%, and $\Delta E_\gamma/E_\gamma$ for $^{162-164}$Er goes from 11.6% to 2.6%.

In summary, this new phenomenon of SIBs is found most often in stable to the most neutron-rich Sm to Yb nuclei known with $N = 94$–108. Studies of their heavier nuclei could give us insight into why such bands occur but will have to await radioactive ion beam accelerators. Comparisons of SIB with the N_pN_n scheme and deformation and its saturation indicate that one must go beyond global collective features to find an understanding of this new phenomenon. These SIBs with remarkably constant E_γ shifts and marked differences in size and sign of κ for even neighboring pairs clearly present challenges for more microscopic theoretical approaches.

ACKNOWLEDGMENTS

The work at VU, INEEL, LBNL, and MSU was supported by US DOE grants and contracts DE-FG05-88ER40407, DE-AC07-76ID01570, DE-AC03-76SF00098, and DE-FG05-95ER40939, and Tsinghua University by National Natural Science

Foundation of China and Science Foundation for Nuclear Industry. The Joint Institute for Heavy Ion Research is supported by University of Tennessee, Vanderbilt University, Oak Ridge National Laboratory, and US DOE.

REFERENCES

1. C. Baktash, B. Haas, and W. Nazarewicz, Annu. Rev. Nucl. Part. Sci. **45**, 485 (1995).
2. R. F. Casten *et al.,* Phys. Rev. C **45**, R1413 (1992).
3. J. H. Hamilton *et al.,* Prog. Part. Nucl. Phys. **35**, 635 (1995).
4. E. F. Jones *et al.,* in *Proceedings of the Second International Conference on Exotic Nuclei and Atomic Masses, Michigan, 1998*, Ed. by B. M. Sherrill *et al.* (AIP, New York, 1998), p. 523.
5. M. A. J. Mariscotti, G. Scharff-Goldhaber, and B. Buck, Phys. Rev. C **178**, 1864 (1969).
6. J. H. Hamilton, in *Treatise on Heavy Ion Science,* Ed. by Allan Bromley (Plenum, New York, 1989), Vol. 8, p. 2.

Physics of Atomic Nuclei, Vol. 64, No. 7, 2001, pp. 1165–1168. From Yadernaya Fizika, Vol. 64, No. 7, 2001, pp. 1242–1245.

Proceedings of the International Conference "Nuclear Structure and Related Topics"

Neutrino–^{12}C Reactions and the LSND and KARMEN Experiments on Neutrino Oscillations*

C. Volpe[**], **N. Auerbach**[1)], **G. Colò**[2)], **T. Suzuki**[3)], **and N. Van Giai**

Groupe de Physique Theorique, Institut de Physique Nucléaire, Orsay Cedex, France

Received October 25, 2000

Abstract—We present new theoretical results of the flux-averaged ^{12}C$(\nu_e, e^-)^{12}$N and ^{12}C$(\nu_\mu, \mu^-)^{12}$N cross sections with $\nu_\mu(\nu_e)$ coming from the decay-in-flight (decay-at-rest) of $\pi^+(\mu^+)$. These cross sections are relevant for the interpretation of the recent experiments on neutrino oscillation performed by the LSND and KARMEN collaborations. The microscopic approaches used are charge-exchange random phase approximation (RPA), charge-exchange RPA among quasiparticles (QRPA), and the Shell Model. We show that the exclusive cross sections are in nice agreement with the experimental values for both reactions when a large-scale shell-model calculation is performed. Concerning the inclusive cross section for ν_μ coming from the decay-in-flight of π^+, the calculated value keeps overestimating the experimental one by 20–30%, while the inclusive cross section due to ν_e coming from the decay-at-rest of μ^+ is in agreement within experimental error bars with the measured values. The shell-model prediction for the decay-in-flight neutrino cross section is reduced compared to the RPA one because of the different kind of correlations in the calculation of the spin modes (in particular, the quenching of the 1^+) and partially due to the shell-model configuration basis, which is not large enough, as we show using arguments based on sum rules. © *2001 MAIK "Nauka/Interperiodica".*

In current experiments on neutrinos, either aiming at studying the properties of neutrinos such as their mass or using neutrinos to learn something on astrophysical objects like the sun and supernovae, nuclei are often used as neutrino detectors. For example, ^{12}C has been used in recent experiments performed both by the LSND and the KARMEN collaborations, looking for $\nu_\mu \to \nu_e$ [1, 2], $\bar{\nu}_\mu \to \bar{\nu}_e$ [3, 4], or $\nu_\mu \to \nu_x$ [5] oscillations with neutrinos produced by accelerators. An accurate knowledge of the cross sections of the reactions induced by neutrinos on ^{12}C is therefore necessary to interpret these experiments. In fact, recently, significant discrepancies between the experimental values and the theoretical predictions of some cross sections have stimulated many calculations: (i) a discrepancy up to a factor of 4 on the cross section for the charged-current (CC) reaction $\nu_e + {}^{12}\mathrm{C} \to e^- + {}^{12}\mathrm{N}_{\mathrm{g.s.}}$ with ν_e coming from the decay-at-rest (DAR) of μ^+; (ii) a discrepancy up to a factor 2 on the cross section of $\nu_\mu + {}^{12}\mathrm{C} \to \mu^- + {}^{12}\mathrm{N}$ with ν_μ coming from the decay-in-flight (DIF) of π^+. If, on one hand, the former has been measured by different collaborations, the latter has only been measured by the LSND collaboration, the detector used being the same as the one used in the oscillation experiments. Because only one experimental value is available in this case, it is even more important to understand from the theoretical point of view what can be at the origin of these discrepancies. The microscopic theoretical approaches used are either the charge-exchange random phase approximation (RPA) or the shell model (SM). Both these models present approximations that render it difficult to take into account the many aspects of the nuclear structure of the nuclei involved in these reactions, aspects which are necessary for an accurate prediction of the cross sections. In fact, it has been known since the very first shell-model calculations in light nuclei [6] that ^{12}C is not a well-closed subshell nucleus. Actually, a good prediction of the exclusive cross sections (in which ^{12}N is left in its ground state) needs a good description of the ground state to ground state transition probability. On the other hand, the inclusive cross sections (in which ^{12}N is left either in the ground state or in an excited state) require the use of approaches capable of describing high-lying excited states, in the giant resonance region or

*This article was submitted by the authors in English.

[1)]School of Physics and Astronomy, Tel Aviv University, Israel.
[2)]Dipartimento di Fisica, Università degli Studi, Milano, Italy.
[3)] Department of Physics, College of Humanities and Science, Nihon University, Tokyo, Japan.
[**]e-mail: volpe@ipnost.in2p3.fr

above, the average energy transferred to the nucleus being of several tens of MeV. Within RPA, it is easy to perform calculations in large model spaces and therefore to include high-lying states, whereas the ground state to ground state transition probability is not well described, as is known from other weak processes in these nuclei, namely, $^{12}\mathrm{N}(\beta^+)^{12}\mathrm{C}$ and $^{12}\mathrm{C}(\mu^-)^{12}\mathrm{B}$. On the contrary, within SM, it is not so easy to perform large-scale calculations because of computational reasons. The prediction of these cross sections is therefore a challenging task from the theoretical point of view.

We present new theoretical results on the exclusive and inclusive cross sections, both for the reaction $\nu_e + ^{12}\mathrm{C} \to e^- + ^{12}\mathrm{N}_{\mathrm{g.s.}}$ with ν_e coming from the DAR of μ^+ and the reaction $\nu_\mu + ^{12}\mathrm{C} \to \mu^- + ^{12}\mathrm{N}$ with ν_μ coming from the DIF of π^+ [7]. The calculations are performed within two microscopic approaches. The first is the RPA among quasiparticles (QRPA) where we introduce the configuration mixing present in the ground state of ^{12}C by including "ad hoc" pairing, as was first suggested in [8]. In [9], this is done by performing RPA with fractional occupancies. The second approach used is SM where we use a model space which is larger than the one used in [10].

The expression for the cross section of the reaction $\nu_l + ^{12}\mathrm{C} \to l + ^{12}\mathrm{N}$ ($l = e,\ \mu$) is [11]

$$\sigma = \frac{G^2}{2\pi}\cos^2\theta_{\mathrm{C}} \sum_f p_l E_l \int_{-1}^{1} d(\cos\theta) M_\beta, \qquad (1)$$

where $G\cos\theta_{\mathrm{C}}$ is the weak coupling constant, θ is the angle between the directions of the incident neutrino and the outgoing lepton, and M_β is given by

$$M_\beta \equiv M_{\mathrm{F}}|\langle f|\tilde{1}|i\rangle|^2 + M_{\mathrm{G0}}\frac{1}{3}|\langle f|\tilde{\sigma}|i\rangle|^2 + M_{\mathrm{G2}}\Lambda, \qquad (2)$$

where the expression for the squared nuclear matrix elements which are related either to Fermi type or Gamow–Teller type transitions can be found in [11]. A correction to (1) must be introduced to account for the distortion of the outgoing lepton wave function due to the Coulomb field of the daughter nucleus, either by multiplying (1) by the Fermi function [12] or by using the "Effective Momentum Approximation" [13], according to the energy of the outgoing leptons.

Concerning the transition matrix elements (2), we perform a self-consistent RPA calculation where the residual interaction among particle–hole states is derived from the same Skyrme force used to produce the mean field. The forces used are either SGII [14] or SIII [15]. We have checked that the results are not very sensitive to the choice of the force. To go beyond the closed-subshell approximation for the ^{12}C ground state, pairing correlations are taken into account in the HF+BCS approximation. Constant pairing gaps Δ_p and Δ_n for protons and neutrons are introduced and are set at 4.5 MeV. A large pairing gap is unrealistic for states far from the Fermi surface, and an energy cutoff is required, such that the states above this cutoff have $\Delta = 0$. The cutoff is set at the $2s_{1/2}$ state. We have then performed a QRPA calculation [16] in order to get the transition matrix elements. We simply note that the particle–particle matrix elements are renormalized here by means of a parameter g_{pp} that has been chosen to be smaller than 1 (typically 0.7) to avoid the well-known ground-state instabilities.

Concerning the SM approach, we perform calculations in the $0s$–$0p$–$1s0d$–$1p0f$ shell-model space and include configurations up to $3\hbar\omega$ excitations for negative parity states and up to $2\hbar\omega$ excitations for positive parity states. No ^{4}He core is assumed in the present calculations. The spurious center-of-mass states are eliminated here by using the method of Lawson [17]. We adopt here the effective interaction of Warburton and Brown [18] for use in the present $0s$–$0p$–$1s0d$–$1p0f$ model space, and we use the set WB10 [19], which is based on the WBT interaction [18]. In the shell model, the reduced matrix elements of transition operators are expressed as linear combinations of the reduced matrix elements of single-particle states with coefficients given by one-body density matrix elements. The form factors in the coefficients M_{F}, M_{G0}, M_{G2} in (2) have to be corrected for the center-of-mass motion. This is done by multiplying the matrix elements by the Tassie–Barker function, $\exp(b^2q^2/2A)$, with b being the oscillator length parameter [20].

In order to compare the theoretical cross sections to the experimental data, the energy-dependent cross section (1) is weighted by the neutrino impinging flux $\tilde{f}(E_\nu)$ (depending on the neutrino source used)

$$\langle\sigma\rangle_f = \int dE_\nu \sigma(E_\nu)\tilde{f}(E_\nu). \qquad (3)$$

Tables 1, 2, and 3 show the calculated flux-averaged cross sections obtained in the different approaches used in comparison with the results of [9] and [10] and with the experimental data. First, let us discuss the results obtained for the exclusive cross sections. As we mentioned above, the RPA value presents a factor 4 discrepancy with the experimental data. This disagreement is strongly reduced when RPA with fractional occupancies is used [9], whereas the QRPA value is only slightly different from the RPA one. Within SM in a $0s$–$0p$–$1s0d$ ($(0+1+2)\hbar\omega$) model space, the exclusive cross sections for both the DIF and the DAR cases agree with the experimental data. These results are not very sensitive to

Table 1. Flux averaged exclusive cross sections $\langle\sigma\rangle_f$ within the different approaches used, namely, SM, RPA, and QRPA [7]

	(ν_μ, μ^-)DIF $\langle\sigma\rangle_f, 10^{-40}$ cm^2	(ν_e, e^-)DAR $\langle\sigma\rangle_f, 10^{-42}$ cm^2
RPA	2.09	49.47
QRPA	1.97	42.92
CRPA [9]	1.06(1.03)	13.88(12.55)
SM(HF wf) $(0+1+2)\hbar\omega$	0.65	8.11
SM(WS wf) $(0+1+2)\hbar\omega$ [10]	0.58	8.4
Experiment	$0.66 \pm 1.0 \pm 1.0$ [21]	$10.5 \pm 1.0 \pm 1.0$ [22]
		$9.1 \pm 0.4 \pm 0.9$ [23]
		$9.1 \pm 0.5 \pm 0.8$ [24]

Note: In the SM calculation in the $(0+1+2)\hbar\omega$ model space, Hartree–Fock wave functions (HF wf) have been used. Comparison with CRPA with fractional occupancies [9] and a recent shell-model calculation [10] is made. In the former case, the results are obtained with the finite-range G matrix derived from the Bonn NN potential (BP) and with the Landau–Migdal (LM) force (in brackets). In the latter case, Woods–Saxon wave functions (WS wf) have been used.

the choice of the wave functions, which are either Hartree–Fock (HF) in our calculation or Woods–Saxon (WS) in [10]. Concerning the inclusive cross section without the contribution of the ground state to ground state transition for the DAR case (Table 2), we see that calculations within RPA and RPA with fractional occupancies give values in agreement with the experiment. This cross section is very sensitive to any shift of the strength distribution. In fact, the cross section (1) goes almost like the square of the lepton energy E_l, which is equal to the difference between the energy of the impinging neutrino and the energy transferred to the nucleus, i.e., $E_\nu - E_{fi}$. As a consequence, for example, we can see that the QRPA result is almost a factor 2 larger than the RPA value. This is because the QRPA strength functions are, as a rule, shifted downward in energy compared to RPA due to the particle–particle correlations. The SM cross sections are very close to the experimental values both in our calculation and in the one of [10] with the difference that our result slightly overestimates the data, whereas the one in [10] slightly underestimates it. Finally, let us look at the inclusive cross sections for the DIF case. We see (Table 3) that the QRPA and RPA with fractional occupancies give cross sections very similar to RPA, that is, a factor 2 larger than the experimental values, as we expect because the inclusion of configuration mixing does not strongly affect the transition probabilities to high-lying states with respect to the RPA values. On the contrary, the SM results are very close to the experimental cross section within error bars. This reduction of the cross sections compared to the RPA values is due partially to the better description of certain modes such as the Gamow–Teller transition between the ground states and the spin dipole modes and partially due to the shell-model space. In fact, we have evaluated energy-weighted sum rules for different multipolarities. This has shown that, for some of them, the sum rules were not completely satisfied and pointed out that the model space should be enlarged.

Table 2. Same as Table 1 for flux-averaged inclusive cross sections but excluding the ground state [7] (our results are obtained within the $(0+1+2+3)\hbar\omega$ model space, whereas the results of [10] in the same model space (in brackets) are obtained by extrapolation)

	(ν_e, e^-)DAR $\langle\sigma\rangle_f, 10^{-42}$ cm^2
RPA	5.63
QRPA	9.08
CRPA [9]	5.4(5.6)
SM(HF wf) $(0+1+2+3)\hbar\omega$	8.28
SM(WS wf) $(0+1+2+3)\hbar\omega$ [10]	(3.8)
Experiment	5.4 ± 1.9 [22]
	$5.7 \pm 0.6 \pm 0.6$ [23]
	5.1 ± 0.8 [24]

In conclusion, we have shown that detailed large-scale calculations are needed to accurately predict the reaction cross sections induced by neutrinos on ^{12}C. The exclusive cross sections for the charged-current $\nu_l + {}^{12}\mathrm{C} \to l^- + {}^{12}\mathrm{N}$ $(l = e, \mu)$ with ν_e coming from the DAR of μ^+ or with ν_μ coming from the DIF of π^+ are in agreement with the experimental

Table 3. Same as Table 1 for the flux-averaged DIF inclusive cross section [7] (our results are obtained within the $(0+1+2+3)\hbar\omega$ model space, whereas the results of [10] in the same model space (in brackets) are obtained by extrapolation)

	(ν_μ, μ^-)DIF $\langle\sigma\rangle_f, 10^{-40}$ cm^2
RPA	19.23
QRPA	20.29
CRPA [9]	18.18 (17.80)
SM(HF wf) $(0+1+2+3)\hbar\omega$	15.18
SM(WS wf) $(0+1+2+3)\hbar\omega$ [10]	(13.2)
Experiment	$12.4 \pm 0.3 \pm 1.8$ [9, 21]

values, when a SM calculation is performed within $0s$–$0p$–$1s0d$–$1p0f$ model space, showing that the inclusion of configuration mixing is necessary. Concerning the inclusive reaction cross sections, the values obtained within SM are (i) 16.4×10^{-42} cm^2 for the reaction due to ν_e coming from the DAR of μ^+, which agrees within experimental error bars with the measured values; (ii) 15.2×10^{-40} cm^2 for the one due to ν_μ coming from the DIF of π^+, to be compared to the experimental value of $(12.4 \pm 0.3 \pm 1.8) \times 10^{-40}$ cm^2. The latter SM result is much closer to the data than the RPA one. This is due, on one hand, to a better description of the 1^+ and spin dipole contribution and, on the other hand, to the model space used. In fact, the calculation of energy-weighted sum rules for some multipolarities shows that the model space used is not large enough for them to be satisfied.

REFERENCES

1. C. Athanassopoulos (LSND Collab.), Phys. Rev. Lett. **81**, 1774 (1998); Phys. Rev. C **58**, 2489 (1998).
2. K. Eitel, in *Proceedings of the 32nd Rencontres de Moriond, Electroweak Interactions and Unified Theories, Les Arcs, France, 1997*.
3. C. Athanassopoulos (LSND Collab.), Phys. Rev. Lett. **77**, 3082 (1996); **75**, 2650 (1995).
4. K. Eitel and B. Zeitnitz (KARMEN Collab.), Nucl. Phys. B (Proc. Suppl.) **77**, 212 (1999).
5. B. Armbruster *et al.,* Phys. Rev. C **57**, 3414 (1998).
6. S. Cohen and D. Kurath, Nucl. Phys. **73**, 1 (1965).
7. C. Volpe, N. Auerbach, G. Colò, T. Suzuki, and N. Van Giai, Phys. Rev. C **62**, 015501 (2000).
8. N. Auerbach, N. Van Giai, and O. K. Vorov, Phys. Rev. C **56**, R2368 (1997).
9. E. Kolbe, K. Langanke, and P. Vogel, Nucl. Phys. A **652**, 91 (1999).
10. A. C. Hayes and I. S. Towner, Phys. Rev. C **61**, 044603 (2000).
11. T. Kuramoto, M. Fukugita, Y. Kohyama, and K. Kubodera, Nucl. Phys. A **512**, 711 (1990).
12. D. H. Wilkinson and B. E. F. Macefield, Nucl. Phys. A **232**, 58 (1974).
13. J. Engel, Phys. Rev. C **57**, 2004 (1998).
14. N. Van Giai and H. Sagawa, Phys. Lett. B **106B**, 379 (1981).
15. M. Beiner, H. Flocard, N. Van Giai, and Ph. Quentin, Nucl. Phys. A **238**, 29 (1975).
16. K. Grotz and H. V. Klapdor, *The Weak Interaction in Nuclear-, Particle- and Astrophysics* (Adam Hilger, Bristol, 1990).
17. D. H. Gloeckner and R. D. Lawson, Phys. Lett. B **53B**, 313 (1974).
18. E. K. Warburton and B. A. Brown, Phys. Rev. C **46**, 923 (1992).
19. B. A. Brown, A. Etchegoyen, and W. D. M. Rae, MSU Cyclotron Laboratory Report No. 524 (1986) (OXBASH — The Oxford, Buenos-Aires, Michigan State, Shell Model Program).
20. L. J. Tassie and F. C. Barker, Phys. Rev. **111**, 940 (1958).
21. C. Athanassopoulos (LSND Collab.), Phys. Rev. C **56**, 2806 (1997); M. Albert *et al.,* Phys. Rev. C **51**, R1065 (1995).
22. D. A. Krakauer *et al.,* Phys. Rev. C **45**, 2450 (1992); R. C. Allen *et al.,* Phys. Rev. Lett. **64**, 1871 (1990).
23. C. Athanassopoulos (LSND Collab.), Phys. Rev. C **55**, 2078 (1997).
24. B. E. Bodmann (KARMEN Collab.), Phys. Lett. B **332**, 251 (1994); J. Kleinfeller *et al.,* in *Neutrino 96,* Ed. by K. Enquist, H. Huitu, and J. Maalampi (World Sci., Singapore, 1997).

Physics of Atomic Nuclei, Vol. 64, No. 7, 2001, pp. 1169–1173. From Yadernaya Fizika, Vol. 64, No. 7, 2001, pp. 1246–1250.

Proceedings of the International Conference "Nuclear Structure and Related Topics"

Strength of Spin–Isospin Transitions in $A = 28$ Nuclei*

V. A. Kuz'min**, **T. V. Tetereva**[1)], **and K. Junker**[2)]

Joint Institute for Nuclear Research, Dubna, Moscow oblast, 141980 Russia

Received October 25, 2000

Abstract—The relations between the strengths of spin–isospin transition operators extracted from direct nuclear reactions, magnetic electron scattering, and processes of semileptonic weak interaction are discussed. © *2001 MAIK "Nauka/Interperiodica".*

1. INTRODUCTION

Studies of spin–isospin excitations in nuclei have a long history. Detailed discussions of it are given in [1, 2]. We dwell upon only a few points that are important for our purposes. The first manifestation of spin–isospin transitions was detected in beta decay as Gamow–Teller transitions ($\Delta J^\pi = 1^+$) for which we have

$$ft_{1/2} = \frac{6135}{(g_A/g_V)^2 B^\pm(\mathrm{GT})},$$

where the strength of the Gamow–Teller (GT) transition is introduced as

$$B_f^\pm(\mathrm{GT}) = \frac{1}{2J_f+1}\left|\langle J_f \left\| \sum_{k=1}^{A} \sigma_k\, t_k^\pm \right\| J_i\rangle\right|^2. \quad (1)$$

In this article, we will only discuss the $0^+ \to 1^+$ transitions. The discovery of isobar analog states in (p,n) reactions was followed by the prediction of a new nuclear collective excitation—the giant GT resonance—as the reason for the lack of σt^- strength observed in β-decay studies. In the early 1980s, giant GT resonances were experimentally discovered and studied in (p,n) and other nuclear charge-exchange (CEX) reactions at intermediate energies. By using some additional assumptions, it was shown in [3] that the zero-angle (p,n) cross sections are proportional to $B(\mathrm{GT})$. A comparison of $B(\mathrm{GT})$ values extracted from the cross sections of CEX reactions with those obtained from β decay reveals that there are some distinctions between them [4]. The origin of these distinctions was explained by the fact that transitions characterized by small $B(\mathrm{GT})$ are observed even in fast beta decay. For small $B(\mathrm{GT})$, however, other spin multipoles strongly contribute to CEX cross sections, leading to a considerable deviation from the proportionality between the zero-angle cross sections and $B(\mathrm{GT})$ values. Therefore, large errors may appear in $B(\mathrm{GT})$ values obtained from CEX cross sections [5].

Recent experiments that study exclusive muon capture in sd-shell nuclei [6] make it possible to compare the characteristics of strong GT transitions measured in a weak interaction process with those obtained from CEX reactions. The energy released in nuclear muon capture is determined by the muon mass. Limitations on the transition energy that exist in beta decay are absent in muon capture. During muon capture, the nucleus acquires a nonzero linear momentum. Therefore, kinematics in muon capture differs from that in beta decay and zero-angle CEX reactions. For this reason, the matrix elements for the $0^+ \to 1^+$ transition obtained in muon capture cannot be compared directly with $B(\mathrm{GT})$ values extracted from (p,n) reactions. One is therefore forced to address a different problem, that of assessing the extent to which the wave functions of the isovector states will simultaneously describe the experimental $B(\mathrm{GT})$ values and the rates of ordinary muon capture (Λ_f).

2. RATE OF NUCLEAR MUON CAPTURE

Our calculations of exclusive-muon-capture rates are based on the approach described in [7]. If the matrix elements of the operator $\sum_{k=1}^{A} j_0(E_\nu r_k)\,\sigma_k\, t_k^+$ are dominant, the rates of the $0^+_{\mathrm{g.s.}} \to 1^+_f$ partial transitions are given by (only the final result is shown here)

$$\Lambda_f \approx \frac{2}{3} V g_A^2 [101]^2 \left\{ 1 + \frac{2}{3}\eta + \frac{8}{3}\frac{g_V + g_M}{g_A}\eta \right. \quad (2)$$
$$\left. -\frac{2}{3}\frac{g_P}{g_A}\eta + \frac{1}{3}\left(\frac{g_P}{g_A}\eta\right)^2 \right.$$

*This article was submitted by the authors in English.

[1)]Institute of Nuclear Physics, Moscow State University, Vorob'evy gory, Moscow, 119899 Russia.

[2)]Paul Scherrer Institut, CH-5232 Villigen PSI, Switzerland.

**e-mail: kuzmin@thsun1.jinr.ru

$$+\sqrt{\frac{8}{9}}\left[2\left(1+\frac{g_V+g_M}{g_A}-\frac{g_P}{g_A}\right)\eta+\left(\frac{g_P}{g_A}\right)^2\right]\frac{[121]}{[101]}$$
$$+2\left(1-\frac{g_P}{g_A}\right)\eta\frac{[111p]}{M[101]}-\sqrt{\frac{8}{9}}\,\frac{g_V}{g_A}\,\frac{[011p]}{M[101]}\Bigg\},$$

where $\eta=\dfrac{E_\nu}{2\,M_p}$ and the nuclear matrix elements are defined by

$$[101]=\sqrt{\frac{1}{4\pi}}\langle 1_f^+ \parallel \sum_{k=1}^{A}\varphi_\mu(r_k)\,j_0(E_\nu r_k)$$
$$\times\, Y_0(\hat{r}_k)\,\sigma_k\,t_k^+ \parallel 0^+_{\text{g.s.}}\rangle,$$

$$[121]=\sqrt{\frac{1}{4\pi}}\langle 1_f^+ \parallel \sum_{k=1}^{A}\varphi_\mu(r_k)\,j_2(E_\nu r_k)$$
$$\times\big[Y_2(\hat{r}_k)\otimes\sigma_k\big]_1\,t_k^+ \parallel 0^+_{\text{g.s.}}\rangle,$$

$$[111p]=\sqrt{\frac{1}{4\pi}}\langle 1_f^+ \parallel \sum_{k=1}^{A}\varphi_\mu(r_k)\,j_1(E_\nu r_k)$$
$$\times\big[Y_1(\hat{r}_k)\otimes\nabla_k\big]_1\,t_k^+ \parallel 0^+_{\text{g.s.}}\rangle,$$

$$[011p]=\sqrt{\frac{1}{12\pi}}\langle 1_f^+ \parallel \sum_{k=1}^{A}\varphi_\mu(r_k)\,j_1(E_\nu r_k)\,Y_1(\hat{r}_k)$$
$$\times\big(\boldsymbol{\nabla}_k,\boldsymbol{\sigma}_k\big)\,t_k^+ \parallel 0^+_{\text{g.s.}}\rangle.$$

Here, $\varphi_\mu(r)$ is the muon radial wave function. We approximate φ_μ, as one usually did for light and medium-mass nuclei, by the average value calculated in [8].

3. COMPARISON OF THE RESULTS OF CALCULATIONS WITH EXPERIMENTAL DATA

The calculations were performed on the basis of a many-particle shell model by using the Hamiltonian of Wildenthal [9] and an unrestricted sd-shell space. The computer code OXBASH [10] was employed in the calculations. Theoretical and experimental GT- and $M1$-strength functions are presented in the figure. The theoretical results obtained with the eigenfunctions of Wildenthal's Hamiltonian are labeled with (a). The quantities $B(\mathrm{GT})$ for the 1^+ states with excitation energies below 6 MeV are shown in the upper left part of the figure. The energies are measured from the ground state of ^{28}P. The experimental GT strength function was obtained from the cross sections for the reaction $^{28}\mathrm{Si}(p,n)^{28}\mathrm{P}$ [11]. All states whose excitation energy is below 5 MeV are shown in the figure. Only a small fraction of entire experimental GT strength goes to the states with higher excitation energies [11]. Additionally, the exact spins and parities of high-lying states have not yet been determined experimentally. For these two reasons, we neglect high-lying states that are not shown in the figure in the ensuing analysis. In the energy region up to 12.6 MeV, one observes an experimental $B(\mathrm{GT})$ strength of 2.595; the $B(\mathrm{GT})$ values summed over the states shown in the figure amount to 2.301. The theoretical $B(\mathrm{GT})$ values summed over the first ten eigenstates with J^π, $T=1^+,1$ (shown in the figure) give 3.492. Therefore, a rather standard value of GT quenching, $\dfrac{\sum B_{\text{expt}}(\mathrm{GT})}{\sum B_{\text{theor}}(\mathrm{GT})}=0.66$, is obtained from this comparison.

The figure also shows the theoretical and experimental $M1$ strength functions. It is known [12] that the shell model with the Hamiltonian from [9] faithfully reproduces the energies of 1^+ isovector states in ^{28}Si. However, the theoretical dependence of $B(M1)$ values on the excitation energy considerably differs from the experimental dependence obtained in [13]. The calculations were performed with a "free" value of g_s, and the summed theoretical $B(M1)$ is larger than the experimental one: $\dfrac{\sum B_{\text{expt}}(M1)}{\sum B_{\text{theor}}(M1)}=\dfrac{7.360}{8.623}=0.85$. Even in that case, however, the experimental $B(M1)$ value exceeds considerably the theoretical value for the strongest transition that goes to the 1^+ isovector state at 11.445 MeV (see figure).

Therefore, we can conclude that the shell model with the Hamiltonian from [9] describes qualitatively the main features of GT and $M1$ strength functions in the sense that small theoretical $B(\mathrm{GT})$ and $B(M1)$ values correspond to small experimental values. However, the theoretical distributions of the transition strength over the states that absorb the largest part of the total strength differ considerably from the experimental strength functions.

According to (2), the nuclear matrix element [101], having the σt^+ operator as the spin–angular part, contributes mainly to the rate of fast allowed muon capture. Therefore, the differences between the theoretical and experimental values of $B(\mathrm{GT})$ and $B(M1)$ led to the discrepancies between the theoretical and experimental values of Λ_f. The Λ_f values calculated with the eigenfunctions of the Wildenthal Hamiltonian are shown in the table (column a). Also, the values of $B(M1)$ and $B(\mathrm{GT})$ for the members of the same isotopic triplets are presented in the table, together with the corresponding experimental values. The only conclusion that one can draw from a comparison of experimental data with the results of calculation (a) is that the difficulties in the description

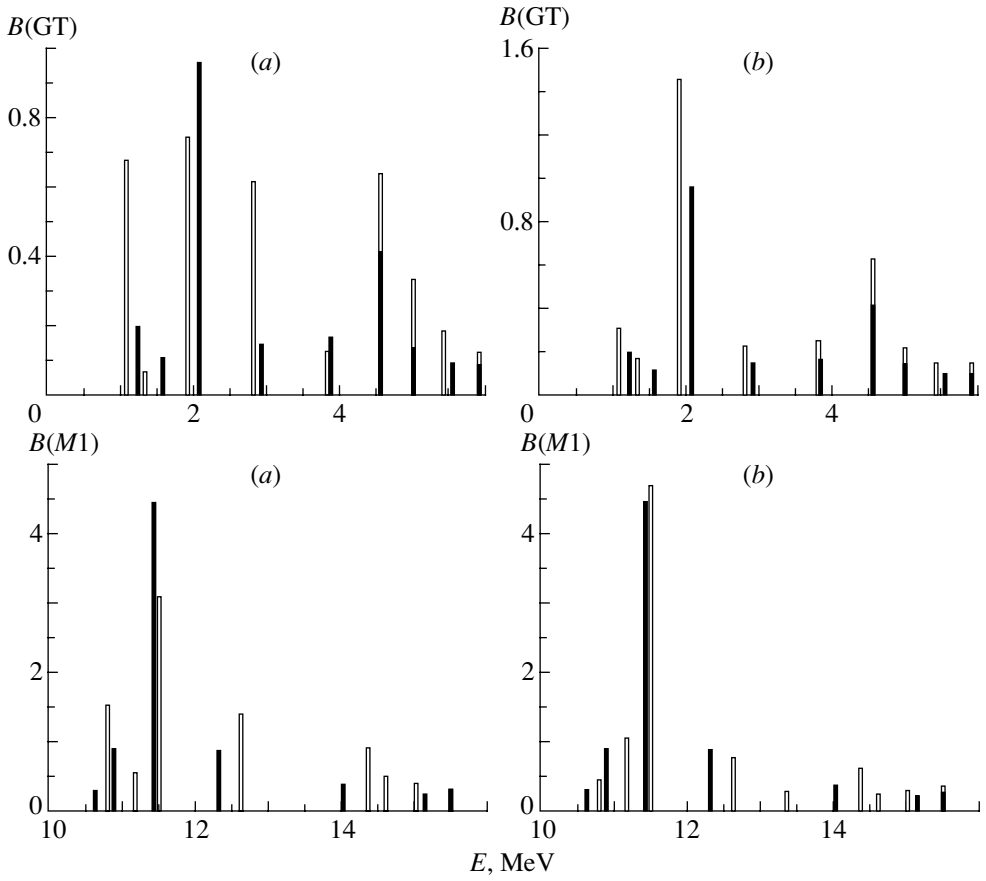

Fig. 1. Strength functions of GT and $M1$ transitions in ^{28}Si. Experimental data and the results of calculations are represented by, respectively, closed and open bars. The calculations have been performed (a) with the eigenfunctions of the Hamiltonian from [9] and (b) with transformed wave functions.

of GT and $M1$ transitions have a counterpart in the description of muon capture rates.

In this situation, it might be reasonable to use available experimental information about GT and $M1$ strength functions in the calculations of muon capture rates. For this purpose, an orthogonal transformation acting in the subspace spanned by the wave functions of the 1^+ isovector states was proposed in [14]. According to that study, the parameters of the transformation must be chosen in such a way that the GT and $M1$ strength functions calculated with transformed wave functions differ from the experimental GT and $M1$ strength functions only by a constant factor. Therefore, the transformation parameters do not depend on any relation between the experimental and theoretical values of the summed GT and $M1$ strengths and are determined only by the shapes of experimental GT and $M1$ strength functions. The orthogonality of the transformation will support the mutual orthogonality and normalization of the resulting wave functions. For the same reason, the theoretical total GT and $M1$ transition strengths will be conserved.

Isotopic invariance of strong interactions ensures that the transformation of the 1^+ isovector states in ^{28}P will induce the transformations of the $1^+, 1$ states in ^{28}Si and ^{28}Al. In addition, the transformation matrix will not depend on the value of the third component of the total isospin. Therefore, exactly the same transformation will be applied to the corresponding subspaces of the wave functions for ^{28}Si and ^{28}Al.

The next section describes how this transformation can be constructed.

4. TRANSFORMATION OF WAVE FUNCTIONS

The transformation of the wave functions for excited states,

$$\phi_k \to \psi_k = U_{k,k'}\,\phi_{k'} \qquad (k = 1, 2, \ldots, N),$$

causes a transformation of the transition matrix elements,

$$\langle \phi_k|\mathcal{O}|\Phi\rangle \to \langle \psi_k|\mathcal{O}|\Phi\rangle = U^*_{k,k'}\langle \phi_{k'}|\mathcal{O}|\Phi\rangle$$

$$= \langle \phi_{k'}|\mathcal{O}|\Phi\rangle\, U^\dagger_{k',k}.$$

Considering the transformation within the subspace of multiparticle wave functions as a transformation in a linear space of the vectors composed of the transition amplitudes, we simplify the determination of the transformation matrix.

An orthogonal $N \times N$ matrix is determined by $N(N-1)/2$ free parameters. To reduce the number of required parameters, one should use matrices of a less general structure. The simplest orthogonal transformation of a vector is its reflection with respect to a plane [15, 16],

$$v = v_{\|} + v_{\perp} \to v' = v_{\|} - v_{\perp}.$$

Here, the vector $v_{\|}$ is parallel to a plane, while $v_{\perp}$ is orthogonal to it. If the plane is determined by the equation $(b, x) = b_k x_k = 0$, where b is a nonzero vector, $(b, b) > 0$, then the transformation is given by [15, 16]

$$v_k \to v' = R(b)\, v \qquad (3)$$

$$\text{with} \quad R_{k,l}(b) = \delta_{k,l} - 2\,\frac{b_k b_l}{(b,b)}.$$

This equation also gives a solution to our problem: for any two vectors u and w of the same length, $|u| = |w|$, the matrix $R(b)$ with $b = u - w$ will transform u into w, and vice versa.

From the calculations within the shell model, we know the vector formed by the theoretical GT amplitudes. A second vector is assembled from the experimental amplitudes. After proper normalization, we can construct the matrix given by (3). However, we can get only the absolute values of the transition amplitudes from experimental data. Therefore, we are forced to consider all possible distributions of signs within the "experimental vector." Each distribution has its own reflection matrix that will transform the wave functions in such a way that the new theoretical GT strength function will coincide in shape with the experimental one. In order to select the best transformation, we consider the $M1$ strength function in ^{28}Si. Due to isotopic invariance, the 1^+ states in ^{28}Si and ^{28}P are transformed by the same matrix. Therefore, the theoretical $M1$ strength function will change too. The magnetic-dipole-transition operator differs from the GT transition operator, and the vectors constructed from the GT and $M1$ amplitudes will be linearly independent. Therefore, the transformed theoretical $M1$ strength function will have a shape differing from the experimental one. We use the transformation that leads to the smallest deviation of the theoretical from experimental $M1$ shapes.

Properties of spin–isospin transitions in $A = 28$ nuclei (references to experimental data and details of the calculations are given in the main body of the text)

E_f, MeV	Experiment	Calculations	
		(a)	(b)
Λ_f (in $10^3\,s^{-1}$) for ^{28}Si$(0^+_{g.s.})$ (μ,ν) ^{28}Al(1^+_f)			
1.62	12.9 ± 2.1	3.1	7.6 ± 0.2
2.20	62.8 ± 7.4	34.1	63.6 ± 2.4
3.11	14.7 ± 2.6	26.1	11.2 ± 0.5
$B_f(M1)$ (in μ_N) for ^{28}Si$(0^+_{g.s.})$ (e,e') ^{28}Si(1^+_f)			
10.90	0.90 ± 0.02	0.538	1.044
11.45	4.42 ± 0.20	3.064	4.461
12.33	0.87 ± 0.06	1.387	0.764
$B^-_f(GT)$ for ^{28}Si$(0^+_{g.s.})$ (p,n) ^{28}P(1^+_f)			
1.59	0.109 ± 0.002	0.069	0.165
2.10	0.956 ± 0.005	0.774	1.451
2.94	0.146 ± 0.003	0.613	0.222

5. CALCULATIONS WITH TRANSFORMED WAVE FUNCTIONS

The GT and $M1$ strength functions calculated with the transformed wave functions are presented in the right panels of the figure (*b*). The subspace where the transformation acts includes all states shown in the figure. The transformation causes a significant redistribution of transition strengths over the excitation energies. As a result, the shape of the GT strength function is exactly restored and the shape of the $M1$ strength function is approximately reproduced. The muon-capture rates calculated with the transformed wave functions are given in the table (column b). The new theoretical rates are very close to the experimental ones. The errors in Λ_f are the estimated uncertainties in the calculated rates as induced by the errors in the experimental values of B(GT) and $B(M1)$ used in constructing the transformation. It should be pointed out again that the experimental values of B(GT) and $B(M1)$ themselves have not been used in the transformation matrix; only the shapes of the experimental GT and $M1$ strength functions were important for the transformation. Moreover, no effective charges were introduced in the calculations. The B(GT) and $B(M1)$ values calculated with the transformed wave functions can be compared with the experimental values. The result is given in the table (column b).

The calculations for the strongest transitions with the transformed wave functions produce surprising

results: the theoretical ordinary-muon-capture rates are very close to the experimental values; the theoretical $B(M1)$ values are close to the experimental ones, but the theoretical $B(\mathrm{GT})$ values are 1.5 times greater than those extracted from the cross sections for the reaction $^{28}\mathrm{Si}(p,n)^{28}\mathrm{P}$. Due to the similarity of the spin–isospin parts of the operators describing CEX reactions, magnetic electron scattering, and muon capture, this disagreement could not have been expected.

6. CONCLUSION

We have constructed a set of wave functions for the excited 1^+ isovector states in $A = 28$ nuclei, starting from the wave functions calculated within a many-particle shell model, using the Hamiltonian from [9], and introducing phenomenological corrections by means of an orthogonal transformation in a subspace of shell-model wave functions. Some characteristics of spin–isospin transitions have then been calculated with the new wave functions. The calculations have been performed without introducing any effective charges. From a comparison of the theoretical results with experimental data, the following has been deduced for the strongest $0^+ \to 1^+$ isovector transitions:

(i) The theoretical ordinary-muon-capture rates are very close to the relevant experimental values.

(ii) The theoretical $B(M1)$ values are close to the experimental ones.

(iii) The theoretical $B(\mathrm{GT})$ values are 1.5 times greater than those extracted from the cross sections for the reaction $^{28}\mathrm{Si}(p,n)^{28}\mathrm{P}$. This disagreement is unexpected mainly because of the similarity of the spin–isospin parts of the operators describing CEX reactions, magnetic electron scattering, and muon capture.

We have shown that experimental data on partial muon-capture rates can be used to obtain important spectroscopic information, because fast spin-flip transitions were observed and because the rates of weak-interaction processes were measured for such fast transitions.

In contrast to the generally accepted opinion, the relation between cross sections for CEX reactions and $B(\mathrm{GT})$ can be quite complicated even for strong GT transitions. It seems necessary to find how spin-quadrupole transitions and two-step processes can contribute to cross sections for CEX reactions even for strong GT transitions.

REFERENCES

1. F. Osterfeld, Rev. Mod. Phys. **64**, 491 (1992).
2. W. P. Alford and B. M. Spicer, Adv. Nucl. Phys. **24**, 2 (1998).
3. C. D. Goodman *et al.,* Phys. Rev. Lett. **44**, 1755 (1980).
4. T. N. Taddeucci *et al.,* Nucl. Phys. A **469**, 125 (1987); E. G. Adelberger *et al.,* Phys. Rev. Lett. **67**, 3658 (1991).
5. S. M. Austin, N. Anantaraman, and W. G. Love, Phys. Rev. Lett. **73**, 30 (1994).
6. T. P. Gorringe *et al.,* Phys. Rev. C **60**, 055501 (1999).
7. V. V. Balashov and R. A. Eramzhyan, At. Energy Rev. (Vienna) **5**, 3 (1967).
8. K. W. Ford and J. G. Wills, Nucl. Phys. **35**, 295 (1962).
9. B. H. Wildenthal, Prog. Part. Nucl. Phys. **11**, 5 (1984).
10. B. A. Brown, A. Etchegoyen, and W. D. M. Rae, OXBASH, Report No. 524, MSU Cyclotron Laboratory (Michigan, 1986).
11. B. D. Anderson *et al.,* Phys. Rev. C **43**, 50 (1991); P. von Neumann-Cosel *et al.,* Phys. Rev. C **55**, 532 (1997).
12. P. M. Endt and J. G. L. Booten, Nucl. Phys. A **555**, 499 (1993).
13. C. Lüttge *et al.,* Phys. Rev. C **53**, 127 (1996); Y. Fujita *et al.,* Phys. Rev. C **55**, 1137 (1997).
14. V. A. Kuz'min and T. V. Tetereva, Phys. At. Nucl. **63**, 1874 (2000).
15. E. Cartan, *Leçons sur la theórie des spineurs* (Actualités Scientifiques et Industrielles, Paris, 1938).
16. A. S. Householder, *The Theory of Matrices in Numerical Analysis* (Blaisdel, New York, 1964).

Physics of Atomic Nuclei, Vol. 64, No. 7, 2001, pp. 1174–1180. From Yadernaya Fizika, Vol. 64, No. 7, 2001, pp. 1251–1257.

Proceedings of the International Conference "Nuclear Structure and Related Topics"

Structure of Nuclear Multipole Resonances as a Function of Momentum Transfer*

N. G. Goncharova** **and A. A. Dzhioev**

Institute of Nuclear Physics, Moscow State University, Vorob'evy gory, Moscow, 119899 Russia

Received October 25, 2000

Abstract—The momentum-transfer dependence of transverse and longitudinal isovector form factors is studied for the electroexcitation of *sd*-shell self-conjugate nuclei. The effect of the interference between the orbital and spin components of the intranuclear current on the behavior of transverse form factors is traced. The results of the particle–core version of the shell model are compared with experimental data on $E1$ and $M6$ multipole resonances. © *2001 MAIK "Nauka/Interperiodica".*

1. INTRODUCTION

Multipole resonances in reaction cross sections provide the main piece of information about the modes of nuclear response to an excitation. The possibility of varying the momentum transfer to a nucleus in inelastic-electron-scattering reactions opens broad vistas in studying nuclear excitations. The structure of the electroexcitation cross section changes drastically as the momentum transfer q becomes higher. The behavior of transverse multipole resonances in nuclear cross sections versus momentum transfer is determined primarily by the interplay of the orbital and spin nucleon currents. The relative contribution of the spin components grows with momentum transfer and with the multipolarity of multipole resonances.

Nuclear theory must give an adequate interpretation of data obtained in (e, e') reactions in a wide range of momentum transfers. There is a very well established fact that the higher the momentum transfer, the higher the multipolarity of the multipole resonances dominating electroexcitation; in addition, the cross section is strongly affected by individual properties of the target nucleus. Special features of nuclear structure are most clearly revealed in reactions on light nuclei. The excitation spectra of light nuclei give a clear manifestation of the properties of single-particle transitions contributing to multipole resonances, while the spectra of heavier nuclei are usually governed by collective effects.

The objective of this study is to analyze the transverse and longitudinal isovector form factors for 1-$\hbar\omega$ transitions in self-conjugate *sd*-shell nuclei (^{28}Si, ^{32}S, and ^{40}Ca) within the particle–core-coupling (PCC) version of the shell model. The role of the interference between the orbital and spin components of the intranuclear current in the transverse form factors at various momentum transfers will also be considered.

2. FORM FACTORS FOR THE ELECTROEXCITATION OF *sd*-SHELL NUCLEI

For the inclusive cross sections of electron scattering on a nucleus, the entire body of information about the nuclear structure is concentrated in the longitudinal (Coulomb) and transverse form factors F_L^2 and F_T^2 [1],

$$\frac{d\sigma}{d\Omega} = \frac{4\pi\sigma_{\rm M}}{\eta_R} \times \left[F_L^2(q,\omega) + \left(\frac{1}{2} + \tan^2\frac{\Theta}{2}\right) F_T^2(q,\omega)\right]. \quad (1)$$

Here, Θ is the electron-scattering angle, $\sigma_{\rm M}$ is the Mott cross section for electron scattering on a structureless charge, and η_R is the recoil factor. The longitudinal form factor F_L^2 can be represented as the sum of multipole form factors F_{CJ}^2 related to the charge density through the matrix elements of the multipole operator $\hat{M}_J^{\rm Coul}$. The transverse form factor F_L^2 can be represented as the sum of electric (F_{EJ}^2) and magnetic (F_{MJ}^2) multipole form factors related to the nuclear current density through the matrix elements of the multipole operators $\hat{T}_J^{\rm el}$ and $\hat{T}_J^{\rm mag}$, respectively,

$$F_L^2 = \sum_{J=0}^{\infty} F_{CJ}^2 = (2J_i+1)^{-1} \sum_{J=0}^{\infty} \left|\langle J_f \| \hat{M}_J^{\rm Coul} \| J_i\rangle\right|^2, \quad (2)$$

*This article was submitted by the authors in English.

**e-mail: ngg@srdlan.npi.msu.su

1063-7788/01/6407-1174$21.00

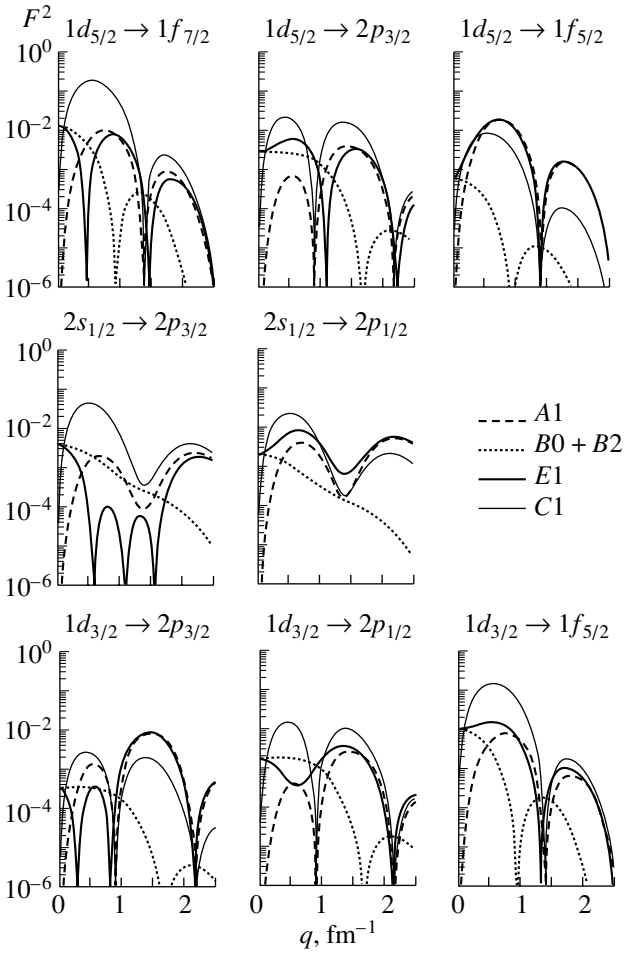

Fig. 1. Squared transverse $[F^2_{E1}(q)]$ and longitudinal $[F^2_{C1}(q)]$ form factors for single-particle isovector $E1$ transitions.

$$F_T^2 = \sum_{J=1}^{\infty} \left\{ F_{EJ}^2 + F_{MJ}^2 \right\} \tag{3}$$
$$= (2J_i+1)^{-1} \times \sum_{J=1}^{\infty} \left\{ \left| \langle J_f \| \hat{T}_J^{\rm el} \| J_i \rangle \right|^2 + \left| \langle J_f \| \hat{T}_J^{\rm mag} \| J_i \rangle \right|^2 \right\},$$

$$\hat{M}_J^{\rm Coul} = \sum_{j=1}^{A} \hat{e}_j j_J(qr_j) Y_J(\Omega_j), \tag{4}$$

$$\hat{T}_J^{\rm el} = \frac{q}{2M} \sum_{j=1}^{A} \left\{ \hat{\mu}_j j_J(qr_j) [Y_J \times \bar{\sigma}_j]^J \right. \tag{5}$$
$$+ \frac{2\hat{e}_j}{q} \left(\sqrt{\frac{J+1}{2J+1}} j_{J-1}(qr_j) [Y_{J-1}(\Omega_j) \times \bar{\nabla}_j]^J \right.$$
$$\left. \left. - \sqrt{\frac{J+1}{2J+1}} j_{J+1}(qr_j) [Y_{J+1}(\Omega_j) \times \bar{\nabla}_J]^J \right) \right\},$$

$$\hat{T}_J^{\rm mag} = \frac{iq}{2M} \tag{6}$$
$$\times \sum_{j=1}^{A} \left\{ \hat{\mu}_j \left(\sqrt{\frac{J+1}{2J+1}} j_{J-1}(qr_j) [Y_{J-1}(\Omega_j) \times \bar{\sigma}_j]^J \right. \right.$$
$$\left. - \sqrt{\frac{J}{2J+1}} j_{J+1}(qr_j) [Y_{J+1}(\Omega_j) \times \bar{\sigma}_j]^J \right)$$
$$\left. - \frac{2\hat{e}_j}{q} j_J(qr_j) [Y_{J+1}(\Omega_j) \times \bar{\nabla}_J]^J \right\}.$$

All transverse multipole form factors for the electroexcitation of sd-shell nuclei, except for $M6$ excitation, contain contributions from both the spin and the orbital currents.

Analysis of the contribution from the spin and orbital components of the nucleon current to the sd-shell nuclei is based on studying the single-particle form-factor structure of $1\text{-}\hbar\omega$ transitions forming multipole resonances. The behavior of the squared transverse and longitudinal form factors for single-particle isovector $E1$ transitions is shown in Fig. 1. The contributions to the transverse form factors from the spin and orbital components of nucleon current are represented in Fig. 1 by the dashed and the dotted curves, respectively. The matrix elements for single-particle transitions were calculated by using the harmonic-oscillator wave functions.

The most significant feature of this set of pictures is the behavior of the dipole transverse form factor for the $1d_{5/2} \to 1f_{7/2}$ transition. Because of the destructive interference between the orbital and spin components of the nucleon current, the transverse form factor goes through zero at a momentum transfer of about 0.5 fm^{-1}. At this q value, the longitudinal form factor of the same single-particle transition is close to a maximum. Analysis of transverse and longitudinal form factors for $1l_{j=l+1/2} \to 1(l+1)_{j=l+3/2}$ single-particle transitions revealed that this effect is universal and follows from the expressions

$$F_{EJ}(y) = K(J,l) \exp(-y) \tag{7}$$
$$\times \left[\mu_T y^{\frac{J+1}{2}} F(-l + \frac{J-1}{2}; \frac{2J+3}{2}; y) \right.$$
$$\left. - e_T \frac{d}{dy} y^{\frac{J+1}{2}} F(-l + \frac{J-1}{2}; \frac{2J+3}{2}; y) \right],$$

$$F_{CJ}(y) = D(J,l) \exp(-y) e_T y^{J/2} \tag{8}$$
$$\times F(-l + \frac{J-1}{2}; \frac{2J+3}{2}; y),$$

which describe form factors for all EJ transitions.

On the contrary, the q dependences of transverse and longitudinal form factors are similar for all EJ $1l_{j=l+1/2} \to 1(l+1)_{j=l+1/2}$ transitions.

Analysis of the form-factor behavior for single-particle $C1$ and $E1$ transitions (Fig. 1) shows that the ratio F^2_{C1}/F^2_{E1} for individual resonances is sensitive to the details of the configuration structure of dipole-excitation wave functions. Therefore, a comparison of the q dependences of the longitudinal and transverse form factors at $q < 1.0$ fm^{-1} can help to identify the quantum numbers of the transition dominating the multipole-resonance wave function.

The interference between the orbital and spin currents is also revealed in the minimum of the $E3$ form factors for the $1d_{5/2} \to 1f_{7/2}$ transitions at $q \approx 0.75$ fm^{-1} and, owing to the appearance of this nondiffraction minimum, in the small values of the transverse $E3$ form factors compared to the longitudinal $C3$ ones for all excited states where this transition is dominant. For all other octupole transitions from $1d$ subshells, the contribution of the orbital current to $E3$ excitations is small and the structure of the transverse form factors is determined exclusively by the contribution of the spin current. In this case, the $E3$ and $C3$ form factors exhibit similar q dependences. The contributions of the orbital currents to $E3$ transitions from the $2s$ subshell are completely absent [2].

The contribution of the orbital current to the $E5$ form factors is very small for all transitions from sd shell, and the $E5$ and $C5$ form factors behave similarly.

For $M2$ resonances in sd shell nuclei, the interplay of orbital and spin currents is revealed most significantly in the $1d_{3/2} \to 1f_{5/2}$ and $1d_{3/2} \to 2p_{1/2}$ transitions leading to small values of the corresponding $M2$ form factors at low q. For other $M2$ form factors, the contribution of the orbital current is rather small; it is manifested only in a small shift of the position of the diffraction minimum.

The contribution of the orbital current to the $M4$ form factors is negligible for all transitions. The $M6$ resonances in the sd shell are generated exclusively by the contribution of the spin current.

3. MULTIPOLE RESONANCES IN sd-SHELL NUCLEI IN PARTICLE–CORE-COUPLING APPROACH

In the PCC version of the shell model, the wave functions of excited nuclear states are expanded in a set of low-lying states of residual $(A-1)$ nuclei coupled to a nucleon in a free orbit [3],

$$|J_f T_f\rangle = \sum \alpha_f |(J'T'E')_{A-1} \times (n'l'j') : J_f T_f\rangle. \quad (9)$$

The PCC approach takes into account the fragmentation of hole configurations among the states of residual nuclei. This version of the shell model also naturally restricts the full 1-$\hbar\omega$ basis by including only core states with a nonvanishing coefficient of fractional parentage connected with the ground state of a target nucleus A,

$$|J_i T_i\rangle = \sum_{j,J'E'T'} C_j^{J'E'T'} |(J'E'T')_{A-1} \times (nlj) : J_i T_i\rangle. \quad (10)$$

Spectroscopic factors for ^{28}Si, ^{32}S, and ^{40}Ca

E', MeV	J^π	S_j
	^{28}Si	
0	$5/2^+$	3.4
0.84	$1/2^+$	0.8
1.01	$3/2^+$	0.5
2.73	$5/2^+$	0.41
2.98	$3/2^+$	0.5
3.68	$1/2^+$	0.06
4.05	$1/2^-$	1.5
4.41	$5/2^+$	0.29
	^{32}S	
0	$1/2^+$	0.93
1.27	$3/2^+$	0.98
2.23	$5/2^+$	1.84
3.13	$1/2^+$	0.11
3.30	$5/2^+$	0.67
4.19	$5/2^+$	0.65
4.78	$5/2^+$	0.20
5.26	$1/2^+$	0.10
5.89	$5/2^+$	0.15
6.33	$1/2^+$	0.11
7.16	$5/2^+$	0.79
7.98	$1/2^-$	0.82
	^{40}Ca	
0	$3/2^+$	3.7
2.52	$1/2^+$	1.65
2.81	$7/2^-$	0.6
4.10	$1/2^+$	0.1
5.26	$5/2^+$	0.9
5.60	$5/2^+$	0.65
6.36	$5/2^+$	1.25
7.43	$5/2^+$	0.47

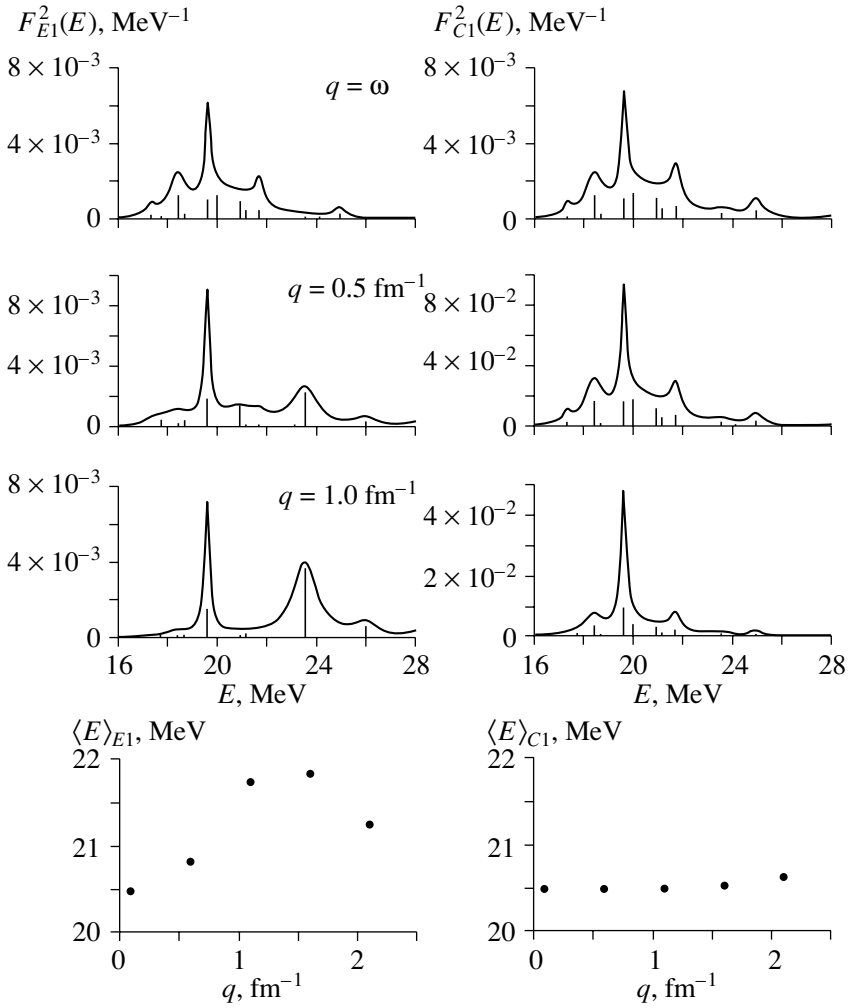

Fig. 2. Isovector dipole form factors and mean energies of $E1$ and $C1$ resonances for ^{28}Si.

For self-conjugate nuclei discussed in this study—^{28}Si, ^{32}S, and ^{40}Ca—the basis for excited states was constructed in terms of all states of $A-1$ nuclei with nonzero spectroscopic factors of direct pickup reactions listed in the table [4–6]. Without violating the Pauli exclusion principle, the PCC basis can easily be extended to include the doorway configuration coupled to the collective excitation of the target nucleus.

In the following parts of this article, we will discuss the $E1$ and $M6$ resonances in the electroexcitation of self-conjugate sd-shell nuclei. The structure of dipole resonances at various momentum transfers is strongly influenced by the interplay of the orbital and spin currents. Hole fragmentation over the states of residual nuclei plays an important role in the dipole-resonance structure, but its effect is partly overshadowed by the influence of configuration mixing and interference of current components. The structure of $M6$ resonances reveals the hole fragmentation most clearly, since its wave function consists of the configuration $|(5/2^+, E', 1/2) \times (1f_{7/2}) : 6\ 1\rangle$, and $M6$ excitations are created exclusively by the spin-current operator.

4. DIPOLE RESONANCES IN THE ELECTROEXCITATION OF sd-SHELL SELF-CONJUGATE NUCLEI

The results of the PCC calculation of isovector dipole form factors for ^{28}Si, ^{32}S, and ^{40}Ca nuclei are shown in Figs. 2, 3, and 4 for three values of the momentum transfer. These pictures also show the dependences of the mean energies for $C1$ and $E1$ (transverse) dipole resonances in these three nuclei.

At $q = \omega$ (photon point), the pictures of electroexcitation are very close to the cross sections for photonuclear reactions [7–9], and the $E1$ and $C1$ form factors behave similarly. At low momentum transfers,

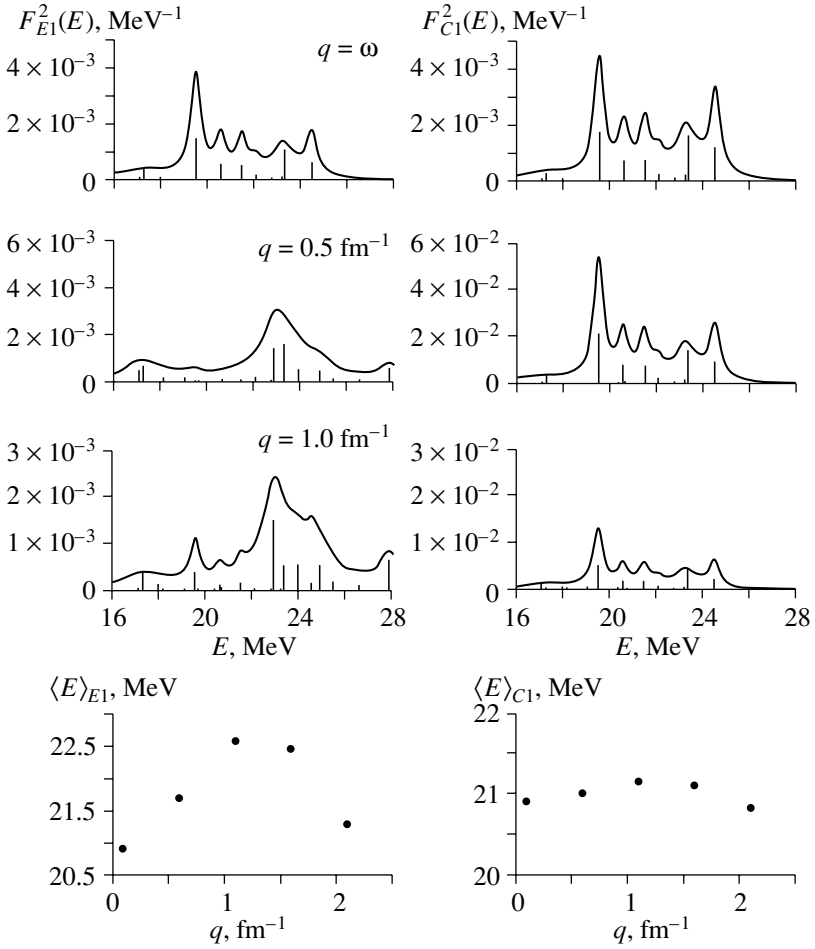

Fig. 3. Isovector dipole form factors and mean energies of $E1$ and $C1$ resonances for ^{32}S.

the $E1$ distribution is dominated by the giant-dipole-resonance bump, which is formed by the orbital component of the nucleon current. At a momentum transfer of about 0.5 fm^{-1}, similarity of the $C1$ and $E1$ form factors disappears for all nuclei. The dipole "photonuclear" peak in ^{28}Si is formed by transitions not only from the $1d_{5/2}$ subshell but also from the $1p$ shell. The transverse form factor for ^{32}S undergoes the most significant changes, because the main peak of the $E1$ resonance near 19 MeV receives the main contribution from the $|(5/2^+, 2.2\ \text{MeV}, 1/2) \times (1f_{7/2}) : 1\ 1\rangle$ configuration. The destructive interference between the nucleon components of the current is responsible for the vanishing of the transverse $E1$ strength at $E < 22$ MeV. Similar configurations in ^{40}Ca are embedded in the resonances occurring at 22–24 MeV. The $1d_{5/2} \to 1f_{5/2}$ spin-flip transitions are responsible for dipole excitations above 23 MeV in ^{28}Si and ^{32}S and above 25 MeV in ^{40}Ca. Their contributions to transverse form factors grow with q in the range 0.5–1.0 fm^{-1} and cause a shift of the mean energies of $E1$ resonances shown in the figures.

5. STRETCHED-STATE DISTRIBUTIONS IN ^{28}Si, ^{32}S, AND ^{40}Ca NUCLEI

In the last decade, special attention has been given to stretched states (or maximum-spin states) in nuclei because of their unique features: (1) only the spin component of the nucleon current is responsible for the excitation of these transitions; (2) on the level of a doorway excitation, stretched states in self-conjugate nuclei consist of a unique particle–hole configuration coupled to the maximum angular momentum allowable in the $1\hbar\omega$ basis; and (3) a comparative analysis of the excitation of stretched states with various test particles makes it possible to separate nuclear-structure effects from the dynamics of interaction between a test particle and a target nucleus.

Owing to the simplicity of the structure, stretched states can be used to test nuclear models. The $M6$ form factors in sd-shell nuclei have been investigated

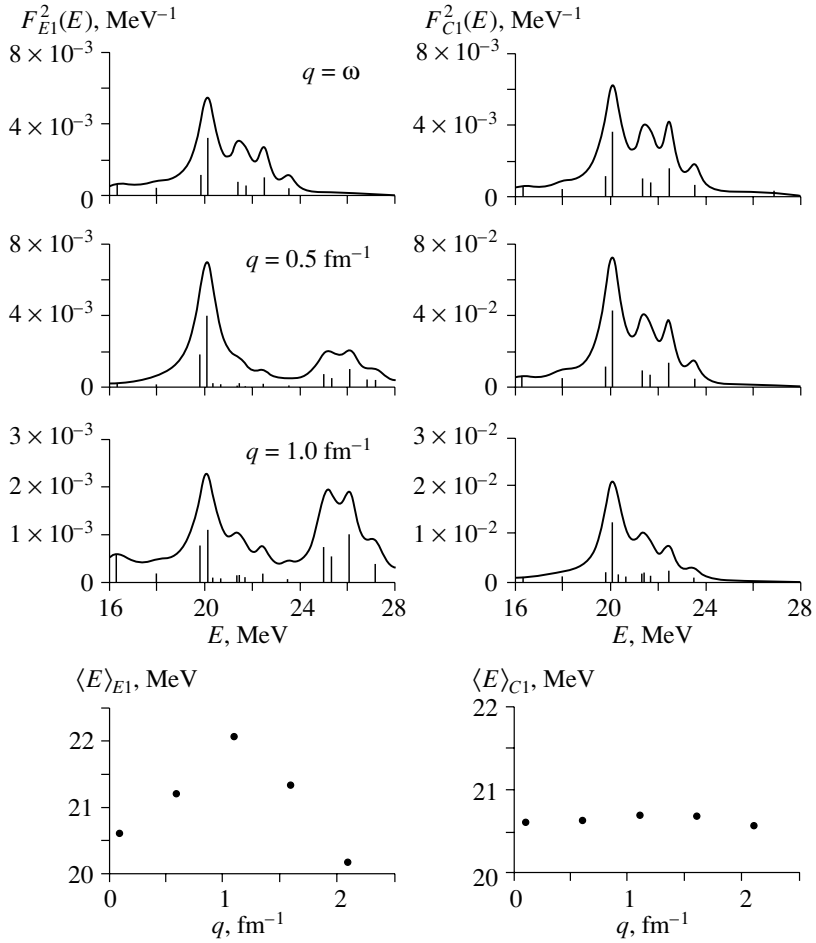

Fig. 4. Isovector dipole form factors and mean energies of $E1$ and $C1$ resonances for ^{40}Ca.

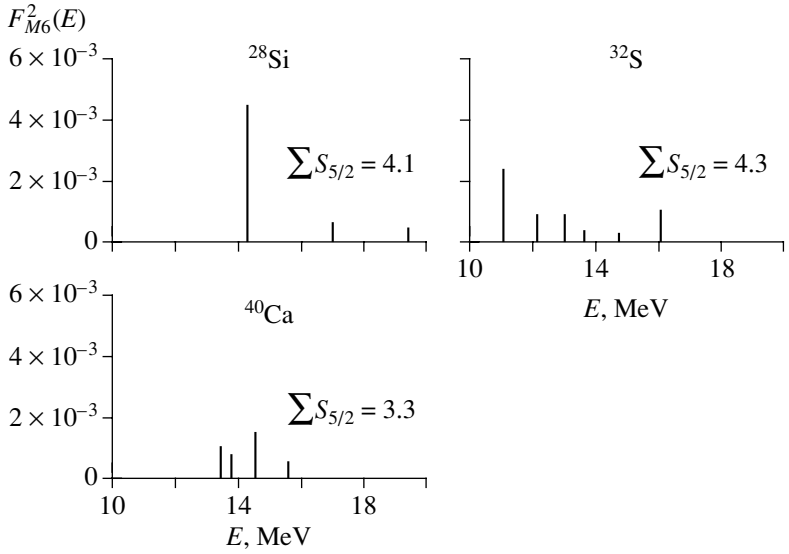

Fig. 5. Energy distributions of $M6$ resonances for ^{28}Si, ^{32}S, and ^{40}Ca.

by using various test particles. Experimental data for ^{28}Si show the main part of the entire observable stretched isovector strength found in a single peak [10]. In contrast to this result, the $M6$ distribution in ^{32}S is strongly fragmented [11]. So far, no $M6$ peaks have been observed in the electroexcitation of

the ^{40}Ca nucleus. From the point of view of the PCC shell-model approach, the distribution of the $M6$ strength in all these nuclei is strongly affected by the fragmentation of hole configurations among the states of residual nuclei. The results of the PCC calculations for the $M6$ form factors are shown in Fig. 5, together with the summed spectroscopic factors for these resonances. The energy distributions of the $M6$ strength for ^{28}Si and ^{32}S are close to the experimental distributions. According to the PCC model, the $M6$ state in ^{40}Ca has a smaller strength in relation to those in ^{28}Si and ^{32}S and is rather strongly fragmented.

6. CONCLUSIONS

(i) The destructive interference between the orbital and spin components of the nucleon current leads to the appearance of zeros of a nondiffractive origin in the transverse form factors for some single-particle 1-$\hbar\omega$ transitions. For all $1l_{j=l+1/2} \to 1(l+1)_{j=l+3/2}$ 1-$\hbar\omega$ electric transitions, the zeros of the transverse form factors F_{EJ} are close, on the q axis, to the positions of the maxima of the longitudinal form factor F_{CJ}. For all $1l_{j=l+1/2} \to 1(l+1)_{j=l+1/2}$ 1-$\hbar\omega$ electric transitions, the transverse (F_{EJ}) and longitudinal (F_{CJ}) form factors exhibit similar momentum-transfer dependences. A comparison of the q dependences of the longitudinal and transverse form factors for an electric resonance could be used to identify the wave-function configuration structure.

(ii) Multipole resonances in the electroexcitation of ^{28}Si, ^{32}S, and ^{40}Ca have been described on the basis of the PCC version of the shell model by taking into account experimental data on direct pickup reactions. The results on the energy dependence of $E1$ strengths at low momentum transfers for all these nuclei are close to photonuclear-cross-section data. Analysis of transverse ($E1$) and longitudinal ($C1$) form factors for all these nuclei has revealed that, because of the orbital and spin components of the nucleon current in the transverse form factor, the $E1$ and $C1$ energy distributions cease to be similar at $q = 0.5$ fm^{-1}. The mean energies of multipole resonances in backward electron scattering would shift upward as q grows from the photon point up to 1 fm^{-1}.

(iii) Experimental data on $M6$ strength distributions in the (e, e') cross sections for the ^{28}Si and ^{32}S nuclei agree well with the results of the calculations based on the PCC version of the shell model. The deviation of the ground states of the sd-shell self-conjugate nuclei ^{28}Si, ^{32}S, and ^{40}Ca from the closed subshell is the main origin of the observed fragmentation of the multipole strength.

REFERENCES

1. T. W. Donnelly and J. D. Walecka, Annu. Rev. Nucl. Sci. **225**, 329 (1975).
2. N. G. Goncharova and A. A. Dzhioev, Vestn. Mosk. Univ., Ser. 3: Fiz., Astron., No. 5, 30 (1997).
3. N. G. Goncharova and N. P. Yudin, Phys. Lett. B **29B**, 272 (1969).
4. H. Mackh, G. Mairle, *et al.,* Z. Phys. A **269**, 353 (1974).
5. J. Vernotte, G. Berrier-Ronsin, *et al.,* Nucl. Phys. A **655**, 415 (1999).
6. K. Doll *et al.,* Nucl. Phys. A **263**, 210 (1976).
7. R. E. Pywell *et al.,* Phys. Rev. C **27**, 960 (1983).
8. V. V. Varlamov, B. S. Ishkhanov, *et al.,* Izv. Akad. Nauk SSSR, Ser. Fiz. **43**, 186 (1979).
9. A. Veyssiere *et al.,* Nucl. Phys. A **227**, 513 (1974).
10. S. Yen, T. E. Drake, *et al.,* Phys. Lett. B **289**, 22 (1992).
11. B. L. Clausen, R. A. Lindgren, *et al.,* Phys. Rev. Lett. **65**, 547 (1990).

Physics of Atomic Nuclei, Vol. 64, No. 7, 2001, pp. 1181–1185. From Yadernaya Fizika, Vol. 64, No. 7, 2001, pp. 1258–1262.

Proceedings of the International Conference "Nuclear Structure and Related Topics"

Measurement of the g Factors of Isomers Near the Proposed $N \approx 40$ Subshell Closure*

G. Georgiev[**], **D. L. Balabanski**[1),2)], **C. Bingham**[1)], **C. Borcea**[3)], **N. Coulier**, **R. Coussement**, **J. M. Daugas**[4)], **G. Defrance**[4)], **F. de Oliveira Santos**[4)], **G. Goldring**[5)], **M. Górska**[6)], **H. Grawe**[6)], **R. Grzywacz**[1),7)], **M. Hass**[5)], **C. O'Leary**[8)], **M. Lewitowicz**[4)], **H. Mach**[9)], **I. Macovei**[3),4)], **R. Page**[8)], **M. Pfützner**[7)], **Yu. E. Penionzkevich**[10)], **Zs. Podolyák**[11)], **P. H. Regan**[11)], **K. Rykaczewski**[12)], **M. Sawicka**[7)], **N. A. Smirnova**[4)], **Yu. G. Sobolev**[10)], **M. Stanoiu**[3),4)], **S. Teughels**, **K. Vyvey**, and **G. Neyens**[4)]

University of Leuven, Belgium

Received October 25, 2000

Abstract—We report results from a pioneering experiment to measure the g factors of isomeric states of neutron-rich nuclei around ^{68}Ni, far from the valley of β stability. For the first time, the time-dependent perturbed angular distribution method was applied in combination with the heavy-ion–γ correlation technique to study g factors of spin-aligned isomers produced in a projectile fragmentation reaction and mass-separated. Some technical aspects are discussed and illustrated with preliminary results. © *2001 MAIK "Nauka/Interperiodica".*

1. INTRODUCTION

Nuclear magnetic moments are very sensitive probes of the intrinsic structure and especially of the single-particle nature of nuclear states. Measurements of nuclear magnetic moments can also serve as a stringent test for the spin and parity assignments of nuclear states, especially in regions where they are based on systematics and comparison with theoretical predictions.

The nuclear shell model describes well the properties of nuclei close to the β-stability line. Some recent experiments on nuclei far from stability [1–3] have shown evidence for disappearance of the shell closures. Another interesting phenomenon is the appearance of new shell closures. Indications for the presence of a new subshell closure in the vicinity of ^{68}Ni were given by the observation of a relatively high excitation energy of the first 2^+ state and the identification of a 5^- isomer by Broda *et al.* [4]. Many yrast isomers in neighboring nuclei have been identified. Their structure is explained as particle–hole excitations from the νfp shell into the $\nu 1g_{9/2}$ orbit [4–7] across the subshell gap. On the other hand, the two-neutron separation energies S_{2n} for the Ni isotopes [8] do not provide evidence for subshell closure. Relativistic mean field theory [9] predicts the appearance of a subshell closure at $N = 40$. Measurements of the g factors of the isomeric states in the vicinity of ^{68}Ni can shed more light over the nuclear structure in the region and test the presence of a subshell closure at $N = 40$. In the current work, we report a measurement of several g factors of isomeric states in the region of ^{68}Ni.

2. EXPERIMENTAL METHOD

The experimental method which we used is the Time-Dependent Perturbed Angular Distribution (TDPAD) [10] method in combination with ion–γ correlations. So far the TDPAD method was applied to nuclei produced in a fusion-evaporation

*This article was submitted by the authors in English.

[1)]University of Tennessee, Knoxville, USA.
[2)]Faculty of Physics, St. Kliment Ohridski University of Sofia, Bulgaria.
[3)]IFIN, Bucharest, Romania.
[4)]GANIL, Caen, France.
[5)]The Weizmann Institute, Rehovot, Israel.
[6)]GSI, Darmstadt, Germany.
[7)]IEP, Warsaw University, Poland.
[8)]University of Liverpool, UK.
[9)]Uppsala University, Studsvik, Sweden.
[10)]Flerov Laboratory for Nuclear Reactions, JINR, Dubna, Russia.
[11)]University of Surrey, Guilford, UK.
[12)]Oak Ridge National Laboratory, Physics Division, USA.
[**]e-mail: Georgi.Georgiev@fys.kuleuven.ac.be

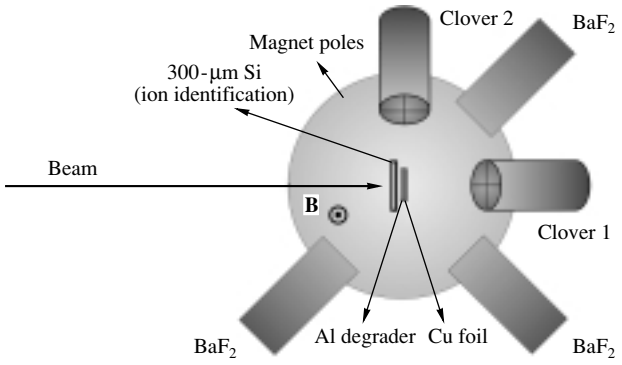

Fig. 1. Schematic drawing of the experimental setup used for the g-factor measurement at GANIL (top view).

reaction, where a high amount of spin orientation is obtained. Such a type of reaction is not applicable for production of very neutron-rich nuclei for which one is forced to other production mechanisms like projectile fragmentation. Schmidt-Ott *et al.* [11] have proven that a spin-aligned ensemble of isomeric states can be obtained in a projectile-fragmentation reaction as well. We applied the TDPAD for the first time to measure g factors of nuclei produced in a projectile-fragmentation reaction and separated via in-flight mass separation.

Following the fragmentation process, the spin-aligned ensemble is obtained with its symmetry axis parallel to the primary beam. During the passage of the ensemble through the spectrometer, the nuclear spins interact with the magnetic field of the dipole magnets, which causes a Larmor precession of the spin orientation. Finally, at the exit of the spectrometer, the spin-orientation axis is deflected at an angle α with respect to the beam axis [12]:

$$\alpha = \theta_C \left(1 - \frac{gA\mu_N}{Z\hbar}\right), \qquad (1)$$

where θ_C is the rotation angle in the spectrometer (90° in this case), g is the isomeric g factor, A is the mass of the implanted ion, and Z is charge.

In a TDPAD experiment, the spin-oriented ensemble of nuclei is immersed in a magnetic field **B** with a direction perpendicular to the spin-orientation axis. This causes a Larmor precession of the nuclear spins around **B**, with a frequency $\omega_{\rm L} = -\dfrac{g\mu_N B}{\hbar}$ which depends directly on the g factor of the nuclear state of interest. The precession of the nuclear spins is monitored via measurement of the γ asymmetry as a function of time. For this reason, γ-ray detectors are positioned at 90° with respect to each other in a plane perpendicular to the magnetic field. A signature of the precession pattern is the $R(t)$ function [10, 13]:

$$R(t) = \frac{I_1(\theta,t) - \epsilon I_2(\theta+\frac{\pi}{2},t)}{I_1(\theta,t) + \epsilon I_2(\theta+\frac{\pi}{2},t)} \qquad (2)$$
$$\sim A_2 B_2^0(t=0)\cos(2(\omega_{\rm L}t + \alpha - \theta)),$$

where ϵ is the relative efficiency between both detectors, A_2 is the radiation parameter of the γ transition, B_2^0 is the orientation of the isomeric state at the moment of implantation, θ is the angle between the beam axis and the first γ detector, and α is the angle between the beam axis and the symmetry axis of the spin-oriented ensemble. Note that both the frequency $\omega_{\rm L}$ and the phase α (1) depend on the g factor and we used this dependence to fit the data.

In order to perform a TDPAD measurement, one needs to preserve the spin orientation after the implantation of the nuclei till the moment of their radioactive decay. For this reason, we choose a high-purity Cu foil as a stopper. Copper has a cubic crystal-lattice structure that is free of perturbation, and the nuclei which we investigated (Cu, Ni, and Co) are expected to take a substitutional [14] site as they have the same electronegativity and very similar atomic radius as Cu.

In our experiment, the isomers of interest were produced via the fragmentation of a ^{76}Ge, 61.4 MeV/u beam onto a 145 mg/cm^2 ^{9}Be target which was mounted on the rotating target wheel at the entrance of the LISE spectrometer at GANIL. In order to maintain the spin orientation during the passage of the nuclei through the LISE spectrometer, it is important that fully stripped ions are being selected [15]. We could not avoid that some fragments pick up an electron when passing through a 300-μm Si detector which was used for the ion identification [16]. The ion arrival time also served as time $t = 0$ signal to start the Larmor precession measurement. The probability of electron pickup was estimated to be of the order of 30–40% using the LISE [17] and the ETACHA [18] programs. This means that for 30–40% of the implanted nuclei the spin orientation is reduced due to interaction of the coupled electron and nuclear spins with the external magnetic field [19–21]. This will reduce the measured amplitude of the oscillations in the γ anisotropy as a function of time.

3. EXPERIMENTAL SETUP

The setup we used in this experiment (Fig. 1) was positioned at the focal plane immediately after the LISE spectrometer in order to decrease as much as possible the time of flight of the produced species and this way to decrease the amount of nuclei which decay in flight and are lost for the measurement. The

ΔE Si detector and the Cu foil in which the nuclei are implanted are both fixed in a vacuum chamber positioned between the poles of an electromagnet. This magnet provides a constant magnetic field of $\mathbf{B} = 0.3753(50)$ T in a direction perpendicular to the plane of the beam and the orientation axis. The Larmor precession of the aligned isomeric spins is monitored by measuring the γ decay as a function of time, using two Clover Ge detectors and three BaF_2 detectors positioned in the horizontal plane. The two Clover detectors are positioned at 0° and 90° with respect to the beam axis.

The data collection was done in an event-by-event mode. The data acquisition system was triggered from a coincidence between the heavy-ion passing through the Si detector and a delayed γ, registered within a 20-μs time window, in any of the γ detectors. A two-dimensional plot of ΔE in the Si detector vs. time of flight (TOF) is shown in Fig. 2 ("potato plot"). Each of these "potatoes" represents a different isotope which is clearly distinguished from the others. As a delayed γ is triggering the data acquisition system, mainly isotopes containing an isomer are detected. During the off-line analysis, projections for different isotopes were made and this way each heavy-ion was correlated to the γ rays detected spontaneously after its implantation.

Gamma-ray time spectra were started by the ion arrival time, and stopped by detection of a delayed γ. To extract the precession pattern out of the individual time spectra, detectors at 90° with respect to each other are combined to find the $R(t)$ function (2).

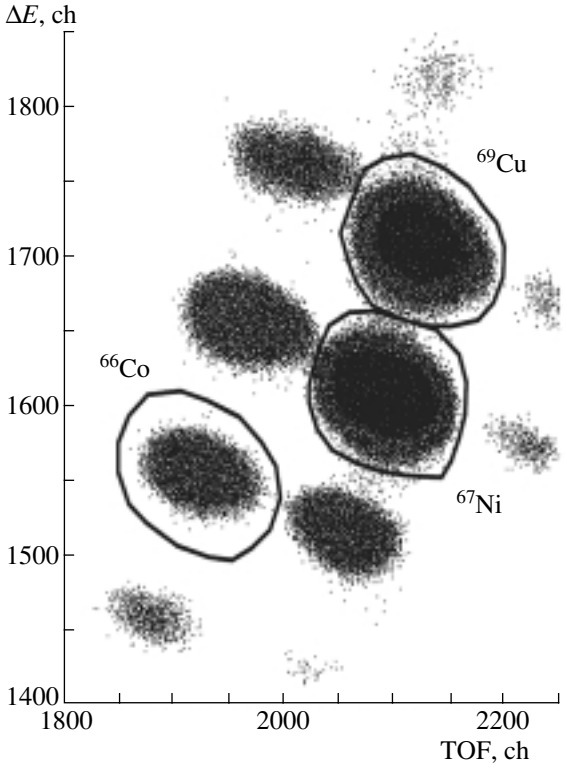

Fig. 2. ΔE vs. time of flight for the heavy ions passing through the Si detector ("potato plot"). In circles are shown the "potatoes" for the different nuclei.

4. RESULTS AND DISCUSSION

For three of the produced isomers (^{69m}Cu, ^{67m}Ni, and ^{66m}Co), the lifetimes and the implantation rates were suitable for g-factor measurements. Here, we present the results from the analysis of the $13/2^+$, $T_{1/2} = 354(2)$-ns isomer in ^{69}Cu. The results for the isomers in ^{67}Ni and in ^{66}Co will be finalized and published soon.

Projection of the data for the different isotopes was made using the "potato plot" (Fig. 2). This way, we created separate data sets for the different isotopes produced in the reaction. In the best case, one would expect that all of the γ in each data set are coming from the decay of that particular isomer (100% pure identification) without any contaminating γ lines from other isomers or isotope decays. In reality, there is also a contamination from noncorrelated γ-ray background from long-lived activities like long-lifetime isomers or β decay. This contamination depends on the isomeric ratio and on the lifetime of the selected isomer.

In the case of ^{69}Cu, each of the stronger γ lines was identified and for each of them a decay curve was produced and the lifetime was measured. During the fitting procedure, a sum of exponential function together with a constant background was used. We have found that all of the γ lines (also the contaminants) have a similar lifetime (in the range of 300–380 ns). This is due to the fact that no $\gamma\gamma$ coincidences were required and under each photo peak line there is a time-dependent Compton background. The Compton background have two different components—one comes from Compton scattered γ originating from the isomer decay, and the second one comes from Compton scattered γ of contaminating lines.

Choosing a line that is not correlated to the decay of the isomer, one has the inversed situation—the events that are in the photopeak have random time distribution and contribute to the background in the time spectra, while some of the Compton scattered events (originating from the isomeric decay) have the correct timing and contribute to the exponential decay in the time spectrum. Thus, one has to be very careful assigning a certain γ line to a particular isomer using only lifetime arguments.

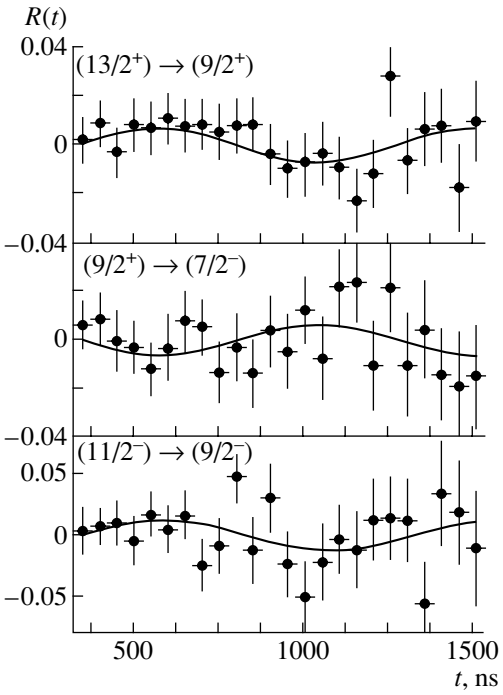

Fig. 3. Some typical TDPAD curves obtained for the 190, 680, and 486 keV transitions (from top to bottom) in ^{69}Cu isomer. The spins and parities of the connected nuclear levels are shown as inset.

Several γ lines from the decay of ^{69m}Cu had sufficient statistics to be analyzed using the $R(t)$ function. The TDPAD curves for the 190, 680, and 486 keV transitions are presented in Fig. 3. Note that there is a phase difference of π between the different transitions which is due to the difference in their multipolarities. The experimental asymmetry parameter A_2 for the 680 keV ($(9/2^+) \to (7/2^-)$) [22, 23] transition has opposite sign to that of the 190 keV ($(13/2^+) \to (9/2^+)$) transition. This is in agreement with the assumption that the former is an $E1$ transition and the latter is an $E2$ transition. Note that the 486 keV transition ($(11/2^-) \to (9/2^-)$) which is expected to be $M1$, has the same phase as the 190 keV transition. This indicates that 486 keV is not a pure $M1$ transition but has mixed $M1/E2$ multipolarity. From the experimentally measured amplitudes of the wiggles, we can set a lower limit on the mixing ratio ($\delta > 0.3$).

For the fit shown in Fig. 3, we use both the dependence of frequency and the phase of the g factor. There then arises the question of whether the sign of the g factor can be determined from a TDPAD measurement after a fragmentation reaction. Nuclei with different g factors have different rotation (α) of their spin ensembles passing through the spectrometer and consequently different direction of their initial orientation. Thus, from the phase of the wiggles in a TDPAD experiment, one can determine the sign of the g factor. But there are some specific configurations in which due to internal symmetries of the system this is not possible. The geometry in which this experiment was performed, selecting the secondary beam, with the LISE spectrometer ($\theta_C = 90°$) and γ detectors positioned at 0° and 90° with respect to the beam does not allow one to deduce the sign of the g factor. In this particular case, the $R(t)$ formula has the form

$$R(t) = \frac{I_1(0,t) - \epsilon I_2(\frac{\pi}{2},t)}{I_1(0,t) + \epsilon I_2(\frac{\pi}{2},t)} \sim A_2 B_2^0(t=0)\cos(2(\omega_{\rm L} t + \alpha)); \quad (3)$$

introducing the explicit dependence of α on the g factor, one gets

$$R(t) \approx A_2 B_2^0(t=0)\cos(\pi + g \cdot \text{const}) \equiv A_2 B_2^0(t=0)\cos(\pi - g \cdot \text{const}). \quad (4)$$

Thus, in our experiment (choosing this particular arrangement of the detectors), we are only sensitive to the absolute value of the g factor.

Note that the data depend on the isomeric g factor and not on the magnetic moment (which is $\mu = gI\mu_N$). This means that when comparing experimental results to magnetic moment calculations from a shell model, we need to assume a particular spin for the isomer, which has not been derived experimentally for all cases.

From the fit of the $R(t)$ function of the 190, 680, and 486 keV transitions of the $I^\pi = 13/2^+$ isomer in ^{69}Cu, we deduced the results shown in the table. The mean value is $g(^{69}\text{Cu}, 13/2^+) = 0.195(9)$. Corrections for knight-shift are negligible, and also paramagnetic corrections are less than the mentioned uncertainties [24]. The error bars correspond to statistical errors only. An additional systematic error of about 2% due to the uncertainty in the field should also be included. This value is in a reasonably good agreement with the value for a pure $\pi p_{3/2} \nu p_{1/2}^{-1} g_{9/2}$ configuration ($g = +0.244$) or a $\pi p_{3/2} \nu f_{5/2}^{-1} g_{9/2}$ configuration ($g = +0.237$), if one uses empirical single-particle moments for the individual orbits. The g factors of these two configurations are very close to each other, which does not allow us to distinguish between them. In [22], the configuration is assigned to be $\pi p_{3/2} \nu p_{1/2}^{-1} g_{9/2}$ based on analogy to the 5^- isomer observed in ^{68}Ni. In a shell-model calculation using a realistic interaction (S3V [25]) and single-particle energies fitted to data in this mass region to correct for the monopole term of the two-body matrix element, these $13/2^+$ states occur at an energy difference of only a few hundred keV. The shell-model g factors

List of the measured g factors for the 190, 680, and 486 keV transitions in ^{69}Cu. (The quoted value for the lifetime is the mean value of the most intense γ transitions observed in the current work)

Ion	I^π	$T_{1/2}$, μs		E_γ, keV	$g_{\exp}$
^{69}Cu	$13/2^+$	0.360(50)*	0.354(2)**	190	0.199(13)
				680	0.187(17)
				486	0.196(17)
				Mean	0.195(9)

* Value reported in [6].

** Value derived in the present work.

using free nucleon g factors are $g = +0.280$ and $g = +0.304$, respectively. The best agreement with the experimental result is achieved when effective $M1$ matrix elements from measured g factors are used, giving corrected values of $g = +0.194$ and $+0.189$, respectively.

5. CONCLUSION

In a pioneering experiment, we have shown the feasibility of application of TDPAD in combination with ion–γ correlation on nuclei produced in fragmentation reactions. This opens a new area for studies of nuclear moments of high-spin isomeric states in neutron-rich nuclei which are not reachable with fusion-evaporation reactions. There are still some possibilities for optimization of such type of experiments like using a primary beam having higher energy which will avoid pickup of electrons in the Si detector. Using more Ge Clover detectors would increase the sensitivity of the setup and would push down the necessary intensity (in this experiment we had a rate of a few hundred implanted isomers per second). BaF_2 detectors have proven not to be very useful unless a single isomer with few γ transitions is selected.

ACKNOWLEDGMENTS

This work has been supported by the Access to Large-Scale Facility program under the Training and Mobility of Researchers program of the European Union, under contract no. ERBFMGECT950036. We are grateful to the CEA (France), EPSRC (UK), and NBI (Denmark) for providing Clover detectors. G.N. is a postdoctoral researcher of the FWO–Vlaanderen Belgium and is grateful for the hospitality received at the GANIL facility during the year preceding the experiment. Partial financial support under DOE contract DE-FG02-96ER40983 and by the Polish Committee of Scientific Research under grant KBN 2 P03B 036 15 is also acknowledged.

REFERENCES

1. N. A. Orr *et al.,* Phys. Lett. B **258**, 29 (1991).
2. G. Klotz *et al.,* Phys. Rev. C **47**, 2502 (1993).
3. T. Motobayashi *et al.,* Phys. Lett. B **346**, 9 (1995).
4. R. Broda *et al.,* Phys. Rev. Lett. **74**, 868 (1995).
5. T. Pawlat *et al.,* Nucl. Phys. A **574**, 623 (1994).
6. R. Grzywacz *et al.,* Phys. Rev. Lett. **81**, 766 (1998).
7. W. F. Mueller *et al.,* Phys. Rev. Lett. **83**, 3613 (1999).
8. H. L. Seifert *et al.,* Z. Phys. A **349**, 25 (1994).
9. M. Bender *et al.,* in *Proceedings of the XXVI International Workshop on Gross Properties of Nuclei and Nuclear Excitations, Hirchegg, Austria, 1998.*
10. G. Goldring and M. Hass, in *Treatise in Heavy-Ion Sciences,* Ed. by D. E. Bromley (Plenum, New York, 1985), Vol. 3, p. 539.
11. W.-D. Schmidt-Ott *et al.,* Z. Phys. A **350**, 215 (1994).
12. G. Neyens *et al.,* Nucl. Instrum. Methods Phys. Res. A **340**, 555 (1994).
13. G. Neyens, in *Proceedings of Ecole Joliot-Curie de Physique Nucleaire, 1999,* p. 256.
14. W. Hume-Rothery *et al., Structure of Metals and Alloys* (Institute of Metals, London, 1969).
15. M. Hass *et al.,* in *Proceedings of the First International Conference on Radioactive Nuclear Beams* (World Sci., Singapore, 1989), p. 193.
16. D. Bazin *et al.,* Nucl. Phys. A **515**, 349 (1990).
17. D. Bazin, O. Sorlin, and O. B. Tarasov, www.ganil.fr/lise/prog.html.
18. J. P. Rozet *et al.,* Nucl. Instrum. Methods Phys. Res. B **107**, 67 (1996).
19. G. Goldring *et al.,* Phys. Rev. Lett. **28**, 763 (1972).
20. G. Goldring, in *Heavy-Ion Collisions,* Ed. by R. Bock (North-Holland, Amsterdam, 1982), p. 483.
21. K. Vyvey *et al.,* Phys. Rev. C (in press).
22. R. Broda *et al.,* in *Proceedings of the International Conference on Fission and Properties of Neutron-Rich Nuclei* (World Sci., Singapore, 1998), p. 202.
23. T. Ishii *et al.,* Phys. Rev. Lett. **84**, 39 (2000).
24. H. Haas, private communication.
25. J. Sinatkas *et al.,* J. Phys. G **18**, 1377, 1401 (1992).

Physics of Atomic Nuclei, Vol. 64, No. 7, 2001, pp. 1186–1193. From Yadernaya Fizika, Vol. 64, No. 7, 2001, pp. 1263–1270.

Proceedings of the International Conference "Nuclear Structure and Related Topics"

Level Density and Thermal Properties in Rare Earth Nuclei*

A. Schiller**, **M. Guttormsen, M. Hjorth-Jensen, E. Melby, J. Rekstad, and S. Siem**

Department of Physics, University of Oslo, Norway

Received October 25, 2000

Abstract—A convergent method to extract the nuclear level density and the γ-ray strength function from primary γ-ray spectra has been established. Thermodynamical quantities have been obtained within the microcanonical and canonical ensemble theory. Structures in the caloric curve and in the heat capacity curve are interpreted as fingerprints of breaking of Cooper pairs and quenching of pairing correlations. The strength function can be described using models and common parametrizations for the $E1$, $M1$, and pygmy resonance strength. However, a significant decrease of the pygmy resonance strength at finite temperatures has been observed. © *2001 MAIK "Nauka/Interperiodica".*

1. INTRODUCTION

Investigation of nuclear level density is an old problem in nuclear physics. The first theoretical attempt to describe nuclear level density was done by Bethe in 1936 [1]. In order to do so, he introduced thermodynamical quantities like temperature and entropy, showing how closely related nuclear level density and thermodynamics in nuclei are. With the discovery of pairing correlations, their effect on nuclear level density, temperature, and heat capacity was explored early in schematic calculations [2]. Today, the Monte Carlo shell model technique [3] can estimate nuclear level density [4] reliably for heavy midshell nuclei like dysprosium [5].

On the experimental side, the main sources of information on nuclear level density have been counting of discrete levels in the vicinity of the ground state (see, e.g., [6]) and neutron resonance spacing data (see, e.g., [7]). Recently, the Oslo group has reported on a new method to extract level density and γ-ray strength function from primary γ-ray spectra [8].

Important applications of nuclear level densities are Hauser–Feshbach type of calculations [9] of nuclear reaction cross sections. These reaction cross sections are important input parameters in large network calculations of stellar evolution [10]. The reaction cross sections can also be used to estimate the efficiency of accelerator-driven transmutation of nuclear waste.

Also, radiative strength functions have been examined for a long time. The first estimate of γ-ray strength functions within the single-particle shell model was done by Weisskopf in 1951 [11]. However, this model of energy-independent strength functions failed particularly badly with $E1$ transitions. First, some ten years later [12], experimental data on electric dipole transitions over a large energy range could be explained consistently within one model. Today, refined schematic models of the giant dipole resonance, taking into account temperature dependence, are available [13, 14], while low-lying dipole strength can be reliably estimated within microscopic random-phase approximation calculations for rare earth nuclei [15, 16].

Experimentally, the total radiative strength function can be measured by absorption methods [17]. At energies below the neutron separation energy, it can be estimated from radiative neutron capture, usually assuming a model for the nuclear level density. These experiments involve either the total γ-ray spectrum [18] or two-step γ cascades [19] (see also the talk of A.M. Sukhovoj in this issue). Our newly developed method [8] gives now for the first time the opportunity to extract level density and radiative strength function simultaneously without assuming any model for either of them.

Applications of radiative strength functions can again be found in nuclear astrophysics. Especially, the existence of a soft dipole mode in neutron-rich nuclei can have a large impact on the (n, γ) reaction rates of r-process nuclei [20].

In Section 2, we discuss the experimental details and the main assumptions of our data analysis method. In Section 3, results for the level density and thermodynamical quantities are shown. In Section 4, the radiative strength function is discussed, and we conclude the talk in Section 5.

*This article was submitted by the authors in English.

**e-mail: Andreas.Schiller@fys.uio.no

1063-7788/01/6407-1186$21.00

2. EXPERIMENTAL DETAILS AND DATA ANALYSIS

The experiments were carried out at the Oslo Cyclotron Laboratory at the University of Oslo, using an MC35 Scanditronix cyclotron with a ^{3}He beam energy of 45 MeV and a beam intensity of typically 1 nA. The experiments were usually running for two weeks. The targets consist of self-supporting, isotopically enriched ($\sim$95%) metal foils of $\sim$2.0 mg/cm^2 thickness, glued on an aluminum frame. Particle identification and energy measurements were performed by a ring of 8 Si(Li) particle telescopes mounted at 45° with respect to the beam axis. The telescopes consist of a front and end detector with thicknesses of some 150 and 3000 μm, respectively, and can effectively stop α particles with energies up to 60 MeV. The γ rays were detected by an array of 28 5″ × 5″ NaI(Tl) detectors (CACTUS) [21] covering a solid angle of $\sim$15% of 4π. Three 60% Ge(HP) detectors were used to monitor the selectivity of the reaction and the entrance spin distribution of the product nuclei. During one experimental run, data can be recorded and sorted out simultaneously for the (^{3}He,^{3}He′) and the (^{3}He,α) reaction on the same target.

In the data analysis, the ejectile energy can be transformed into excitation energy of the product nucleus, since the reaction kinematic is uniquely determined. In the next step, the γ-ray spectra are unfolded [22], using measured response functions of the CACTUS detector array. Afterwards, the primary γ-ray spectra can be extracted, using the subtraction technique of [23]. In order to be able to apply this technique, the entrance point in excitation energy of the product nucleus has to be known and all excitation energies up to a certain limit have to be scanned in the experiment. The basic assumption behind the first-generation method is that the γ-ray spectrum of any excitation-energy bin is independent of the way that states in this bin are populated (e.g., direct population by a nuclear reaction, or population by the same nuclear reaction at some higher entrance energy and followed by one or several subsequent γ rays). This assumption is not completely valid at low excitation energies where γ decay competes effectively with thermalization processes and the nuclear reactions applied exhibit a more direct than compound character. Also, possibly different spin and parity distributions of levels populated at different excitation energies by the same nuclear reaction can violate this assumption. However, in a recent investigation of this matter, we could not find any severe problems with the first-generation method [24].

The primary γ-ray spectra (see Fig. 1) are the starting point of the discussion in this talk. According to the Brink–Axel hypothesis [25, 12], the primary γ-ray matrix can be factorized into two functions of one variable using

$$\Gamma(E_x, E_\gamma) \propto \rho(E_x - E_\gamma)\, F(E_\gamma), \qquad (1)$$

where ρ is the level density and F is a γ-ray energy-dependent factor, proportional to the total radiative strength function, i.e.,

$$F(E_\gamma) \propto \sum_{XL} E_\gamma^{(2L+1)}\, f_{XL}(E_\gamma). \qquad (2)$$

In (1), a temperature-independent radiative strength function f is assumed. Today, we know that at least the $E1$ strength function is temperature dependent, a fact which has already been incorporated in several models [13, 14]. However, we found for our data that the factorization according to (1) works remarkably well (see Fig. 1), which indicates that, for low and slowly varying temperatures, as in our case, the Brink–Axel hypothesis is approximately valid.

The details of the method to extract level density and radiative strength function from primary γ-ray spectra can be found in [8]. An extension of this method to temperature-dependent radiative strength functions is discussed in Section 4. One detail of the method should be mentioned here. The method does not yield absolute values of the level density and the radiative strength function. Also, the slope of these two functions is undetermined. Actually, all functions $\tilde{\rho}$ and $\tilde{F}$ obtained by the transformation

$$\tilde{\rho}(E_x - E_\gamma) = A\, \exp(\alpha\, [E_x - E_\gamma])\, \rho(E_x - E_\gamma), \qquad (3)$$

$$\tilde{F}(E_\gamma) = B\, \exp(\alpha\, E_\gamma)\, F(E_\gamma) \qquad (4)$$

of any particular solution (ρ, F) will fit our primary γ-ray matrix equally, since the areas of the first-generation spectrum are normalized to unity for every excitation energy bin E_x, i.e.,

$$\Gamma(E_x, E_\gamma) = \frac{\rho(E_x - E_\gamma)\, F(E_\gamma)}{\sum_{E_\gamma} \rho(E_x - E_\gamma)\, F(E_\gamma)}. \qquad (5)$$

In order to determine the parameters A and α, i.e., the absolute value and the slope of the level density, we fit our extracted level density curve to the known number of discrete levels in the vicinity of the ground state [6] and to the level density estimate obtained from neutron resonance spacing data [7] at the neutron binding energy. The only remaining free parameter then is the absolute value of the γ-ray energy-dependent factor F, which can be determined from the average total radiative width of neutron capture resonances [26] by

$$\langle \Gamma_\gamma(E, I, \Pi) \rangle = \frac{1}{\rho(E, I, \Pi)} \qquad (6)$$

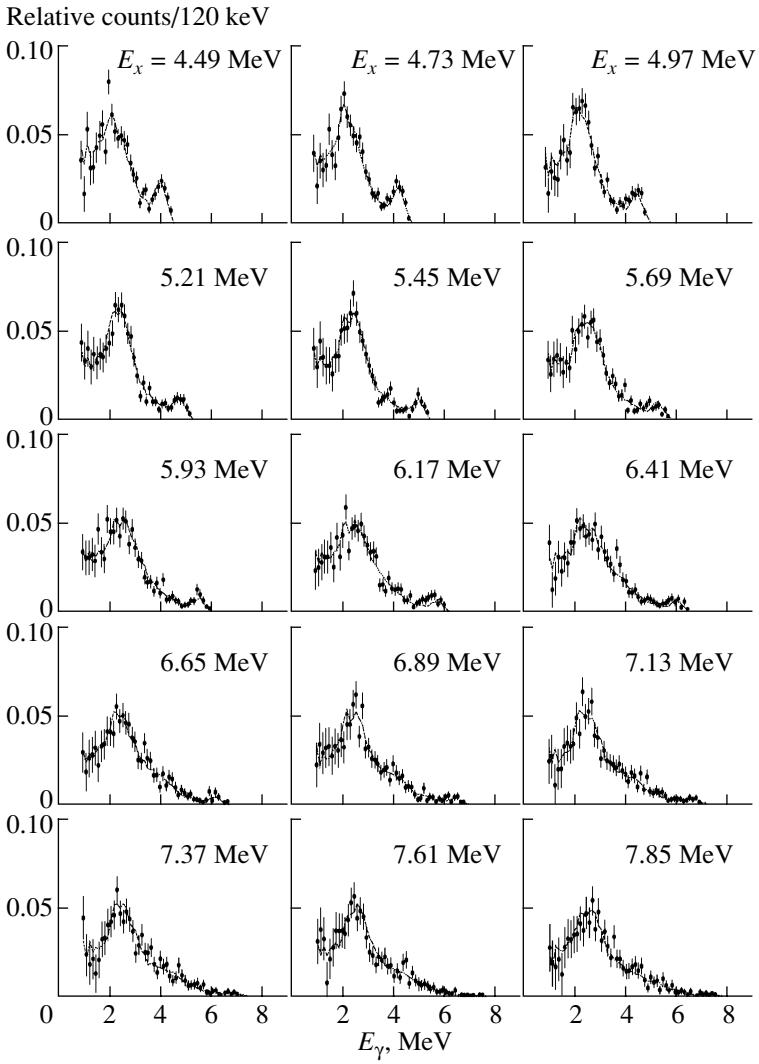

Fig. 1. Normalized experimental primary γ-ray spectra with estimated errors (data points) and fit using the factorization of (1) (solid curves). The data are taken from the ^{162}Dy(^{3}He,^{3}He′)^{162}Dy reaction.

$$\times \sum_{XL} \sum_{I_f,\Pi_f} \int_{E_\gamma=0}^{E} dE_\gamma\, E_\gamma^{2L+1}\, f_{XL}(E_\gamma) \times \rho(E - E_\gamma, I_f, \Pi_f)$$

(see, e.g., [27]).

In this talk, we will discuss the level density and radiative strength function of ^{161,162}Dy and ^{171,172}Yb obtained from (^{3}He, α) reaction data and the radiative strength function of ^{162}Dy obtained from (^{3}He,^{3}He′) reaction data.

3. LEVEL DENSITY AND THERMODYNAMICAL QUANTITIES

In Fig. 2, the nuclear level density and the γ-ray energy-dependent factor $F(E_\gamma)$ for the nuclei ^{161,162}Dy and ^{171,172}Yb are shown. In this section, we will mainly discuss the physics of the nuclear level density. First of all, the experimental curves can be compared to popular parametrizations of the nuclear level density, like those of Gilbert and Cameron [28] or of von Egidy *et al.* [29]. This has been done in [30], and the conclusion is that neither of the two parametrizations can describe our data well. However, the data favor the concept of a composite level density formula as proposed in [28] with a constant-temperature level density part from above 1–2 MeV and up to approximately the neutron binding energy B_n. Another important aspect is that the experimental data of the odd and even nuclei show a relative shift of the order of the effective pairing energy $\Delta^{\text{eff}}(N,Z) = \Delta_p(N,Z) + \Delta_n(N,Z) - \Delta_p(N -$

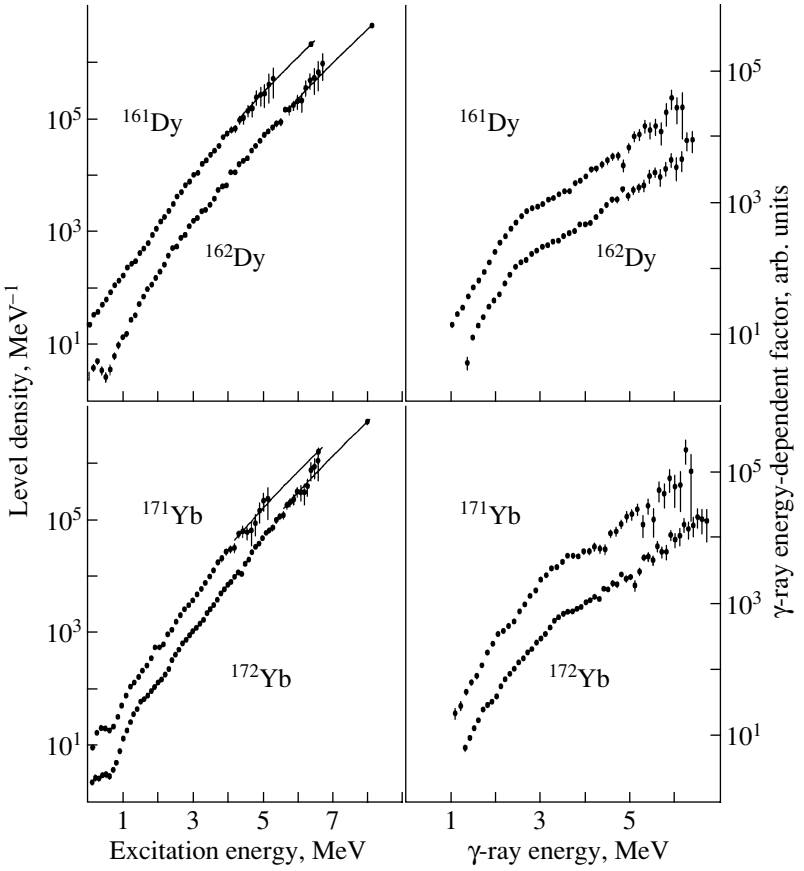

Fig. 2. Level density and γ-ray energy-dependent factor $F(E_\gamma)$ of ^{161,162}Dy and ^{171,172}Yb from (^{3}He,α) reaction data. The error bars show the experimental uncertainties. The solid curves are extrapolations based on a shifted Fermi gas model. The isolated points at the neutron binding energy were obtained from neutron resonance spacing data.

$1, Z$) [30]; thus, the data support the concept of shifted level density formulas.

From level densities, one can easily calculate thermodynamical quantities like entropy S, temperature T, heat capacity C_V, the canonical partition function Z, and the average excitation energy in the canonical ensemble $\langle E\rangle$. Within the microcanonical ensemble, one obtains (in this work $k_\mathrm{B} = 1$)

$$S(E_x) = \ln\rho(E_x) + S_0, \tag{7}$$

$$T(E_x) = \left(\frac{\partial S(E_x)}{\partial E_x}\right)^{-1}_V, \tag{8}$$

$$C_V(E_x) = \left(\frac{\partial T(E_x)}{\partial E_x}\right)^{-1}_V, \tag{9}$$

and in the canonical ensemble, one gets

$$Z(T) = \int_0^\infty N\rho(E_x)\exp(-E_x/T)dE_x, \tag{10}$$

$$S(T) = \frac{\partial}{\partial T}[T\ln Z(T)], \tag{11}$$

$$\langle E(T)\rangle = T^2\frac{\partial}{\partial T}\ln Z(T), \tag{12}$$

$$C_V(T) = \left(\frac{\partial\langle E(T)\rangle}{\partial T}\right)_V. \tag{13}$$

The quantities S_0 and N are necessary, since the level density is only proportional to the energy surface in the phase space W.

In principle, one should only consider the microcanonical ensemble, since the nucleus is a closed system. However, the canonical and even the grand-canonical ensemble have often been used [1, 3] to describe thermodynamical properties of nuclei. In [31], the microcanonical and canonical entropy is discussed and compared to a simple model. One result of this discussion is that the small bumps in the experimental level density curves (see Fig. 2) can be interpreted in terms of breaking of Cooper pairs. These bumps can even be enhanced by derivation [see (8)], yielding the experimental caloric curve in the microcanonical ensemble (see data points in Fig. 3 and discussion in [32]). Another important result is that the entropy excess of the odd nuclei relative to

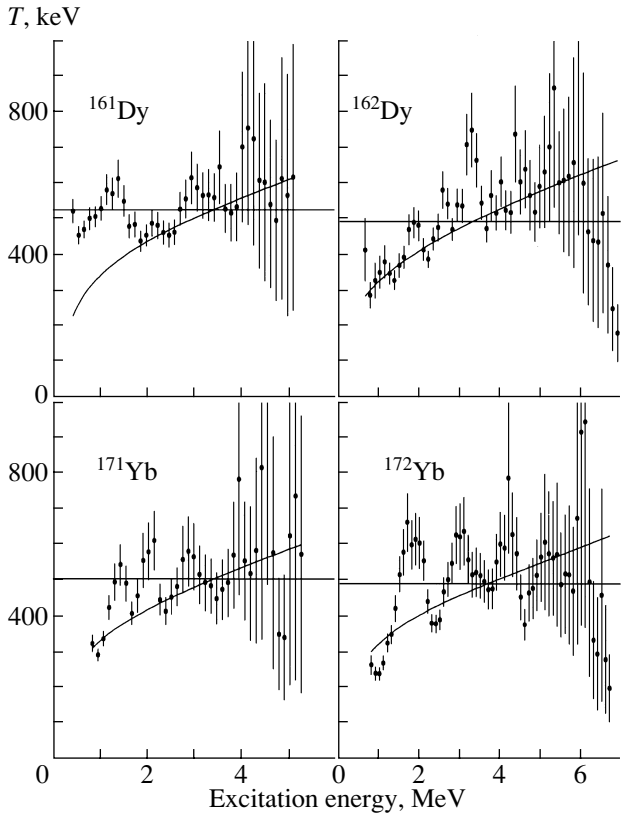

Fig. 3. Caloric curve of ^{161,162}Dy and ^{171,172}Yb in the microcanonical ensemble (data points) and the canonical ensemble (curve). The straight line indicates the critical temperature T_c.

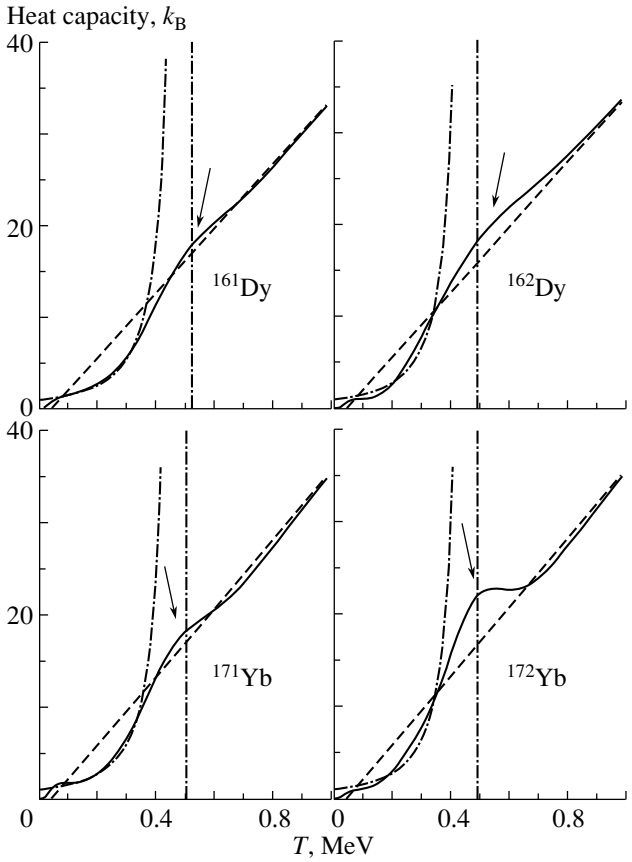

Fig. 4. Semiexperimental heat capacity as function of temperature in the canonical ensemble for ^{161,162}Dy and ^{171,172}Yb (solid curves). The dashed lines describe the approximate Fermi gas heat capacity. The arrows indicate the first local maxima of the experimental curves relative to the Fermi gas estimates. The dash-dotted curves describe estimates according to a constant-temperature level density formula, where T is set equal to the critical temperature T_c (vertical lines).

the even nuclei can be used to calculate the entropy of one quasiparticle. It is surprising that the quasiparticle entropy is constant $1.70(15)\,k_B$ over the whole excitation energy region investigated in [31].

When calculating the partition function in the canonical ensemble [see (10)], a strong smoothing is introduced due to the Laplace transformation involved. It is also worth noting that, in order to calculate thermodynamical quantities reliably up to $T \sim 1$ MeV, one has to know the level density up to about 40 MeV. Since the experimental level density curves are only known up close to the neutron binding energy, they had to be extrapolated by a model. We have chosen the shifted Fermi gas parametrization of von Egidy *et al.* [29] multiplied by a constant factor in order to match the neutron resonance spacing data.

Due to this strong smoothing over a huge range of excitation energies, one does not expect to see fine structures in the canonical ensemble. This is clearly demonstrated in Fig. 3, where the canonical caloric curve is smooth and the breaking of individual Cooper pairs is completely washed out. However, the quenching of pairing correlations is manifested in the canonical heat-capacity curves (see Fig. 4). Deviating from a Fermi gas estimate, the heat-capacity curves show pronounced S shapes with local maxima relative to the smooth Fermi gas estimate. This behavior can be explained by the fact that the level density exhibits a constant-temperature part at low excitation energies. Therefore the canonical heat capacity curve $C_V = (1 - T/\tau)^{-2}$ for a constant-temperature level density $\rho = C\exp(E/\tau)$ has been fitted to the data at low temperatures, and the parameter τ is interpreted as the critical temperature for the quenching of pairing correlations [33]. The resulting critical temperatures are given as horizontal and vertical lines in Figs. 3 and 4, respectively. We interpret the S shape of the heat capacity as a fingerprint of a second-order phase-transition-like phenomenon in finite systems, where the transition goes from a phase with strong pairing correlations (usually

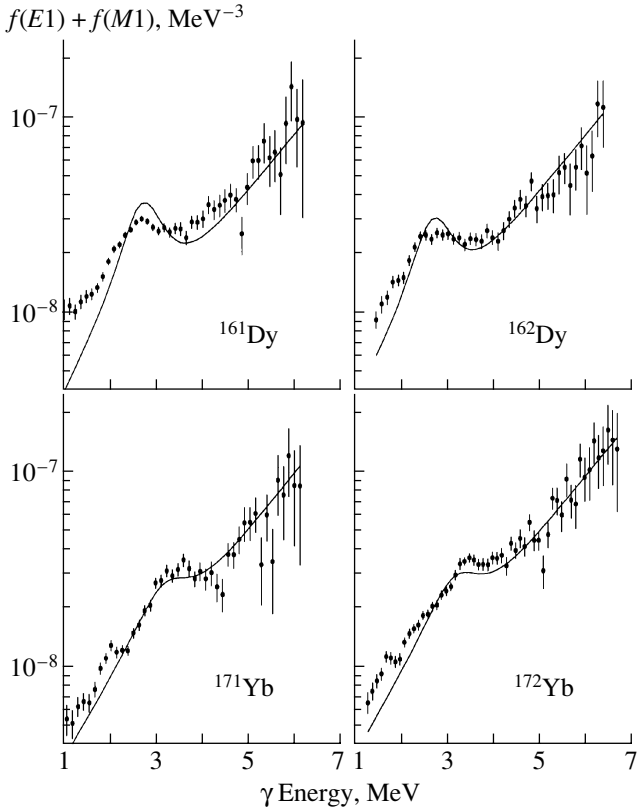

Fig. 5. Radiative strength function of ^{161,162}Dy and ^{171,172}Yb (data points). The absolute normalization of the data is still preliminary. The error bars show the experimental uncertainties only. The solid curves are strength function models (see text), where all parameters are taken from other experimental systematics and nothing was fitted to our data besides $k\sigma_p$ (see text).

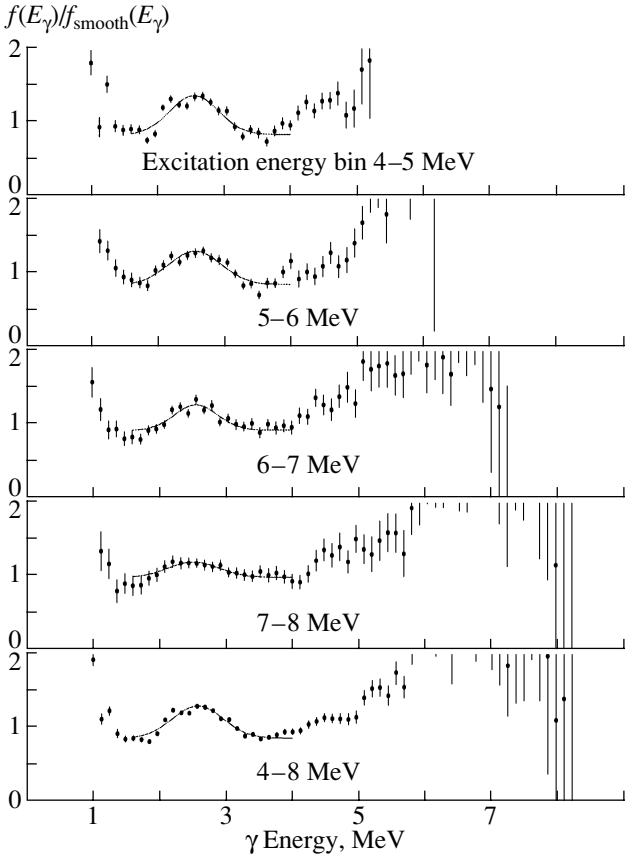

Fig. 6. Relative radiative strength functions extracted from different excitation energy bins. The data here and in the following discussion are from the ^{162}Dy(^{3}He,^{3}He′)^{162}Dy reaction. The radiative strength functions are all divided by the same smooth strength function CE_γ^n with $n \approx 1.2$ in order to enhance the pygmy resonance structure. The solid curves are Gaussian fits to the pygmy resonance structure.

referred to as a superfluid phase) to a phase with weak pairing correlations (normal fluid phase). This phase-transition-like phenomenon has been anticipated by many theoretical works [2, 4, 34, 35].

4. RADIATIVE STRENGTH FUNCTION

Figure 5 shows the radiative strength functions of ^{161,162}Dy and ^{171,172}Yb compared to model calculations. For the theoretical calculation, we have used the $E1$ model of Sirotkin [14], where we take the expression for the temperature-dependent width of Kadmensky *et al.* [13]. The parameters are taken from an interpolation of the experimental systematics of [17]. The temperature has been assumed as constant with $T \sim 500$ keV. For the $M1$ model, we simply take a Lorentzian, where the parameters for the centroids and widths are taken from [27] and the parameters for the resonance strengths are taken from f_{M1}/f_{E1} systematics [36], evaluated at $E_\gamma = B_n - 1$ MeV. For the pygmy resonance, we use again a Lorentzian with parameters from an interpolation based on the experimental systematics [18]. It is amazing that the model calculation can fit our data so well. Both the absolute value and the slope of the experimental strength functions could be reproduced without fitting any parameter from the models except $k\sigma_p$ of [18]. Here, we had to reduce the parameters for the pygmy resonance strength $k\sigma_p$ by 30–70% compared to [18] as the only compromise to our data.

In the following, we want to investigate the strength of the pygmy resonance, which is the only parameter we had to fit in order to describe our data. For this reason, we divide our primary γ-ray matrix into four subsets of distinct excitation energy bins. Each excitation energy bin is 1 MeV broad; thus, we can assume that the nuclear temperature within every excitation energy bin is constant and the Brink–Axel hypothesis remains valid. However, for the different excitation energy bins the nuclear temperature is

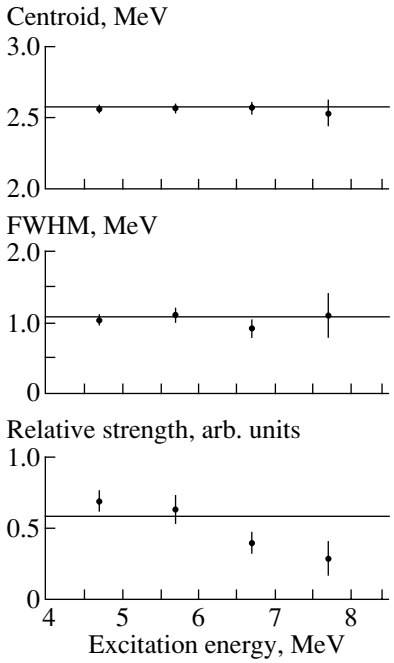

Fig. 7. Fit parameters from a Gaussian fit to the pygmy resonance structure (see Fig. 6) for different excitation energy bins. The centroid and the width are constant and fit nicely into the systematics of [18]. The relative strength is decreasing with increasing excitation energy. The lines indicate average values, taking into account the whole data set.

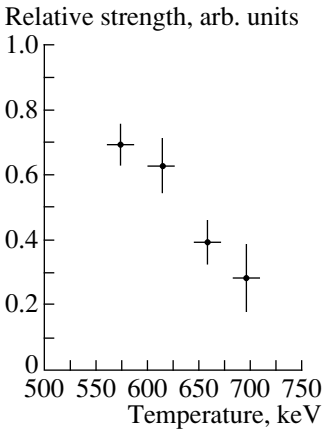

Fig. 8. Temperature dependence of the relative pygmy resonance strength.

in general different. We extract radiative strength functions from those four excitation energy bins. In that way, we obtain radiative strength functions for four different nuclear temperatures. This provides an easy way to investigate the temperature dependence of the radiative strength function.

In Fig. 6, the relative radiative strength functions from the different excitation energy bins are plotted. One can see immediately that the pygmy resonance strength is highly temperature dependent. On the other hand, the general slope of the radiative strength function is constant; thus, the gross features of the strength function are rather independent of nuclear temperature, justifying the use of the Brink–Axel hypothesis for our data analysis. The fit parameters of the pygmy resonance for the different excitation energy bins are shown in Fig. 7. Obviously, only the resonance strength of the pygmy resonance shows a pronounced temperature dependence, whereas the centroid and the width are nearly independent of temperature. The temperature dependence becomes even much more obvious when we actually translate the excitation energy bins into nuclear temperature using the canonical caloric curve of Fig. 3. The result is given in Fig. 8, where the temperature dependence of the pygmy resonance strength is shown. A clear quenching of the pygmy resonance strength as a function of temperature is observed.

We have to speculate on the physical origin of the observed quenching. In the first place, it is not at all clear if the pygmy resonance is a phenomenon in the electric or magnetic dipole strength function. Igashira *et al.* [18] favor electric dipole strength without measuring the parity of the transition, whereas, in other works, spin-flip [37] or orbital [38] (scissors mode) $M1$ strength has been proposed. Anyhow, we might assume a strong dependence of the pygmy resonance strength on the deformation parameter δ (as is observed for the scissors mode [39]). A quenching of the pygmy resonance strength would then correspond to a shape transition of the nucleus from deformed to spherical. This temperature-induced shape transition was indeed anticipated for ^{170}Dy in [3] at temperatures around 500 keV. Therefore, we speculatively interpret the quenching of the pygmy resonance strength as a fingerprint for a temperature-induced shape transition.

5. CONCLUSION

A method to extract simultaneously level density and radiative strength function from primary γ-ray spectra without assuming any model for either of them has been presented. Thermodynamical quantities have been deduced within the microcanonical and the canonical ensemble. We observe structures in these quantities which can be interpreted as breaking of Cooper pairs and quenching of pairing correlations, and we observe a fingerprint of the phase-transition-like phenomenon from a superfluid-like phase to a normal-fluid-like phase. Further, the critical temperature of this transition has been determined. We are able to reproduce our experimental strength functions by the use of models, where all parameters save the pygmy resonance strength are taken from

other experimental systematics. The temperature dependence of the pygmy resonance strength has been investigated, and a significant quenching around $T \approx 500$ keV has been observed, which we interpret tentatively as the result of a temperature-induced shape transition.

The authors are grateful to E.A. Olsen and J. Wikne for providing the excellent experimental conditions. We thank A. Voinov for many interesting discussions. We wish to acknowledge the support from the Norwegian Research Council (NFR).

REFERENCES

1. H. A. Bethe, Phys. Rev. **50**, 332 (1936).
2. M. Sano and S. Yamasaki, Prog. Theor. Phys. **29**, 397 (1963).
3. S. E. Koonin, D. J. Dean, and K. Langanke, Phys. Rep. **278**, 1 (1997).
4. H. Nakada and Y. Alhassid, Phys. Rev. Lett. **79**, 2939 (1997).
5. J. A. White, S. E. Koonin, and D. J. Dean, Phys. Rev. C **61**, 034303 (2000).
6. R. B. Firestone and V. S. Shirley, *Table of Isotopes* (Wiley, New York, 1996, 8th ed.), Vol. II.
7. A. S. Iljinov, M. V. Mebel, N. Bianchi, *et al.,* Nucl. Phys. A **543**, 517 (1992).
8. A. Schiller, L. Bergholt, M. Guttormsen, *et al.,* Nucl. Instrum. Methods Phys. Res. A **447**, 498 (2000).
9. W. Hauser and H. Feshbach, Phys. Rev. **87**, 366 (1952).
10. Thomas Rauscher, Friedrich-Karl Thielemann, and Karl-Ludwig Kratz, Phys. Rev. C **56**, 1613 (1997).
11. V. Weisskopf, Phys. Rev. **83**, 1073 (1951).
12. P. Axel, Phys. Rev. **126**, 671 (1962).
13. S. G. Kadmensky, V. P. Markushev, and V. I. Furman, Yad. Fiz. **37**, 277 (1983) [Sov. J. Nucl. Phys. **37**, 165 (1983)].
14. V. K. Sirotkin, Yad. Fiz. **43**, 570 (1986) [Sov. J. Nucl. Phys. **43**, 362 (1986)].
15. V. G. Soloviev, A. V. Sushkov, N. Yu. Shirikova, and N. Lo Iudice, Nucl. Phys. A **613**, 45 (1997).
16. V. G. Soloviev, A. V. Sushkov, and N. Yu. Shirikova, Phys. Rev. C **56**, 2528 (1997).
17. G. M. Gurevich, L. E. Lazareva, V. M. Mazur, *et al.,* Nucl. Phys. A **351**, 257 (1981).
18. M. Igashira, H. Kitazawa, M. Shimizu, *et al.,* Nucl. Phys. A **457**, 301 (1986).
19. F. Bečvář, P. Cejnar, J. Honžatko, *et al.,* Phys. Rev. C **52**, 1278 (1995).
20. S. Goriely, Phys. Lett. B **436**, 10 (1998).
21. M. Guttormsen, A. Atac, G. Løvhøiden, *et al.,* Phys. Scr. T **T32**, 54 (1990).
22. M. Guttormsen, T. S. Tveter, L. Bergholt, *et al.,* Nucl. Instrum. Methods Phys. Res. A **374**, 371 (1996).
23. M. Guttormsen, T. Ramsøy, and J. Rekstad, Nucl. Instrum. Methods Phys. Res. A **255**, 518 (1987).
24. A. Schiller, M. Guttormsen, E. Melby, *et al.,* Phys. Rev. C **61**, 044324 (2000).
25. D. M. Brink, Ph.D. Thesis (Oxford Univ., 1955).
26. S. F. Mughabghab, *Neutron Cross Sections* (Academic, New York, 1984), Vol. 1, Part B.
27. J. Kopecky and M. Uhl, Phys. Rev. C **41**, 1941 (1990).
28. A. Gilbert and A. G. W. Cameron, Can. J. Phys. **43**, 1446 (1965).
29. T. von Egidy, H. H. Schmidt, and A. N. Behkami, Nucl. Phys. A **481**, 189 (1987).
30. M. Guttormsen, M. Hjorth-Jensen, E. Melby, *et al.,* Phys. Rev. C **61**, 067302 (2000).
31. M. Guttormsen, A. Bjerve, M. Hjorth-Jensen, *et al.,* Phys. Rev. C **62**, 024306 (2000).
32. E. Melby, L. Bergholt, M. Guttormsen, *et al.,* Phys. Rev. Lett. **83**, 3150 (1999).
33. A. Schiller, A. Bjerve, M. Guttormsen, *et al.,* Phys. Rev. C **63**, 021306 (2001).
34. D. J. Dean, S. E. Koonin, K. Langanke, *et al.,* Phys. Rev. Lett. **74**, 2909 (1995).
35. S. Rombouts, K. Heyde, and N. Jachowicz, Phys. Rev. C **58**, 3295 (1998).
36. J. Kopecky and M. Uhl, in *Proceedings of a Specialists' Meeting on Measurement, Calculation and Evaluation of Photon Production Data, Bologna, Italy, 1994* (NEA/NSC/DOC(95)1), p. 119.
37. M. Guttormsen, J. Rekstad, A. Henriquez, *et al.,* Phys. Rev. Lett. **52**, 102 (1984).
38. C. Wesselborg, P. von Brentano, K. O. Zell, *et al.,* Phys. Lett. B **207**, 22 (1988).
39. N. Pietralla, P. von Brentano, R.-D. Herzberg, *et al.,* Phys. Rev. C **58**, 184 (1998).

Physics of Atomic Nuclei, Vol. 64, No. 7, 2001, pp. 1194–1198. From Yadernaya Fizika, Vol. 64, No. 7, 2001, pp. 1271–1274.

Proceedings of the International Conference "Nuclear Structure and Related Topics"

Estimations of Level Densities and Radiative Strength Functions from Experimental Data and Probable Change in the Properties of Nuclei at $E_{\mathrm{exc}} \simeq 3$–$4$ MeV*

V. A. Khitrov and A. M. Sukhovoj**

Joint Institute for Nuclear Research, Dubna, Moscow oblast, 141980 Russia

Received October 25, 2000

Abstract—Investigations of two-step γ cascades following thermal-neutron capture by heavy nuclei reveal that the density of excited levels is significantly smaller than that which is predicted by an exponential extrapolation like that of the back-shifted Fermi gas model. Data on two-step cascades allow one to determine in a model-independent way the most probable energy dependences of the level density and radiative strength functions, virtually over the whole excitation-energy interval below the neutron binding energy B_n. Data for more than 30 heavy nuclei cannot be understood without assuming a considerable change in the nuclear properties at $E_{\mathrm{exc}} \simeq 3$–$4$ MeV. © *2001 MAIK "Nauka/Interperiodica".*

The level density $\rho(J^\pi, E_{\mathrm{exc}})$ and the partial radiative widths $\Gamma_{\lambda i}(E_\gamma)$ for states at an arbitrary excitation energy E_{exc} contain information on the wave functions for these states. Below the neutron binding energy B_n, there are a few other similar parameters that can be measured experimentally and used to test nuclear models.

The excitation energy region $E_{\mathrm{exc}} < B_n$ is of special interest because, here, nuclear structure undergoes radical changes: states described by the simplest (often, one-component) wave functions transform into Bohr compound states. From a comparison with physical phenomena of macrocosm, one can assume that an experimental study of this change will provide exclusive information about the properties of nuclear matter.

Therefore, an experiment should be aimed at obtaining data as complete, precise, and reliable as possible on $\rho(J^\pi)$ and $\Gamma_{\lambda i}$ in the widest interval of nuclear excitation energies. Unfortunately, available information about these nuclear properties does not meet these demands. The level density for 3–5 MeV $< E_{\mathrm{exc}} < B_n$ is extracted from nuclear-reaction cross sections by using some model assumptions (with unknown accuracy) about reaction yields. The situation concerning the determination of the partial widths $\Gamma_{\lambda i}$ and the corresponding radiative strength functions with respect to $E1$ and $M1$ transitions,

$$f = \langle\Gamma_{\lambda i}\rangle/(E_\gamma^3 \times A^{2/3} \times D_\lambda), \qquad (1)$$

is even worse (here, A is the nuclear mass and D_λ is the spacing between decaying states). Therefore, new experimental methods for independently determining the parameters of a cascade γ decay in the nuclear-excitation-energy region around $E_{\mathrm{exc}} \simeq B_n$ are required. The first example of such a method is an analysis of the intensities of two-step γ cascades proceeding between neutron resonances and low-lying levels [1]. This analysis shows that the actual number of cascades populating a given low-lying level is many times less than theoretical predictions based on the following two assumptions: (a) ρ is an exponential function of the excitation energy [2] [a consequence of the idea that (n,γ) reactions are nonselective]. (b) Fluctuations of primary transition widths follow the Porter–Thomas distribution [3].

The unique possibility of simultaneously estimating ρ and radiative strength functions for dipole transitions is provided by the study of the cascade of two successive γ transitions following thermal-neutron capture. Using ordinary Ge detectors, one can measure intensity

$$i_{\gamma\gamma} = (\Gamma_{\lambda i}/\Gamma_\lambda) \times (\Gamma_{if}/\Gamma_i) \qquad (2)$$

of an individual cascade connecting three states ($\lambda \to i \to f$) up to the energy $E_i \sim 3$–5 MeV and the total intensity of the cascades,

$$I_{\gamma\gamma} = \sum_{J,\pi}(\Gamma_{\lambda i}/(\langle\Gamma_{\lambda i}\rangle m_{\lambda i})) \qquad (3)$$
$$\times n_{\lambda i} \times (\Gamma_{if}/(\langle\Gamma_{if}\rangle m_{if})).$$

Summation in (3) is performed over a certain set of the quantum numbers J and π of $n_{\lambda i} = \rho_i \times \Delta E$

*This article was submitted by the authors in English.

**e-mail: suchovoj@nf.jinr.ru

intermediate and, if necessary, initial and final cascade states. This summation takes into account the parity selection rule.

Simple algorithms [4] applied to analyze this experiment are physically substantiated and easily realized within the maximum-likelihood method. As a result, the total cascade intensities (summed over 0.5-MeV energy bins) as functions of the energy of the cascade intermediate level were obtained nearly up to $E_{\rm exc} \simeq B_n$. The level schemes and main modes of their decay up to $E_{\rm exc} \simeq 3$–4 MeV were also derived.

The experimental distribution of random deviations of the cascade intensities from their mean value was approximated by some function. An extrapolation of this function to the region below the detection threshold L_c of the spectrometer $0 < i_{\gamma\gamma} < L_c$ allowed one to estimate ρ independently up to $E_{\rm exc} \simeq 3$–4 MeV in many nuclei from the mass region $114 \leq A \leq 200$ [5]. The results of the analysis confirmed the conclusions [1] that the density of levels excited in (n, γ) reactions deviates significantly from the exponential extrapolation [2] and manifested an unexpected effect—ρ is almost constant or slowly increases with $E_{\rm exc}$ in the interval from 1–2 to 3–4 MeV.

The only theoretical elaboration providing a similar result is the analysis by Ignatyuk [6] of the pairing-interaction effect on ρ. This analysis, performed within the generalized model of a superfluid nucleus, predicted a stepwise behavior of the level density due to breaking of nucleon pairs.

Unfortunately, the modern version of the generalized model of a superfluid nucleus [7] considers the pairing-interaction effect in terms of Bardeen–Cooper–Schrieffer theory [8] as a phase transition only between a purely boson and a purely fermion system. This condition cannot be realized in a nucleus because, at the energy of an expected phase transition (exceeding B_n), some part of Cooper pairs have already been broken. This effect is well known for a mixture of liquid He isotopes. The authors of [9] made an attempt at extrapolating this effect to a nucleus by using an extremely simple model and found that the energy and temperature T_c of a phase transition from a superfluid to a normal phase can be considerably less than a known thermodynamic value [8] $T_c = 0.567\delta$.

The conclusions drawn in [5] were confirmed by using a new probabilistic, model-independent method for simultaneously estimating basic parameters of cascade γ decay. An analysis of experimental data revealed that the cascade intensities $I_{\gamma\gamma}$ (3) observed for N energy intervals of intermediate levels and the experimental total radiative widths of capturing states,

$$\Gamma_\lambda = \langle \Gamma_{\lambda i} \rangle m_{\lambda i}, \tag{4}$$

combined with the physical constraints

$$\rho(\pi = +) > 0; \quad \rho(\pi = -) > 0, \tag{5}$$
$$\Gamma(E1) > 0; \quad \Gamma(M1) > 0$$

(separately for primary and secondary transitions) effectively restrict the interval of allowed level densities and partial radiative widths, which provides an explanation of the values of $\Gamma_\lambda^{\rm expt}$ and $I_{\gamma\gamma}^{\rm expt}$. It is implied in Eqs. (3) and (4) that the parameters under investigation can be expressed in terms of sums over m or n levels excited by the corresponding transitions and the mean (for this interval) partial widths. This approach is necessary for comparing experimental data and the results of the calculations.

At present, such an extraction of the most probable parameters of a cascade γ decay requires only a few assumptions concerning the spin dependence of ρ and the ratio of the energy dependences of the radiative strength functions for primary and secondary cascade transitions [10]. Moreover, the results of a simulation should be compared, first of all, with the sums $\rho(\pi = +) + \rho(\pi = -)$ and $f(E1) + f(M1)$. This compromising approach is due to a rather strong mutual correlation of deviations of the parameters from their most probable values. It can be seen from (3) that, in general, ρ and f values satisfying relations (3) and (4) can be determined only numerically by using some random simulations—i.e., via an iterative process. The possibility of realizing this procedure and its convergence to some narrow interval of ρ and f values were established in simulations [10] for a wide set of initial ρ and f values (some of them were quite unrealistic).

By way of example, Figs. 1 and 2 show the intervals of the most probable values of ρ and f for several nuclei. It should be noted, however, that, in contrast to [10], these results were obtained without using the assumption that $\rho(\pi = +) = \rho(\pi = -)$. Experimental cascade intensities employed in the simulations can be found elsewhere [11].

The intensities of the two-step cascades following thermal-neutron capture in nuclei from the region of the $4s$ resonance of the neutron strength function and the densities of levels excited by primary dipole transitions were analyzed by the algorithms developed in [5, 10]. The basic result of the analysis is that ρ is noticeably less than that which is predicted by the Fermi gas model [2] for $E_{\rm exc} \geq 1$ MeV in N-odd nuclei and for $E_{\rm exc} \geq 2$ MeV in N-even nuclei. The discrepancy is maximal at $E_{\rm exc} \sim 3$–4 MeV. The question of whether it is true for the total nuclear level

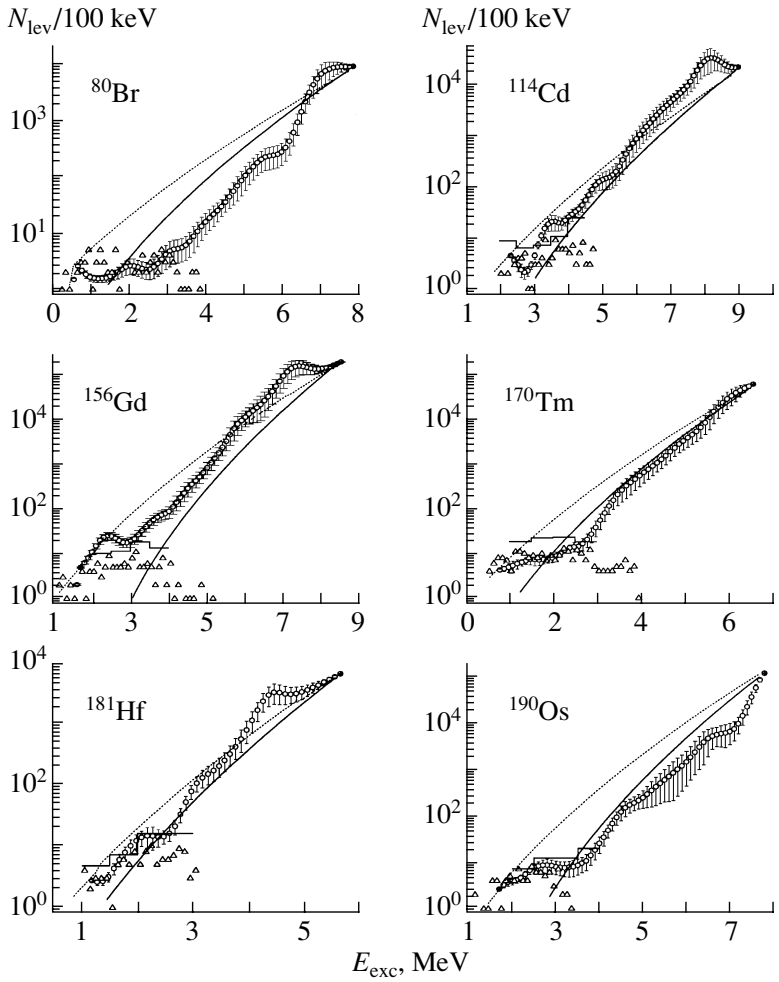

Fig. 1. Number of levels of both parities with errors (circles with bars) in ^{80}Br, ^{114}Cd, ^{156}Gd, ^{170}Tm, ^{181}Hf, and ^{190}Os. The histogram represents the data [5], while the triangles show the number of intermediate levels of intense cascades. The upper and lower curves represent the predictions of the models proposed in [2] and [6], respectively.

density (or this effect results from a strong selectivity of (n, γ) reactions) is still open.

In order to understand processes occurring in a nucleus at low excitation energies, serious theoretical investigations of nuclear properties at $E_{exc} >$ 1–2 MeV are nevertheless required. If the model proposed in [6] is valid, the description of nuclear properties at this excitation energy calls for a more correct treatment of pairing correlations than in the existing nuclear models. Most probably, this should be done for a bounded region of excitations because the pairing-interaction effect on nuclear properties may become weaker at low excitation energies because the Bogolyubov coefficients u and v are not equal to unity. It is obvious that the consequences of incorrectly treating the pairing interaction are not so dramatic at higher excitations.

If the hypothesis of a phase transition in a nucleus is valid, the energy of a captured neutron is shared not only among quasiparticle excitations but also among phonon-type excitations. It is possible that, at higher energies, there is a multiquasiparticle state whose wave function has a structure markedly different from the wave function for low-lying states and involves one or several phonons. According to [14], the fragmentation of so complicated a state must be very weak and its strength can be concentrated on one or a few neighboring levels. Possibly, this effect was observed in [15] as an equidistant spacing between intermediate levels or their multiplets of the most intense two-step cascades.

As can be seen from Fig. 2, a decrease in the level density is followed by an increase in the sum of the radiative strength functions for cascade transitions. On one hand, this means that the assumed influence of boson-type excitations manifests itself in the probability of the primary transition. On the other hand,

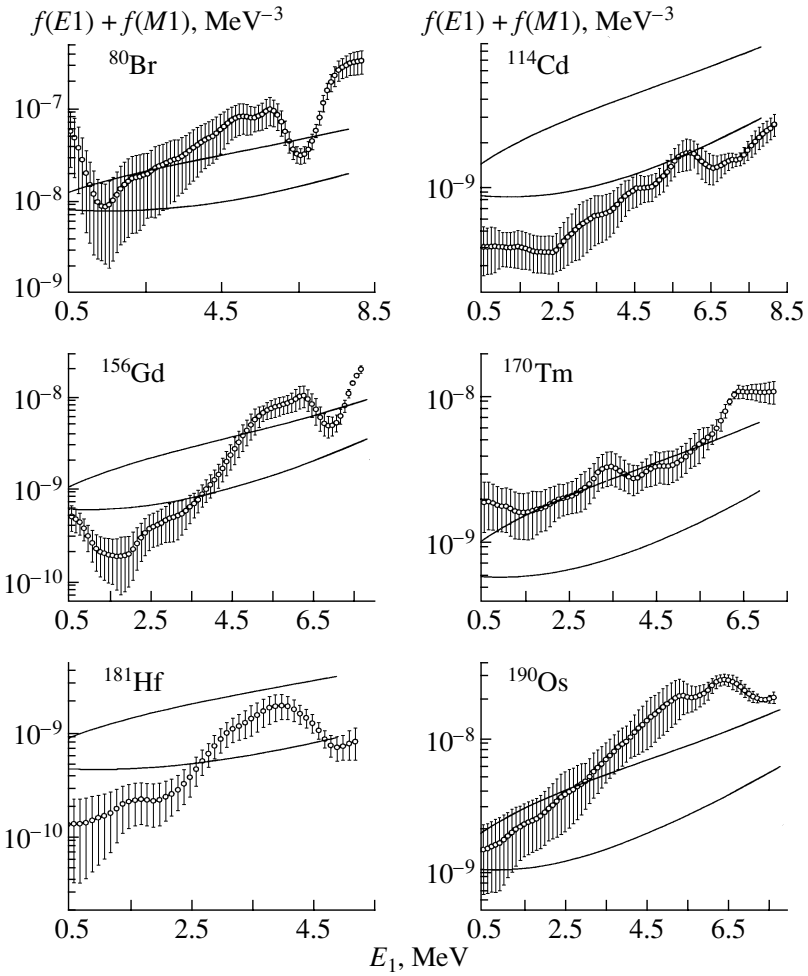

Fig. 2. Sum of the probable radiative strength functions for $E1$ and $M1$ transitions (with estimated errors) in the same nuclei as in Fig. 1. The upper and lower solid curves represent the predictions of the models from [15] and [14], respectively, the value of $f(M1) = \text{const}$ normalized to the experimental value being added here.

this explains the impossibility of observing this effect in experiments of other types.

The proposed picture of the processes occurring in a nucleus at excitation energy of a few MeV seems very preliminary. A further improvement of experimental techniques can make it more adequate, but the final conclusion on the dynamics of intranuclear processes can be obtained only upon a serious theoretical analysis or in the conjunction of it with the relevant experiments.

The data obtained can form a basis for developing new models of heavy nuclei for predicting at least the parameters of γ decays with a required accuracy as well as for better understanding processes that occur in nuclei at low excitation energies.

ACKNOWLEDGMENTS

This work was supported by the Russian Foundation for Basic Research (project no. 99-02-17863).

REFERENCES

1. V. A. Khitrov *et al.,* in *Proceedings of the International Symposium on Neutron-Capture Gamma-Ray Spectroscopy* (Plenum, New York, 1979), p. 655.
2. W. Dilg, W. Schantl, H. Vonach, and M. Uhl, Nucl. Phys. A **217**, 269 (1973).
3. C. F. Porter and R. G. Thomas, Phys. Rev. **104**, 483 (1956).
4. S. T. Boneva *et al.,* Nucl. Phys. A **589**, 293 (1995).
5. A. M. Sukhovoj and V. A. Khitrov, Yad. Fiz. **62**, 24 (1999) [Phys. At. Nucl. **62**, 19 (1999)].
6. A. V. Ignatyuk, in *Proceedings of the IAEA Consultants Meeting on the Use of Nuclear Theory in Neutron Nuclear Data Evaluation, Italy, 1976,* IAEA-190, Vol. 1, p. 211.
7. E. M. Rastopchin, M. I. Svirin, and G. N. Smirenkin, Yad. Fiz. **52**, 1258 (1990) [Sov. J. Nucl. Phys. **52**, 799 (1990)].
8. J. Bardin, L. Cooper, and J. Schrieffer, Phys. Rev. **108**, 1175 (1957).
9. S. T. Boneva, V. A. Khitrov, Yu. P. Popov, and

A. M. Sukhovoj, in *Proceedings of the 9th International Symposium on Capture Gamma-Ray Spectroscopy and Related Topics, Budapest, Hungary, 1996* (Springer-Verlag, Berlin, 1997), Vol. 1, p. 483.
10. E. V. Vasilieva, A. M. Sukhovoj, and V. A. Khitrov, Preprints Nos. R3–99-202, R3–99–203, OIYaI (Joint Institute for Nuclear Research, Dubna, 1999).
11. P. Axel, Phys. Rev. **126**, 683 (1962).
12. S. G. Kadmensky, V. P. Markushev, and V. I. Furman, Yad. Fiz. **37**, 581 (1983) [Sov. J. Nucl. Phys. **37**, 345 (1983)].
13. S. T. Boneva *et al.,* Yad. Fiz. **62**, 892 (1999) [Phys. At. Nucl. **62**, 832 (1999)].
14. L. A. Malov and V. G. Soloviev, Yad. Fiz. **26**, 729 (1977) [Sov. J. Nucl. Phys. **26**, 384 (1977)].
15. A. M. Sukhovoj and V. A. Khitrov, Izv. Akad. Nauk, Ser. Fiz. **61**, 2068 (1997).

Physics of Atomic Nuclei, Vol. 64, No. 7, 2001, pp. 1199–1205. From Yadernaya Fizika, Vol. 64, No. 7, 2001, pp. 1275–1280.

Proceedings of the International Conference "Nuclear Structure and Related Topics"

Gamma Deexcitation of the ^{180m}Ta Isomer*

V. G. Soloviev†, A. V. Sushkov, **and N. Yu. Shirikova**

Joint Institute for Nuclear Research, Dubna, Moscow oblast, 141980 Russia

Received October 25, 2000

Abstract—Vibrational states built on the $K^\pi = 9^-$ isomer and on the ground state ($K^\pi = 1^+$) in ^{180}Ta are calculated within the quasiparticle–phonon nuclear model using the ^{178}Hf nucleus as a core. A procedure for calculating the rates of K-allowed γ-ray transitions from vibrational states built on the isomer to those built on the ground state is presented. The probabilities of two-step processes consisting of a dipole excitation of the isomer and successive $E1$ and $E2$ transitions from them to vibrational states built on the ground state of the ^{180}Ta nucleus are calculated. Two-step transitions from the isomer to vibrational states below 2.7 MeV and to the vibrational states built on the ground state appear to be very weak. There are many $E1$ transitions from the vibrational states built on the isomer to the vibrational states built on the ground state. They are weak and cannot be responsible for the strong deexcitation of ^{180m}Ta in the relevant (γ, γ') reaction. A decisive role is played by collective $E2$ transitions from dipole excitations in several excitation energy intervals ranging between 2.7 and 4.0 MeV. These highly intense K-allowed two-step γ-ray transitions can be responsible for the strong deexcitation of the ^{180m}Ta state in the (γ, γ') reactions.

1. INTRODUCTION

The problem of the production and survival of the very long-lived isomeric state in the ^{180}Ta nuclide is a real challenge for the theory of nucleosynthesis. The isomeric state ^{180m}Ta identified as a $I^\pi K = 9^-9$ two-quasiparticle configuration has an energy of 75.3 keV and a half-life of 1.2×10^{15} yr, whereas the ground state of ^{180}Ta, with $I^\pi K = 1^+1$, has a half-life of only 8.1 h. Despite so long a half-life of the isomer, the existence of its sizable amount at present raises some questions. Indeed, after the birth of ^{180m}Ta, indirect transitions from this state to the ground state of ^{180}Ta seem possible. This may proceed via an excitation into a higher lying intermediate state due to γ capture and a subsequent decay to the short-lived ground state.

Intensive experimental efforts were devoted to studying the level structure of ^{180}Ta [1–3] and seeking γ transitions that link the isomer and the ground state. A depletion of ^{180m}Ta to the ground state in (γ, γ') reactions was studied in [4–8]. The activation function for the ^{180m}Ta$(\gamma, \gamma')^{180}$Ta reaction was measured in the energy range 2–7 MeV, and intermediate levels can be identified at 2.8 and 3.6 MeV [4]. Improved photoactivation experiments with ^{180m}Ta were performed at the Stuttgart Dinamitron facility by the Darmstadt–Karlsruhe–Munich–Stuttgart collaboration and succeeded in observing the depopulation of the isomer state down to bremsstrahlung-endpoint energies of about 1.1 MeV [9]. The depopulation of ^{180m}Ta was the subject of several investigations in Coulomb excitation experiments with heavy ions [10–12] and p and α beams [13].

Theoretical investigations, based on a two-quasiparticle-configuration picture, were conducted to seek γ-ray transitions linking the isomer and the ground state in ^{180}Ta, but without any success. Therefore, it seems promising to investigate γ-ray transitions linking the isomer and the ground state in ^{180}Ta by using collective (e.g., one- and two-phonon) configurations built on the isomer and on the ground state. These studies are performed within the quasiparticle–phonon nuclear model (QPNM) [14–16] by using the formalism developed in [17].

We assume the following picture of the two-step process of γ deexcitation of the isomer. At the first step, dipole transitions from the isomer ^{180m}Ta with $I^\pi K = 9^-9$ feed the dipole states built on it ($|\text{ism}\rangle \otimes |\text{vibr}\rangle$). At the second step, the states $|\text{ism}\rangle \otimes |\text{vibr}\rangle$ decay into various excited states of the type $|\text{grs}\rangle \otimes |\text{vibr}\rangle$—i.e., into vibrational states built on the ground state. After that, the last states decay into the ground state itself. These transitions seem to be the most important because they are of the most probable one-phonon-exchange type.

*This article was submitted by the authors in English.

†Deceased.

**e-mail: sushkov@thsun1.jinr.ru

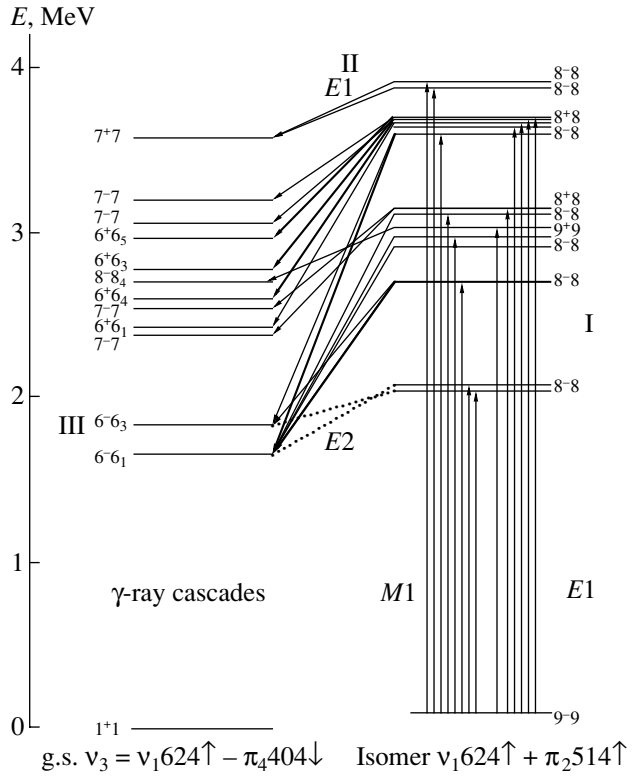

Fig. 1. Three steps of the deexcitation of ^{180m}Ta. The first step is the dipole excitation of the isomer. The second step is (thin lines) $E1$ or (thick lines and points) $E2$ transitions from the dipole vibrational states built on the isomer to the vibrational states built on the ground state. The third step is γ cascades involving many intermediate states and finally reaching the ground state.

2. BRIEF DESCRIPTION OF THE MODEL

The description of the QPNM can be found elsewhere [15, 16]. We briefly recall here the basic points of the model. The QPNM Hamiltonian in terms of nucleon variables contains average fields of a neutron and a proton system with the shape of the axisymmetric Woods–Saxon potential. As effective nucleon–nucleon forces, the QPNM Hamiltonian includes the monopole (Bardeen–Cooper–Schrieffer) pairing and isoscalar and isovector particle–hole (ph) and particle–particle (pp) interactions. The last terms have a separable form and are written as a series of multipoles and spin-multipoles.

To describe nonrotational states of an even–even nucleus, we use a trial wave function consisting of the sum of one- and two-phonon terms,

$$\Psi_n(\bar{\mu}^\pi,\sigma) = \Omega^+_{n\sigma}(\bar{\lambda}\bar{\mu})\Psi_0, \tag{1}$$

$$\Omega^+_{n\sigma}(\bar{\lambda}\bar{\mu}) = \sum_i R^n_i(\bar{\lambda}\bar{\mu})Q^+_{\bar{\lambda}\bar{\mu}i\sigma} \tag{2}$$

$$+\frac{1}{2}\sum_{\substack{g_5 g_6\\ \sigma_5\sigma_6}} S^{\bar{\mu}}_{g_5g_6}\delta_{\sigma_5\mu_5+\sigma_6\mu_6,\sigma\bar{\mu}}P^n_{g_5g_6}(\bar{\lambda}\bar{\mu})Q^+_{g_5\sigma_5}Q^+_{g_6\sigma_6},$$

where $g_5 = \lambda_5\mu_5 i_5$ and $g_6 = \lambda_6\mu_6 i_6$; the index $n = 1, 2, 3, \ldots$ numbers $\bar{\mu}^\pi$ states in accordance with their excitation energies; Ψ_0 is the phonon vacuum state and, at the same time, the wave function of the ground state of an even–even nucleus; and

$$S^{\bar{\mu}}_{g_5g_6} = (1+\delta_{g_5g_6})^{-1/2}[1+\delta_{\bar{\mu}0}(1-\delta_{\mu_5 0})]^{-1/2}.$$

We follow the procedure developed in [18] in describing two-quasiparticle configurations in odd–odd nuclei. The basic idea is to use the so-called "fragmented" phonons in the wave function of an excited state, in accordance with that suggested in [15]. The same procedure was used to describe low-energy dipole transitions in odd-mass deformed nuclei [19], as well as transitions to vibrational states built on isomers [17].

The wave function of a two-quasiparticle state consisting of one quasineutron and one quasiproton is

$$\alpha^+_{s_1\sigma_1}\alpha^+_{r_2\sigma_2}\Psi_0, \tag{3}$$

where the indices $s\sigma$ and $r\sigma$ stand for single-particle neutron and proton quantum numbers, respectively. Our trial wave function is

$$\Psi_n(K^\pi,\bar{\lambda}\bar{\mu}) \tag{4}$$
$$= \delta_{\bar{\sigma}\bar{\mu}+\sigma_1K_1+\sigma_2K_2,K}\Omega^+_{n\bar{\sigma}}(\bar{\lambda}\bar{\mu})\alpha^+_{s_1\sigma_1}\alpha^+_{r_2\sigma_2}\Psi_0,$$

where $\bar{\lambda}\bar{\mu}$ characterizes the operator $\Omega^+_{n\sigma}(\bar{\lambda}\bar{\mu})$ on the two-quasiparticle configuration. The normalization condition for (4) is

$$\delta_{\bar{\sigma}\bar{\mu}+\sigma_1K_1+\sigma_2K_2,K} \tag{5}$$
$$\times\{\sum_i (R^n_i(\bar{\lambda}\bar{\mu}))^2[1-\mathcal{L}(s_1\sigma_1,\bar{g}\bar{\sigma})-\mathcal{L}(r_2\sigma_2,\bar{g}\bar{\sigma})]$$
$$+\sum_{g_5\geq g_6}(P^n_{g_5g_6}(\bar{\lambda}\bar{\mu}))^2[1+\mathcal{K}^{\bar{\mu}}(g_5g_6)]\} = 1,$$

where $\bar{g} = \bar{\lambda}\bar{\mu}i$ and

$$\mathcal{L}(q_1\sigma_1,\bar{g}\bar{\sigma}) \tag{6}$$
$$= \sum_q\{(\tilde{\phi}^{\bar{g}}_{q_1q})^2\delta_{\sigma_1(K_1-K),\bar{\sigma}\bar{\mu}} + (\bar{\phi}^{\bar{g}}_{q_1q})^2\delta_{\bar{\sigma},\sigma_1}\delta_{K_1+K,\bar{\mu}}\}.$$

The $\mathcal{L}$ and $\mathcal{K}$ functions appearing in (5) and (6) take into account the Pauli blocking effect in, respectively, one- and two-phonon terms of the wave function (4).

The reduced probability of the $E\lambda$ transition from the two-quasiparticle state (3) to the excited state (4) has the form

$$B(E\lambda; I^\pi_{s_1r_2}K_{s_1r_2}\to I^\pi Kn(\bar{\lambda}\bar{\mu})) \tag{7}$$
$$= \langle I_{s_1r_2}\ K_{s_1r_2}\ \bar{\lambda}\ \pm\bar{\mu}|I\ K\rangle^2$$
$$\times|\sum_i R^n_i(\bar{\lambda}\bar{\mu})\mathcal{M}^{\rm ph}_i(E\bar{\lambda}\bar{\mu})|^2,$$

where $\mathcal{M}^{\rm ph}_i$ is the matrix element for the $E\lambda$ transition to the one-phonon state i. The reduced probability of the $M1$ transition has a similar form.

We assume that the isomer wave function is a pure two-quasiparticle one,

$$\Psi_{\rm is}(9^-) = \alpha^+_{s_1,+1}\alpha^+_{r_2,+1}\delta_{K_1+K_2,9}\Psi_0, \qquad (8)$$

with the one-quasineutron $s_1 = \nu 624\uparrow$ and one-quasiproton $r_2 = \pi 514\uparrow$ configurations. We consider only those vibrational states built on the isomer that have the projections $K_0 \le 9$ onto the symmetry axis and which are excited by $M1$ and $E1$ transitions from the isomer. We do not take into account the vibrational states built on the $K_0 > 9$ isomer because there are no γ transitions from these states to the vibrational states built on the ground state with an energy below 4 MeV. The wave function of the state $|{\rm ism}\rangle \otimes |{\rm vibr}\rangle$ is

$$\Psi_{n_0}(K_0^{\pi_0}, \lambda_0\mu_0) = \delta_{-\mu_0+K_1+K_2,K_0} \qquad (9)$$
$$\times\Omega^+_{n_0,\sigma_0=-1}(\lambda_0\mu_0)\alpha^+_{s_1,+1}\alpha^+_{r_2,+1}\Psi_0$$

with $\lambda_0\mu_0 = 21, 30$, and 31.

The ground state of ^{180}Ta with quantum numbers $K^{\pi_{\rm g.s}}_{\rm g.s.} = 1^+$ is identified as a $\nu 624\uparrow - \pi 404\downarrow$ two-quasiparticle configuration. Its wave function is supposed to be

$$\Psi_{\rm g.s}(1^+) = \alpha^+_{s_1,+1}\alpha^+_{r_4,-1}\delta_{K_1-K_4,1}\Psi_0, \qquad (10)$$

where $s_1 = \nu 624\uparrow$ and $r_4 = \pi 404\downarrow$. The wave function of the state $|{\rm grs}\rangle \otimes |{\rm vibr}\rangle$ is assumed to have the form

$$\Psi_{n_f}(K_f^{\pi_f}, \lambda_f\mu_f) = \delta_{\mu_f+K_1-K_4,K_f} \qquad (11)$$
$$\times\Omega^+_{n_f,\sigma_f=+1}(\lambda_f\mu_f)\alpha^+_{s_1,+1}\alpha^+_{r_4,-1}\Psi_0.$$

The operator $\Omega^+_{n\sigma}(\bar\lambda\bar\mu)$ is given by (2), while $\lambda_f\mu_f = 55, 65, 66, 76$, and 77.

Let us consider $E\lambda$ transitions from states (9) to the $K_f \le K_0$ states (11). The $E\lambda$ transitions to $K_f > K_0$ states are very weak, and we do not take them into account. The reduced $E\lambda$ transition probability has the form

$$B(E\lambda\mu, \sigma = -1; I_0^{\pi_0}K_0n_0(\lambda_0\mu_0) \to I_f^{\pi_f}K_fn_f(\lambda_f\mu_f)) = \langle I_0\ K_0\ \lambda\ -\mu | I_f\ K_f\rangle^2 \qquad (12)$$
$$\times|(\Psi^*_{n_f}(K_f^{\pi_f}, \lambda_f\mu_f)\mathcal{M}^{\rm sp}(E\lambda, \mu = K_0 - K_f)\Psi_{n_0}(K_0^{\pi_0}, \lambda_0\mu_0))|^2,$$

where $\mathcal{M}^{\rm sp}$ is the single-particle matrix element of the $E\lambda$ operator. Equation (12) involves three terms. Let us write them in a symbolic form,

$$B(E\lambda\mu, \sigma = -1; I_0^{\pi_0}K_0n_0(\lambda_0\mu_0) \to I_f^{\pi_f}K_fn_f(\lambda_f\mu_f)) \qquad (13)$$
$$= |({\rm exchange\ of\ quasiproton}) + \sum_{i_fi_0} R^{n_f}_{i_f}R^{n_0}_{i_0}\mathcal{M}_{\rm I} + \sum_{i_fi_0i_1} R^{n_f}_{i_f}P^{n_0}_{i_0i_1}\mathcal{M}_{\rm II}|^2.$$

The first term in (13) is the contribution of the direct $E\lambda$ transition between two-quasiparticle components of the initial and final states. Only proton single-particle states participate in $E\lambda$ transitions. The second term in (13) is the contribution of the transition between one-phonon components. The third term in (13) is the contribution of the transition between the two-phonon components of the initial wave function and the one-phonon components of the final wave function. The quantities $\mathcal{M}_{\rm I}$ and $\mathcal{M}_{\rm II}$ are the corresponding matrix elements of the $E\lambda$ operator. There are no $E\lambda$ transitions between the one-phonon components of the initial state $|{\rm ism}\rangle \otimes |{\rm vibr}\rangle$ and the two-phonon components of the final state $|{\rm grs}\rangle \otimes |{\rm vibr}\rangle$ at energies below 4 MeV.

As was mentioned in the Introduction, we consider the transition from the isomer to the ground state in the reaction $^{180m}{\rm Ta}(\gamma,\gamma')^{180}{\rm Ta}$ as a three-step process. The three steps are shown in Fig. 1. According to our calculation, the rates of the $M1$ transitions from the states $|{\rm ism}\rangle \otimes |{\rm vibr}\rangle$ to the states $|{\rm grs}\rangle \otimes |{\rm vibr}\rangle$ in ^{180}Ta are very low; for this reason, we do not take these transitions into account.

3. NUMERICAL RESULTS AND DISCUSSION

In the present calculations, we use the even–even nucleus ^{178}Hf as a core; i.e., the properties of phonons are calculated for that nucleus [20].

Calculating the $E\lambda$ transition rate, we take into account γ transitions between all relevant rotational states. The intensities of $E1$ and $E2$ transitions between the rotational states are three times as large as the intensity between the heads of the rotational bands.

We calculate only the probabilities of K-allowed γ transitions. The Coriolis interaction is not taken into account because it does not affect the total transition strength.

We compute the $B(E1)$ and $B(M1)$ values and the intensities per second W of the corresponding transitions from the isomer states (8) to states (9). We also compute the $B(E1)$ ($\Delta K = 1$) and $B(E2)$ values and the relevant intensities per second for transitions from states (9) to states (11). The corresponding formulas are

$$W(E1) = 1.59 \times 10^{15} E_\gamma^3 B(E1), \qquad (14)$$

$$W(E2) = 1.22 \times 10^{9} E_\gamma^5 B(E2),$$

$$W(M1) = 1.76 \times 10^{13} E_\gamma^3 B(M1).$$

Here, E_γ is in MeV, $B(E\lambda)$ is in units of e^2 fm$^{2\lambda}$, and $B(M1)$ is in units of μ_N^2. The total intensities of the relevant γ transitions per second for two-step cascades are

$$W(\text{IS}\rightarrow\text{vib.st. on IS}(I_0^{\pi_0} K_0 n_0, \lambda_0\mu_0)\rightarrow\text{vib.st. on g.s.}(I_f^{\pi_f} K_f n_f, \lambda_f\mu_f))$$

$$= \left(\frac{1}{W(\text{ IS}\rightarrow\text{ vib.st. on IS})} + \frac{1}{W(\text{ vib. st. on IS}\rightarrow\text{ vib. st. on g.s.})}\right)^{-1}. \qquad (15)$$

In our case, the intensities of the first step are the intensities of the $M1$ and $E1$ transitions from the isomer to the dipole excitations built on the isomer. The intensities of the second step are the intensities of the $E1$ and $E2$ transitions from the $|\text{ism}\rangle \otimes |\text{vibr}\rangle$ states to $|\text{grs}\rangle \otimes |\text{vibr}\rangle$. If the first transition is fast and if the second transition is slow, the intensity of the two-step process is approximately equal to the intensity of the slow transition. For the majority of the two-step processes being considered, the intensity W of the $E1$ or the $M1$ transition from the isomer to the $|\text{ism}\rangle \otimes |\text{vibr}\rangle$ states in the energy range 2–4 MeV is much greater than the intensity W of the $E1$ or the $E2$ transition from the $|\text{ism}\rangle \otimes |\text{vibr}\rangle$ state to the $|\text{grs}\rangle \otimes |\text{vibr}\rangle$ one. Therefore, the intensities of the two-step processes are virtually identical to the intensities $W(E1)$ or $W(E2)$ of the transitions from the vibrational states built on the isomer to the vibrational states built on the ground state. The intensities of the two-step processes summed in bins of 0.1 MeV are shown in Fig. 2.

There are very many $E1$ and $E2$ transitions between the $|\text{ism}\rangle \otimes |\text{vibr}\rangle$ and $|\text{grs}\rangle \otimes |\text{vibr}\rangle$ states. The majority of these transitions are very weak. Nevertheless, there are many relatively weak and several strong transitions. In the table, we therefore give the $B(E1)$ and $B(E2)$ values in the excitation energy range 2.4–4.0 MeV that are summed in bins of 0.1 MeV. In the table, we include the $B(E1)$ values larger than $10^{-11} e^2$ fm^2 and the $B(E2)$ values larger than 10^{-3} s.p.u. There are also very many γ transitions with $B(E1) < 10^{-11} e^2$ fm^2 and $B(E2) < 10^{-3}$ s.p.u.

The rates of $\Delta K = 0$ $M1$ and $E1$ transitions are very low. Therefore, they are not included in the numerical results presented in the table or in the figures.

Let us consider the $E1$, $\Delta K = 1$ transitions from the dipole states built on the isomer to the vibrational states built on the ground state. These $E1$ transitions, with $B(E1) > 10^{-11} e^2$ fm^2, proceed only from a small part (10–20%) of the dipole excitations to one to six final states built on the ground state. The number of nonrotational initial states in the energy interval of width 0.1 MeV varies from one to five. In several cases, the number of $E1$ transitions from the energy range of width 0.1 MeV is quite large. For example, the number of $E1$ transitions from the $K_0^{\pi_0} = 8^-$ states in the energy range 3.7–3.8 MeV to the $K_f^{\pi_f} = 7^-$ states is equal to 18. The $E1$ strength for the transitions from the $K_0^{\pi_0} = 9^+(\lambda_0\mu_0 = 30)$ states in the energy range 2–4 MeV to the $K_f^{\pi_f} = 8^-(\lambda_f\mu_f = 77)$ states is equal to $2.5 \times 10^{-7} e^2$ fm^2. The $E1$ strength for the transitions from the $K_0^{\pi_0} = 8^+(\lambda_0\mu_0 = 31)$ states in the energy range 2–4 MeV to the $K_f^{\pi_f} = 7^-(\lambda_f\mu_f = 76)$ states is $10^{-5} e^2$ fm^2. The $K_0^{\pi_0} = 8^-(\lambda_0\mu_0 = 21) \rightarrow K_f^{\pi_f} = 7^+(\lambda_f\mu_f = 66)$ transitions are weak. The $E1$ strength summed in the energy range 2.0–3.8 MeV is $5 \times 10^{-10} e^2$ fm^2. All the $E1$ transitions from the dipole states built on the isomer to the vibrational states built on the ground state play a minor role. These transitions proceed through the first and second terms in expression (13); therefore, they are weak.

As can be seen from the table, the largest $B(E1)$ values are 10^{-6}–$10^{-8} e^2$ fm^2. According to experimental data, the $B(E1)$ values for the transitions between one-phonon components in the nuclei ^{168}Er [21] and ^{156}Gd [22] are 10^{-4}–$10^{-7} e^2$ fm^2. According to the calculations within the QPNM [23, 24], similar small $B(E1)$ values are obtained for $E1$ transitions between one-phonon states in many nuclei. The computed $B(E1)$ values for the transitions from the dipole excitations built on the isomer to the states $|\text{grs}\rangle \otimes |\text{vibr}\rangle$ are smaller than the $B(E1)$ values for transitions between one-phonon states. These small $B(E1)$ values cannot be responsible for the fast de-

excitation of the isomeric state ^{180m}Ta in the relevant (γ,γ') reaction.

The $E2$ transitions from the states $|\mathrm{ism}\rangle \otimes |\mathrm{vibr}\rangle$ proceed through the second and the third term in expression (13). The third term is very important. According to our present calculations, the $B(E2)$ value for the $E2$ transitions from the initial $K_0^{\pi_0} = 8^-(\lambda_0\mu_0 = 21)$ 2.71-MeV state to the final $K_f^{\pi_f} = 6^-(\lambda_f\mu_f = 55)$ states at energies 1.7 and 2.2 MeV (including $E2$ transitions between rotational levels) is 3 s.p.u. So strong an $E2$ transition is due to the large two-phonon component $\{(22)_1,(33)_2\}$ in the wave function of the initial state. The value of $B(E2) = 5.25$ s.p.u. for the transitions from the three initial $K_0^{\pi_0} = 8^+(\lambda_0\mu_0 = 31)$ states in the energy range 3.66–3.67 MeV to the four final $K_f^{\pi_f} = 6^+(\lambda_f\mu_f = 65)$ states in the energy range 2.4–3.0 MeV and relevant transitions between rotational levels. The two-phonon components $\{(22)_1,(43)_1\}$ and $\{(22)_2,(43)_1\}$ are responsible for these very strong $E2$ transitions. There are many $E2$ transitions with $B(E2)$ in the range from 0.1 to 1.4 s.p.u. and very many weak transitions.

Collective $E2$ transitions from two-phonon components of the wave functions of the initial states play such an important role owing to the gamma-vibrational $(22)_1$ or $(22)_2$ phonon. These strong $E2$ transitions demonstrate a very important role of the two-phonon components of the excited states built on the isomer.

Below 2.4 MeV, there are a few $E1$ transitions with W values equal to 10^7 s^{-1} or less. All these γ transitions proceed through very small components of the initial-state wave functions.

The high intensities of the two-step processes from the isomer to the $K_0^{\pi_0} = 8^\pm$ states and to the $K_f^{\pi_f} = 6^\pm$ states built on the ground state are displayed in Fig. 2 as a histogram. There are very intense two-step processes in the excitation energy intervals 2.7–2.8, 2.9–3.0, 3.1–3.5, 3.6–3.7, and 3.8–4.0 MeV. The peaks of this distribution correspond to the strong $B(E2)$ transitions shown in the table.

The running sum of the intensities per second of the two-step processes consisting of the dipole excitations of the isomer and further $E2$ transitions to the states $|\mathrm{grs}\rangle \otimes |\mathrm{vibr}\rangle$ is also given in Fig. 2. This running sum in the energy interval 2.7–2.8 MeV increases by a factor of 500 in relation to its value for energies below 2.7 MeV. The running sum increases by an order of magnitude from 2.8 MeV to 3.6 MeV. Such high intensities of the two-step process can be responsible for a strong deexcitation of ^{180m}Ta in the relevant (γ,γ') reaction.

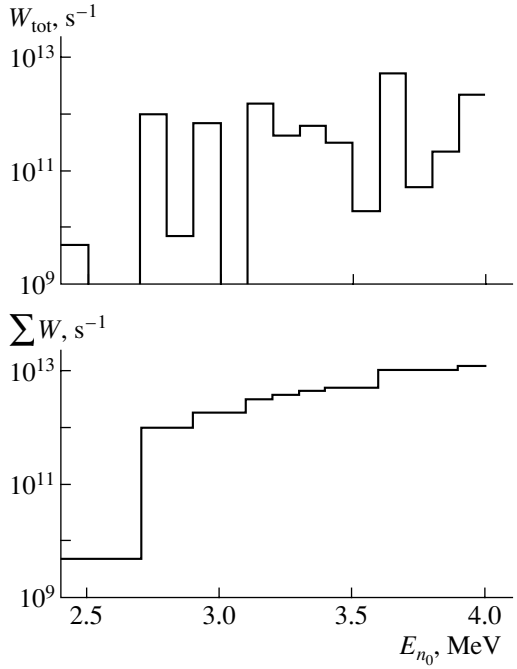

Fig. 2. Computed high intensities W_{tot} per second of the two-step transitions from the isomer to the dipole excitations and from the dipole excitations built on the isomer to the vibrational states built on the ground state in the 2.4–4.0 MeV excitation-energy range. The displayed results represent the intensities summed in a bin of 0.1 MeV (upper panel) and the running sum of them (lower panel).

As soon as the states $|\mathrm{grs}\rangle \otimes |\mathrm{vibr}\rangle$ in ^{180}Ta are populated, the third step of the process starts. Probably, there are several γ cascades from these states to many intermediate states and finally to the ground state of ^{180}Ta. It is possible that γ cascades proceed through strong K-mixed states at fairly low excitation energies. In any case, the γ transitions finally reach the ground state.

We consider backward γ transitions from the vibrational state built on the ground state, including the vibrational states populated from the vibrational states built on the isomer, to the vibrational states built on the isomer. According to our estimates, backward γ transitions from the vibrational states below 3 MeV to the vibrational states built on the isomer are very weak.

Our final conclusions are the following:

(i) There is strong deexcitation of the isomer ^{180m}Ta in the relevant (γ,γ') reaction by the three-step process. Strong two-step γ transitions are determined by the fast dipole excitation of the isomer through the one-phonon components of the vibrational states built on the isomer, as a first step, and the successive collective $E2$ transitions from the two-phonon components of these states to the vibrational

Computed $B(E1)$ and $B(E2)$ values for transitions from the vibrational states that occur at energy E and which are built on the $K^\pi = 9^-$ isomer to the vibrational states built on the $K^\pi = 1^+$ ground state of ^{180}Ta.

E, MeV	$B(E1; K_0^{\pi_0}(\lambda_0\mu_0) \to K_f^{\pi_f}(\lambda_f\mu_f))$, e^2 fm^2				$B(E2; K_0^{\pi_0}(\lambda_0\mu_0) \to K_f^{\pi_f}(\lambda_f\mu_f))$, s.p.u.		
	$9^+(30) \to 8^-(77)$	$8^+(31) \to 7^-(76)$	$8^-(21) \to 7^+(66)$	total	$8^+(31) \to 6^+(65)$	$8^-(21) \to 6^-(55)$	total
2.4–2.5	–	–	–	–	–	0.06	0.06
2.5–2.6	–	–	–	–	–	–	–
2.6–2.7	–	4×10^{-8}	–	4×10^{-8}	–	–	–
2.7–2.8	2×10^{-7}	2×10^{-8}	1×10^{-11}	2.2×10^{-7}	–	3.0	3.0
2.8–2.9	3×10^{-9}	–	–	3×10^{-8}	–	0.11	0.11
2.9–3.0	–	–	2×10^{-10}	2×10^{-10}	–	1.4	1.4
3.0–3.1	4×10^{-8}	2×10^{-7}	–	2.4×10^{-7}	–	–	–
3.1–3.2	1×10^{-8}	7×10^{-6}	5×10^{-11}	7×10^{-6}	4×10^{-3}	0.71	0.71
3.2–3.3	–	–	–	–	–	0.14	0.14
3.3–3.4	–	–	5×10^{-11}	5×10^{-11}	–	0.14	0.14
3.4–3.5	–	–	3×10^{-11}	3×10^{-11}	9×10^{-3}	0.05	0.06
3.5–3.6	–	–	1×10^{-10}	1×10^{-10}	0.04	0.02	0.06
3.6–3.7	–	6×10^{-9}	1×10^{-10}	6×10^{-9}	5.25	0.47	5.72
3.7–3.8	–	2×10^{-6}	–	2×10^{-6}	0.47	–	0.47
3.8–3.9	–	7×10^{-7}	–	7×10^{-7}	0.008	0.13	0.014
3.9–4.0	–	–	1×10^{-8}	1×10^{-8}	0.002	0.07	0.072

states built on the ground state, as a second step. Several γ-ray cascades from the vibrational states built on the ground state to many intermediate states finally reach the ground state of ^{180}Ta. This is the third step. The strong deexcitation of the isomer ^{180m}Ta in the (γ, γ') reaction is due to collective $E2$ transitions from the vibrational states built on the isomer to the vibrational states built on the ground state.

(ii) Very large probabilities per second of the two-step process via intermediate states that occur near 2.7 and 3.6 MeV and which are built on the isomer generally agree with the deexcitation of the isomer in the (γ, γ') reaction observed in [4].

(iii) The probability of deexcitation of ^{180m}Ta from the dipole excitations built on it below 2.7 MeV is very weak. A strong deexcitation of the isomer occurs in several energy intervals from 2.7 to 4.0 MeV.

(iv) Since the present analysis employs the phonons calculated for the ^{178}Hf nucleus, all constants are fixed (see [20]) and there are no free parameters in our calculations.

ACKNOWLEDGMENTS

We are grateful to Ch. Briançon, N. Lo Iudice, and V. Ponomarev for stimulating discussions.

REFERENCES

1. E. Warde, G. J. Costa, D. Magnac, *et al.,* Phys. Rev. C **27**, 98 (1983).
2. R. A. Dewberry and R. A. Naumann, Phys. Rev. C **28**, 2259 (1983).
3. G. D. Dracoulis, S. M. Mullins, F. G. Kondev, *et al.,* Phys. Rev. C **58**, 1444 (1998).
4. C. B. Collins *et al.,* Phys. Rev. C **42**, R1813 (1990).
5. Zs. Nemeth, Phys. Rev. C **45**, 467 (1992).
6. J. J. Carrol, C. B. Collins, P. von Neumann-Cosel, *et al.,* Phys. Rev. C **45**, 470 (1992).
7. A. G. Belov, Yu. P. Gangrsky, A. P. Tonchev, and P. Zuzaan, Hyperfine Interact. **107**, 167 (1997).
8. S. A. Karamian, C. B. Collins, J. J. Carroll, and J. Adam, Phys. Rev. C **57**, 1812 (1998).
9. U. Kneissl, in *Proceedings of WE–Heraues Seminar "Exotic High-Spin Isomers in Heavy Deformed Nuclei," Bad Honnef, 1998*.
10. C. Schlegel, P. von Neumann-Cosel, F. Neumeyer, *et al.,* Phys. Rev. C **50**, 2198 (1994).

11. P. von Neumann-Cosel *et al.,* Nucl. Phys. A **621**, 278c (1997).
12. M. Loewe *et al.,* Z. Phys. A **356**, 9 (1996).
13. M. Schumann, F. Käppeler, R. Böttger, and H. Schlölermann, Phys. Rev. C **58**, 1790 (1998).
14. V. G. Soloviev, Fiz. Élem. Chastits At. Yadra **9**, 860 (1978) [Sov. J. Part. Nucl. **9**, 343 (1978)].
15. V. G. Soloviev, *Theory of Atomic Nuclei: Quasiparticles and Phonons* (Institute of Physics, Bristol, 1992).
16. V. G. Soloviev, A. V. Sushkov, and N. Yu. Shirikova, Fiz. Élem. Chastits At. Yadra **25**, 377 (1994) [Phys. Part. Nucl. **25**, 157 (1994)].
17. V. G. Soloviev, Nucl. Phys. A **633**, 247 (1998).
18. V. G. Soloviev, Yad. Fiz. **40**, 1163 (1984) [Sov. J. Nucl. Phys. **40**, 740 (1984)].
19. V. G. Soloviev, A. V. Sushkov, N. Yu. Shirikova, and N. Lo Iudice, Nucl. Phys. A **613**, 45 (1997).
20. V. G. Soloviev, A. V. Sushkov, and N. Yu. Shirikova, Yad. Fiz. **60**, 1754 (1997) [Phys. At. Nucl. **60**, 1599 (1997)].
21. P. Petkov, W. Andrejtscheff, J. Copnell, and S. J. Robinson, Nucl. Phys. A **533**, 49 (1991).
22. J. Klora *et al.,* Nucl. Phys. A **561**, 1 (1993).
23. V. G. Soloviev, A. V. Sushkov, and N. Yu. Shirikova, J. Phys. G **20**, 113 (1994).
24. V. G. Soloviev, A. V. Sushkov, and N. Yu. Shirikova, Nucl. Phys. A **568**, 244 (1994).

Physics of Atomic Nuclei, Vol. 64, No. 7, 2001, pp. 1206–1209. From Yadernaya Fizika, Vol. 64, No. 7, 2001, pp. 1281–1284.

Proceedings of the International Conference "Nuclear Structure and Related Topics"

Toward Isovector $M1$ Transitions in Odd–Odd $N = Z$ Nuclei*

A. F. Lisetskiy**, **C. Frießner, A. Schmidt, I. Schneider, N. Pietralla**[1)], **P. von Brentano, R. V. Jolos**[2)], **T. Otsuka**[3)], **T. Sebe**[3)], **and Y. Utsuno**[3)]

Institut für Kernphysik, Universität zu Köln, Germany

Received October 25, 2000

Abstract—Isovector $M1$ transitions between low-lying $T = 1$ and $T = 0$ states in odd–odd $N = Z$ nuclei are discussed. The data on low-spin states in the odd–odd nuclei ^{46}V and ^{50}Mn investigated with the ^{46}Ti$(p, n\gamma)^{46}$V and ^{50}Cr$(p, n\gamma)^{50}$Mn fusion evaporation reactions at the FN–TANDEM accelerator in Cologne are reported. A simple explanation of the enhancement of the $M1$ transitions is given in terms of quasideuteron configurations. The fragmentation of the strong $M1$ transitions is shown to be due to the coupling of the two-particle configurations to the rotating core. © *2001 MAIK "Nauka/Interperiodica".*

1. INTRODUCTION

Investigation of the proton–neutron interaction in different isospin channels is one of the most active areas of current research in nuclear structure physics (see [1] and references therein). This direction is naturally related to the $N = Z$ nuclei, where the proton–neutron pairing is expected to play a much more important role as in $N > Z$ nuclei. The odd–odd $N = Z$ nuclei are especially interesting objects. In these nuclei, the $T = 0$ and $T = 1$ states are almost degenerate, which makes it convenient to study their properties by means of γ-ray spectroscopy. As was recently shown [2, 3], the phenomenon of degeneracy of the $T = 0$ and $T = 1$ states means that in odd–odd $N = Z$ nuclei the symmetry and pairing energies are equal in magnitude, i.e., almost exactly cancel each other. Another interesting phenomenon is an occurrence of very strong $M1$ transitions in odd–odd $N = Z$ nuclei. The enhancement of $M1$ transitions in near-spherical odd–odd $N = Z$ nuclei was recently understood to be due to the positive interference of orbital and spin parts of $M1$ matrix elements for two-nucleon (one proton and one neutron) configurations in single $j = l + 1/2$ orbital [4]. The fragmentation of this strength in deformed odd–odd $N = Z$ nuclei can be understood as the coupling of these configurations to the axially symmetric rotor [5].

2. REGULARITIES FOR $M1$ TRANSITIONS IN ODD–ODD $N = Z$ NUCLEI

The interesting properties of the odd–odd $N = Z$ nuclei mentioned in the previous section motivate the study of the $T = 0$ and $T = 1$ states in heavy odd–odd $N = Z$ nuclei. Recently, the low-spin structure of the odd–odd $N = Z$ nucleus ^{54}Co was investigated up to an excitation energy of 4 MeV [6].

To get a qualitative understanding of the structure of the low-lying states in ^{54}Co, we have performed spherical-shell-model calculations. With the calculated $B(E2)$ and $B(M1)$ values, we can reproduce the new experimental branching ratios and $E2/M1$ mixing ratios.

It is interesting to note that the $M1$ strengths are found to be very large in the shell-model calculations and the $\left[\pi(f_{7/2}^{-1}) \times \nu(f_{7/2}^{-1})\right]_{J,T}$ configurations dominate in the wave functions of the low-lying states in ^{54}Co. To get a feeling of how strong realistic $M1$ transitions could be in ^{54}Co, we have supposed that $B(E2; 2_1^+ \to 0_1^+)$ values for the nuclei belonging to one isospin triplet, e.g., for ^{54}Fe, ^{54}Co, and ^{54}Ni, are rather similar. Then (see for details [6]) using the known $B(E2; 2_1^+ \to 0_1^+)$ value for ^{54}Fe and the intensity ratio $I(2_1^+ \to 0_1^+)/I(2_1^+ \to 1_1^+)$ for the ^{54}Co nucleus, we can get the value of $M1$ $2_1^+ \to 1_1^+$ transition strength of 4.2 μ_N^2, which is in very good agreement with the shell-model value of 4.17 μ_N^2. Furthermore, we found that the shell model predicts very strong $M1$ $0_1^+ \to 1_1^+$ transition with the strength of 12 μ_N^2.

To get an understanding of the phenomenon, we have analyzed the known experimental data for odd–odd $N = Z$ nuclei and a simple model was proposed

*This article was submitted by the authors in English.

[1)]Wright Nuclear Structure Laboratory, Yale University, New Haven, USA.

[2)]Bogolyubov Laboratory of Theoretical Physics, JINR, Dubna, Russia.

[3)]Department of Physics, University of Tokyo, Hongo, Bunkyo-ku, Japan.

**e-mail: lis@ikp.uni-koeln.de

for the interpretation of the data [4]. We have found that some of the odd–odd $N = Z$ nuclei, as, e.g., ^{6}Li, ^{10}B, ^{18}F, ^{22}Na, ^{26}Al, and ^{42}Sc, exhibit very strong isovector $M1$ transitions between low-lying states with quantum numbers $(J_i^\pi, T) = (0_1^+, 1)$ and $(1_1^+, 0)$, while other odd–odd $N = Z$ nuclei, as, e.g., ^{14}N, ^{30}P, ^{34}Cl, ^{38}K, have considerably weaker transitions, in some cases with almost vanishing $M1$ strengths. We have shown that the strong $M1$ transitions are due to the one-proton one-neutron configurations within the single-j orbital with "spin-up" orientation ($j = l + 1/2$). In generalization of the deuteron case, we denoted such configurations as quasideuteron configurations. In other cases ("spin-down", $j = l - 1/2$), $M1$ strengths vanish due to the destructive interference of the orbital and spin parts of the matrix elements of $M1$ transition operator:

$$B(M1; 0^+ \to 1^+) = \frac{3}{4\pi} j(j+1) \left(g_p^j - g_n^j \right)^2 \quad (\mu_N^2), \tag{1}$$

where

$$g_p^j - g_n^j = \frac{l + 4.706}{j} \quad \text{for} \quad j = l + 1/2$$

and

$$g_p^j - g_n^j = \frac{l - 3.706}{j+1} \quad \text{for} \quad j = l - 1/2.$$

The results of calculations using (1) and the experimental data are given in [4]. For spherical nuclei like ^{6}Li, ^{18}F, and ^{42}Sc, the total large $M1$ strength is concentrated in one 1_1^+ state, while in other nuclei which are deformed it is distributed among several low-lying 1^+ states. To understand the fragmentation, we have considered another model which we discuss in the following section.

3. DISTRIBUTION OF QUASIDEUTERON $M1$ STRENGTHS

It was shown already in the 1960s that the symmetric-core collective model can explain quite successfully the low-lying level structure of odd–odd nuclei in the *sd* shell [7, 8]. However, the available experimental data at that moment were not sufficient to investigate $M1$ transitions. Here, we applied the simplified version of this model called rotor plus quasideuteron model [5] in order to explain the distribution of the strengths of isovector $M1$ transitions between low-lying states in odd–odd $N = Z$ nuclei. The basic assumption of our approximation is that one has one proton and one neutron outside a deformed rotating core. Then, the model basis is taken to be similar to the one for the *rotor plus particle* model in a strong-j-coupling approximation [9]:

$$|JMKT\rangle = \sum_{R,J_s} \sqrt{\frac{2(2R+1)}{2J+1}} C^{JK}_{R0J_sK} \left[|R\rangle \otimes |J_s\rangle \right]^{JT}_{MK}, \tag{2}$$

where the single-particle wave function $|J_s\rangle$ is to be replaced with the two-particle (one proton and one neutron) wave function $|J_q\rangle$ of the following form:

$$|J_q\rangle \equiv |J_q M_q K T\rangle = \sum_{j_p, j_n} \chi^{\Omega_p}_{j_p} \chi^{\Omega_n}_{j_n} C^{J_qK}_{j_p\Omega_p j_n\Omega_n} \left[|j_p\rangle \otimes |j_n\rangle \right]^{J_qT}_{M_q}, \tag{3}$$

where Ω_p (Ω_n) is the Nilsson asymptotic quantum number of angular-momentum projection onto the symmetry axis for odd proton (neutron). The χ^Ω_j coefficients (see [10]) are projection amplitudes of the Nilsson basis onto the spherical basis, $C^{J_qK}_{j_p\Omega_p j_n\Omega_n}$ are Clebsch–Gordan coefficients, T is isospin, K is total angular-momentum projection on the symmetry axis, and R is angular momentum of the core. Using wave functions (2) defined in the laboratory frame and expressed in terms of spherical shell-model weak-coupled $[|j_p\rangle \otimes |j_n\rangle]^{J_qT}_{M_q}$ configurations, we have calculated $M1$ reduced matrix elements [5]. We have obtained the following analytical expressions for the $B(M1; J_i \to J_f)$ values:

$$B(M1; J_i, K = 0 \to J_f, K) = \frac{3}{4\pi} \left[C^{J_fK}_{J_i01K} \sum_j \chi^\Omega_j \chi^{\Omega'}_j C^{j\Omega'}_{j\Omega 1K} \sqrt{(2j+1)j(j+1)} \times (g_p^j - g_n^j) \right]^2 (\mu_N^2), \tag{4}$$

where $g_p^j - g_n^j$ is given by (1), $\Omega' = |K| \pm |\Omega_g|$, and Ω_g is the Nilsson asymptotic quantum number of single-particle angular-momentum projection which is used for the building of the $K^\pi = 0^+$ band.

It is interesting to note that, for the 0^+ to 1^+ transitions, taking just one of the spherical orbitals in (4) (for example, quasideuteron $j = l + 1/2$) and summing up over all allowed Ω' and K values, one obtains an expression which is identical to the formulas given by (1). It means that coupling of the two-nucleon configurations to the rotating core results in the fragmentation of the strength of $M1$ transition caused by these two-particle quasideuteron configurations. It is one of the best examples of the interplay between collective and single-particle motions in odd–odd nuclei.

In order to test the model, we have applied it to *sd*-shell nuclei and have obtained reasonably good

Calculated and experimental $B(M1;\ J_i \to J_f)$ values (in μ_N^2 units) for ^{46}V and ^{50}Mn. (In the column labeled with R + QD, the results of the *rotor plus quasideuteron* model are given; in column KB3, shell-model results are given with KB3 interaction; and "Expt." denotes experimental data)

$J_i \to J_f$ ($\Delta T = 1$)	^{46}V			^{50}Mn	
	R + QD	KB3	Expt.	R + QD	KB3
$0_1^+ \to 1_1^+$	2.46	3.80	$\geq$2.31	5.9	8.7
$0_1^+ \to 1_2^+$	6.56	5.01	–	3.3	–
$0_1^+ \to 1_3^+$	8.20	–	–	5.6	–
$2_1^+ \to 1_1^+$	0.99	0.80	–	2.37	1.94
$3_1^+ \to 2_1^+$	0.0	0.21	$\leq$0.012	2.54	3.73
$3_2^+ \to 2_1^+$	1.06	1.25	1.98(71)	0.0	0.0
$4_2^+ \to 3_1^+$	0.0	0.08	–	2.63	2.71
$4_2^+ \to 3_2^+$	1.10	0.85	$\geq$0.52	0.0	0.0
$5_1^+ \to 4_2^+$	0.0	0.02	$\geq$0.02	0.0	0.04
$5_2^+ \to 4_2^+$	1.12	1.17	$\geq$0.41	2.69	3.46

agreement with experimental data. As an example, in Fig. 1 the experimental $M1$ strengths for the ^{22}Na nucleus are compared to the calculated $B(M1)$ values using (4). One can note rather good agreement for many $M1$ transitions. Having these interesting results for the *sd* shell, it is intriguing to find what can be expected for the heavier odd–odd $N = Z$ nuclei in *pf* shell.

4. COLLECTIVITY AND $M1$ TRANSITIONS IN ^{46}V AND ^{50}Mn

Recently [11–13], the low-spin structure of the odd–odd $N = Z$ nuclei ^{46}V and ^{50}Mn up to an excitation energy of $E_x \approx 3.5$ MeV was investigated

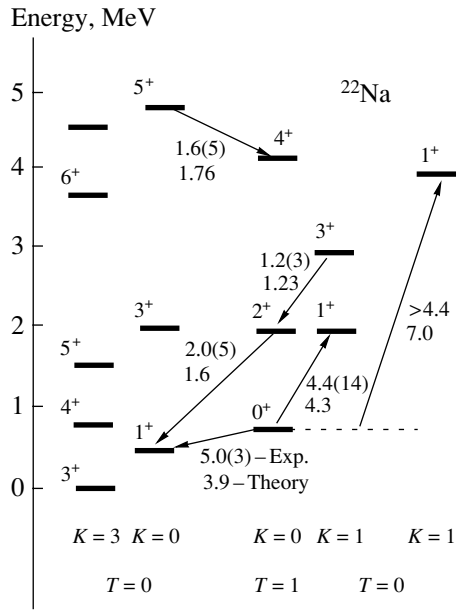

Fig. 1. Experimental and calculated $B(M1)$ values (in μ_N^2 units) for the isovector transitions in ^{22}Na nucleus.

in Cologne. Low-spin states of ^{46}V and ^{50}Mn were populated using the fusion evaporation reactions ^{46}Ti(p, $n\gamma$)^{46}V and ^{50}Cr(p, $n\gamma$)^{50}Mn, respectively, at a proton beam energy $E_p = 15$ MeV. The beam was delivered by the FN–TANDEM accelerator of the University of Cologne. From the analysis of coincidence spectra, many new transitions were placed in the level scheme, establishing new levels and confirming some of the previously observed levels. Our new data together with some recent high spin data for ^{50}Mn from Svensson *et al.* [14] and for ^{46}V from O'Leary *et al.* [15] give a consistent and extensive level scheme for the studied nuclei.

The experimental data were compared to shell-model (SM) calculations of the positive-parity states of both nuclei in the full *pf* shell without truncation [11, 13]. The Hamiltonian matrix in the full *pf* shell was diagonalized without any truncation using the Tokyo shell-model code [16]. The calculated excitation energies for the $T = 0$ and $T = 1$ positive-parity levels with spin quantum numbers $J = 0$–7 below 3 MeV were compared to the data in [11, 13]. The calculations lead to reasonable agreement with experiment. We have found that observed and calculated branching ratios, as well as $E2/M1$ multipole-mixing ratios δ, agree rather well. It indicates that relative intensities of observed electromagnetic transitions are reproduced well by the shell model. Furthermore, the absolute values of calculated $E2$ transition strengths were carefully analyzed [5]. We have found that $B(E2)$ values from the shell model are well matched by the *rotor plus quasideuteron* model, in which the expression for $B(E2)$ values is the same as in the Bohr–Mottelson geometrical model [9]. This comparison helps to assign additional quantum number $K^\pi = 0^+$ to $T = 1$ states and to separate $T = 0$ states into $K^\pi = 0^+$ and $K^\pi = 3^+$ bands in ^{46}V and into $K^\pi = 0^+$ and $K^\pi = 5^+$ bands in ^{50}Mn, as is

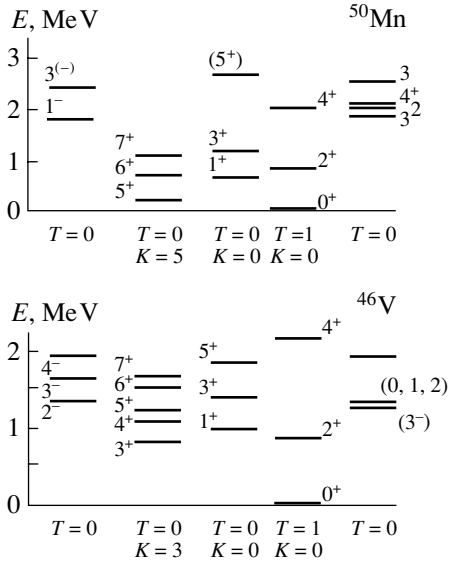

Fig. 2. Experimental low-energy spectra of ^{50}Mn and ^{46}V. The construction of the bands is based on the analysis of the experimental and theoretical $E2$ transition strengths.

shown in Fig. 2. The interpretation of the experimental and shell-model results for $E2$ transitions in terms of the *rotor plus quasideuteron* model immediately explains why strong isovector $M1$ transitions can be observed between $T = 1$, $K^\pi = 0^+$ and $T = 0$, $K^\pi = 0^+$ states ($\Delta K \leq 1$ selection rule for $M1$ transitions) and why there are no strong isovector $M1$ transitions between $T = 1$, $K^\pi = 0^+$ and $T = 0$, $K^\pi = 3^+$ ($K^\pi = 5^+$ for ^{50}Mn) states in ^{46}V ($M1$ transitions are forbidden for $\Delta K > 1$). Moreover, the *rotor plus quasideuteron* model gives a quantitative description of the $M1$ transitions in ^{50}Mn and ^{46}V. The results of this model (4), of the shell model (KB3 interaction), and some experimental data for ^{50}Mn and ^{46}V are shown in the table. From this comparison, one can note that very strong $M1$ transitions are expected in both nuclei. One can also expect fragmentation of the total $M1$ $0^+ \to 1^+$ transition strength over three low-lying 1^+ states. These expected strong $M1$ transitions, as follows from the rotor plus quasideuteron model, are caused by odd proton and odd neutron motions; i.e., they are not collective in contrast to the $E2$ transitions, which are related mainly to the core's rotational motion.

5. SUMMARY

The spectroscopy of the low spin structure of odd–odd $N = Z$ nuclei is of great current interest, and many laboratories around the world are working in this field. We focus here on experimental and theoretical study of the electromagnetic transitions in odd–odd $N = Z$ nuclei. The interesting result of our study is an identification of strong noncollective (quasideuteron mechanism) isovector $M1$ transitions between low-lying states. The enhancement of $M1$ strengths in nearly spherical nuclei is found to be due to the constructive interference of orbital and spin parts of the $M1$ reduced matrix elements between the states having predominantly quasideuteron $(\pi j \times \nu j)_{J,T}$ structure, where $j = l + 1/2$. Coupling of the quasideuteron configurations to the collective rotating core results in the fragmentation of the $M1$ strengths in deformed odd–odd $N = Z$ nuclei. A comparison of the results obtained within the shell model and within the *rotor plus quasideuteron* model gives evidence for strong isovector $M1$ transitions in ^{46}V and ^{50}Mn.

ACKNOWLEDGMENTS

We thank A. Dewald, J. Eberth, G.F. Filippov, A. Gelberg, and K. Jessen for valuable discussions. One of us (R.V.J.) thanks the Universität zu Köln for a Georg Simon Ohm guest professorship.

This work supported in part by the DFG under contracts nos. Br 799/10-1, Br 799/9-1, Pi 393/1-1 and in part by the Grant-in-Aid for Scientific Research (A) (2) (10304019) from the Ministry of Education, Science, and Culture (of Japan) and by the JSP–DFG collaboration.

REFERENCES

1. P. von Brentano, A. F. Lisetskiy, I. Schneider, *et al.,* Prog. Part. Nucl. Phys. **44**, 29 (2000).
2. A. O. Macchiavelli *et al.,* Phys. Rev. C **61**, 041303 (2000).
3. P. Vogel, Nucl. Phys. A **662**, 148 (2000).
4. A. F. Lisetskiy, R. V. Jolos, N. Pietralla, and P. von Brentano, Phys. Rev. C **60**, 064310 (1999).
5. A. F. Lisetskiy *et al.,* submitted for publication in Phys. Lett. B.
6. I. Schneider *et al.,* Phys. Rev. C **61**, 044312 (2000).
7. R. J. Ascuitto, D. A. Bell, and J. P. Davidson, Phys. Rev. **176**, 1323 (1968).
8. P. Wasilewski and F. B. Malik, Nucl. Phys. A **160**, 113 (1971).
9. A. Bohr and B. R. Mottelson, *Nuclear Structure* (Benjamin, New York, 1974; Mir, Moscow, 1977), Vol. II.
10. J. M. Irvine, *Nuclear Structure Theory* (Pergamon, Oxford, 1972).
11. C. Frießner *et al.,* Phys. Rev. C **60**, 011304 (1999).
12. I. Schneider, Ph.D. Thesis (University of Cologne, 2000).
13. A. Schmidt *et al.,* Phys. Rev. C 62, 044319 (2000).
14. C. E. Svensson *et al.,* Phys. Rev. C **58**, R2621 (1998).
15. C. D. O'Leary *et al.,* Phys. Lett. B **459**, 73 (1999).
16. T. Sebe, *Shell-Model Code*, University of Tokyo (unpublished).

Physics of Atomic Nuclei, Vol. 64, No. 7, 2001, pp. 1210–1214. From Yadernaya Fizika, Vol. 64, No. 7, 2001, pp. 1285–1289.

Proceedings of the International Conference "Nuclear Structure and Related Topics"

^{102}Ag: In-Beam Gamma-Ray Spectroscopy*

S. Rastikerdar**

Physics Department, Isfahan University, Iran

Received October 25, 2000

Abstract—Gamma-rays associated with the decay of states in the ^{102}Ag nucleus have been identified, sixty-four of them for the first time following the reaction ^{50}Cr(^{56}Fe, $3pn$)^{102}Ag at a mean energy of 195 MeV. Identification was made using an array of nine escape-suppressed Ge detectors coupled to the Daresbury Recoil Separator. Excited states in ^{102}Ag were identified using recoil-gamma and $\gamma\gamma$ coincidences. From the intensity balance and the coincidence data, a new set of levels was identified which may be interpreted as reminiscent of "three-quasiparticle" bands in neighboring odd-mass nuclei and similar to a four-quasi-particle band observed in ^{106}Ag. © *2001 MAIK "Nauka/Interperiodica".*

1. INTRODUCTION

The study of the transitional odd–odd silver isotopes such as ^{102}Ag, which can provide information on different modes of coupling mechanisms between the odd proton and the odd neutron, is challenging, both experimentally and theoretically. Treherne *et al.* [1] produced the ^{102}Ag nucleus and compared its high-spin level structure with two-quasiparticle rotor-model calculations. Then, Kumar *et al.* [2] extended the negative-parity band in the level scheme of the ^{102}Ag nucleus up to 19^-, and they also observed a new band in their study. In the present work, the heavy-ion reaction ^{50}Cr(^{56}Fe, $3pn$) at 195 MeV energy was used to study the in-beam gamma-ray spectroscopy of the ^{102}Ag nucleus.

2. EXPERIMENTAL PROCEDURE

Gamma rays from the reaction ^{50}Cr(^{56}Fe, $3pn$) were detected using an array of nine BGO shielded, intrinsic germanium detectors coupled to the Daresbury recoil separator to record the recoil-gamma and $\gamma\gamma$-coincidence events on tapes.

A full description of the design and performance of the Daresbury recoil separator has been given by James *et al.* [3]. In brief, it allows one to determine A and Z for the recoils in coincidence with an array of BGO Compton suppressed Ge detectors.

3. ANALYSIS OF THE DATA

Manipulation of the data permitted a "pure" ^{102}Ag gamma-ray spectrum to be created (Fig. 1). The energies and relative intensities of the gamma rays obtained from this spectrum are shown in the table. One hundred twelve gamma-ray lines were identified, 64 of them for the first time. Comparisons were made with the data published by Treherne *et al.* [1] and Kumar *et al.* [2]. Good agreements were obtained in both cases. Almost all gamma rays seen by both authors are observed here too. Also, 64 new gamma rays are observed here, which are marked by asterisks in the table.

A careful analysis of the coincidence data was made in order to establish the sequence of decays of sidebands in order to get information on various experimentally unknown coupling mechanisms of the two unpaired particles but predicted by the theory [2, 4]. Due to poor statistics, we were not able to arrive at firm conclusive evidence of these decay patterns. However, from the intensity balance and the coincidences, a new set of levels was found from which the 473-keV line feeds the 1706-keV level, which in turn mainly feeds the band head of the 8^- band through the 157-keV line. Figures 2 and 3 show the spectra corresponding to gates set on the 473- and 404-keV gamma lines, respectively. Figure 4 shows the level scheme for ^{102}Ag. New transitions and new levels are indicated by * and **, respectively. The rest of the level scheme has been taken from Kumar *et al.* [2] and Treherne *et al.* [1].

4. DISCUSSION

In ^{102}Ag ($Z = 47$), an odd–odd transitional nucleus, the unpaired proton is likely to fill up a large

*This article was submitted by the author in English.

**e-mail: samadr1@yahoo.com

A compilation of gamma-ray energies and relative intensities assigned to ^{102}Ag (D stands for the doublet and the new transitions are indicated by asterisks)

E, keV	I_γ (rel.)	E, keV	I_γ (rel.)	E, keV	I_γ (rel.)	E, keV	I_γ (rel.)
40.0 ± 0.2	20 ± 4	349.4 ± 0.2	100 ± 12	686.0 ± 0.2	6 ± 3	1120.4 ± 0.2	9 ± 4
46.0 ± 0.2	21 ± 4	*354.2 ± 0.2	45 ± 9	*695.9 ± 0.3	8 ± 3	1147.2 ± 0.2	D
*76.3 ± 0.3	6 ± 2	397.7 ± 0.2	113 ± 0.2	705.0 ± 0.3	22 ± 5	*1164.9 ± 0.4	D
89.7 ± 0.2	36 ± 7	*403.7 ± 0.2	40 ± 8	*714.9 ± 0.3	5 ± 3	1183.1 ± 0.4	8 ± 4
97.5 ± 0.2	45 ± 8	415.1 ± 0.3	8 ± 4	*721.8 ± 0.3	5 ± 3	*1185.0 ± 0.4	7 ± 4
*108.1 ± 0.4	3 ± 2	*420.5 ± 0.4	Weak	*742.0 ± 0.3	4 ± 2	*1196.4 ± 0.4	Weak
*116.0 ± 0.4	5 ± 3	*428.8 ± 0.2	6 ± 3	746.0 ± 0.3	20 ± 7	1247.4 ± 0.3	25 ± 7
130.2 ± 0.3	6 ± 3	*452.0 ± 0.5	6 ± 4	748.0 ± 0.3	7 ± 4	*1264.3 ± 0.2	4 ± 3
141.0 ± 0.2	100	466.6 ± 0.2	170 ± 20	*758.0 ± 0.3	9 ± 4	*1291.5 ± 0.3	7 ± 3
149.2 ± 0.2	78 ± 9	*473.2 ± 0.2	80 ± 16	*776.0 ± 0.3	D	*1320.9 ± 0.3	10 ± 4
157.5 ± 0.2	124 ± 12	483.4 ± 0.3	55 ± 12	*788.8 ± 0.3	8 ± 4	*1356.6 ± 0.3	6 ± 3
*167.5 ± 0.4	5 ± 4	*489.3 ± 0.3	35 ± 9	816.2 ± 0.3	Weak	*1365.2 ± 0.3	28 ± 6
174.5 ± 0.2	30 ± 7	*494.9 ± 0.4	9 ± 4	819.6 ± 0.3	20 ± 7	1367.8 ± 0.3	20 ± 5
180.8 ± 0.4	7 ± 4	503.0 ± 0.3	46 ± 8	*831.2 ± 0.3	14 ± 5	*1387.4 ± 0.2	25 ± 7
187.2 ± 0.2	26 ± 7	*510.3 ± 0.2	30 ± 7	839.1 ± 0.2	220 ± 15	*1417.0 ± 0.3	5 ± 4
196.2 ± 0.2	28 ± 6	517.4 ± 0.2	32 ± 7	*851.4 ± 0.2	105 ± 12	*1427.4 ± 0.2	7 ± 4
*214.2 ± 0.4	7 ± 3	*524.8 ± 0.3	12 ± 5	860.7 ± 0.2	26 ± 6	*1446.0 ± 0.3	Weak
*229.0 ± 0.4	5 ± 2	*529.4 ± 0.3	30 ± 7	875.7 ± 0.2	158 ± 13	*1483.5 ± 0.5	Weak
236.0 ± 0.3	30 ± 6	540.1 ± 0.2	36 ± 8	*888.5 ± 0.2	61 ± 10	*1501.2 ± 0.5	Weak
*240.5 ± 0.3	24 ± 6	*548.0 ± 0.2	12 ± 4	920.9 ± 0.3	Weak	*2287.4 ± 0.3	5 ± 3
260.7 ± 0.3	60 ± 10	555.0 ± 0.2	13 ± 4	951.0 ± 0.2	114 ± 12	*2298.6 ± 0.3	6 ± 3
*262.3 ± 0.3	25 ± 7	*577.8 ± 0.3	Weak	*967.0 ± 0.3	D	*2336.9 ± 0.3	Weak
268.1 ± 0.4	7 ± 4	*617.6 ± 0.3	8 ± 4	*985.2 ± 0.3	D		
274.5 ± 0.2	95 ± 15	*626.4 ± 0.3	6 ± 3	*998.3 ± 0.3	Weak		
279.5 ± 0.2	61 ± 10	637.0 ± 0.2	50 ± 9	*1043.9 ± 0.4	7 ± 4		
*284.0 ± 0.5	7 ± 3	*646.7 ± 0.3	23 ± 7	*1052.5 ± 0.4	7 ± 4		
304.8 ± 0.3	38 ± 8	651.0 ± 0.3	17 ± 6	*1076.9 ± 0.4	6 ± 4		
*309.8 ± 0.4	12 ± 4	*656.0 ± 0.3	18 ± 6	1084.0 ± 0.3	Weak		
*329.0 ± 0.4	D	664.2 ± 0.2	90 ± 11	*1087.4 ± 0.3	Weak		
336.1 ± 0.2	36 ± 8	*673.5 ± 0.2	25 ± 7	*1103.9 ± 0.3	9 ± 4		

$\Omega(7/2, 9/2)$ state arising from the $\pi g_{9/2}$ orbital, whereas the neutron Fermi level lies near the low Ω states of the $\nu d_{5/2}, g_{7/2}$ orbitals. Therefore, the Coriolis response of the neutron and proton motion to the rotation of the core will be quite different. Since there are many excited states with configurations such as $(\nu h_{11/2} \otimes \pi g_{9/2}), (\nu g_{7/2} \otimes \pi g_{9/2}), \quad (\nu d_{5/2} \otimes \pi g_{9/2}), (\nu h_{11/2} \otimes \pi p_{1/2})$, etc., one would expect to find different types of coupling mechanisms in the level structure. This idea is confirmed by the richness of the number of new gamma rays seen in the present work.

As is seen from Fig. 4, the level diagram of ^{102}Ag can be grouped into five bandlike structures. Three of them (the two positive-parity bands and

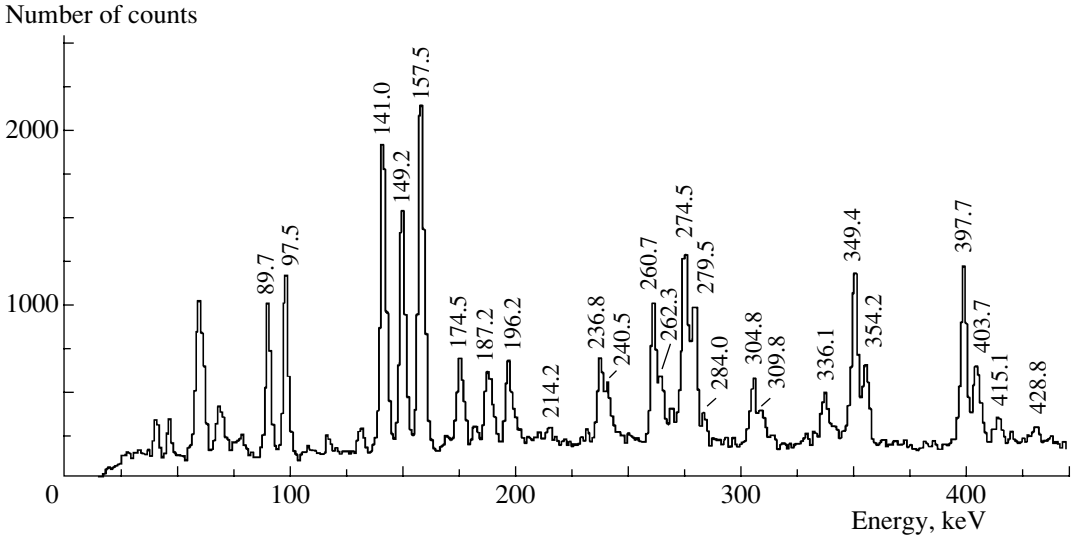

Fig. 1. The "pure" gamma-ray spectrum of ^{102}Ag (lower-energy part of the spectrum only).

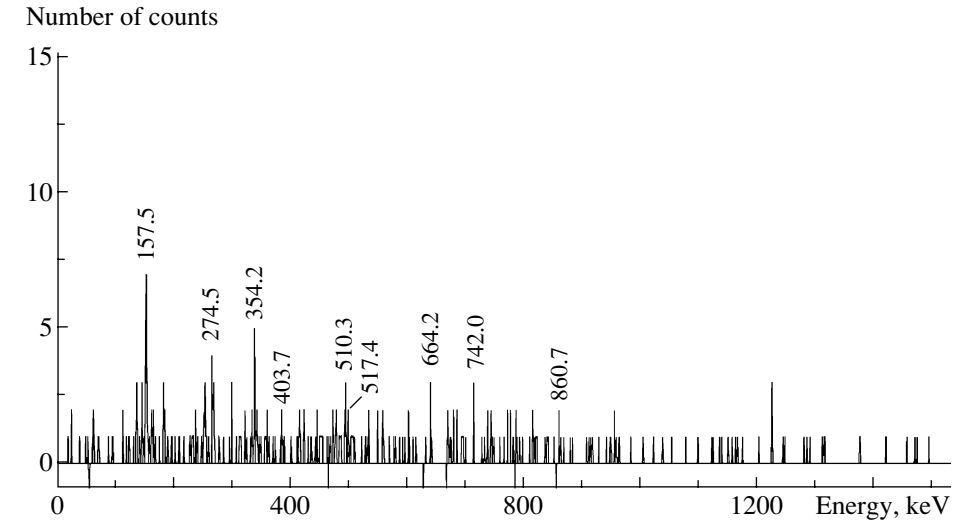

Fig. 2. The spectrum resulting from a gate set on the 473-keV transition.

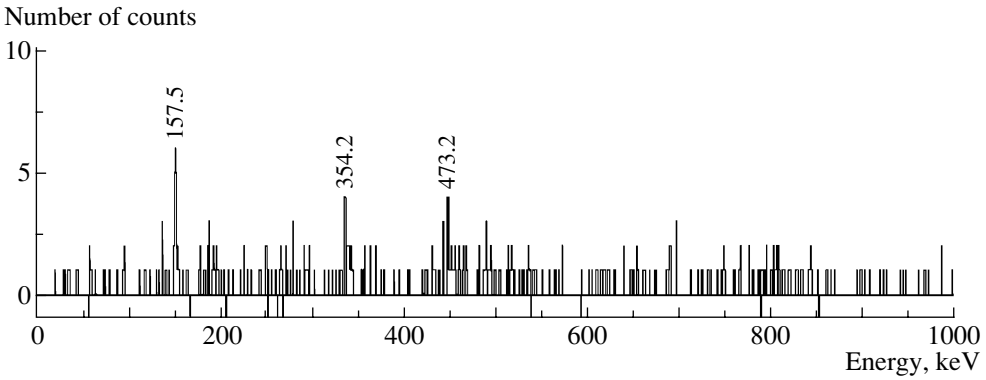

Fig. 3. The spectrum resulting from a gate set on the 404-keV transition.

the main negative-parity band) were observed by Treherne *et al.* [1], and the one shown on the left was observed by Kumar *et al.* [2]. The positive-parity bands based on the two 7^+ states at energies 181 and 382 keV have been interpreted as quasirotational bands with band head configurations $[\pi g_{9/2} \otimes \nu d_{5/2}]$

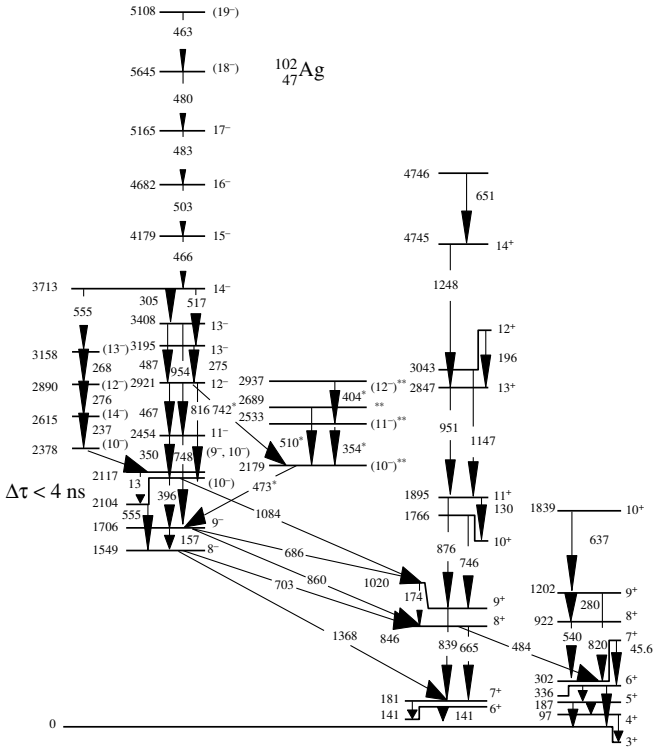

Fig. 4. The level scheme of ^{102}Ag. New transitions and new levels (from the present work) are indicated by * and **, respectively. The rest of the level scheme has been taken from Kumar *et al.* [2] and Treherne *et al.* [1].

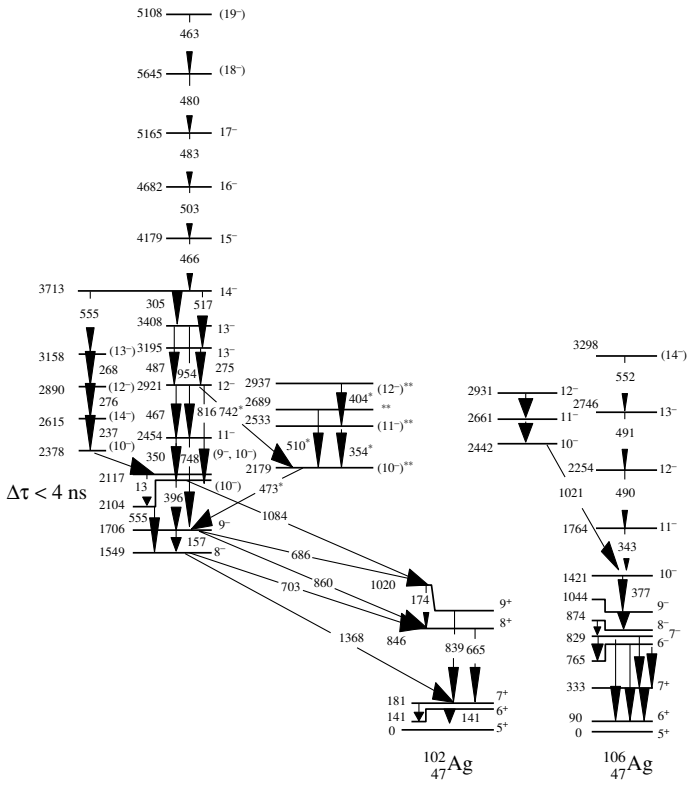

Fig. 5. Comparison of negative-parity bands in ^{102}Ag and ^{106}Ag. New transitions and new levels are shown by * and **, respectively.

and $[\pi g_{9/2} \otimes \nu d_{7/2}]$, respectively. The main negative-parity band based on the 1549 keV state was interpreted as a two-quasiparticle band based on the $[\pi g_{9/2} \otimes \nu h_{11/2}]$ configuration. The fourth one

shown on the left has been suggested to have a four-quasiparticle configuration similar to $[\pi(g_{9/2})^2(p_{1/2})^1 \otimes \nu(d_{5/2})^1]_{10^-}$.

The new set of levels observed at the present work and shown in the middle of the level diagram is suggested to be the fifth band with the head at 2179 keV. From the coincidences, it was observed that this level was fed from the 12^- state in the main negative-parity band through the 742-keV transition. It has been observed in ^{106}Ag, ^{104}Ag, ^{102}Ag, and other nuclei in this region that, in general, parity-changing transitions are highly retarded and cannot compete with $M1$ or $E2$ transitions of comparable energy. In fact, almost all gamma rays for which their multipolarities have been measured in ^{102}Ag [2] are $M1$, $E2$, or $M1 + E2$. Therefore, the spin of the 2179-keV level should be 10 or higher, but based on systematics, spin 11 or more should happen at higher energies. This argument was used to assign spin and parity 10^- tentatively to the 2179-keV state. Suggested spins and parities to the states at 2533 and 2937 keV are based on the similarities to the spins between 10^- to 12^- states in ^{106}Ag (Fig. 5). Since all these spins and parities are tentatively assigned, they were placed in parentheses. If these assignments are correct, then the 2179-keV level observed in the present work might be viewed as the head of a band with low energy, $\Delta I = 1$ γ rays. A similar negative-parity band with the band head energy at 2442 keV has been observed in ^{106}Ag and suggested to have a four-quasiparticle structure [4]. In fact, the new band observed in the present work is very reminiscent of "three-quasiparticle" bands in neighboring odd-mass nuclei, both in terms of band head energy and level spacing. For example, there is a $\Delta I = 1$ band in ^{103}Pd based on $17/2^+$ state at 2109 keV with γ-ray energies of 237 and 311 keV [5], or there is a $\Delta I = 1$ band in ^{105}Pd based on $17/2^+$ state at 2552.3 keV with γ-ray energies of 255 and 313 keV [6]. Therefore, the (10^-) state at 2179 keV observed in the present work is suggested to have a four-quasiparticle structure similar to the one observed at the 2441 keV state in ^{106}Ag with spin and parity 10^- (Fig. 5). However, transition probability data and four-quasiparticle calculations are required to get some more insight into the possible structures of these bands.

The assistance given by the crew and staff of the NSF at Daresbury (Great Britain) and also the support given by Isfahan University (Iran) are greatly acknowledged.

REFERENCES

1. J. Treherne *et al.,* Phys. Rev. C **27**, 166 (1983).
2. V. Kumar *et al.,* Z. Phys. A **351**, 249 (1995).
3. A. N. James *et al.,* Nucl. Instrum. Methods Phys. Res. A **267**, 144 (1988).
4. R. Popli, F. A. Rickey, L. E. Samuelson, and P. C. Simms, Phys. Rev. C **23**, 1085 (1981).
5. J. A. Grau, F. A. Rickey, G. J. Smith, *et al.,* Nucl. Phys. A **229**, 345 (1974).
6. F. A. Rickey, J. A. Grau, L. E. Samuelson, and P. C. Simms, Phys. Rev. C **15**, 1530 (1977).

Physics of Atomic Nuclei, Vol. 64, No. 7, 2001, pp. 1215–1222. From Yadernaya Fizika, Vol. 64, No. 7, 2001, pp. 1290–1297.

Proceedings of the International Conference "Nuclear Structure and Related Topics"

Few-Body Cluster Models for Borromean Halo Nuclei*

B. D. Danilin[**], **I. J. Thompson**[1)], **M. V. Zhukov**[2)], **and J. S. Vaagen**[3)]
and RNBT (Russian–Nordic–British Theory) Collaboration
Russian Research Centre Kurchatov Institute, pl. Kurchatova 1, Moscow, 123182 Russia
Received October 25, 2000

Abstract—Modern few-body methods for investigating Borromean two-neutron halo nuclei are discussed together with recent experiments. Advances in the studies of ^{6}He and ^{11}Li are analyzed. Some new problems created by a large neutron excess and a halo phenomenon are considered. © *2001 MAIK "Nauka/Interperiodica".*

1. INTRODUCTION

Triggered by Tanihata's discovery [1] of nuclei abnormally extended in space (^{6,8}He, ^{11}Li, ^{11}Be) at the neutron drip line, the initial idea of (binary) halos was suggested by Hansen and Jonson [2]. Subsequent developments deepened and enriched the picture of halos as outstanding structural drip-line phenomena with extreme clustering into an ordinary core nucleus and a veil of halo nucleons forming exceptionally dilute neutron matter. The origin of the stratification is of purely quantum-mechanical character and is only partly understood, but prerequisites are a low angular momentum for halo particles and few-body dynamics such as in Borromean nuclei [3] characterized by pairwise constituents with no bound states. In the limit of vanishing binding, extremely large halos may occur.

Few-body dynamics plays a crucial role in any adequate description of halo properties, since, for halo bound states, the wave function is predominantly concentrated in the classically forbidden region, where the behavior is dictated by the type of dynamics—from two-body to extremely rich three- and few-body. The chain of He isotopes with an alpha core has become particularly useful as benchmark systems. The binding of ^{6,8}He and the observation, a few years ago, of a narrow low-lying ^{10}He resonance, as well as in ^{5}H, gave clear evidence that genuine few-body features of the neutron veil have to be taken seriously. Thus, a diversity of few-body-inspired methods with different virtues have been developed and tested against each other for the ^{6}He and ^{11}Li benchmark systems. For ^{14}Be and ^{19}B, we are only at the very beginning of detailed explorations. Presently, the only two-proton halo candidate is ^{17}Ne, while ^{6}Be and ^{12}O are precursors of diproton radioactivity. These systems are topics of current explorations of isospin and charge symmetries in the presence of a substantial proton excess.

A variety of few-body methods, such as Faddeev, hyperspherical-harmonic (HH), resonating-group, and Green's function Monte Carlo methods, were used for bound states, but only a few of these are suitable for a continuum analysis. We will, however, focus on the three-body structure of Borromean halo nuclei, explored in a $core + n + n$ cluster decomposition within a full range of three-body dynamics. In relation to a two-body problem, there appear new features: the Efimov effect [4] and the Thomas collapse [5].

Experimentally, the entire body of information about drip-line nuclei is extracted from elastic and breakup reactions. Apart from highly integrated observables like elastic and reaction cross sections and momentum distributions of fragments, it is still possible, in modern experiments, to measure different correlations between fragments, including a kinematically complete experiment.

An important probe is the Coulomb breakup cross section for cases where nuclei are incident on highly charged targets. Experiments find an unusually large electromagnetic-dissociation (EMD) cross section per unit charge and a strong concentration of the dipole breakup strength for halo nuclei at low continuum energies. There has been much debate among theorists on the question of whether (or not) the particles still attract each other sufficiently to form a "soft

*This article was submitted by the authors in English.

[1)]Department of Physics, University of Surrey, Guildford, GU2 7XH, UK.
[2)]Department of Physics, Göteborg University and Chalmers University of Technology, S-41296 Göteborg, Sweden.
[3)]SENTEF, Institute of Physics, University of Bergen, Allégaten 55, N-5007 Bergen, Norway.
[**]e-mail: danilin@cerber.mbslab.kiae.ru

dipole" excited state or a resonance at low energies in the breakup continuum.

The kinematically complete breakup of ^{6}He on heavy and light targets was measured at GSI [6]. This allows energy and angular correlations of various subsystems to be measured, as well as the full three-body breakup energy distribution.

The ^{11}Li nucleus is still very puzzling, despite the great number of experiments and theories that attempt to elucidate its structure. A soft dipole mode in ^{11}Li was detected in three recent experiments [7–9]. Angular and energy correlations in two-body subsystems were also measured [10]. A comparison of the dipole-mode predictions of the intruder-state models with these EMD data shed further light on the importance of the s intruder state.

The experimental advances are discussed in recent reviews of experiments [11, 12].

There are open problems created by new features, such as a halo structure, soft modes, and three-body continuum effects (continuum pairing): (1) extraction of the matter radii of halo nuclei from experimental data (for example, three Glauber-type methods using the total matter density [13], *core* + *valence neutron* density [14], and granularity of the ^{6}He structure with quantum interference [15] give the rms radii of 2.48, 2.57 ± 0.1, and 2.54 ± 0.04 fm, respectively); (2) the longitudinal- and transverse-momentum distributions of the core and the valence neutron in fragmentation experiments (these can be explained by two extreme models: the Serber (or sudden) approximation without final-state interaction (FSI) and nuclear breakup via halo excitation with FSI fully taken into account); and (3) the nature of soft dipole modes in halo nuclei (there arises the question of whether they represent a resonance or a giant induced dipole moment; the second aspect is that the most elaborate three-body calculations give an overly soft dipole response in relation to experimental data on ^{6}He and ^{11}Li).

2. THEORETICAL DEVELOPMENTS

When experiments indicate a cluster structure in many light nuclei, theorists can approximate the many-nucleon problem by a few-body one, and a number of methods have been developed for the treatment of the latter problem. Faddeev's [16] and Schrödinger's effective few-body formulations have successfully been solved with the aid of direct, variational [17–19], hyperspherical-harmonic [3], and Faddeev equations with adiabatic hyperspherical methods [20]. All of them treat clusters as pointlike particles and use few-body dynamics. Interactions between the species are realistic as much as possible, but they are still effective, describing the bound-state and continuum properties in each binary subsystem. For that, we need to know their properties, which are sometimes poorly defined because of experimental difficulties; sometimes, we have absolutely no information. The complex structure of clusters leads to nonlocal interactions, instead of which the phase-equivalent l-dependent local interactions can be employed. Antisymmetrization with respect to valence nucleons is easily performed correctly, but the general Pauli exclusion principle is usually treated in an effective way.

Within few-body cluster models such as the resonating-group method (RGM) [21–24] and the generator-coordinate method (GCM) [25], the composite structure of clusters manifests itself through nonlocal exchange integral kernels. They treat clusters as "frozen" objects with their wave functions (as simple as possible) describing the main characteristics of the free clusters. The relative motion of their centers of mass is then calculated in some restricted basis. A full antisymmetrization of the total wave function guarantees a strict treatment of the Pauli exclusion principle between all nucleons. The effective NN interaction has as many realistic features as possible and has the same form for all (sub)systems. A good effective interaction will give a simultaneous description of the internal properties of clusters and two-cluster subsystems and will rarely be a free NN interaction.

The orthogonality-condition model [26], derived from the RGM, reduces the complicated Hill–Wheeler equation to a Schrödinger one with a physically transparent projection of Pauli-blocked states out of the spectrum of the binary Hamiltonian. An alternative method, generating a spectrally equivalent Hamiltonian, is to use the double supersymmetric transform [27]. The two approaches give the same on-shell behavior, but they are different off the shell, the latter becoming critical in the three-body situation.

The strict calculations of A-nucleon system—Green's function Monte Carlo method—should be mentioned as well [28].

Within some of these methods, only a few continuum explorations were performed. There are full-scale $3 \to 3$ scattering, complex energies (Gamow states) [29] and the Feshbach-type approach [29] in the method of hyperspherical harmonics [30]; $3 \to 3$ scattering, complex energies in the adiabatic hyperspherical method [31]; and $3 \to 3$ scattering in the algebraic version of the RGM [32] and the J-matrix method [19], the complex rotation method in the RGM [21], and the cluster oscillator-shell model [33].

The method of hyperspherical harmonics [30], which treats bound states and a continuum on equal footing, was incorporated in developed four-body Glauber theory [15] and the DWBA [34].

2.1. Three-Body Ground States

^{6}He. All models listed above give similar weights of partial components of the wave function in the ground state of ^{6}He. However, the effective three-body methods with any realistic pair interactions show the common problem of underbinding, with three-body energies of about -0.4 MeV instead of -0.97 MeV. This underbinding is most likely caused by the influence of other closed channels, the most important of these being $t+t$ [22, 23, 35], or the polarization of the α cluster [22, 36]. Calculations of the RGM type [22, 23, 35, 36] show that the inclusion of the $t+t$ closed channel (or the polarization of the α particle) gives a value very close to the total needed correction to the binding energy and improves the small radius of ^{6}He. In the shell-model language, this corresponds to polarizing the α particle by adding two extra nucleons. This can be taken approximately into account in two ways: (i) by increasing (as in [3]) the radius of the α particle and, consequently, the radius $R_{\alpha n}$ of the αn interaction or (ii) by effectively renormalizing the force [30].

We compare the calculated ground states for all methods treating the Pauli exclusion principle, and rather similar characteristics for ^{6}He emerge once again. The matter radii are 2.43–2.44 fm for a Gaussian basis and 2.44–2.61 fm for a hyperspherical one.

Few-body cluster approaches (RGM-based) give a similar partial content but smaller matter radii (2.36–2.46 fm). This could be due to an incorrect asymptotic behavior or to an effective character of NN forces, which do not contain a strong repulsion at short distances.

^{11}Li. The ^{11}Li nucleus is still very puzzling, despite a great number of experiments and theories that attempt to elucidate its structure. A study of ^{11}Li analogous to that of ^{6}He is hampered by the lack of information about the n–^{9}Li channel. Since the n–^{9}Li interaction is not accurately known, it is necessary to explore a range of scenarios with varying mixtures of s-wave intruder states and p-wave resonances.

In recent years, there has been considerable theoretical interest in the possible role of the s-wave intruder state in the structure of the ^{11}Li halo [37]. There are various pieces of experimental evidence for virtual states in ^{10}Li, and they are sometimes conflicting [38, 39]. The antisymmetrized RGM [40] and GCM [41] models are unable to find s-wave poles, but few-body *core + nucleon(s)* models can begin to explain their presence in a semimicroscopic treatment [42] by the coupling of a quadrupole core deformation (which simulates the mixture of configurations) to s- and d-wave single-particle states.

The observed momentum distributions [43] are found [37] to support strongly an intruder state, but the predicted matter radii are overly large in relation to the analysis of the data from [44]. There is now evidence [15] that the radii from [44] are overly small, but an independent probe of the halo structure would still be useful.

An n–^{9}Li virtual state increases the s^2 components and the matter radius of the ground state. We may conclude that a model with a p^2 admixture of about 60% in the ^{11}Li ground state and a radius close to that which fits [15] the experimental reaction cross section fits best. This is also in approximate agreement with the results of calculations [45] analyzing the ^{11}Li β-decay experiments.

2.2. Three-Body Continuum

An extended analysis of three-body continuum theory was performed in [30].

Resonances and other structures. Physically, long-lived states of three types can exist in three-body systems [46]: (I) "true" three-body resonances; (II) long-lived binary virtual states or resonances; and (III) multichannel resonances due to the distributed moderate coupling of all channels [47]—in particular, so-called "coupled channel" (CC) resonances.

Spatial correlations. The difference of the correlated densities of an exact solution and an (antisymmetrized) six-dimensional plane wave as a reference is an original measure of spatial correlations, which are analogous to ground-state spatial correlations. In the case of ^{6}He, the former exhibited dineutron and cigar configurations [3], which were observed in the Dubna experiment reported in [48].

Correlated spatial densities for narrow resonances (2^+_1 in ^{6}He) revealed a compact internal structure and large-scale spatial correlations for monopole and dipole modes in the same nucleus.

^{6}He. Summarizing the extended analysis that was performed in [30], we present the positions and widths of possible resonances in the table. We also list the positions obtained in the complex-scaling (CS) methods of [21, 33]. All of the methods give very similar positions, but somewhat different widths should be tested experimentally.

^{11}Li. In [50], in just the same way as in [51] for ^{6}He, many resonances were indicated (even though

Comparison of resonance positions and widths in ^{6}He

	HH [30]		CS1 [21]		CS2 [33]		Expt. [49]	
J^π	E, MeV	Γ, MeV	E, MeV	Γ, MeV	E, MeV	Γ, MeV	E, MeV	Γ, MeV
0_1^+	−0.98		−0.6		−0.78		−0.97	
2_1^+	0.8	0.10	0.74	0.06	0.8	0.26	0.822	0.113
2_2^+	2.7	1.2	–	–	2.5	4.7	–	–
1^-	Not found		Not found		Not found		–	–
1^+	3.2	1.8	–	–	3.0	6.4	–	–
^{6}He, 0_2^+	5.4	6.0	–	–	3.9	9.4	–	–

all of these did not manifest themselves unambiguously in the phase shifts).

Channels other than dipole excitations may be generated in nuclear collisions with smaller impact parameters. The two neutrons in ^{11}Li begin (in our inert-core model) in a 0^+ state, but they may be excited to 1^- and 2^+ states by $\mathcal{E}1$ and $\mathcal{E}2$ excitations, respectively, and also to 0^- states, to a second 0^+ state, and to 1^+ states by nuclear mechanisms.

Experimental evidence for excited states of the ^{11}Li halo points to a state at 0.9 MeV above the threshold [52] and possibly further states at 2.1, 4.55, and 5.9 MeV [53]. We have more than one, however: a 0^+ resonance at 0.3 MeV, a 0^- resonance at 0.5 MeV, a 1^+ resonance at 1.6 MeV, and a 1^- "bump" at 0.5 MeV. It is not clear which of our three resonances and a bump corresponds to the observed peak at 0.9 MeV. The 0^+ continuum states are orthogonal to the ground state and will be excited only weakly. To understand this and other experiments, our continuum wave functions will be used to calculate the transition densities and then breakup cross sections, as has already been done for ^{6}He [34].

3. NUCLEAR BREAKUP AND MOMENTUM DISTRIBUTIONS OF THE NEUTRONS AND THE CORE

The momentum distributions of fragments are the most integrated characteristics of the system, which can be obtained from the six-dimensional differential cross section integrated with respect to the unobserved five Cartesian momenta. Let us discuss two extreme models for the fragmentation of halo nuclei—the Serber approximation and nuclear breakup via halo excitation.

In the Serber approximation, the transition operator is unity, and a plane wave is a final state in the transition-matrix element. It corresponds to the sudden approximation, and the observed longitudinal- and transverse-momentum distributions of the core and valence neutron are momenta in the ground state, which reflect the extension of the halo structure due to the uncertainty principle.

Only the natural parity states ($J^\pi = 0^+, 1^-, 2^+$) and the lowest pair angular momenta must be considered in nuclear breakup via halo excitation for ^{6}He, ^{11}Li, and other Borromean nuclei.

A simple analytic expression was derived in [54], where the Breit–Wigner energy dependence of a resonance was replaced by a delta function.

Analytically, the ratio of the half-width at half-maximum (HWHM) $\Gamma_{\rm HWHM}$ for, say, the neutrons and the core is

$$\frac{\Gamma^n_{\rm HWHM}}{\Gamma^{\rm core}_{\rm HWHM}} = \sqrt{\frac{1}{2}\,(1 + 1/A_{\rm core})}. \qquad (1)$$

Taking into account only the lowest 2^+ state, we find for the ^{6}He nucleus that $\Gamma^n_{\rm HWHM} = 22$ MeV/c and $\Gamma^{\rm core}_{\rm HWHM} = 29$ MeV/c; these results are very close to experimental values. In the case of ^{11}Li, the lowest peak, identified in almost all experiments, is located at about 1 MeV above the three-body threshold. With this value, we have $\Gamma^n_{\rm HWHM} = 26$ MeV/c and $\Gamma^{\rm core}_{\rm HWHM} = 35$ MeV/c, results that are also very close to experimental values.

This fact brings about the question of what we observe in momentum distributions, the size of the halo or low-energy resonances in halo excitation. Recently, a four-body DWIA theory for the breakup of Borromean nuclei was developed in [34] and was applied to ^{6}He nuclei in [55]. The results on both ^{4}He and neutron-momentum distributions confirm our qualitative estimates. This should be clarified in correlation experiments since the Serber mechanism will give correlations in the ground state, but diffraction-type breakup will reveal the structure of excited states (2^+ in the ^{6}He nucleus and 0^- or 1^- in ^{11}Li in relation to the mutual 0^+ ground state).

4. SOFT DIPOLE MODE

At present, the origin of accumulation of the dipole strength at a very low continuum energy is a key question. Nevertheless, the nature of the so-called "soft dipole mode" [12] responsible for abnormally large EMD cross section still needs clarification. Various attempts, based on the same cluster representation of ^{6}He, have not given a definite answer [18, 21, 51, 56] as to the presence of dipole resonance state in ^{6}He.

In [57], several Pauli principle treatments at the level of one-neutron–core exchange were applied to the soft dipole mode, and a rather significant difference was found because of the sensitivity of the three-body problem to the off-shell behavior of binary interactions. But the first experimental result on ^{6}He EMD [6] shows the absence of a peak at 1 to 2 MeV in the dipole strength function.

It could be a manifestation of the need for taking into account "two-neutron–core" exchange, which, at the physical level, corresponds to a change in the NN interaction within the core. At a phenomenological level, this means that, if the attractive NN s-wave interaction is replaced by a repulsive one within the core, we improve the dipole response but hardly change the ground state (see Fig. 1).

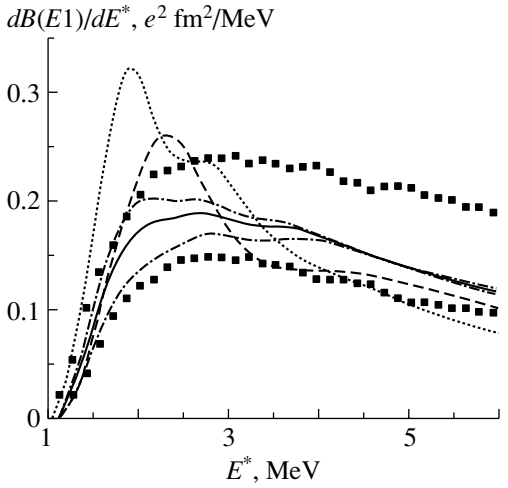

Fig. 1. Dipole response for ^{6}He: (solid and dash-dotted lines) results of new theoretical calculations; (dashed and dotted lines) results of theoretical calculations from [30] and [51], respectively; and (dark squares) distribution boundaries from [6], which were derived experimentally.

5. TWO-DIMENSIONAL ENERGY CORRELATIONS: INSIGHT INTO THE NATURE OF RESONANCES

Actually, all possible information about the three-body continuum structure is extracted from nuclear reactions, where the interplay of the reaction mechanism and the structure of the initial and final states make this task very difficult. Only one-step nuclear reactions and reactions with well-defined mechanisms (e.g., electromagnetic, charge-exchange) enable us to perform reasonable analysis.

There are several main sources of the amplification of the continuum cross sections: (i) true three-body resonances, which are due to the interaction of all three particles in the interior domain; (ii) a long-lived binary resonance in one of the pairs; and (iii) the response of an extended system to long-range transition operators, as was mentioned above.

The existence and the properties of any intrinsic resonance states should not depend on the excitation mechanism (electromagnetic, strong or weak interaction, etc.) that produces them.

To conclude our discussion of three-body properties or, in particular, of binary subsystems, it is necessary to inspect FSI (resembling ground-state energy–momentum correlations); intrinsic continuum correlations; and FSI transitions, where the intrinsic properties of the continuum are intertwined with ground-state correlations. From the theoretical point of view, the Jacobi coordinates and the corresponding energies of the relative motion of two particles (ϵ_x) and of the center of mass of these particles and the third particle (ϵ_y) are the most adequate to describing the internal excitations of the system.

The expression for the correlation function can be obtained from the differential cross section [30, 34] for $3 \to 3$ scattering (intrinsic properties of the continuum) or for reactions (transition properties) by performing integration with respect to the four-dimensional angular part of the momenta of scattered particles, averaging over the initial spins, and summation over the final spins.

Ground-state energy–momentum correlations. If we take an antisymmetrized plane wave for the final state, the correlated response gives the ground-state energy–momentum correlations for the T_{000} transition operator, which is often used as the Serber-type reaction cross section (Fig. 2). Other transition multipoles T_{jls} serve as "no-FSI" breakup reaction cross sections with zero-range perturbation $V(\mathbf{r}) = \sum \eta_i \delta(\mathbf{r} - \mathbf{r_i})$. They reflect only ground-state correlations and, every time, should be treated as a reference for the cases where the FSI is switched on.

Intrinsic and transition energy–momentum correlations. The intrinsic properties of halo excitations are contained in scattering amplitudes, which characterize the large-distance asymptotic behavior of the wave function. For sharp three-body resonances, the poles in the S matrix coincide with the

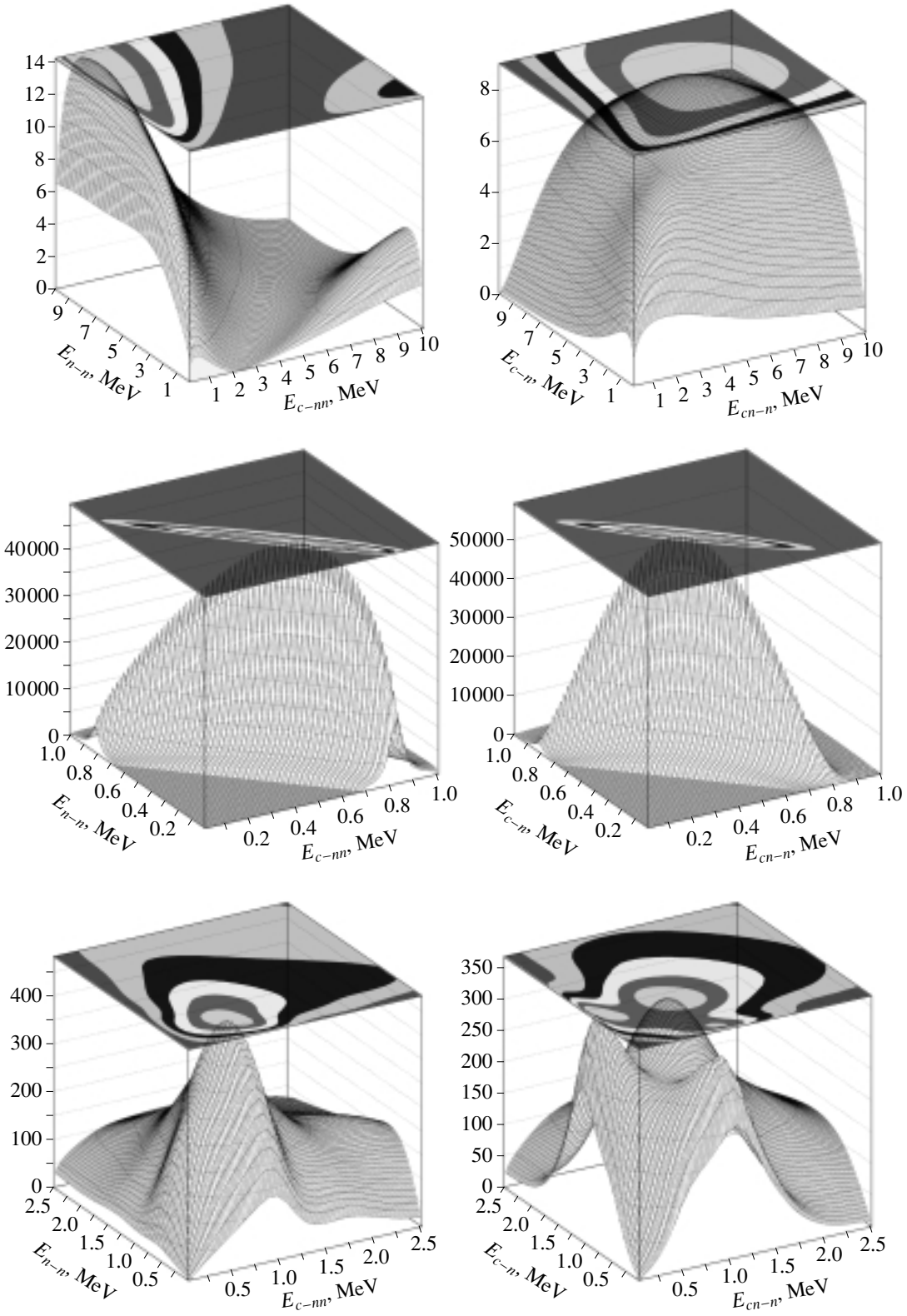

Fig. 2. Energy-correlation plot for the 0^+, 2^+, and 1^-states in ^{6}He: (upper row) transition with antisymmetrized plane wave (no FSI) for 0^+, (lower row) with 1^- FSI, and (middle row) intrinsic correlations for 2^+. The results in the left and the right column were obtained in, respectively, the cluster **T** basis and the "quasishell"-model **Y** basis.

peak energy in the resonance amplification of the interior part of the wave function, and intrinsic energy–momentum correlations for $3 \to 3$ scattering should almost coincide with transition energy–momentum

correlations for reactions. This can serve as a unique signal of the three-body resonance nature of the observed resonance-like enhancement in the cross section.

For qualitative understanding, we can apply the above analytic properties to the $3 \to 3$ scattering amplitudes in the true three-body resonance region (E_0, Γ_0). For the former, we have

$$\frac{d^2\sigma(3)}{d\epsilon_x d\epsilon_y} \sim \frac{A_3^2(E)}{(E-E_0)^2 + \Gamma_0^2/4}\sqrt{\epsilon_{xi}\epsilon_{yi}}. \qquad (2)$$

Considering that $E = \epsilon_{xi} + \epsilon_{yi}$ is invariant (for any pair and the third particle), we can clearly see that the correlation plot should have a straight-line maximum $E_0 = \epsilon_{xi} + \epsilon_{yi}$ and equilateral surfaces (contour plot) of an elliptic type with a "width" of about Γ influenced by the phase space $\sqrt{\epsilon_{xi}\epsilon_{yi}}$ and the partial structure of the state.

This can serve as a discriminating tool in cases of doubt, as was mentioned in the Introduction.

We will illustrate the general properties of correlations using ^{6}He as an example.

The ground-state-correlation plot for the 0^+ monopole and the continuum demonstrates the uncertainty principle for the ground state: the spatial correlations reflect the "Pauli-focusing" effect [3] generating "dineutron" and "cigar" configurations, which correspond to two wings in the E_{n-n}–E_{c-nn} correlation plot. A higher probability of the narrow core–nn energy distribution should be seen, to some extent, in the distributions of longitudinal and transverse momenta measured in fragmentation experiments.

The correlation plots for the well-known 2^+ resonance (Fig. 2) represent a classical example of a three-body resonance, where, in both coordinate systems, the maximum lines follow the $E_0 = \epsilon_{xi} + \epsilon_{yi}$ law, which results from the analytic structure of the scattering amplitude.

We may draw a number of conclusions. The correlations between the 0^+ monopole and the continuum reveal the absence of three-body resonance behavior and reflect the strong influence of FSI.

The correlations between the 1^- dipole and the continuum (Fig. 2) are very similar to those involving the monopole and also reflect the strong influence of FSI.

Thus, the well-known 2_1^+ state is the real three-body resonance, while the 1^- and 0^+ excitations are not.

A correlation analysis of the 2_2^+ and 1^+ states confirms their three-body resonance nature.

6. CONCLUSION

Advances in few-body dynamics have deepened and enriched the understanding of halos as an outstanding structural drip-line phenomenon with extreme clustering into an ordinary core nucleus and a veil of halo nucleons. A large neutron excess creates new phenomena, such as the rearrangement of shells and the intruder s level, which seems to be a feature common to extremely light drip-line nuclei. Then, there is a soft dipole mode, which is responsible for abnormally large EMD cross sections. There are some unsolved problems, such as the structure of halo excitations, the nature of the dipole mode, the matter radii of halo nuclei, and the nature of extremely narrow momentum distributions in fragmentation reactions. These new phenomena and problems stimulate further theoretical and experimental developments and will bring deeper insights into nuclear physics.

ACKNOWLEDGMENTS

The work of B.V. Danilin was supported by the Russian Foundation for Basic Research (project nos. 99-02-17610 and 00-15-96590), and I.J. Thompson acknowledges support from the EPSRC grant no. GR/J/95867.

REFERENCES

1. I. Tanihata, H. Hamagaki, O. Hashimoto, *et al.,* Phys. Lett. B **160B**, 380 (1985).
2. P. G. Hansen and B. Jonson, Europhys. Lett. **4**, 409 (1987).
3. M. V. Zhukov, B. V. Danilin, D. V. Fedorov, *et al.,* Phys. Rep. **231**, 151 (1993).
4. V. M. Efimov, Comments Nucl. Part. Phys. **19**, 271 (1990).
5. R. G. Thomas, Ann. Phys. (Paris) **48**, 231 (1958).
6. T. Aumann *et al.,* Phys. Rev. C **59**, 1252 (1999).
7. K. Ieki *et al.,* Phys. Rev. Lett. **70**, 730 (1993); D. Sackett *et al.,* Phys. Rev. C **48**, 118 (1993).
8. F. Shimoura *et al.,* Phys. Lett. B **348**, 29 (1995).
9. M. Zinser *et al.,* Nucl. Phys. A **619**, 151 (1997).
10. H. Simon *et al.,* Phys. Rev. Lett. **83**, 496 (1999).
11. I. Tanihata, J. Phys. G **22**, 157 (1996).
12. P. G. Hansen, A. S. Jensen, and B. Jonson, Annu. Rev. Nucl. Part. Sci. **45**, 591 (1995).
13. I. Tanihata *et al.,* Phys. Lett. B **289**, 261 (1992).
14. L. V. Chulkov, B. V. Danilin, V. D. Efros, *et al.,* Europhys. Lett. **8**, 245 (1989).
15. J. S. Al-Khalili and J. A. Tostevin, Phys. Rev. Lett. **76**, 3903 (1996); J. S. Al-Khalili, J. A. Tostevin, and I. J. Thompson, Phys. Rev. C **54**, 1843 (1996).
16. J. Bang and C. Gignoux, Nucl. Phys. A **313**, 119 (1979).
17. V. I. Kukulin, V. N. Pomerantsev, K. D. Razikov, *et al.,* Nucl. Phys. A **586**, 151 (1995).
18. S. Funada, H. Kameyama, and Y. Sakuragi, Nucl. Phys. A **575**, 93 (1994).

19. Yu. A. Lurie, A. M. Shirokov, and Yu. F. Smirnov, Rev. Mex. Fis. **40** (Suppl. 1), 63 (1994); Yu. A. Lurie and A. M. Shirokov, Bull. Russ. Acad. Sci., Phys. Ser. **61**, 1665 (1997).
20. D. V. Fedorov, A. S. Jensen, and K. Riisager, Phys. Rev. C **50**, 2372 (1994).
21. A. Csótó, Phys. Lett. B **315**, 24 (1993); Phys. Rev. C **48**, 165 (1993); **49**, 3035 (1994); **49**, 2244 (1994).
22. K. Arai, Y. Suzuki, and K. Varga, Phys. Rev. C **51**, 2488 (1995).
23. J. Wurzer and H. M. Hofmann, Phys. Rev. C **55**, 688 (1997).
24. G. F. Filippov, I. Yu. Rybkin, S. V. Korennov, and K. Kato, J. Math. Phys. **36**, 4571 (1995).
25. D. Baye, Y. Suzuki, and P. Descouvemont, Prog. Theor. Phys. **91**, 271 (1994).
26. S. Saito, Prog. Theor. Phys. **41**, 705 (1969).
27. D. Baye, Phys. Rev. Lett. **58**, 2738 (1987).
28. B. S. Pudliner, V. R. Pandharipande, J. Carlson, *et al.,* Phys. Rev. C **56**, 1720 (1997); R. B. Wiringa, Nucl. Phys. A **631**, 70c (1998).
29. B. V. Danilin, Izv. Akad. Nauk SSSR, Ser. Fiz. **54**, 2212 (1990).
30. B. V. Danilin, I. J. Thompson, M. V. Zhukov, and J. S. Vaagen, Nucl. Phys. A **632**, 383 (1998).
31. E. Garrido, D. V. Fedorov, and A. S. Jensen, Nucl. Phys. A **617**, 153 (1997).
32. G. F. Filippov, Yad. Fiz. **62**, 1237 (1999) [Phys. At. Nucl. **62**, 1164 (1999)].
33. S. Aoyama, S. Mukai, K. Kato, and K. Ikeda, Prog. Theor. Phys. **93**, 99 (1995); **94**, 343 (1995); K. Kato, S. Aoyama, S. Mukai, and K. Ikeda, Nucl. Phys. A **588**, 29c (1995).
34. S. N. Ershov, T. Rogde, B. V. Danilin, *et al.,* Phys. Rev. C **56**, 1483 (1997).
35. A. Csótó, Phys. Rev. C **48**, 165 (1993); A. Csótó and G. M. Hale, Phys. Rev. C **55**, 536 (1997).
36. K. Arai, Y. Suzuki, and R. G. Lovas, Phys. Rev. C **59**, 1432 (1999).
37. I. J. Thompson and M. V. Zhukov, Phys. Rev. C **49**, 1904 (1994).
38. M. Zinser *et al.,* Phys. Rev. Lett. **75**, 1719 (1995).
39. M. Thoennessen, S. Yokoyama, A. Azhari, *et al.,* Phys. Rev. C **59**, 111 (1999).
40. J. Wurzer, H. M. Hofmann, *et al.,* Z. Phys. A **354**, 135 (1996).
41. P. Descouvemont, Nucl. Phys. A **626**, 647 (1997).
42. F. M. Nunes, I. J. Thompson, and R. C. Johnson, Nucl. Phys. A **596**, 171 (1996).
43. N. A. Orr *et al.,* Phys. Rev. Lett. **69**, 2050 (1992).
44. I. Tanihata, T. Kobayashi, O. Yamakawa, *et al.,* Phys. Lett. B **206**, 592 (1988).
45. M. J. G. Borge *et al.,* Phys. Rev. C **55**, R8 (1997).
46. A. I. Baz' and S. P. Merkuriev, Teor. Mat. Fiz. **70**, 397 (1976).
47. A. I. Baz', Zh. Éksp. Teor. Fiz. **70**, 397 (1976) [Sov. Phys. JETP **43**, 205 (1976)].
48. Yu. Ts. Oganessian, V. I. Zagrebaev, and J. S. Vaagen, Phys. Rev. C **60**, 044605 (1999).
49. F. Ajzenberg-Selove, Nucl. Phys. A **490**, 1 (1988).
50. A. Cobis, D. V. Fedorov, and A. S. Jensen, Nucl. Phys. A **631**, 793c (1998); Phys. Rev. C **58**, 1403 (1998).
51. A. Cobis, D. V. Fedorov, and A. S. Jensen, Phys. Rev. Lett. **79**, 2411 (1997).
52. A. A. Korsheninnikov *et al.,* Phys. Rev. C **53**, R537 (1996).
53. H. G. Bohlen *et al.,* Z. Phys. A **351**, 7 (1995).
54. M. V. Zhukov, L. V. Chulkov, D. V. Fedorov, *et al.,* J. Phys. G **20**, 201 (1994).
55. S. N. Ershov, B. V. Danilin, T. Rogde, and J. S. Vaagen, Phys. Rev. Lett. **82**, 908 (1999).
56. B. V. Danilin, T. Rogde, S. N. Ershov, *et al.,* Phys. Rev. C **55**, R577 (1997).
57. I. J. Thompson, B. V. Danilin, V. D. Efros, *et al.,* Phys. Rev. C **61**, 24318 (2000).

Physics of Atomic Nuclei, Vol. 64, No. 7, 2001, pp. 1223–1228. From Yadernaya Fizika, Vol. 64, No. 7, 2001, pp. 1298–1303.

Proceedings of the International Conference "Nuclear Structure and Related Topics"

Four-Body Distorted-Wave Theory for Halo Excitations in Peripheral Fragmentation Reactions*

S. N. Ershov[**], **B. V. Danilin**[1)], **and J. S. Vaagen**[2)]

Joint Institute for Nuclear Research, Dubna, Moscow oblast, 141980 Russia

Received October 25, 2000

Abstract—A microscopic approach to breakup into the low-energy continuum of Borromean two-neutron-halo nuclei is developed by quantum mechanically taking into account both Coulomb and nuclear dissociation. The crucial role of both elastic and inelastic fragmentation is demonstrated for ^{6}He breakup on C and Pb targets at intermediate energies in kinematically complete experiments. For the first time, recent GSI experimental data are analyzed quantitatively, and a rich and complex interplay of reaction mechanisms and low-lying halo excitations is revealed. © *2001 MAIK "Nauka/Interperiodica".*

At least four-body dynamics is necessary for probing the detailed Borromean halo excitation structure. Within a microscopic four-body distorted-wave theory, it was shown in [1] that, in diffractive (elastic) breakup of Borromean halo nuclei on proton target, the correlated continuum excitations play a crucial role for fragment momentum distributions. We have extended this approach to breakup reactions on heavier targets. It is especially suitable for a complete kinematic experiment, which furnishes information about all beam and fragment momenta (with the exception of the recoil of the target nucleus). Such experiments allow a sophisticated analysis of the data and make it possible to reconstruct projectile excitation spectra and various correlations between fragments. Yet, some uncertainty remains since the energy transfer to the target can be distributed in different ways between internal excitations and center-of-mass motion. Theoretical models must take into account the presence of different reaction mechanisms leading to elastic and inelastic fragmentations—i.e., when the target remains in the ground state or goes over to excited states, respectively.

The Borromean nucleus that has received the most thorough theoretical and experimental study is ^{6}He, the testbench for a series of Borromean halo nuclei, such as ^{11}Li and ^{14}Be. Nevertheless, the question of the nature of low-lying soft modes—in particular, a dipole mode—is still under discussion since the theoretical analysis of [2–5] disagrees with recent experimental results [6].

Below, we present the first study of continuum excitations for both elastic and inelastic ^{6}He breakup on ^{12}C (nuclear interaction dominates) and ^{208}Pb (Coulomb dissociation is the main process) targets and compare our theoretical results with recent experimental data from GSI [6] at a collision energy of 240 MeV per projectile nucleon. Other breakup scenarios are discussed in [7].

The amplitude T_{fi} of the breakup reaction $a + A \to \alpha + n_1 + n_2 + A'$ induced by a collision of the projectile a (two-neutron halo) and the target A includes entirely interaction dynamics and is given by

$$T_{fi} = \langle \Psi^{(-)}_{A'}(\mathbf{k}_x, \mathbf{k}_y, \mathbf{k}_f)\, \Phi_{A'} \mid \sum_{p,t} V_{p,t} - U_{aA} \mid \Psi_0\, \Phi_0\, \chi^{(+)}_0(\mathbf{k}_i)\rangle, \quad (1)$$

where Ψ_0 is the halo ground-state wave function, while $\Psi^{(-)}_{A'}(\mathbf{k}_x, \mathbf{k}_y, \mathbf{k}_f)$ is the exact continuum wave function, which describes the relative motion of halo fragments and the target in the excited state $\Phi_{A'}$ ($A' = 0$ labels the ground state). The Jacobi vectors $(\mathbf{k}_x, \mathbf{k}_y)$ characterize the relative motion of three projectile-breakup fragments, and $\mathbf{k}_f$ characterizes the relative target–projectile center-of-mass motion [2, 8]. The sum $\sum_{p,t} V_{p,t}$ is composed of effective NN

*This article was submitted by the authors in English.

[1)]Russian Research Centre Kurchatov Institute, pl. Kurchatova 1, Moscow, 123182 Russia.

[2)]SENTEF, Department of Physics, University of Bergen, Allégaten 55, N-5507 Bergen, Norway.

[**]e-mail: ershov@thsun1.jinr.ru

interactions $V_{p,t}$ between the projectile p and target t nucleons and governs the fragmentation process in the breakup reactions. The optical potential U_{aA} depends on the center-of-mass distance between the a and A nuclei and defines the distorted wave $\chi_0^{(+)}(\mathbf{k}_i)$, which describes the relative motion of colliding nuclei in the input channel. To get $\Psi_{A'}^{(-)}$, some approximations are required. We use approximations at the level of the reaction mechanism, but we treat the three-body structure of the halo projectile in a consistent way, retaining the characteristics of the halo structure. These are contained directly in the halo ground-state wave function and in the spectra of low-lying excitations, where the strength concentration of transitions of different multipolarities, so-called "soft modes," is formed. If there is no direct knockout of a projectile fragment, we cannot neglect any of the mutual interactions. All projectile fragments take a similar part in the interaction process. This is realized for the soft section of the halo spectrum, where the relative fragment velocities are small and are restricted kinematically by a low excitation energy E^*. At low E^*, there are no spectator particles. Also, the reaction should be fast, and the loss of energy has to be small in relation to the initial collision energy. Hence, we factorize the exact scattering wave function $\Psi_{A'}^{(-)}(\mathbf{k}_x, \mathbf{k}_y, \mathbf{k}_f)$ explicitly, isolating the wave function of the excited projectile. Thus, the reaction amplitude can be written as

$$T_{fi} = \langle \chi_{A'}^{(-)}(\mathbf{k}_f)\, \Phi_{A'}\, \Psi^{(-)}(\mathbf{k}_x,\ \mathbf{k}_y) \mid \sum_{p,t} V_{p,t} \mid \Psi_0\, \Phi_0\, \chi_0^{(+)}(\mathbf{k}_i) \rangle\,, \qquad (2)$$

where $\Psi^{(-)}(\mathbf{k}_x,\ \mathbf{k}_y)$ is the three-body continuum wave function of the halo system, while $\chi_{A'}^{(-)}(\mathbf{k}_{i,f})$ is a distorted wave that describes the relative motion of the projectile and target in the state A'. The optical potential U_{aA} does not contribute to (2) because of the orthogonality of the bound state Ψ_0 and the excited states $\Psi^{(-)}(\mathbf{k}_x,\ \mathbf{k}_y)$ of a halo projectile. The post and prior forms of the breakup amplitude are equal in our approximation, since the decomposition of the Hamiltonian in the perturbed and the unperturbed part is the same for the input and the output channel. According to this approach, the nature of breakup is inelastic excitations of the projectile directly to a continuum. Whether this continuum state will be resonant or nonresonant depends on the final-state interactions between the fragments.

To calculate the reaction amplitude, it is necessary to precompute the bound-state (Ψ_0) and continuum [$\Psi^{(-)}(\mathbf{k}_x, \mathbf{k}_y)$] wave functions. For the ^{6}He nucleus, the essential halo structure was obtained within the three-body $\alpha + N + N$ model [2, 9]. In this model, the total wave function is represented by the product of wave functions describing the internal structure of the α core and the relative motion of three interacting constituents. The method of hyperspherical harmonics [2] was used to treat the three-body dynamics of both bound and scattering states and gave [1, 8, 10] a comprehensive description of a variety of data for $A = 6$ systems. For the present calculations, the hyperspherical-harmonic method was extended in an effective way to include core polarization and two-nucleon exchange with the core by modifying the NN interaction within the core. The details of the method will be published elsewhere. We used the Feshbach reduction to an active subspace and, in all partial states, reduced the initial $K \sim 40$ hyperharmonic space (sufficient for practical convergence) to $K \sim 10$, which gives the same results as a strict calculation in a large initial space. Exchange effects are responsible for the difference between the dipole strength functions as calculated in the simple [2, 5] and the improved cluster model, but they affect only slightly the ground-state wave function. In the present calculations, we used the improved cluster wave functions, which give a dipole strength distribution (solid line in Fig. 1) that is consistent with GSI experimental data. The boundaries of the theoretical uncertainties are shown by the dash-dotted lines. It is important to emphasize that, in the calculations of the continuum wave functions $\Psi^{(-)}(\mathbf{k}_x, \mathbf{k}_y)$, the final-state interaction (the pair interactions between all projectile constituents) is fully taken into account.

For a consistent treatment of electromagnetic dissociation, Coulomb and nuclear interactions must be treated on equal footing. The interactions $V_{p,t}$ between projectile and target nucleons have a short-range part due to strong forces, but they also include the Coulomb repulsion for the case where the two nucleons involved are protons. This allows quantum-mechanical calculations of nuclear and Coulomb excitations, including their interference, without an ad hoc partition into different mechanisms.

Inclusive cross sections take into account both elastic and inelastic breakup reactions. To single out these contributions, we use the method from [11–13]. Thus, the inclusive cross section $\sigma = \sigma_{\rm el} + \sigma_{\rm in}$ is decomposed into the elastic ($\sigma_{\rm el}$) and the inelastic

Theoretical (integrated over the excitation-energy region $E^* \leq 10$ MeV) cross sections (mb) for the inelastic excitation of ^{6}He on the ^{208}Pb and ^{12}C targets at an energy of 240 MeV per nucleon {N (C) label calculations with purely nuclear (Coulomb) forces; (a) [15] and (b) [16] label the optical potentials used in the calculations; experimental data [6] include cross sections up to $E^* \leq 12.3$ MeV}

	Total	Elastic	Inelastic	0^+	1^-	2^+	$2^+_{\rm res}$
			^{208}Pb				
N	218	73	145	20	112	87	41
C	299	267	32	0	293	1.3	0.4
$N+C$	480	333	147	20	378	82	40
Expt. [6]	650 ± 110						14 ± 4
			^{12}C				
N^a	16.9	8.6	8.3	1.3	6.9	8.7	4.5
C^a	1.9	1.7	0.2	0	1.9	0.02	0.01
$(N+C)^a$	16.8	9.3	7.5	1.3	7.2	8.4	4.4
$(N+C)^b$	20.6	11.0	9.6	2.7	9.2	8.7	4.5
Expt. [6]	30 ± 5						4 ± 0.8

($\sigma_{\rm in}$) part given by

$$\sigma_{\rm el} = \frac{(2\pi)^4}{\hbar v_i}\int d\mathbf{k}_x\, d\mathbf{k}_y\, d\mathbf{k}_f\, \delta(\varepsilon_i - \varepsilon_f - E^*) \times |\langle \chi_0^{(-)}(\mathbf{k}_f)\Phi_0\Psi^{(-)}(\mathbf{k}_x,\, \mathbf{k}_y)| \times \sum_{p,t} V_{p,t} |\Psi_0\Phi_0\chi_0^{(+)}(\mathbf{k}_i)\rangle|^2,$$

$$\sigma_{\rm in} = \frac{(2\pi)^4}{\hbar v_i}\int d\mathbf{k}_x\, d\mathbf{k}_y \int d\mathbf{r}\, \frac{1}{\pi}(-{\rm Im}\, U_{aA}(\mathbf{r})) \times |\langle G_{\rm opt}(\mathbf{r},\omega)\Phi_0\Psi^{(-)}(\mathbf{k}_x,\, \mathbf{k}_y)| \times \sum_{p,t} V_{p,t} |\Psi_0\Phi_0\chi_0^{(+)}(\mathbf{k}_i)\rangle|^2,$$

where $\varepsilon_{i,f}$ are the kinetic energies of relative center-of-mass motion in the channels, $\omega = \varepsilon_i - E^*$, and the optical-model Green's function $G_{\rm opt}(\mathbf{r},\mathbf{r}',\omega)$ is a solution to the Schrödinger equation with the optical potential U_{aA}.

The calculations employed an effective NN interaction with the parametrization of [14] for the nucleon–nucleon t matrix. The optical potentials [15] for ^{12}C scattering on ^{12}C and ^{208}Pb at 200 MeV per nucleon were used with the radius parameters scaled to the number of nucleons in ^{6}He and are the same for both the input and the output channel.

The table shows total theoretical cross sections integrated with respect to the excitation energy up to 10 MeV for inelastic excitations of ^{6}He on ^{208}Pb and ^{12}C targets. Figures 2 and 3 show the corresponding spectra, along with experimental data [6]. The calculations correctly describe the absolute values and the spectral shape for both reactions, in spite of their different mechanisms. Yet, the theory somewhat underestimates the total cross sections because of insufficient contributions at higher E^*. In this respect, the calculations can be improved by including excitations of higher multipolarities [8] currently not taken into account.

The contributions (Fig. 2a) of various multipole excitations in ^{6}He to the inclusive spectra for the reaction on the lead target display a small monopole contribution; the dipole is dominant; and the well-known three-body 2^+ resonance at 1.8 MeV is strongly excited (the total cross section is about 40 mb). Since the calculated resonance width (about 60 keV) is less than the experimental value (about 113 keV) and since no energy averaging with experimental resolution is performed, the peak in the theoretical cross section exceeds the experimental one. A steep increase in the cross section at the threshold is due exclusively to dipole excitations. Figure 2b shows the cross sections calculated with allowance for only the Coulomb or for only the nuclear interaction. Coulomb dissociation is dominant, but it cannot alone saturate the absolute values of experimental data. The contributions to the cross section from elastic and inelastic fragmentation are shown in Fig. 2c. Although the elastic fragmentation dominates the low-energy part of the spectrum, both contributions must be taken into account simultaneously to obtain an adequate quantitative description. The elastic-fragmentation cross section decreases fast with energy, while the inelastic component is rather flat. In total, $\sigma_{\rm in}$ for the reaction on ^{208}Pb

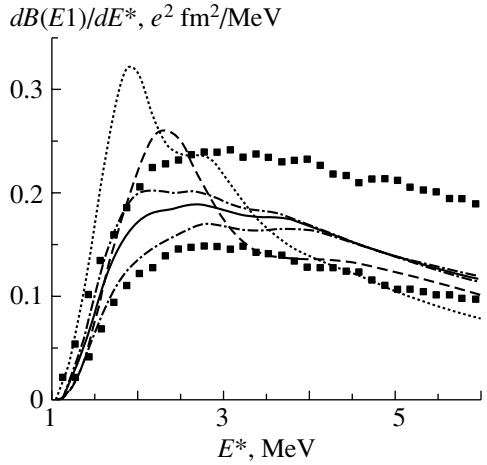

Fig. 1. Dipole strength distributions for ^{6}He. The solid and dash-dotted lines show the distribution and the theoretical uncertainty in the present improved calculations. The dashed and dotted lines represent the results of the theoretical calculations from [2] and [5], respectively. Dark squares indicate the experimentally derived boundaries from [6].

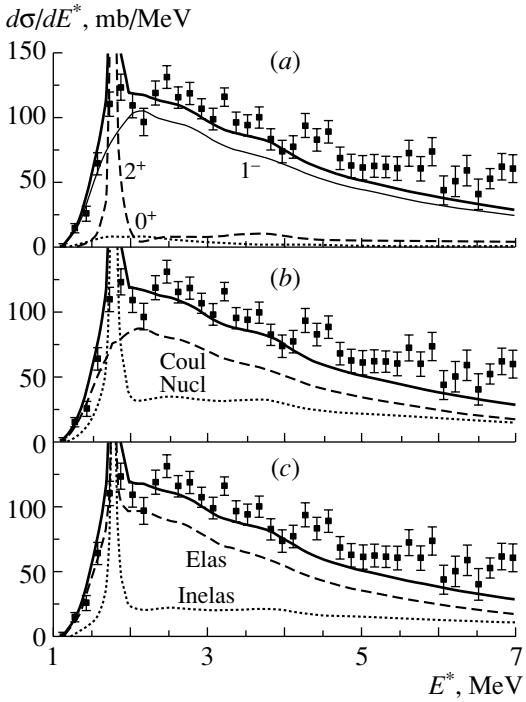

Fig. 2. Theoretical ^{6}He excitation spectrum (thick solid line) for ^{6}He + ^{208}Pb breakup at 240 MeV per nucleon, along with experimental data [6]. (*a*) The thin solid, dashed, and dotted lines show the dipole 1^-, quadrupole 2^+, and monopole 0^+ contributions; (*b*) the dashed (dotted) lines represent the results of the calculations taking into account only nuclear (Coulomb) interactions; and (*c*) the dashed (dotted) lines correspond to the contributions from elastic (inelastic) fragmentation.

contributes about 30% to the total cross section for $E^* \leq 10$ MeV.

Figure 3 shows the results of the theoretical calculations, along with experimental data from [6] for ^{6}He + ^{12}C interactions at 240 MeV per nucleon. The peak, the most pronounced feature in the spectrum, is again due to the excitation of the 2^+ resonance (Fig. 3*a*), with the total cross section being about 4 mb. Above the resonance, approximately half of the strength in the flat part of the spectrum is due to the dipole, third quadrupole, and the rest of the monopole excitations. For a carbon target, the inclusive excitation spectrum is completely determined by the nuclear interaction, the contributions from elastic and inelastic fragmentation being approximately equal (Fig. 3*c*).

Figure 4 illustrates, in particular, the (*a*, *c*) quadrupole and (*b*, *d*) dipole excitations of ^{6}He for a reaction on ^{12}C and ^{208}Pb targets. For quadrupole transitions, the Coulomb interaction is immaterial. The rate of dipole nuclear fragmentation on ^{12}C is more than twice as high as that of Coulomb fragmentation. Its cross section for ^{208}Pb is roughly an order of magnitude larger, but that for dipole Coulomb dissociation increases by more than two orders of magnitude. This factor is similar to the square of the ratio of the target charges and is expected for pure Coulomb excitations. When both interactions are present, the picture becomes more complicated: there are a destructive interference in the internal region and Coulomb excitation in the external region.

To check sensitivity to optical potentials, the calculations for fragmentation on ^{12}C have also been performed with the potential from [16]. This optical potential has a shallow imaginary part and may represent a reasonable variation of a potential family. The calculations show only minor changes for quadrupole transitions; at the same time, the dipole cross sections increase by 30%, and the contribution from monopole excitations is doubled. The total cross section for $E^* \leq 10$ MeV increases by 20%. It is clearly demonstrated that the use of a transparent potential more strongly affects the excitations concentrated more deeply in the interior of the nucleus.

Figure 5 shows the energy spectra of different fragments for ^{6}He breakup on a ^{208}Pb target. The α–neutron and neutron–neutron relative-energy distributions are compared with experimental data [6] in Figs. 5*a* and 5*c*. The α-particle and neutron energy spectra in the projectile rest frame are shown in Figs. 5*b* and 5*d*. The thick solid, thin solid, dashed, and dotted lines represent the total, dipole 1^-, quadrupole 2^+, and monopole 0^+ contributions, respectively. The theoretical two-body energy correlations (Figs. 5*a* and 5*c*) correctly reproduce the fall of the cross section with increasing fragment relative

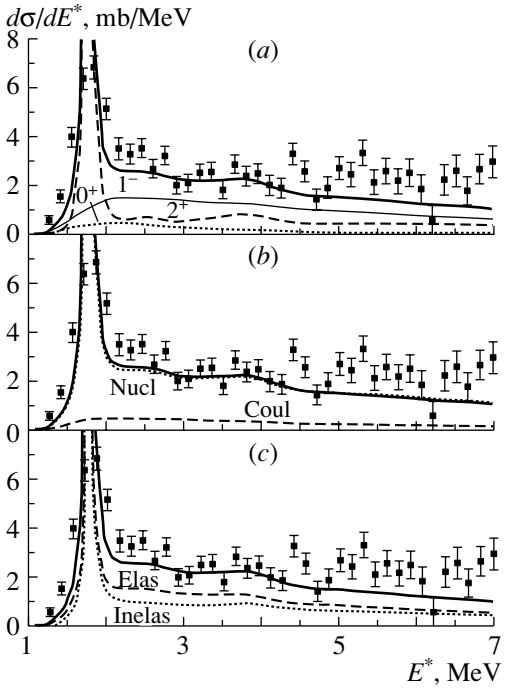

Fig. 3. As in Fig. 2, but for ^{6}He + ^{12}C interactions.

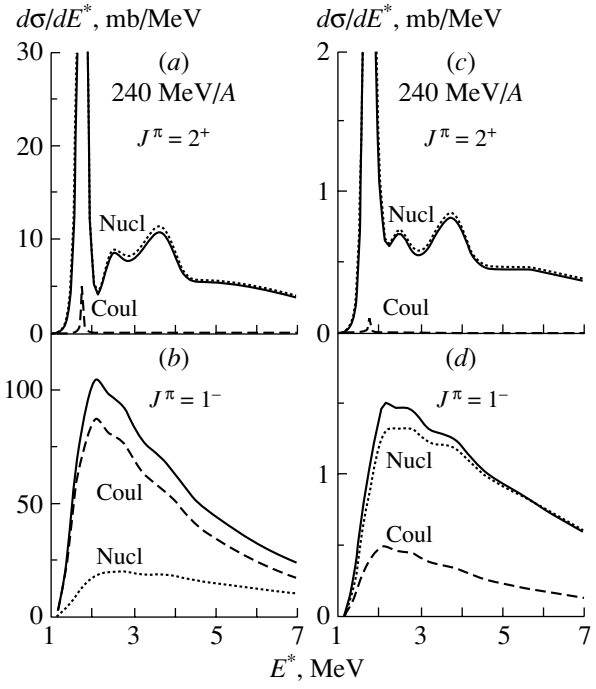

Fig. 4. (*a*) Quadrupole and (*b*) dipole excitations of ^{6}He on ^{208}Pb, and (*c*) quadrupole and (*d*) dipole excitations of ^{6}He on ^{12}C (solid lines). The dashed (dotted) lines represent the results of the calculations taking into account only Coulomb (nuclear) interactions.

energy, but there are some deviations from the measured data at low energies. For a fair comparison with experimental data, the results of theoretical calculations must be convoluted with an instrumental response in order to correct for the efficiency and for the solid-angle acceptance of fragment detectors. Since these experimental distortions are not included in the calculations, it is premature to draw definitive conclusions from this comparison. Decays from dipole excitations dominate the energy spectra and define the slope at high energies. Decays from quadrupole states (from the three-body 2^+ resonance) are important at low energies. The neutron–neutron spectrum (Fig. 5*c*) from the 2^+ resonance has a peak close to the threshold, revealing strong nucleon–nucleon correlations. The shapes of the 2^+ α-particle and neutron spectra (Figs. 5*b* and 5*d*, dashed lines) are qualitatively similar to the shapes that were measured for the decay of the 2^+ resonance populated in the reaction ^{7}Li(d, ^{3}He)^{6}He($J^\pi = 2^+$, $E^* = 1.8$ MeV) [17, 18]. It is interesting to note that the shape of the total α-particle spectrum (Fig. 5*b*, thick solid line) is in perfect agreement with experimental data for neutron–α correlations (Fig. 5*a*). To demonstrate the importance of final-state interactions, the dash-dotted lines in Fig. 5 represent the results of the calculations without taking into account the interactions of the fragments in the output channel (the relative motions of the fragments are described by three-body plane waves), but the halo ground-state wave function preserves a complex correlated structure. We see that only the spectrum of the single heavy fragment (Fig. 5*b*) has a shape qualitatively similar to that in a full calculation (yet, the width of the peak is significantly broader), while all other spectra differ markedly from it.

In summary, we have developed a microscopic four-body DWIA theory for two-neutron halo breakup reactions that is suitable for elastic and inelastic fragmentation processes leading to low-lying halo excitations. Within this approach, Coulomb and nuclear dissociation have been included in a consistent way with allowance for Coulomb–nuclear interference. The method of hyperspherical harmonics has been used to describe consistently the genuine features of the halo bound state and final-state interactions between all halo fragments. The procedure can be applied to an analysis of complete kinematic experiments, which allow a reconstruction of the halo excitation spectrum and single out events carrying the most valuable information about correlations peculiar to two-neutron halo systems. The model has been used to analyze recent experimental data [6] on ^{6}He fragmentation on ^{12}C and ^{208}Pb targets at an energy of 240 MeV per projectile nucleon. In addition to accurate simultaneous descriptions of absolute cross sections and excitation spectra for both reactions, new insights into the intertwining of reaction mechanisms and correlated continuum

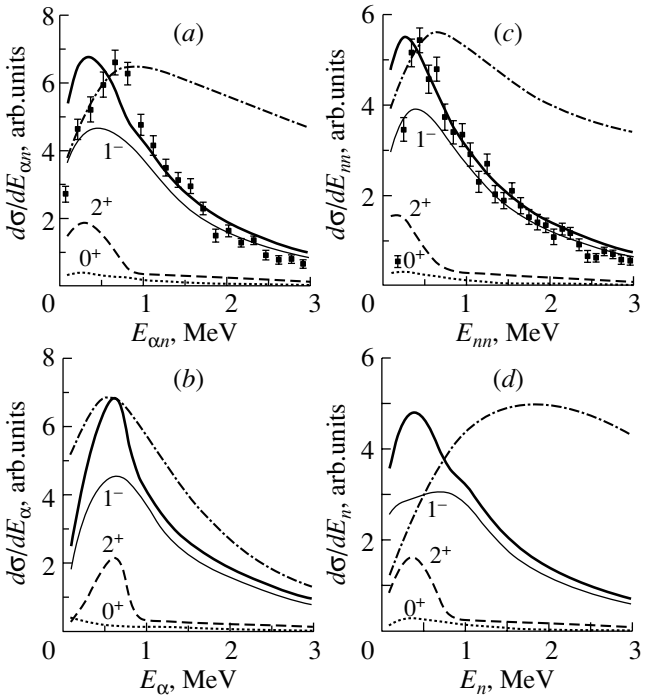

Fig. 5. Theoretical spectra of the relative energy of the (*a*) α particle and the neutron and (*c*) two neutrons for ^{6}He + ^{208}Pb breakup at 240 MeV per nucleon, along with experimental data [6]; (*b*) α-particle and (*d*) neutron energy spectra in the projectile rest frame. The thick solid, thin solid, dashed, and dotted lines represent the total, dipole 1^-, quadrupole 2^+, and monopole 0^+ contributions, respectively. The dash-dotted lines correspond to the calculations of the total spectra without final-state interactions.

structure have been obtained. The important role found for inelastic fragmentation and Coulomb–nuclear interference is consistent with experimental data. Application of the approach to other Borromean nuclei is in progress.

ACKNOWLEDGMENTS

We are grateful to Prof. M.V. Zhukov for stimulating discussions.

This work was performed under financial support from the Bergen member of the RNBT collaboration and BCPL project. The work of B.V. Danilin was supported by the Russian Foundation for Basic Research (project no. 99-02-17610). B.V. Danilin and S.N. Ershov are indebted to the University of Bergen for hospitality.

REFERENCES

1. S. N. Ershov, B. V. Danilin, T. Togde, and J. S. Vaagen, Phys. Rev. Lett. **82**, 908 (1999).
2. B. V. Danilin, I. J. Thompson, J. S. Vaagen, and M. V. Zhukov, Nucl. Phys. A **632**, 383 (1998).
3. A. Csótó, Phys. Rev. C **49**, 3035 (1994).
4. S. Aoyaama, S. Mukai, K. Kato, and K. Ikeda, Prog. Theor. Phys. **93**, 99 (1995).
5. A. Cobis, D. Fedorov, and A. Jensen, Phys. Rev. Lett. **79**, 2411 (1997).
6. T. Aumann *et al.,* Phys. Rev. C **59**, 1252 (1999).
7. G. F. Bertsch, K. Hencken, and H. Esbensen, Phys. Rev. C **57**, 1366 (1998).
8. S. N. Ershov, T. Togde, B. V. Danilin, *et al.,* Phys. Rev. C **56**, 1483 (1997).
9. M. V. Zhukov, B. V. Danilin, D. V. Fedorov, *et al.,* Phys. Rep. **231**, 151 (1993).
10. B. V. Danilin, M. V. Zhukov, S. N. Ershov, *et al.,* Phys. Rev. C **43**, 2835 (1991).
11. N. Austern and C. M. Vincent, Phys. Rev. C **23**, 1847 (1981).
12. T. Udagawa and T. Tamura, Phys. Rev. C **24**, 1348 (1981).
13. A. Kasano and M. Ichimura, Phys. Lett. B **115B**, 81 (1982).
14. M. A. Franey and W. G. Love, Phys. Rev. C **31**, 488 (1985).
15. J. Y. Hostachy, M. Buenard, J. Chauvin, *et al.,* Nucl. Phys. A **490**, 441 (1988).
16. M. E. Brandan, Phys. Rev. Lett. **60**, 784 (1988).
17. O. V. Bochkarev, A. A. Korsheninnikov, E. A. Kuz'min, *et al.,* Yad. Fiz. **46**, 12 (1987) [Sov. J. Nucl. Phys. **46**, 7 (1987)].
18. O. V. Bochkarev, A. A. Korsheninnikov, E. A. Kuz'min, *et al.,* Yad. Fiz. **57**, 1351 (1994) [Phys. At. Nucl. **57**, 1281 (1994)].

Physics of Atomic Nuclei, Vol. 64, No. 7, 2001, pp. 1229–1235. From Yadernaya Fizika, Vol. 64, No. 7, 2001, pp. 1304–1310.

Proceedings of the International Conference "Nuclear Structure and Related Topics"

Light Exotic Nuclei: A New Explanation of Halo*

G. S. Anagnostatos, **C. Politis**, **A. Vahlas**, **J. Giapitzakis**, **A. N. Antonov**[1)], **and M. Avrigeanu**[2)]

Institute of Nuclear Physics, National Center for Scientific Research Demokritos, Aghia Paraskevi, Attiki, Greece

Received October 25, 2000

Abstract—The experimental Tanihata density distributions for both protons and neutrons in ^{6,8}He are very well reproduced here without an increase of the $1p$ neutron orbital size. Instead, an internal collective rotation, due to the invalidity of the adiabatic approximation, leads to the same measurable increase in the radius and to a simultaneous decrease in the separation energy of the nucleons participating in this rotation. Further support of the approach presented is gained by the reproduction of the ground-state properties of $^{7-11}$Be and of the excited (particle and rotational) states of ^{11}Be. © *2001 MAIK "Nauka/Interperiodica".*

1. INTRODUCTION

Light exotic nuclei constitute a hot subject of nuclear physics today, due to new very interesting phenomena observed during their research. These phenomena include the neutron (or even proton) halo, the weak binding of the last one or two neutrons, the inverse sequence of energy levels, the huge moment of inertia of certain rotational bands, etc. [1–3]. This exciting new physics stimulated new experimental research and attracted many theorists for its explanation. The first experiments referring to nucleon distributions of ^{6}He, ^{8}He, and ^{11}Li are interpreted by assuming that the nucleons responsible for the very large radius are, in some unusual way, far away from the nuclear core [1]. This assumption leads simultaneously to the increase in the nuclear radius and to the weak binding of the halo nucleons. However, this assumption does not explain either the inversion of levels or other phenomena observed in halo nuclei. Moreover, this assumption does not explain due to what mechanism nucleons, despite the apparent attractive forces, prefer to stay far away from the core and, in general, why light nuclei should differ so much from the other nuclei. Through the present work, an alternative explanation of the halo phenomenon and other related phenomena mentioned above is attempted. This alternative explanation considers that halo (and in general exotic) nuclei have a structure similar to other nuclei and what is really different in these nuclei is an extra degree of freedom responsible for all related phenomena. This additional degree of freedom is an internal collective rotation mixed with the usual internal motion (of shell-model type) and is an indispensable part of the nucleon motion even in the nuclear ground state. This mixing is inevitable due to the adiabatic approximation invalidity (since $\omega_{\rm rot} \approx \omega_{\rm intr}$) in very light nuclei in contrast to heavy nuclei where this approximation is valid (since $\omega_{\rm rot} \ll \omega_{\rm intr}$) and the collective rotation appears as an excitation in rotational bands. The reason behind this internal collective rotation is the polarization of the core, which leads to an internal angular momentum $J = 2^+$, which should be compensated (counterbalanced) by a rotation $R = 2^+$ of opposite direction in such a way that, for example, in even–even nuclei, the total angular momentum is zero, i.e., $\mathbf{I} = \mathbf{J} + \mathbf{R} = \mathbf{0}$. This polarization, which in other words means no perfect pairing of the nucleon angular momenta, is the result of a huge deformation appearing in very light nuclei. Indeed, these nuclei can have an even planar average structure. The good results obtained here lend support to our alternative explanation of halo and related phenomena.

2. THE MODEL

The model employed here is the isomorphic shell model (ISM), which is a microscopic nuclear structure model that incorporates into a hybrid model the prominent features of single-particle and collective approaches in conjunction with the nucleon finite size.

*This article was submitted by the authors in English.

[1)]Institute of Nuclear Research and Nuclear Energy, Sofia, Bulgaria.

[2)]"Horia Hulubei" National Institute of Physics and Nuclear Engineering, Bucharest, Romania.

**e-mail: anagnos@mail.demokritos.gr

The model consists of two complementary parts, namely, the semiclassical part [4] and the quantum mechanical part [5]. Both the parts give very good results which are consistent with each other.

2.1. The Quantum Mechanical ISM

The Hamiltonian of the model is analyzed into partial state-dependent Hamiltonians which are different for neutrons (N) and for protons (Z) as follows, where crossing terms between partial Hamiltonians of different shells, H_{ij}, have been omitted:

$$H = {}_{N}H_{1s} + {}_{N}H_{1p} + {}_{N}H_{1d2s} + ... \qquad (1)$$
$$+ {}_{Z}H_{1s} + {}_{Z}H_{1p} + {}_{Z}H_{1d2s} + ...,$$

where a harmonic oscillator is taken as the central potential.

The different ω_i are not taken as adjusted parameters, but all are determined from the harmonic oscillator relation

$$\hbar\omega_i = \left(\frac{\hbar^2}{m\langle r_i^2\rangle}\right)\left(n_i + \frac{3}{2}\right), \qquad (2)$$

where $\langle r_i^2\rangle^{1/2}$ is the root-mean-square radius of nucleon centers for the particular neutron or proton shell under consideration and is estimated in the semiclassical part of the model (given below) with respect to only two numerical parameters.

In addition to eigenvalues for the energy derived from (1), Coulomb, spin-orbit, isospin, and last odd nucleon (neutron or proton, if it exists) energies are introduced in the estimation of the binding energy of a nucleus as usual.

2.2. The Semiclassical ISM

This part of the model is based on two assumptions, namely, that of an equilibrium of nucleon average positions on spherical shells and that of packing of the average forms of nuclear shells. The first leads uniquely to the conclusion that the average forms of nuclear shells have the high symmetry of equilibrium (regular) polyhedra, while the second leads uniquely to the sizes of these polyhedra, when they are considered superimposed with a common center and nucleons are taken with finite size ($r_p = 0.860$ fm and $r_n = 0.974$ fm).

Figure 1 shows the average forms of the first three neutron shells and those of the first three proton shells in relative size and orientation, while Fig. 1 of [4] shows the average polyhedral forms of all nuclear shells up to ^{208}Pb. The sizes of these polyhedra are also given at the bottom of each block of these figures. From Fig. 1 here and from Fig. 1 of [4], it is apparent that a magic number is reproduced, all the way up to ^{208}Pb, each time a polyhedron is completed.

One should further notice in Fig. 1 that the vectors labeled ${}_{n}\theta_l^m$ precisely represent the orbital angular momentum quantization of directions and that the value labeled ρ at the low right corner of each block of Fig. 1 stands for the maximum possible distance of the polyhedral vertices from these vectors. These ρ values are used for the estimation of the kinetic-energy part due to nucleon orbiting, as will be understood shortly.

In this part of the model, the binding energy of a nucleus is given by

$$E_B = \sum_{ij} V_{ij} + \sum_{nlm}\langle T_{nlm}\rangle + \sum_{ij}(E_{\rm C})_{ij} \qquad (3)$$
$$+ \sum(E_{\rm SO}) + E_{\rm ISO} + E_{\text{odd } n},$$

where the expressions for the last four terms are taken in the usual way as mentioned in the quantum-mechanical part of the model [4, 5], while the first two terms are computed by using the following two equations:

$$V_{ij} = \frac{\left[3.7\,(10)^{16}\,\exp(-30.187 r_{ij}) \;-\; 363\exp(-1.632 r_{ij})\right]}{r_{ij}}, \qquad (4)$$

$$\langle T_{nlm}\rangle = \frac{\hbar^2}{2m}\left[\frac{1}{R_{\rm max}^2} + \frac{l(l+1)}{\rho_{nlm}^2}\right], \qquad (5)$$

where $R_{\rm max}$ is the outermost polyhedral radius (R) plus the relevant nucleon radius (i.e., $r_n = 0.974$ fm and $r_p = 0.860$ fm), i.e., it is the radius of the nuclear volume in which the nucleons are confined, and ρ_{nlm} is as explained earlier.

The mass nuclear radius for both the parts of the model is given by

$$\langle r^2\rangle_{\rm mass}^{1/2} \qquad (6)$$
$$= \left[\frac{\sum_{i=1}^{Z} R_i^2 + \sum_{i=1}^{N} R_i^2 + Z(0.8)^2 + N(0.91)^2}{Z+N}\right]^{1/2},$$

from which one can get the expression for the neutron radius by taking $Z = 0$ or the expression for

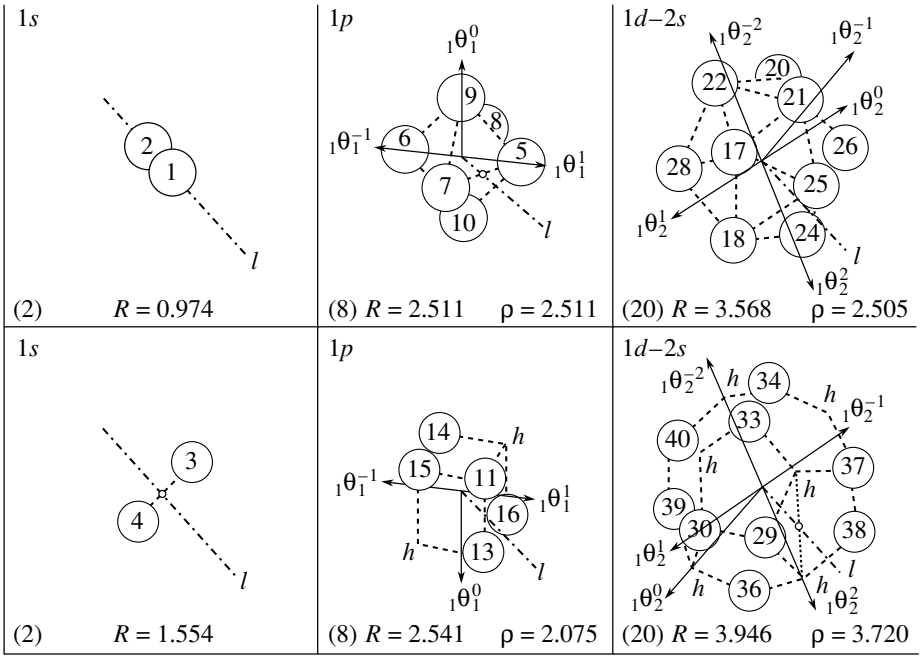

Fig. 1. First three average neutron shells and first three average proton shells in relative size and orientation [4].

the charge radius by taking $N = 0$. In the latter case one could consider an extra small term equal to $-0.116(N)$, where -0.116 fm^2 is the mean square charge radius of a neutron.

2.3. The Model for Very Light Nuclei

When either of the two parts of the model is applied to determine binding energies and radii for all existing nuclei, the following observation is made. The predictions for both properties are in very good agreement with the experimental data except for the very light nuclei, where the model binding energies are systematically larger than the experimental values, while the model radii are systematically smaller than the data. This observation implies that for very light nuclei there is a phenomenon which is not sufficiently described in the framework of the model so far [6].

Here, we rewrite the Hamiltonian of (1) to include rotation:

$$H = H_0(r') + H_{\rm rot} + H', \qquad (7)$$

where the three terms on the right-hand side describe the motion of the internal degree of freedom [of shell-model type as in (1)], the collective rotation of nucleons, and the coupling between the previous two terms, respectively.

By taking $\mathbf{I} = \mathbf{R} + \mathbf{J}$ (where $\mathbf{R}$ is the angular momentum due to rotation, $\mathbf{J}$ is the internal angular momentum, and $\mathbf{I}$ is the total angular momentum), for the ground state where $I = 0$, e.g., for even–even nuclei, (7) becomes

$$H = H_0(r') + \frac{\hbar^2}{2\Im}\mathbf{J}^2, \qquad (8)$$

where $\Im$ is the moment of inertia and both terms on the right-hand side refer to the internal motion of the nucleons. That is, even for the ground state with $\mathbf{I} = 0$, there is an additional term in the Hamiltonian if the internal angular momenta do not couple to zero. In other words, if the spins ($\mathbf{s}$) or the individual total angular momenta ($\mathbf{j}$) of certain nucleons do not pair perfectly but they lead to an internal total angular momentum $\mathbf{J}$, then an internal rotation $\mathbf{R}$ is needed to compensate $\mathbf{J}$ and to lead to total nuclear angular momentum $\mathbf{I} = 0$. It is considered that the aforementioned deviations of the binding energies and radii are due to this internal rotation. In other words, one may say that for the very light nuclei the deformation is very large and does not permit perfect pairing, a fact which leads to an internal $\mathbf{J} \neq 0$. In addition, the internal rotation $\mathbf{R}$, necessary to compensate $\mathbf{J}$, cannot be separated from the usual internal motion since the adiabatic approximation is not valid for these nuclei, where $\omega_{\rm rot} \approx \omega_{\rm intr}$. This is in contrast to what happens in nuclei of the well-deformed region where $\omega_{\rm intr} \approx 100\omega_{\rm rot}$ and the total wave function can be written as a product of the internal wave function and the rotational wave function. Under the valid conditions for very light nuclei, the internal wave function (up to a normalization factor) can be assumed as

$$\psi \propto \chi^{\tau}_{K=0}(r'), \qquad (9)$$

where K is the projection of the total angular momentum on the axis (z') and τ stands for the rest of the quantum numbers. In other words, the usual internal motion and the internal collective rotation are coupled in the form of (9).

It can be derived from (8) that the mass radius of a nucleus is given by

$$\langle r^2\rangle_{\rm mass} = \frac{\sum_{i=1}^{Z}\langle r_i^2\rangle + \sum_{i=1}^{N}\langle r_i^2\rangle + \Im_Z + \Im_N}{Z+N}, \tag{10}$$

where $\Im_Z$ and $\Im_N$ are the proton and the neutron moments of inertia due to the rotation coming from the second term of (8). If the proton or the neutron radii are needed, they can be derived from (10) in an obvious way.

3. APPLICATIONS TO SPECIFIC VERY LIGHT NUCLEI

3.1. Support of Internal Collective Rotation from ^{6}He and ^{8}He

The isotopes ^{6}He and ^{8}He are employed to demonstrate that the assumption of an internal collective rotation of certain nucleons leads to the same measurable density distribution like the assumption of an increase in the radius of certain orbitals.

Figure 2 demonstrates the proton and the neutron density distributions for ^{6}He (Fig. 2*a*) and ^{8}He (Fig. 2*b*) according to Tanihata's experiments [1]. Tanihata was able to fit these curves by assuming that the same orbitals, namely $1s$ and $1p$, are involved as in the conventional shell model, and that the only difference is the size of the $1p$ neutron orbital, which takes on the values 3.22 and 3.05 fm for ^{6}He and ^{8}He, instead of 2.13 and 2.24 fm, respectively. As a consequence of this increase in the orbital size, the separation energy of a $1p$ neutron is reduced. Equation (11) is the Tanihata equation for the proton and neutron density distributions, and only one free parameter, as explained in [1], is necessary for the reproduction of each of the four curves in Fig. 2:

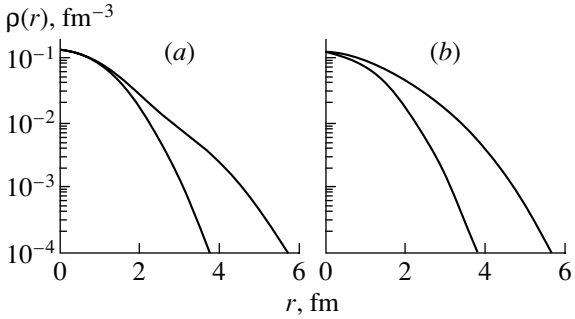

Fig. 2. Tanihata and ISM neutron (higher curve) and proton (lower curve) density distributions for (*a*) ^{6}He and for (*b*) ^{8}He.

$$\rho_X(r) = \frac{1}{4\pi}\left[2\Re_{1s}^2(r) + (X-2)\Re_{1p}^2(r)\right],\ X = N, Z. \tag{11}$$

Here, we present the density distributions in the natural orbital representation (e.g., [7]), which is a convenient method to describe nucleon–nucleon correlation effects in a given correlated nuclear state. This method reflects the depletion of the states below the Fermi level (hole states) and the partial occupancy of the states above it (particle states). Such a particle state is the $1d$ state for nucleons in ^{6}He and ^{8}He. The neutron and proton densities for both isotopes have the form

$$\rho_X(r) = \frac{1}{4\pi}\left[2\lambda_{1s}\Re_{1s}^2(r) + (X-2)\lambda_{1p}\Re_{1p}^2(r) + \frac{X}{2}10\lambda_{1d}\Re_{1d}^2(r)\right],\quad X = N, Z. \tag{12}$$

According to our approach, the occupancy of the $1s$ state is reduced ($\lambda_{1s} < 1$) and, keeping $\lambda_{1p} = 1$, again only one free parameter (λ_{1s}) is needed to describe the density distributions due to the relationship

$$2\lambda_{1s} + (X-2)\lambda_{1p} + \frac{X}{2}10\lambda_{1d} = X. \tag{13}$$

This is true since all $\hbar\omega$ of $\Re_{nl}$ functions come from the geometry of ISM and (2). As can be seen from Fig. 2, the reproduction of the densities via (12) is almost identical to that of Tanihata to the degree that the two fittings cannot be distinguished from each other in the figure. The identity of the two fittings is also apparent from the neutron, proton, and mass rms radii of ^{6}He and ^{8}He [1]. The values of these radii up to the second decimal are identical for both the Tanihata (11) and the present (12) approach. The parameter values of the ISM approach are as follows:

for protons: in ^{6}He $\lambda_{1s} = 0.96$, $\lambda_{1d} = 0.008$, $\hbar\omega_{1s} = 25.76$ MeV, and $\hbar\omega_{1d} = 439.87$ MeV; in ^{8}He $\lambda_{1s} = 0.98$, $\lambda_{1d} = 0.004$, $\hbar\omega_{1s} = 25.76$ MeV, and $\hbar\omega_{1d} = 28.13$ MeV;

for neutrons: in ^{6}He $\lambda_{1s} = 0.655$, $\lambda_{1p} = 1.0$, $\lambda_{1d} = 0.0345$, $\hbar\omega_{1s} = 42.71$ MeV, $\hbar\omega_{1p} = 16.44$ MeV, and $\hbar\omega_{1d} = 11.22$ MeV; in ^{8}He $\lambda_{1s} = 0.555$, $\lambda_{1p} = 1.0$, $\lambda_{1d} = 0.0297$, $\hbar\omega_{1s} = 42.71$ MeV, $\hbar\omega_{1p} = 16.44$ MeV, and $\hbar\omega_{1d} = 10.94$ MeV.

The extra state $1d$ appearing in (12), as explained in [6], could be attributed to the rotation implied by

Table 1. ISM predictions for internal vibrational, internal rotational, and binding energies, together with the experimental binding energies (in MeV) for the isotopes $^{7-10}$Be [also, model predictions for total (finite nucleons), neutron, and proton (point nucleons) moments of inertia (in fm^2)]

Nucleus	Vertex config.	$E_{\text{intr.vibr.}}$	$E_{\text{intr.rot.}}$	$E_{B\ \text{model}}$	$E_{B\ \text{expt}}$	$\Im_{n+p}$	$\Im_n$	$\Im_p$
^{7}Be	p: 3, 4, 12, 14	50.39	−13.96	36.43	37.60	8.91	3.16	4.30
	n : 1, 2, 8							
^{8}Be	p: 3, 4, 12, 14	64.30	−7.37	56.93	56.50	16.44	6.31	8.61
	n : 1, 2, 6, 8							
^{9}Be	p: 3, 4, 12, 14	65.12	−7.65	57.47	58.17	16.26	9.12	4.30
	n : 1, 2, 6–8							
^{10}Be	p: 3, 4, 12, 14	63.91	–	63.91	64.98	–	–	–
	n : 1, 2, 5–8							

(8). Indeed, the parameters of $1d$ states given above come from the rotation properties of the valence neutrons and protons of ^{6}He and ^{8}He.

From the discussion in this section, one can realize that, according to the present work, exotic nuclei are equally compact as the usual nuclei and what really gives the increase of nuclear radius and the decrease of separation energy for certain nucleons is an extra degree of freedom, that of an internal collective rotation, appearing due to the adiabatic approximation invalidity in these nuclei.

In the analytical expression for the density (12) based on the natural orbital representation, the phenomenon of the internal collective rotation is reflected by the existence of the term containing the particle d state (above the Fermi level in the He isotopes) which is occupied with probability value λ_{1d}. The latter is closely related to beyond-mean-field correlations at short distances between nucleons [7].

3.2. Support from the Chain of $^{7-10}$Be

Further support to the existence of an internal collective rotation in explaining experimental data on very light nuclei (either exotic or not) is provided here by the chain of Be isotopes with $A = 7$–10.

Taking ^{7}Be as a usual nucleus (i.e., equally compact as any other nucleus), it has been found that, if the places numbered 1, 2, and 8 for neutrons and 3, 4, 12, and 14 for protons (among all possibilities offered from Fig. 1) are chosen to accommodate the average positions of the three neutrons and of the four protons in ^{7}Be, the maximum binding energy (3) results (50.39 MeV). For such a nucleus, the point proton rms radius is 2.11 fm. Further, if a rotation is considered around the axis (x, y) (i.e., around the axis in 45° with both $+x$, $+y$ axes), the moment of inertia of the valence (finite size) nucleons is 8.91 fm^2 (namely, 4.30 fm^2 for the point protons and 3.16 fm^2 for the point neutrons), for which the rotation energy for $J = 2$ is 13.96 MeV, according to the formula ($\Im$ being in fm^2)

$$E_R = \frac{\hbar^2}{2m}\,\frac{J(J+1)}{\Im}. \tag{14}$$

Hence, the model binding energy is 36.43 MeV ($= 50.39 - 13.96$). Also, the corresponding point proton rms radius due to rotation is 1.04 fm, according to the formula

$$r^2_{p(\text{rot})} = \frac{\Im_p}{Z}. \tag{15}$$

Thus, the effective point proton rms radius, due to the intrinsic proton distribution and to the internal collective rotation, is 2.35 fm, according to the formula

$$r^2_{p(\text{eff})} = r^2_{p(\text{intr})} + r^2_{p(\text{rot})}. \tag{16}$$

It is satisfying that the experimental point proton rms radius for this nucleus is 2.36(2) fm [8], thus being in good agreement with our prediction. Following a similar reasoning, the point neutron intrinsic (shell-model type) rms radius is 1.65 fm and that due to internal rotation is 1.03 fm and, hence, that of effective radius is 1.95 fm. For these neutron radii, there are not experimental values for comparison. All aforementioned values of moments of inertia, energies, and radii for ^{7}Be are listed in Tables 1 and 2.

Thus, considering for ^{7}Be an internal collective rotation of the valence nucleons, we simultaneously find a rotational energy and a rotational radius that are needed to lead to binding energy and the effective point proton rms radius very close to the experimental

Table 2. ISM proton, neutron, and mass rms radii for point nucleons, together with available experimental values [8] (in fm)

Nucleus	$r_{p\,\mathrm{intr.vibr.}}$	$r_{p\,\mathrm{intr.rot.}}$	$r_{p\,\mathrm{model}}$	$r_{p\,\mathrm{expt}}$	$r_{n\,\mathrm{intr.vibr.}}$	$r_{n\,\mathrm{intr.rot.}}$	$r_{n\,\mathrm{model}}$	$r_{m\,\mathrm{model}}$
^{7}Be	2.11	1.04	2.35	2.36(2)	1.65	1.03	1.95	2.19
^{8}Be	2.11	1.47	2.57	–	1.91	1.26	2.29	2.43
^{9}Be	2.11	1.04	2.35	2.34(1)	2.04	1.35	2.45	2.41
^{10}Be	2.11	–	2.11	2.24(8)	2.13	–	2.13	2.12

Table 3. Same as in Table 1, but for the low excitation spectrum of ^{11}Be

State	Vertex config.	$E_{\mathrm{intr.vibr.}}$	$E_{\mathrm{intr.rot.}}$	$E_{B\,\mathrm{model}}$	$E_{\mathrm{exc.\,model}}$	$E_{\mathrm{exc.\,expt}}$	$\Im_{n+p}$	$\Im_n$	$\Im_p$
$1/2^+$	p: 3, 4, 12, 14	77.34	−9.87	67.47	0.0	0.0	12.61	12.05	–
	n: 1, 2, 5–8, 27								
$1/2^-$	p: 3, 4, 11, 14	80.02	−13.15	66.87	0.60	0.32	9.46	–	8.61
	n: 1, 2, 5–9								
$5/2^+$	p: 3, 4, 12, 14	72.15	−6.47	65.68	1.79	1.778	19.23	9.21	8.61
	n: 1, 2, 5–8, 27								
$3/2^-$	p: 3, 4, 12, 14	72.30	−9.05	63.25	4.22	3.956	13.75	–	12.91
	n: 1, 2, 6–10								

Table 4. Same as in Table 2, but for the low excitation spectrum of ^{11}Be

State	$r_{p\,\mathrm{intr.vibr.}}$	$r_{p\,\mathrm{intr.rot.}}$	$r_{p\,\mathrm{model}}$	$r_{n\,\mathrm{intr.vibr.}}$	$r_{n\,\mathrm{intr.rot.}}$	$r_{n\,\mathrm{model}}$	$r_{m\,\mathrm{model}}$	$r_{m\,\mathrm{expt}}$
$1/2^+$	2.11	–	2.11	2.39	1.31	2.73	2.52	2.58(2) [9]
$1/2^-$	2.11	1.47	2.57	2.19	–	2.19	2.33	–
$5/2^+$	2.11	1.47	2.57	2.39	1.17	2.66	2.62	–
$3/2^-$	2.11	1.80	2.77	2.19	–	2.19	2.42	–

values, without considering any adjustable parameter and any increase for the size of the $1p$ orbitals involved.

Similar calculations for the remaining isotopes of the chain up to ^{10}Be are listed in Tables 1 and 2. The previous explanations given for ^{7}Be are sufficient for understanding all pieces of information provided in these tables for all remaining isotopes of the chain. It is interesting to notice that ^{10}Be does not possess the internal collective rotation and, indeed, its binding energy and radius are sufficiently reproduced by considering this nucleus as a usual nucleus, where a binding energy and a radius are reproduced by considering shell-model type motion alone.

3.3. Support from the Low Excitation Spectrum of ^{11}Be: $2s_{1/2}$ Intruder State

The calculations for determining the low-energy excitation spectrum of ^{11}Be are summarized in Tables 3 and 4, and are similar to those of Tables 1 and 2.

First, the vertex configuration corresponding to each of the low-lying states of this nucleus is determined (namely, the vertex configurations for the states $2s^+_{1/2}$, $1p^-_{1/2}$, $1d^+_{5/2}$, and $1p^-_{3/2}$). The configuration chosen for each state corresponds to the maximum binding energy for this state. Then, for each of such configurations, all quantities included in the tables are computed. According to the net energy of each of these states from Table 3, we conclude that the order of the levels is $1/2^+$, $1/2^-$, $5/2^+$, and $3/2^-$, i.e., exactly as the experimental order. The appearance of the $2s_{1/2}$ intruder state in the ground state of ^{11}Be is well understood here, as a cumulative effect of all energy components included in Table 3 for this nucleus.

In Table 4, one also observes the relative size of the rms neutron and proton radii for each state. Thus, for the ground state of ^{11}Be, it is apparent that the neutron radius is much larger than that of the protons,

while for the state $5/2^+$ both the neutron and proton radii are extended but are almost equal, and for the state $1/2^-$ the proton radius is much larger than that of the neutrons, what is also true for the $3/2^-$ state. Thus, in the low-lying excitation spectrum of ^{11}Be, the relative size of neutron and proton radii changes from state to state.

3.4. Support from the $3/2^-$ Rotational Band of ^{11}Be

In [3], the experimental rotational band of ^{11}Be is provided with the state $3/2^-$ as a band head. The experimental moment of inertia of this band is 91.23 fm^2 and is interpreted as due to a large ($\sim$5–6 fm) separation of the two α-like particles in this nucleus. In the model here, a compact structure of ^{11}Be leads to a large moment of inertia, 92.32 fm^2, by simply considering a simultaneous rotation around three perpendicular axes (which is almost equivalent to a rotation around the nuclear center), instead of a rotation around a single axis as usual. This is possible in the framework of the model, where the nucleon average positions constitute a distinct and not a continuous structure. For such an average structure, there are several axes of symmetry and several axes of rotation. The specific components of the moment of inertia for finite nucleons rotating around the x, y, z axes are $\Im_x = 27.52$ fm^2, $\Im_y = 28.68$ fm^2, and $\Im_z = 36.18$ fm^2, respectively.

4. CONCLUSIONS

A new approach in studying exotic nuclei is presented according to which these nuclei are equally compact as ordinary nuclei. The main difference between these two groups of nuclei is that the exotic ones have an extra degree of freedom—the internal collective rotation. It appears due to the adiabatic approximation invalidity which is responsible for the new phenomena observed in these nuclei.

Ground-state properties of ^{6,8}He and $^{7-11}$Be and excited-state properties (including the $2s\,1/2$ intruder state and the rotational band based on the $3/2^-$ state) of ^{11}Be lend support to the present approach.

REFERENCES

1. I. Tanihata *et al.,* Phys. Lett. B **289**, 261 (1992).
2. M. V. Zhukov *et al.,* Phys. Rep. **231**, 151 (1993).
3. H. G. Bohlen *et al.,* Prog. Part. Nucl. Phys. **42**, 17 (1999).
4. G. S. Anagnostatos, Int. J. Theor. Phys. **24**, 579 (1985).
5. G. S. Anagnostatos, Can. J. Phys. **70**, 361 (1992).
6. G. S. Anagnostatos *et al.,* Phys. Rev. C **58**, 2115 (1998).
7. A. N. Antonov, P. E. Hodgson, and I. Zh. Petkov, *Nucleon Momentum and Density Distributions in Nuclei* (Clarendon Press, Oxford, 1988); *Nucleon Correlations in Nuclei* (Springer-Verlag, Berlin, 1993).
8. P. Navratil and B. R. Barrett, Phys. Rev. C **57**, 3119 (1998).
9. M. Lassaut and R. J. Lombard, Z. Phys. A **341**, 125 (1992).

Physics of Atomic Nuclei, Vol. 64, No. 7, 2001, pp. 1236–1239. From Yadernaya Fizika, Vol. 64, No. 7, 2001, pp. 1311–1314.

Proceedings of the International Conference "Nuclear Structure and Related Topics"

Nature of Halo in Light Nuclei*

G. F. Filippov**

Bogolyubov Institute for Theoretical Physics, National Academy Sciences of Ukraine, Metrologicheskaya ul. 14b, UA-252143 Kiev, Ukraine

Received October 25, 2000

Abstract—A feature peculiar to light neutron-rich nuclei is that their lowest decay thresholds are only slightly above their ground states. Among them, ^{6}He and ^{11}Li are two most striking examples. The energy needed to break ^{6}He (^{11}Li) into an alpha particle (^{9}Li) and two neutrons is about 1 MeV (300 keV). So small a value prompts one to construct their theory by analogy with the zero-range-nuclear-force approximation previously applied to the deuteron. A more detailed analysis shows, however, that the simple version of this approximation applied to systems that decay through a three-particle channel does not take into account some important features of these systems and requires significant improvements. First, with increasing distance between three particles, the potential energy decreases, in contrast to what is observed for binary systems, in inverse proportion to the hyperradius cubed. Second, the Pauli exclusion principle adds complexity even in the asymptotic domain, and we meet its demands in constructing the ^{6}He and ^{11}Li wave functions in the continuum. An approach is proposed to analyze weakly bound three-cluster systems that takes into account the aforementioned features and which describes correctly the experimentally observed structure of bound and unbound states above the threshold for three-particle decay.

1. INTRODUCTION

A number of interesting properties of light neutron-rich nuclei were found in experimental and, later, in theoretical studies. In this article, I consider two examples of these nuclei, ^{6}He and ^{11}Li. The first has become the best known member of the family, while the latter has happened to receive the most thorough study.

In each of these nuclei, there is one bound state just below the threshold for three-body decay. The binding energies of ^{6}He and ^{11}Li are about 1 MeV and 300 keV, respectively. Such small values of the binding energies imply the possibility of considering them within a theoretical framework similar to the zero-range-nuclear-force approximation for the deuteron. The most important consequence of this approximation is that the deuteron is a weakly bound system extending far beyond the range of nuclear forces. Let me recall how one arrives at this conclusion. Beyond the range of nuclear forces, the wave function $\psi(r)$ of the deuteron falls exponentially with increasing distance r between the proton and the neutron,

$$\psi(r) \to C\frac{\exp(-\alpha r)}{r}, \qquad (1)$$

$$\alpha = \sqrt{\frac{2m\epsilon}{\hbar^2}},\ r = \frac{|\mathbf{r}_1 - \mathbf{r}_2|}{\sqrt{2}},$$

where $\epsilon = 2.3$ MeV is the binding energy of the deuteron. It is the small value of ϵ that causes a large value of the deuteron root-mean-square (r.m.s.) radius in relation to the range of nuclear forces.

Being applied to ^{6}He and ^{11}Li, this approximation leads to the conclusion that these nuclei have large r.m.s. radii. The radius of ^{6}He should be much larger than that of ^{4}He (^{6}He breaks into ^{4}He and two neutrons), and, similarly, the radius of ^{11}Li should be much larger than that of ^{9}Li. This is confirmed by experimental data. Moreover, both nuclei feature neutron halos, in agreement with what is predicted within the zero-range-nuclear-force approximation.

A more detailed analysis shows, however, that, if applied to nuclear systems having a three-body decay channel, the simplest version of the zero-range approximation proves to be too naive and requires significant modifications. First, with increasing distance between three particles, the potential energy of the nucleon–nucleon interaction decreases much more slowly than in the binary case. Second, the Pauli exclusion principle affects the picture even in the asymptotic region, and it should be taken into account in constructing the continuum wave functions for ^{6}He and ^{11}Li.

*This article was submitted by the author in English.

**e-mail: gfilippov@gluk.org

2. THREE-CLUSTER MODEL

In the case of three-body decay of, say, ^{6}He, Eq. (1), written in the c.m. frame, must be modified as

$$\Psi(\rho) \to \phi_0 \frac{\exp(-\alpha\rho)}{\rho^{5/2}}, \qquad (2)$$

$$\alpha = \sqrt{\frac{2m\epsilon}{\hbar^2}}, \;\; \rho = \sqrt{r^2 + q^2},$$

$$\mathbf{r} = \frac{\mathbf{r}_2 - \mathbf{r}_3}{\sqrt{2}}, \; \mathbf{q} = \frac{2}{\sqrt{3}} \left(\mathbf{r}_1 - \frac{\mathbf{r}_2 + \mathbf{r}_3}{2} \right),$$

where $\mathbf{r}_1$ is the c.m. position vector of the ^{4}He cluster, $\mathbf{r}_2$ and $\mathbf{r}_3$ are the position vectors of the valence neutrons (neutron clusters), and ρ is the so-called hyperradius. A normalization of the Jacobi vectors $\mathbf{r}$ and $\mathbf{q}$ involves the reduced mass of the clusters. The factor $\rho^{5/2}$ in the denominator of the wave function (2) appears for the same reasons as the factor r in the denominator of the wave function (1). Finally, the factor ϕ_0 ensures antisymmetrization of the wave function.

In the attempt at extending the ideas of the zero-range approximation to systems having three-body decay channels, we must clarify the limiting expression (2) for the wave function. Before that, however, let us specify the model to be applied here. The model wave function Ψ for the ^{6}He nucleus is to be found within the resonating-group method (RGM) in the form of the antisymmetrized product

$$\Psi = \hat{\mathrm{A}}\{\psi_1\psi_2\psi_3 f(\mathbf{r}, \mathbf{q})\}, \qquad (3)$$

where $\hat{\mathrm{A}}$ is the antisymmetrization operator (the operator of nucleon-coordinate permutations), ψ_1 is the predefined wave function for the ground-state ^{4}He cluster, ψ_2 and ψ_3 are predefined wave functions for the neutron clusters, and $f(\mathbf{r}, \mathbf{q})$ is the wave function describing the relative motion of three clusters. The form (3) of the wave function as such does not ensure any practical advancements, so that further simplifications are needed. It is convenient to represent the function f as an expansion in the three-body hyperharmonics $\Phi_{K,\lambda}(\theta_i)$, where K is the hyperspherical number (grand orbital), all additional quantum numbers are denoted by λ, and $\{\theta_i\}$ are the hyperangles; that is,

$$f(\mathbf{r}, \mathbf{q}) = \sum_{K,\lambda} \phi_{K,\lambda}(\rho)\Phi_{K,\lambda}(\theta_i). \qquad (4)$$

In the six-dimensional space spanned by two vectors $\mathbf{r}$ and $\mathbf{q}$, the grand orbital plays a role similar to that of the angular momentum l in the three-dimensional space, while the hyperharmonic $\Phi_{K,\lambda}$ is a natural generalization of the spherical harmonic Y_{lm}. Harmonic functions are eigenfunctions of the Laplace operator; hyperharmonics in turn are eigenfunctions of the same operator defined in a multidimensional space.

It is known that, for a two-nucleon system at low energies, states characterized by low values of the angular momentum l are of greatest physical importance. For a three-cluster system at low energies, the most important states appear to be those that have low values of the grand orbital. The version of the hyperharmonic method where the value of the grand orbital is restricted to the lowest one is referred to as the minimal approximation.

If the ground state of ^{6}He is expanded as in (4), there arises the question of whether it is possible to apply the minimal approximation with the restriction $K = 0$. The answer is negative. Antisymmetrization of the wave function produces the $K = 2$ hyperharmonic from the $K = 0$ one. Therefore, the simplest function of ^{6}He respecting the Pauli exclusion principle has the form of a superposition of the $K = 0$ and $K = 2$ states, their weights being about 5 and 95%, respectively. By the way, the same weight factors appear in the grand-orbital expansion of the $L^\pi = 0^+$ state in the oscillator shell model.

Our conventional approach, the algebraic version of the RGM (AVRGM) [1], utilizes an expansion of the wave function (3) in the basis of the Pauli-allowed states $\Phi_{\nu,\mu}$ of the harmonic oscillator,

$$\Psi = \sum_{\nu,\mu} C_{\nu,\mu}\Phi_{\nu,\mu}. \qquad (5)$$

The expansion coefficients $C_{\nu,\mu}$ are then determined by solving the set of AVRGM equations. The summation index ν is the number of hyperradial-oscillator-excitation quanta, while all other quantum numbers are denoted by μ. The allowed basis states are in general some superpositions of hyperharmonics with different values of K. Maybe, the most interesting property of the coefficients $C_{\nu,\mu}$ is that they are known at large values of ν, because they can be expressed in terms of the S matrix. This is the key point of our approach. As soon as we have realized this fact, it becomes clear that the set of linear equations for the coefficients $C_{\nu,\mu}$ can easily be solved.

One may wonder why the hyperharmonics are used even if their superpositions are to be constructed. The answer is the following. First, the minimal approximation involves only hyperharmonics with the lowest values of K. Thus, the hyperharmonics are of use in classifying various approximations. Second, the asymptotic behavior of hyperharmonics at large value of the hyperradius (or at large values of the number ν of quanta) is well known and simple,

and this fact is employed when the asymptotic values of $C_{\nu,\mu}$ are determined.

Thus, the index μ is set to some value μ_0 in the minimal approximation, and a set of equations for C_{ν,μ_0} is constructed,

$$\sum_{\tilde{\nu}=0}^{\infty}\{\langle\nu,\mu_0|\hat{H}|\tilde{\nu},\mu_0\rangle - E\delta_{\nu,\tilde{\nu}}\}C_{\tilde{\nu},\mu_0} = 0, \quad (6)$$

$$0 \le \nu \le \infty.$$

Evidently,

$$\langle\nu,\mu_0|\hat{H}|\tilde{\nu},\mu_0\rangle \quad (7)$$
$$= \langle\nu,\mu_0|\hat{T}|\tilde{\nu},\mu_0\rangle + \langle\nu,\mu_0|\hat{U}|\tilde{\nu},\mu_0\rangle,$$

and we have to decide whether we can neglect the second term on the right-hand side of (7) within the minimal, zero-range-nuclear-force approximation. This problem is discussed in the next section.

3. NUCLEON–NUCLEON INTERACTION IN ALLOWED STATES

In a state characterized by a specific value of K, a short-range nucleon–nucleon potential decreases in proportion to A/ρ^3 with increasing ρ. This result may seem unexpected, but it is well known to specialists who use the hyperharmonic method. It is valid for almost any kind of nucleon–nucleon interaction, be it of an exponential or of a Gaussian form, or a potential well, etc. So slowly decreasing a potential energy cannot be neglected in calculating the matrix elements $\langle\nu,\mu_0|\hat{U}|\tilde{\nu},\mu_0\rangle$ to be substituted into (7). Nevertheless, there is a very important property of these matrix elements that was proven in [2]. At large values of ν and $\tilde{\nu}$, the matrix

$$||\langle\nu,\mu_0|\hat{U}|\tilde{\nu},\mu_0\rangle||$$

is identical to a diagonal matrix with the elements

$$V_{\nu,\tilde{\nu}} = \delta_{\nu,\tilde{\nu}}\frac{A}{(4\nu+q_0)^{3/2}}, \quad (8)$$

where q_0 is the doubled number of the zero-point-oscillation quanta.

The factor A in (8) (it is negative because of the attractive character of the potential) can easily be calculated for a semirealistic interaction. For some reasons, we prefer the Minnesota interaction, although it is not ideal. For instance, as opposed to the popular Volkov force, the Minnesota interaction does not bind two neutrons, which is important in describing systems that have two neutron clusters.

The inclusion of the matrix $V_{\nu,\tilde{\nu}}$ provides for an explanation of the high diffuseness of ^{6}He and ^{11}Li. Within the potential range, the ground-state wave function decreases more slowly than an exponential like that in (2), with the result that the r.m.s. radius appears to be large.

The second consequence of taking into consideration the matrix $V_{\nu,\tilde{\nu}}$ is related to the continuous-spectrum states above the threshold. The phase shift for $3 \to 3$ scattering is proportional to the square root of energy, and this dependence is formed in the asymptotic region, where an attractive potential decreases slowly.

4. RESULTS

On the basis of the above, we have considered a wide range of practical problems.

We have calculated the wave functions for the ground 0^+ state of ^{6}He and for the 1^- state, which lies in the continuum and which is responsible for the formation of the soft dipole mode [3]. The latter is due both to the proximity of the ^{6}He ground state to the decay threshold and to the 1^- resonance, whose existence does not contradict theoretical estimates. At the same time, it was clarified how one can define the angular and energy distributions of products of the electric-dipole photodisintegration of ^{6}He.

It was shown how we must treat clusters having a structure more complicated than that of an α particle, like ^{6}He, ^{8}He, and ^{9}Li, and, in particular, how we can consider degrees of freedom that are responsible for the excitation of these clusters [4]. It has become clear how it is possible to study the origin of the soft dipole mode in ^{11}Li [5]. The energy and the r.m.s. radius of the ground $3/2^-$ state of ^{11}Li has been explained, as well as of the continuum of the final states fed by $E1$ transitions from the ground state. The theory predicts two resonances in ^{11}Li: $3/2^+$ and $5/2^+$. The total effective cross section for dipole photodisintegration with the excitation of these resonances appears to be in good agreement with experimental data. Also, the cross section for two-neutron radiative capture by ^{9}Li has been calculated. It may be of interest for those who study neutron stars with large neutron fluxes.

Our calculations have shown that ^{10}He is unbound, but that there exists a resonance at $E_r \sim 1.6$ MeV with a width $\Gamma \sim 0.5$ MeV [6]. At present, experimental data only set an upper limit on the width, $\Gamma < 1.4$ MeV.

In addition, we have estimated the energy and the width of a resonance state of another three-cluster nucleus, ^{5}H [7].

We have given special attention to the problem of neutron scattering on ^{9}Li and to ^{9}Li–n interaction [8]. The energy and the width of the $1/2^+$ state in ^{10}Li have also been found.

5. CONCLUSION

We conclude that our relatively simple theoretical approach has been checked for many cases. It opens exciting prospects for studying new interesting objects that are of interest for both theorists and, we hope, experimentalists.

REFERENCES

1. G. F. Filippov, Riv. Nuovo Cimento **9**, 1 (1989).
2. G. F. Filippov, A. D. Bazavov, K. Kato, and S. V. Korennov, Yad. Fiz. **60**, 635 (1997) [Phys. At. Nucl. **60**, 554 (1997)].
3. G. F. Filippov, Yu. A. Lashko, and L. P. Shvedov, Yad. Fiz. **62**, 1772 (1999) [Phys. At. Nucl. **62**, 1651 (1999)].
4. G. F. Filippov, K. Kato, and S. V. Korennov, in *Proceedings of the International Conference "Large-Scale Collective Motion of Atomic Nuclei," Brolo, Messina, Italy, 1996* (World Sci., Singapore, 1997); G. F. Filippov, Yad. Fiz. **62**, 1237 (1999) [Phys. At. Nucl. **62**, 1164 (1999)].
5. G. F. Filippov and Ya. A. Lashko, Yad. Fiz. **64**, 229 (2001) [Phys. At. Nucl. **64**, 186 (2001)].
6. G. F. Filippov and L. P. Shvedov, in *Abstracts of 16th European Conference on Few-Body Problems in Physics, Autrans, France, 1998,* p. 57.
7. G. F. Filippov, A. D. Bazavov, and K. Kato, Yad. Fiz. **62**, 1763 (1999) [Phys. At. Nucl. **62**, 1642 (1999)].
8. G. F. Filippov, S. V. Korennov, and K. Kato, in *Proceedings of 17th International Conference on Clustering Aspects of Nuclear Structure and Dynamics, Island of Rab, Croatia, 1999, Summaries,* p. 71.

Physics of Atomic Nuclei, Vol. 64, No. 7, 2001, pp. 1240–1243. From Yadernaya Fizika, Vol. 64, No. 7, 2001, pp. 1315–1318.

Proceedings of the International Conference "Nuclear Structure and Related Topics"

Remarks on Halo Nuclei*

R. J. Lombard**

Groupe de Physique Théorique, Institut de Physique Nucléaire, 91406 Orsay Cedex, France

Received October 25, 2000

Abstract—On the ground of a relationship between the rms radius and the separation energy, we compare halo nuclei to diffuse diatomics. It underlines the essential difference between these two kinds of weakly bound systems: whereas the two-body approximation seems well justified in the case of diatomics, it becomes questionable in the nuclear case when the separation energy approaches zero. Because of this particular situation, we conjecture that the Efimov states have less chances to be observed in nuclear than in molecular cases. Discussing possibilities of measuring accurately the rms radius of halo wave function, we propose a strategy based on the parallel momentum distribution measured in dissociation experiments, together with the use of an Abel transform. © *2001 MAIK "Nauka/Interperiodica"*.

The purpose of the present work is to compare two kinds of weakly bound systems with respect to a general property. We consider two bodies in a relative s state, linked by such a weak potential that only one single bound state exists. The eigenvalue E_{1s} necessarily equals the separation energy S. In this framework, we have studied [1, 2] the dimensional relationship

$$\langle r^2 \rangle \;=\; \frac{3\hbar^2}{2\mu}\,\frac{1}{S}\varphi \quad \text{with} \quad \frac{1}{6} \le \varphi \le 1. \qquad (1)$$

Here, r is the relative distance between the two bodies, and μ the reduced mass. The conditions of applicability of (1) are given explicitly in [1]. The factor φ depends on the potential. However, we have shown that for finite range potentials having a hard-core component, φ admits a kind of universal behavior

$$\varphi(\varepsilon) \cong \frac{1}{6}(1 + 2\sqrt{\varepsilon} + 2\varepsilon), \qquad (2)$$

where

$$\varepsilon = S/E_{1s,\,\max}.$$

For each considered potential, E_{1s} depends on the strength of the attractive part. Increasing this strength, $E_{1s,\,\max}$ is the maximum of the eigenvalue under the condition of a single bound state. Equation (2) is strictly valid for a hard-core radius $r_c \to \infty$. In practice however, it constitutes already an excellent approximation for very finite values of r_c, typically $r_c \ge 2.5$ fm in the nuclear case. In order to give an insight into the actual influence of r_c, we first display the factor $\varphi(\varepsilon)$ calculated by using the modified Pöschl–Teller potential for the attractive part:

$$V(r) = \begin{cases} \infty & \text{for } r \le r_c, \\ \dfrac{-V_0}{\cosh^2(r - r_c)} & \text{for } r \ge r_c. \end{cases}$$

In three dimensions, the ground state solution of the Schrödinger equation is of the form [3]

$$\Psi_{1s}(r) = \frac{N_0}{r}\sinh(r - r_c)\cosh^{-\lambda}(r - r_c)\,. \qquad (3)$$

The eigenvalue is given by

$$E_{1s} = -\frac{1}{2}(\lambda - 1)^2\,;\;\; V_0 = \frac{\lambda(\lambda + 1)}{2}. \qquad (4)$$

The maximal value $E_{1s,\max}$ is given by the critical λ for the $\ell = 1$ state, i.e., the λ for which $E_{1p} = 0$. It has been determined numerically, requiring an accuracy of the order of 10^{-7}. The resulting $\varphi(\varepsilon)$ are drawn in Fig. 1 for $r_c = 0.2$ and 0.4 fm. At $r_c = 1$ fm, the universal curve (2) is already met at better than 1%. In view of the systems we are considering, it means that the universal curve (2) can be used safely.

The variable ε is not measurable. Thus, except for the limit $\varepsilon \to 0$, which is independent of the potentials and yields an absolute lower bound, φ is not directly given by S. Consequently, (1) does not yield the rms radius of the weakly bound system in terms of the separation energy. However, if the two quantities $\langle r^2 \rangle$ and S are known, either from experiments or models, φ can be determined and the comparison between various values brings interesting information. Roughly speaking, it gives a way of comparing weakly bound systems governed by different forces. This is

*This article was submitted by the author in English.

**e-mail: lombard@ipno.in2p3.fr

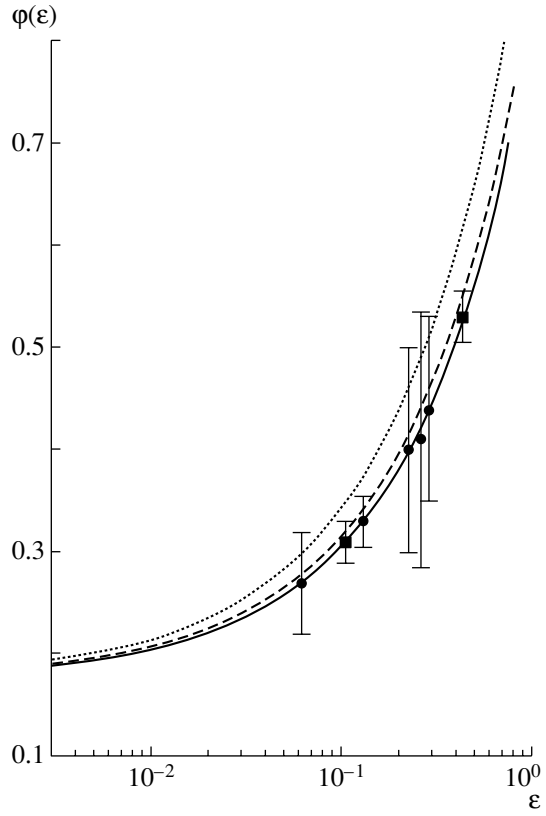

Fig. 1. The three curves $\varphi(\varepsilon)$ correspond to the modified Pöschl–Teller potential with a hard-core component of $r_c = 0.2$ fm (dotted curve), $r_c = 0.4$ fm (dashed curve) and the asymptotic expression (2) (solid curve). In increasing order, the filled circles are the experimental values of φ for ^{19}C, ^{11}Be, ^{17}C, ^{15}C, and ^{14}B, respectively, displayed on the asymptotic curve. The filled squares are the experimental values for ^{11}Li and ^{6}He treated in the dineutron approximation.

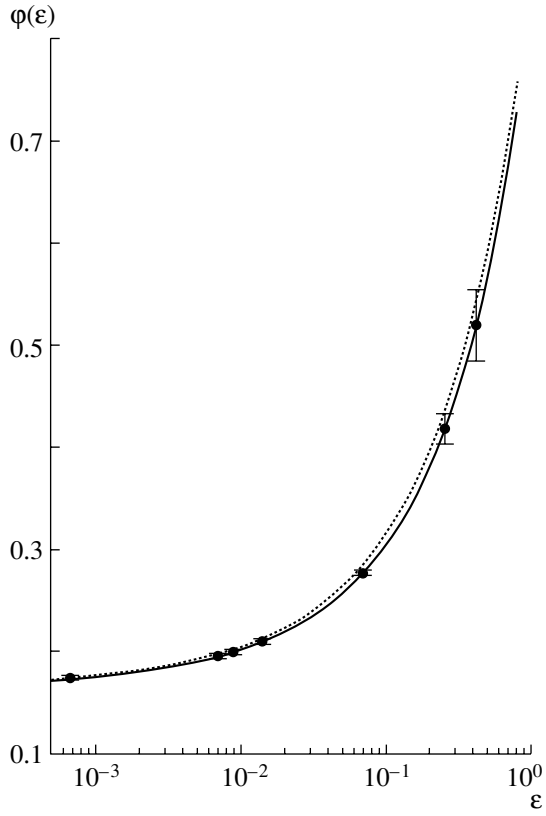

Fig. 2. The two curves $\varphi(\varepsilon)$ correspond to the modified Pöschl–Teller potential with a hard-core component of $r_c = 0.4$ fm (dotted curve) and to the asymptotic expression (2) (solid curve), respectively. In increasing order, the filled circles are the values of φ for ^{4}He–^{6}Li, ^{3}He–^{23}Na, ^{4}He–^{7}Li, ^{4}He–^{40}K, ^{3}He–^{40}K, ^{4}He–^{85}Rb, and ^{3}He–^{85}Rb, respectively. These values are derived from the calculations of [8].

illustrated here by comparing the results obtained for halo nuclei and diffuse diatomic molecules.

As far as nuclei are concerned, we select a few relevant cases of single neutron halo nuclei, namely, ^{11}Be, ^{14}B, ^{15}C, ^{17}C, and ^{19}C. Values of $\langle r^2 \rangle$ were derived from the data analysis by Al-Khalili, Tostevin, and Thompson [4], as well as Liatard *et al.* [5]. For ^{19}C, we take the recent measurements of Nakamura *et al.* [6].

To this sample, we add the two-neutron halo nuclei ^{6}He and ^{11}Li, treated in the two-body approximation. The rms radius of their halo wave function has been calculated by using values obtained in [4], assuming a pinpoint dineutron.

The derived values of φ have been drawn in Fig. 1, on the universal curve at their corresponding ε. The way the points fall on the curve indicates that ε is roughly proportional to the separation energy, but not quite. The error bars are much too large to draw conclusions concerning the possibility of a universal potential for halo nuclei.

The same analysis, has been made for loosely bound diatomics. Experimentally, the dimer molecule (^{4}He–^{4}He) has been observed [7]. This object is bound by 1.1×10^{-13} MeV, and the mean interdistance $\langle r \rangle = 62 \pm 10$ Å. Assuming a wave function of the form $\sin(kr/r)$ leads to $\langle r^2 \rangle^{1/2} = 72 \pm 12$ Å. With these figures, we get from (1) $\varphi = 0.18$, which comes very close to the absolute lowest limit.

For the sake of comparison, a sample of diffuse diatomics have been considered. The ensemble consists of seven cases: ^{4}He–^{6}Li, ^{3}He–^{23}Na, ^{4}He–^{7}Li, ^{4}He–^{40}K, ^{3}He–^{40}K, ^{4}He–^{85}Rb, and ^{3}He–^{85}Rb. These molecules have not been observed yet. Consequently we rely on the calculations that have been performed by Kleinekathöfer, Lewerenz, and Mladenović [8] by using various sophisticated potentials. We have selected about half of the calculated cases; the chosen set is well representative of the situation. The

results displayed on Fig. 2 represent an average over 3–4 potentials for each case. Particularly interesting is the molecule ^{4}He–^{6}Li, because its binding energy is predicted to be even smaller than for the dimer. The prediction yields $\varphi = 0.175$.

While comparing Figs. 1 and 2, the striking difference is the fact that the diffuse diatomics are spread over the whole range of ε. Some cases approach closely the lower limit, like ^{4}He–^{6}Li. This result is more or less expected, since the calculations have been made in the very frame of two-body quantum mechanics. In this respect, the actual observation of the dimer provides the calculations with a key support.

On the contrary, the halo nuclei all lie above $\varphi = 0.27$. Even if a lower value is not yet excluded, due to the size of the error bars (the lowest value compatible with experiments is $\varphi = 0.19$ for ^{19}C), there seems to be a qualitative difference between the two kinds of weakly bound systems. It represents a different regime: the range of molecular forces is certainly larger than the one of nuclear forces. It also suggests the two-body approximation to be more justified in the molecular than in the nuclear case.

Further arguments confirm that a halo nucleus has less chances to approach $\varepsilon = 0$ than a diatomic molecule. They stress the many-body aspect of the nuclear case, which cannot be forgotten in the extreme limit. Relevant to this discussion is the fact that, in a nucleus, one has to distinguish the separation energy and single-particle energy. This can be illustrated as follows. For instance, if use is made of the density functional method, it is possible to generate a s-state neutron with a single-particle energy approaching zero, accompanied with a large extension of the wave function. This is achieved by suitably varying the parameters of the functional. As concrete examples, calculations have been performed for ^{21}C and ^{23}O. In these two nuclei, the valence neutron lies in the $2s$ orbital. In both cases, however, the nucleus is found to be particle unstable much before the limit $E_{2s} = 0$ is reached. This result is rather general and is not expected to depend sensitively on models, i.e., on the specific form of the functional. It is corroborated by the observation that ^{21}C is actually unstable [9].

Going beyond the mean-field approximation requires introducing dynamical correlations. This was done, for instance, in a perturbative way for the description of ^{11}Be by Vinh Mau [10]. In this model, the ground state is obtained by coupling the $1d$ neutron to the collective states of the core, especially the 2^+ state. The coupling is proportional to the reduced transition probability $B(E2)$ of the core phonon. Thus, to soften the coupling and give the ground state a chance to approach zero energy, it suffices to weaken the $B(E2)$ value. However, it is well known that, in practice, the fraction of the sum rule that is taken by the low-energy phonon is constant. In other words, the product $E_2B(E2)$ is a constant. It means that lowering $B(E2)$ must be accompanied by an increase of E_2, in order to remain in a realistic situation. The immediate consequence is that the coupling cannot be made arbitrarily small since the phonon energy will reach the threshold of particle instability.

Obviously, these two arguments are not a proof but merely a challenging conjecture. It deserves further experimental and theoretical investigations.

If this conjecture is confirmed—in other words, if the coupling in nuclei cannot be made arbitrarily small—its immediate consequence is that the Efimov states [11] have more chances to be observed in molecular systems than in nuclei. Again, this deduction is a conjecture, because the step from the two- to the three-body situation is not straightforward. Equation (2) cannot be applied to three-body case, except in the dineutron approximation, which is too crude to enforce the conjecture. In this respect, the points drawn in Fig. 1 merely indicate that the two-neutron halo nuclei behave similarly to the one-neutron case in the dineutron limit.

In view of the large error bars displayed in Fig. 1, it is clear that precise measurements of both the separation energies and the rms radii of the halo wave functions are very desirable. The separation energy of ^{19}C, for instance, is known only within 25%. As far as the radii are concerned, many values are coming from total reaction cross sections, the analysis being subject to a number of controversies.

Relying on a few-body description, one can measure the halo wave function in elastic scattering at sufficient energy for the Glauber model to be valid [12]. However, it requires a beam quality capable of disentangling the elastic channel from the others, which is not met at present.

On the other hand, the parallel momentum distribution of inclusive dissociation scattering has been claimed on several occasions to be the clue to the problem [13]. Considering single neutron halo nuclei, in the Glauber model [12], this distribution takes the form

$$\frac{d\sigma}{dk_\parallel} = \int |\Gamma(\mathbf{x}, \boldsymbol{\beta})|^2 \, |\phi(\boldsymbol{\beta}, k_\parallel)|^2 d^2x \, d^2\beta \, . \qquad (5)$$

This is a convolution integral between the interaction, represented by the profile function Γ, and the square of the equivalent to the thickness function

$$\phi(\boldsymbol{\beta}, k_\parallel) = \left(\frac{1}{2\pi}\right)^{1/2} \int_{-\infty}^{\infty} e^{ik_\parallel \sigma} \Psi(\boldsymbol{\xi}) d\sigma. \qquad (6)$$

Here, $\Psi(\boldsymbol{\xi})$ is the halo wave function, $\boldsymbol{\xi} = (\boldsymbol{\beta}, \sigma)$ with σ directed along the incident direction and $\boldsymbol{\beta}$ in a plane perpendicular to it containing the impact parameter. The total profile function has Coulomb, neutron-target, and core-target components:

$$\Gamma(\mathbf{x}, \boldsymbol{\beta}) = \Gamma_{\mathrm{C}}(\mathbf{x} - \boldsymbol{\beta}) + e^{-i\eta_c(\mathbf{x}-\boldsymbol{\beta})} \times \Big[\Gamma_{nT}(\mathbf{x}) + \Gamma_{cT}(\mathbf{x} - \boldsymbol{\beta}) - \Gamma_{nT}(\mathbf{x})\Gamma_{cT}(\mathbf{x} - \boldsymbol{\beta})\Big]. \quad (7)$$

The single and double scattering structure of Γ is easily recognized. The contributions to $d\sigma/dk_\parallel$ can be collected in two parts. For the simple one, two-dimensional integration with respect to x and β are separable and the results take the form

$$\frac{d\sigma^{(s)}}{dk_\parallel} = \Sigma_0\, \overline{S_d^2}(k_\parallel), \quad (8)$$

where Σ_0 is a number, and $\overline{S_d^2}(k_\parallel) = \int |\phi(\boldsymbol{\beta}, k_\parallel|^2 d^2\beta$.

The mixed contributions, $d\sigma/dk_\parallel^{(m)}$, actually require a convolution integral. If the halo wave function is separable in $\boldsymbol{\beta}$ and σ, like the Gaussian, it is easy to show that these terms also take the simple form (8). On the other hand, we have verified on a specific example that the modification of the shape brought by the mixed terms is relatively small. Negligible in the forward direction, it reaches about 5% at half of the height. The calculation was done [12] with

$$\Psi(\boldsymbol{\xi}) = N_0\Big[e^{-\mu\xi/2} - \frac{5}{4}e^{-\mu\xi} + \frac{1}{4}e^{-2\mu\xi}\Big]/\xi. \quad (9)$$

This wave function has the advantage of behaving like a Yukawa at large distances while remaining finite at the origin. The profile functions were taken as Gaussian, ignoring the Coulomb interaction. Although more critical tests would be desirable, it suggests a way of combining data to achieve a fair analysis.

Since the corrections to (8) are small, they can be estimated numerically, by using realistic or even semirealistic ingredients. Furthermore, the importance of the corrections, as well as the departure from a Gaussian, can be checked quantitatively by comparing

$$\overline{S_d^2}(k_\parallel) = \frac{d\sigma}{dk_\parallel}\Big/\frac{d\sigma}{dk_\parallel}(0) \quad (10)$$

obtained from different targets and energies.

The next step consists in analyzing $\overline{S_d^2}(k_\parallel)$ in a model-independent way. This can be performed by noticing that

$$\overline{S_d^2}(k_\parallel) = \int |S_d(\mathbf{k})|^2 d^2k_\perp\,, \quad (11)$$

with

$$S_d(\mathbf{k}) = \Big(\frac{1}{2\pi}\Big)^{3/2} \int e^{i\mathbf{k}\cdot\boldsymbol{\xi}}\Psi(\boldsymbol{\xi})d^3\xi. \quad (12)$$

Then, by using an Abel transform and assuming spherical symmetry, we have

$$|S_d(k)|^2 = -\frac{1}{2\pi}\frac{1}{k}\frac{\partial}{\partial k}\overline{S_d^2}(k), \quad (13)$$

where $k = |\mathbf{k}|$. This procedure gives access to the Fourier transform of the wave function, which is handled by means of usual techniques.

In conclusion, the comparison between halo nuclei and diffuse diatomic molecules underlines the essential difference between these two kinds of weakly bound systems. Whereas the two-body approximation seems well justified in the case of diatomics, it becomes questionable in the nuclear case when the separation energy approaches zero.

It suggests that the extreme limit of zero binding energy, which is required to observe the Efimov states, has more chance to be met in molecules than in nuclei. This is, however, only a conjecture, which deserves more theoretical and experimental investigations.

The quantities relevant to the present work are still poorly known, and more accurate experimental data are needed, for the rms radii of the halo wave functions as well as for the separation energies. As far as the measurements of the radii are concerned, we propose a strategy based on the parallel momentum distribution. It consists in the extraction of $\overline{S_d^2}(k_\parallel)$ from the data, followed by an Abel transform leading to the Fourier transform of the wave function.

REFERENCES

1. M. Lassaut, M. Keriaki, and R. J. Lombard, J. Phys. A **30**, 2467 (1997).
2. M. Lassaut and R. J. Lombard, Eur. Phys. J. A **2**, 111 (1999).
3. M. M. Nieto, Phys. Rev. A **17**, 1273 (1978).
4. J. S. Al-Khalili, J. A. Tostevin, and I. J. Thompson, Phys. Rev. C **54**, 1843 (1996).
5. E. Liatard *et al.,* Europhys. Lett. **13**, 401 (1990).
6. T. Nakamura *et al.,* Phys. Rev. Lett. **83**, 1112 (1999).
7. W. Schöllkopf and J. P. Toennies, Science **266**, 1345 (1994).
8. U. Kleinekathöfer, M. Lewerenz, and M. Mladenović, Phys. Rev. Lett. **83**, 4717 (1999); M. Lewerenz, private communication.
9. M. Langevin *et al.,* Phys. Lett. B **150B**, 71 (1985).
10. N. Vinh Mau, Nucl. Phys. A **592**, 33 (1995).
11. V. Efimov, Phys. Lett. B **33B**, 563 (1970).
12. J. Formanek, R. J. Lombard, and J.-P. Maillet, J. Phys. G **25**, 2107 (1999).
13. P. G. Hansen, Phys. Rev. Lett. **77**, 1016 (1996), and references therein.

Physics of Atomic Nuclei, Vol. 64, No. 7, 2001, pp. 1244–1248. From Yadernaya Fizika, Vol. 64, No. 7, 2001, pp. 1319–1323.

Proceedings of the International Conference "Nuclear Structure and Related Topics"

Spectroscopy of ^{7}He and Superheavy Hydrogen Isotope ^{5}H*

M. S. Golovkov[1),2)], A. A. Korsheninnikov[1),2)], I. Tanihata[2)], D. D. Bogdanov, M. L. Chelnokov, A. S. Fomichev, V. A. Gorshkov, Yu. Ts. Oganessian, A. M. Rodin, S. I. Sidorchuk, S. V. Stepantsov, G. M. Ter-Akopian[**], R. Wolski[3)], W. Mittig[4)], P. Roussel-Chomaz[4)], H. Savajols[4)], E. A. Kuzmin[5)], E. Yu. Nikolskii[5)], B. G. Novatskii[5)], and A. A. Ogloblin[5)]

Joint Institute for Nuclear Research, Dubna, Moscow oblast, 141980 Russia

Received October 25, 2000

Abstract—The neutron-transfer reaction $d(^6\mathrm{He}, p)^7\mathrm{He}$ is investigated. The data obtained show that, in the range between 1 and 7 MeV above its ground-state resonance, ^{7}He does not have well-pronounced narrow excited states with a single-particle structure. A resonance state of ^{5}H with an energy of 2 MeV above the $n + n + ^3\mathrm{H}$ decay threshold is obtained for the first time by making use of the reaction $p(^6\mathrm{He}, ^2\mathrm{He})^5\mathrm{H}$. © *2001 MAIK "Nauka/Interperiodica".*

1. INTRODUCTION

The ^{7}He nucleus has been repeatedly studied for 30 years, and its well-known ground-state resonance decaying into $n+^6$He has been obtained in many reactions (see [1]). However, excited states ($E^* < 10$ MeV, $\Gamma < 2$ MeV) were not found in this nucleus until very recent time. Particularly, a negative conclusion has been drawn from the energy spectra of ^{7}Be and ^{8}B obtained, respectively, in the reactions $^7\mathrm{Li}(^7\mathrm{Li}, ^7\mathrm{Be})^7\mathrm{He}$ and $^9\mathrm{Be}(^6\mathrm{Li}, ^8\mathrm{B})^7\mathrm{He}$ [2]. More recent experiments that employed transfer reactions with stable heavy-ion beams also yielded negative results in what is concerned with excited states in ^{7}He [3–5].

It is evident that radioactive nuclear beams provide the best conditions for studying nuclei with a high neutron excess, such as ^{7}He. As reactions that are induced by neutron-rich projectiles and which lead to ^{7}He become simpler, their cross sections grow, while physical backgrounds decrease. These observations were justified in [6], where a ^{7}He nucleus was obtained in the reaction $p(^8\mathrm{He}, d)^7\mathrm{He}$ at a ^{8}He beam energy of 50 MeV per projectile nucleon. The detection of deuterons in correlation with other particles emitted in the decay of ^{7}He allowed the authors to obtain, for the first time, an excited state of ^{7}He at 3.3 ± 0.3 MeV above the $n+^6$He threshold. The width of this resonance state is $\Gamma = 2.2 \pm 0.3$ MeV. It decays predominantly into $3n+^4$He, though the energy of its $n+^6$He decay is higher. One can put forth arguments in favor of the assumption [6] that, most likely, this state has a structure with a neutron in the $p_{1/2}$ state coupled to the ^{6}He core, which itself is in the excited 2^+ state. A tentative spin–parity assignment for this state is $J^\pi = 5/2^-$. To all appearance, ^{8}He is a "suitable" projectile for populating this excited state in ^{7}He after one-neutron stripping because, as is expected (see [6, 7]), the ground state of ^{8}He contains mainly a ^{6}He subsystem in the excited 2^+ state.

In this connection, the question of whether there are excited states in ^{7}He with a single-particle structure is still open, despite the fact that this problem remains persistently interesting. It was expected that ^{7}He could have an excited $1/2^-$ state of this nature. The observation of such a state in ^{7}He could shed light upon spin–orbit interaction in neutron-halo nuclei. Theoretical predictions (see [8] and references

*This article was submitted by the authors in English.

[1)]On leave of absence from Russian Research Centre Kurchatov Institute, pl. Kurchatova 1, Moscow, 123182 Russia.

[2)]RIKEN, Hirosawa 2-1, Wako, Saitama 351-01, Japan.

[3)]Joint Institute for Nuclear Research, Dubna, Russia, and Institute of Nuclear Physics, ul. Kawiory 26a, PL-30-055 Cracow, Poland.

[4)]GANIL, BP 5027; F-14021 Caen Cedex, France.

[5)]Russian Research Centre Kurchatov Institute, pl. Kurchatova 1, Moscow, 123182 Russia.

[**]e-mail: gurgen2@suntimpx.jinr.ru

therein) also attract one's attention to searches for new excited states in ^{7}He.

The question of whether there exists a superheavy hydrogen ^{5}H has been discussed for more than 40 years. Simple physical arguments were invoked to show that a resonance state of ^{5}H should exist [9, 10]. In [11], a complete dynamical investigation of ^{5}H was performed within the three-body $n + n + ^3$H model.

Numerous attempts at observing either a stable or a resonance state of ^{5}H yielded negative results (see the review article [12] and references therein). At the same time, there were several claims to the observation of the ^{5}H nucleus among the products of reactions with pions [13, 14] and with stable (^{6}Li) [15] and radioactive (^{6}He) [16] nuclear beams. In addition to the fact that all these results are mutually conflicting, there are other reasons to conclude that searches for a resonance state of ^{5}H still make a topical problem.

2. EXPERIMENTAL LAYOUT

We used the pickup reaction $d(^6\mathrm{He}, ^7\mathrm{He})p$ to carry out searches for new excited states in the ^{7}He nucleus. One could anticipate a relatively high population probability for a single-particle $1/2^-$ state in this reaction, which would be a single-step transfer in contrast to the stripping reaction $p(^8\mathrm{He}, ^7\mathrm{He})d$, where a two-step process is required, if one assumes, for ^{8}He, the structure [6, 7] mentioned above.

The reaction $p(^6\mathrm{He}, ^5\mathrm{H})^2$He was employed in experiments devoted to the superheavy hydrogen isotope ^{5}H. The presented notation underlines that accent was placed on the detection of two correlated protons emitted from the decay of ^{2}He at small angles in the laboratory frame. The measurement of the energy and angle for each proton allowed us to know the energy of the residual system ^{5}H. This is an analog of the missing-mass method where a recoil particle d from a reaction $a(b,c)d$ is unstable (the virtual state of ^{2}He), and this particle is detected by measuring the characteristics of its decay products.

The experiments were carried out at the U-400M cyclotron of the Flerov Laboratory of Nuclear Reactions (JINR, Dubna). The experimental setup is shown schematically in Fig. 1. A primary beam of ^{11}B ions with an energy of 42 MeV per projectile nucleon was used to obtain a secondary ^{6}He beam of energy 37 MeV per nucleon in the focal plane of the ACCULINNA separator [17]. In long-term experimental runs, the average intensity of the ^{6}He beam on the target was 5×10^4 s^{-1}. Of the total beam flux hitting the target, tritons and ^{8}Li ions comprised,

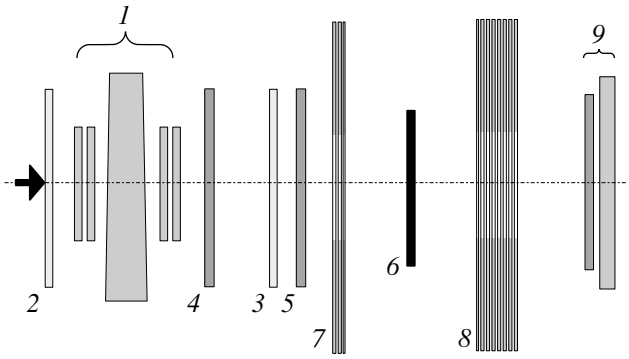

Fig. 1. Schematic diagram of the experimental setup: (*1*) group of units symbolizing one-half of the ACCULINNA beam line (i.e., a dipole magnet with two pairs of quadrupole lenses on the two sides); (*2, 3*) time-of-flight plastic scintillators, (*4, 5*) multiwire proportional chambers, (*6*) gas target, (*7*) detector telescope used in experiments aimed at ^{7}He, (*8*) detector telescope used in experiments dedicated to ^{5}H, (*9*) telescope involving one Si detector and one large-area thick BGO crystal for $\Delta E \times E$ measurements of long-range charged reaction products emitted from the target in the forward direction.

respectively, $\sim$55% and $<$1%. While the energy spread of the beam ions amounted to 5% (FWHM), the energy of individual ^{6}He ions was defined with an accuracy of $\Delta E/E \leq 2\%$ by means of time-of-flight (TOF) measurements. For each event associated with the detection of reaction products, the measured time of flight and the energy loss in the second TOF plastic (plastic *3* in Fig. 1) allowed us to identify unambiguously the incoming ion that had generated the reaction products. Two multiwire proportional chambers (positions *4* and *5* in Fig. 1) were used for tracking individual beam ions.

The GANIL gas target filled with pure hydrogen isotopes was employed in these experiments. The length of the target cell along the beam axis was 10 mm, its entrance and exit window diameters being 15 mm. In the case where the reaction $d(^6\mathrm{He}, ^7\mathrm{He})p$ was studied, the target filling was 3 atm of pure deuterium gas cooled down to 40 K. The target windows were 10-μm stainless steel foils. In the case of the reaction $p(^6\mathrm{He}, ^5\mathrm{H})^2$He, the target cell having 20-μm stainless-steel windows was filled with a pure hydrogen gas at a pressure of 11 atm. The gas was cooled down to 35 K.

An array of three annular Si-strip detectors from the RIKEN telescope [6] was employed to observe protons originating from the reaction $d(^6\mathrm{He}, ^7\mathrm{He})p$. Covering an angular range between 170.8° and 154.3° in the laboratory frame (see Fig. 1, position *7*), this array was intended for detecting low-energy ($E = 2.5$–6.0 MeV) protons emitted at small c.m.

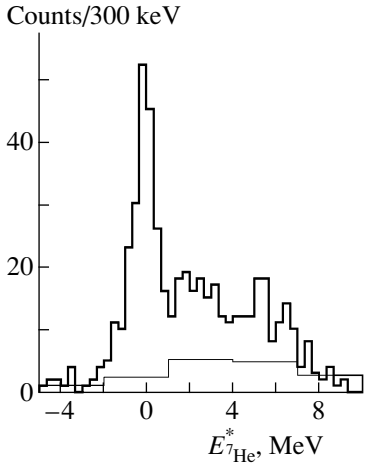

Fig. 2. Excitation-energy spectrum of ^{7}He nuclei from the reaction $^6\mathrm{He}+d \rightarrow {}^7\mathrm{He}+p$ (thick solid line). The background obtained with the deuterium gas evacuated from the target is shown with a thin line.

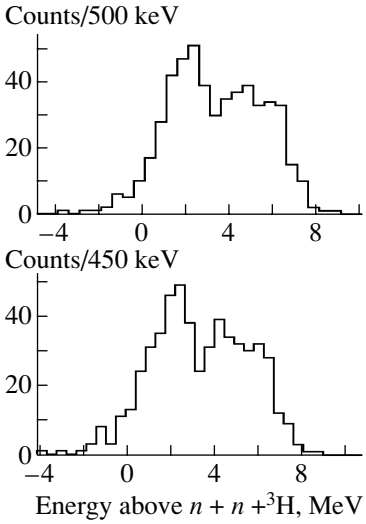

Fig. 3. Energy distribution obtained for the ^{5}H system formed in the reaction $^6\mathrm{He} + p \rightarrow {}^5\mathrm{He} + p + p$. The upper and lower panels show the same distribution in two different bin widths. The distribution was obtained from the energy–angle correlations of the two protons emerging in this reactions. The condition of coincidence with tritons from the decay $^5\mathrm{H} \rightarrow n + n + {}^3\mathrm{H}$ was included in the analysis. The observed resonance state of the ^{5}H nucleus shows up as a maximum in the spectrum centered at about 2 MeV above the threshold for the decay $^5\mathrm{H} \rightarrow n + n + {}^3\mathrm{H}$. The bump seen on the right side is due to space–volume events extending to the left of this bump and smoothly vanishing at zero energy. The right-side cutoff of the space–volume distribution is caused by the energy threshold. Only a very few events were obtained in the background spectrum when the hydrogen gas was evacuated from the target.

angles. In the case of an event being detected, the time delay between the signals coming from the Si detector telescope and plastic *3* was used to derive the particle velocity. The energy–velocity correlation allowed us to make a selection for protons. In addition to protons, we detected ^{6}He nuclei originating from the decay of ^{7}He into $^6\mathrm{He}+n$. The $\Delta E \times E$ telescope *9* (see Fig. 1) provided an unambiguous identification of those ^{6}He nuclei that moved in a axis close to the beam axis and had, on average, the energy 15% lower than that of the ^{6}He beam ions traversing the target.

When ^{5}H obtained in the reaction $p(^6\mathrm{He}, {}^5\mathrm{H})^2\mathrm{He}$ was the subject of interest, the RIKEN telescope equipped with eight annular strip detectors was installed in the forward direction (position *8* in Fig. 1). The telescope could detect proton pairs emerging from the target with their center of mass moving in the laboratory frame within the angular range 10°–18°. The maximum energy of protons stopped in the telescope was about 30 MeV. The particles involved were identified on the basis of $\Delta E \times E$ data. Apart from the two protons, the charged particle (^{3}H) from the decay $^5\mathrm{H} \rightarrow n + n + {}^3\mathrm{H}$ was detected by telescope *9* at small angles in the laboratory frame.

For either of the reactions $d(^6\mathrm{He}, {}^7\mathrm{He})p$ and $p(^6\mathrm{He}, {}^5\mathrm{H})^2\mathrm{He}$, the angle between the trajectories of the detected protons and the ^{6}He beam ion was measured with a precision of 0.4° in the laboratory frame. The same was true for the angle between the trajectories of two protons emitted as a pair in the second reaction.

The total fluxes of ^{6}He ions that traversed the deuterium and hydrogen targets were, respectively, 5.4×10^9 and 3.2×10^{10}. Each experimental run was supplemented with the irradiation performed with the gas evacuated from the target. The doses of the ^{6}He beam in these background measurements amounted to one-half of the values achieved in the measurements of the effect.

3. RESULTS AND DISCUSSION

One could readily see the locus of protons originating from the reaction $d(^6\mathrm{He}, {}^7\mathrm{He})p$ in the $E_p \times \theta_{\mathrm{lab}}$ plot constructed for protons coinciding with ^{6}He nuclei observed as ^{7}He decay products (E_p and θ_{lab} are the measured proton energy and angle in the laboratory frame). The proton energy–angle values were converted to obtain the ^{7}He excitation-energy spectrum shown in Fig. 2. The peak corresponding to the population of the ^{7}He ground-state resonance is well seen in this spectrum. The background lying under this peak is negligible. Any other resonance states of ^{7}He are not seen in the excitation-energy region extending up to 8 MeV.

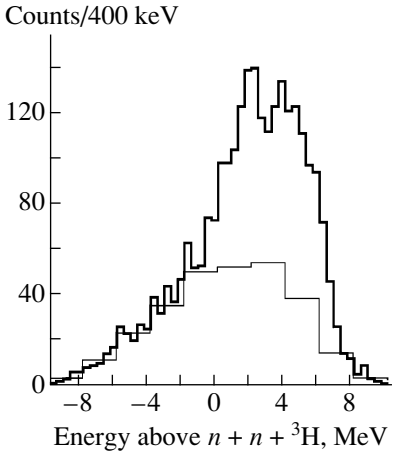

Fig. 4. The same distribution as in Fig. 3 (thick solid line), except that the coincidence with tritons was not required. The thin solid line represents the background obtained with the hydrogen gas evacuated from the target.

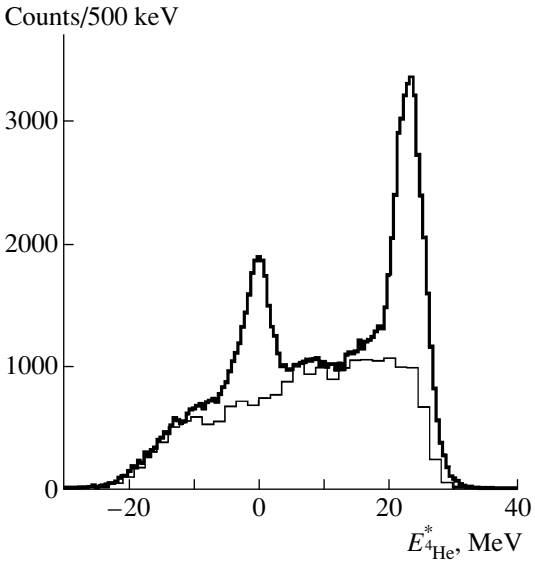

Fig. 5. Excitation-energy spectrum of ^{4}He nuclei from the reaction $^6\mathrm{He}+p \rightarrow {}^4\mathrm{He}+{}^3\mathrm{H}$ (thick solid line). The finite width of the maximum corresponding to the ^{4}He ground state displays the limited energy resolution of the setup. The background obtained with the hydrogen gas evacuated from the target is shown by the thin line.

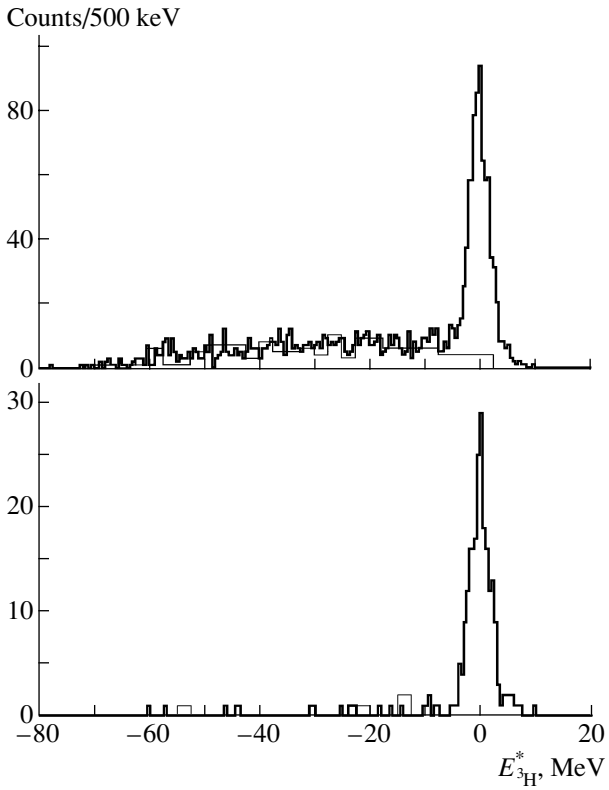

Fig. 6. Excitation energy spectra of tritons (thick solid lines) from the reactions (upper panel) $^6\mathrm{He}+p \rightarrow p+{}^3\mathrm{H}+X$ and (lower panel) $^6\mathrm{He}+p \rightarrow p+{}^3\mathrm{H}+{}^3\mathrm{H}$. The background obtained with the hydrogen gas evacuated from the target is shown by thin lines in the two panels.

As was noted above, the reaction used appears to be the most favorable for populating a single-particle $1/2^-$ state in ^{7}He. One could assume that, if this nucleus had such a narrow state notable for its simple, single-particle structure it would show a clear resonance that would be comparable in value with the ^{7}He ground-state resonance seen in Fig. 2. Therefore, the absence of any other resonance in the spectrum shown in Fig. 2 gives a strong support to the conclusion that, in the range between 1 and 7 MeV above is ground-state resonance, ^{7}He does not have well-pronounced narrow excited states with a single-particle structure.

After the irradiation of the hydrogen target, a clear picture was obtained when, for each detected event, the energy of the ^{5}H nucleus was derived from the energies and angles of two protons detected in coincidence with ^{3}H originating from the decay $^5\mathrm{H}\rightarrow n+n+{}^3\mathrm{H}$. Two spectra shown in Fig. 3 with respect to the ^{5}H energy counted from the $n+n+{}^3$H decay threshold were obtained after such a data treatment. A distinct peak centered at about 2 MeV above this threshold obviously represents the sought resonance of ^{5}H. A similar spectrum (see Fig. 4) obtained when all detected proton pairs, irrelative to the ^{3}H observation, were involved in the analysis also shows this resonance peak. The consistency of the peak characteristics seen in Figs. 3 and 4 gives additional grounds to believe that this state of ^{5}H does indeed exist. The analogous spectra that were obtained for α particles emitted as the result of $2n$ transfer $p(^6\mathrm{He}, \alpha)^3\mathrm{H}$ and for tritons from $^6\mathrm{He}+p \rightarrow p+{}^3\mathrm{H}+X$

and $^6\mathrm{He} + p \rightarrow p + {}^3\mathrm{H} + {}^3\mathrm{H}$ processes and which are shown in Figs. 5 and 6 prove the proper operation of the whole setup and, hence, the correctness of the ^{5}He resonance seen in Fig. 3.

Thus, the data obtained make us confident that, for the first time, we have found a resonance state of ^{5}H lying at an energy of about 2 MeV above the $^5\mathrm{H} \rightarrow n + n + {}^3\mathrm{H}$ decay threshold. This is the only channel of ^{5}H decay because its energy is below the threshold of the decay $^5\mathrm{H} \rightarrow n + {}^4\mathrm{H}$.

A more comprehensive analysis of the data will be made in the near future. Therefore, one should regard the results presented here as preliminary ones. In particular, the intrinsic width of the 2-MeV ^{5}H resonance has not yet been obtained, though one could expect that it will be quite small, on the order of or even less than 1 MeV.

ACKNOWLEDGMENTS

This work was supported in part by the Russian Foundation for Basic Research (project no. 99-02-17968) and INTAS (grant no. INTAS97-1668).

REFERENCES

1. F. Aizenberg-Selove, Nucl. Phys. A **490**, 1 (1988).
2. D. V. Alexandrov, E. A. Ganza, Yu. A. Glukov, *et al.,* Vopr. At. Nauki Tekh., No. 2, 3 (1985).
3. H. G. Bohlen, in *Proceedings of the International Symposium "Structure and Reactions with Unstable Nuclei," Niigata, Japan, 1991* (World Sci., Singapore, 1991), p. 13.
4. H. G. Bohlen, in *Proceedings of the International School–Seminar on Heavy-Ion Physics, Dubna, Russia, 1993* (JINR, Dubna, 1993), p. 17.
5. H. G. Bohlen *et al.,* Nucl. Phys. A **583**, 775c (1995).
6. A. A. Korsheninnikov, M. S. Golovkov, A. Ozawa, *et al.,* Phys. Rev. Lett. **82**, 3581 (1999).
7. M. V. Zhukov, private communication.
8. N. A. F. M. Poppelier, A. A. Wolters, and P. W. M. Glaudemans, Z. Phys. A **346**, 11 (1993).
9. C. H. Blanchard and R. G. Winter, Phys. Rev. **107**, 774 (1957).
10. A. I. Baz', V. I. Goldansky, and Ya. B. Zel'dovich, *Light and Medium-Mass Nuclei Close to the Border of Nuclear Stability* (Nauka, Moscow, 1972).
11. N. V. Shulgina, B. V. Danilin, L. V. Grigorenko, *et al.,* Internal Report Chalmers SP-99/15 (Göteborg, Sweden, 1999).
12. A. A. Ogloblin and Yu. E. Penionzhkevich, in *Treatise on Heavy-Ion Science,* Ed. by D. A. Bromley (Plenum, New York, 1989), Vol. 8, p. 261.
13. K. K. Seth, in *Proceedings of the International Conference on Nuclei Far from Stability, Helsingør, Denmark, 1981* (CERN 81-90), p. 655.
14. M. G. Gornov, Yu. B. Gurov, P. V. Morokhov, *et al.,* Nucl. Phys. A **531**, 613 (1991).
15. D. V. Aleksandrov, E. Yu. Nikolskii, B. G. Novatskii, and D. N. Stepanov, in *Proceedings of the International Conference on Exotic Nuclei and Atomic Masses, Arles, France, 1995* (Editions Frontières, Gif-sur-Yvette Cedex, 1995), p. 329.
16. T. Kobayashi, K. Yoshida, A. Ozawa, *et al.,* Nucl. Phys. A **616**, 223c (1997).
17. A. M. Rodin *et al.,* Nucl. Instrum. Methods Phys. Res. B **126**, 236 (1997).

Physics of Atomic Nuclei, Vol. 64, No. 7, 2001, pp. 1249–1253. From Yadernaya Fizika, Vol. 64, No. 7, 2001, pp. 1324–1328.

Proceedings of the International Conference "Nuclear Structure and Related Topics"

Microscopic Calculation of Nuclear Systems Involving Nonspherical Clusters*

S. V. Korennov[1), **] **and G. F. Filippov**

Bogolyubov Institute for Theoretical Physics, National Academy of Sciences of Ukraine, Metrologicheskaya ul. 14b, UA-252143 Kiev, Ukraine

Received October 25, 2000

Abstract—The algebraic version of the resonating-group method is extended to cover cases where one of the clusters has an open p shell. A basis of Pauli-allowed states labeled with the symmetry indices of irreducible representations of the $SU(3)$ group is constructed in the Fock–Bargmann representation. Dynamical variables that describe nonspherical degrees of freedom of the cluster are introduced. The matrix elements of the nucleon–nucleon interaction are analytically found by using the operator-representation method. The nuclear system $^9\mathrm{Li} + n$ is taken as an example. © *2001 MAIK "Nauka/Interperiodica"*.

1. INTRODUCTION

Recent developments of experimental techniques opened new possibilities for exploring drip-line and exotic nuclei. This in turn gave impetus to searches for new approaches to theoretically describing various features of such nuclei like a neutron skin, a halo, or the inverted order of energy levels. Many of those nuclei involve $A = 10, ..., 20$ nucleons and have a well-defined cluster structure. One typical example is provided by the ^{11}Li nucleus, which is very weakly bound below the $^9\mathrm{Li}+2n$ threshold. In view of this, it is necessary to find a microscopic approach that takes into account the Pauli exclusion principle and the cluster structure and which is able to allow for internal degrees of freedom of nonspherical clusters such as ^{9}Li.

At present, the computational technique within the resonating-group method (RGM) or its algebraic version (AVRGM) [1] has been developed for those cases where the clusters involved are spherical. In terms of Elliott's model [2], their wave functions are transformed according to the irreducible representation $(\lambda, \mu) = (0, 0)$. In [3], one of the present authors discussed for the first time an extension of the AVRGM to the case of p clusters. In that study, the three-cluster case was discussed and a universal basis of allowed states was constructed. Here, we analyze binary systems, where it is simpler to take exactly into account the Pauli exclusion principle.

In the following, we consider the interaction of a ^{9}Li cluster with a valence neutron. Nevertheless, the procedure is basically applicable to a wide range of cluster systems.

2. ANSATZ: BRINK ORBITALS AND NORM OVERLAP

2.1. Brink Orbitals for the Core

Having adopted the $(1, 2)$ representation space for the core (^{9}Li), we make no further restrictions, thus allowing the angular momentum L_9 of the core to be 1, 2, or 3 and negative parity. The introduction of Brink orbitals is similar to any calculation within the generator-coordinate method (GCM) with some technical modifications. First, we define the normalized s-shell orbit for four nucleons as

$$|s\rangle = \frac{1}{\pi^{3/4}} \exp\{-\mathbf{r}^2/2\}. \tag{1}$$

Second, we define the p orbit as

$$|p_1\rangle = \frac{\sqrt{2}}{\pi^{3/4}} (\mathbf{u} \cdot \mathbf{r}) \exp\{-\mathbf{r}^2/2\}, \tag{2}$$

where $\mathbf{u}$ is a unit vector directed along the z axis of the frame rigidly bound to the core. We place the remaining proton and two neutrons on this orbital. Along with the ket states, we introduce bra states in the form

$$\langle s| = \frac{1}{\pi^{3/4}} \exp\{-\mathbf{r}^2/2\}, \tag{3}$$

$$\langle p_1| = \frac{\sqrt{2}}{\pi^{3/4}} (\mathbf{u}^* \cdot \mathbf{r}) \exp\{-\mathbf{r}^2/2\}. \tag{4}$$

*This article was submitted by the authors in English.

1)Present address: Graduate School of Science, Hokkaido University, Sapporo 060, Japan.

**e-mail: korennov@nova.sci.hokudai.ac.jp

1063-7788/01/6407-1249$21.00

The overlaps $\langle m \mid n\rangle = \int |n\rangle\langle m| d\mathbf{r}$ are

$$\langle s \mid s\rangle = 1, \quad \langle p_1 \mid p_1\rangle = (\mathbf{u}\cdot\mathbf{u}^*), \quad \langle s \mid p_1\rangle = 0. \quad (5)$$

For the remaining two neutrons, another p orbit must be defined,

$$|p_2\rangle = \frac{\sqrt{2}}{\pi^{3/4}}\frac{([\mathbf{w}\times\mathbf{u}^*]\cdot\mathbf{r})}{(\mathbf{u}\cdot\mathbf{u}^*)}\exp\{-\mathbf{r}^2/2\}, \quad (6)$$

$$\langle p_2| = \frac{\sqrt{2}}{\pi^{3/4}}\frac{([\mathbf{w}^*\times\mathbf{u}]\cdot\mathbf{r})}{(\mathbf{u}\cdot\mathbf{u}^*)}\exp\{-\mathbf{r}^2/2\}, \quad (7)$$

where the vector $\mathbf{w}$ ($\mathbf{w}^*$) is orthogonal to $\mathbf{u}$ ($\mathbf{u}^*$). Due to biorthogonality, the total overlap for the core is

$$\langle\Psi_9|\Psi_9\rangle = (\mathbf{u}\cdot\mathbf{u}^*)(\mathbf{w}\cdot\mathbf{w}^*)^2. \quad (8)$$

2.2. Brink Orbital for the Valence Neutron

The valence neutron is a separate cluster with $(0,0)$ symmetry; therefore, its Brink orbitals are

$$|R\rangle = \frac{1}{\pi^{3/4}}\exp\{-\mathbf{r}^2/2 + \sqrt{2}(\mathbf{R}\cdot\mathbf{r}) - \mathbf{R}^2/2\}, \quad (9)$$

$$\langle R| = \frac{1}{\pi^{3/4}}\exp\{-\mathbf{r}^2/2 + \sqrt{2}(\mathbf{R}^*\cdot\mathbf{r}) - \mathbf{R}^{*2}/2\}, \quad (10)$$

where $\mathbf{R}$ ($\mathbf{R}^*$) is the (cluster) generating vector for the harmonic-oscillator basis. Clearly, the form of the basis reflects the cluster structure.

The function in (9) is obviously not biorthogonal to the core orbitals. Biorthogonalization leads to the following orbital:

$$|n\rangle = |R\rangle - |s\rangle - \frac{(\mathbf{u}^*\cdot\mathbf{R})}{(\mathbf{u}\cdot\mathbf{u}^*)}|p_1\rangle - \frac{([\mathbf{w}\times\mathbf{u}^*]\cdot\mathbf{R})}{(\mathbf{u}\cdot\mathbf{u}^*)}|p_2\rangle, \quad (11)$$

$$\langle n| = \langle R| - \langle s| - \frac{(\mathbf{u}\cdot\mathbf{R}^*)}{(\mathbf{u}\cdot\mathbf{u}^*)}\langle p_1| - \frac{([\mathbf{w}^*\times\mathbf{u}]\cdot\mathbf{R}^*)}{(\mathbf{u}\cdot\mathbf{u}^*)}\langle p_2|. \quad (12)$$

The norm overlap is

$$\langle n \mid n\rangle = \exp(\mathbf{R}\cdot\mathbf{R}^*) - 1 - (\mathbf{R}\cdot\mathbf{R}^*) + \frac{(\mathbf{w}\cdot\mathbf{R})(\mathbf{w}^*\cdot\mathbf{R}^*)}{(\mathbf{w}\cdot\mathbf{w}^*)}. \quad (13)$$

The norm overlap for the entire nucleus is the product of (8) and (13). Upon the separation of the center-of-mass part, the result takes the form

$$\langle\Psi_{10} \mid \Psi_{10}\rangle = \sum_{n=2}^{\infty} C_n\mathcal{N}_n + \sum_{n=1}^{\infty} B_n\mathcal{M}_n, \quad (14)$$

$$\mathcal{N}_n = (\mathbf{u}\cdot\mathbf{u}^*)(\mathbf{w}\cdot\mathbf{w})^2(\mathbf{R}\cdot\mathbf{R}^*)^n,$$

$$\mathcal{M}_n = (\mathbf{u}\cdot\mathbf{u}^*)(\mathbf{w}\cdot\mathbf{w})(\mathbf{w}\cdot\mathbf{R})(\mathbf{w}^*\cdot\mathbf{R}^*)(\mathbf{R}\cdot\mathbf{R}^*)^{n-1},$$

$$C_n = \frac{1}{n!}\{1 + (-1)^n\frac{10n-1}{9^n}\}, \quad B_n = \frac{1}{n!}\frac{(-1)^{n-1}10n}{9^n}.$$

3. PROJECTION OF THE NORM OVERLAP

The norm overlap depends on the generating parameters $\mathbf{u}$, $\mathbf{w}$, and $\mathbf{R}$ and those conjugate to them. These parameters express the degrees of freedom we are interested in. Our basis functions will depend on them, being images of real-space harmonic-oscillator basis functions. The space of generating parameters will be referred to as Fock–Bargmann space, and we will be work in this representation.

In this space, the relation between the norm overlap and the basis functions has the simple form

$$\langle\Psi_{10} \mid \Psi_{10}\rangle = \sum_{\alpha} N_\alpha^2\psi_\alpha(\mathcal{R})\psi_\alpha(\mathcal{R}^*), \quad (15)$$

where, for the sake of brevity, we denote by α all quantum numbers and by $\mathcal{R}$ the set of the vectors $\mathbf{u}$, $\mathbf{w}$, and $\mathbf{R}$ and where N_α^2 is the weight of a function in the norm kernel (in other words, the squared norm of a function).

As discussed above, the basis will be labeled with the indices (λ,μ) of an $SU(3)$ irreducible representation in accordance with which the functions transform. The overlap in (14) is a superposition of terms having different $SU(3)$ symmetries. Nevertheless, it is possible to define the most symmetric (leading) term. Other terms and their weights are obtained by iteratively applying the Casimir operator $\hat{G}_2$ of the $U(3)$ group to the leading state.

The result of this operation is shown in Table 1. Thus, we arrive to the expansion

$$\langle\Psi_{10} \mid \Psi_{10}\rangle = \sum_{n,(\lambda',\mu)} (C_nW_{(n+\lambda',\mu)}\mathcal{N}_{n,(\lambda',\mu)} + B_nV_{(n+\lambda',\mu)}\mathcal{M}_{n,(\lambda',\mu)}), \quad (16)$$

where $\lambda = \lambda' + n$. Evidently, n is yet another quantum number, the number of oscillator quanta. It is easy to verify that $n = 2\nu + 1$ and $n = 2\nu$ correspond to, respectively, a positive and a negative parity. In this manner, the parity projection is performed.

The expressions for $\mathcal{N}_{n,(\lambda',\mu)}$ and $\mathcal{M}_{n,(\lambda',\mu)}$ must be further projected onto the overlaps of basis states with definite angular momenta. This procedure was described by Elliott and involves expansions in Wigner's D functions. The result of this projection is the following expansion:

$$\langle\Psi_{10} \mid \Psi_{10}\rangle = \sum_{n,(\lambda',\mu),L} (C_nW_{(n+\lambda',\mu),L}\mathcal{N}_{n,(\lambda',\mu),L} + B_nV_{(n+\lambda',\mu),L}\mathcal{M}_{n,(\lambda',\mu),L}). \quad (17)$$

The construction of the basis functions in the Fock–Bargmann space is performed in a straightforward way. Some basis functions and their weights are shown in Table 2. Their norms are defined as

$$N^2_{n,(\lambda',\mu),L} = C_nW_{(n+\lambda',\mu),L} + B_nV_{(n+\lambda',\mu),L}. \quad (18)$$

Table 1. $SU(3)$ projections $\mathcal{N}_n$ and $\mathcal{M}_n$ (g_2 is the eigenvalue of $\hat{G}_2$, and $d_{11}^{\lambda}d_{33}^{\mu}$ is the leading function in this representation)

	(λ,μ)	$g_2(\lambda,\mu)$	$W(\lambda,\mu)$	$V(\lambda,\mu)$	$d_{11}^{\lambda}d_{\mu}^{\mu}$
1	$(n+1,2)$	$n+1$	1		$d_{11}^{n+1}d_{33}^{2}$
2	$(n-1,3)$	0	$\frac{n}{n+1}$		$d_{11}^{n-1}d_{33}^{3}$
3	$(n,1)$	-3	$\frac{8n}{3(n+4)}$	1	$d_{11}^{n}d_{33}$
4	$(n-2,2)$	$-(n+3)$	$\frac{2(n-1)}{n+3}$	$\frac{(n-1)}{n}$	$d_{11}^{n-2}d_{33}^{2}$
5	$(n-1,0)$	$-(n+5)$	$\frac{8n(n-1)}{(n+3)(n+2)}$	$\frac{3(n-1)}{2(n+2)}$	d_{11}^{n-1}
6	$(n-3,1)$	$-2(n+2)$	$\frac{6(n+1)n(n-2)}{(n+2)(3n+5)(2n+1)}$	$\frac{(n-2)}{(n+1)}$	$d_{11}^{n-3}d_{33}$

Table 2. Some $SU(3)$ basis functions

(λ,μ)	n	L	Explicit form	$W(L)$
$(2\nu+2,2)$	$2\nu+1$	0	$(\mathbf{u}\cdot\mathbf{R})w^2R^{2\nu}-\frac{\nu}{\nu+2}(\mathbf{u}\cdot\mathbf{R})(\mathbf{w}\cdot\mathbf{R})^2R^{2\nu-2}$	$\frac{\nu+2}{(2\nu+3)(2\nu+5)}$
$(2\nu,0)$	$2\nu+1$	0	$(\mathbf{u}\cdot\mathbf{R})(\mathbf{w}\cdot\mathbf{R})^2R^{2\nu-2}$	$\frac{1}{(2\nu+1)}$
$(2\nu-2,2)$	2ν	0	$([\mathbf{u}\times\mathbf{w}]\cdot\mathbf{R})(\mathbf{w}\cdot\mathbf{R})R^{2\nu-2}$	$\frac{\nu}{(2\nu-1)(2\nu+1)}$
$(2\nu+1,1)$	$2\nu+1$	1	$\{[\mathbf{u}\times\mathbf{w}]R^{2\nu}-2\nu[\mathbf{w}\times\mathbf{R}](\mathbf{u}\cdot\mathbf{R})R^{2\nu-2}\}(\mathbf{w}\cdot\mathbf{R})$	$\frac{3}{2(2\nu+1)}$

4. MATRIX ELEMENTS OF THE INTERACTION

Calculation of the matrix elements of nucleon–nucleon interaction is the most tedious task in microscopic approaches like those based on the RGM [4]. In the AVRGM, the task is divided into two parts: first, we find the GCM kernel of the interaction; then, we project it onto the basis states, thereby determining the matrix elements.

In the following, the nucleon–nucleon interaction is assumed to be of the Gaussian form

$$\hat{U}_{\mathbf{r}_1,\mathbf{r}_2}=U_0\exp\{-(r_1-r_2)^2/b^2\}.$$

If Brink orbitals are biorthogonal (as in our case), the GCM kernel is calculated by the formula

$$\langle\Psi_{10}\mid\hat{U}\mid\Psi_{10}\rangle$$
$$=\sum_{i<j}(U_d\langle i(\mathbf{r}_1),j(\mathbf{r}_2)\mid\hat{U}\mid i(\mathbf{r}_1),j(\mathbf{r}_2)\rangle$$
$$-U_e\langle i(\mathbf{r}_1),j(\mathbf{r}_2)\mid\hat{U}\mid i(\mathbf{r}_2),j(\mathbf{r}_1)\rangle)\frac{\langle\Psi_{10}\mid\Psi_{10}\rangle}{\langle i\mid i\rangle\langle j\mid j\rangle},$$

where U_d and U_e are spin–isospin-averaged constants for direct and exchange interactions, respectively, while $|i\rangle$ and $|j\rangle$ are Brink orbitals ($|s\rangle$, $|p_1\rangle$, $|p_2\rangle$, and $|n\rangle$).

There is a large number of terms in (19). However, there is a way to calculate all of them if we know just one term; namely,

$$\langle\mathbf{R}^*(\mathbf{r}_1),\mathbf{S}^*(\mathbf{r}_2)\mid\hat{U}\mid\mathbf{R}(\mathbf{r}_1),\mathbf{S}(\mathbf{r}_2)\rangle \qquad (19)$$
$$=\exp\left\{\frac{1}{2}[(\mathbf{R}+\mathbf{S})\cdot(\mathbf{R}^*+\mathbf{S}^*)]\right.$$
$$+\frac{z}{2}[(\mathbf{R}-\mathbf{S})\cdot(\mathbf{R}^*-\mathbf{S}^*)]$$
$$\left.+\frac{z-1}{4}[(\mathbf{R}-\mathbf{S})^2+(\mathbf{R}^*-\mathbf{S}^*)^2]\right\},$$

where $z=(1+2/b^2)^{-1}$ and the orbital $|\mathbf{R}(\mathbf{r})\rangle$ has the same form as in (9). We can define all other orbitals in terms of $|\mathbf{R}\rangle$; for example, we have

$$|s\rangle=|\mathbf{R}\rangle\mid_{R=0},\quad|p_1\rangle=(\mathbf{u}\nabla_{\mathbf{R}})|\mathbf{R}\rangle\mid_{R=0},$$
$$|p_2\rangle=\frac{1}{(\mathbf{u}\mathbf{u}^*)}([\mathbf{w}\mathbf{u}^*]\nabla_{\mathbf{R}})|\mathbf{R}\rangle\mid_{R=0},\text{ etc.}$$

By way of example, the expression $\langle p_1,s\mid\hat{U}\mid p_1,s\rangle$ can be calculated as

$$\langle p_1,s\mid\hat{U}\mid p_1,s\rangle$$
$$=(\mathbf{u}^*\cdot\nabla_{\mathbf{R}^*})(\mathbf{u}\cdot\nabla_{\mathbf{R}})\langle\mathbf{R}^*,\mathbf{S}^*\mid\hat{U}\mid\mathbf{R},\mathbf{S}\rangle\mid_0$$
$$=\frac{z+1}{2}(\mathbf{u}\cdot\mathbf{u}^*).$$

In this way, all terms in (19) can be found analytically.

For each of the terms in (19), it is now necessary to construct an expansion in the basis states, which is similar to the expansion (15) of the norm overlap. One way to do this is to integrate the product of the kernel and the basis functions with respect to all variables. However, it is next to impossible to do this analytically (even with the help of computers). As to a numerical way, it will take a huge amount of computer time, since the process must be repeated for each pair of basis functions. To solve this problem, we make use of the operator representation of the interaction kernel. In other words, we find the corresponding operator in the Fock–Bargmann space for each of the terms entering into (19).

In general, $\langle\Psi_{10} \mid \hat{U} \mid \Psi_{10}\rangle$ consists of a number of terms u having the form [5]

$$u = u_0 P(\mathcal{R}, \mathcal{R}^*) \times \exp\{A(\mathbf{R}\cdot\mathbf{R}^*) + BR^2 + B^*R^{*2}\}, \tag{20}$$

where A, B, B^*, and u_0 are some constants, while $P(\mathcal{R}, \mathcal{R}^*)$ is the product of k scalar products (k can be equal 1 or 0, too). In turn, each of these scalar products can be of the form $(\mathbf{X}\cdot\mathbf{Y})$, $(\mathbf{X}\cdot\nabla_{\mathbf{Y}})$, or $(\nabla_{\mathbf{X}}\cdot\nabla_{\mathbf{Y}})$, where $\mathbf{X}$ and $\mathbf{Y}$ are variables from the sets $\mathcal{R}$ and $\mathcal{R}^*$. The presence of the polynomial $P(\mathcal{R}, \mathcal{R}^*) = 1$ is due to a nonspherical shape of the core cluster.

We first consider the case where $B = B^* = 0$ and $A = u_0 = 1$. We then have

$$u = P(\mathcal{R}, \mathcal{R}^*)\exp\{(\mathbf{R}\cdot\mathbf{R}^*)\} = \sum_{\alpha^*\alpha} |\alpha\rangle\langle\alpha \mid u \mid \alpha^*\rangle\langle\alpha^*|, \tag{21}$$

where $\alpha \equiv \{n, (\lambda', \mu), L\}$. Let us now compare this formula with the expansion of the reduced norm overlap [see Eq. (14)]:

$$\langle\Psi_{10} \mid \Psi_{10}\rangle_{\text{red}} = (\mathbf{u}\cdot\mathbf{u}^*)(\mathbf{w}\cdot\mathbf{w}^*)^2\exp(\mathbf{R}\cdot\mathbf{R}^*) = \sum_{\alpha}\frac{1}{n!}W_\alpha|\alpha\rangle\langle\alpha|. \tag{22}$$

Suppose that we have found an operator $\mathcal{P}_\mathcal{R}$ that satisfies the equation

$$\mathcal{P}_\mathcal{R}\langle\Psi_{10} \mid \Psi_{10}\rangle_{\text{red}} = P(\mathcal{R}, \mathcal{R}^*)\exp(\mathbf{R}\cdot\mathbf{R}^*). \tag{23}$$

From (23) and (22), we then obtain

$$\mathcal{P}_\mathcal{R}\langle\Psi_{10} \mid \Psi_{10}\rangle_{\text{red}} = \sum_{\alpha}\frac{1}{n!}W_\alpha\langle\alpha|(\mathcal{P}_\mathcal{R}|\alpha\rangle) = \sum_{\alpha}\sum_{\beta}|\beta\rangle\langle\beta \mid u \mid \alpha\rangle\langle\alpha|,$$

where

$$\mathcal{P}_\mathcal{R}|\alpha\rangle = \sum_{\beta} P_\alpha^\beta|\beta\rangle, \tag{24}$$

$$\langle\beta \mid u \mid \alpha\rangle = \frac{1}{n!}W_\beta P_\alpha^\beta.$$

The last formula is nothing but the sought-for matrix element.

It is easy to generalize this formula to the case of $u_0 \neq 1$ and $A \neq 1$ (by scaling $\mathbf{R} \to \mathbf{R}/\sqrt{A}$). It is also straightforward to expand the expressions $\exp\{BR^2\}|\beta\rangle$ (and $\exp\{BR^{*2}\}\langle\alpha|$) [6].

Finally, we present a general formula for the matrix element of operator (20) between the basis states $|n, (\lambda', \mu)\rangle$ (they are diagonal in L; therefore, this index is dropped here):

$$\langle n^*, (\lambda', \mu)^* \mid u \mid n^*, (\lambda', \mu)\rangle = \frac{z^{3/2}u_0}{N_{n^*,(\lambda',\mu)^*}N_{n,(\lambda',\mu)}} \times \sum_{m=0(1)}^{\min(n-p,n^*)} \left\{W_{(n+\lambda',\mu),L}\, P_{m,(\lambda',\mu)}^{m+p,(\lambda,\mu)'} \times \frac{A^m B^{(n-p-m)/2}(B^*)^{(n^*-m)/2}}{(\frac{n-p-m}{2})!(\frac{(n^*-m)}{2})!m!}\right\}. \tag{25}$$

Here, the parity of m must be identical to that of n and n^*. The index p is one of $\{0, 2, -2, 4, -4, ...\}$, depending on the ratio of creation and annihilation operators in $\mathcal{P}_\mathcal{R}$.

5. SOLVING THE AVRGM EQUATIONS

In the AVRGM, the set of equations to be solved is

$$\sum_{\nu^*,\beta^*}\langle\nu^*\beta^* \mid \hat{H} - E \mid \nu, \beta\rangle C_\nu^\beta = 0, \tag{26}$$

where all quantum numbers, with the exception of ν, are denoted by β and take those values that are of physical interest, thereby specifying a channel. Finally, C_ν^β are the sought-for coefficients in the expansion of the total wave function in the basis states.

If the continuum spectrum is under investigation, the coefficients C_ν^β oscillate, mimicking the wavefunction behavior. If the basis is truncated at $\nu_{\max}$ and if Eq. (26) is solved, this means that $C_\nu^\beta = 0$ for all $\nu > \nu_{\max}$. We refer to this way as a diagonalization method. But $\nu_{\max}$ cannot be set to very large value because of computational limitations. Therefore, it is advisable to determine the asymptotic behavior of the coefficients C_ν^β and match it with a solution to (26) at $\nu_{\max}$, thereby closing up the set of equations. We refer to this as an asymptotic method.

The asymptotic behavior of the coefficients C_ν^β was studied in [7].

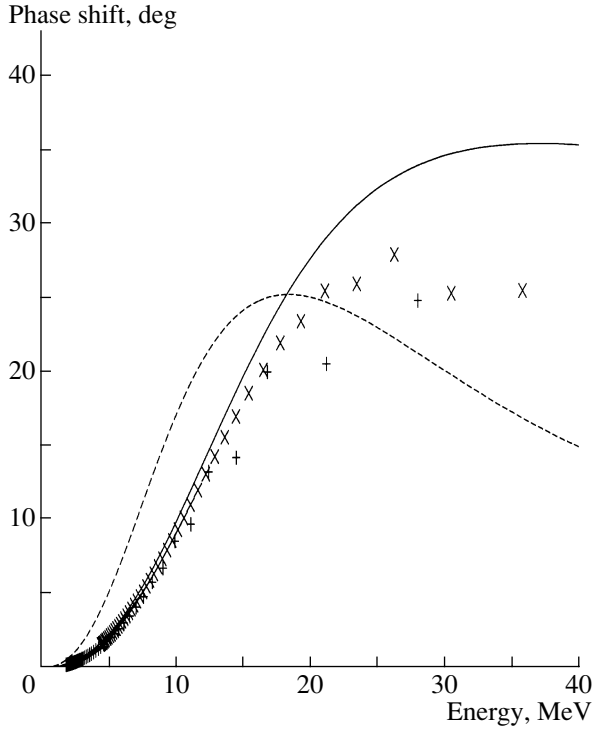

The 0^-, $(\lambda, \mu) = (2\nu - 2, 2)$ phase shift. The result of the calculations with the Minnesota potential and the Volkov potential no. 2 are represented by the solid and dashed curves, respectively. For the Minnesota potential, the results of the calculations based on the diagonalization method are shown by crosses and X-shaped symbols for the dimensions of 50 and 70, respectively.

The figure shows the behavior of the phase shift in the $^9\mathrm{Li} + n$ system for the case of $\beta = \{(2\nu - 2, 2), L = 0\}$ (0^- spectrum). The difference between the behavior of the phase shift obtained by the diagonalization and by the asymptotic method is noticeable at higher energies. Also, the dependence on the N–N interaction is evident. In any case, however, the phase shift shows a nonresonance behavior.

6. CONCLUSION

Extending the applicability region of the AVRGM to the nuclear systems featuring clusters with an open p shell, we have developed an algorithm for constructing the basis of harmonic oscillator Pauli-allowed states in the Fock–Bargmann space. The generating-coordinate technique has been used to construct the norm and Hamiltonian overlaps (kernels). In the two-cluster case, the indices of the irreducible representation of the $SU(3)$ group have been chosen to classify the basis states. The projection of the kernels onto the states with definite values of the quantum numbers has been performed. In terms of the operator-representation technique, we have presented an algorithm for calculating the matrix elements of a Gaussian nucleon–nucleon interaction.

By way of example, we have illustrated the implementation of the method for the $^9\mathrm{Li} + n$ system. At present, the analysis of this case is still under way. We also intend to use the results to study the $^9\mathrm{Li} + n + n$ system and other systems of interest.

ACKNOWLEDGMENTS

We are grateful to Prof. K. Katō and all members of the Nuclear Theory Laboratory of Hokkaido University for stimulating discussions.

REFERENCES

1. G. F. Filippov, Riv. Nuovo Cimento **9**, 1 (1989).
2. J. P. Elliott, Proc. R. Soc. London **245**, 128 (1958); **245**, 562 (1958).
3. G. F. Filippov, Yad. Fiz. **62**, 1237 (1999) [Phys. At. Nucl. **62**, 1164 (1999)].
4. J. A. Wheeler, Phys. Rev. **52**, 1083, 1107 (1937).
5. S. V. Korennov, in *Proceedings of INNOCOM'97, Osaka, Japan, 1997* (World Sci., Singapore, 1998), p. 117.
6. G. F. Filippov, A .V. Nesterov, I. Yu. Rybkin, and S. V. Korennov, Fiz. Élem. Chastits At. Yadra **25**, 1347 (1994) [Phys. Part. Nucl. **25**, 569 (1994)].
7. G. F. Filippov, A. D. Bazavov, K. Katō, and S. V. Korennov, Yad. Fiz. **60**, 635 (1997) [Phys. At. Nucl. **60**, 554 (1997)].

Physics of Atomic Nuclei, Vol. 64, No. 7, 2001, pp. 1254–1268. Translated from Yadernaya Fizika, Vol. 64, No. 7, 2001, pp. 1329–1343.

NUCLEI
Experiment

Multipole Mixtures in Gamma Transitions in ^{158}Gd from the $(n, n'\gamma)$ Reaction

L. I. Govor, A. M. Demidov, and I. V. Mikhailov

Russian Research Centre Kurchatov Institute, pl. Kurchatova 1, Moscow, 123182 Russia

Received March 31, 2000

Abstract—The energy spectrum, the angular distributions, and the linear polarizations of gamma radiation emitted by ^{158}Gd are measured in the $(n, n'\gamma)$ reaction induced by fast reactor neutrons. The known diagram of levels and gamma transitions is extended. The multipole-mixing ratio δ is found for many gamma transitions between levels with known spin–parity values. © *2001 MAIK "Nauka/Interperiodica".*

1. INTRODUCTION

A review of data on the energies of the levels and gamma transitions in ^{158}Gd can be found in [1]. That the cross section for thermal-neutron capture by ^{157}Gd is very large made it possible to obtain, with the aid of a diffraction spectrometer and an internal-conversion-electron spectrometer, a vast body of information about the energies, intensities, and conversion coefficients for almost 1000 transitions in ^{158}Gd. In view of this, the ^{158}Gd nucleus is the most convenient object for drawing a comparison with new theoretical concepts. Therefore, additional information about this nuclear species would of course be useful.

Our procedure of measurement and data treatment [2, 3] is advantageous in that it enables us to deduce information about multipole-mixing ratios in gamma transitions (prior to the present investigation, there was virtually no such information for ^{158}Gd, with the exception of estimates that were obtained from the internal-conversion ratios, which are insufficient for determining the sign of the multipole-mixing ratios). Measurement of the gamma spectrum and analysis of photon linear polarizations and angular distributions with respect to the direction of the beam of fast reactor neutrons permitted us to draw conclusions on the multipole-mixing ratios or on the multipole order for 50 gamma transitions in ^{158}Gd; we were also able to discover previously unknown gamma transitions and to extend the known diagram of levels for energies above 2 MeV.

2. RESULTS OF THE MEASUREMENTS

The gamma spectra of ^{158}Gd were measured in our experiment by using the $(n, n'\gamma)$ reaction induced by a fast-neutron beam extracted from the IR-8 reactor installed at the Russian Research Centre Kurchatov Institute (Moscow). The measurements were performed with a $^{158}Gd_2O_3$ sample of mass 23 g and thickness 1.13 g/cm^2, its enrichment in ^{158}Gd being 97.3% (the concentrations of the $A = 155$, 156, 157, and 160 gadolinium isotopes were 0.17, 0.33, 0.78, and 1.42%, respectively). The gamma radiation in question was recorded by a detector from ultrapure germanium with an efficiency of 10% and a resolution of 2.1 keV at $E_\gamma = 1.3$ MeV. In the measured gamma spectra, we singled out 410 gamma lines associated with ^{158}Gd. The angular distributions were investigated at angles of 90°, 105°, 115°, 125°, 135°, 142°, and 150° with respect to the neutron beam. In order to normalize the intensities of gamma radiation at the various angles, we used the isotropic 1663.54-keV $0_4^+ - 2_1^+$ gamma transition. The linear polarization of the radiation from ^{158}Gd was measured by a two-crystal Compton polarimeter. A more detailed account of our experimental procedure is given in [2].

Table 1 displays the energy values for the angle of $\theta = 90°$ between the direction of gamma-radiation detection and the neutron-beam direction and data on the relative intensities of gamma transitions in ^{158}Gd at $\theta = 125°$. The energies (E_i) of the ^{158}Gd levels from which the aforementioned gamma transitions proceed are quoted in the third column of Table 1. The spectrum of photons from the reaction ^{158}Gd$(n, n'\gamma)$ induced by fast neutrons was previously measured at a reactor in Riga with a resolution of 3 keV at 1.3 MeV [4]. While being consistent, for intense gamma lines, with the results presented in [4], our data show many deviations from those for transitions of low intensity (the authors of [4] did not eliminate some background gamma lines and the gamma lines associated with the capture of intermediate-energy neutrons that are present in the beam). For this reason, we deemed it appropriate to quote here our data on the spectrum in Table 1.

1063-7788/01/6407-1254$21.00

Table 1. Energies and intensities of gamma transitions in ^{158}Gd

E_γ, keV	I_γ, arb. units	E_i, keV	E_γ, keV	I_γ, arb. units	E_i, keV
79.51(2)	–	80	539.58(5)	1.05(8)	1920
135.25(14)	0.26(2)	1159	546.4(3)	0.057(11)	
155.09(18)	0.20(2)	1636?	558.20(10)	0.28(2)	
181.94(2)	100	261	587.43(15)	0.26(2)	
212.98(6)	0.62(4)	1372	$\sim$ 592.87(17)	–	1856
218.01(7)	0.49(4)	1717	606.52(4)	1.40(11)	1794
230.14(12)	0.21(2)	1407	619.4(2)	0.134(16)	1978
235.42(9)	0.48(4)	1717	622.5(3)	0.031(10)	
255.65(2)	3.18(22)	1636	631.31(12)	0.16(2)	1895
277.54(2)	17.0(12)	539	637.46(3)	1.57(12)	1176
282.75(8)	0.38(3)	1260	646.47(11)	0.22(2)	2049
301.1(2)	< 0.08	2018	654.1(2)	0.18(2)	
314.9(2)	< 0.08	1814	670.0(4)	0.099(17)	1856
332.65(11)	0.115(14)	1814	672.30(7)	0.72(6)	
336.21(5)	0.51(4)	1717	674.31(8)	0.52(4)	1862
339.14(10)	0.20(2)	1381	676.3(2)	0.162(19)	1941+^{159}Gd
341.75(14)	0.104(14)		680.85(11)	0.35(3)	2084
365.10(3) m	1.87(16)	904	688.74(5) m	1.07(8)	1952
		1407			1954
408.63(12)	0.32(3)		698.88(14)	0.33(3)	1964
410.75(19)	0.20(2)		701.2(3)	0.19(2)	
417.90(11)	0.20(2)	1917	707.82(7)	0.53(4)	1895
435.48(14)	0.30(3)	1917	713.31(10)	0.36(3)	
439.21(7)	0.45(4)		725.3(4)	0.068(12)	1901
444.87(25)	0.080(16)		735.36(7)	0.61(5)	
455.1(3)	0.109(13)	1954?	743.05(5)	1.01(8)	1930
466.65(13)	0.19(2)	2260	750.06(4)	1.05(8)	1792
475.64(15) m	0.15(2)	1452?	768.60(10)	0.58(5)	2034
		1517	771.9(2)	0.18(2)	
479.71(9)	0.22(2)	1743	777.34(17)	0.161(15)	1964
502.85(12)	$\sim$ 0.27(2)	1862	780.16(2)	7.0(5)	1042
518.55(18)	$\sim$ 0.30(3)	2018	782.65(8)	0.50(4)	1941
524.77(17)	0.116(13)		785.66(13)	0.21(2)	2049
528.13(4) m	0.67(5)	1792	790.97(12)	0.35(3)	1978
		1794	795.0(2)	0.27(2)	1954
537.05(8)	0.51(4)		800.1(5)	0.054(11)	

Table 1. (Contd.)

E_γ, keV	I_γ, arb. units	E_i, keV	E_γ, keV	I_γ, arb. units	E_i, keV
808.9(4)	< 0.05		944.13(2)	23.4(18)	1024
814.69(8)	0.43(4)	1792	948.51(18)	0.190(18)	
816.45(12)	0.31(3)	1794	953.34(9)	0.31(3)	
820.01(6) m	0.67(6)	1861	955.05(16)	0.28(3)	
		2084	962.08(2)	14.9(10)	1042
824.10(6)	0.73(6)	1848	977.13(2)	13.2(8)	977
832.97(5) m	1.08(9)	1372	982.50(10)	0.29(3)	
		1856	987.50(8)	0.38(3)	1964?
836.3(3)	0.137(20)		994.29(11)	0.28(2)	
843.4(3)	0.047(10)		1003.95(2)	2.61(17)	1265
847.13(18)	0.23(3)	2034?	1007.25(9)	0.45(4)	2049
851.15(5)	0.89(7)		1010.35(14)	0.30(3)	2034
852.84(5)	0.96(8)	1894	1018.9(2)	0.17(2)	2215?
856.2(3)	0.16(2)		1021.9(2)	0.132(19)	
859.83(11)	0.45(4)	1901	1024.93(10)	0.35(3)	2049?
865.94(11)	–		1028.31(9)	0.38(3)	2215
867.90(4)	$< 1.34(11)$	1407	1034.67(8)	0.45(4)	2222?
870.74(3) m	2.41(19)	1848	1046.07(6)	0.62(5)	
		1894	1050.7(2)	0.129(19)	
874.9(2)	0.23(2)	2034	1052.9(2)	0.22(2)	2095?
879.28(5)	0.80(6)	1856	1060.64(9)	0.30(3)	2326
884.7(3)	0.138(19)	1862	1062.31(9)	0.29(3)	2249?
887.51(14)	0.22(2)	2084	1072.08(16)	0.23(2)	
891.9(3)	0.030(10)		1077.32(11)	0.41(4)	
897.59(2) m	19.6(8)	977	1080.86(9)	0.38(3)	
		1159	1090.75(14)	0.19(2)	
902.38(4)	0.88(7)	2090	1094.17(4)	0.75(6)	
906.64(10)	0.25(2)	1930	1097.03(2)	5.6(4)	1359
915.00(2)	5.2(4)	1176	1100.74(12)	0.22(2)	1640
917.54(3) m	1.34(11)	1894	1107.63(2)	10.6(8)	1187
		1895	1116.47(2)	4.7(3)	1196
922.65(8)	0.41(4)	1964	1119.20(2)	9.4(7)	1381
925.52(18)	0.178(21)	1187	1126.06(15)	0.171(19)	
928.3(2)	0.074(16)		1128.91(12)	0.20(2)	1667?
934.2(5)	0.085(18)		1130.59(14)	0.162(18)	
936.1(3)	0.057(16)	1978	1141.45(2)	3.6(3)	1403

Table 1. (Contd.)

E_γ, keV	I_γ, arb. units	E_i, keV	E_γ, keV	I_γ, arb. units	E_i, keV
1145.35(5)	0.75(6)	1407	1371.38(3)	1.09(9)	
1153.7(3)	0.058(13)		1372.98(3)	2.29(16)	1452
1157.4(3)	0.063(14)		1378.19(11)	0.36(3)	1640
1159.8(2)	0.089(15)		1386.3(3)	0.068(14)	
1166.81(12)	0.22(2)		1389.39(9)	0.30(3)	
1173.26(11)	0.113(16)		1392.62(8)	0.48(4)	
1180.38(4)	1.99(14)	1260	1401.8(2)	0.119(16)	
1184.05(4)	7.6(5)	1264	1405.84(4)	0.87(7)	1667
1185.87(4)	12.1(9)	1265	1419.6(2)	0.117(14)	
1187.13(3)	5.8(4)	1187	1428.48(14)	0.155(16)	
1196.4(2)	0.140(15)		1437.89(3)	2.6(2)	1517
1204.68(11)	0.30(3)		1455.10(17)	0.25(3)	
1208.5(3)	0.106(15)		1460.0(4)	0.126(19)	
1215.55(11)	0.18(2)		1483.2(4)	0.045(11)	
1218.77(3)	0.47(4)	2260	1499.5(4)	0.055(12)	
1220.15(2)	2.6(2)	1482	1504.7(3)	0.036(9)	
1221.41(3)	0.55(4)		1509.04(19)	0.150(16)	
1234.8(2)	0.149(18)		1517.36(3)	1.85(15)	1517
1237.60(2)	2.8(2)	1499	1522.3(4)	0.122(13)	^{159}Gd?
1244.3(3)	0.191(17)		1530.09(6)	0.55(5)	1792
1250.21(18)	0.20(2)		1540.3(3)	0.104(12)	
1256.00(4)	0.89(7)	1517	1564.05(17)	0.125(14)	
1259.90(4)	3.6(3)	1260	1570.7(7)	0.058(11)	
1263.58(4)	4.6(3)	1264	1577.2(7)	0.073(12)	
1271.85(8)	0.27(2)		1587.71(5)	0.97(7)	1667
1275.84(16)	0.159(18)		1617.6(6)	0.043(14)	2805
1279.01(3)	1.77(13)	1359	1622.2(3)	0.098(17)	
1284.6(2)	0.122(13)		1625.8(3)	0.110(16)	
1301.20(3)	2.12(17)	1381	1632.8(7)	0.048(11)	1894
1312.23(14)	0.173(17)		1637.5(2)	0.172(19)	
1314.81(16)	0.110(15)		1640.4(3)	0.113(17)	1901
1323.44(2)	4.1(3)	1403	1644.2(2)	0.163(18)	
1327.26(3)	2.5(2)	1407	1650.8(2)	0.149(17)	2675
1347.98(6)	0.45(4)	2325	1657.5(3)	0.040(9)	
1353.97(5)	0.76(6)		1663.54(5)	0.69(6)	1743
1360.67(15)	0.26(3)		1674.0(2)	0.138(15)	

Table 1. (Contd.)

E_γ, keV	I_γ, arb. units	E_i, keV	E_γ, keV	I_γ, arb. units	E_i, keV
1682.39(18)	0.156(16)		2035.6(6)	0.076(15)	2035
1692.46(18)	0.26(2)	1954	2040.63(8)	0.34(3)	
1697.3(6)	0.030(9)	2675	2060.40(14)	0.21(2)	
1703.0(3)	0.100(17)	1964	2068.3(2)	0.21(2)	
1707.4(3)	0.138(19)		2071.51(14)	0.30(3)	
1721.7(3)	0.119(18)		2073.88(16)	0.151(18)	
1725.9(5)	0.135(18)		2102.3(5)	0.056(16)	
1735.5(5)	0.060(15)		2107.3(2)	0.19(2)	
1739.1(4)	0.087(16)		2122.48(15)	0.29(2)	
1749.9(2)	0.20(2)		2135.26(13)	0.31(3)	2215
1756.5(4)	0.15(2)		2138.51(8)	0.63(5)	
1774.44(17)	0.49(4)	2035?	2148.80(13)	0.27(2)	
1782.03(12)	0.30(3)	1862	2154.48(14)	0.22(2)	
1786.2(2)	0.17(2)		2163.07(13)	0.24(2)	
1799.2(5)	0.096(13)		2170.90(19)	0.126(14)	
1815.30(18)	0.32(3)	1895	2180.52(14)	0.45(4)	2260
1833.73(16)	0.30(2)	2095	2187.9(2)	0.20(2)	2267
1838.9(3)	0.073(11)		2196.26(17)	0.29(3)	
1856.38(6)	0.49(4)	1856	2202.83(10)	0.59(4)	
1858.83(8)	0.31(3)		2210.2(3)	0.161(15)	2289?
1864.81(7)	0.35(3)		2215.18(17)	0.33(3)	2215
1877.76(9)	0.40(3)	1957	2233.3(2)	0.153(16)	
1884.64(14)	0.31(3)	1964	2242.20(17)	0.23(2)	
1891.4(3)	0.076(17)		2246.48(12)	0.33(3)	2326
1930.9(3)	0.137(15)	1930?	2250.5(4)	0.121(16)	
1940.78(10)	0.52(4)		2260.16(16)	0.31(3)	2260
1944.35(9)	0.45(4)	2024	2267.04(12)	0.37(3)	2267
1955.76(6)	0.84(7)	2035	2273.29(17)	0.25(2)	
1971.0(2)	0.23(2)		2276.3(2)	0.155(18)	
1977.8(3)	0.25(2)		2289.44(12) m?	0.33(3)	2289?
1988.6(6)	0.071(17)		2304.42(13)	0.30(3)	
1998.5(3)	0.074(13)		2314.01(9)	0.27(2)	
2009.9(3)	0.24(2)	2090?	2327.4(2)	0.19(2)	
2014.8(3)	0.20(2)	2095?	2337.4(2)	0.117(13)	
2023.77(12)	0.33(3)	2024	2344.6(5)	0.058(10)	
2028.0(4)	0.089(16)		2366.8(2)	0.20(2)	2446

Table 1. (Contd.)

E_γ, keV	I_γ, arb. units	E_i, keV	E_γ, keV	I_γ, arb. units	E_i, keV
2369.7(2)	0.19(2)		2767.1(7)	0.068(14)	
2389.6(5)	0.17(2)		2775.4(5)	0.095(16)	2855
2395.2(3)	0.134(19)		2783.1(6)	0.085(16)	
2401.3(3)	0.171(19)		2791.2(7)	0.051(10)	
2412.3(2)	0.145(18)		2798.9(6)	0.093(16)	
2418.30(17)	0.27(3)		2805.1(3)	0.14(2)	2805
2434.8(3)	0.119(16)		2816.4(6)	0.118(16)	
2437.8(3)	0.100(16)		2822.8(7)	0.063(16)	2822
2446.26(16)	0.26(2)	2446	2832.0(3)	0.21(2)	2832
2450.70(12)	0.37(3)	2451	2839.4(6)	0.095(17)	
2458.51(12)	0.20(2)		2850.0(10)	0.059(14)	
2474.4(5)	0.064(11)		2854.6(5)	0.125(16)	2855
2485.7(4)	0.057(11)	2565	2869.0(11)	0.056(16)	
2498.8(2)	0.125(14)		2879.6(7)	0.082(16)	
2505.5(3)	0.048(11)		2885.1(10)	0.077(16)	2964
2515.2(2)	0.29(3)	2595	2895.9(7)	0.062(15)	
2520.8(3)	0.18(2)	2600	2904.7(6)	0.090(15)	
2550.8(4)	0.071(11)		2916.1(7)	0.062(13)	
2564.82(18)	0.24(2)	2565	2920.6(6)	0.061(14)	
2577.04(16)	0.21(2)		2932.5(5)	0.119(16)	
2600.1(3)	0.25(2)	2600	2946.6(12)	0.041(15)	
2607.5(4)	0.103(13)	2687	2952.2(11)	0.039(14)	
2626.5(6)	0.113(14)		2964.2(5)	0.137(15)	2964
2641.5(5)	0.094(17)		2980.4(6)	0.077(16)	3060
2646.8(5)	0.14(2)		2986.0(7)	0.074(15)	3065
2654.0(4)	0.119(17)		3006.4(5)	0.101(16)	
2663.7(5)	0.117(16)		3026.9(4)	0.078(12)	
2670.2(6)	0.122(17)	2750	3038.1(4)	0.109(13)	3038
2674.8(4)	0.17(2)	2675	3059.8(9)	0.053(12)	3060
2678.2(6)	0.096(16)		3064.7(5)	0.093(14)	3065
2686.3(8)	0.16(2)	2687	3083.2(4)	0.072(13)	
2702.0(3)	0.31(3)	2702	3097.9(8)	0.027(11)	
2720.4(7)	0.071(16)		3109.9(14)	0.022(12)	
2727.8(5)	0.120(18)		3119.3(8)	0.064(14)	
2742.0(8)	0.147(17)	2822	3135.2(6)	0.035(8)	
2750.4(2)	0.141(17)	2750	3175.5(8)	0.077(11)	

Table 1. (Contd.)

E_γ, keV	I_γ, arb. units	E_i, keV	E_γ, keV	I_γ, arb. units	E_i, keV
3188.1(9)	0.048(9)		3299.2(6)	0.050(9)	
3227.6(11)	0.047(10)		3318.1(6)	0.053(11)	
3237.1(5)	0.072(11)		3341.8(8)	0.056(11)	

Note: The label "m" indicates cases where we are dealing with a multiplet.

The diagram of ^{158}Gd levels and of the relevant gamma transitions that was composed on the basis of our results is given in Table 2, along with the results that we found for the coefficients a_2 and a_4 in the Legendre polynomial expansion $W(\theta) = A_0(1 + a_2P_2(\cos\theta) + a_4P_4(\cos\theta))$ of the angular distributions; also displayed in this table are the relative populations $P_s = \sum I_\gamma^{\text{out}} - \sum I_\gamma^{\text{in}}$ of the levels in the $(n, n'\gamma)$ reaction induced by fast reactor neutrons and the values found for the multipole-mixing ratio δ or for the multipole order ML. The uncertainties in a_2, a_4, and δ correspond to a 68% confidence level. The uncertainties in the δ values and their signs are given according to the system adopted in [5]: for example, $\delta = -4.5(+20, -17) = -2.8 > \delta > -6.5$. Here, we will not consider the dependence $P_s(E_i)$ for ^{158}Gd, since it was discussed in [6] on the basis of data from [4] and the diagram of gamma transitions that was composed in [7].

Table 3 lists the results obtained by measuring the linear polarization of photons for ^{158}Gd. The last column of this table presents the conclusion on the δ-ellipse branch on which the required value of δ resides ($a_4 \sim 0$ or $|a_4| > 0$, which usually corresponds to small or large values of $|\delta|$, respectively).

3. DISCUSSION OF THE RESULTS

In composing Table 2, we relied on information compiled in the review article of Helmer [1]. In particular, the features of the levels other than those based on our new data were borrowed from that review article. An analysis of the dependence $P_s(E_i)$ and the fact that the most intense transitions have already been included in the diagram give every reason to state that the ^{158}Gd nucleus has no other $J < 5$ levels at energies below 1.7 MeV. At energies above 2 MeV, the diagram of ^{158}Gd levels is obviously not complete. In this section of the diagram, we either present the deexcitation of a level that is known from a different reaction or propose an alternative version of deexcitation; there are also cases where we introduce an additional level, provided that this is suggested by the population of the level, the presumed diagram of deexcitation, and the angular distributions of emitted photons. For some levels, such arguments will be specified below.

In order to choose unambiguously δ (from two possible values) on the basis of measurement of angular distributions of photons alone, it was necessary that errors in determining the coefficient a_4 be very small. Since it was impossible to achieve this for many transitions, the choice among the two possible values of δ was sometimes based on the conclusion drawn from the data in Table 3 or on the values of the internal-electron-conversion coefficient from [1].

Discussed below are the results that we obtained for some individual levels.

1187-keV level. The δ value that we obtained for the 1107.63-keV transition complies with the $E2$ multipolarity found in studying internal-conversion electrons. The second, very small, value of δ is ruled out by the data on the linear polarization.

1260-keV level. A comparison of the multipole-mixing ratio expected on the basis of the known conversion ratio and the δ value that we found for the 1180.38-keV transition leads to the conclusion that there is a contribution from an $E0$ transition. The value of $\delta = -0.70(7)$ for this transition was chosen here by taking into account the value of P_γ. Since the lifetime of the initial level is known, we can find, for this level, the reduced matrix element $\rho(0)$ for the $E0$ transition in question.

1264-keV level. The internal-conversion coefficient for the 1184.05-keV transition is indicative of the presence of an $(E1 + M2)$ mixture. For an $E1$ transition, we expect $\alpha = 0.00085$, but the observed value is $\alpha = 0.00196$ [1]. Our data ($\delta = +0.11(8)$) also suggest the presence of a nonzero contribution from an $M2$ radiation. The second value of $\delta = -6(3)$ is inconsistent with the known value of α.

1265-keV level. For the 1185.87- and 1003.95-keV transitions, the values of δ are determined unambiguously on the basis of large a_4 values for both transitions. The value chosen here for the 1003.95-keV gamma transition is confirmed by the value of P_γ.

1358-keV level. The value of α for the 1097.03-keV transition favors the greater value δ. The second value is shown parenthetically. The data on P_γ give no way to make a reliable choice.

1381-keV level. For the 1119.20-keV transition, the second value of $\delta = -1.6(4)$ cannot be ruled out reliably on the basis of the value of α; however, the data on P_γ definitively indicate that this value of δ is impossible.

Table 2. Diagram of levels and gamma transitions in ^{158}Gd

E_i, keV	J_i^π	E_γ, keV	I_γ, arb. units	E_f, keV	J_f^π	P_s	a_2	a_4	δ, ML
79.51(2)	2^+	79.51	–	0	0^+				
261.45(3)	4^+	181.94	100	80	2^+	23	+0.237(18)	−0.070(20)	$E2$
538.99(4)	6^+	277.54	17	261	4^+	12.3			
904.1	8^+	365.10 m	~ 1.4	539	6^+	~ 1.4			
977.13(2)	1^-	977.13	13.2	0	0^+	< 28	−0.108(15)	0	$E1$
		897.59 m	< 19.6	80	2^+				
1023.64(3)	2^-	944.13	23.4	80	2^+	19.5			
1041.60(3)	3^-	962.08	14.9	80	2^+	17.1	−0.166(16)	+0.001(22)	$E1$
		780.16	7.0	261	4^+				
1158.85(14)	4^-	897.59 m	< 19.6	261	4^+	< 18.7			
		135.25	0.26	1024	2^-				
1176.45(4)	5^-	915.00	5.2	261	4^+	6.6			
		637.46	1.57	539	6^+				
1187.13(3)	2^+	1187.13	5.8	0	0^+	10.9	+0.284(26)	−0.100(35)	$E2$
		1107.63	10.6	80	2^+		0.066(15)	−0.029(22)	$+80 < \delta < -25$
		925.52	0.18	261	4^+				
1195.98(3)	0^+	1116.47	4.7	80	2^+	4.5	+0.028(22)	+0.035(32)	
1259.90(7)	2^+	1259.90	3.6	0	0^+	10.4	+0.247(15)	−0.083(20)	$E2$
		1180.38	1.99	80	2^+		−0.144(15)	−0.008(25)	−0.70(7)
		998.47	4.7	261	4^+		+0.081(19)	+0.002(21)	$E2$
		282.75	0.38	977	1^-				
1263.57(4)	1^-	1263.58	4.6	0	0^+	9.3	−0.150(15)	+0.003(22)	$E1$
		1184.05	7.6	80	2^+		−0.037(15)	0	+0.11(8)
1265.40(4)	3^+	1185.87	12.1	80	2^+	11.5	+0.105(25)	+0.091(35)	$+30(+32,-14)$
		1003.95	2.61	261	4^+		−0.132(14)	+0.075(21)	$-23(+19,-7)$
1358.50(4)	4^+	1279.01	1.77	80	2^+	7.1	+0.271(16)	−0.072(22)	$E2$
		1097.03	5.6	261	4^+		−0.078(15)	−0.024(23)	$+6.4(+14,-10)$ or $(-0.73(4))$
1371.94(15)	6^-	832.97 m	~ 0.98	539	6^-	~ 1.6			
		212.98	0.62	1159	4^-				
1380.68(4)	4^+	1301.20	2.12	80	2^+	7.5	+0.276(21)	−0.071(27)	$E2$
		1119.20	9.4	261	4^+		−0.219(14)	−0.066(22)	$-4.5(+20,-17)$
		339.14	0.20	1041	3^-				
1402.93(3)	3^-	1323.44	4.1	80	2^+	7.5	−0.182(15)	+0.029(23)	−0.02(3)
		1141.45	3.6	261	4^+		−0.03(2)	+0.02(4)	$-0.04(+4,-2)$

Table 2. (Contd.)

E_i, keV	J_i^π	E_γ, keV	I_γ, arb. units	E_f, keV	J_f^π	P_s	a_2	a_4	δ, ML
1406.78(4)	4^+	1327.26	2.5	80	2^+	5.3	+0.33(2)	−0.03(3)	$E2$
		1145.35	0.75	261	4^+		+0.30(5)	−0.06(7)	+1.0(2)
		867.90	< 1.34	539	6^+				
		365.10 m	~ 0.5	1042	3^-				
		230.14	0.21	1176	5^-				
1452.50(4)	0^+	1372.98	2.29	80	2^+	2.3			
		475.64?	< 0.15	977	1^-				
1481.60(4)	5^+	1220.15	2.6	261	4^+	1.5			
1499.05(4)	5^+	1237.60	2.8	261	4^+	1.7			
1517.39(3)	2^+	1517.36	1.85	0	0^+	5.5	+0.254(16)	−0.107(21)	$E2$
		1437.89	2.6	80	2^+		−0.227(17)	−0.021(24)	−1.5(4)
		1256.00	0.89	261	4^+		+0.082(20)	+0.002(24)	$E2$
		475.64	< 0.15	1042	3^-				
1636.33(4)	4^-	255.65	3.18	1381	4^+	3.4			
		155.09?	0.20	1482	5^+				
1639.69(11)	(5^-)	1378.19	0.36	261	4^+	0.58			
		1100.74	0.22	539	6^+				
1667.26(5)	4^+	1587.71	0.97	80	2^+	2.0	+0.28(3)	−0.01(4)	$E2$
		1405.84	0.87	261	4^+		−0.09(4)	−0.02(5)	+6(2) or (−0.76(11))
		1128.91?	0.20	539	6^+				
1716.95(6)	5^-	336.21	0.51	1381	4^+	1.5			
		235.42	0.48	1482	5^+				
		218.01	0.49	1499	5^+				
1743.06(5)	0^+	1663.54	0.69	80	2^+	0.91			
		479.71	0.22	1264	1^-				
1791.60(5)	2^+	1530.09	0.55	261	4^+	< 2.7	+0.09(3)	0	$E2$
		814.69	0.43	977	1^-				
		750.02	1.05	1042	3^-				
		528.13 m	< 0.67	1264	1^-				
1793.60(5)	2^-	816.45	0.31	977	1^-	< 2.2			
		606.52	1.40	1187	2^+				
		528.13 m	< 0.67	1265	3^+				
1814.25(12)	6^-	332.65	0.115	1482	5^+	< 0.2			
		314.9	< 0.08	1499	5^+				
1847.74(7)	1^+	870.74 m	~ 0.70	977	1^-	~ 1.4			
		824.10	0.74	1024	2^-				

Table 2. (Contd.)

E_i, keV	J_i^π	E_γ, keV	I_γ, arb. units	E_f, keV	J_f^π	P_s	a_2	a_4	δ, ML
1856.40(5)	1^-	1856.38	0.49	0	0^+	~ 1.0			
		879.28	0.33	977	1^-				
		832.97 m	~ 0.10	1024	2^-				
		670.0	0.099	1187	2^+				
		592.87	–	1264	1^-				
1861.45(9)	3^-	1782.03	0.30	80	2^+	~ 1.3			
		884.7	0.138	977	1^-				
		820.01 m	~ 0.08	1042	3^-				
		674.31	0.52	1187	2^+				
		502.85	~ 0.27	1358	4^+				
1894.40(4)	(2^+)	1632.8	0.048	261	4^+	~ 3.4			
		917.54 m?	~ 0.68	977	1^-				
		870.74 m	~ 1.71	1024	2^-				
		852.84	0.96	1042	3^-				
1894.93(8)	2^-	1815.30	0.32	80	2^+	~ 1.6			
		917.54 m?	~ 0.66	977	1^-				
		707.82	0.53	1187	2^+				
		631.31	0.16	1264	1^-				
1901.49(11)	4^+	1640.4	0.113	261	4^+	< 0.63			
		859.83	< 0.45	1042	3^-				
		725.3	0.068	1176	5^-				
1917.00(11)	$(4,5,6)^-$	435.48	0.30	1482	5^+	0.50			
		417.90	0.20	1499	5^+				
1920.26(6)	4^+	539.58	1.05	1381	4^+	1.05	+0.35(4)	+0.02(6)	−0.02(9) (or +1.08(17))
1930.21(6)	1^+	1930.9?	0.137	0	0^+	1.26			
		906.6	0.25	1024	2^-				
		743.05	1.01	1187	2^+		−0.05(3)	0.00(5)	+0.17(15)
1941.50(16)	3^+	782.65	0.50	1159	4^-	0.66			
		676.3	0.162	1265	3^+				
1952.3	$(0)^+$	688.74 m	~ 0.50	1264	1^-	~ 0.5			
1953.90(18)	4^-	1692.46	0.26	261	4^+	~ 1.1			
		795.0	0.27	1159	4^-				
		688.74 m	~ 0.57	1265	3^+				
		455.1?	0.109	1499	5^+				
1957.28(9)	0^+	1877.76	0.40	80	2^+	0.40	−0.03(6)	0.00(10)	$E2$

Table 2. (Contd.)

E_i, keV	J_i^π	E_γ, keV	I_γ, arb. units	E_f, keV	J_f^π	P_s	a_2	a_4	δ, ML
1964.24(8)	2^+	1884.64	0.31	80	2^+	1.31	+0.21(9)	−0.01(15)	−0.08(12) or +2.9(+18, −9)
		1703.0	0.100	261	4^+				
		922.65	0.41	1042	3^-				
		777.34	0.161	1187	2^+				
		698.88	0.33	1265	3^+				
1978.01(12)	3^-	936.1	0.057	1042	3^-	0.54			
		790.97	0.35	1187	2^+				
		619.4	0.134	1358	4^+				
2017.9(2)	(5^+)	518.55	~ 0.30	1499	5^+	~ 0.3			
		301.1	< 0.08	1717	5^-				
2023.83(9)	1	2023.77	0.33	0	0^+	0.78	−0.08(7)	−0.02(12)	$M1$ or $E1$
		1944.35	0.45	80	2^+				
2034.00(11)	3^+	1010.35	0.30	1024	2^-	1.11			
		874.9	0.23	1159	4^-				
		847.13?	0.23	1187	2^+				
		768.60	0.58	1265	3^+				
2035.28(6)	2^+	2035.6	0.076	0	0^+	1.41?			
		1955.76	0.84	80	2^+		+0.30(3)	+0.03(5)	+0.06(6) or +2.0(3)
		1774.44?	0.49	261	4^+				
2049.09(9)	2^-	1024.93?	0.35	1024	2^-	1.23?			
		1007.25	0.45	1042	3^-				
		785.66	0.21	1264	1^-				
		646.47?	0.22	1403	3^-				
2083.64(7)	2^+	887.51?	0.22	1196	0^+	~ 1.16			
		820.01 m	~ 0.59	1264	1^-				
		680.85	0.35	1403	3^-				
2089.51(5)	3^+	2009.9	0.24	80	2^+	1.12	+0.26(15)	−0.05(20)	+0.45(20) or +7(+70, −4)
		902.38	0.88	1187	2^+		+0.49(4)	+0.09(5)	+1.5(7)
2094.8(2)	4^+	2014.8	0.20	80	2^+	0.72	+0.35(17)	−0.09(23)	$E2$
		1833.73	0.30	261	4^+		+0.18(9)	−0.02(13)	−0.25(13) or +1.8(6)
		1052.9	0.22	1042	3^-				
2120.22(8)	$2^+, 3$	2040.63	0.34	80	2^+	0.65	−0.22(8)	−0.08(12)	
		1858.83	0.31	261	4^+				

Table 2. (Contd.)

E_i, keV	J_i^π	E_γ, keV	I_γ, arb. units	E_f, keV	J_f^π	P_s	a_2	a_4	δ, ML
2214.93(13)	1	2215.18	0.33	0	0^+	0.81	−0.07(10)	0	$E1$ or $M1$
		2135.26	0.31	80	2^+				
		1018.9	0.17	1196	0^+				
2215.44(9)	$(1,2)^+$	1028.31	0.38	1187	2^+	0.38			
2221.80(9)	$2^-,\ 3^-$	1034.67	0.45	1187	2^+	0.45			
2249.44(9)		1062.31	0.29	1187	2^+	0.29			
2260.11(14)	2^+	2260.16	0.31	0	0^+	0.76	+0.35(11)	−0.04(15)	$E2$
		2180.52	0.45	80	2^+				
2260.36(4)?		1218.77	0.47	1042	3^-	0.47			
2267.15(12)	$(1)2^+$	2267.04	0.37	0	0^+	0.57	+0.09(9)	+0.01(12)	
		2187.9	0.20	80	2^+				
2289.46(12)	$1, 2^+$	2289.14	0.33	0	0^+	0.49			
		2210.2	0.161	80	2^+				
2325.11(6)		1347.98	0.45	977	1^-	0.45			
2326.02(9)		2246.48	0.33	80	2^+	0.63			
		1060.64	0.30	1265	3^+				
2446.28(16)		2446.26	0.26	0	0^+	0.46			
		2366.8	0.20	80	2^+				
2450.72(12)	2^+	2450.70	0.37	0	0^+	0.37	+0.13(7)	−0.02(13)	$E2$
2564.88(18)	$1^{(+)}$	2564.84	0.24	0	0^+	0.30	−0.09(8)	0	$E1$ or $M1$
		2485.7	0.057	80	2^+				
2594.7(2)		2515.2	0.29	80	2^+	0.29			
2600.2(3)	$1^{(+)}$	2600.1	0.25	0	0^+	0.43	−0.04(8)	0	$E1$ or $M1$
		2520.8	0.18	80	2^+				
2674.5(4)	$(1), 2^+$	2674.8	0.17	0	0^+	0.35	+0.10(15)	−0.10(25)	$(E2)$
		1697.3	0.030	977	1^-				
		1650.8	0.149	1024	2^-				
2686.9(4)	1	2686.3	0.16	0	0^+	0.26	−0.09(9)	0.00(14)	$E1$ or $M1$
		2607.5	0.103	80	2^+				
2702.0(3)	2^+	2702.0	0.31	0	0^+	0.31	+0.10(7)	−0.01(10)	$E2$
2750.3(2)	$1(2^+)$	2750.4	0.141	0	0^+	0.26	−0.05(20)	0	
		2670.2	0.122	80	2^+				
2805.1(3)	1	2805.1	0.14	0	0^+	0.18			
		1617.6?	0.043	1187	2^+				
2822.2(7)	1^-	2822.8	0.063	0	0^+	0.21			
		2742.0	0.147	80	2^+				

Table 2. (Contd.)

E_i, keV	J_i^π	E_γ, keV	I_γ, arb. units	E_f, keV	J_f^π	P_s	a_2	a_4	δ, ML
2832.0(3)	1	2832.0	0.21	0	0^+	0.21	−0.11(13)	0	$E1$ or $M1$
2854.8(5)	$1, 2^+$	2854.6	0.125	0	0^+	0.22			
		2775.4	0.095	80	2^+				
2964.2(5)	2^+	2964.2	0.137	0	0^+	0.21	+0.11(16)	−0.04(21)	$E2$
		2885.1	0.077	80	2^+				
3038.1(4)	1	3038.1	0.109	0	0^+	0.11			
3059.9(6)	$1, 2^+$	3059.8	0.053	0	0^+	0.13			
		2980.4	0.077	80	2^+				
3065.0(5)	$1, 2^+$	3064.7	0.093	0	0^+	0.17			
		2986.0	0.074	80	2^+				

1407-keV level. For the 1145.35-keV transition, we found that $\delta = +1.0\,(2)$, which leads to $\alpha_K = 0.0023$. It is likely that, in the review article of Helmer [1], this transition was assigned the $E2$ type on the basis of the value of $\alpha_K = 0.0018\,(6)$ quoted in [8]. For the $E2$ transition, it is expected that $\alpha_K = 0.00177$. The second value ($\delta \sim 0$) is ruled out by the value of α_K.

1499-keV level. From the data on P_γ for the 1237.60-keV gamma transition, it follows that $|\delta| > 1$, which is consistent with the value of α (see [1]).

1517-keV level. In a study devoted to the Coulomb excitation of ^{158}Gd, the value of $\delta = -1.6\,(15)$ was obtained for the 1437.89-keV transition; we found $\delta = -1.5\,(4)$. That the conversion coefficient is large suggests the presence of an $E0$ transition. The lifetime of this level is known, which makes it possible to find $\rho\,(0)$ for the 1437.89-keV transition. That δ and $P_\gamma^{\rm calc}$ have been determined unambiguously is due to the proximity of the experimental value of a_2 to the minimum possible value calculated for the δ ellipse.

1667-keV level. The angular distribution for the 1587.71-keV transition complies with that which is expected for the $(4^+{-}2^+)$ transition; therefore, this level can be definitively assigned the spin–parity of $J^\pi = 4^+$. The value of P_γ favors $\delta = +6\,(2)$ for the 1405.84-keV transition, while the value of α (see [1]) suggests the presence of a contribution from an $E0$ transition. The second value of $\delta = -0.76\,(11)$ is given parenthetically.

1920-keV level. Of the two values of δ for the 539.58-keV transition, we have chosen the smaller one, since the value of a_4 favors it as the more probable. This value is consistent with the $M1$ multipolarity, which follows from the data on the conversion ratio. However, a contribution from an $E0$ transition can be expected for the transition being considered, since the initial and the final state both have $K^\pi = 4^+$ (see [1]).

1957-keV level. An isotropic angular distribution of 1877.76-keV photons and a relatively low population of this level are consistent with the $J^\pi = 0^+$ assignment for it.

2024-keV level. The angular distribution of 2023.77-keV photons is at odds with the $J^\pi = 2^+$ assignment for this level, but it complies with $J = 1$.

2089-keV level. The spin–parity value of $J^\pi = 2^+$ was adopted in [1] for this level. The angular distribution of 902.38-keV photons complies neither with $J^\pi = 2^+$ nor with 4^+ for this level. We assume that $J^\pi = 3^+$.

2120-keV level. The value of a_2 for the 2040.63-keV transition rules out the assumption of $J^\pi = 4^+$ or 2^- for the level being discussed.

2215-keV level. The angular distribution of 2215.18-keV photons does not comply with $J^\pi = 2^+$ for this level.

2260.1-keV level. The value of a_2 for the 2260.16-keV transition is at odds with the spin value of $J = 1$ for the level being considered. The relationship between the intensities of the 2180.52- and 1218.77-keV transitions that was found in our previous study and which was quoted in [1] gives sufficient grounds to assume that they proceed from different levels. There are no strong arguments in support of the introduction of a level at 2260.4 keV.

2451-keV level. The value of a_2 for the 2450.70-keV transition does not comply with the spin value of $J = 1$ for this level.

Table 3. Results obtained by measuring the linear polarization of gamma rays from ^{158}Gd

E_γ, keV	J_i^π	J_f^π	P_γ^{calc}		P_γ^{expt}	Conclusions
			$a_4 \sim 0$	$\lvert a_4\rvert > 0$		
780.16	3_1^-	4_1^+			1.2 (2)	Corresponds to $E1$
944.13	2_1^-	2_1^+			0.56 (10)	Corresponds to $E1$
962.08	3_1^-	2_1^+			1.8 (+4, −3)	Corresponds to $E1$
977.13	1_1^-	0_1^+	1.36 (6)		1.5 (3)	Corresponds to $E1$
998.47	2_3^+	4_1^+	1.30 (8)		1.3 (3)	Corresponds to $E2$
1003.95	3_1^+	4_1^+	0.84 (2)	0.60 (1)	0.49 (13)	$\lvert a_4\rvert > 0$
1097.03	4_2^+	4_1^+	1.61 (6)	0.51 (1)	1.2 (+3, −2)	
1107.63	2_2^+	2_1^+	2.00 (2)	0.81 (1)	0.88 (16)	$\lvert a_4\rvert > 0$
1116.47	0_2^+	2_1^+	1.00 (3)		0.94 (20)	
1119.20	4_3^+	4_1^+	1.00 (13)	0.63 (8)	0.47 (10)	$\lvert a_4\rvert > 0$
1180.38	2_3^+	2_2^+	1.64 (4)	0.96 (3)	1.7 (+8, −5)	$a_4 \sim 0$
1237.60	5_2^+	4_1^+			1.4 (+4, −3)	$\lvert a_4\rvert > 0, \quad \lvert\delta\rvert > 1$
1259.90	2_3^+	0_1^+		2.2 (2)	1.9 (+8, −5)	Corresponds to $E2$
1263.58	1_2^-	0_1^+	1.52 (6)		1.3 (3)	Corresponds to $E1$
1323.44	3_2^-	2_1^+	1.7 (2)		2.6(+13, −6)	Corresponds to $E1$
1405.84	4^+	4_1^+	1.70 (15)	0.59 (1)	0.7 (+6, −4)	$\lvert a_4\rvert > 0$
1437.89	2_4^+	2_1^+	1.3 (3)		1.9 (+9, −5)	
1517.36	2_4^+	0_1^+		2.2 (3)	2.0(+19, −8)	Corresponds to $E2$

Table 4. Some features of the gamma transitions in the deexcitation of the $K^\pi = 0_2^+$ and 0_3^+ levels

E_i, keV	E_γ, keV	$J_i^\pi K - J_f^\pi K$	δ	q^2	$\rho(0)$
1260	1180.38	$2^+0_2 - 2^+0_1$	−0.70(7)	0.79(65)	0.055(23)
1517	1437.89	$2^+0_3 - 2^+0_1$	−1.5(4)	6.8(13)	0.44(6)
1407	1145.35	$4^+0_2 - 4^+0_1$	+1.0(2)	∼0.0	−
1667	1405.84	$4^+0_3 - 4^+0_1$	+6(2)	3.4(6)	−

2565- and 2600-keV levels. The values of a_2 for the transitions from these levels to the ground state support the $J = 1$ assignment.

2687- and 2832-keV levels. The angular distributions of photons that are associated with the transitions to the ground state rule out the spin-parity of $J^\pi = 2^+$, but they are consistent with $J = 1$.

2702- and 2964-keV levels. The values of a_2 for the transitions to the ground state comply with $J^\pi = 2^+$.

At energies above 2100 keV, we introduced only a few previously unknown levels in Table 2 (those at 2214.93, 2289.46, 2674.5, 2686.9, 2854.8, and 2964.2 keV), relying on the occurrence of gamma transitions to the ground state and to the first 2^+ level (with the exception of 2674.5-keV level). The remaining levels in Table 2 at energies in excess of 2100 keV manifested themselves either through a gamma transition in the (n, γ) reaction from a state formed upon neutron capture or in the (γ, γ'), (d, p), and (d, t) reactions. In such cases, we present our version of the deexcitation of such levels. For the levels at 2215.41, 2260.08, and 2326.28 keV, the diagrams of deexcitation adopted in [1] are incorrect

since they lead to unrealistically high populations P_s of the levels in the reactions being studied.

4. DEEXCITATION OF THE $K^\pi = 2^+_\gamma$, 0^+_2, AND 0^+_3 ROTATIONAL BANDS

In the sample of data that we obtained for multipole mixtures, information about the deexcitation of the levels that belong to the $K^\pi = 2^+_\gamma$, 0^+_2, and 0^+_3 rotational bands is of particular interest. In [9], it was found that, for the majority of even–even nuclei where the number of neutrons is in the range $90 < N < 110$, the values of δ have the same sign for the $(2^+2_\gamma - 2^+0_1)$ and $(4^+2_\gamma - 4^+0_1)$ transitions and opposite signs for the $(2^+2_\gamma - 2^+0_1)$ and $(2^+0_\beta - 2^+0_1)$ transitions. Here, the indices γ, β, and 1 correspond to, respectively, gamma rotational bands, beta rotational bands, and rotational bands built on the ground state. For the ^{158}Gd nucleus, we were unable to establish the sign of δ for the $(2^+2_\gamma - 2^+0_1)$ transition ($E_\gamma = 1107.63$ keV). If, however, we assume that it is identical to the analogous sign for the $(4^+2_\gamma - 4^+0_1)$ transition, the second rule of opposite signs is satisfied for both $K^\pi = 0^+_2$ and 0^+_3 bands.

Data on some features of gamma transitions from the 2^+ and 4^+ levels of these bands are quoted in Table 4. These include $q^2 = J_K(E0)/J_K(E2)$, the ratio of the intensity of K electrons for the $E0$ transition to the intensity of K electrons for the $E2$ transition, and $\rho(0)$, the reduced nuclear matrix element for the $E0$ transition (see [10]). The value of $\rho(0)$ for the 1180.38-keV transition is close to that which is expected for the deexcitation of the levels of the gamma rotational band; this is due to the mixing of the $K^\pi = 2^+_\gamma$ and 0^+_2 bands because of their proximity in the excitation energy. For the 1437.89-keV transition, the value of $\rho(0)$ corresponds to that which is observed in the neighboring nuclei in the deexcitation of the beta rotational band. For the 1145.35- and 1405.84-keV $(4^+ - 4^+)$ transitions, the relationship between the relevant values of q^2 is similar to that in $(2^+ - 2^+)$ transitions. Unfortunately, the lifetimes of the 1407- and 1667-keV levels are not known; therefore, we do not quote the relevant values of $\rho(0)$.

REFERENCES

1. R. G. Helmer, Nucl. Data Sheets **77**, 481 (1996).
2. A. M. Demidov, L. I. Govor, and K. A. Baskova, in *Investigation of Excited Nuclear States* (Nauka, Alma-Ata, 1986), p. 70.
3. A. M. Demidov and I. V. Mikhaĭlov, Yad. Fiz. **58**, 2115 (1995) [Phys. At. Nucl. **58**, 2001 (1995)].
4. Ya. Ya. Berzin', T. V. Guseva, and Yu. Ya. Tamberg, Izv. Akad. Nauk Lat. SSR, Ser. Fiz. Tekh. Nauk, No. 3, 12 (1982).
5. K. S. Krane, At. Data Nucl. Data Tables **25**, 29 (1980).
6. Yu. G. Kosyak, L. V. Chekushina, S. Arynov, and Zh. I. Adamov, Izv. Akad. Nauk, Ser. Fiz. **60** (1), 193 (1996).
7. E. P. Grigor'ev, in *Investigation of Excited Nuclear States* (Nauka, Alma-Ata, 1986), p. 140.
8. R. C. Greenwood, C. W. Reich, and H. A. Baader, Nucl. Phys. A **304**, 327 (1978).
9. A. M. Demidov, L. I. Govor, V. A. Kurkin, and I. V. Mikhaĭlov, Yad. Fiz. **62**, 1349 (1999) [Phys. At. Nucl. **62**, 1271 (1999)].
10. A. V. Aldushchenkov and N. A. Voinova, Nucl. Data Tables **11**, 299 (1973).

Translated by A. Isaakyan

Physics of Atomic Nuclei, Vol. 64, No. 7, 2001, pp. 1269–1272. Translated from Yadernaya Fizika, Vol. 64, No. 7, 2001, pp. 1344–1348.

NUCLEI
Experiment

^{236}U and ^{238}U Fission Induced by Linearly Polarized Photons in the Region of a Giant Dipole Resonance

V. M. Khvastunov and V. V. Denyak

National Research Center Kharkov Institute for Physics and Technology, Akademicheskaya ul. 1, Kharkov, 310108 Ukraine

Received February 10, 2000; in final form, June 15, 2000

Abstract—The asymmetry Σ in ^{236}U and ^{238}U photofission induced by linearly polarized photons obtained by passing electrons through a silicon crystal under conditions close to the conditions of planar channeling is measured. This asymmetry is found to depend on the mass of the nucleus. The measured asymmetry is compared with data from other studies performed either with a polarized or an unpolarized photon beam. It is shown that the asymmetry value cannot be explained by a dominant role of any of the dipole fission channels, but that it is in accord with the currently prevalent idea that $E1$ transitions play the most important part in the energy region under investigation. It is assumed that the asymmetry Σ is sensitive to the relative height of the inner and the outer hump of the fission barrier, and this is manifested in the distinctions between the asymmetry values for nuclei having the same Z. © *2001 MAIK "Nauka/Interperiodica"*.

1. INTRODUCTION

The use of polarized photons in studying nuclear fission opens new possibilities for exploring the mechanism of the fission process and the structure of excited nuclear states. The first studies along these lines were performed in Hessen [1, 2] and in Kharkov [3]. The data from those experiments revealed that the contributions of the electric-quadrupole and the magnetic-dipole fission channel are not observed in the photon-energy region studied there.

The present article reports on the results obtained by experimentally studying ^{236}U and ^{238}U photofission induced by linearly polarized photons in the region of a giant dipole resonance. Our experiment was performed at the LUE-2000 Kharkov linear electron accelerator. A beam of polarized photons was formed by passing 1200-MeV electrons through a silicon crystal under conditions close to the conditions of channeling. The silicon crystal was arranged in a goniometer and was oriented with respect to the electron beam to a precision of 5×10^{-5} rad. The orientation of the crystal was monitored by determining the photon yield in the soft section of the spectrum with the aid of an ionization chamber. The number of electrons that had traversed the crystal was estimated by measuring the current of secondary electron emission in the crystal. The total photon flux was measured by a quantameter. The degree of linear polarization of the photon beam, P_γ, was determined with a gas deuterium polarimeter by measuring the yield of protons from the reaction $\vec{\gamma}d \to pn$ by a silicon semiconductor detector. The recorded protons were interpreted as those that originate from direct deuteron photodisintegration, and the photon energy was reconstructed on the basis of this hypothesis. Upon traversing the polarimeter, the photon beam hit the nuclear target being investigated. The targets were prepared in the form of ^{236}U and ^{238}U films 186 and 233 μg/cm^2 thick, respectively, deposited onto aluminum substrates of thickness 10 μm. Fission fragment were recorded at an angle of 90° with respect to the photon-beam direction by using a silicon semiconductor detector of thickness 100 μm positioned at a distance of 35 mm from the target.

The amplitude spectra of the yield of protons from the reaction $\vec{\gamma}d \to pn$ and of the fragments originating from the fission of ^{236}U and ^{238}U nuclei were measured simultaneously for each of three positions of the silicon crystal; that is, $N_\parallel$ and $N_\perp$ are the yields for the photon-polarization-vector direction, respectively, parallel and orthogonal to the reaction plane, while N_p are the relevant yields for a disoriented crystal.

From the amplitude spectra of the proton yields, we deduced the quantity $\beta = \left(N_\parallel + N_\perp\right)/2N_p$, which gives the ratio of the intensity of the radiation from the oriented crystal to the intensity of the radiation from the disoriented crystal. From the values of β, we can see that, with increasing energy, the relative yield of photons decreases sharply from 5.6 at 5 MeV, approaching 1 at 18 MeV; that is, the photon spectrum from the oriented crystal is enriched in heavy nuclei at energies in the region of the giant dipole

1063-7788/01/6407-1269$21.00

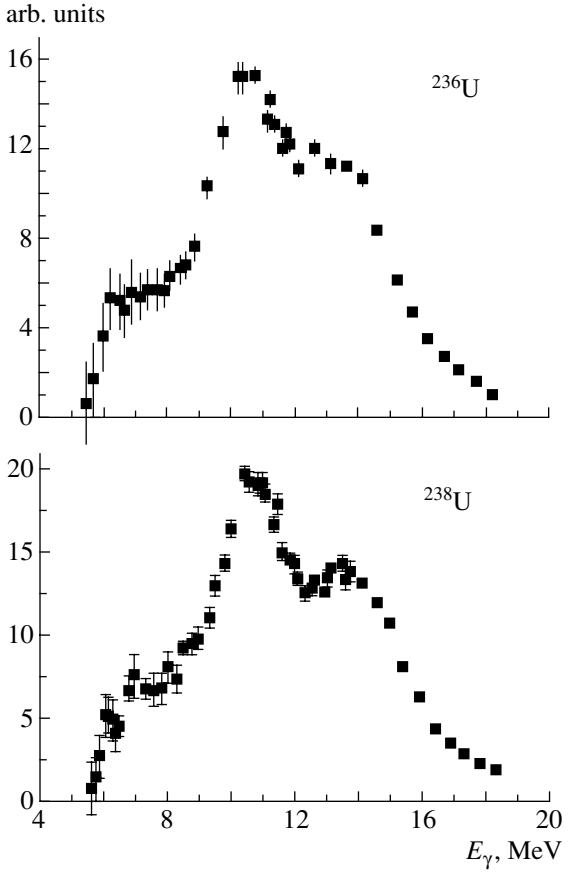

Fig. 1. Result obtained by evaluating the convolution of the cross sections for uranium-isotope photofission with the photon spectrum used in the present experiment.

resonance. In order to eliminate the effect of photons with energies above 18 MeV on the yield of reaction products, we subtracted the yield of reaction products for the disoriented crystal from the analogous yield for the oriented crystal; that is, we obtained the result only for the coherent part $(\beta - 1)\, N_\gamma^{\mathrm{br}}$ of the photon spectrum (N_γ^{br} is the spectrum of photons from the disoriented crystal). For a detailed description of our experimental setup and of the procedure used to process the results of our measurements, the interested reader is referred to [3].

The majority of previous experiments devoted to fission employed bremsstrahlung photons. The spectrum of the photons used in our experiment differs from the bremsstrahlung spectrum. In order to take into account special features of the spectrum of the polarized photons that we obtained and to determine the region of nuclear excitation energies, we evaluated the convolution of the polarized-photon spectrum with the cross sections for ^{236}U and ^{238}U fission. The results are presented in Fig. 1. The cross sections for ^{236}U and ^{238}U fission were taken from [4]. From Fig. 1, it can be seen that we have investigated the photofission process in the energy region of the giant dipole resonance and measured its major part up to an energy of 18 MeV.

The theoretical formalism developed in [1, 5] for describing the fission process makes it possible to relate, provided that the multipole structure of photon interaction with a nucleus is known, the asymmetry in fission induced by polarized photons to the coefficients in the angular distribution of fission fragments from measurements with unpolarized photons. Previous investigations into the fission of the nuclei being discussed revealed the dominant role of $E1$ transitions in the energy region around the giant dipole resonance. The contribution of the $E2$ and $M1$ components that was discovered in [6, 7] is much less than the $E1$ contribution.

In the $E1$ approximation, the asymmetry in fission has the form

$$\Sigma = b/(a+b) \tag{1}$$

with

$$\sigma(\theta) = a + b\sin^2\theta. \tag{2}$$

The coefficients a and b can be expressed in terms of the cross sections $\sigma(J^\pi, K)$ for the excitation of nuclear states characterized by fixed values of the following quantum numbers: J, the spin of a compound nucleus; π, its parity; and K, the projection of J onto the symmetry axis of the nucleus. Specifically, we have

$$a = \frac{3}{2}\sigma\left(1^-, \pm 1\right), \tag{3}$$

$$b = \frac{3}{4}\sigma\left(1^-, 0\right) - \frac{3}{4}\sigma\left(1^-, \pm 1\right).$$

If there is only one state in the energy region being studied, the asymmetry has an excitation-energy-independent value:

$$\Sigma\left(1^-, 0\right) = 1, \tag{4}$$

$$\Sigma\left(1^-, \pm 1\right) = -1.$$

2. ASYMMETRY Σ OF ^{236}U PHOTOFISSION

The value that we obtained for the asymmetry in ^{236}U fission; the result presented in [2]; and the asymmetry values from [8], which were rescaled from the coefficients a and b, are displayed in Fig. 2 versus the maximum energy $E_\gamma^{\max}$ in the photon spectrum. The value of the asymmetry Σ according to [2] was obtained on the basis of the polarization degree quoted in [1]. The result of our measurements for the asymmetry Σ is given at the energy of $E_\gamma^{\max} = 18$ MeV.

From Fig. 2, it can be seen that neither the $(1^-, 0)$ nor the $(1^-, \pm 1)$ state is dominant in the region

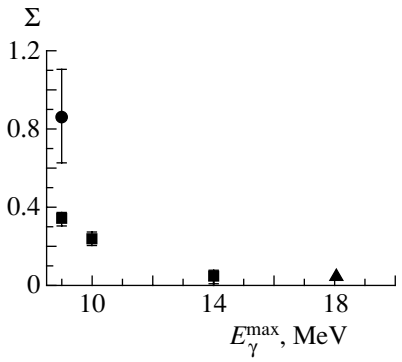

Fig. 2. Asymmetry in ^{236}U fission: (●) data from [2], (■) data from [8], and (▲) data from our present study.

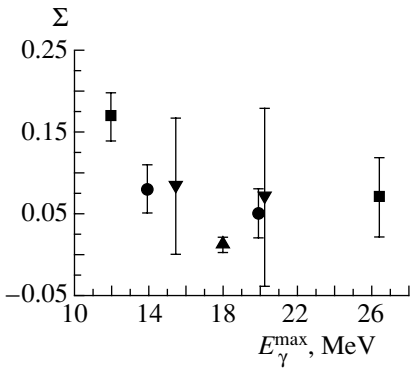

Fig. 3. Asymmetry in ^{238}U fission: (●) data from [8, 10], (■) data from [11], (▼) data from [12], and (▲) data from our present study.

of the giant dipole resonance. The asymmetry in the fission process from [2] and our result have the same sign, but the former is much greater in magnitude. This may be due to a dominant role of the $(1^-, 0)$ state at low energies. With increasing E_γ^{max}, the contribution of the $(1^-, \pm 1)$ state increases and the coefficient b (or the ratio b/a) tends to zero (the angular distribution of fission fragments becomes ever more isotropic), with the result that the asymmetry decreases. The measurements in [8] were performed in the region closest to ours. There, the ratio b/a decreases with increasing energy, approaching zero at $E_\gamma^{max} = 14$ MeV; it follows from expression (1) that the asymmetry will also tend to zero in this case. Our value of the asymmetry Σ complies with the behavior of the asymmetry deduced from the data presented in [8], but it should be borne in mind that the value that we obtained still differs from zero; that is, the angular distribution of fission fragments must not be isotropic in the region of the giant dipole resonance.

3. ASYMMETRY Σ IN ^{238}U PHOTOFISSION

Figure 3 shows the result of our measurements for the asymmetry in ^{238}U fission and the values of Σ that were obtained from the coefficients a and b for various E_γ^{max} values under the assumption of the $E1$ transition. Presented here is the entire body of currently available data corresponding to E_γ^{max} in excess of 12 MeV, with the exception of data from [9], which were taken at $E_\gamma^{max} = 12.01$ and 14.02 MeV and which agree, within the experimental errors, with the values displayed in Fig. 3. In order to obtain a clearer graphical representation, the value based on the data from [12] at $E_\gamma^{max} = 20$ MeV is shifted by 0.3 MeV. Our experimental value of the asymmetry Σ is shown at $E_\gamma^{max} = 18$ MeV.

In just the same way as for ^{236}U, the measured value of Σ differs markedly from the value of Σ for any dipole channel of fission [$(1^-, 0)$ or $(1^-, \pm 0)$].

From a comparison of the results of our measurements with the data obtained by means of rescaling from the coefficients a and b, it can be seen that, although the measurements of the angular distributions were performed by different experimental groups who used photon spectra somewhat different from that in our experiment, the results of these calculations comply with the data from a direct measurement of the asymmetry. Thus, the new experimental data on the asymmetry Σ of the cross section do not show deviations from the pattern based on the $E1$ transition.

4. MASS DEPENDENCE OF ASYMMETRY

The asymmetry values obtained in our experiments for the even–even nuclei ^{236}U and ^{238}U and previously for ^{232}Th [3] markedly differ from one another. In Fig. 4*a*, the results of our measurements for the asymmetry Σ are plotted versus the nuclear mass number A. It can be seen that the asymmetry decreases with increasing A.

Since, for all three elements, the numerical value of asymmetry is described well, within the experimental errors, in terms of the coefficients a and b under the assumption of the $E1$ transition, it would be of interest to analyze the behavior of the asymmetry rescaled from these coefficients as a function of the nuclear mass number A near the fission threshold, where the errors are much less than those in the available experimental data around $E_\gamma^{max} = 20$ MeV. In order to rule out systematic effects that could be different in different experiments, it is advisable to compare data obtained for the coefficients a and b by the same experimental group. For $E_\gamma^{max} = 7$ MeV, Fig. 4*b* displays the asymmetry Σ as a function of A according to our calculations on the basis of data from [13, 14].

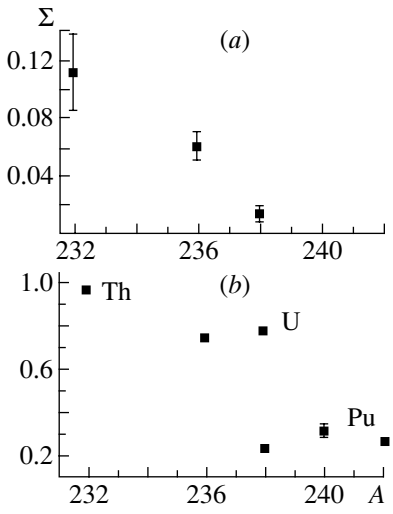

Fig. 4. Asymmetry in fission as a function of nuclear mass: (*a*) data from our present study and (*b*) data from [13, 14] at $E_\gamma^{\max} = 7$ MeV.

If there were no data for this $E_\gamma^{\max}$ value, the required result was obtained by means of a linear interpolation between the two neighboring values of $E_\gamma^{\max}$. From Fig. 4*b*, it can be seen that the rescaled asymmetry values have a pronounced dependence on the nuclear charge, but they show virtually no variations in response to changes in the number N of neutrons for nuclei with the same Z. Such a dependence is a corollary of the well-known effect that manifests itself as an anomaly in the angular distribution of fission fragments and which stems from the Z dependence of the relative height of the inner and the outer fission barrier (see, for example, [15]).

The accuracy in the asymmetry value that we obtained is much higher than the accuracy of the rescaled data in the close region of $E_\gamma^{\max}$. The asymmetries for ^{236}U and ^{238}U differ by three standard deviations, and it is highly improbable that this distinction is accidental. That the asymmetry depends not only on Z but also on N suggests either the presence of the contribution in it from multipoles other than $E1$ (for example, $E2$ or $M1$) or a high sensitivity of measurements like that described here to the relative height of the humps in the fission barrier (and the latter is observed in our experiment for nuclei with identical Z).

5. CONCLUSION

Our measurements of the asymmetry Σ of the cross sections for ^{236}U and ^{238}U fission induced by polarized photons in the region of the giant dipole resonance have revealed (as previously for ^{232}Th [3]) that the fission cross section is sensitive to the direction of the photon-polarization vector. The resulting value of the asymmetry cannot be explained by a dominant role of any channel, $(1^-, 0)$ or $(1^-, \pm 1)$, but it corresponds to modern concepts according to which the $E1$ transition prevails in the energy region being studied.

The asymmetry in the fission process has been found to depend on the nuclear mass. The existence of this dependence cannot be explained on the basis of the $E1$ transition and available experimental data obtained with an unpolarized-photon beam. In this connection, it would be of great interest to perform a systematic investigation of the asymmetry as a function of nuclear mass for even–even nuclei, especially in the region closer to the threshold.

REFERENCES

1. R. Ratzek, W. Wilke, J. Drexler, *et al.,* Z. Phys. A **308**, 63 (1982).
2. F. Steiper, T. Frommhold, W. Henkel, *et al.,* Nucl. Phys. A **563**, 282 (1993).
3. V. M. Khvastunov, V. V. Denyak, I. G. Evseev, *et al.,* Yad. Fiz. **57**, 1930 (1994) [Phys. At. Nucl. **57**, 1858 (1994)].
4. J. T. Caldwell, E. J. Dowdy, B. L. Berman, *et al.,* Phys. Rev. C **21**, 1215 (1980).
5. V. Bellini, M. Di Toro, S. Lo Nigro, and G. S. Pappalardo, Lett. Nuovo Cimento **26**, 173 (1979).
6. J. D. Arruda-Neto, S. B. Herdade, B. L. Berman, and I. C. Nascimento, Phys. Rev. C **22**, 1996 (1980).
7. J. D. Arruda-Neto, S. B. Herdade, B. L. Berman, and I. C. Nascimento, Phys. Rev. C **18**, 863 (1978).
8. A. P. Baerg, R. M. Bartoholomew, F. Brown, *et al.,* Can. J. Phys. **37**, 1418 (1959).
9. E. I. Winhold and I. Halpern, Phys. Rev. **103**, 990 (1956).
10. L. Katz, A. P. Baerg, and F. Brown, in *Proceedings of the International Conference on Peaceful Uses of Atomic Energy* (United Nations, Geneva, 1958), Vol. 15, p. 188.
11. A. I. Baz, N. M. Kulikova, L. E. Lazareva, *et al.,* in *Proceedings of the International Conference on Peaceful Uses of Atomic Energy* (United Nations, Geneva, 1958), Vol. 15, p. 2037.
12. H. G. Carvalwo, A. G. Silva, and J. Goldemberg, Nuovo Cimento **19**, 1131 (1961).
13. N. S. Rabornov, G. N. Smirenkin, A. S. Soldatov, *et al.,* Yad. Fiz. **11**, 508 (1970) [Sov. J. Nucl. Phys. **11**, 285 (1970)].
14. V. E. Zhuchko, Yu. B. Ostapenko, G. N. Smirenkin, *et al.,* Yad. Fiz. **30**, 634 (1979) [Sov. J. Nucl. Phys. **30**, 326 (1979)].
15. Yu. B. Ostapenko, G. N. Smirenkin, A. S. Soldatov, and Yu. M. Tsipenyuk, Fiz. Élem. Chastits At. Yadra **12**, 1364 (1981) [Sov. J. Part. Nucl. **12**, 545 (1981)].

Translated by A. Isaakyan

Physics of Atomic Nuclei, Vol. 64, No. 7, 2001, pp. 1273–1281. Translated from Yadernaya Fizika, Vol. 64, No. 7, 2001, pp. 1349–1357.

NUCLEI
Theory

Role of the Nuclear Surface in the Formation of Total Cross Sections for Heavy-Ion Reactions

V. K. Lukyanov, B. Słowinski[1)], and E. V. Zemlyanaya

Joint Institute for Nuclear Research, Dubna, Moscow oblast, 141980 Russia

Received May 11, 2000; in final form, August 24, 2000

Abstract—Within the Glauber–Sitenko approach, a procedure for calculating cross sections for intermediate-energy heavy-ion reactions is developed by using the analytic form of the eikonal phase for the symmetrized Woods–Saxon potential. The differential and total cross sections obtained on this basis comply well with the results derived by numerically solving the wave equation. A clear and instructive model of the phase is constructed, which makes it possible to separate, in total reaction cross sections, the contributions of the internal and the peripheral region of interaction. It is found that the nuclear surface plays an important role in the formation of reaction cross sections, and the effect of the Coulomb field on these cross sections is investigated. The origin of a continuous ambiguity in optical potentials is revealed in interpreting total cross sections. © *2001 MAIK "Nauka/Interperiodica".*

1. INTRODUCTION

Interest in investigations into total cross sections for heavy-ion reactions at energies E ranging from a few tens of MeV to 1 GeV per nucleon is provoked both by the fundamental problem of the mechanism of nuclear interaction and by applied problems—for example, the problem of transmutation of nuclear wastes (see [1]). Under such conditions, where $E \gg U$, $kR \gg 1$ (U is the potential of nuclear interaction with a characteristic radius R, and k is the momentum of the relative motion of the nuclei involved), the cross sections can be calculated within the Glauber–Sitenko approach [2, 3]; that is,

$$\sigma_R = 2\pi \int_0^\infty db\, b\,(1 - e^{-2Im\ \Phi_N}), \qquad (1.1)$$

where b is the impact parameter and Φ_N is the nuclear component of the total eikonal phase

$$\Phi(b) = -\frac{1}{\hbar v}\int_{-\infty}^{\infty} dz\, U(\sqrt{b^2+z^2}) = -\frac{U_0}{\hbar v} I(b), \qquad (1.2)$$

which is expressed in terms of the profile integral

$$I(b) = \int_{-\infty}^{\infty} dz\, u(\sqrt{b^2+z^2}). \qquad (1.3)$$

Here, $U_0 = V_0 + iW_0$, where V_0 and W_0 are the depth parameters of, respectively, the real and the imaginary part of the optical potential, and $u(r)$ is its spatial distribution. Integration in (1.3) is performed along the trajectory of motion—more specifically, along the z axis that is chosen to be aligned with the projectile momentum $\mathbf{k}_i$.

In general, heavy-ion optical potentials are obtained by fitting the differential cross sections for elastic scattering and total cross sections at a given collision energy to experimental data. Their energy dependence can be established if the phase $\Phi(b)$ is calculated in the approximation of multiple diffractive scattering, where it is expressed in terms of the total cross section $\sigma_{NN}(E)$ for nucleon–nucleon scattering, a quantity whose energy dependence is known. In this approximation, we can also determine the impact-parameter (b) dependence of the phase by taking the convolution of the distributions of nucleons in the projectile and in the target nucleus (ρ_p and ρ_t, respectively); eventually, this requires evaluating profile integrals that belong to the type in Eq. (1.3) and which involve the function $\rho(\sqrt{b^2+z^2})$ in the integrand.

As a rule, such calculations rely on Gaussian distributions, since this makes it possible to obtain analytic expressions for total cross sections (see, for example, [4–6]). However, Gaussian distributions of potentials and densities are adequate to the purpose predominantly for light nuclei—in medium-mass and heavy nuclei, the relevant distributions are quite extended. Most often, these are the Fermi functions

[1)]Institute of Atomic Energy, Otwock-Swierk, Poland, and Warsaw University of Technolgy, Warsaw, Poland.

$u_{\rm F}(r)$, but their emergence leads to serious mathematical and computational difficulties. Sometimes, they can be overcome by representing $u_{\rm F}(r)$ as the sum of Gaussian functions [7]

$$u_{\rm F}(r,R,a) = \frac{1}{1+\exp[(r-R)/a]} = \sum_{n=1}^{N} c_n \exp\left(-\frac{r^2}{d_n^2}\right), \quad (1.4)$$

which yields

$$I_{\rm F}(b) = \int_{-\infty}^{\infty} \frac{dz}{1+\exp[(\sqrt{b^2+z^2}-R)/a]} = \sum_{n=1}^{N} \sqrt{\pi}\, c_n\, d_n \exp\left(-\frac{b^2}{d_n^2}\right). \quad (1.5)$$

Here, the quantities c_n, d_n, and N are fitted to a preset form of $u_{\rm F}(r)$; for each set of specific values of the radius R and the diffuseness parameter a in the Fermi function (1.4), such a fit must be constructed anew. Alternatively, Shepard and Rost [8] proposed to represent the function in (1.3) as

$$I_{\rm F}(b) = 2R - 2\pi i a \sum_{p=1,3,5\ldots}^{\infty} \left\{ \frac{b_p^+}{\lambda_p^{(+)}} + \frac{b_p^-}{\lambda_p^{(-)}} \right\}, \quad (1.6)$$

where $b_p^{\pm} = R \pm i\pi a p, p = 1,3,5,\ldots$ are the poles of the function $u_{\rm F}(b)$ and $\lambda_p^{(\pm)} = (b_p^{\pm 2} - b^2)^{1/2}$ and where the condition $\mathrm{Im}\,\lambda_p^{(\pm)} \geq 0$ must be satisfied. Retaining, in expression (1.6), a few tens of the terms in the sum, we can reproduce the behavior of the function $I_{\rm F}(b)$ in the region of b from zero to values slightly exceeding the radius R. At larger values of b, however, a correct exponential decay of $I_{\rm F}(b)$ cannot be obtained even with a few hundred terms.

In order to calculate total reaction cross sections, we propose here to use a different, rather simple, analytic expression that can represent the profile integral (1.3) and which was obtained in [9] for a realistic distribution in the form of the symmetrized Fermi function $u_{\rm SF}$. This expression faithfully reproduces the exact behavior of the above function over the entire region of real b values and retains the aforementioned pole singularities at $b = b_p^{\pm}$. The differential cross sections computed in [10] on this basis proved to be in agreement with the results obtained by numerically solving the wave equation.

The ensuing exposition is organized as follows. In Section 2, we show that the same expression can be used to calculate total cross sections. In Section 3, we construct a clear and instructive model for analytically calculating total reaction cross sections that makes it possible to separate the contributions from the internal and the peripheral region of interaction, to trace the mechanism through which the Coulomb field affects the distribution of these contributions, and to study the nuclear-transparency effect. In the last section, we indicate one of the factors that can be responsible for the ambiguity of the optical potentials used in a fit to experimental data and draw general conclusions.

2. EIKONAL PHASE FOR THE SYMMETRIZED FERMI FUNCTION AND CALCULATION OF TOTAL REACTION CROSS SECTIONS

The spatial distribution of an extended Woods–Saxon potential, which is very popular in nuclear physics, corresponds to the behavior of the Fermi function $u_{\rm F}(r)$ as given by (1.4). However, it is more justifiable to use its symmetrized form

$$u_{\rm SF}(r) = \frac{\sinh(R/a)}{\cosh(R/a)+\cosh(r/a)} = u_{\rm F}(r) - \delta(r), \quad (2.1)$$

where

$$\delta(r) = \frac{\exp(-R/a)}{\exp(r/a)+\exp(-R/a)}. \quad (2.2)$$

Indeed, the potential in (2.1) has ever more often taken the place of $u_{\rm F}$ since the studies reported in [11, 12] and devoted to calculating nuclear form factors. For $R \gg a$, in which case we have $\delta(r) \ll 1$, the functions $u_{\rm F}(r)$ and $u_{\rm SF}(r)$ nearly coincide in the region $r \geq 0$—that is, they can be used with the same degree of reliability to parametrize the distributions of matter in medium-mass and heavy nuclei and to construct nucleus–nucleus potentials. However, these forms are markedly different for light nuclei, which have a highly developed surface ($a \simeq R$). Strictly speaking, a parametrization of the distributions in terms of a conventional Fermi function is inappropriate from the physical point view, since $u_{\rm F}$ has a nonzero derivative at the center of the nucleus, $u'_{\rm F}(0) \neq 0$, whereas $u'_{\rm SF}(0) = 0$. Because of the same flaw in the Fermi function, the use of it in the complex plane in calculating scattering amplitudes involves serious problems: for some integrals, it is difficult to obtain explicit expressions with it (see, for example, [13, 14]). At the same time, it was with the function $u_{\rm SF}$ that a fairly accurate explicit expression was obtained in [9] for the profile integral, and this expression will be used below. Inserting (2.1) into (1.3) and making the substitutions $\zeta = z/a$, $\beta = b/R$, and $C = R/a$, we represent the profile integral in the more convenient form

$$I(b) \equiv I(\beta R) = 2R\mathcal{I}(\beta), \quad (2.3)$$

$$\mathcal{I}(\beta) = \frac{1}{C}\int_0^\infty \frac{\sinh C\, d\zeta}{\cosh C + \cosh\sqrt{(\beta C)^2+\zeta^2}} \quad (2.4)$$
$$= u_{\rm SF}(\beta)P(\beta, C).$$

It turns out that, here, the impact-parameter or the β dependence is determined primarily by the symmetrized Fermi function

$$u_{\rm SF}(\beta) = \frac{\sinh C}{\cosh C + \cosh \beta C} \quad (2.5)$$

and that the second, correcting, function $P(\beta, C)$ depends only slightly on β at a fixed value of C. For this function, it is possible to obtain the compact expression [9]

$$P(\beta, C) \simeq P_a(x) = \frac{1}{C}\ln(4/x), \quad (2.6)$$

where

$$x(\beta, C) = \frac{2}{\kappa}\,\frac{1}{1+\dfrac{\cosh C}{\cosh \beta C}}\left\{1+\frac{\kappa-1}{\cosh \beta C}\right\}. \quad (2.7)$$

Here, the parameter κ is related to C and is given by

$$\log\kappa = 0.47909 + 0.15025C - 0.001938C^2. \quad (2.8)$$

This expression was deduced in [9] by fitting the results obtained by calculating the integral $\mathcal{I}(\beta)$ according to an approximate analytic expression [right-hand side of (2.4)] to precise values of this integral that result from a numerical integration with a mesh of the parameters β and C from the region of their typical physical values that is specified by the inequalities $0 < \beta < 2$ and $5 \le C \le 20$. We consider that, for heavy ions, the main contribution comes from the region of the nuclear surface; that is, $b = R$ or $\beta = 1$. We then have $x \simeq 1/\kappa$, and the correcting function assumes the simple form

$$P_a(1, C) \simeq \frac{1}{C}\ln 4\kappa \quad (2.9)$$
$$= \frac{1}{C}\left[2.489453 + 0.34597C - 0.0046C^2\right]. \quad (2.10)$$

The corresponding nuclear phase becomes

$$\Phi_N(b) = -\frac{2RU_0}{\hbar v}\,\frac{\sinh(R/a)}{\cosh(R/a)+\cosh(b/a)}P_a(1, C).$$

From Fig. 1, it can be seen that the profile integrals calculated for various combinations of colliding nuclei by using the analytic formula (2.6) for $P_a(\beta, C)$ show nearly the same behavior in the most important impact-parameter region $0 \le b \le 2R$. The agreement is somewhat poorer for $P_a(1, C)$. This is noticeable, however, only for $b < R$ in the strong-absorption region, and it will be shown below that such a distinction affects only slightly the behavior of the cross sections. The $C = R/a$ values indicated in the figure correspond to the geometric parameters of the Fermi distributions for the Woods–Saxon potentials fitted to experimental data in [15, 16]. In order to assess the degree to which the analytic expressions for nuclear eikonal phases make it possible to reproduce the differential cross sections obtained by numerically solving the wave equation, we will draw a relevant comparison. Within the Glauber–Sitenko approach [2, 3], the scattering amplitude has the form

$$f(q) = ik\int_0^\infty db\, bJ_0(qb)\,(1 - e^{i\Phi_N + i\Phi_c}),$$
$$q < \sqrt{2k/R}. \quad (2.11)$$

A feature peculiar to nucleus–nucleus scattering is that Coulomb interaction plays an important role here. As a rule, it is legitimate to use the explicit expression for the eikonal Coulomb phase Φ_c for the potential generated by a uniform charge distribution over a sphere of radius R_u, in which case this phase is given by

$$\Phi_{uc}(b) = \begin{cases} 2\eta\left[\ln(kR_u) + \ln\left(1+\sqrt{1-\dfrac{b^2}{R_u^2}}\right) - \frac{1}{3}\sqrt{\dfrac{1-b^2}{R_u^2}}\left(4-\dfrac{b^2}{R_u^2}\right)\right], & b \le R_u \\ \Phi_{pc}(b), & b > R_u, \end{cases} \quad (2.12)$$

where $\eta = Z_1Z_2e^2/\hbar v$ is the Sommerfeld parameter and $\Phi_{pc}(b) = 2\eta\ln(kb)$ is the eikonal phase shift for scattering in the field of a pointlike charge. It follows that, as soon as the Coulomb phases are included in the scattering amplitude (2.11), divergent terms of the form $\exp(2\eta i\ln(kb))$ generate the problem of integration at large distances. This problem can be sidestepped by adding and subtracting, in the parenthetical factor of the integrand on the right-hand side of (2.11), the eikonal function for a pointlike charge, $\exp(i\Phi_{pc})$. We then obtain

$$f(q) = f_{pc}(q) \quad (2.13)$$
$$+ ik\int_0^\infty db\, bJ_0(qb)\, e^{i\Phi_{pc}}\left(1 - e^{i\Phi_N + i\delta\Phi_{uc}}\right),$$

where the quantity $\delta\Phi_{uc} = \Phi_{uc} - \Phi_{pc}$ added to the nuclear phase no longer involves a logarithmic term at large b, while $\Phi_N(b \to \infty) = 0$. The quantity

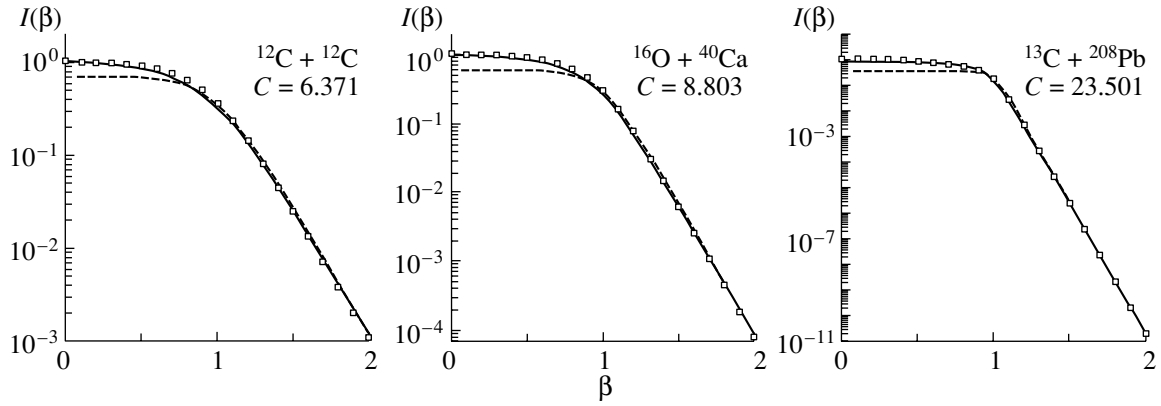

Fig. 1. Comparison of precise (solid curves) and approximate profile functions calculated with the correcting functions $P_a(\beta, C)$ (2.6) (boxes) and $P_a(1, C)$ (2.9) (dashed curves) for symmetrized Fermi functions.

$f_{pc}(q)$ that represents the amplitude for scattering by a pointlike charge and which now appears as a separate term in (2.13) is known in the explicit form [2]

$$f_{pc}(q) = -ik\int\limits_0^\infty db\, b^{1+2i\eta} J_0(qb) \qquad (2.14)$$
$$= -\frac{2k\eta}{q^2}\, e^{-2i\eta\ln(q/2k)+2i\arg\Gamma(1+i\eta)}.$$

This is the way in which one can solve the problem of numerically integrating the scattering amplitude at high energies in the presence of the Coulomb phase.

In the case of heavy-ion scattering, one has to make yet another modification to the amplitude in (2.11), because the original trajectory deflects from a straight line in the field of a long-range Coulomb potential. This distortion effect can be taken into account [17] by adding, to the momentum transfer q in (2.11), the momentum $q_c = 2k\sin(\theta_c(b)/2)$, where θ_c is the angle of deflection of the trajectory in the Coulomb field. But if use is made of the transformed amplitude (2.13), one must here merely replace, in the nuclear eikonal, the impact parameter b in the asymptotic region by b_c in the region where the nuclei involved come into contact and the probability flux v by $(b/b_c)v$ [18]. The quantity

$$b_c = \bar{a} + \sqrt{b^2 + \bar{a}^2}, \qquad (2.15)$$

where $\bar{a} = \eta/k = (R_c/2)(U_c(R_c)/E)$ is half the distance of the closest approach of the nuclei in the Coulomb field at $b = 0$, while $U_c = Z_1Z_2e^2/R_c$ is the potential of interaction between the charges Z_1e and Z_2e occurring at a distance of about the characteristic radius R_c of the charged system being considered.

By way of example, the calculated differential cross sections for ^{12,13}C and ^{16}O scattering on some nuclei are shown in Fig. 2 at various energies. Relevant experimental data were borrowed from [15, 16, 19]. Also presented in this figure are theoretical curves that were obtained by fitting numerical solutions of the wave equation with the Woods–Saxon optical potential to experimental points. The relevant values of the potential parameters are used in our ensuing calculations based on the approach proposed here. It can be seen that the Glauber–Sitenko approach employing analytic eikonal phases provides fairly good agreement with experimental data. Here, one can use (see $^{12}C + ^{12}C$ and $^{16}O + ^{40}Ca$ cross sections) either the $P_a(\beta, C)$ [Eq. (2.6)] or the $P_a(1, C)$ [Eq. (2.9)] approximation (solid or dashed curves, respectively). For $^{13}C + ^{208}Pb$ interactions at $E = 390$ MeV, we also present (dashed curve) the results of the calculations performed without taking into account the Coulomb distortion of the trajectory. It can be seen that the inclusion of this distortion is of importance in this case, but that this has virtually no effect on the result in the other two cases considered here. As might have been expected, such distortions manifest themselves in scattering on heavier nuclei and at comparatively low energies; otherwise, their effect is insignificant.

In Table 1, the results of our calculations of the total reaction cross sections by formula (1.1) with the analytic phases of nuclear eikonals are contrasted against the results of precise calculations on the basis of numerical solutions to the wave equation [15, 16]. It should be borne in mind that the precise calculations employed the Woods–Saxon potential, while our calculations relied on its symmetrized analog, these two potential types being markedly different for light $^{12}C + ^{12}C$ systems. Yet another distinction is that the precise calculations take automatically into account the effect of both the real and the imaginary part of the optical potential, and not only of the latter as in the high-energy approximation specified by Eq. (1.1). Nonetheless, the distinction between the

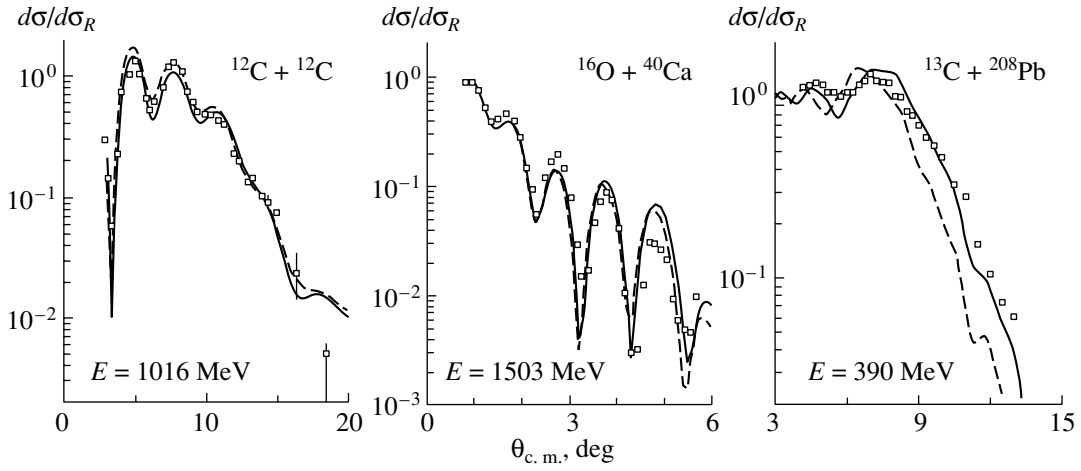

Fig. 2. Differential cross sections for heavy-ion scattering. Experimental data are represented by boxes. The theoretical results in the left and the middle panel were calculated with analytic phases by using $P_a(\beta, C)$ (solid curve) and $P_a(1, C)$ (dashed curves). The dashed curve in the right panel was computed without allowing for the Coulomb distortion of the trajectory.

results does not exceed 1% of the cross-section values for all cases considered here, with the exception of $^{12}C + ^{12}C$ interaction at 360 MeV, where it is 9%, which is due to the enhanced role of the real part of the potential at this comparatively low energy.

3. POLYGONAL-TRAPEZOID MODEL AND REACTION CROSS SECTION

In the preceding section, we have shown that the eikonal nuclear phase with the profile integral (2.4) in the form of the symmetrized Fermi distribution $u_{\rm SF}(b)$ describes fairly well the differential cross sections for scattering and total reaction cross sections. The form of this function is such that the surface of radius R, where $u_{\rm SF}(R) \simeq 1/2$ and where the derivative of this function is $u'_{\rm SF}(R) = -1/4a$, is singled out explicitly in it; therefore, it falls off over a distance of $4a$ from a value of $u_{\rm SF}(b < R - 2a) \simeq 1$ to $u_{\rm SF}(b > R + 2a) = 0$. One can approximate this form by a conventional trapezoid (see, for example, [20]) and obtain an analytic expression for the total reaction cross section (1.1). However, this model is overly rough for heavy-ion reactions, since it does not take into account smoother variations in the function $u_{\rm SF}$ in the region $b < R_2 = R - a$ and in the region $b > R_3 = R + a$. This drawback can be remedied by introducing additional cusps at the ends of these regions and by setting the slopes of sides in the corresponding sections to $u'_{\rm SF}(R_1 < b < R_2) = -1/2a$ and $u'_{\rm SF}(R_3 < b < R_{4(5)}) = -1/2a(-1/3a)$ (see Fig. 3), where $R_1 = R - 3a$ and $R_{4(5)} = R + 3a(4a)$. On the basis of this model, we will present the required calculations and a perform a comparison with the results of precise computations and an analysis of experimental data.

The total cross section (1.1) will be given in the approximation where expression (2.10) is taken for the eikonal nuclear phase and where effects associated with the distortion of the trajectory by the Coulomb field are taken into account through the above substitutions $b \to b_c(b)$ and $v \to (b/b_c)v \simeq [1 - U_c(R_c)/E]^{1/2}v$, with b_c being represented in the form (2.15). Transforming $bdb = (b_c - \bar{a})db_c$ on the basis of (2.15), we then obtain

$$\sigma_R = 2\pi \int\limits_0^\infty db\, b\, \left(1 - \tilde{T}(b_c)\right) \qquad (3.1)$$

$$= 2\pi \int\limits_{2\bar{a}}^\infty db_c\, (b_c - \bar{a})\, \left(1 - \tilde{T}(b_c)\right),$$

where the transparency function is defined as

$$\tilde{T}(b_c) = e^{-\chi(b_c)}$$

$$= \left(\tilde{T}_0\right)^{u_{\rm SF}(b_c)}, \quad \tilde{T}_0 = e^{-\tilde{\chi}_0}, \qquad (3.2)$$

$$\tilde{\chi}_0 \simeq \frac{\chi_0}{\sqrt{1 - U_c(R_c)/E}}, \quad \chi_0 = \frac{4RW_0}{\hbar v} P_a(1, C).$$

The symmetrized Fermi function is now approximated by a polygonal trapezoid as $u_{\rm SF}(b) \simeq u_{{\rm bt}(b)}$,

$$u_{\rm bt} = \Theta(R_1 - b) + \sum_{n=2,3,4(5)} u_{\rm bt}^{(n)}(b). \qquad (3.3)$$

Here, each of the three sections in the surface region is specified by the function

$$u_{\rm bt}^{(n)} = \left[A_n + \frac{1}{a_n}(R_{k(n)} - b)\right] \Theta(R_n \qquad (3.4)$$

Table 1. Total cross sections for heavy-ion reactions in the Glauber–Sitenko approach, along with the results of precise calculations from [15, 16, 19]

Reaction	$E_{\rm lab}$, MeV	$\sigma_R^{\rm appr}$(SF), mb	$\sigma_R^{\rm precise}$(F), mb
^{16}O+^{40}Ca	1503	1983	1996
^{16}O+^{90}Zr	1503	2711	2749
^{16}O+^{208}Pb	1503	3614	3602
^{13}C+^{208}Pb	390	2868	2898
^{12}C+^{12}C	1016	1093	1040
^{12}C+^{12}C	360	1147	1258

$$- b)\Theta(b - R_{k(n)}),$$

where

$$A_n = \frac{6 - n - \delta_{n,4}}{4}, \quad a_n = 4(n - 2 + 2\delta_{n,2})a, \tag{3.5}$$
$$n = 2, ..., 5;$$

$$R_p = R + (2p - 5 - \delta_{p,5})a, \quad p = 1, ..., 5; \tag{3.6}$$
$$k(n) = n - 1 - \delta_{n,5}, \quad n = 2, ..., 5.$$

Substituting (3.3) into (3.2) and then into (3.1) and introducing the width of each of the sections,

$$\Delta_n = R_n - R_{k(n)} = (2 + \delta_{n,5})a, \quad n = 2, ..., 5, \tag{3.7}$$

we find, after an elementary integration, that

$$\sigma_R = \pi R_1^2 \left[1 - \frac{2\bar{a}}{R_1}\right]\left(1 - \tilde{T}_0\right) \tag{3.8}$$
$$+ \sum_{n=2,3,4(5)} \left\{ 2\pi\Delta_n R_{k(n)} C_{k(n)} + \pi\Delta_n^2 \right.$$
$$- 2\pi \frac{a_n R_{k(n)} C_{k(n)}}{\tilde{\chi}_0} \tilde{T}_0^{A_n - \Delta_n/a_n}$$
$$\times \left[1 - \frac{\Delta_n}{R_{k(n)} C_{k(n)}} - \tilde{T}_0^{\Delta_n/a_n} \right.$$
$$\left.\left. + \frac{a_n}{R_{k(n)} C_{k(n)}} \frac{1}{\tilde{\chi}_0}\left(1 - \tilde{T}_0^{\Delta_n/a_n}\right)\right]\right\},$$

where

$$C_{k(n)} = 1 - \frac{\bar{a}}{R_{k(n)}} = 1 - \frac{1}{2}\frac{R_c}{R_{k(n)}}\frac{U_c(R_c)}{E} \tag{3.9}$$

is a factor that appears along with other modifications in (3.1) and (3.2) owing to taking into account the Coulomb distortion.

In the absence of a Coulomb field, we have $\eta = 0$ and $\bar{a} = 0$; we must then make the substitution $C_{k(n)} = 1$ in (3.8) and consider that $\tilde{T} \to T_0 = \exp(-\chi_0)$. As a result, we obtain

$$\sigma_R = \pi R_1^2 (1 - T_0) + \sum_{n=2,3,4(5)} \left\{ 2\pi\Delta_n R_{k(n)} \right. \tag{3.10}$$
$$+ \pi\Delta_n^2 - 2\pi \frac{a_n R_{k(n)}}{\chi_0} T_0^{A_n - \Delta_n/a_n} \left[1 \right.$$
$$\left.\left. - \frac{\Delta_n}{R_{k(n)}} - T_0^{\Delta_n/a_n} + \frac{a_n}{R_{k(n)}}\frac{1}{\chi_0}\left(1 - T_0^{\Delta_n/a_n}\right)\right]\right\}.$$

As a rule, the parameters of the potentials in intermediate-energy heavy-ion collisions are such that $\chi_0 \gg 1$ and $T_0 \ll 1$ (strong absorption in the interior of the nuclei involved). For a rough estimate of the relevant cross sections, we can make use of the expression

$$\sigma_R \simeq \pi R_1^2 + \sum_{n=2,3,4(5)} \left(2\pi\Delta_n R_{k(n)} + \pi\Delta_n^2\right), \tag{3.11}$$

which represents, as might have been expected, the sum of the area of the internal region of a circle of radius $R_1 = R - 3a$ and the areas of the external rings having a total width of $6a$ to $7a$.

The calculated total cross sections for the reactions induced by collisions of ^{16}O projectile nuclei with ^{40}Ca, ^{90}Zr, and ^{208}Pb target nuclei are compiled in Table 2, where the contributions from individual regions of interaction are singled out in accordance with the values of the impact parameter b that are given in Fig. 3 for the polygonal trapezoidal model. The results are quoted for three models of the distribution of the imaginary part of the optical potential: the symmetrized Fermi function (SF); a polygonal-trapezoid (PT); and a step, which is represented by a uniform distribution (U) of radius $R_u = R[1 + (7/3)(\pi a/R)^2]^{1/2}$ and which is equivalent to the SF form. In all cases, the calculations were performed with (+C) and without allowance for the Coulomb distortion of the trajectory. The kinetic energy of projectile nuclei, $E = 94$ MeV per nucleon, and the values of the parameters R and a were taken to be identical to those in [19], where the cross sections were calculated on the basis of numerical solutions to the wave equation with the Woods–Saxon potential (F distribution). These cross sections are quoted in Table 1 and are equal to 1996, 2749, and 3602 mb for ^{40}Ca, ^{90}Zr, and ^{208}Pb target nuclei, respectively. From a comparison of the precise values and the results of the calculations performed in the Glauber–Sitenko approach (see Table 2), we can conclude that the square-well model (U distribution), which is sometimes used to analyze experimental data (see, for example, [6]), is very rough. Indeed,

Table 2. Distribution of the contributions to the cross sections from the internal and the peripheral region in various models with and without allowance for the Coulomb distortion of the trajectory (partition of the contributions into sections I–V are given in Fig. 3)

Target	Model	I	II	III	IV (V)	(R_5, ∞)	σ_R, mb
^{40}Ca	SF	517.7	425.5	538.4	462.5 (494.9)	59.8	2036.3
	SF+C	517.7	425.4	533.3	382.4 (454.6)	51.7	1982.7
	PT	517.7	425.5	537.5	407.1 (590.3)		2050.9
	PT+C	517.7	425.5	531.8	465.5 (549.2)		2025.3
	U	517.5	424.8	528.3	13.4 (13.4)		1530.7
	U +C	517.5	424.9	537.5	50.8 (50.8)		1484.0
^{90}Zr	SF	568.3	500.7	657.3	707.9 (917.2)	172.8	2816.8
	SF+C	568.3	500.7	656.8	667.7 (845.1)	139.9	2710.8
	PT	568.3	500.7	657.2	770.6 (1008.5)		2734.7
	PT+C	568.3	500.7	656.7	749.1 (934.7)		2660.4
	U	568.3	500.7	656.2	96.6 (96.6)		1821.8
	U +C	568.3	500.7	655.3	13.9 (13.8)		1738.1
^{208}Pb	SF	1495.2	687.2	805.7	634.2 (765.3)	95.6	3849.0
	SF+C	1495.2	687.2	783.9	500.9 (587.5)	60.2	3614.1
	PT	1495.2	687.2	804.7	737.6 (899.6)		3886.8
	PT+C	1495.2	687.2	784.5	634.8 (683.4)		3650.3
	U	1495.0	686.1	715.9			2897.0
	U+C	1495.0	685.2	513.0			2693.1

the calculations based on the realistic SF model and the polygonal-trapezoid (PT) model reveal that the contributions to the total cross section from the inner and the outer region of interaction, which are by convention separated by the value of $b = R$, are approximately equal to each other. This indicates that the specific form of potential in the surface region of colliding nuclei plays an important role in the formation of the total reaction cross section. Owing to its simplicity, the trapezoid model makes it possible to visualize the mechanism of addition of the cross sections from different segments in the interaction-surface region. As to the Coulomb distortion of the trajectory, it also manifests itself predominantly in the peripheral region, and the inclusion of this effect in the computational scheme reduces the cross section by about 20% for the heavy target nucleus ^{208}Pb and by 10% for the interaction with medium-mass nuclei. It is clear that, with decreasing collision energy, the deflection of Coulomb trajectories from the region where the nuclei involved would come into contact becomes more pronounced; therefore, the reaction cross section decreases faster.

4. AMBIGUITY OF THE POTENTIAL AND CONCLUSIONS

Yet another advantage of our analytic approach is that it enables us to obtain deeper insight into the mechanism behind the manifestation of the so-called continuous ambiguity in the choice of potential parameters. This ambiguity is associated with the fact that, because of strong absorption in the interior of the nucleus, a fit to experimental data is determined primarily by the peripheral region of interaction [21]. For the first time, this was demonstrated by Igo [22], who employed, in calculating the cross sections for the scattering of fast alpha particles by nuclei, the exponential potential $[U\exp(R/a)]\exp(-r/a)$ instead of the Woods–Saxon potential. Although these two potentials coincide only for $r \gg R$—they are markedly different in the nuclear interior—a sample of data on the differential cross sections could be explained with the above exponential potential by varying, in it, the parameter a and the "strength" $[U\exp(R/a)]$. Obviously, the same value of the bracketed expression can be obtained for continuous sets of R and U values. In Section 3, we have seen that experimental data

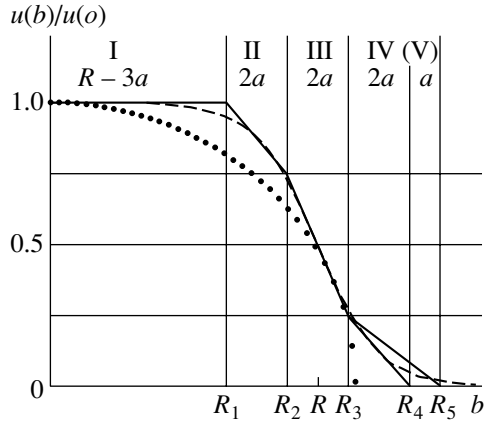

Fig. 3. Symmetrized Fermi function (dashed curve) with the parameter R equal to the radius value at which this function decreases by a factor of 2 and the parameter a characterizing the surface-layer thickness and its approximation by a three-section polygonal trapezoid in the surface region (solid broken line). The dotted curve represents the phase for a square-well potential having an equivalent radius R_u.

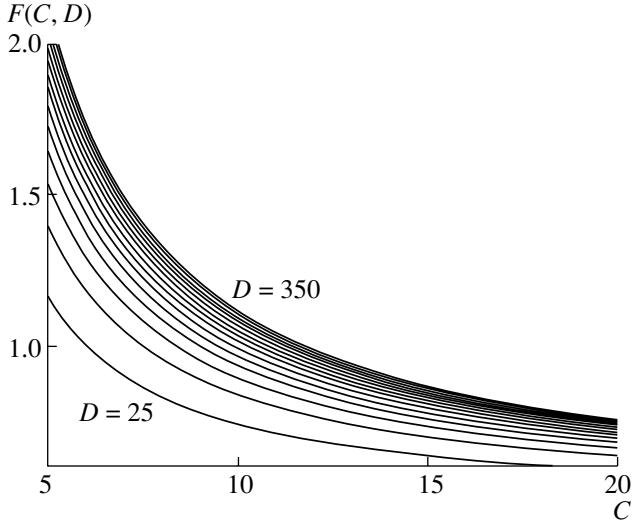

Fig. 4. Pattern of a continuous ambiguity of the fitting parameters R, a, and W_0 of the imaginary part of the potential in the form of a symmetrized Fermi function, in which case the reaction cross section depends on their combinations $C = R/a$ and $D = 9.11RW_0/\hbar v$.

can also be reproduced when the original phase is replaced by a polygonal trapezoid, which, in contrast to the above exponential function, preserves the form of the phase in the nuclear interior, approximating its behavior in the peripheral region by different, linear, functions.

In order to investigate the origin of the ambiguity within our approach, it is not necessary to replace the original potential by a different one—in particular, by that which approximates it at the surface of interaction. The mechanism behind its manifestation can be revealed in the very expression (3.1) for the cross section. In order to prove this, we represent this cross section, by means of the substitutions $b = \beta R$ and $C = R/a$, in the form

$$\sigma_R = 2\pi R^2 \left[1 - \frac{U_c(R_c)}{E_{\rm c.m.}}\right] F(C, D), \qquad (4.1)$$

where

$$F(C, D) = \int_0^\infty d\beta\, \beta \left[1 - e^{-0.4391\, D\, u_{\rm SF}(\beta,C) P_a(\beta,C)}\right], \qquad (4.2)$$

$$D = \sqrt{\frac{A_2}{A_1 + A_2}\frac{1}{\epsilon_{\rm c.m.}}}\, RW_0, \quad \epsilon_{\rm c.m.} = \frac{E_{\rm c.m.}}{A_1}. \qquad (4.3)$$

Here, the symmetrized Fermi function $u_{\rm SF}(\beta, C)$ and the correcting function $P_a(\beta, C)$ are given by (2.5) and (2.6), respectively. The above expressions, which provide a solution to the problem in question, involve the combined parameter D depending on the following input quantities: the atomic numbers of the nuclei involved, A_1 and A_2; the collision energy $\epsilon_{\rm c.m.}$(MeV) per projectile nucleon; the depth of the imaginary part of the potential, W_0(MeV); and the radius R(fm). The function $F(C, D)$ is calculated once for the entire region of possible values of C and D and is further used to scan these values in a comparison with experimental data. By way of example, the curves representing $F(C, D)$ are plotted in Fig. 4 in the interval of D from 25 to 350 with a step of 25 units as a function of C in the range 5–20. As a matter of fact, such curves cover the figure plane continuously.

A procedure for choosing the parameters of the imaginary part of the optical potential can be conveniently constructed in the following way. The experimental value of the cross section at a given energy is divided by $2\pi R^2[1 - U_c(R_c)/E_{\rm c.m.}]$ in order to obtain $F(C, D)$ with the aim of comparing it with the calculated curves in Fig. 4. After that, one selects the values of the radii R and R_c in order to fix this quantity. Further, the corresponding horizontal straight line is drawn in the plane where the function $F(C, D)$ is depicted and the values of C and D (continuous set) are determined at the intersection points and are then used to find the diffuseness parameters a and W_0. It is interesting to note that, at each given value of the radius R, there exists a continuous set of a values, so that all phase curves $\Phi_N(b)$ intersect in the surface region at one point $b = R$, an individual value of W_0, different from other of its values, corresponding to each such curve. Since a, R, and W_0 are potential parameters, an ambiguity in the

phases is a manifestation of an ambiguous choice of potential—for example, the point of intersection of the potentials in the diffuseness region $r \simeq R\cos^{-1}\theta_c$, where $\theta_c \simeq U_c(R_c)/E_{\mathrm{c.m.}}$, corresponds to the point of intersection of the phases at $b = R$. In order to select sets of physically significant parameter values, we can use the condition of conservation of the volume of the potential and the condition of conservation of its root-mean-square range, as well as some other physical criteria. The procedure of fitting is entirely repeated if different values of the radii R and R_c are specified initially. Thus, we can see that the transparency $T(b)$ depends not on the three parameters a, R, and W_0 individually but on two combinations of these quantities, RW_0 and $C = R/a$. These combinations represent a kind of calibration that one can use in fitting the calculated cross sections to experimental data, thereby constraining the possible parameter sets.

In summary, we can conclude that, at projectile energies in excess of 10 MeV per nucleon, the Glauber–Sitenko approach is applicable to calculating and analyzing differential cross sections for scattering and total cross sections for heavy-ion reactions. Within this framework, the use of the analytic expression (2.4), which represents the profile integral for a realistic optical potential with the SF distribution and which has been tested here, makes it possible not only to construct faster computational procedures but also (and this is more important) to develop analytic methods for calculating observables, whereby one can analyze the mechanism responsible for the formation of the relevant cross sections and investigate explicit dependences on potential parameters. Having at our disposal explicit expressions for reaction amplitudes and cross sections, we can easily take into account, by means of a formal renormalization of the impact parameter, the effect of Coulomb distortion on the eventual results of the calculations. This can be done without changing the original scheme of the high-energy approximation. In all the cases where the results of our calculations based on the above analytic expressions have been compared, for the same choice of potentials, with the results obtained by numerically solving the Schrödinger equation, the agreement was fairly good in the case of differential cross sections for elastic scattering and in the case of total cross sections for heavy-ion collisions.

ACKNOWLEDGMENTS

This work was supported by the Infeld–Bogolyubov Program. V.K. Lukyanov is grateful to the Foundation for the Support of Leading Scientific Schools of the Russian Federation (grant no. 00-15-96737) and the Foundation for Fundamental Natural Sciences at the Ministry of the General and Special Education of the Russian Federation (grant no. 97-40-1.6-6). The work of E.V. Zemlyanaya was supported by the Russian Foundation for Basic Research (project no. 0001-006-17).

REFERENCES

1. J.-S. Wan *et al.,* Kerntechnik **63**, 167 (1998).
2. R. J. Glauber, in *Lectures on Theoretical Physics* (Interscience, New York, 1959), Vol. 1.
3. A. G. Sitenko, Ukr. Fiz. Zh. **4**, 152 (1957).
4. P. J. Karol, Phys. Rev. C **11**, 1203 (1975).
5. S. Charagi and G. Gupta, Phys. Rev. C **41**, 1610 (1990).
6. A. Abul-Magd and A. Talib Ali-Alhinai, Nuovo Cimento A **110**, 1281 (1997).
7. O. D. Dalkarov and V. A. Karmanov, Nucl. Phys. A **445**, 579 (1985).
8. J. R. Shepard and E. Rost, Phys. Rev. C **25**, 2660 (1982).
9. V. K. Lukyanov and E. V. Zemlyanaya, J. Phys. G **26**, 357 (2000); Preprint No. E4-99-260, JINR (Joint Institute for Nuclear Research, Dubna, 1999).
10. V. K. Lukyanov, E. V. Zemlyanaya, and A. V. Embulaev, Preprint No. E4-99-291, JINR (Joint Institute for Nuclear Research, Dubna, 1999).
11. Yu. N. Eldyshev, V. K. Luk'yanov, and Yu. S. Pol', Yad. Fiz. **16**, 506 (1972) [Sov. J. Nucl. Phys. **16**, 282 (1973)].
12. V. V. Burov, Yu. N. Eldyshev, V. K. Lukyanov, and Yu. S. Pol', Preprint No. E4-8029, JINR (Joint Institute for Nuclear Research, Dubna, 1974).
13. M. Grypeos, C. Koutroulos, V. Lukyanov, and A. Shebeko, J. Phys. G **24**, 1913 (1998).
14. D. W. L. Sprung and J. Martorell, J. Phys. A **30**, 6525 (1997).
15. M. Buenerd *et al.,* Nucl. Phys. A **424**, 313 (1984).
16. J. Y. Hostachy *et al.,* Phys. Lett. B **184**, 139 (1987).
17. V. K. Lukyanov, Yad. Fiz. **58**, 1955 (1995) [Phys. At. Nucl. **58**, 1848 (1995)].
18. A. Vitturi and F. Zardi, Phys. Rev. C **38**, 2086 (1988).
19. P. Rossel-Chomaz *et al.,* Nucl. Phys. A **477**, 345 (1988).
20. B. Slowinski, Yad. Fiz. **19**, 595 (1974) [Sov. J. Nucl. Phys. **19**, 301 (1974)].
21. G. D. Satchler, *Direct Nuclear Reactions* (Clarendon, Oxford, 1983).
22. G. Igo, Phys. Rev. **115**, 1665 (1959).

Translated by A. Isaakyan

Physics of Atomic Nuclei, Vol. 64, No. 7, 2001, pp. 1282–1287. Translated from Yadernaya Fizika, Vol. 64, No. 7, 2001, pp. 1358–1363.

ELEMENTARY PARTICLES AND FIELDS
Theory

Effects of Vacuum Polarization and of Proton Polarizability in the Lamb Shift of Muonic Hydrogen

A. P. Martynenko and R. N. Faustov[1)]

Samara State University, ul. Akademika Pavlova 1, Samara, 443011 Russia

Received March 6, 2000

Abstract—The contributions to the Lamb shift in muonic hydrogen from hadronic vacuum polarization and from the correction associated with electron vacuum polarization and with the proton polarizability are calculated by using present-day experimental data on the cross section for e^+e^- annihilation into hadrons and on structure functions for deep-inelastic ep scattering. The numerical value of the total contribution to the $(2P–2S)$ shift in muonic hydrogen is found to be 10.95 μeV. © *2001 MAIK "Nauka/Interperiodica".*

Extremely simple atomic systems like positronium, muonium, the hydrogen atom, muonic hydrogen, dimuonium, and pionium appear to be a unique laboratory for studying various types of elementary-particle interactions. Experimental accuracies in measuring energy levels of hydrogen-like atoms and the anomalous magnetic moments of the electron and the muon have been considerably improved in recent years. In some problems, these accuracies have achieved so high a level that a theoretical evaluation of the relevant quantities requires correctly taking into account the contributions of strong and even weak interactions. By way of example, we indicate that, according to the calculations of various authors [1–6], the contribution of hadronic vacuum polarization (HVP) to the anomalous magnetic moment of the muon is

$$a_\mu^{\rm HVP} = (6738 \pm 70) \times 10^{-11}. \qquad (1)$$

It is assumed that, in the E821 experiment to be performed at the Brookhaven National Laboratory (BNL), the accuracy in measuring the muon anomalous magnetic moment will be as high as one to two 10^{-10} units [6]. In a new Los Alamos experiment aimed at measuring the hyperfine splitting of the muonium ground state, the accuracy of the measurement reached a few hundredths of a kilohertz: $\Delta\nu = 4463302765(53)$ Hz [7]. This requires taking into account, in the hyperfine structure, both higher order contributions in α (α is the fine-structure constant) and the contribution from hadronic vacuum polarization, the latter being [8]

$$\Delta E_{\rm hfs}^{\rm HVP}(\mu e) = 0.2397 \pm 0.0070 \text{ kHz}. \qquad (2)$$

In the near future, it is planned to measure the Lamb shift in the muonic-hydrogen atom (μp). This may present yet another problem that admits an experimental verification of the contribution from hadronic vacuum polarization [9]. The energy levels of this system are determined in just the same way as for conventional hydrogen. However, effects associated with the distribution of the proton charge, magnetic moment, and polarizability, as well as corrections stemming from vacuum polarization (including hadronic vacuum polarization), are much greater for muonic hydrogen since the electron-to-muon mass ratio is $m_e/m_\mu = 4.836332 \times 10^{-3}$. Measurement of the $(2P$-$2S)$ Lamb shift in muonic hydrogen would make it possible to estimate, with a higher precision, the proton charge radius $R_p = \sqrt{\langle r^2 \rangle}$ [10, 11], an important characteristic of the proton indeed. One method for determining the proton charge radius—that which involves measuring the Lamb shift in muonic hydrogen [12]—leads to the value of $R_p = 0.883(14)$ fm [13]. Another possibility of obtaining a more precise value of R_p is based on measuring the Lamb shift in the muonic-hydrogen atom to within 2 μeV. In view of this, it is necessary to calculate various contributions to the Lamb shift with the same or a higher precision. In the present study, we evaluate some corrections to the Lamb shift in (μp) that are associated with hadronic vacuum polarization, electron vacuum polarization, and the proton polarizability.

Within the quasipotential approach to describing the energy spectrum of muonic hydrogen, the particle-interaction operator that takes into account 1γ and 2γ interactions has the form [14]

$$V = V_{1\gamma} + V_{2\gamma} = V^c + \Delta V, \qquad (3)$$

[1)] Scientific Council for the Interdisciplinary Problem Cybernetics, Russian Academy of Sciences, ul. Vavilova 40, Moscow, 117967 Russia.

1063-7788/01/6407-1282$21.00

$$V_{1\gamma} = T_{1\gamma}, \quad V_{2\gamma} = T_{2\gamma} - T_{1\gamma} \times G^f \times T_{1\gamma}, \qquad (4)$$

where V^c is the Coulomb potential; $T_{1\gamma}$ and $T_{2\gamma}$ are the off-energy-shell amplitudes for 1γ and 2γ interaction, respectively; and $[G^f]^{-1} = (b^2 - \mathbf{p}^2)/2\mu_R$. The main contribution of hadronic vacuum polarization to the Lamb shift in muonic hydrogen is represented by the diagram in Fig. 1. The corresponding modification to the photon propagator is

$$\frac{-ig^{\mu\nu}}{q^2 + i\epsilon} \to \frac{-i}{q^2 + i\epsilon}\Pi^{\mu\nu}(q)\frac{-i}{q^2 + i\epsilon}. \qquad (5)$$

The self-energy operator $\Pi^{\mu\nu}(q) = (g^{\mu\nu}q^2 - q^\mu q^\nu) \times \Pi(q^2)$ satisfies the dispersion relation

$$\Pi(q^2) = \frac{q^2}{\pi}\int\limits_{4m_\pi{}^2}^{\infty} \frac{\mathrm{Im}\Pi(s)ds}{s(s - q^2 - i\epsilon)}. \qquad (6)$$

In the coordinate representation, the corresponding correction to the quasipotential of muon–proton interaction then assumes the form [15]

$$\Delta V_{\mathrm{Ls}}^{\mathrm{HVP}}(\mathbf{r}) = -4\alpha(Z\alpha)\int\limits_{4m_\pi^2}^{\infty} \frac{\rho(s)ds}{s}\delta(\mathbf{r}), \qquad (7)$$

where the spectral function $\rho(s)$ is related to the well-known cross section for e^+e^- annihilation into hadrons, σ^h, by the equation

$$\rho(s) = \frac{R(s)}{3s} = \frac{\sigma^h(e^+e^- \to \text{ hadrons})}{3s\sigma_{\mu\mu}(e^+e^- \to \mu^+\mu^-)}, \qquad (8)$$

while $\sigma_{\mu\mu}(e^+e^- \to \mu^+\mu^-) = 4\pi\alpha^2/3s$ is the cross section for e^+e^- annihilation into a muon pair. The shift of S levels in muonic hydrogen is obtained by averaging expression (7) over the Coulomb wave functions. The result has the form

$$\Delta E_{\mathrm{Ls}}^{\mathrm{HVP}} = -\frac{4\alpha(Z\alpha)^4\mu^3}{\pi n^3}\int\limits_{4m_\pi^2}^{\infty} \frac{\rho(s)ds}{s}. \qquad (9)$$

The accuracy in measuring the cross section σ^h for various energy intervals has been improved considerably in recent years [16, 17]. The main contribution to σ^h comes from the process $e^+ + e^- \to \pi^+ + \pi^-$, whose cross section is proportional to the squared modulus of the π-meson form factor F_π. Our calculation of the contribution from hadronic vacuum polarization will employ experimental data on the form factor F_π in the energy range $0.61 \le \sqrt{s} \le 0.96$ GeV that were obtained in new experiments with the CMD-2 detector in Novosibirsk. These data are well described by the Gounaris–Sakurai model with allowance for $\rho\omega$ interference:

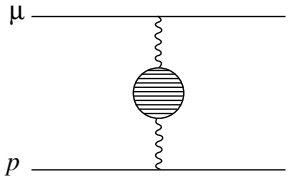

Fig. 1. Diagram for the one-photon hadronic-vacuum-polarization contribution to the Lamb shift in (μp).

$$F_\pi(s) = \frac{\mathrm{BW}_{\rho(770)}^{GS}(s)\frac{1+\delta\ \mathrm{BW}_\omega(s)}{1+\delta} + \beta\,\mathrm{BW}_{\rho(1450)}^{GS}(s)}{1+\beta}. \qquad (10)$$

The values of the parameters of $\rho(770)$, $\rho(1450)$, and ω and the values of β and δ were borrowed from [16, 18]. Upon substituting expression (10) into the spectral function

$$\rho_{\pi\pi}(s) = \frac{(s - 4m_\pi^2)^{3/2}}{12s^{5/2}}|F_\pi(s)|^2, \qquad (11)$$

we have performed a numerical integration in (9) for the energy interval $4m_\pi^2 \le \sqrt{s} \le 0.95$ GeV. The contribution from other energy intervals to $\Delta E_{\mathrm{Ls}}^{\mathrm{HVP}}$ was evaluated in just the same way as in [3, 8, 19]. The results of a numerical integration of expression (9) are quoted in the table. As can be seen from the table, the main contribution to $\Delta E_{\mathrm{Ls}}^{\mathrm{HVP}}$ comes from the form factor F_π; therefore, it was instructive to compare the contributions to the shift of S levels for expression (11) and for the π-meson form factor proposed in [20]. It turned out that the corresponding contributions to $\Delta E_{\mathrm{Ls}}^{\mathrm{HVP}}$ are identical.

Let us now consider the two-photon contribution of hadronic vacuum polarization to the Lamb shift of the energy levels in muonic hydrogen (see Fig. 2). The required correction associated with hadronic vacuum polarization in the one-loop amplitudes $T_{2\gamma}$ arises if, in the propagator of one of exchange photons, use is made of the substitution

$$\frac{1}{k^2 + i\epsilon} \to \frac{\alpha}{\pi}\int\limits_{s_{\mathrm{th}}}^{\infty} \frac{\rho(s)ds}{k^2 - s + i\epsilon}. \qquad (12)$$

The shift of the energy levels of S states can then be represented as [21]

$$\Delta E_{\mathrm{Ls},\,2\gamma}^{\mathrm{HVP}} = -\frac{2\mu^3}{\pi^2 n^3}\delta_{l0}\alpha(Z\alpha)^5\int\limits_0^\infty V(k)dk\int\limits_{s_{\mathrm{th}}}^{\infty} \frac{\rho(s)ds}{k^2 + s}, \qquad (13)$$

$$V(k) = \frac{2kF_1^2}{m_1 m_2} + \frac{k^3}{2m_1^3 m_2^3}\left[2F_1^2(m_1^2 + m_2^2)\right. \qquad (14)$$

Contributions from hadronic vacuum polarization to the $(2P–2S)$ Lamb shift in (μp) for various energy ranges

Final state	Energy range $\sqrt{s}$, GeV	$\Delta E_{\rm Ls}^{\rm HVP}(\mu p)$, μeV
$\rho, \omega \to 2\pi, \omega \to 3\pi$	(0.28, 0.95)	7.035 ± 0.193
ϕ		0.625 ± 0.023
J/ψ		0.115 ± 0.010
Υ		0.001
Hadrons	(0.95, 1.4)	1.766 ± 0.073
"	(1.4, 2.2)	0.602 ± 0.039
"	(2.2, 3.1)	0.279 ± 0.024
"	(3.1, 5.0)	0.181 ± 0.012
"	(5.0, 10.0)	0.099 ± 0.002
"	(10.0, 40.0)	0.034 ± 0.001
"	$\sqrt{s} \geq 40.0$	0.003
Contribution of the diagram in Fig. 1		10.740 ± 0.377
Contribution of the diagrams in Figs. 2*a* and 2*b*		0.047
Contribution of the diagram in Fig. 2*c*		−0.015
Total contribution		10.772 ± 0.377

$$+ 4m_1^2F_1F_2 + 3m_1^2F_2^2\Big] + \frac{\sqrt{k^2+4m_1^2}}{2m_1^3m_2(m_1^2-m_2^2)}$$
$$\times \Bigg[k^2(2m_2^2F_1^2 + 4m_1^2F_1F_2 + 3m_1^2F_2^2) + 8m_1^4F_1F_2 + \frac{16m_1^4m_2^2F_1^2}{k^2}\Bigg] - \frac{\sqrt{k^2+4m_2^2}m_1}{2m_2^3(m_1^2-m_2^2)}$$
$$\times \Bigg[k^2(2F_1^2 + 4F_1F_2 + 3F_2^2) - 8m_2^2F_1F_2 + \frac{16m_2^4F_1^2}{k^2}\Bigg]$$

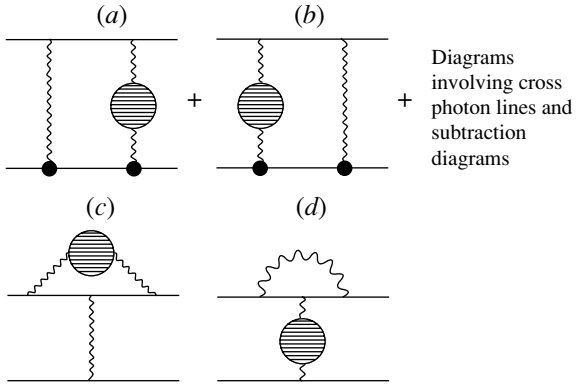

Fig. 2. Diagrams for the two-photon hadronic-vacuum-polarization contribution to the Lamb shift in (μp).

$$+\frac{8m_1[F_2(0) + 4m_2^2F_1'(0) - 2m_2^2/k^2]}{m_2(m_1+m_2)},$$

where the contribution of the iterative component was taken into account in constructing the quasipotential (4). Expression (13) does not involve infrared divergences. In performing numerical calculations on the basis of this expression, the proton form factors F_1 and F_2 were parametrized as (dipole parametrization) [22]

$$F_1(k^2) = \frac{G_E - \dfrac{k^2}{4m_2^2}G_M}{1 - \dfrac{k^2}{4m_2^2}}, \quad F_2(k^2) = \frac{G_M - G_E}{1 - \dfrac{k^2}{4m_2^2}}, \tag{15}$$
$$G_M = \frac{1+\kappa}{\left(1 - \dfrac{k^2}{\Lambda^2}\right)^2}, \quad G_E = \frac{1}{\left(1 - \dfrac{k^2}{\Lambda^2}\right)^2},$$

where the proton-structure parameter is $\Lambda = 0.898m_2$ [22] and $\kappa = 1.792847337$ is the proton anomalous magnetic moment. With allowance for (11), the numerical value of the contribution in (13) to the shift $(2P–2S)$ is

$$\Delta E_{\rm Ls,\,2\gamma(a+b)}^{\rm HVP} = 0.047\ \mu\text{eV}. \tag{16}$$

The hadronic-vacuum-polarization-induced contribution of the same order in α to the energy spectrum is determined by the diagram in Fig. 2*c*. Assuming that the muon and proton momenta are on

the mass shell, we can represent this contribution as

$$\Delta E_{2\gamma\,(c)} = \frac{\mu^3(Z\alpha)^4}{m_1^2 n^3} \times \left[4m_1^2\rho'_{\rm HVP}(0)\delta_{l0} + f_{\rm HVP}(0)\frac{C_{jl}}{2l+1}\right], \quad (17)$$

$$C_{jl} = \delta_{l0} + (1-\delta_{l0})\frac{j(j+1) - l(l+1) - 3/4}{l(l+1)}, \quad (18)$$

where the quantities $\rho'_{\rm HVP}(0)$ and $f_{\rm HVP}(0)$ stand for the contributions of hadronic vacuum polarization to, respectively, the slope of the muon charge form factor and the muon anomalous magnetic moment. In order to calculate $f_{\rm HVP}(0)$, use is usually made of the integral representation

$$f_{\rm HVP}(0) = \frac{1}{3}\left(\frac{\alpha}{\pi}\right)^2 \int\limits_{s_{\rm th}}^{\infty} \frac{R(s)ds}{s} \int\limits_0^1 \frac{y^2(1-y)dy}{(y^2 + \frac{s}{m_1^2}(1-y))}. \quad (19)$$

The numerical value of $f_{\rm HVP}(0)$ has been refined in recent years as the result of new calculations [1], and we take it to be $f_{\rm HVP}(0) = 673.8 \times 10^{-10}$. The contribution of hadronic vacuum polarization to the slope of the charge form factor can also be represented in an integral form of the type in (19). To do this, we consider the on-mass-shell vertex of the interaction of a virtual photon with a muon (see the diagram in Fig. 2*c*). We have

$$\Gamma^\mu = e^3\bar{u}(q_1)\gamma^\lambda \int \frac{\hat{q}_1 - \hat{q} + m}{(q_1-q)^2 - m^2 + i\epsilon}\gamma^\mu \times \frac{\hat{p}_1 - \hat{q} + m}{(p_1-q)^2 - m^2 + i\epsilon}\gamma^\sigma u(p_1)\frac{d^4q}{(2\pi)^4}\frac{4\pi}{q^2}\frac{\Pi(q^2)}{q^2} \times \left(g^{\lambda\sigma} - \frac{q^\lambda q^\sigma}{q^2}\right). \quad (20)$$

By using the Feynman parametrization in calculating the relevant loop integral and the dispersion relation (6) for the self-energy operator [23], we can single out the contributions to the form factors $\rho(k^2)$ and $f(k^2)$ and represent the slope of the charge form factor as

$$\rho'_{\rm HVP}(0) = \frac{1}{12}\left(\frac{\alpha}{\pi}\right)^2 \frac{1}{m_1^2}\int\limits_{s_{\rm th}}^{\infty}\frac{R(s)ds}{s}\int\limits_0^1 ydy \times \left[\frac{1}{30}\frac{y^2(36y - y^2 - 40)}{D^2(y,s)} - \frac{1}{6}\frac{(22 - 14y - y^2)}{D(y,s)} + \frac{m_1^2}{s}\ln\left(\frac{y^2}{D(y,s)}\right)\right], D(y,s) = y^2 + \frac{s}{m_1^2}(1-y). \quad (21)$$

The integral with respect to y in (21) can be calculated exactly. According to the calculations based on expressions (19), (21), and (11), the numerical value of the correction in (17) to the $(2P-2S)$ Lamb shift in muonic hydrogen is

$$\Delta E^{\rm HVP}_{{\rm Ls},\,2\gamma(c)} = -0.015\ \mu{\rm eV}. \quad (22)$$

The contribution of the diagram in Fig. 2*d* to the energy spectrum is an $O(\alpha^8)$ quantity and can therefore be disregarded. The total value of the hadronic-vacuum-polarization-induced correction to the $(2P-2S)$ Lamb shift in muonic hydrogen is quoted in the table. It is in fairly good agreement with the results presented in [24, 25].

The strong-interaction contribution to the energy spectrum of (μp) comes not only from hadronic vacuum polarization but also from the proton polarizability [21, 26–29]. In just the same way as in the case of hadronic vacuum polarization, strong-interaction effects can be taken into account here phenomenologically on the basis of present-day data on the structure functions $F_2(x,Q^2)$ and $R(x,Q^2)$ for deep-inelastic scattering [30, 31]. Since electron vacuum polarization plays a dominant role among various QED corrections to the $(2P-2S)$ Lamb shift in (μp), we have evaluated the contribution of the diagrams in Fig. 3. They are associated with two effects, electron vacuum polarization and the proton polarizability. By using the substitution in (12), we can represent the corresponding correction to S levels in muonic hydrogen as [21]

$$\Delta E^{\rm Ls}_{\rm vp,\,pol} = -\frac{16\mu^3\alpha(Z\alpha)^5 m_1}{\pi^3 n^3} \times \int\limits_0^\infty \frac{dk}{k}\int\limits_0^\pi \sin^2\phi d\phi \int\limits_{\nu_0}^\infty dy \frac{1}{k^2 + 4m_1^2\cos^2\phi} \times \int\limits_{s_{\rm th}}^\infty \frac{\rho(s)ds}{s+k^2}\frac{F_2(y,k^2)}{(y^2 + k^2\cos^2\phi)} \times \left[(1+2\cos^2\phi)\frac{\left(1+\frac{k^2}{y^2}\right)\cos^2\phi}{1+R(y,k^2)} + \sin^2\phi\right], \quad (23)$$

where $R(y,k^2) = \sigma_L/\sigma_T$ is the ratio of the cross sections for the absorption of longitudinally and transversely polarized photons by hadrons and $\rho(s) = \sqrt{1-4m_e^2/s}\frac{(1+2m_e^2/s)}{3s}$. In order to perform numerical calculations on the basis of expression (23), we need experimental data on the structure function $F_2(x,Q^2)$ and on the ratio $R(x,Q^2)$. There exist a number of parametrizations of experimental data on the function $F_2(x,Q^2)$ over a wide region of Q^2

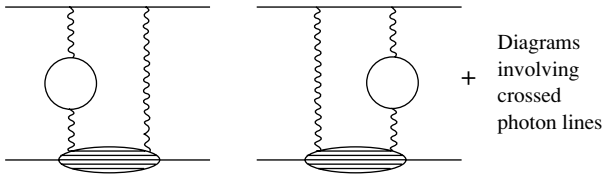

Fig. 3. Diagrams for the electron-vacuum-polarization and the proton-polarizability contribution to the Lamb shift in (μp).

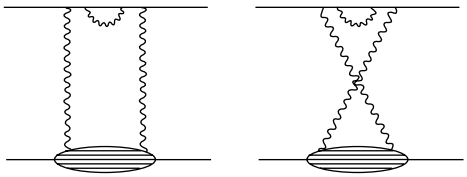

Fig. 4. Diagrams for the muon-self-energy and the proton-polarizability contribution to the Lamb shift in (μp).

and x [31]; we have used that which was proposed in [30, 31]. For the contribution in (23), the numerical integration eventually yields

$$\Delta E^{\rm Ls}_{\rm vp,\,pol} = -1.52\frac{1}{n^3}\ \mu{\rm eV}. \qquad (24)$$

Other corrections of order α^6 that are associated with the proton polarizability are much less. For example, the muon self-energy correction (Fig. 4) is determined by the following substitution in the muon propagator [32]:

$$\frac{1}{\hat p - m_1} \to \frac{1}{\hat p - m_1}\Sigma^{(R)}_{1\gamma}(p)\frac{1}{\hat p - m_1}, \qquad (25)$$

$$\Sigma^{(R)}_{1\gamma}(p) = (\hat p - m_1)^2\left(-\frac{3\alpha\hat p}{4\pi m_1^2}\right)\frac{1}{1-\rho} \qquad (26)$$
$$\times\left[1+\frac{\rho}{1-\rho}\ln\rho\right],\ \rho = \frac{m_1^2-p^2}{m_1^2}.$$

Averaging the relevant amplitude over the proton and muon spins, we can represent its contribution to the shift of S levels in the form [21]

$$\Delta E^{\rm Ls}_{\rm se,\,pol} = \frac{3\alpha(Z\alpha)^5\mu^3}{2n^3\pi^4 m_1^2}\int\frac{d^4k}{(k^2)^2}\int\limits_{\nu_0}^{\infty}\frac{dy}{(y^2-k_0^2)} \qquad (27)$$
$$\times F_2(y,k^2)\left\{\left(\frac{1}{2}m_1 - 3k_0 - \frac{2m_1k_0^2}{k^2}\right)\right.$$
$$\times\frac{\left(1+\frac{y^2}{k^2}\right)\frac{k_0^2}{y^2}}{1+R(y,k^2)} + \frac{3}{2}m_1 - k_0 - \frac{7}{2}\frac{m_1k_0^2}{k^2} +$$
$$\left.+\frac{k_0^3}{k^2} + \frac{2m_1k_0^4}{k^4}\right\}$$
$$\times\frac{1}{1-\rho_1}\left[1+\frac{\rho_1}{1-\rho_1}\ln\rho_1\right],\quad \rho_1 = -\frac{k^2+2m_1k_0}{m_1^2}.$$

Going over to integration over four-dimensional Euclidean space ($k_0 \to ik_0$), as in evaluating expression (23), we obtain

$$\Delta E^{\rm Ls}_{\rm se,\,pol} = 0.092\frac{1}{n^3}\ \mu{\rm eV}. \qquad (28)$$

The above analysis of strong-interaction contributions has revealed that, in the Lamb shift of muonic-hydrogen levels, the contribution of hadronic vacuum polarization is on the same order of magnitude as corrections associated with the proton polarizability and structure [21, 24, 26, 27]. The contributions obtained in the present study make it possible to improve the theoretical accuracy in determining the Lamb shift of (μp) levels. In order to demonstrate this, we note that, by taking into account the hadronic-vacuum-polarization-induced contribution evaluated in the present study [see Eqs. (24) and (28)], the main contribution of the proton polarizability from [21], and the results quoted in [9, 25], we can reprsent the total expression for the $(2P\text{–}2S)$ Lamb shift in muonic hydrogen in the form

$$\Delta E_{\rm Ls} = (206.085(2) - 5.1975R_p^2)\ \mu{\rm eV}. \qquad (29)$$

The uncertainty in the first term in expression (29) is associated with the experimental errors in measuring the structure functions for deep-inelastic ep scattering [30] and the cross section σ^h [16, 17]. Expression (29) must be used in extracting the proton charge radius R_p from data of future experiments aimed at measuring the Lamb shift in muonic hydrogen.

ACKNOWLEDGMENTS

We are grateful to M.J. Eides, S. G. Karshenboim, Yu. G. Kerner, R. A. Sen'kov, and I. B. Khriplovich for stimulating discussions and to H. Abramowicz for sending the corrected values of the parameters for the structure function $F_2(x,Q^2)$.

This work was supported by the Russian Foundation for Basic Research (project no. 00-02-17771) and by the Russian Universities—Fundamental Research Program (grant no. 990192).

REFERENCES

1. V. W. Hughes and T. Kinoshita, Rev. Mod. Phys. **71**, S133 (1999).
2. M. Davier and A. Hocker, Phys. Lett. B **435**, 427 (1998).

3. S. Eidelman and F. Jegerlehner, Z. Phys. C **67**, 585 (1995).
4. M. Steinhauser, hep-ph/9904373.
5. A. Czarnecki and W. J. Marciano, Nucl. Phys. B (Proc. Suppl.) **76**, 245 (1999).
6. B. Lee Roberts, Int. J. Mod. Phys. A **15**, 386 (2000).
7. W. Liu *et al.,* Phys. Rev. Lett. **82**, 711 (1999).
8. R. N. Faustov, A. Karimkhodzaev, and A. P. Martynenko, Phys. Rev. A **59**, 2498 (1999).
9. K. Pachucki, Phys. Rev. A **53**, 2092 (1996).
10. S. G. Karshenboim, in *Proceedings of the International Workshop "Hadronic Atoms and Positronium in the Standard Model", Dubna, 1998,* p. 224; hep-ph/9712347.
11. R. Rosenfelder, Phys. Lett. B 479, 381 (2000); nucl-th/9912031.
12. C. Schwob *et al.,* Phys. Rev. Lett. **82**, 4960 (1999).
13. K. Melnikov and T. Ritbergen, Preprint No. SLAC-PUB-8281 (1999).
14. A. P. Martynenko and R. N. Faustov, Teor. Mat. Fiz. **64**, 765 (1985).
15. V. P. Gerdt, A. Karimkhodzaev and R. N. Faustov, in *Proceedings of International Seminar on High Energy Physics and Quantum Field Theory, IHEP, Protvino, 1978,* p. 289.
16. R. R. Akhmetshin *et al.,* Preprint No. BUDKERINP-99-10 (1999); hep-ex/9904027.
17. J. Z. Bai *et al.,* Phys. Rev. Lett. **84**, 594 (2000).
18. Particle Data Group, Eur. Phys. J. C **3** (1–4) (1998).
19. A. P. Martynenko and R. N. Faustov, Yad. Fiz. **61**, 534 (1998) [Phys. At. Nucl. **61**, 471 (1998)].
20. F. Guerrero and A. Pich, Phys. Lett. B **412**, 382 (1997).
21. A. P. Martynenko and R. N. Faustov, Yad. Fiz. **63**, 915 (2000) [Phys. At. Nucl. **63**, 845 (2000)].
22. G. T. Bodwin and D. R. Yennie, Phys. Rev. D **37**, 498 (1988).
23. B. E. Lautrup, A. Peterman, and E. de Rafael, Phys. Rep. C **3**, 194 (1972).
24. J. L. Friar, J. Martorell, and D. W. L. Sprung, Preprint No. LA-UR-98-5728 (1998); nucl-th/9812053.
25. T. Kinoshita and M. Nio, Phys. Rev. Lett. **82**, 3240 (1999).
26. S. A. Startsev, V. A. Petrun'kin, and A. L. Khomkin, Yad. Fiz. **23**, 1233 (1976) [Sov. J. Nucl. Phys. **23**, 656 (1976)].
27. I. B. Khriplovich and R. A. Sen'kov, Phys. Lett. A **249**, 474 (1998).
28. R. Rosenfelder, Phys. Lett. B 463, 317 (1999); hep-ph/9903352.
29. K. Pachucki, Phys. Rev. A 60, 3593 (1999); hep-ph/9906002.
30. H. Abramowicz and A. Levy, Preprint No. DESY-97-251 (1997).
31. B. Badelek and J. Kwiecinski, Rev. Mod. Phys. **68**, 445 (1996); F.W. Brasse, W. Flauger, J. Gayler, *et al.*, Nucl. Phys. B **110**, 413 (1976).
32. M. I. Eides, S. G. Karshenboim, and V. A. Shelyuto, Ann. Phys. (N.Y.) **205**, 231 (1991).

Translated by A. Isaakyan

Physics of Atomic Nuclei, Vol. 64, No. 7, 2001, pp. 1288–1291. From Yadernaya Fizika, Vol. 64, No. 7, 2001, pp. 1364–1367.

ELEMENTARY PARTICLES AND FIELDS
Theory

Search for Quark Compositeness at LHC: Dijet Angular Distributions*

Z. U. Usubov** **and O. B. Abdinov**

Joint Institute for Nuclear Research, Dubna, Moscow oblast, 141980 Russia

Received January 21, 2000; in final form, May 10, 2000

Abstract—Effects of dijet angular distributions coming from a model of quark compositeness are presented. The influence of the parton distribution, calorimeter nonlinearity, and energy resolution is investigated. The sensitivity of data to the quark-compositeness scale for a low and a high LHC luminosity is studied. © *2001 MAIK "Nauka/Interperiodica".*

The existence of an underlying substructure will be a good key to understanding unresolved problems of the Standard Model (SM), such as the presence of a few generations of quarks and leptons and the fundamental properties of particles.

The quark substructure would appear as an excess of the high-P_T jets in relation to the level predicted by QCD, with dijet angular distributions being more isotropic than what is expected from a pointlike-quark theory, and/or as the discovery of excited quarks. Dijet angular distributions were studied by the CDF [1] and D0 [2] experiments at a c.m. energy of 1.8 TeV. The highest E_T reached so far at the Tevatron, about 500 GeV, corresponds to a distance scale of 10^{-17} cm. The data from these experiments were compared with QCD predictions, including compositeness. No evidence of quark substructure was found. Previous studies of dijet invariant-mass spectra reported by UA1 [3] and UA2 [4] at $\sqrt{s} = 630$ GeV and by CDF [5] also showed that the data were consistent with QCD predictions. The CDF [6] and D0 [7] results of high-mass Drell–Yan cross section measurements set a lower limit on the quark–electron compositeness scale (about 5.5 TeV). From the measurement of the ratio of charged-to-neutral-current cross sections in the CCFR fixed-target neutrino experiment [8] at the Tevatron, a limit of $\Lambda \sim 8$ TeV was achieved.

Searches for the quark substructure will continue at future hadron colliders. Here, we investigate the effect of quark compositeness in dijet angular distributions as would be seen by ATLAS [9] at LHC. The same problem for high-E_T jet spectrum was indicated earlier [10]. The event generator PYTHIA-5.7 [11] was used to simulate a scenario with quark substructure. This allowed us to use a simple phenomenological approach of contact interactions between quark constituents with a compositeness scale Λ [12], where the sign of the effective Lagrangian for a flavor-diagonal current of definite chirality is positive (destructive interference) or negative (constructive interference). The data simulated within the SM are compared with those obtained under the assumption of quark compositeness. The analysis is based on a sample of about 280800 pp interactions at $\sqrt{s} = 14$ TeV, which corresponds to the sample of dijet events expected after one month of LHC operation at a luminosity of $\mathcal{L} = 10^{33}$ cm^{-2}s^{-1}. The simulated event sample included the following hard-scattering subprocesses: qq, qg, gg, $g\gamma$, $q\gamma$, and $\gamma\gamma$. The γ^*/Z, W, tt production subprocesses were also taken into account. To get a sufficiently large number of events with high-P_T jets within a reasonable central-processor-unit time, a cut on the transverse momentum of the hard scattering subprocess was set to 600 GeV. Under these conditions, the contributions from the qq, qg, and gg processes saturate 97.5% of the total cross section of 3.370×10^{-7} mb. Initial- and final-state QCD and QED radiation, the fragmentation and decay of partons and particles, and multiple interactions were taken into account. First-order running α_s calculations were applied. The $\Lambda_{\rm QCD}$ value was chosen according to the parton-distribution parametrizations used in PYTHIA. For the Q^2 scale in the $2 \to 2$ hard-scattering process, $Q^2 = (m_{T1}^2 + m_{T2}^2)/2$ was used. The detector performance was simulated by using the ATLFAST [13] package, which provides a reliable estimate of the detector response to hadronic jets. Jets were reconstructed with ATLFAST by using the standard procedure for summing the energy deposited in a cone of radius $\Delta R = \sqrt{\Delta\eta^2 + \Delta\phi^2} = 0.7$. All calorime-

*This article was submitted by the authors in English.

**e-mail: usubov@nusun2.jinr.ru

Characteristics of the invariant-mass bins for high-E_T jets

Mass bins, GeV	E_T thresholds, GeV	N_{ev}	Average M_{jj}, GeV
2000–2300	400	18562	2136
2300–2800	400	15781	2512
2800–3400	400	7722	3050
> 3400	400	5228	4048

ter cells with $E_T > 1.5$ GeV were taken as possible initiators of clusters. The total transverse energy E_T summed over all cells in a cone ΔR should be greater than 15 GeV. Jets were reconstructed down to $|\eta| \leq 5.0$.

The analysis was performed in terms of the angular variable $\chi \equiv e^{|\eta_1 - \eta_2|}$, where $\eta_{1,2}$ are the pseudorapidities of the two leading jets. For the case of $2 \to 2$ parton scattering, it is related to the c.m. scattering angle θ^* by the equation

$$\chi = \frac{1 + |\cos\,\theta^*|}{1 - |\cos\,\theta^*|}. \qquad (1)$$

This definition renders a comparison with theory more straightforward [14]. The investigation of the dijet angular distribution $(1/N)(dN/d\chi)$ was performed in four dijet-invariant-mass bins. The dijet invariant mass is defined as

$$M_{jj} = \sqrt{(E_1 + E_2)^2 - (P_1 + P_2)^2}, \qquad (2)$$

where $(E_{1,2}, P_{1,2})$ are the 4-momenta of the two leading jets. For all dijet-invariant-mass bins, the E_T threshold for the highest-E_T jet was 400 GeV. The table shows the selection cuts for the highest-E_T jet for various invariant-dijet-mass bins, together with the average M_{jj} and the number of events per bin.

The dijet angular distributions for these dijet-mass bins are shown in Fig. 1 for constructive interference. The case of destructive interference is similar. From this figure, one can see that quark compositeness leads to an enhancement in the distribution at low values of χ in relation to the SM prediction. The dijet mass region above 3400 GeV is good for determining isotropic contributions to the dijet angular distribution in pp interactions at $\sqrt{s} = 14$ TeV for Λ up to 8 TeV. It should be noted that the effect is slightly lower for destructive interference and that the sensitivity is higher for constructive interference than for destructive interference.

To estimate limits on the quark-compositeness scale, the CDF group used the variable R_χ defined as the ratio of the number of events with $\chi < \chi_0$ to the number of events with $\chi > \chi_0$. In our case, a value of $\chi_0 = 5$ was used. For the constructive case where all quarks are composite, Fig. 2 shows R_χ as

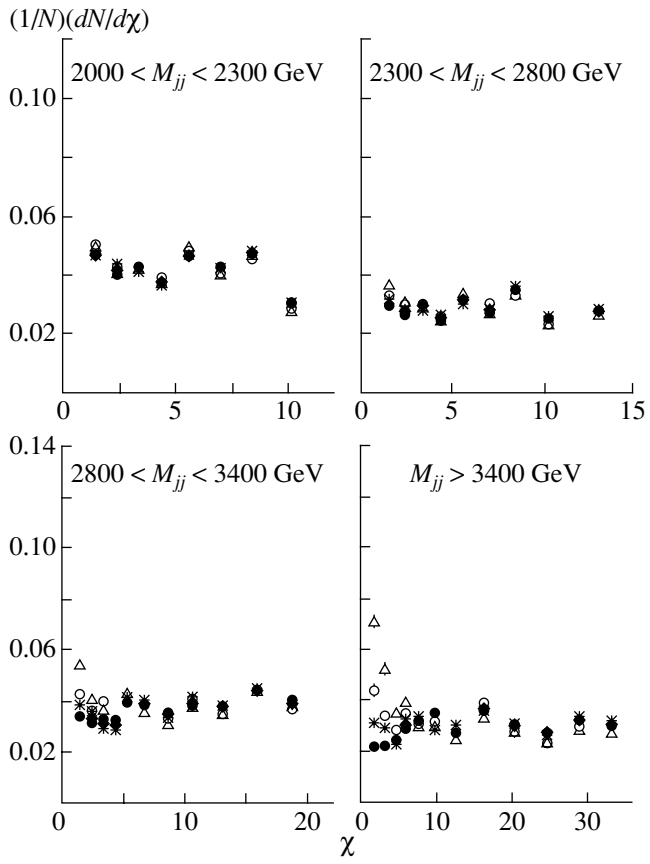

Fig. 1. Dijet angular distributions for various mass bins for the case of constructive interference (two quarks are composite): (•) SM prediction, (△) $\Lambda_{ud} = 8000$ GeV, (○) $\Lambda_{ud} = 10000$ GeV, and (*) $\Lambda_{ud} = 14000$ GeV.

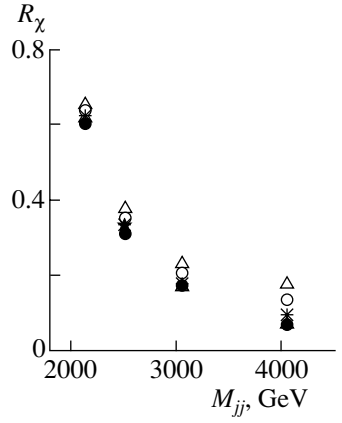

Fig. 2. R_χ as a function of the dijet mass M_{jj} for various values of the compositeness scale Λ (all quarks are composite): (•) SM prediction, (△) $\Lambda = 8000$ GeV, (○) $\Lambda = 10000$ GeV, (*) $\Lambda = 14000$ GeV, and (⋆) $\Lambda = 16000$ GeV.

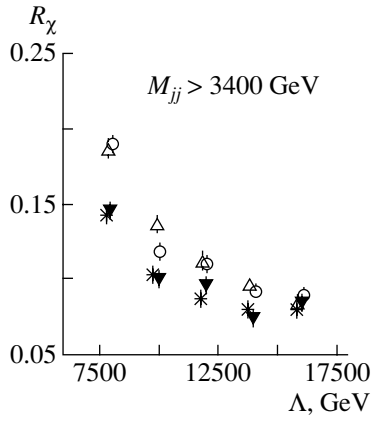

Fig. 3. R_χ as a function of the scale Λ: (○ and △) constructive interference (two and all quarks are composite) and (▼ and ✳) destructive interference (two and all quarks are composite).

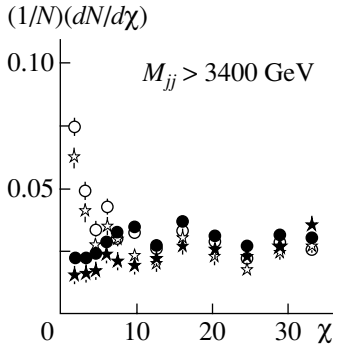

Fig. 4. Influence of the calorimeter nonlinearity on the quark-compositeness effect. (● and ★) SM prediction without and with calorimeter nonlinearity and (○ and ☆) $\Lambda_{\text{all}} = 8000$ GeV without and with calorimeter nonlinearity.

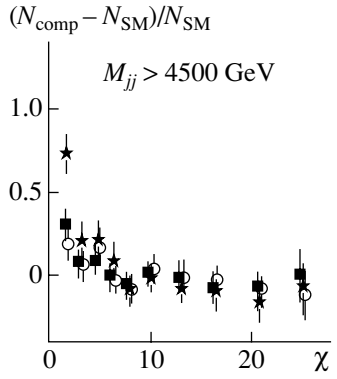

Fig. 5. Difference of the quark-compositeness and SM predictions that is divided by the SM predictions for the dijet angular distribution at an integrated luminosity of $L = 30$ fb^{-1}: (★) $\Lambda_{\text{all}} = 15000$ GeV, (■) $\Lambda_{\text{all}} = 20000$ GeV, and (○) $\Lambda_{\text{all}} = 25000$ GeV.

a function of the dijet mass for various values of the compositeness scale Λ. The case where two quarks are composite is very similar. The data are plotted at the average mass for each mass bin. In the case where all quarks are composite and for the compositeness scale of $\Lambda = 16$ TeV, the data differ from the SM predictions by 1.5σ and 3.5σ for destructive and constructive interference, respectively.

Figure 3 displays R_χ as a function of the scale Λ for the constructive and destructive cases and for the case where two and all quarks are composite. It is clear that the sensitivity is insufficient for distinguishing the case where two quarks are composite from the case where all quarks are composite.

From the study of R_χ with different parton distributions, it was found that the quark-compositeness effect is not sensitive to the parton distribution. Note that, in the rest of the analysis, PYTHIA was used with the default structure function CTEQ2L. The quantity R_χ is also insensitive to the jet cone radius ΔR.

The sensitivity to the calorimeter resolution was studied in [15]. In ATLFAST, the jet energy is smeared according to $\sigma_E/E \sim 50\%/\sqrt{E} + 2\%$ in the central region ($|\eta| < 3$) and $\sigma_E/E \sim 100\%/\sqrt{E} + 7\%$ in the forward calorimeters ($3 < |\eta| < 5$).

In order to investigate the influence of a change in the constant term on $(1/N)(dN/d\chi)$, we simply multiplied and divided the constant term by two. Changes in the stochastic term were also considered. There is no significant effect of those changes on the dijet angular distribution.

The nonlinear response of the hadron calorimeter can affect the observed difference between the SM and compositeness scenario or mimic a compositeness signal. To study this effect, we considered the nonlinearity of the jet E_T scale according to the relation [16]

$$E_T(\text{meas}) = E_T \frac{1.0}{c(1.0 + (e/h - 1.0) \cdot 0.11 \cdot \ln E_T)}, \quad (3)$$

where E_T(meas) and E_T are, respectively, the measured and true jet transverse energy; $e/h = 1.36$; and c is adjusted in such a way that the scale is unchanged at 50 GeV. Such a dependence on E_T leads to a deviation of 6.5, 9.3, and 12.3% from linearity for 400, 1000, and 3000 GeV, respectively. In Fig. 4 we compare the SM and quark-compositeness predictions with and without nonlinearity effects. For this choice of dijet-mass-bin intervals and jet E_T, we see that no spurious signal is created and that the

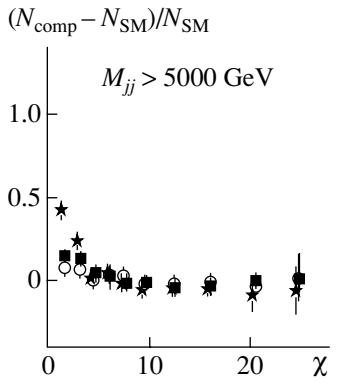

Fig. 6. As in Fig. 5, but for $L = 300$ fb^{-1}: (★) $\Lambda_{all} =$ 20000 GeV, (■) $\Lambda_{all} = 30000$ GeV, and (○) $\Lambda_{all} =$ 40000 GeV.

angular distribution is quite insensitive to effects of nonlinearity.

To study the sensitivity of data to the quark-compositeness signal for a higher scale Λ_{all}, an analysis was performed for integrated luminosities of 30 and 300 fb^{-1}. For dijet angular distributions, Figs. 5 and 6 show the difference of the quark-compositeness and SM predictions divided by the SM predictions. The integrated luminosity of 300 fb^{-1} can allow one to reach a 95% C.L. limit of $\Lambda = 40$ TeV.

In conclusion, the study based on a sample of events generated by PYTHIA-5.7 and processed through ATLFAST shows that high-mass-dijet angular distributions have a high potential for discovering quark compositeness. A low sensitivity to the choice of parton distributions, the energy resolution of the calorimeter, and nonlinearity effects make the dijet angular distribution a powerful tool for future high-statistics data analyses. One month of LHC operation at 10^{33} cm^{-2}s^{-1} and $\sqrt{s} = 14$ TeV would allow the discovery of quark substructure if the constituent coupling constant is on the order of 14 TeV. To reach a lower limit of 25 (40) TeV for the coupling constant, data taking at an integrated luminosity of 30 (300) fb^{-1} would be required.

ACKNOWLEDGMENTS

We would like to thank D. Froidevaux, F. Gianotti, I. Hinchliffe, and M. Bosman for help and enlightening comments.

REFERENCES

1. F. Abe *et al.,* Phys. Rev. Lett. **77**, 5336 (1996).
2. B. Abbott *et al.,* Phys. Rev. Lett. **80**, 666 (1998).
3. C. Albajar *et al.,* Phys. Lett. B **209**, 127 (1988).
4. J. Alitti *et al.,* Z. Phys. C **49**, 17 (1991).
5. F. Abe *et al.,* Phys. Rev. D **41**, 1722 (1990); Phys. Rev. Lett. **71**, 2542 (1993).
6. F. Abe *et al.,* Phys. Rev. Lett. **79**, 2198 (1997).
7. B. Abbott *et al.,* Phys. Rev. Lett. **82**, 4769 (1999).
8. K. S. McFarland *et al.,* Eur. Phys. J. C **1**, 509 (1998).
9. ATLAS Collab., Technical Proposal, CERN/LHCC/94-43.
10. Z. U. Usubov, Yad. Fiz. **64**, 382 (2001).
11. T. Sjostrand, Comput. Phys. Commun. **82**, 74 (1994); Preprint LU tp 95-20.
12. E. Eichten, K. Lane, and M. Peskin, Phys. Rev. Lett. **50**, 811 (1983); E. Eichten *et al.,* Rev. Mod. Phys. **56**, 579 (1984).
13. E. Richter-Was, D. Froidevaux, and L. Poggioli, ATLAS Internal Note PHYS-No-079 (1996).
14. V. Barger and R. J. N. Phillips, *Collider Physics* (Addison-Wesley, Reading, 1987).
15. F. Ariztizabal *et al.,* Nucl. Instrum. Methods Phys. Res. A **349**, 384 (1994).
16. M. Bosman, in *Proceedings of VI International Conference on Calorimetry in High Energy Physics, Frascati, 1996,* Frasc. Phys. Ser. **VI**, 299 (1996).

Physics of Atomic Nuclei, Vol. 64, No. 7, 2001, pp. 1292–1298. Translated from Yadernaya Fizika, Vol. 64, No. 7, 2001, pp. 1368–1374.

ELEMENTARY PARTICLES AND FIELDS
Theory

Phenomenological Model for Describing Pion-Pair Production on a Proton by Virtual Photons in the Energy Region of Nucleon-Resonance Excitation

V. I. Mokeev[1)], M. Ripani[1)], M. Anginolfi[1)], M. Battaglieri[1)], E. N. Golovach[1)], B. S. Ishkhanov[2)], M. V. Osipenko[2)], G. Ricco[1),3)], V. V. Sapunenko[1)], M. Taiuti[1)], and G. V. Fedotov[2)]

Institute of Nuclear Physics, Moscow State University, Vorob'evy gory, Moscow, 119899 Russia
Received January 12, 2000; in final form, July 17, 2000

Abstract—A phenomenological model is developed for describing the production of $\pi^+\pi^-$ pairs on a proton by virtual photons in the energy region of nucleon-resonance excitation. The cross sections are calculated for the channels $\gamma p \to \pi^-\Delta^{++}$, $\gamma p \to \pi^+\Delta^0$, and $\gamma p \to \rho p$, which make a dominant contribution to pion-pair production, and the results are compared with available experimental data. The contributions of nucleon resonances to the cross section for the reaction $\gamma p \to \pi^-\Delta^{++}$ are predicted within the developed approach. © *2001 MAIK "Nauka/Interperiodica".*

1. INTRODUCTION

Investigation of the exclusive channel of pion-pair production on a proton by photons is an efficient tool for exploring the structure of high-lying nucleon resonances N^* ($M_{N^*} > 1.6$ GeV) and for seeking nucleon resonance states that are predicted by constituent quark models, but which have not yet been discovered experimentally (missing resonances [1]). Presently, a vast program of investigations of nucleon resonances in the exclusive reactions of pion-pair production on a proton by virtual photons is being performed at the Thomas Jefferson National Accelerator Facility (TJNAF, USA) [2, 3]. A feature peculiar to these exclusive channels is that they receive a considerable contribution from nonresonance channels, and this impedes the use of model-independent approaches in extracting information about the structure of nucleon resonances. Data on their structure can be obtained only within models that relate the electromagnetic form factors for nucleon resonances to the measured differential cross sections for the reactions $\gamma_{r,v}p \to \pi^+\pi^-p$. [4)]

A description of interactions in the initial and the final reaction state with open inelastic channels is an important problem in studying nucleon resonances. Models that make it possible to take into account channel-coupling effects by using the entire body of data on processes featuring both hadrons and photons and leading to the formation of the state being studied were proposed in [4–6] to solve this problem. These approaches take consistently into account the requirements imposed by the unitarity of the S matrix. The set of meson- and baryon-interaction mechanisms is parametrized at the level of effective model Lagrangians. The number of such mechanisms becomes greater with increasing total energy W. Since our knowledge of the effective vertices for meson–baryon interaction (above all, of their off-mass-shell behavior) is incomplete and since it is difficult to allow for a large number of different mechanisms, approaches similar to those presented in [4–6] are applied predominantly to the channel of single-meson production in the region $W < 1.7$ GeV. Presently, such calculations have been performed only for reactions induced by real photons.

Nucleon resonances of mass in excess of 1.6 GeV predominantly decay into final states featuring a few pions. In order to study high-lying nucleon resonances, it is therefore of crucial importance to examine exclusive reaction channels leading to the production of a few pions. The cross section for pion-pair production on a proton increases fast from the threshold at $W = 1.21$ GeV, becoming commensurate with the cross section for single-pion production

[1)]Istituto Nazionale di Fisica Nucleare, Sezione di Genova, Genova, Italy.
[2)]Faculty of Physics, Moscow State University, Vorob'evy gory, Moscow, 119899 Russia, and Institute of Nuclear Physics, Moscow State University, Vorob'evy gory, Moscow, 119899 Russia.
[3)]Universitá di Genova, via Dodecaneso 33, I-16146 Genova, Italy.
[4)]The subscripts r and v label real and virtual photons, respectively.

at $W = 1.5$–1.7 GeV. Concurrently, the contribution of this channel to the total cross section for photon–proton interaction grows with increasing W.

Thus, investigation of pion-pair production on a proton by real and virtual photons is of great interest both for exploring the structure of nucleon resonances and for examining the dynamics of nonresonance mechanisms in the region of nonperturbative QCD. Moreover, an analysis of pion-pair production makes it possible to determine the cross sections for the reactions $\gamma_{r,v}p \to \pi^-\Delta^{++}$ and $\gamma_{r,v}p \to \rho p$, which lead to the formation of unstable particles in the final state.

Information about the cross sections for such reactions is necessary for extending models of the type from [4–6] to the region $W > 1.7$ GeV.

In [7–11], a model was developed for describing dominant quasi-two-body channels of the reaction $\gamma_{r,v}p \to \pi^+\pi^-p$:

$$\gamma_{r,v}p \to \pi^-\Delta^{++}, \quad (1)$$

$$\gamma_{r,v}p \to \pi^+\Delta^0, \quad (2)$$

$$\gamma_{r,v}p \to \rho p. \quad (3)$$

In that model, the quasi-two-body processes (1)–(3) are described as a superposition of nucleon-resonance excitations in the s channel and nonresonance processes, which, for channels (1) and (2), are determined by a minimal set of Born tree diagrams in terms of meson–baryon degrees of freedom. For channel (3), nonresonance processes are treated in the diffraction approximation [12]. In describing channels (1) and (2) for $W > 1.6$ GeV, it is especially important to take into account the coupling of the initial and the final state with open inelastic channels. For the quasi-two-body reactions (1) and (2), an approach was developed in [7–11] that makes it possible to obtain a model-dependent description of initial- and final-state interaction. The set of these effects is considered as the absorption of incident and emitted particles in the initial and in the final reaction state [13]. The coefficients of transmission (absorption) are related to the amplitudes for elastic $\pi\Delta$ and ρp scattering. These amplitudes in turn are calculated within the isobaric model [14], which employs the set of world-averaged data on the amplitudes of pion–nucleon scattering.

In [7, 8, 15], a model was proposed for describing the cross sections for the reaction $\gamma p \to \pi^+\pi^-p$ at the photon point ($Q^2 = 0$) by using the model from [9–11] for the quasi-two-body processes (1)–(3). In the present study, this approach is generalized to describe the fivefold differential cross sections for the virtual-photon-induced reaction $\gamma_{r,v}p \to \pi^+\pi^-p$ in a full kinematics. The only limitation on the approach is that the square of the virtual-photon 4-momentum, $Q^2 = -q_\mu^2$, must lie in the region where the reaction amplitude can be described in terms of meson–baryon degrees of freedom. The question of the boundary where a transition between meson–baryon and quark–gluon degrees of freedom occurs remains open; it can only be solved on the basis of a comparison of theoretical results with future experimental data. The expected applicability range of the proposed approach corresponds to $Q^2 < 3 - 4$ GeV^2.

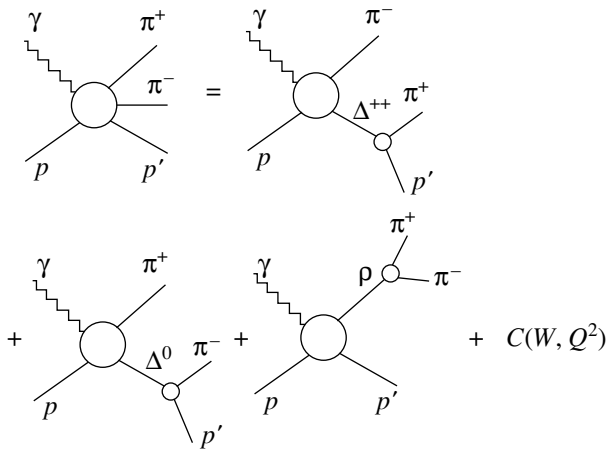

Fig. 1. Dominant mechanisms of the reaction $\gamma_{r,v}p \to \pi^+\pi^-p$.

2. DESCRIPTION OF THE PRODUCTION OF $\pi^+\pi^-$ PAIRS ON A PROTON BY VIRTUAL PHOTONS

The Dalitz distributions of $\pi^+\pi^-$ and π^+p systems show pronounced features—these are bands corresponding to the formation of particles in the intermediate state and their subsequent decays, $\Delta^{++} \to \pi^+p$, $\Delta^0 \to \pi^-p$, and $\rho \to \pi^+\pi^-$. In accordance with these data, the mechanisms of the reaction $\gamma_v p \to \pi^+\pi^-p$ are represented by the sum of diagrams in Fig. 1. The set of other processes contributing to the amplitude of the reaction $\gamma_v p \to \pi^+\pi^-p$ is described by the amplitude $C(W, Q^2)$ that depends neither on the helicities of the particles involved in the reaction being considered nor on the kinematical variables of the final state, but which is dependent on W and Q^2. In the model used, the amplitude $C(W, Q^2)$ is the only free parameter, which is determined from a fit to the measured double differential cross section $d^2\sigma/(dM_{\pi^+\pi^-}dM_{\pi^+p})$ or $d\sigma/dM_{\pi^+\pi^-}$ and $d\sigma/dM_{\pi^+p}$ (or all of them), where $M_{\pi^+\pi^-}$ and M_{π^+p} are the invariant masses of the $\pi^+\pi^-$ and π^+p systems at various values of W and Q^2.

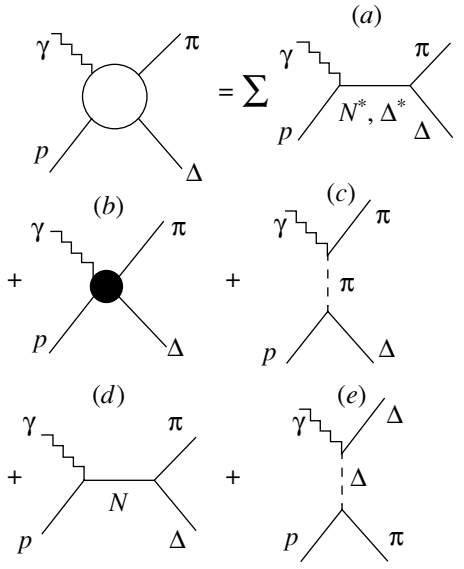

Fig. 2. Diagrams describing $\pi\Delta$ photo- and electroproduction on a proton.

For the processes described by the diagrams in Fig. 1, the amplitude is calculated in the Breit–Wigner approximation. The total amplitude $\langle\lambda_f\,|T|\,\lambda_\gamma\lambda_p\rangle$ for the reaction $\gamma_{r,v}p \to \pi^+\pi^-p$ is given by

$$\begin{aligned}\langle\lambda_f\,|T|\,\lambda_\gamma\lambda_p\rangle &= \sum_{\lambda_{\Delta^{++}}} \frac{\langle\lambda_{\Delta^{++}}\pi^-\,|T|\,\lambda_\gamma\lambda_p\rangle\langle\pi^+\lambda_{p'}\,|T|\,\lambda_{\Delta^{++}}\rangle}{S_{\pi^+p} - M_\Delta^2 + i\Gamma_\Delta(S_{\pi^+p})M_\Delta} \\ &+ \sum_{\lambda_{\Delta^0}} \frac{\langle\lambda_{\Delta^0}\pi^+\,|T|\,\lambda_\gamma\lambda_p\rangle\langle\pi^-\lambda_{p'}\,|T|\,\lambda_{\Delta^0}\rangle}{S_{\pi^-p} - M_\Delta^2 + i\Gamma_\Delta(S_{\pi^-p})M_\Delta} \\ &+ \sum_{\lambda_\rho} \frac{\langle\lambda_\rho\lambda_{p'}\,|T|\,\lambda_\gamma\lambda_p\rangle\langle\pi^+\pi^-\,|T|\,\lambda_\rho\rangle}{S_{\pi^+\pi^-} - M_\rho^2 + i\Gamma_\rho(S_{\pi^+\pi^-})M_\rho} \\ &+ C(Q^2, W),\end{aligned} \tag{4}$$

where the amplitudes $\langle\lambda_{\Delta^{++}}\pi^-\,|T|\,\lambda_\gamma\lambda_p\rangle$, $\langle\lambda_{\Delta^0}\pi^+\,|T|\,\lambda_\gamma\lambda_p\rangle$, and $\langle\lambda_\rho\lambda_{p'}\,|T|\,\lambda_\gamma\lambda_p\rangle$ correspond to the quasi-two-body processes (1)–(3) with the initial-state photon and proton helicities equal to λ_γ and λ_p, respectively, and the final-state Δ^{++}, Δ^0, ρ, and p' helicities equal to $\lambda_{\Delta^{++}}$, λ_{Δ^0}, λ_ρ, and $\lambda_{p'}$, respectively; the amplitudes $\langle\pi^+\lambda_{p'}\,|T|\,\lambda_{\Delta^{++}}\rangle$, $\langle\pi^-\lambda_{p'}\,|T|\,\lambda_{\Delta^0}\rangle$, and $\langle\pi^+\pi^-\,|T|\,\lambda_\rho\rangle$ describe the decay processes $\Delta^{++} \to \pi^+p$, $\Delta^0 \to \pi^-p$, and $\rho \to \pi^+\pi^-$, respectively; M_Δ and M_ρ are the masses of Δ and ρ; $\Gamma_\Delta(S_{\pi p})$ and $\Gamma_\rho(S_{\pi^+\pi^-})$ are their widths; $C(Q^2, W)$ is the amplitude corresponding to the three-body phase space; and $S_{\pi^+\pi^-}$, S_{π^-p}, and S_{π^+p} are the squares of the invariant masses of the $\pi^+\pi^-$, π^-p, and π^+p systems, respectively. A detailed account of the models for describing the amplitudes for the quasi-two-body processes (1)–(3) is given in [9–11]. The amplitudes for the decay processes $\Delta^{++} \to \pi^+p$, $\Delta^0 \to \pi^-p$, and $\rho \to \pi^+\pi^-$ were calculated in the approximation of effective Lagrangians with the s-channel form factors [16] depending on the invariant mass of the products in the initial state and were discussed in detail elsewhere [15]; the relations between the amplitudes in Eq. (4) and the fivefold differential cross sections for the reactions $\gamma_{r,v}p \to \pi^+\pi^-p$ are also presented in [15]. Here, we focus on special features in describing the amplitudes for the quasi-two-body reactions (1)–(3) induced by virtual photons.

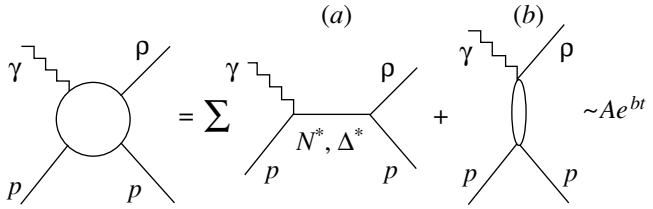

Fig. 3. Diagrams describing ρp photo- and electroproduction (the quantities A and b are defined according to [12]).

The nonresonance mechanisms in the quasi-two-body reactions being considered are described by the set of diagrams in Figs. 2 and 3. In dealing with virtual-photon interaction, the $\gamma\pi\pi$ vertex function $F_{\gamma\pi\pi}(Q^2)$ is introduced in the diagram in Fig. 2c (pion in flight), the effects of the internal structure of the π, p, and Δ particles in the strong-interaction vertex being taken into account in our approach through the vertex function $F_{\pi p\Delta}(t)$, which is determined from data on nucleon–nucleon scattering [17]. Data from [18] on the pion electromagnetic form factor are used as input information for reconstructing the vertex function $F_{\gamma\pi\pi}(Q^2)$ [18]. In [18], the pion form factor was determined from experimental data on single-pion electroproduction at small c.m. angles of $\theta < 5^\circ (t \simeq 0)$ under the assumption of $F_{\pi p\Delta} = 1$. Therefore, the vertex function $F_{\gamma\pi\pi}(Q^2)$ used in our approach is related to the pion electromagnetic form factor $F_\pi(Q^2)$ defined in [18] by the relation

$$F_{\gamma\pi\pi}(Q^2) = \frac{F_\pi(Q^2)}{F_{\pi p\Delta}(t = t_{\min})}, \tag{5}$$

where $t_{\min}$ is the Mandelstam t invariant at zero pion emission angle in the c.m. frame. The vertex function

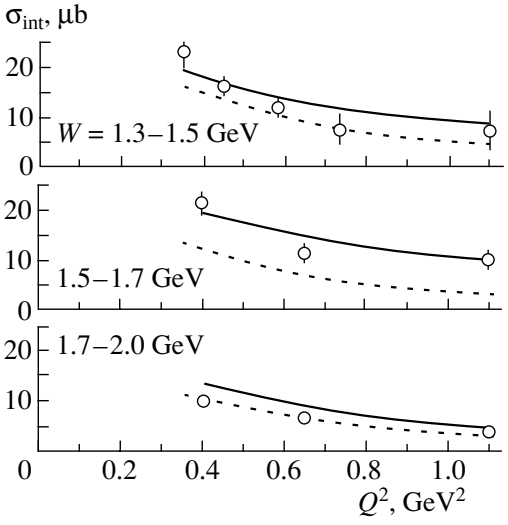

Fig. 4. Integrated cross sections for the reaction $\gamma_v p \to \pi^- \Delta^{++}$ versus Q^2: (dashed curve) results of the calculations that take into account the contributions from only nonresonance terms and (solid curve) results of the calculations that take into account the contributions from nucleon resonances and from nonresonance processes. Experimental data were borrowed from [19].

for the contact term, $F_c(Q^2, t)$ (Fig. 2*b*), is given by [9]

$$F_c(Q^2, t) = F_{\gamma\pi\pi}(Q^2) F_{\pi p\Delta}(t). \qquad (6)$$

In describing the nucleon term (see Fig. 2*d*), the proton form factor $F_p(Q^2)$ in the dipole approximation of experimental data, which has the form

$$F_p(Q^2) = \frac{1}{(1 + Q^2/0.71)^2}, \qquad (7)$$

where Q^2 is measured in GeV^2, is introduced in the electromagnetic vertex. In our model, the initial- and the final-state interaction with open inelastic channels is effectively described by the complex-valued absorption factors $f^j_{\rm ISI}$ and $f^j_{\rm FSI}$, which are dependent on the total channel spin J and which are related to the S-matrix elements for elastic ρp and $\pi\Delta$ scattering by the equations [7, 11]

$$f^j_{\rm ISI} = \langle \rho p \left| S^J \right| \rho p \rangle^{1/2} \qquad (8)$$
$$f^j_{\rm FSI} = \langle \pi\Delta \left| S^J \right| \pi\Delta \rangle^{1/2}.$$

Within the approach proposed in [7, 11, 14], these matrix elements were determined from experimental data on pion–nucleon scattering. That the photon is off the mass shell leads to the Q^2 dependence of initial-state-interaction effects. Assuming that transitions of the initial-state photon into hadrons are governed primarily by vector dominance, we obtain the Q^2 dependence in the form

$$f^j_{\rm ISI}(Q^2) = \frac{\Lambda_\pi^2 f^j_{\rm ISI}(Q^2 = 0) + Q^2}{\Lambda_\pi^2 + Q^2}, \qquad (9)$$

where the parameter Λ_π^2 determined from data on single-pion electroproduction is 0.46 GeV^2 [18].

The Q^2 dependence of nonresonance processes in the quasi-two-body reaction (3) is described within the diffraction vector-dominance model [18]. The relevant amplitude determined at the photon point is multiplied by the quantity

$$g(Q^2) = \frac{1}{1 + \dfrac{Q^2}{m_\rho^2}} \sqrt{\frac{P_\gamma(Q^2 = 0)}{P_\gamma(Q^2)}}, \qquad (10)$$

where m_ρ is the ρ-meson mass and P_γ is the absolute value of the photon momentum at given W. The first factor on the right-hand side of Eq. (10) is the ρ-meson propagator, while the second corresponds to the transformation of the flux in going over from real to virtual photons.

3. DISCUSSION OF THE RESULTS

Experimental data on the reaction $\gamma_v p \to \pi^+\pi^- p$ and on its quasi-two-body channels (1)–(3) are systematized in [19]. The integrated cross sections for the quasi-two-body channel (1) that were calculated within the approach proposed here are displayed in Fig. 4 versus Q^2, along with data from [19]. The nucleon-resonance electromagnetic form factors as functions of Q^2 were obtained on the basis of the approach developed by Burkert [20], who used the entire body of available experimental data on the Q^2 dependences of the electromagnetic form factors for nucleon resonances. In the case where there were no relevant data, the electromagnetic form factors for nucleon resonances were determined from the relations of $SU(6)$ symmetry for the electromagnetic-transition operator and the wave functions for states entering into the $SU(6)$ multiplets. In order to investigate the nucleon-resonance contributions to the cross section for reaction (1), we have performed calculations with allowance for only Born terms (dashed curves in Fig. 4) and with allowance for the superposition of Born terms and nucleon-resonance contributions (solid curves in Fig. 4). In comparing the results of the calculations with experimental data from [19], it should be borne in mind that these data were averaged over wide regions of W (≥ 0.26 GeV) and Q^2 (≥ 0.26 GeV^2) (this was necessary for experimentally collecting required statistics). Over the interval of averaging, the cross section changes within a factor of 1.5, these changes being even more

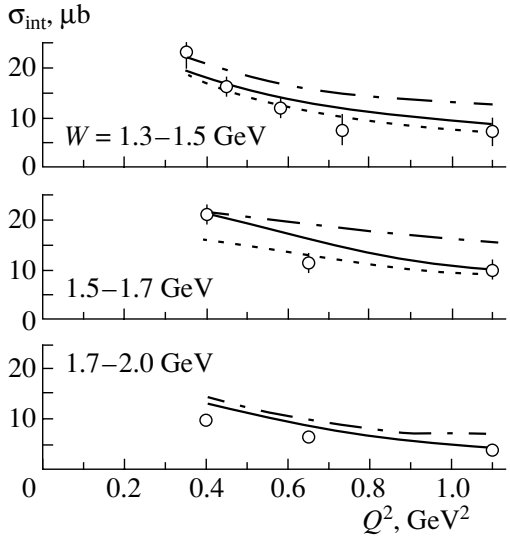

Fig. 5. As in Fig. 4 but for model calculations employing γpN^* vertices from the study of Burkert [20], who relied on an $SU(6)$ interpolation of experimental data (solid curve), and the γpN^* vertices as computed within the quark models from [21] (dashed curve) and from [22] (dash-dotted curve).

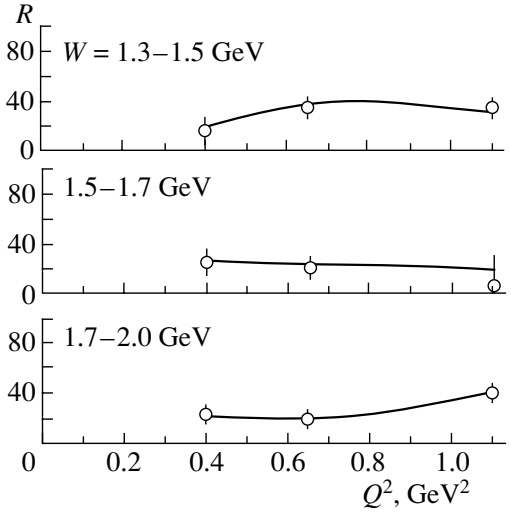

Fig. 6. Results obtained from a fit to experimental data on the contribution R of the three-body phase space to the cross section for the reaction $\gamma_v p \to \pi^+\pi^- p$ by varying the amplitude $C(W, Q^2)$ [see Eq. (4)] in accordance with the concepts of the model proposed in the present study.

pronounced at small W. As can be seen from Fig. 4, the calculations faithfully reproduce the entire body of experimental data on the quasi-two-body channel (1). The observed deviations are within the aforementioned systematic uncertainty in the experimental data.

The nucleon-resonance contribution to the integrated cross section for channel (1) grows sharply with increasing Q^2. In the interval of W from 1.5 to 1.7 GeV at Q^2 above 0.8 GeV^2, the nucleon-resonance contribution exceeds 50%, while it is below 20–30% at the photon point. Thus, experiments with virtual-photon beams at 0.8 GeV^2 open a good possibility for obtaining experimental data on the structure of nucleon resonances at distances corresponding to the transition between confinement and perturbative QCD.

The integrated cross sections for channel (1) that were calculated with the nucleon-resonance electromagnetic form factors as determined from the analysis of experimental data in [20] are displayed in Fig. 5, along with analogous results based on the form factors calculated on the basis of quark models [21, 22]. Within the model used in [22], a nucleon resonance is described as a system of three constituent quarks in a one-gluon-exchange confining potential, the $SU(6)$ configurations being mixed here. Additionally, allowances are made for the effects of three-particle interactions between the quarks. In the model developed in [21], the motion of the quarks in a nucleon resonance is described in the approximation of two-particle interactions between the quarks; however, the algebraic approach used leads to a significant expansion of the basis configuration space in relation to the model from [22], with the result that two-particle correlations in the motion of the quarks can efficiently be taken into account within this approach. From Fig. 5, we can see that the calculations performed in [20–22] reproduce basic features in the behavior of experimental data, and we can hardly give preference to one of the approaches in view of the aforementioned uncertainties in the data. However, there are noticeable distinctions between the cross sections calculated with the different nucleon-resonance electromagnetic form factors from [21] and [22]. By comparing the results obtained by calculating, within the model proposed here, the integrated cross sections for the processes $\gamma_{r,v} p \to \pi^+\pi^- p$ with effective nucleon-resonance form factors evaluated on the basis of various model approaches and the future precision experimental data from TJNAF [2, 3] on the Q^2 dependences of the integrated cross sections, one would therefore be able to choose the most adequate model approximations for describing the structure of nucleon resonances and to reveal thereby mechanisms that determine the formation of this structure in the transition region between confinement and the asymptotic freedom of quarks.

It was noted above that, in describing the total cross sections for the reaction $\gamma_v p \to \pi^+\pi^- p$, our model involves only one free parameter, the amplitude $C(W, Q^2)$, which was determined from a fit to exper-

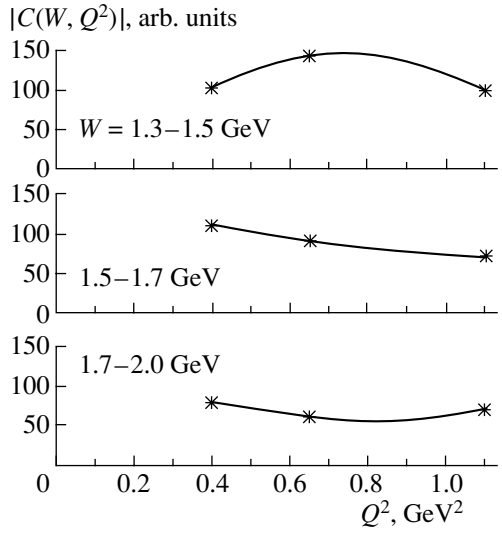

Fig. 7. Amplitudes $C(W, Q^2)$ [see Eq. (4)] deduced from a fit to data from [19] on the relative contribution of the three-body phase space to the cross section for the reaction $\gamma_v p \to \pi^+\pi^- p$.

imental data from [19] on the relative contribution of the three-body phase space to the cross section for the reaction $\gamma_v p \to \pi^+\pi^- p$. This fit is illustrated in Fig. 6, while the resulting values of $C(W, Q^2)$ are given in Fig. 7. At intermediate kinematical points (W, Q^2), the amplitude $C(W, Q^2)$ was determined by interpolating the values displayed in Fig. 7.

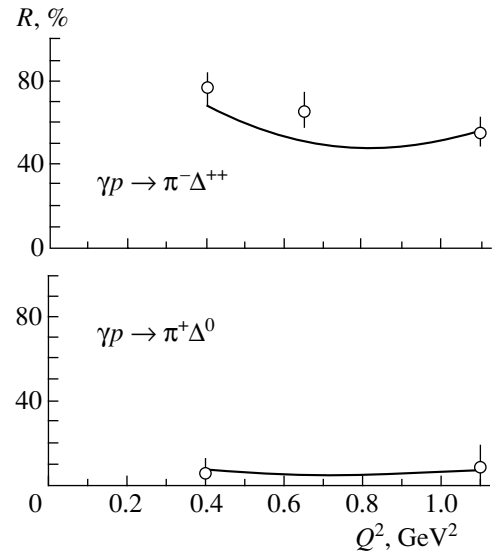

Fig. 8. Comparison of data from [19] with the results of the calculations based on the model developed in the present study and performed for the relative contribution R of the quasi-two-body channels (1)–(3) to the cross section for the reaction $\gamma_v p \to \pi^+\pi^- p$ in the range W = 1.3–1.5 GeV.

Figures 8–10 show the experimental data from [19] on the relative contribution of the quasi-two-body channels (1)–(3) to the total cross section for the reaction $\gamma_v p \to \pi^+\pi^- p$. Within the model developed in the present study, we have calculated the total integrated cross sections for this reaction as functions of Q^2 and determined the contributions of the quasi-two-body channels (1)–(3) to the total cross section for this reaction. The results are shown in Figs. 8–10 by solid curves. The data from [19] are faithfully reproduced in the regions W = 1.3–1.5 GeV and 1.5–1.7 GeV. In the interval W = 1.7–2.0 GeV, the calculated contribution of channel (1) is above the data from [19], while the calculated contribution of channel (3) is below them. These discrepancies may be due both to the aforementioned uncertainties in the data (they are especially pronounced in the range W = 1.7–2.0 GeV) and to additional mechanisms that manifest themselves in nonresonance processes of the quasi-two-body channel (1), where the t-channel diagram (Fig. 2*b*) may receive contributions not only from the exchange of a π meson but also from exchanges of other particles. According to [23], such processes can be effectively taken into account by replacing the exchange of a π meson by the exchange of the π-meson Regge trajectory. The discrepancies can also be associated with the contributions of high-lying nucleon resonances ($M_{N^*} > 1.9$ GeV). For want of experimental data, the electromagnetic form factors for such resonances were estimated on the basis of the model from [20]. There is yet another factor that could be invoked in explaining the above discrepancies: according to [24], the energy region being discussed may house missing resonances, baryonic states involving a considerable

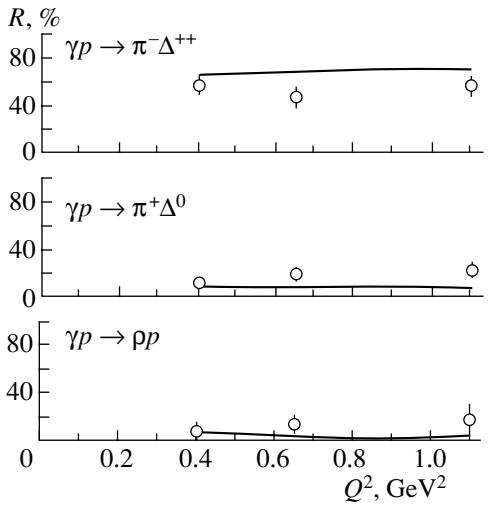

Fig. 9. As in Fig. 8, but for the range W = 1.5–1.7 GeV.

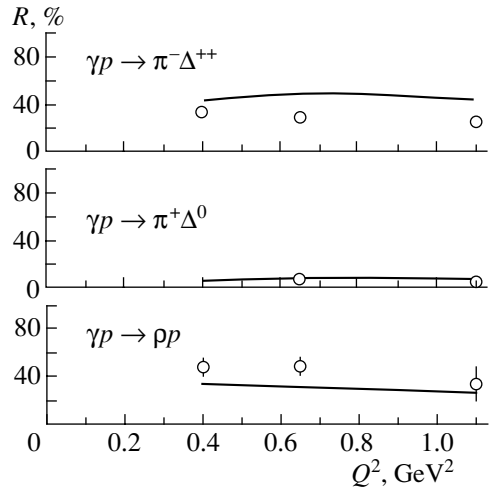

Fig. 10. As in Fig. 8, but for the range $W = 1.7$–2.0 GeV.

fraction of decays into final states that contain pion pairs.

4. CONCLUSION

A phenomenological model has been developed for describing the production of $\pi^+\pi^-$ pairs on a proton by virtual photons in the energy region of nucleon-resonance excitation ($W \leq 2.0$ GeV). The proposed approach can be used to study this exclusive channel for Q^2 less than 3 to 4 GeV^2, in which case the amplitude of the process can be defined in terms of meson–baryon degrees of freedom. Our model describes satisfactorily the entire body of experimental data on the Q^2 dependences of the cross sections for the reaction $\gamma_v p \to \pi^+\pi^- p$ and for its quasi-two-body channels in the energy region of nucleon-resonance excitation ($W \ll 2.0$ GeV) and for $Q^2 < 1$ GeV^2. The nucleon-resonance contribution to the cross section for the reaction $\gamma_v p \to \pi^+\pi^- p$ increases sharply with Q^2, exceeding 50% at Q^2 around 1.0 GeV^2 (Fig. 5). A comparative analysis has revealed considerable distinctions between the cross sections calculated by using different model descriptions of the electromagnetic form factors for nucleon resonances. A comparison of the calculated integrated and differential cross sections for the reactions $\gamma_{r,v} p \to \pi^+\pi^- p$ with TJNAF experimental data [2, 3] would make it possible to choose the most adequate description of these form factors and to pinpoint specific mechanisms that form the structure of nucleon resonances in the transition region between confinement and perturbative QCD.

REFERENCES

1. V. D. Burkert, in *Proceedings on Joint ECT*/JLAB Workshop on N* Physics and Nonperturbative QCD, Trento, Italy, 1998,* Ed. by S. Simula *et al.;* Few-Body Syst. Suppl. **11**, 1 (1999).
2. V. D. Burkert, M. Ripani, *et al.,* Jlab Internal Document CEBAF Experiment E-93-006.
3. M. Ripani, Nucl. Phys. A **623**, 110c (1997); **664**, 675 (2000).
4. S. Nozava, B. Blankleider, and T.-S. H. Lee, Nucl. Phys. A **513**, 459 (1990).
5. I. Surya and F. Gross, Preprint CEBAF-TH-95-04 & WM-95-101.
6. T. Feuster and U. Mosel, Phys. Rev. C **59**, 460 (1999).
7. V. Mokeev *et al.,* in *Proceedings on Joint ECT*/JLAB Workshop on N* Physics and Nonperturbative QCD, Trento, Italy, 1998,* Ed. by S. Simula *et al.;* Few-Body Syst. Suppl. **11**, 293 (1999).
8. M. Ripani, in *Proceedings on Joint ECT*/JLAB Workshop on N* Physics and Nonperturbative QCD, Trento, Italy, 1998,* Ed. by S. Simula *et al.;* Few-Body Syst. Suppl. **11**, 284 (1999).
9. M. Anghinolfi *et al.,* Yad. Fiz. **62**, 1522 (1999) [Phys. At. Nucl. **62**, 1437 (1999)].
10. M. Anghinolfi, M. Battaglieri, E. N. Golovach, *et al.,* Yad. Fiz. **63**, 85 (2000) [Phys. At. Nucl. **63**, 76 (2000)].
11. M. Ripani, V. Mokeev, *et al.,* Nucl. Phys. A **672**, 220 (2000).
12. D. G. Cassel *et al.,* Phys. Rev. D **24**, 2787 (1981).
13. K. Gottfried and J. Jackson, Nuovo Cimento **34**, 735 (1964).
14. V. I. Mokeev and M. V. Osipenko, Vest. Mosk. Univ., Ser. 3: Fiz., Astron., No. 6, 14 (1999).
15. M. Ripani, V. Mokeev, M. Battaglieri, *et al.,* Yad. Fiz. **63**, 2036 (2000) [Phys. At. Nucl. **63**, 1943 (2000)].
16. R. R. Longacre and J. Dolbeu, Nucl. Phys. B **122**, 493 (1977).
17. R. Machleidt, K. Holinde, and Ch. Elster, Phys. Rep. **149**, 1 (1987).
18. C. J. Bebek *et al.,* Phys. Rev. D **17**, 1693 (1978).
19. K. Wacker *et al.,* Nucl. Phys. B **144**, 269 (1978).
20. V. D. Burkert, Preprint CEBAF-PR-93-035.
21. R. Bijker, F. Iachello, and A. Levitan, Phys. Rev. C **54**, 1935 (1996).
22. M. M. Giannini and E. Santopinto, in *Proceedings of the Joint ECT*/JLAB Workshop on N* Physics and Nonperturbative QCD, Trento, Italy, 1998,* Ed. by S. Simula *et al.;* Few-Body Syst. Suppl. **11**, 37 (1999).
23. M. Guidal, J. M. Laget, and M. Vanderhaeghen, Phys. Lett. B **400**, 6 (1997).
24. S. Capstik and W. Roberts, Phys. Rev. D **49**, 4570 (1994).

Translated by A. Isaakyan

Physics of Atomic Nuclei, Vol. 64, No. 7, 2001, pp. 1299–1314. Translated from Yadernaya Fizika, Vol. 64, No. 7, 2001, pp. 1375–1390.

ELEMENTARY PARTICLES AND FIELDS
Theory

Infrared Quasifixed Solutions in a Nonminimal Supersymmetric Standard Model

R. B. Nevzorov and M. A. Trusov

Institute of Theoretical and Experimental Physics, Bol'shaya Cheremushkinskaya ul. 25, Moscow, 117259 Russia

Received March 24, 2000; in final form, June 28, 2000

Abstract—The constraints from LEPII on the mass of the lightest Higgs boson are such that, in the parameter space of the minimal supersymmetric standard model (MSSM), a considerable part of the region that corresponds to the scenario of an infrared fixed point is virtually ruled out by available experimental data. In a nonminimal supersymmetric standard model (NMSSM), the mass of the lightest Higgs boson takes its maximum value in the regime of strong Yukawa coupling, in which case the Yukawa coupling constants are much greater than the gauge coupling constants at the Grand Unification scale ($Y_i(0) \gg \tilde{\alpha}_i(0)$). In this limiting case, solutions to the renormalization-group equations are attracted to Hill and infrared fixed lines or surfaces in the space of Yukawa coupling constants; for $Y_i(0) \to \infty$, they are concentrated in the vicinities of quasifixed points. However, this attraction is quite weak. For this reason, solutions to the renormalization-group equations are grouped near some line on the Hill surface when all $Y_i(0)$ are close to unity. Approximate solutions for the Yukawa coupling constants within the NMSSM are presented. In addition, the possibility of unifying the Yukawa coupling constants for the b quark and the τ lepton at the scale M_X is discussed. © *2001 MAIK "Nauka/Interperiodica".*

1. INTRODUCTION

The existence of quasifixed points is among the most spectacular and the most interesting properties of renormalization-group equations. A feature characteristic of those solutions to renormalization-group equations that approach such points is that a number of fundamental parameters of the theory are focused in a narrow interval in the infrared region. This means that, at the electroweak scale, some constants or their combinations cease to depend on the boundary conditions. That solutions to renormalization-group equations behave in so peculiar a way in the vicinities of quasifixed points results in that the parameter space of the theory being considered is constrained for a wide class of such solutions. As a result, the predictive power of the theories being discussed becomes higher near these points. Nonetheless, it turns out that, within the minimal Standard Model (SM), the quasifixed-point scenario leads to overly high a value for the mass of the t quark, that which contradicts experimental data obtained at FNAL.

In contrast to the SM, its supersymmetric (SuSy) generalization—the minimal SuSy standard model (MSSM)—features two Higgs doublets (not one), H_1 and H_2. Upon a spontaneous breakdown of symmetry, they develop nonzero vacuum expectation values v_1 and v_2, with the constraint $v^2 = v_1^2 + v_2^2 = (246\ \text{GeV})^2$ being satisfied. In relation to what occurs in the SM, the t-quark running mass m_t that is generated within SuSy models upon the breakdown of $SU(2) \times U(1)$ gauge symmetry involves an additional factor $\sin\beta$,

$$m_t(M_t^{\text{pole}}) = \frac{h_t(M_t^{\text{pole}})}{\sqrt{2}} v \sin\beta, \qquad (1)$$

where $\tan\beta = v_2/v_1$ and h_t is the Yukawa coupling constant for the t quark. Since $\sin\beta \le 1$, $m_t(M_t^{\text{pole}})$ is always less in the MSSM than in the SM at the same values of the Yukawa coupling constants. Recent experimental data on the t-quark mass make it possible to determine $m_t(M_t^{\text{pole}})$ within the $\overline{MS}$ scheme [1]. It proves to be $m_t(M_t^{\text{pole}}) = 165 \pm 5$ GeV. The uncertainty in the determination of the running mass of the t quark stems predominantly from the experimental error with which its pole mass was measured ($M_t^{\text{pole}} = 174.3 \pm 5.1$ GeV [2]).

Equation (1) unambiguously relates $\tan\beta$ to the value of the Yukawa coupling constant for the t quark at the electroweak scale. At modest values of $\tan\beta$ ($\tan\beta \ll 50 - 60$), the Yukawa coupling constants for the b quark, h_b, and for the τ lepton, h_τ, are negligibly small, which makes it possible to obtain an analytic solution to the renormalization-group equation within the MSSM [3]. In this case, the boundary conditions are imposed at the scale $M_X \approx 3 \times$

10^{16} GeV, where the gauge coupling constants are naturally unified within the MSSM. For the t-quark Yukawa coupling constant, it is convenient to represent an exact solution to the renormalization-group equations in the form

$$Y_t(t) = \frac{E(t)}{6F(t)}\left(1 + \frac{1}{6Y_t(0)F(t)}\right)^{-1}, \qquad (2)$$

where $Y_t(t) = h_t^2(t)/(4\pi)^2$ and $t = \ln(M_X^2/q^2)$. The explicit expressions for the functions $E(t)$ and $F(t)$ are presented in the Appendix [see (A.4)]. At the electroweak scale, the second term in parentheses is much less than unity for $h_t^2(0) \geq 1$. The dependence of $h_t^2(t)$ on the initial conditions at $t = 0$ is weak, and the relevant solution to the renormalization-group equations approaches a quasifixed point [4]: $Y_{\rm QFP}(t) = E(t)/6F(t)$. Formally, a solution of this type can be obtained by making $Y_t(0)$ tend to infinity in expression (2). The situation here is, however, different from that near the Pendleton–Ross infrared fixed point [5–8], which solutions to the renormalization-group equations approach only in the asymptotic regime for $q^2 \to 0$: the deviation from $Y_{\rm QFP}(t)$ at finite values of $Y_t(0)$ is determined by the ratio $Y_{\rm QFP}(t)/(E(t)Y_t(0))$, which is of order $1/(10h_t^2(0))$ at the electroweak scale and which is small at comparatively large $h_t^2(0)$ ($h_t^2(0) \geq 1$). For a wide class of solutions, this interesting property of the renormalization-group equations within the MSSM makes it possible to predict quite precisely the value of the Yukawa coupling constant for the t quark at the scale $q = M_t^{\rm pole}$,

$$h_{\rm QFP}^2(t_0) = 0.87g_3^2(t_0) = 1.26, \qquad (3)$$

where g_3 is the gauge coupling constant for strong interaction and $t_0 = 2\ln(M_X/M_t^{\rm pole})$. The accuracy of this prediction becomes higher with increasing $h_t^2(0)$. At sufficiently large initial values of $Y_t(t)$, it would be illegitimate to restrict the analysis to one-loop renormalization-group equations—it is necessary to take into account higher order perturbative corrections. Moreover, the value of the Yukawa coupling constant for the t quark at the electroweak scale depends on the strong-interaction coupling constant, which we set to $\alpha_3(M_Z) = 0.118$. Nevertheless, all these uncertainties do not lead to significant deviations from (3). By way of example, we indicate that the calculations that were performed in [9] and which employed the four-loop beta function showed that deviations from (3) are within 2%.

For each fixed value of $Y_t(0)$, the Yukawa coupling constant for the t quark at the electroweak scale can be evaluated by using the exact analytic solution (2), whereupon $\tan\beta$ can be determined by substituting the resulting value of $h_t(t_0)$ into (4). The theoretical analysis performed in [10–13] revealed that, for the renormalization-group equations within the MSSM, a broad class of solutions corresponding to the infrared-quasifixed-point regime leads to $\tan\beta$ values ranging between 1.3 and 1.8. With increasing Yukawa coupling constant for the t quark, the corresponding trilinear coupling constant A_t for the interaction of scalar particles and the combination $\mathfrak{M}_t^2 = m_Q^2 + m_U^2 + m_2^2$ of the scalar-particle masses cease to depend on the initial conditions. In the vicinity of the quasifixed point, they are expressed in terms of only the gaugino mass at the scale M_X, with the result that the parameter space is further constrained. In the infrared-quasifixed-point regime at $\tan\beta \sim 1$, the properties of solutions to the set of renormalization-group equations and the spectrum of particles were investigated in [8, 12–16].

Finally, there is yet another circumstance that appears as an incentive to study the limit of strong Yukawa coupling within the MSSM. Minimal schemes that are used to unify gauge interactions and which are based on gauge groups like $SU(5)$, E_6, or $SO(10)$ predict the equality of the Yukawa coupling constants h_b and h_τ for, respectively, the b quark and the τ lepton at the scale M_X [17]. Within the MSSM, h_b and h_τ are unified at two specific values of $h_t(M_t^{\rm pole})$. One of these falls within a narrow region near $h_{\rm QFP}(t_0)$, while the other corresponds to the scenario of large $\tan\beta$. In more detail, the problem of $b\tau$ unification within the MSSM was discussed in [7, 15, 16, 18–20].

The spectrum of the Higgs sector of the MSSM contains four massive states: two CP-odd states, one CP-even state, and one charged state. The presence of a light Higgs boson in the CP-even sector is an important feature of SuSy models. The upper limit on its mass greatly depends on $\tan\beta$. A reduction of the number of independent parameters in the infrared-quasifixed-point regime made it possible to determine, to a sufficiently high degree of precision, an upper limit on the mass of the lightest CP-odd Higgs boson. In the case being considered, comparatively small values of $\tan\beta$ result in that its mass does not exceed 94 ± 5 GeV [11–13]. This limit is 25–30 GeV lower than the absolute upper limit in the minimal SuSy model. At the same time, the lower limit on the mass of the lightest Higgs boson from LEPII data—in the case of a heavy spectrum of SuSy particles, it coincides with the corresponding limit on the Higgs boson mass in the SM—is 113.3 GeV [21]. Actually, this means that a major part of solutions approaching the infrared quasifixed point within the MSSM have already been ruled out by the existing LEPII data. In order to meet the experimental constraints on the

Values of the Yukawa coupling constants at the electroweak scale for various initial values $\kappa^2(0)$, $\lambda^2(0)$, and $h_t^2(0)$

$\kappa^2(0)$	$\lambda^2(0)$	$h_t^2(0)$	$\kappa^2(t_0)$	$\lambda^2(t_0)$	$h_t^2(t_0)$	$h_t^2(t_0)+$ $0.506\lambda^2(t_0)$	$h_t^2(t_0)+0.72\times$ $\lambda^2(t_0)+0.33\kappa^2(t_0)$
0	10	10	0	0.3220	1.1538	1.3180	1.3857
0	6	10	0	0.2879	1.1675	1.3143	1.3747
0	2	10	0	0.1911	1.1987	1.2962	1.3363
0	10	6	0	0.3492	1.1327	1.3108	1.3841
0	6	6	0	0.3167	1.1475	1.3090	1.3755
0	2	6	0	0.2203	1.1815	1.2939	1.3402
0	10	2	0	0.4209	1.0513	1.2659	1.3543
0	6	2	0	0.3901	1.0715	1.2704	1.3524
0	2	2	0	0.2941	1.1160	1.2660	1.3277
10	10	10	0.1480	0.2480	1.1737	1.3002	1.4011
10	6	10	0.1995	0.1969	1.1904	1.2908	1.3980
10	2	10	0.2956	0.0979	1.2193	1.2692	1.3874
10	10	6	0.1256	0.2801	1.1527	1.2956	1.3958
10	6	6	0.1760	0.2279	1.1712	1.2875	1.3934
10	2	6	0.2785	0.1192	1.2047	1.2655	1.3825
10	10	2	0.0865	0.3601	1.0734	1.2570	1.3612
10	6	2	0.1305	0.3060	1.0984	1.2545	1.3618
10	2	2	0.2385	0.1775	1.1458	1.2363	1.3523
2	10	10	0.0655	0.2941	1.1608	1.3108	1.3942
2	6	10	0.1055	0.2482	1.1767	1.3033	1.3903
2	2	10	0.2059	0.1396	1.2092	1.2804	1.3777
2	10	6	0.0521	0.3244	1.1395	1.3049	1.3903
2	6	6	0.0875	0.2798	1.1567	1.2994	1.3870
2	2	6	0.1865	0.1663	1.1929	1.2778	1.3742
2	10	2	0.0322	0.4007	1.0582	1.2625	1.3573
2	6	2	0.0578	0.3581	1.0810	1.2637	1.3580
2	2	2	0.1464	0.2361	1.1297	1.2501	1.3480

mass of the lightest Higgs boson, it is necessary either to go over to studying solutions that lead to large values of $\tan\beta$ within the MSSM or to extend the Higgs sector of the minimal SuSy model. The detailed investigations that were performed in [13, 16, 19, 22] revealed that, at $\tan\beta \approx 50$–60, solutions to the renormalization-group equations also approach the infrared quasifixed point, the basic properties of the solutions remaining unchanged.

The nonminimal SuSy SM (NMSSM) [23–25] whose Higgs sector contains, in addition to the doublets H_1 and H_2, an extra superfield Y that is a singlet with respect to $SU(2) \times U(1)$ gauge interactions is the simplest extension of the MSSM. In the parameter space of the NMSSM, the region that corresponds to the limit of strong Yukawa coupling, in which case the Yukawa coupling constants $Y_i(0)$ at the Grand Unification scale M_X are much greater than the gauge coupling constant $\tilde{\alpha}(0)$, is that which is the most appealing from the point of view of a theoretical analysis. It is the region where the upper limit on the mass of the lightest Higgs boson takes

a maximum value that is a few GeV greater than the corresponding absolute limit within the MSSM [26]. Moreover, it is possible, in the case being considered, to choose coupling constants in such a way as to obtain the unification of the Yukawa coupling constants for the b quark and the τ lepton at the scale M_X.

For the Yukawa coupling constants in the limit of strong Yukawa coupling, we study here basic properties of solutions to the renormalization-group equations within the NMSSM. We show that, in the limit $Y_i(0) \to \infty$, all solutions in the nonminimal SuSy model are concentrated, as in the MSSM, near quasifixed points that arise as the result of intersections of Hill lines or surfaces with some invariant line in the space of Yukawa coordinates. However, the solutions are rather weakly attracted to these points. For $Y_i(0) \gg \tilde{\alpha}(0)$, all solutions to the renormalization-group equations are therefore nonuniformly distributed near Hill lines or surfaces. Approximate solutions to the set of nonlinear differential equations that describe the evolution of $Y_i(t)$ within the NMSSM are presented in the Appendix. The approximate solutions that are obtained in the present study are compared with the results of numerical calculations within the nonminimal SuSy model.

2. UPPER LIMIT ON THE MASS OF THE LIGHTEST HIGGS BOSON AND RENORMALIZATION-GROUP EQUATIONS IN THE NMSSM

By construction, the superpotential of the NMSSM is invariant under the discrete transformations $y'_\alpha = e^{2i\pi/3} y_\alpha$ of the Z_3 group [24]. The term $\mu(H_1H_2)$ in the superpotential of the NMSSM does not satisfy this requirement. For this reason, an extra superfield Y that is a singlet with respect to $SU(2) \times U(1)$ gauge interactions is introduced in the NMSSM. The superpotential of the Higgs sector of the NMSSM [23–25] has the form

$$W_h = \lambda Y(H_1H_2) + \frac{\kappa}{3} Y^3. \qquad (4)$$

Upon a spontaneous breakdown of $SU(2) \times U(1)$ symmetry, the field Y develops a nonzero vacuum expectation value ($\langle Y \rangle = y/\sqrt{2}$) and there arises an effective μ term ($\mu = \lambda y/\sqrt{2}$).

The introduction of the neutral field Y in the superpotential of the NMSSM leads to the emergence of the corresponding F term in the potential of the interaction of Higgs fields. As a result, the upper limit on the mass of the lightest Higgs boson proves to be greater than in the MSSM. Specifically, we have

$$m_h \le \sqrt{\frac{\lambda^2}{2} v^2 \sin^2 2\beta + M_Z^2 \cos^2 2\beta + \Delta_1 + \Delta_2}, \qquad (5)$$

where Δ_1 and Δ_2 stand for, respectively, one- and two-loop corrections. At $\lambda = 0$, the expressions for the above upper limit within the MSSM and the NMSSM coincide. In the tree approximation, relation (5) was obtained in [25]. The inclusion of loop corrections to the effective potential of Higgs fields leads to a considerable growth of the upper limit on m_h. The main contributions to Δ_1 and Δ_2 come from loops involving a t quark and its superpartners. In the leading approximation, the contribution of loop corrections to the upper limit on the Higgs boson mass within the NMSSM is approximately equal to that within the minimal SuSy model. In calculating the corrections Δ_1 and Δ_2 within the NMSSM, it is necessary, however, to replace the parameter μ by $\lambda y/\sqrt{2}$. One- and two-loop corrections within the MSSM were studied in [27] and [28], respectively. In the leading approximation, these corrections are proportional to m_t^4; they depend logarithmically on the scale of SuSy breaking, $M_S = \sqrt{m_{\tilde{t}_1} m_{\tilde{t}_2}}$ ($m_{\tilde{t}_1}$ and $m_{\tilde{t}_2}$ are the masses of the superpartners of the t quark), and are virtually independent of the choice of $\tan\beta$. The Higgs sector in the nonminimal SuSy model and one-loop corrections to this sector were studied in [29–31]. The possibility of a spontaneous CP violation in the Higgs sector of the NMSSM was considered in [31, 32]. In [33], the upper limit on the mass of the lightest Higgs boson within the NMSSM was compared with the corresponding limits within the minimal SM and minimal SuSy models. The most recent investigations revealed that, in the nonminimal SuSy model, m_h does not exceed 135 GeV [26].

From relation (5), it follows that the upper limit on m_h grows with increasing $\lambda(t_0)$. It should be emphasized that only in the region of small $\tan\beta$ is this limit markedly different from the corresponding limit within the MSSM. At large values of this parameter ($\tan\beta \gg 1$), the quantity $\sin 2\beta$ vanishes, so that the upper limits on the mass of the lightest Higgs boson within the MSSM and the NMSSM virtually coincide. But only in the case of sufficiently large $h_t(t_0)$ is the scenario of small $\tan\beta$ realized, $\tan\beta$ becoming smaller with increasing $h_t(t_0)$, as can be seen from relation (1). An analysis of the renormalization-group equations within the MSSM and the NMSSM reveals that the growth of the Yukawa coupling constants at the electroweak scale is accompanied by an increase in $h_t(0)$ and $\lambda(0)$ at the Grand Unification scale. Thus, it becomes clear that the upper limit on the mass of the lightest Higgs boson within the nonminimal SuSy model attains a maximum value in the limit of strong Yukawa coupling, in which case $Y_t(0), Y_\lambda(0) \gg \tilde{\alpha}(0)$.

From the point of view of a renormalization-group analysis, investigation of the NMSSM presents a much more complicated problem than investigation of the minimal SuSy model. The full set of renormalization-group equations within the NMSSM can be found in [30, 34]. Even in the one-loop approximation, this set of equations is nonlinear and its analytic solution has yet to be obtained. All equations forming this set can be partitioned into two groups, the first containing equations that describe the evolution of gauge and Yukawa coupling constants. In analyzing the nonlinear differential equations entering into this group, it is convenient to go over from h_t, λ, and κ to the quantities ρ_t, ρ_λ, and ρ_κ, which are defined as the ratios of the squares of the corresponding Yukawa coupling constants and the gauge coupling constant for strong interaction,

$$\rho_t(t) = \frac{Y_t(t)}{\tilde{\alpha}_3(t)},\ \rho_\lambda(t) = \frac{Y_\lambda(t)}{\tilde{\alpha}_3(t)},\ \rho_\kappa(t) = \frac{Y_\kappa(t)}{\tilde{\alpha}_3(t)},$$

where $\tilde{\alpha}_3(t) = g_3^2(t)/(4\pi)^2$, $Y_t(t) = h_t^2(t)/(4\pi)^2$, $Y_\lambda(t) = \lambda^2(t)/(4\pi)^2$, and $Y_\kappa(t) = \kappa^2(t)/(4\pi)^2$. The one-loop renormalization-group equations for $\rho_i(t)$ have the form

$$\begin{cases} \frac{d\tilde{\alpha}_3}{dt} &= 3\tilde{\alpha}_3^2, \\ \frac{d\rho_1}{dt} &= -\tilde{\alpha}_3\rho_1\left(\frac{33}{5}\rho_1 + 3\right), \\ \frac{d\rho_2}{dt} &= -\tilde{\alpha}_3\rho_2\left(\rho_2 + 3\right), \\ \frac{d\rho_t}{dt} &= -\tilde{\alpha}_3\rho_t\left(6\rho_t + \rho_\lambda - \frac{7}{3} - 3\rho_2 - \frac{13}{15}\rho_1\right), \\ \frac{d\rho_\lambda}{dt} &= -\tilde{\alpha}_3\rho_\lambda\left(3\rho_t + 4\rho_\lambda + 2\rho_\kappa + 3 - 3\rho_2 - \frac{3}{5}\rho_1\right), \\ \frac{d\rho_\kappa}{dt} &= -\tilde{\alpha}_3\rho_\kappa\left(6\rho_\lambda + 6\rho_\kappa + 3\right), \end{cases} \tag{6}$$

where $\rho_1(t) = \tilde{\alpha}_1(t)/\tilde{\alpha}_3(t)$, $\rho_2(t) = \tilde{\alpha}_2(t)/\tilde{\alpha}_3(t)$, $\tilde{\alpha}_1(t) = g_1^2(t)/(4\pi)^2$, and $\tilde{\alpha}_2(t) = g_2^2(t)/(4\pi)^2$. The second group includes equations for the parameters of a soft breakdown of SuSy, which are necessary for obtaining a phenomenologically acceptable spectrum of the superpartners of observable particles. Since boundary conditions for three Yukawa coupling constants are unknown, it is very difficult to perform a numerical analysis of the equations belonging to the first group and of the full set of the equations given above. In the regime of strong Yukawa coupling, however, solutions to the renormalization-group equations are concentrated in a narrow region of the parameter space near the electroweak scale, and this considerably simplifies the analysis of the set of equations being considered.

3. INVARIANT AND QUASIFIXED LINES: A DETERMINATION OF THE QUASIFIXED POINT

Let us first consider the simplest case of $\kappa = 0$. The growth of the Yukawa coupling constant $\lambda(t_0)$ at a fixed value of $h_t(t_0)$ results in that the Landau pole in solutions to the renormalization-group equations approaches the Grand Unification scale from above. At a specific value $\lambda(t_0) = \lambda_{\max}$, perturbation theory at $q \sim M_X$ ceases to be applicable. With increasing (decreasing) Yukawa coupling constant for the b quark, $\lambda_{\max}$ decreases (increases). In the (ρ_t, ρ_λ) plane, the dependence $\lambda^2_{\max}(h_t^2)$ is represented by a curve bounding the region of admissible values of the parameters $\rho_t(t_0)$ and $\rho_\lambda(t_0)$. At $\rho_\lambda = 0$, this curve intersects the abscissa at the point $\rho_t = \rho_t^{\mathrm{QFP}}(t_0)$. This is the way in which there arises, in the (ρ_t, ρ_λ) plane, the quasifixed (or Hill) line near which solutions to the renormalization-group equations for the initial values of the Yukawa coupling constants in the range $2 \le h_t^2(0), \lambda^2(0) \le 10$ are grouped (see Figs. 1*a*, 1*b*). With increasing $\lambda^2(0)$ and $h_t^2(0)$, the region where the solutions in question are concentrated sharply shrinks. At initial values of the Yukawa coupling constants from the range between 20 and 100, they are grouped in a narrow region near the straight line

$$\rho_t(t_0) + 0.506\rho_\lambda(t_0) = 0.91, \tag{7}$$

which can be obtained by fitting the results of numerical calculations (these results are presented in Figs. 1*c* and 1*d*). Moreover, it follows from the data in the table that the combination $h_t^2(t_0) + 0.506\lambda^2(t_0)$ of the Yukawa coupling constants depends much more weakly on $\lambda^2(0)$ and $h_t^2(0)$ than $\lambda^2(t_0)$ and $h_t^2(t_0)$ individually. In other words, a decrease in $\lambda^2(t_0)$

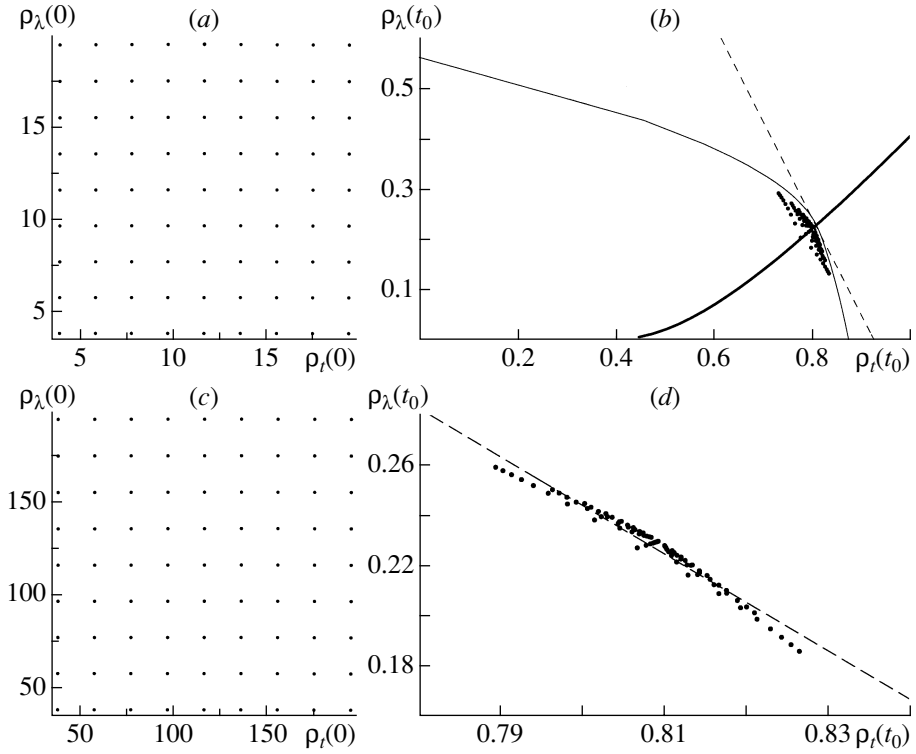

Fig. 1. Boundary conditions imposed on the renormalization-group equations within the NMSSM at the scale $q = M_X$ for $\kappa^2 = 0$ and uniformly distributed in the (ρ_t, ρ_λ) plane: (a) $2 \le h_t^2(0), \lambda^2(0) \le 10$ and (c) $20 \le h_t^2(0), \lambda^2(0) \le 100$. Also shown in this figure are the corresponding values of the Yukawa coupling constants at the electroweak scale (b, d). The thick solid and the thin solid curve in Fig. 1b represent, respectively, the invariant and the Hill line. The dashed lines in Figs. 1b and 1d were obtained as fits to the values of $(\rho_t(t_0), \rho_\lambda(t_0))$ for $20 \le h_t^2(0), \lambda^2(0) \le 100$.

compensates for an increase in $h_t^2(t_0)$, and vice versa. To illustrate this, we indicate that, at initial values $\lambda^2(0)$ and $h_t^2(0)$ from the interval $(2, 10)$, the following occurs upon an increase in $\lambda^2(0)$ and a decrease in $h_t^2(0)$: the constant $\lambda^2(t_0)$ increases monotonically from 0.191 to 0.421, while $h_t^2(t_0)$ decreases from 1.199 to 1.051; at the same time, the sum $h_t^2(t_0) + 0.506\lambda^2(t_0)$ at identical $\lambda^2(0)$ and $h_t^2(0)$ ranges between 1.266 and 1.318. The results in Figs. 2a and 2b, which illustrate the evolution of the above combinations of the Yukawa coupling constants, also confirm that this combination is virtually independent of the initial conditions.

In analyzing the results of numerical calculations, our attention is engaged by a pronounced nonuniformity in the distribution of solutions to the renormalization-group equations along the infrared quasifixed line. The main reason for this is that, in the regime of strong Yukawa coupling, the solutions in question are attracted not only to the quasifixed but also to the infrared fixed (or invariant) line. The latter connects two fixed points. Of these, one is an infrared fixed point of the set of renormalization-group equations within the NMSSM ($\rho_t = 7/18, \rho_\lambda = 0, \rho_1 = (\tilde{\alpha}_1/\tilde{\alpha}_3) = 0$, and $\rho_2 = (\tilde{\alpha}_2/\tilde{\alpha}_3) = 0$) [6], while the other fixed point ($\rho_\lambda/\rho_t = 1$) corresponds to values of the Yukawa coupling constants in the region $Y_t, Y_\lambda \gg \tilde{\alpha}_i$, in which case the gauge coupling constants on the right-hand sides of the renormalization-group equations can be disregarded [35]. The infrared fixed line is invariant under renormalization-group transformations—that is, it is independent of the scale at which the boundary values $Y_t(0)$ and $Y_\lambda(0)$ are specified and of the boundary values themselves. If the boundary conditions are such that $Y_t(0)$ and $Y_\lambda(0)$ belong to a fixed line, the evolution of the Yukawa coupling constants proceeds further along this line toward the infrared fixed point of the set of renormalization-group equations within the NMSSM. With increasing t, all other solutions to the renormalization-group equations are attracted to the infrared fixed line and, for $t/(4\pi) \gg 1$, approach the stable infrared fixed point. Solutions in the regime of strong Yukawa coupling undergo the strongest attraction to the infrared fixed point. From the data in Figs. 1b and 1d, it follows that, with increasing $Y_t(0)$ and $Y_\lambda(0)$, all solutions to the renormalization-group equations are concentrated in the vicinity of the point

of intersection of the infrared fixed and the quasifixed line:

$$\rho_t^{\mathrm{QFP}}(t_0) = 0.803, \;\; \rho_\lambda^{\mathrm{QFP}}(t_0) = 0.224.$$

Hence, this point can be considered as the quasifixed point of the set of renormalization-group equations within the NMSSM at $\kappa = 0$.

Infrared fixed lines and surfaces, as well as their properties in the minimal Standard Model and in the minimal SuSy model, were studied in detail by B. Schrempp [7], B. Schrempp and Wimmer [20], and B. Schrempp and F. Schrempp [36]. Within the NMSSM, the emergence of fixed lines can be traced at $\lambda = 0$, in which case the set of renormalization-group equations for the Yukawa coupling constants reduces to two independent differential equations—of these, one coincides with the equation for $Y_t(t)$ in the minimal SuSy model, while the other describes the evolution of $Y_\kappa(t)$. In the limit being considered, the set of one-loop renormalization-group equations has the exact analytic solution

$$Y_\kappa(t) = \frac{Y_\kappa(0)}{1 + 6Y_\kappa(0)t}, \; Y_t(t) = \frac{Y_t(0)E(t)}{1 + 6Y_t(0)F(t)}, \quad (8)$$

$$\tilde{\alpha}_i(t) = \frac{\tilde{\alpha}_i(0)}{1 + b_i\alpha_i(0)t},$$

where the expressions for $E(t), F(t)$, and b_i are presented in the Appendix. The quasifixed line in the (ρ_t, ρ_κ) plane includes two straight lines parallel to the coordinate axes (see Fig. 3*b*),

$$\begin{aligned} \rho_t &= \frac{E(t_0)}{6\tilde{\alpha}_3(t_0)F(t_0)} \approx 0.876, \\ \rho_\kappa &= \frac{1}{6\tilde{\alpha}_3(t_0)t_0} \approx 0.280, \end{aligned} \quad (9)$$

which intersect at the point (0.876, 0.280). Since the above solutions to the renormalization-group equations are attracted to the invariant line at $t/(4\pi) \gg 1$, unity can be disregarded in the denominators of $Y_t(t)$ and $Y_\kappa(t)$. The infrared fixed line can then be specified parametrically:

$$\begin{cases} \rho_t(t) = \dfrac{E(t)}{6\tilde{\alpha}_3(t)F(t)}, \\ \rho_\kappa(t) = \dfrac{1}{6\tilde{\alpha}_3(t)t}. \end{cases} \quad (10)$$

It can easily be shown that the limit $t \to 0$ corresponds to the values ρ_t and $\rho_\kappa \gg 1$ belonging to this curve, ρ_t and ρ_κ being virtually coincident in this limit. By using the expansions of the functions $E(t)$ and $F(t)$ in the vicinity of the origin, $F(t) \approx t + 0.5E'(0)t^2 + \ldots$ and $E(t) \approx 1 + E'(0)t + \ldots$, we obtain

$$\rho_\kappa = \rho_t - \frac{4}{9} - \frac{\rho_2}{4} - \frac{13}{180}\rho_1. \quad (11)$$

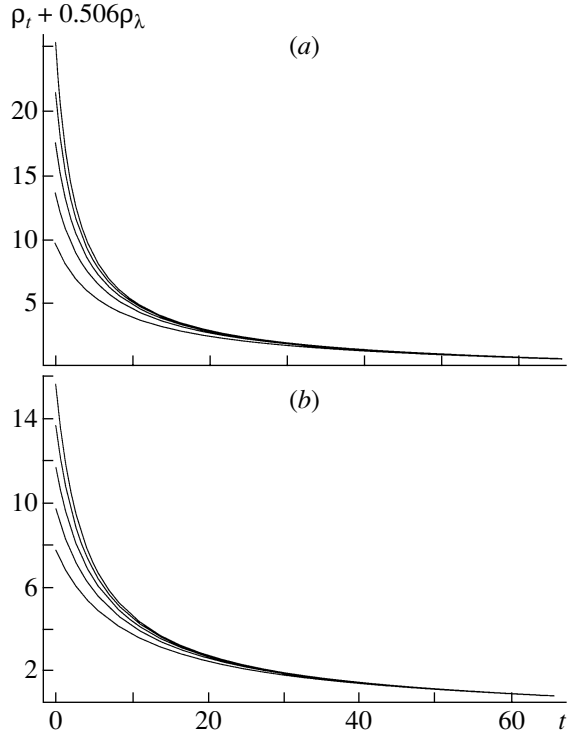

Fig. 2. Evolution of the combination $\rho_t(t) + 0.506\rho_\lambda(t)$ of the Yukawa coupling constants from the Grand Unification scale ($t = 0$) to the electroweak scale ($t = t_0$) at $\kappa^2 = 0$ for various initial values (*a*) $h_t^2(0)$ and (*b*) $\lambda^2(0)$.

The equality $\rho_\kappa = \rho_t$ corresponds to the stable fixed point of the renormalization-group equations in the regime of strong Yukawa coupling ($\rho_\kappa, \rho_t \gg 1$). As $\alpha_3(t)$ tends to the Landau pole for $t \to t_c = 1/[3\tilde{\alpha}_3(0)]$, however, the line given by Eq. (12) approaches the stable infrared point (see Fig. 3*b*); that is, $\rho_t(t)$ tends to 7/18, while $\rho_\kappa(t)$ vanishes: $\rho_\kappa \sim (\rho_t - 7/18)^{9/7}$. The curve given by (10), which connects the fixed points $\rho_\kappa/\rho_t = 1$ and $\rho_\kappa = 0$, $\rho_t = 7/18$ intersects the quasifixed line at the point (0.876, 0.280). As can be seen from Fig. 3*b*, solutions to the renormalization-group equations are concentrated precisely in the vicinity of this point.

Near the infrared fixed point, the curve being investigated is tangent to another invariant line, that which is specified by the equation $\rho_\kappa = 0$. This line connects the unstable fixed point $\rho_\kappa/\rho_t = 0$, which arises in the regime of strong Yukawa coupling ($\rho_t \gg 1$), with other fixed points, those at $\rho_\kappa = 0$, $\rho_t = 7/18$ and at $\rho_\kappa = \rho_t = 0$, the last also being unstable. Yet another infrared fixed line—the attraction of solutions to the renormalization-group equations to this line is the weakest—passes through the points $\rho_t/\rho_\kappa = 0$ and $\rho_t = 7/18, \rho_\kappa = 0$. At $\tilde{\alpha}_1 = \tilde{\alpha}_2 = 0$, it appears to be a straight line parallel to the coordinate axis,

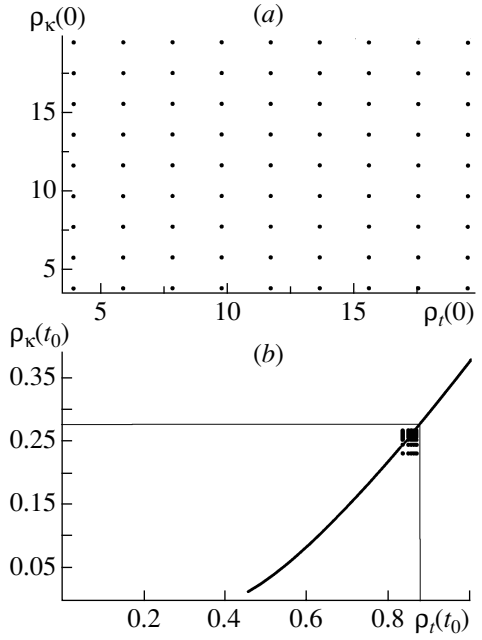

Fig. 3. (*a*) Boundary conditions imposed on the renormalization-group equations within the NMSSM at the scale $q = M_X$ for $\lambda^2 = 0$ and $2 \leq h_t^2(0), \kappa^2(0) \leq 10$ and uniformly distributed in the (ρ_t, ρ_κ) plane and (*b*) corresponding values of the Yukawa coupling constants at the electroweak scale. The thick solid and the thin solid curve in Fig. 1*b* represent, respectively, the invariant and the Hill line.

$\rho_t = 7/18$. However, the inclusion of electroweak interactions leads to a monotonic decrease in $\rho_t(t)$ with increasing $\rho_\kappa(t)$. In the vicinity of the stable infrared fixed point for $t \to t_c$, the equation for this line has the form

$$\begin{cases} \rho_t(t) = \frac{7}{18} - \frac{7}{4}\rho_2(t) - \frac{91}{180}\rho_1(t), \\ \rho_\kappa(t) = \frac{1}{6\tilde{\alpha}_3(t)t}. \end{cases} \qquad (12)$$

Apart from the replacement of ρ_κ by ρ_λ, the same infrared fixed lines are involved in the analysis of renormalization-group equations within the NMSSM in the case where $\kappa = 0$. As before, the invariant line that connects the stable fixed points $\rho_\lambda/\rho_t = 1$ and $\rho_t = 7/18, \rho_\lambda = 0$ attracts most strongly solutions to the renormalization-group equations. Nevertheless, the asymptotic behavior of the curve being studied changes for $\rho_\lambda, \rho_t \gg 1$, where it becomes

$$\rho_\lambda = \rho_t - \frac{8}{15} - \frac{2}{75}\rho_1, \qquad (13)$$

and in the vicinity of the point $\rho_t = 7/18, \rho_\lambda = 0$, where we have $\rho_\lambda \sim (\rho_t - 7/18)^{25/14}$. In analyzing the behavior of solutions to the renormalization-group equations, the other two invariant lines have but a marginal effect. One of these is specified by the equation $\rho_\lambda = 0$. The second connects the unstable fixed point in the regime of strong Yukawa coupling, $\rho_t/\rho_\lambda = 0$, with the stable infrared point, near which we have $\rho_\lambda \sim (7/18 - \rho_t)^{25/18}$.

4. INVARIANT AND HILL SURFACES

In a more complicated case where all three Yukawa coupling constants in the NMSSM are nonzero, analysis of the set of renormalization-group equations presents a much more difficult problem. In particular, invariant (infrared fixed) and Hill surfaces come to the fore instead of the infrared fixed and quasifixed points. For each fixed set of values of the coupling constants $Y_t(t_0)$ and $Y_\kappa(t_0)$, an upper limit on $Y_\lambda(t_0)$ can be obtained from the requirement that perturbation theory be applicable up to the Grand Unification scale M_X. A change in the values of the Yukawa coupling constants h_t and κ at the electroweak scale leads to a growth or a reduction of the upper limit on $Y_\lambda(t_0)$. The resulting surface in the $(\rho_t, \rho_\kappa, \rho_\lambda)$ space is shown in Figs. 4*a* and 4*b*. In the regime of strong Yukawa coupling, solutions to the renormalization-group equations are concentrated near this surface. In just the same way as in the case of $Y_\kappa = 0$, a specific linear combination of Y_t, Y_λ, and Y_κ is virtually independent of the initial conditions for $Y_i(0) \to \infty$:

$$\rho_t(t_0) + 0.72\rho_\lambda(t_0) + 0.33\rho_\kappa(t_0) = 0.98. \qquad (14)$$

For $2 \leq h_t^2(0), \kappa^2(0), \lambda^2(0) \leq 10$, this combination of the coupling constants, $h_t^2(t_0) + 0.72\lambda^2(t_0) + 0.33\kappa^2(t_0)$, ranges between 1.35 and 1.40; at the same time, we have $1.058 \leq h_t^2(t_0) \leq 1.219$, $0.032 \leq \kappa^2(t_0) \leq 0.296$, and $0.098 \leq \lambda^2(t_0) \leq 0.401$ (see table). The evolution of $\rho_t(t) + 0.72\rho_\lambda(t) + 0.33\rho_\kappa(t)$ at various initial values of the Yukawa coupling constants is illustrated in Fig. 5.

On the Hill surface, the region that is depicted in Fig. 4 and near which the solutions in question are grouped shrinks in one direction with increasing initial values of the Yukawa coupling constants, with the result that, at $Y_t(0)$, $Y_\kappa(0)$, and $Y_\lambda(0) \sim 1$, all solutions are grouped around the line that appears as the result of intersection of the quasifixed surface and the infrared fixed surface, which includes the invariant lines lying in the $\rho_\kappa = 0$ and $\rho_\lambda = 0$ planes and connecting the stable infrared point with, respectively, the fixed point $\rho_\lambda/\rho_t = 1$ and the fixed point $\rho_\kappa/\rho_t = 1$ in the regime of strong Yukawa coupling. In the limit $\rho_t, \rho_\kappa, \rho_\lambda \gg 1$, in which case the gauge coupling constants can be disregarded, the fixed points $\rho_\lambda/\rho_t = 1$, $\rho_\kappa/\rho_t = 0$ and $\rho_\kappa/\rho_t = 1$, $\rho_\lambda/\rho_t = 0$ cease to be stable. Instead of them, the stable fixed point $R_\lambda = 3/4, R_\kappa = 3/8$ [35] appears in the (R_λ, R_κ) plane, where $R_\lambda = \rho_\lambda/\rho_t$ and $R_\kappa =$

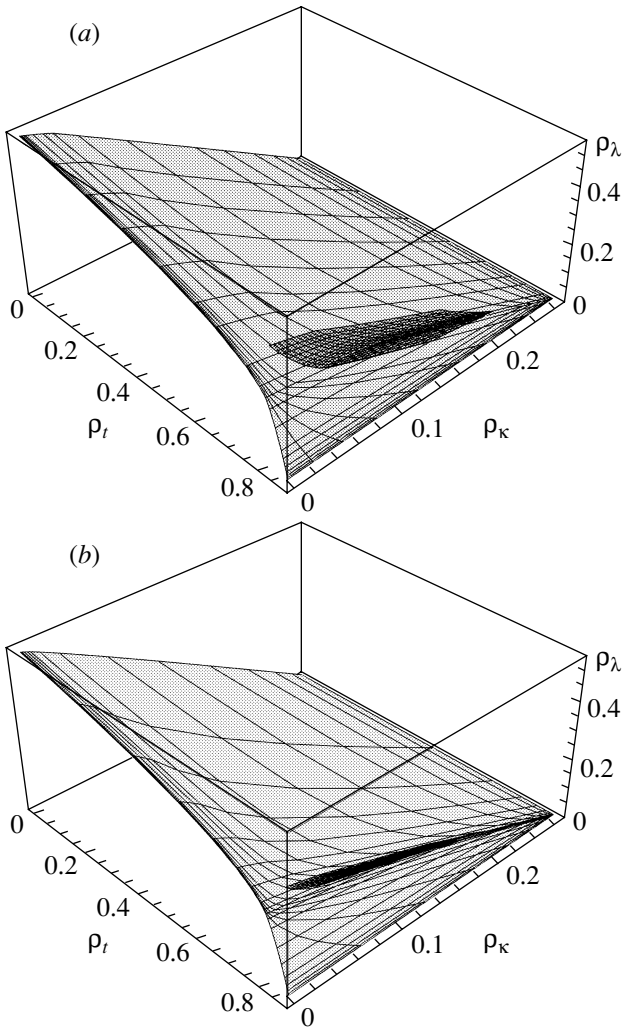

Fig. 4. Quasifixed surface in the $(\rho_t, \rho_\kappa, \rho_\lambda)$ space. The shaded part of the surface corresponds to the region near which the solutions that correspond to the initial values (a) $2 \le h_t^2(0), \kappa^2(0), \lambda^2(0) \le 10$ and (b) $20 \le h_t^2(0), \kappa^2(0), \lambda^2(0) \le 100$ are concentrated.

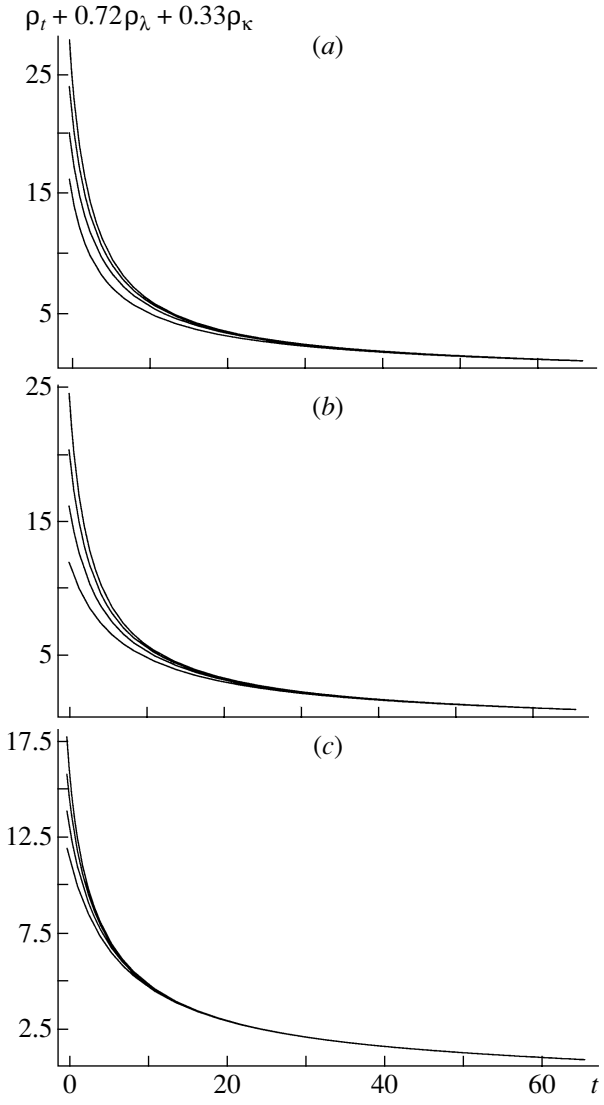

Fig. 5. Combination $\rho_t(t) + 0.72\rho_\lambda(t) + 0.33\rho_\kappa(t)$ of the Yukawa coupling constants as a function of t (which changes from 0 to t_0) for various initial values (a) $h_t^2(0)$, (b) $\lambda^2(0)$, and (c) $\kappa^2(0)$.

ρ_κ/ρ_t. In order to investigate the behavior of the solutions to the renormalization-group equations within the NMSSM, it is necessary to linearize the set of these equations in its vicinity and set $\alpha_i = 0$. As a result, we obtain

$$R_\lambda(t) = \frac{3}{4} \tag{15}$$
$$+ \left(\frac{1}{2}R_{\lambda 0} + \frac{1}{\sqrt{5}}R_{\kappa 0} - \frac{3(\sqrt{5}+1)}{8\sqrt{5}}\right)\left(\frac{\rho_t(t)}{\rho_{t0}}\right)^{\lambda_1}$$
$$+ \left(\frac{1}{2}R_{\lambda 0} - \frac{1}{\sqrt{5}}R_{\kappa 0} - \frac{3(\sqrt{5}-1)}{8\sqrt{5}}\right)\left(\frac{\rho_t(t)}{\rho_{t0}}\right)^{\lambda_2},$$
$$R_\kappa(t) = \frac{3}{8} + \frac{\sqrt{5}}{2}$$
$$\times \left(\frac{1}{2}R_{\lambda 0} + \frac{1}{\sqrt{5}}R_{\kappa 0} - \frac{3(\sqrt{5}+1)}{8\sqrt{5}}\right)\left(\frac{\rho_t(t)}{\rho_{t0}}\right)^{\lambda_1}$$
$$-\frac{\sqrt{5}}{2}\left(\frac{1}{2}R_{\lambda 0} - \frac{1}{\sqrt{5}}R_{\kappa 0} - \frac{3(\sqrt{5}-1)}{8\sqrt{5}}\right)\left(\frac{\rho_t(t)}{\rho_{t0}}\right)^{\lambda_2},$$

where $R_{\lambda 0} = R_\lambda(0), R_{\kappa 0} = R_\kappa(0), \rho_{t0} = \rho_t(0), \lambda_1 = (3+\sqrt{5})/9, \lambda_2 = (3-\sqrt{5})/9$, and $\rho_t(t) = \rho_{t0}/(1 + 7\rho_{t0}t)$. From (15), it follows that the fixed point $R_\lambda = 3/4, R_\kappa = 3/8$ arises as the result of intersection of two fixed lines in the R_λ, R_κ plane. The solutions are attracted most strongly to the line $\frac{1}{2}R_\lambda + \frac{1}{\sqrt{5}}R_\kappa = \frac{3}{8}(1 + \frac{1}{\sqrt{5}})$, since $\lambda_1 \gg \lambda_2$. This line passes through

three fixed points in the (R_λ, R_κ) plane: (1, 0), (3/4, 3/8), and (0, 1). In the regime of strong Yukawa coupling, the fixed line that corresponds, in the $(\rho_t, \rho_\kappa, \rho_\lambda)$ space, to the line mentioned immediately above is that which lies on the invariant surface containing a stable infrared fixed point. The line of intersection of the Hill and the invariant surface can be obtained by mapping this fixed line into the quasifixed surface with the aid of the set of renormalization-group equations. For the boundary conditions, one must then use the values $\lambda^2(0), \kappa^2(0)$, and $h_t^2(0) \gg 1$ belonging to the aforementioned fixed line.

In just the same way as infrared fixed lines, the infrared fixed surface is invariant under renormalization-group transformations. In the evolution process, solutions to the set of renormalization-group equations within the NMSSM are attracted to this surface. If boundary conditions are specified on the fixed surface, the ensuing evolution of the coupling constants proceeds within this surface. To add further details, we note that, near the surface being studied and on it, the solutions are attracted to the invariant line connecting the stable fixed point $(\rho_\lambda/\rho_t = 3/4, \rho_\kappa/\rho_t = 3/8)$ in the regime of strong Yukawa coupling with the stable infrared fixed point within the NMSSM. In the limit $\rho_t, \rho_\kappa, \rho_\lambda \gg 1$, the equation for this line has the form

$$\begin{cases} \rho_\lambda = \dfrac{3}{4}\rho_t - \dfrac{176}{417} + \dfrac{3}{139}\rho_2 - \dfrac{7}{417}\rho_1, \\ \rho_\kappa = \dfrac{3}{8}\rho_t - \dfrac{56}{417} - \dfrac{18}{139}\rho_2 - \dfrac{68}{2085}\rho_1. \end{cases} \tag{16}$$

As one approaches the infrared fixed point, the quantities ρ_λ and ρ_κ tend to zero: $\rho_\lambda \sim (\rho_t - 7/18)^{25/14}$ and $\rho_\kappa \sim (\rho_t - 7/18)^{9/7}$. This line intersects the quasifixed surface at the point

$$\rho_t^{\mathrm{QFP}}(t_0) = 0.82,\ \rho_\kappa^{\mathrm{QFP}}(t_0) = 0.087,$$
$$\rho_\lambda^{\mathrm{QFP}}(t_0) = 0.178.$$

Since all solutions are concentrated in the vicinity of this point for $Y_t(0), Y_\lambda(0),\ Y_\kappa(0) \to \infty$, it should be considered as a quasifixed point for the set of renormalization-group equations within the NMSSM. We note, however, that the solutions are attracted to the invariant line (16) and to the quasifixed points much more weakly than to the infrared fixed surface and to the quasifixed line on the Hill surface. This conclusion can be drawn from an analysis of the behavior of the solutions near the fixed point $R_\lambda = 3/4, R_\kappa = 3/8$ [see Eq. (15)]. Once the solutions have approached the invariant line $\frac{1}{2}R_\lambda + \frac{1}{\sqrt{5}}R_\kappa = \frac{3}{8}\left(1 + \frac{1}{\sqrt{5}}\right)$, their evolution is governed by the expression $[\epsilon(t)]^{0.085}$, where $\epsilon(t) = \rho_t(t)/\rho_{t0}$. This means that the solutions begin to be attracted to the quasifixed point and to the invariant line (16) with a sizable strength only when $Y_i(0)$ reaches a value of 10^2, at which perturbation theory is obviously inapplicable. Thus, it is not the infrared quasifixed point but the quasifixed line on the Hill surface (see Fig. 4) that, within the NMSSM, plays a key role in analyzing the behavior of the solutions to the renormalization-group equations in the regime of strong Yukawa coupling, where all $Y_i(0)$ are much greater than $\tilde{\alpha}(0)$.

Along with the invariant surface, which was studied in detail above, at least three infrared fixed surfaces exist in the $(\rho_t, \rho_\kappa, \rho_\lambda)$ space. They attract solutions to the renormalization-group equations much more weakly. Two of these are specified by the equations $\rho_\lambda = 0$ and $\rho_\kappa = 0$. Yet another infrared fixed surface can be found by analyzing the behavior of the solutions in question near the stable infrared fixed point. Integrating the linearized renormalization-group equations, we obtain

$$\rho_t(t) = \frac{7}{18} + \left(\rho'_{t0} - \frac{7}{33}\rho_{\lambda 0} + \frac{7}{4}\rho_{20} + \frac{91}{180}\rho_{10} - \frac{7}{18}\right) \times \left(\frac{\tilde{\alpha}_{30}}{\tilde{\alpha}_3(t)}\right)^{7/9} + \frac{7}{33}\rho_\lambda(t) - \frac{7}{4}\rho_2(t) - \frac{91}{180}\rho_1(t), \tag{17}$$

$$\rho_\lambda(t) = \rho_{\lambda 0}\left(\frac{\tilde{\alpha}_{30}}{\tilde{\alpha}_3(t)}\right)^{25/18},$$

$$\rho_\kappa(t) = \rho_{\kappa 0}\left(\frac{\tilde{\alpha}_{30}}{\tilde{\alpha}_3(t)}\right),$$

where ρ'_{t0}, ρ_{i0}, and $\tilde{\alpha}_{30}$ are constants of integration. In the limiting case of $\rho_1 = \rho_2 = 0$, the equation of a nontrivial invariant surface is $\rho_t = \frac{7}{18} + \frac{7}{33}\rho_\lambda$. This surface contains nontrivial infrared fixed lines that lie in the $\rho_\lambda = 0$ and $\rho_\kappa = 0$ planes and which weakly attract solutions to the renormalization-group equations. The inclusion of electroweak interactions significantly modifies the asymptotic behavior of this surface near the infrared fixed point. Nonetheless, a solution to the linearized equations (17) does not fix unambiguously an equation for this surface. Considering that, at $\rho_\lambda = 0$, the equation of the surface being studied must reduce to the equation for the invariant line (12), we find, for $t \to t_c$, that

$$\rho_t = \frac{7}{18} + \frac{7}{33}\rho_\lambda - 6t_c\left(\frac{7}{4}\tilde{\alpha}_2(t_c) + \frac{91}{180}\tilde{\alpha}_1(t_c)\right)\rho_\kappa. \tag{18}$$

Relation (18) between ρ_t, ρ_λ, and ρ_κ is valid for $\rho_\kappa \gg \rho_\lambda$. By analyzing the behavior of the solutions in the vicinity of the stable infrared point (17), it can be shown that the invariant surface (18) plays a secondary role in the NMSSM.

5. APPROXIMATE SOLUTIONS FOR THE YUKAWA COUPLING CONSTANTS

By way of example, the emergence of quasifixed lines and surfaces within the NMSSM can be traced by considering approximate solutions to the renormalization-group equations from the Appendix. Recently, approximate solutions of this type were studied within the minimal SuSy model for $\tan\beta \gg 1$ [37], in which case $Y_t \sim Y_b \sim Y_\tau$. In the regime of strong Yukawa coupling within the nonminimal SuSy model, these solutions are given by

$$\rho_t(t) = \frac{E_t(t)}{\tilde{\alpha}_3(t)\left[6F_t(t)(6F_t(t)+2R_{\lambda 0}F_\lambda(t))\right]^{1/2}} + O\left(\frac{1}{Y_t(0)}\right) + ...,$$

$$\rho_\lambda(t) = \frac{R_{\lambda 0}E_\lambda(t)}{\tilde{\alpha}_3(t)\left(6R_{\lambda 0}F_\lambda(t)+6R_{\kappa 0}t\right)^{1/3}\left(6R_{\lambda 0}F_\lambda(t)\right)^{1/6}\left(6F_t(t)+2R_{\lambda 0}F_\lambda(t)\right)^{1/2}} + O\left(\frac{1}{Y_t(0)}\right) + ..., \quad (19)$$

$$\rho_\kappa(t) = \frac{R_{\kappa 0}}{\tilde{\alpha}_3(t)\left(6R_{\lambda 0}F_\lambda(t)+6R_{\kappa 0}t\right)} + O\left(\frac{1}{Y_t(0)}\right) + ...,$$

where the expressions for the functions $E_i(t)$ and $F_i(t)$ are presented in the Appendix. Expressions (19) for $\rho_i(t)$ were formally obtained by expanding approximate solutions in a power series in $1/Y_t(0)$. Each subsequent term in such an expansion is always much less than the preceding one because, in the approximate solutions, the Yukawa coupling constant for the t quark always appears in the form of the combination $Y_t(0)F_t(t)$, which, in the regime of strong Yukawa coupling, leads to values $\frac{1}{Y_t(0)F_t(t)} \ll 1$ at $t \sim t_0$. From relations (19), it follows that, to $O(1/Y_t(0))$ terms, solutions to the renormalization-group equations depend only on the ratios of the Yukawa coupling constants $R_{\lambda 0}$ and $R_{\kappa 0}$ at the Grand Unification scale. Setting $t = t_0$, we obtain a surface in the $(\rho_t, \rho_\kappa, \rho_\lambda)$ space. This surface is specified parametrically; that is, $\rho_i = G_i(R_{\lambda 0}, R_{\kappa 0})$. Deviations from it are determined by $O(1/Y_t(0))$ terms, which are negative and small in magnitude in the limit of strong Yukawa coupling.

However, the approximate solutions (19) poorly describe the evolution of $\rho_\kappa(t)$. By way of example, we indicate that, at the electroweak scale, the relative error is about 20 percent at $\kappa^2(t_0) \sim 0.1$. This is due above all to the fact that the self-interaction constant for the scalar field Y is not renormalized by gauge interactions. The greater the contribution of gauge interactions to the renormalization of Yukawa coupling constants, the higher the accuracy to which the approximate solutions describe their evolution. For example, the relative error in $\rho_t(t_0)$ $[\rho_\lambda(t_0)]$ is 2 to 3 percent (about 5 to 6 percent) at $Y_t(0) \sim Y_\kappa(0) \sim Y_\lambda(0)$.

An approximate solution for $Y_\kappa = 0$ and $Y_t(0)$, $Y_\lambda(0) \gg \tilde{\alpha}_i(0)$ can be obtained by setting $R_{\kappa 0} = 0$ in Eqs. (19). In the regime of strong Yukawa coupling, $\rho_t(t)$ and $\rho_\lambda(t)$ then depend only on $R_{\lambda 0}$, with the result that, in the (ρ_t, ρ_λ) plane, there arises, at $t = t_0$, the Hill line

$$\rho_t^2 + \frac{1}{3}\left(\frac{E_t(t_0)}{E_\lambda(t_0)}\right)^2\left(\frac{F_\lambda(t_0)}{F_t(t_0)}\right)^2\rho_\lambda^2 = \rho_{\mathrm{QFP}}^2, \quad (20)$$

where $\rho_{\mathrm{QFP}} = \frac{E_t(t_0)}{6F_t(t_0)\alpha_3(t_0)}$. With increasing initial values of the Yukawa coupling constants, $O(1/Y_t(0))$ terms, which determine the deviation of the solutions in question from the quasifixed line (20), decrease, so that the approximate solutions to the renormalization-group equations within the NMSSM are attracted to this line. The explicit form of the dependences $\rho_t(t)$ and $\rho_\lambda(t)$ in (19) makes it possible to find that the invariant line lying in the (ρ_t, ρ_λ) plane and corresponding to $R_{\lambda 0} = 1$ can be approximately parametrized as

$$\begin{cases} \rho_t(t) &= \dfrac{E_t(t)}{\tilde{\alpha}_3(t)\left[6F_t(t)(6F_t(t)+2F_\lambda(t))\right]^{1/2}}, \\ \rho_\lambda(t) &= \dfrac{E_\lambda(t)}{\tilde{\alpha}_3(t)\left[6F_\lambda(t)\left(6F_t(t)+2F_\lambda(t)\right)\right]^{1/2}}. \end{cases} \quad (21)$$

The values $\rho_t(t_0)$ and $\rho_\lambda(t_0)$ as calculated by formulas (21) are the coordinates of the point where the Hill fixed line (20) intersects the infrared fixed line (21), which appears to be a quasifixed point for the set of renormalization-group equations within the NMSSM at $Y_\kappa = 0$. Our numerical results, which are displayed in Fig. 6, demonstrate that relations (20) and (21) reproduce quite accurately the quasifixed and the invariant line at $R_{\lambda 0} \leq 1$. Significant deviations are observed only in the infrared region $(t \to t_c)$ and for $R_{\lambda 0} \gg 1$. In general, the relative deviation of the approximate solution in question from the exact one is 5 to 6 percent at $\rho_\kappa = 0$ and $R_{\lambda 0} \sim 1$ and grows fast with increasing ρ_λ/ρ_t.

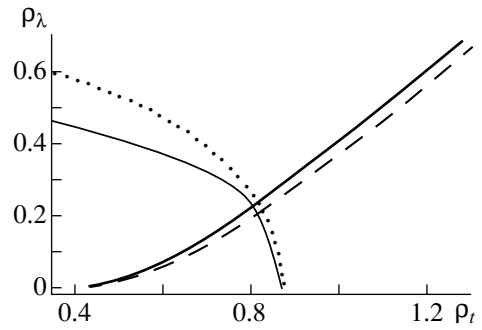

Fig. 6. Invariant and quasifixed lines in the (ρ_t, ρ_λ) plane that were obtained by means of numerical calculations (thick and thin solid curves) and by approximately solving the renormalization-group equations within the NMSSM (dashed and dotted curves). The thick solid and the dashed curve represent the infrared fixed line, while the thin solid and the dotted curve represent the Hill line.

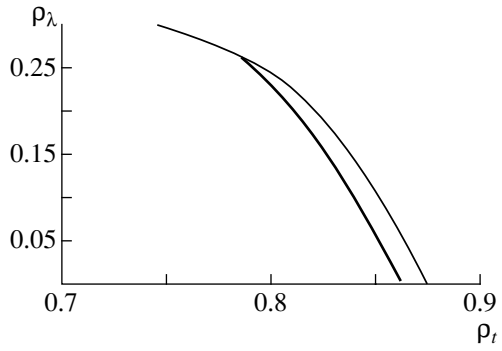

Fig. 7. Curve lying in the (ρ_t, ρ_λ) plane and corresponding to the unification of h_b and h_τ at the scale $q = M_X$ (thick solid curve). The thin solid curve represents the quasifixed line.

6. UNIFICATION OF THE YUKAWA COUPLING CONSTANTS h_b AND h_τ

As was indicated above, Grand Unified Theories impose additional constraints on the parameter space of SuSy models. Among such constraints, the unification of the Yukawa coupling constants for the b quark and the τ lepton at the scale M_X is worthy of note above all. In the nonminimal SuSy model, h_b and h_τ are unified if the constants Y_t, Y_λ, and Y_κ satisfy the relations

$$\frac{Y_t(0)}{Y_t(t_0)} = \left[\frac{R_{b\tau}(0)}{R_{b\tau}(t_0)}\right]^{21/2} \left[\frac{\alpha_3(t_0)}{\alpha_3(0)}\right]^{68/9} \left[\frac{\alpha_2(t_0)}{\alpha_2(0)}\right]^{9/4} \times \left[\frac{\alpha_1(t_0)}{\alpha_1(0)}\right]^{463/396} \left[\frac{Y_\lambda(0)}{Y_\lambda(t_0)}\right]^{1/4},$$

$$\frac{Y_t(0)}{Y_t(t_0)} = \left[\frac{R_{b\tau}(0)}{R_{b\tau}(t_0)}\right]^{9} \left[\frac{\alpha_3(t_0)}{\alpha_3(0)}\right]^{56/9} \times \left[\frac{\alpha_2(t_0)}{\alpha_2(0)}\right]^{3/2} \left[\frac{\alpha_1(t_0)}{\alpha_1(0)}\right]^{197/198} \times \left[\frac{Y_\lambda(0)}{Y_\lambda(t_0)}\right]^{1/2} \left[\frac{Y_\kappa(t_0)}{Y_\kappa(0)}\right]^{1/6}, \quad (22)$$

where $R_{b\tau}(t_0) = m_b(t_0)/m_\tau(t_0)$ is the ratio of the running masses of the b quark and the τ lepton at the electroweak scale; in the minimal unification schemes, we have $R_{b\tau}(0) = \sqrt{\dfrac{Y_b(0)}{Y_\tau(0)}} = 1$. The equation determining $R_{b\tau}(t)$ is presented in the Appendix [see Eq. (A.2)]. The first relation in (22) corresponds to the case of $\kappa = 0$, whereas the second implies a κ value different from zero. Relations (22) can be obtained by directly integrating the renormalization-group equations. Setting $R_{b\tau}(t_0) = 1.61$, which corresponds to $m_b(t_0) = 2.86$ GeV and $m_\tau(t_0) = 1.78$ GeV, we find, for the ratio of the Yukawa coupling constants for the t quark, that

$$\frac{Y_t(0)}{Y_t(t_0)} \approx 3.67 \left[\frac{Y_\lambda(0)}{Y_\lambda(t_0)}\right]^{1/4}, \quad (23)$$

$$\frac{Y_t(0)}{Y_t(t_0)} \approx 2.57 \left[\frac{Y_\lambda(0)}{Y_\lambda(t_0)}\right]^{1/2} \left[\frac{Y_\kappa(t_0)}{Y_\kappa(0)}\right]^{1/6}.$$

The second equation in (23)—it relates Y_t, Y_λ, and Y_κ—determines a surface in the $(\rho_t, \rho_\lambda, \rho_\kappa)$ space; at $Y_\kappa = 0$, this surface degenerates into a line in the (ρ_t, ρ_λ) plane. In this case, $b\tau$ unification is possible under the condition $Y_t(0) \gg Y_t(t_0)$, which is realized only in the regime of strong Yukawa coupling within the NMSSM. In the (ρ_t, ρ_λ) plane, Fig. 7 shows the Hill line and the curve that corresponds to $Y_b(0) = Y_\tau(0)$. As might have been expected, the spacing between them is quite small. In addition, we note that only at sufficiently large values of the t-quark Yukawa coupling constant at the electroweak scale, $Y_t(t_0) > Y_t^0$, is $b\tau$ unification possible. A lower limit on the $Y_t(t_0)$ implies that there exists an upper limit on $\tan\beta$ [see Eq. (1)]. By varying the running b-quark mass at the scale $q = m_b$ between 4.1 and 4.4 GeV, we found that only for $\tan\beta \leq 2$ can the equality of the Yukawa coupling constants at the Grand Unification scale be achieved. The possibility of unifying the Yukawa coupling constants within the NMSSM was investigated in detail elsewhere [38]. The condition $Y_b(0) = Y_\tau(0)$ imposes stringent constraints on the parameter space of the model being studied. Since h_b and h_τ are small in magnitude at $\tan\beta \sim 1$, they can be generated, however, at the Grand Unification scale owing to unrenormalized operators upon a spontaneous breakdown of symmetry, in which case h_b and h_τ can take different values.

7. CONCLUSION

The present analysis has revealed that, in the regime of strong Yukawa coupling, solutions to the renormalization-group equations within the NMSSM, $Y_i(t)$, are attracted to quasifixed lines and surfaces in the space of Yukawa coupling constants and that specific combinations $\rho_i(t)$ are virtually independent of their initial values at the Grand Unification scale. It is for $Y_i(0) \gg \tilde{\alpha}_i(0)$ that the upper limit on the mass of the lightest Higgs boson attains its maximum value. It has also been proven that, in the limit being considered, the values of the constants h_t, λ, and κ can be chosen in such a way as to ensure unification of the Yukawa coupling constants for the b quark and the τ lepton at the scale M_X, a feature usually inherent in Grand Unified Theories. For $Y_i(0) \to \infty$, all solutions to the renormalization-group equations are concentrated near quasifixed points. These points emerge as the result of intersection of Hill lines or surfaces with the invariant line that connects the stable fixed point for $Y_i \gg \tilde{\alpha}_i$ with the stable infrared fixed point. For the renormalization-group equations within the NMSSM, we have listed all the most important invariant lines and surfaces and studied their asymptotic behavior for $Y_i \gg \tilde{\alpha}_i$ and in the vicinity of the infrared fixed point.

With increasing $Y_i(0)$, the solutions in question approach quasifixed points quite slowly; that is, the deviation is proportional to $(\epsilon_t(t))^\delta$, where $\epsilon_t(t) = Y_t(t)/Y_t(0)$ and δ is calculated by analyzing the set of renormalization-group equations in the regime of strong Yukawa coupling. As a rule, δ is positive and much less than unity. By way of example, we indicate that, in the case where all three Yukawa coupling constants differ from zero, $\delta \approx 0.085$. Of greatest importance in analyzing the behavior of solutions to the renormalization-group equations within the NMSSM at $Y_t(0), Y_\lambda(0), Y_\kappa(0) \sim 1$ is therefore not the infrared quasifixed point but the line lying on the Hill surface and emerging as the result of the intersection of the Hill and the invariant surface. This line can be obtained by mapping the fixed line connecting the fixed points (1, 0), (3/4, 3/8), and (0, 1) in the (R_λ, R_κ) plane for $Y_i \gg \tilde{\alpha}_i$ into the quasifixed surface by means of renormalization-group equations.

The emergence of Hill lines and surfaces in the space of Yukawa coupling constants can be traced by considering the examples of approximate solutions that are presented in the Appendix. These solutions lead to qualitatively correct results. However, the approximate solutions poorly describe the evolution of $Y_\kappa(t)$, since the neutral field Y is not renormalized by gauge interactions. At the same time, it has been shown that, at $Y_t(0) \sim Y_\lambda(0)$, the relative deviation of the approximate solution from the exact one is as small as 2 to 3 percent in $Y_t(t_0)$ and about 5 to 6 percent in $Y_\lambda(t_0)$. With increasing $Y_\lambda(t_0)/Y_t(t_0)$, such relative deviations grow quite fast.

ACKNOWLEDGMENTS

We are grateful to M.I. Vysotsky, D.I. Kazakov, and K.A. Ter-Martirosyan for stimulating questions, valuable discussions, and enlightening comments. R.B. Nevzorov is indebted to Istituto Nazionale di Fisica Nucleare (Sezione di Ferrara) for the kind hospitality extended to him.

This work was supported by the Russian Foundation for Basic Research (project nos. 98-02-17372, 98-02-17453, 00-15-96786, and 00-15-96562).

APPENDIX

Set of Renormalization-Group Equations within the NMSSM for Yukawa Coupling Constants and Approximate Solution to It

In the present study, we have analyzed one-loop renormalization-group equations within the NMSSM. These equations can be represented as [34]

$$\frac{d\tilde{\alpha}_i}{dt} = -b_i\tilde{\alpha}_i^2, \qquad \text{(A.1)}$$

$$\frac{dY_t}{dt} = -Y_t\left(Y_\lambda + 6Y_t - \frac{16}{3}\tilde{\alpha}_3 - 3\tilde{\alpha}_2 - \frac{13}{15}\tilde{\alpha}_1\right),$$

$$\frac{dY_\lambda}{dt} = -Y_\lambda\left(4Y_\lambda + 2Y_\kappa + 3Y_t - 3\tilde{\alpha}_2 - \frac{3}{5}\tilde{\alpha}_1\right),$$

$$\frac{dY_\kappa}{dt} = -6Y_\kappa(Y_\lambda + Y_\kappa).$$

On the right-hand sides of these differential equations, we have discarded terms proportional to the Yukawa coupling constants Y_b and Y_τ, since their contribution at $\tan\beta \ll 10$ is negligibly small. The index i runs through the values from 1 and 3, $b_1 = 33/5$, $b_2 = 1$, $b_3 = -3$, $\tilde{\alpha}_i(t) = \frac{\alpha_i(t)}{4\pi} = \left(\frac{g_i(t)}{4\pi}\right)^2$, $Y_t(t) = \left(\frac{h_t(t)}{4\pi}\right)^2$, $Y_\lambda(t) = \left(\frac{\lambda(t)}{4\pi}\right)^2$, and $Y_\kappa(t) = \left(\frac{\kappa(t)}{4\pi}\right)^2$. The variable t is defined in a standard way: $t = \ln\left(M_X^2/q^2\right)$, where $M_X = 3 \times 10^{16}$ GeV.

In analyzing $b\tau$ unification, use was made of the evolution equation for the ratio $R_{b\tau}(t) = \sqrt{Y_b(t)/Y_\tau(t)}$ of the Yukawa coupling constants for the b quark and the τ lepton,

$$\frac{dR_{b\tau}}{dt} = -R_{b\tau}\left(\frac{1}{2}Y_t - \frac{8}{3}\tilde{\alpha}_3 + \frac{2}{3}\tilde{\alpha}_1\right), \qquad \text{(A.2)}$$

where $Y_b(t) = \left(\frac{h_b(t)}{4\pi}\right)^2$ and $Y_\tau(t) = \left(\frac{h_\tau(t)}{4\pi}\right)^2$. The value of $R_{b\tau}(0) = 1$ corresponds to the unification of the Yukawa coupling constants h_b and h_τ. For the Yukawa and gauge coupling constants, the set of two-loop renormalization-group equations within the NMSSM is presented in [30].

The corresponding one-loop equations for the gauge coupling constants can easily be integrated. The result has the form

$$\tilde{\alpha}_i(t) = \frac{\tilde{\alpha}_i(0)}{1 + b_i\tilde{\alpha}_i(0)t}. \qquad (A.3)$$

Since the gauge coupling constants within the MSSM and within the NMSSM coincide at the Grand Unification scale, we have $\tilde{\alpha}_i(0) = \tilde{\alpha}(0) = \tilde{\alpha}_{\rm GUT}$ for all of them. In the case where $\lambda = 0$, there exists an exact analytic solution to the set of renormalization-group equations (A.1). It is specified by relations (2) and (8), with $E(t)$ and $F(t)$ being given by

$$E(t) = \exp\left[\int_0^t H(t')dt'\right]$$
$$= \left[\frac{\tilde{\alpha}_3(t)}{\tilde{\alpha}(0)}\right]^{16/9}\left[\frac{\tilde{\alpha}_2(t)}{\tilde{\alpha}(0)}\right]^{-3}\left[\frac{\tilde{\alpha}_1(t)}{\tilde{\alpha}(0)}\right]^{-13/99},$$
$$F(t) = \int_0^t E(t')dt',$$

where

$$H(t) = \frac{16}{3}\tilde{\alpha}_3(t) + 3\tilde{\alpha}_2(t) + \frac{13}{15}\tilde{\alpha}_1(t). \qquad (A.4)$$

In the regime of strong Yukawa coupling, in which case all $Y_i(0)$ are much greater than $\tilde{\alpha}(0)$, an exact analytic solution to the set of Eqs. (A.1) has not yet been found. An explicit t dependence of the Yukawa coupling constants can be obtained on the basis of an approximate solution to the renormalization-group equations within NMSSM. An approximate solution of this type was first obtained by Kazakov [37], who studied the renormalization-group equations within the MSSM in the limit $\tan\beta \gg 1$. For the Yukawa coupling constants, it has the form

$$Y_\lambda(t) = Y_\lambda(0)E_\lambda(t)P_{H_2}(t)P_{H_1}(t)P_Y(t), \qquad (A.5)$$
$$Y_\kappa(t) = Y_\kappa(0)P_Y^3(t),$$
$$Y_t(t) = Y_t(0)E_t(t)P_Q(t)P_U(t)P_{H_2}(t),$$

where

$$E_t(t) = E(t), \quad E_\lambda(t) = \left(\frac{\tilde{\alpha}_2(t)}{\tilde{\alpha}(0)}\right)^{-3}\left(\frac{\tilde{\alpha}_1(t)}{\tilde{\alpha}(0)}\right)^{-1/11},$$

and $P_i(t)$ is the contribution of the Yukawa coupling constants to the renormalization of $Y_i(t)$ from each of the external legs entering the corresponding vertex:

$$\frac{d\ln P_Q(t)}{dt} = \frac{1}{2}\frac{d\ln P_U(t)}{dt} = -Y_t(t), \qquad (A.6)$$
$$\frac{d\ln P_{H_2}(t)}{dt} = -3Y_t(t) - Y_\lambda(t),$$
$$\frac{d\ln P_{H_1}(t)}{dt} = -Y_\lambda(t),$$
$$\frac{d\ln P_Y(t)}{dt} = -2Y_\lambda(t) - 2Y_\kappa(t).$$

Setting $P_Q(t)P_U(t)P_{H_2}(t) \approx P_{H_2}(t)P_{H_1}(t)P_Y(t) \approx P_Y^3(t) \approx P_0(t)$ and $P_Q^A(t) \approx P_U^B(t) \approx P_{H_2}^{C_2}(t) \approx P_{H_1}^{C_1}(t) \approx P_Y^D(t) \approx P_0(t)$, we find that A, B, C_1, C_2, and D satisfy the relations

$$\frac{1}{A} + \frac{1}{B} + \frac{1}{C_2} = 1, \ \frac{1}{D} + \frac{1}{C_1} + \frac{1}{C_2} = 1, \ D = 3.$$

Since the contribution of the t-quark Yukawa coupling constant to the renormalization of external legs is much greater than the contribution of Y_λ, the constants A, B, and C_2 also satisfy the approximate relations $B \approx A/2$ and $C_2 \approx A/3$, which make it possible to find, for A, B, C_1, and C_2, that

$$A = C_1 = 6, \quad B = 3, \quad C_2 = 2$$

and to obtain, with the aid of the differential equations (A.6) for $P_i(t)$, approximate solutions. The results are

$$P_U(t) = \frac{1}{(1 + 6Y_t(0)F_t(t))^{1/3}} = P_Q^2(t), \qquad (A.7)$$
$$P_{H_2}(t) = \frac{1}{(1 + 6Y_t(0)F_t(t) + 2Y_\lambda(0)F_\lambda(t))^{1/2}},$$
$$P_{H_1}(t) = \frac{1}{(1 + 6Y_\lambda(0)F_\lambda(t))^{1/6}},$$
$$P_Y(t) = \frac{1}{(1 + 6Y_\lambda(0)F_\lambda(t) + 6Y_\kappa(0)t)^{1/3}},$$

where

$$F_t(t) = F(t), \quad F_\lambda(t) = \int_0^t E_\lambda(t')dt'.$$

Substituting the resulting expressions (A.7) for $P_i(t)$ into relations (A.5), we obtain approximate solutions for the Yukawa coupling constants within the NMSSM. In just the same way, we can find approximate solutions for $Y_t(t)$ and $Y_\lambda(t)$ at $\kappa = 0$. As a result, it can easily be proven that the required solutions are obtained by setting $Y_\kappa(0) = 0$ in (A.5) and (A.7).

REFERENCES

1. R. Tallach, Nucl. Phys. B **183**, 384 (1981); S. Narison, Phys. Lett. B **197**, 405 (1987); N. Gray, D. J. Broadhurst, W. Grafe, and K. Schilcher, Z. Phys. C **48**, 673 (1990).
2. L. Demortier *et al*. (the Top Averaging Group for the CDF and DO Collab.), fermilab-TM-2084 (1999).
3. L. E. Ibañez and C. Lopez, Phys. Lett. B **126B**, 54 (1983); Nucl. Phys. B **233**, 511 (1984); W. De Boer, R. Ehret, and D. I. Kazakov, Z. Phys. C **67**, 647 (1995).
4. C. T. Hill, Phys. Rev. D **24**, 691 (1981); C. T. Hill, C. N. Leung, and S. Rao, Nucl. Phys. B **262**, 517 (1985).
5. B. Pendleton and G. G. Ross, Phys. Lett. B **98B**, 291 (1981); D. I. Kazakov, Preprint No. E2-82-880, OIYaI (Joint Institute for Nuclear Research, Dubna, 1982); M. Lanzagorta and G. G. Ross, Phys. Lett. B **349**, 319 (1995); **364**, 163 (1995); M. Bando, J. Sato, and K. Yoshioka, Prog. Theor. Phys. **98**, 169 (1997); B. C. Allanach, G. Amelino-Camelia, and O. Philipsen, Phys. Lett. B **393**, 349 (1997).
6. B. C. Allanach and S. F. King, Phys. Lett. B **407**, 124 (1997); I. Jack and D. R. T. Jones, Phys. Lett. B **443**, 177 (1998).
7. B. Schrempp, Phys. Lett. B **344**, 193 (1995).
8. S. A. Abel and B. C. Allanach, Phys. Lett. B **415**, 371 (1997).
9. P. M. Fereira, I. Jack, and D. R. T. Jones, Phys. Lett. B **392**, 376 (1997).
10. B. Brahmachari, Mod. Phys. Lett. A **12**, 1969 (1997).
11. J. A. Casas, J. R. Espinosa, and H. E. Haber, Nucl. Phys. B **526**, 3 (1998).
12. G. K. Yeghiyan, M. Jurčišin, and D. I. Kazakov, Mod. Phys. Lett. A **14**, 601 (1999).
13. S. Codoban, M. Jurčišin, and D. Kazakov, hep-ph/9912504.
14. M. Carena, M. Olechowski, S. Pokorski, and C. E. M. Wagner, Nucl. Phys. B **419**, 213 (1994); M. Carena and C. E. M. Wagner, Nucl. Phys. B **452**, 45 (1995).
15. V. Barger, M. S. Berger, P. Ohmann, and J. N. Phillips, Phys. Lett. B **314**, 351 (1993); W. A. Bardeen, M. Carena, S. Pokorski, and C. E. M. Wagner, Phys. Lett. B **320**, 110 (1994); S. A. Abel and B. C. Allanach, Phys. Lett. B **431**, 339 (1998).
16. V. Barger, M. S. Berger, and P. Ohmann, Phys. Rev. D **49**, 4908 (1994).
17. M. S. Chanowitz, J. Ellis, and M. K. Gaillard, Nucl. Phys. B **128**, 506 (1977); A. J. Buras, J. Ellis, M. K. Gaillard, and D. V. Nanopoulos, Nucl. Phys. B **135**, 66 (1978).
18. V. Barger, M. S. Berger, and P. Ohmann, Phys. Rev. D **47**, 1093 (1993); M. Carena, S. Pokorski, and C. E. M. Wagner, Nucl. Phys. B **406**, 59 (1993); P. Langacker and N. Polonsky, Phys. Rev. D **49**, 1454 (1994); **50**, 2199 (1994); N. Polonsky, Phys. Rev. D **54**, 4537 (1996).
19. M. Carena, M. Olechowski, S. Pokorski, and C. E. M. Wagner, Nucl. Phys. B **426**, 269 (1994).
20. B. Schrempp and M. Wimmer, Prog. Part. Nucl. Phys. **37**, 1 (1996).
21. P. Igo-Kemenes, in *Proceedings of XXX International Conference of Hihg-Energy Physics, Osaka, 2000* (in press).
22. M. Jurčišin and D. I. Kazakov, Mod. Phys. Lett. A **14**, 671 (1999).
23. P. Fayet, Nucl. Phys. B **90**, 104 (1975); M. I. Vysotskiĭ and K. A. Ter-Martirosyan, Zh. Éksp. Teor. Fiz. **90**, 838 (1986) [Sov. Phys. JETP **63**, 489 (1986)].
24. J. Ellis, J. F. Gunion, H. E. Haber, *et al.,* Phys. Rev. D **39**, 844 (1989).
25. L. Durand and J. L. Lopes, Phys. Lett. B **217**, 463 (1989); L. Drees, Int. J. Mod. Phys. A **4**, 3635 (1989).
26. M. Masip, R. Muñoz-Tapia, and A. Pomarol, Phys. Rev. D **57**, 5340 (1998); G. K. Yeghiyan, Preprint No. 1532(2)-99, YERPHI (1999); hep-ph/9904488; U. Ellwanger and C. Hugonie, hep-ph/9909260.
27. H. E. Haber and R. Hempfling, Phys. Rev. Lett. **66**, 1815 (1991); Y. Okada, M. Yamaguchi, and T. Yanagida, Prog. Theor. Phys. **85**, 1 (1991); J. Ellis, G. Ridolfi, and F. Zwirner, Phys. Lett. B **257**, 83 (1991); **262**, 477 (1991); R. Barbieri, M. Frigeni, and F. Caravaglios, Phys. Lett. B **258**, 167 (1991); Y. Okada, M. Yamaguchi, and T. Yanagida, Phys. Lett. B **262**, 54 (1991); M. Drees and M. Nojiri, Phys. Rev. D **45**, 2482 (1992); D. M. Pierce, A. Papadopoulos, and S. Jhonson, Phys. Rev. Lett. **68**, 3678 (1992); P. H. Chankowski, S. Pokorski, and J. Rosiek, Phys. Lett. B **274**, 191 (1992); H. E. Haber and R. Hempfling, Phys. Rev. D **48**, 4280 (1993); P. H. Chankowski, S. Pokorski, and J. Rosiek, Nucl. Phys. B **423**, 437 (1994); A. Yamada, Z. Phys. C **61**, 247 (1994); A. Dabelstein, Z. Phys. C **67**, 495 (1995); D. M. Pierce, J. A. Bagger, K. Matchev, and R. Zhang, Nucl. Phys. B **491**, 3 (1997).
28. J. R. Espinosa and M. Quiros, Phys. Lett. B **266**, 389 (1991); R. Hempfling and A. H. Hoang, Phys. Lett. B **331**, 99 (1994); M. Carena, J. R. Espinosa, M. Quiros, and C. E. M. Wagner, Phys. Lett. B **355**, 209 (1995); J. A. Casas, J. R. Espinosa, M. Quiros, and A. Riotto, Nucl. Phys. B **436**, 3 (1995); M. Carena, M. Quiros, and C. E. M. Wagner, Nucl. Phys. B **461**, 407 (1996); H. E. Haber, R. Hempfling, and A. H. Hoang, Z. Phys. C **75**, 539 (1997); S. Heinemeyer, W. Hollik, and G. Weiglein, Phys. Rev. D **58**, 091701 (1998); Phys. Lett. B **440**, 296 (1998); R. Zhang, Phys. Lett. B **447**, 89 (1999); S. Heinemeyer, W. Hollik, and G. Weiglein, Phys. Lett. B **455**, 179 (1999).
29. T. Elliott, S. F. King, and P. L. White, Phys. Lett. **319**, 56 (1993); U. Ellwanger, Phys. Lett. B **303**, 271 (1993); U. Ellwanger and M. Lindner, Phys. Lett. B **301**, 365 (1993); P. N. Pandita, Phys. Lett. B **318**, 338 (1993); Z. Phys. C **59**, 575 (1993); T. Elliott, S. F. King, and P. L. White, Phys. Rev. D **49**, 2435 (1994); S. W. Ham, S. K. Oh, and B. R. Kim, J. Phys. G **22**, 1575 (1996); Phys. Lett. B **414**, 305 (1997); P. A. Kovalenko, R. B. Nevzorov,

and K. A. Ter-Martirosyan, Yad. Fiz. **61**, 898 (1998) [Phys. At. Nucl. **61**, 812 (1998)].
30. S. F. King and P. L. White, Phys. Rev. D **52**, 4183 (1995).
31. S. W. Ham, S. K. Oh, and H. S. Song, hep-ph/9910461.
32. A. Pomarol, Phys. Rev. D **47**, 273 (1993); K. S. Babu and S. M. Barr, Phys. Rev. D **49**, 2156 (1994); G. M. Asatrian and G. K. Egiian, Mod. Phys. Lett. A **10**, 2943 (1995); **11**, 2771 (1996); N. Haba, M. Matsuda, and M. Tanimoto, Phys. Rev. D **54**, 6928 (1996).
33. M. A. Diaz, T. A. Ter Veldius, and T. J. Weiler, Phys. Rev. D **54**, 5855 (1996).
34. J.-P. Derendinger and C. A. Savoy, Nucl. Phys. B **237**, 307 (1984).
35. P. Binetruy and C. A. Savoy, Phys. Lett. B **277**, 453 (1992).
36. B. Schrempp and F. Schrempp, Phys. Lett. B **299**, 321 (1993).
37. S. Codoban and D. I. Kazakov, hep-ph/9906256.
38. B. C. Allanach and S. F. King, Phys. Lett. B **328**, 360 (1994).

Translated by A. Isaakyan

Physics of Atomic Nuclei, Vol. 64, No. 7, 2001, pp. 1315–1322. From Yadernaya Fizika, Vol. 64, No. 7, 2001, pp. 1391–1398.

ELEMENTARY PARTICLES AND FIELDS
Theory

Search for SUSY at LHC in Jets + $E_T^{\rm miss}$ Final States for the Case of Nonuniversal Gaugino Masses*

S. I. Bityukov[1)] and N. V. Krasnikov

Institute for Nuclear Research, Russian Academy of Sciences, pr. Shestidesyatiletiya Oktyabrya 7a, Moscow, 117312 Russia

Received January 24, 2000

Abstract—We investigate squark and gluino pair production at LHC (CMS) with subsequent decays into quarks and an LSP for the case of nonuniversal gaugino masses. Visibility of a signal by an excess over the SM background in $(n \geq 2)jets + E_T^{\rm miss}$ events depends rather strongly on the relation between the LSP, gluino, and squark masses and decreases with increasing LSP mass. For a relatively heavy LSP mass close to the squark or the gluino mass and for $m_{\tilde{q}}, m_{\tilde{g}} \geq 1.5$ TeV, the sygnal is overly small to be observable. © *2001 MAIK "Nauka/Interperiodica".*

1. INTRODUCTION

One of the LHC supergoals is the discovery of supersymmetry. In particular, it is very important to investigate the possibility of discovering strongly interacting superparticles (squarks and gluinos). In [1] (see also [2]), the LHC potential for discovering squarks and gluinos was investigated within the minimal SUGRA–MSSM framework [3], where all sparticle masses are determined mainly by two parameters: m_0 (common squark and slepton mass at the GUT scale) and $m_{1/2}$ (common gaugino mass at the GUT scale). The signature used to seek squarks and gluinos at LHC is $(n \geq 0)leptons + (n \geq 2)jets + E_T^{\rm miss}$ events. The conclusion of [1] is that LHC is able to detect squarks and gluinos with masses up to (2–2.5) TeV.

In this article, we investigate the LHC potential for discovering squarks and gluinos in the case of nonuniversal gaugino masses. Despite the simplicity of the SUGRA–MSSM framework, it is a very particular model. The mass formulas for sparticles in this model are derived under the assumption that, at the GUT scale ($M_{\rm GUT} \approx 2 \times 10^{16}$ GeV), soft supersymmetry-breaking terms are universal. However, we can generally expect that real sparticle masses can differ in a drastic way from the sparticle-mass pattern of the SUGRA–MSSM framework for many reasons (see, for instance, [4–7]). Therefore, it is more appropriate to investigate, in a model-independent way, the LHC potential for discovering SUSY.[2)]

The cross section for the production of strongly interacting superparticles,

$$pp \to \tilde{g}\tilde{g}, \tilde{q}\tilde{g}, \tilde{q}\tilde{q}, \quad (1)$$

depends on the gluino and squark masses. Within the SUGRA–MSSM framework, the sparticle masses satisfy the approximate relations

$$m_{\tilde{q}}^2 \approx m_0^2 + 6m_{1/2}^2, \quad (2)$$

$$m_{\tilde{\chi}_1^0} \approx 0.45 m_{1/2}, \quad (3)$$

$$m_{\tilde{\chi}_2^0} \approx m_{\tilde{\chi}_1^\pm} \approx 2m_{\tilde{\chi}_1^0}, \quad (4)$$

$$m_{\tilde{g}} \approx 2.5 m_{1/2}. \quad (5)$$

The decays of squarks and gluinos depend on the relation between the squark and gluinos masses. For $m_{\tilde{q}} > m_{\tilde{g}}$, squarks decay predominantly into gluinos and quarks,

$$\tilde{q} \to \tilde{g}q,$$

while gluinos decay, as a rule, into a quark–antiquark pair and a gaugino,

$$\tilde{g} \to q\bar{q}\tilde{\chi}_i^0,$$

$$\tilde{g} \to q\bar{q}'\tilde{\chi}_1^\pm.$$

For $m_{\tilde{q}} < m_{\tilde{g}}$, gluinos decay mainly into squarks and quarks,

$$\tilde{g} \to \bar{q}\tilde{q}, q\bar{\tilde{q}},$$

*This article was submitted by the authors in English.

[1)]Institute for High Energy Physics, Protvino, Moscow oblast, 142284 Russia.

[2)]The early version of this study was published in [8].

1063-7788/01/6407-1315$21.00

Table 1. Cuts (a) and corresponding number of background events for $L = 10^5$ pb^{-1}

Cut number	E_T^{miss}, GeV	E_{T1}, GeV	E_{T2}, GeV	N_b
1	200	40	40	4995783
2	200	100	100	3292494
3	200	100	150	3097944
4	200	50	100	4478452
5	400	200	200	180868
6	400	200	300	173889
7	400	100	200	247991
8	600	300	300	8992
9	600	300	450	7771
10	600	150	300	17662
11	800	400	400	1120
12	800	400	600	963
13	800	200	400	2708
14	1000	500	500	229
15	1000	500	750	183
16	1000	250	500	616
17	1200	600	600	38
18	1200	600	900	28
19	1200	300	600	115

whereas squarks decay mainly into quarks and a gaugino,

$$\tilde{q} \to q\tilde{\chi}_i^0,$$
$$\tilde{q} \to q'\tilde{\chi}_1^{\pm}.$$

The lightest chargino $\tilde{\chi}_1^{\pm}$ has several leptonic decay modes giving a lepton and missing energy:

the three-body decay

$$\tilde{\chi}_1^{\pm} \longrightarrow \tilde{\chi}_1^0 + l^{\pm} + \nu$$

and the two-body decays

$$\tilde{\chi}_1^{\pm} \longrightarrow \tilde{l}_{L,R}^{\pm} + \nu, \quad \tilde{l}_{L,R}^{\pm} \hookrightarrow \tilde{\chi}_1^0 + l^{\pm}$$

$$\tilde{\chi}_1^{\pm} \longrightarrow \tilde{\nu}_L + l^{\pm}, \quad \tilde{\nu}_L \hookrightarrow \tilde{\chi}_1^0 + \nu$$

$$\tilde{\chi}_1^{\pm} \longrightarrow \tilde{\chi}_1^0 + W^{\pm}. \quad W^{\pm} \hookrightarrow l^{\pm} + \nu$$

The leptonic decays of $\tilde{\chi}_2^0$ give two leptons and missing energy. These are the three-body decays

$$\tilde{\chi}_2^0 \longrightarrow \tilde{\chi}_1^0 + l^+ l^-$$

Table 2. Cuts (b) and corresponding number of background events for $L = 10^5$ pb^{-1}

Cut number	E_T^{miss}, GeV	E_{T1}, GeV	E_{T2}, GeV	E_{T3}, GeV	N_b
1	200	40	40	40	2953667
2	200	100	125	150	957089
3	200	167	208	250	315594
4	200	233	292	350	104932
5	200	300	375	450	79970
6	400	100	125	150	151076
7	400	167	208	250	20392
8	400	233	292	350	9025
9	400	300	375	450	4113
10	600	100	125	150	8774
11	600	167	208	250	4547
12	600	233	292	350	2599
13	600	300	375	450	1701
14	800	100	125	150	1693
15	800	167	208	250	754
16	800	233	292	350	372
17	800	300	375	450	194
18	1000	100	125	150	425
19	1000	167	208	250	234
20	1000	233	292	350	147
21	1000	300	375	450	59
22	1200	100	125	150	99
23	1200	167	208	250	58
24	1200	233	292	350	31
25	1200	300	375	450	22

$$\tilde{\chi}_2^0 \longrightarrow \tilde{\chi}_1^{\pm} + l^{\mp} + \nu, \quad \tilde{\chi}_1^{\pm} \hookrightarrow \tilde{\chi}_1^0 + l^{\pm} + \nu$$

and the two-body decay

$$\tilde{\chi}_2^0 \longrightarrow \tilde{l}_{L,R}^{\pm} + l^{\mp}. \quad \tilde{l}_{L,R}^{\pm} \hookrightarrow \tilde{\chi}_1^0 + l^{\pm}$$

In addition to the classical signature

$$(n \geq 2)\,\mathrm{jets} + E_T^{\mathrm{miss}},$$

the signatures

$$(k \geq 1)\ \mathrm{leptons} + (n \geq 2)\,\mathrm{jets} + E_T^{\mathrm{miss}}$$

Table 3. Numbers of events for the cut with the maximal value of the "significances" S_2 and S_{12} and corresponding values of the 5σ discovery probability for $L = 10^5$ pb^{-1} (case A)

$m_{\tilde{q}}$ ($m_{\tilde{g}}$), GeV	$m_{\tilde{\chi}_1^0}$, GeV	Cut number	Signal	S_2	S_{12}	Probability of discovery	
						$N_{\rm back} = N_b$	$N_{\rm back} = 2N_b$
2450	400	18	33	4.23	2.52	0.667	0.211
(3050)	1200	17	21	2.73	1.52	0.055	0.006
2050	350	19	176	10.32	6.33	1.000	1.000
(3000)	1025	19	63	4.72	2.62	0.684	0.198
	1500					$N_s/N_b < 0.5$	
	1950					$N_s/N_b < 0.5$	
1550	260	16	1773	36.27	24.06	1.000	1.000
(2000)	770	13	1697	25.57	14.33	1.000	1.000
	1162					$N_s/N_b < 0.5$	
	1395					$N_s/N_b < 0.5$	
1050	175	10	18793	98.43	58.03	1.000	1.000
(2000)	525	10	10954	64.75	36.26	1.000	1.000
	788	19	74	5.38	3.02	0.900	0.417
	945	19	86	6.07	3.45	0.983	0.681
550	92	7	180270	275.47	156.43	1.000	1.000
(2000)	225	10	20210	103.85	61.71	1.000	1.000
	412	10	9939	59.82	33.24	1.000	1.000
	495	13	2560	35.27	20.54	1.000	1.000

Note: The N_b values were taken from Table 1.

with leptons and jets in the final state arise owing to the leptonic decays of the chargino and the second neutralino. As was mentioned above, these signatures were used in [1] to investigate the LHC(CMS) potential for discovering squarks and gluinos. This was done within the SUGRA–MSSM framework, where the gaugino masses $m_{\tilde{\chi}_1^0}$ and $m_{\tilde{\chi}_2^0}$ are determined predominantly by the common gaugino mass $m_{1/2}$.

In our study, we consider the general case where the relation between $m_{\tilde{\chi}_1^0}$ and $m_{\tilde{g}}$ is arbitrary. We investigate the detection supersymmetry using the classical signature $(n \geq 2)jets + E_T^{\rm miss}$. Signatures featuring several leptons in the final state are more model-dependent; in addition, the classical signature leads to the highest discovery potential within the SUGRA–MSSM framework. We find that LHC potential for discovering squarks and gluinos depends rather strongly on the relation between the $\tilde{\chi}_1^0$, $\tilde{g}$, and $\tilde{q}$ masses and decreases with increasing LSP mass.

2. SIMULATION OF THE DETECTOR RESPONSE

Our simulations were performed at the particle level with parametrized detector responses based on a detailed detector simulation. To be more specific, our estimates were obtained for the CMS (Compact Muon Solenoid) detector. We used the program CMSJET [9] for a CMS detector simulation. The main aspects of the CMSJET relevant to our study are the following.

Charged particles are tracked in a 4 T magnetic field. A 90% reconstruction efficiency per charged track with $p_T > 1$ GeV within $|\eta| < 2.5$ is assumed.

The geometric acceptances for μ and e are $|\eta| < 2.4$ and 2.5, respectively. The lepton momentum is smeared according to parametrizations obtained from full GEANT simulations. For a 10-GeV lepton, the momentum resolution $\Delta p_T/p_T$ is better than 1% over the full η coverage. For a 100-GeV lepton, the resolution becomes approximately $(1–5)\times 10^{-2}$, depending

Table 4. Numbers of events for the cut with the maximal value of the "significances" S_2 and S_{12} and corresponding values of the 5σ discovery probability for $L = 10^5$ pb^{-1} (case B)

$m_{\tilde{g}}$ ($m_{\tilde{q}}$), GeV	$m_{\tilde{\chi}_1^0}$, GeV	Cut number	Signal	S_2	S_{12}	Probability of discovery	
						$N_{\rm back} = N_b$	$N_{\rm back} = 2N_b$
2000	350	24	18	2.57	1.43	0.031	0.004
(2950)	1000					$N_s/N_b < 0.5$	
1500	251	16	720	21.79	13.75	1.000	1.000
(1950)	750	15	456	13.11	7.32	1.000	1.000
	1125					$N_s/N_b < 0.5$	
	1350					$N_s/N_b < 0.5$	
1000	175	7	10970	61.94	34.29	1.000	1.000
(1950)	500	11	3050	34.99	19.73	1.000	1.000
	750	14	1271	23.34	13.29	1.000	1.000
	900	14	1100	20.81	11.70	1.000	1.000
500	94	2	1164159	530.81	300.77	1.000	1.000
(1950)	250	7	30710	135.85	83.26	1.000	1.000

Note: The N_b values were taken from Table 2.

Table 5. Numbers of events for the cut with the maximal value of the "significances" S_2 and S_{12} and corresponding values of the 5σ discovery probability for $L = 10^5$ pb^{-1} (case C, cuts a)

$m_{\tilde{q}}$ ($m_{\tilde{g}}$), GeV	$m_{\tilde{\chi}_1^0}$, GeV	Cut number	Signal	S_2	S_{12}	Probability of discovery	
						$N_{\rm back} = N_b$	$N_{\rm back} = 2N_b$
2400	400	19	85	6.01	3.41	0.980	0.661
(2300)	1150					$N_s/N_b < 0.5$	
	1700					$N_s/N_b < 0.5$	
2100	350	19	191	10.92	6.77	1.000	1.000
(2000)	1000	19	63	4.72	2.62	0.684	0.198
	1500					$N_s/N_b < 0.5$	

Note: The N_b values were taken from Table 1.

on η. We assumed a 90% triggering plus a reconstruction efficiency per lepton within the geometric acceptance of the CMS detector.

The electromagnetic calorimeter of CMS extends up to $|\eta| = 2.61$. There is a pointing crack in the ECAL barrel/endcap transition region between $|\eta| = 1.478$–1.566 (six ECAL crystals). The hadronic calorimeter covers $|\eta| < 3$. The Very Forward calorimeter extends from $|\eta| < 3$ to $|\eta| < 5$. Noise terms were simulated with Gaussian distributions, and zero suppression cuts were applied.

The e/γ and hadron-shower development are taken into account by parametrizing the lateral and longitudinal profiles of showers. The starting point of a shower is fluctuated according to an exponential law.

For jet reconstruction, we used a slightly modified UA1 Jet Finding Algorithm, with a cone size of $\Delta R = 0.8$ and a 25 GeV transverse-energy threshold for jets.

3. BACKGROUNDS AND SUSY KINEMATICS

All SUSY processes with a full particle spectrum, couplings, production cross section, and decays were generated with ISAJET 7.32 and ISASUSY [10]. The SM backgrounds were also generated with ISAJET 7.32.

Table 6. Numbers of the cut with the maximal value of the "significances" S_2 and S_{12} and corresponding values of the probability of discovery (case C, cuts b)

$m_{\tilde{g}}$ ($m_{\tilde{q}}$), GeV	$m_{\tilde{\chi}_1^0}$, GeV	Cut number	Signal	S_2	S_{12}	Probability of discovery	
						$N_{\rm back} = N_b$	$N_{\rm back} = 2N_b$
2300	400	22	73	5.55	3.16	0.943	0.508
(2400)	1150	24	18	2.57	1.43	0.031	0.004
	1700					$N_s/N_b < 0.5$	
2000	350	16	283	11.06	6.30	1.000	1.000
(2100)	1000	22	51	4.15	2.29	0.446	0.088
	1500					$N_s/N_b < 0.5$	
1500	251	14	2910	42.89	26.70	1.000	1.000
(1550)	750	14	1180	22.01	12.45	1.000	1.000
	1125					$N_s/N_b < 0.5$	
	1350					$N_s/N_b < 0.5$	
1000	167	7	51260	191.50	124.88	1.000	1.000
(1050)	500	7	24240	114.74	68.46	1.000	1.000
	750	10	5700	47.38	26.64	1.000	1.000
	900	14	1460	26.00	15.00	1.000	1.000
500	84	1	4330000	1604.4	980.20	1.000	1.000
(550)	250	1	3456000	1365.1	813.11	1.000	1.000
	375	1	1794000	823.3	460.28	1.000	1.000
	450	6	108528	213.0	120.83	1.000	1.000

Note: The N_b values were taken from Table 2.

The following SM processes make the main contribution to the background: WZ, ZZ, $t\bar{t}$, Wtb, $Zb\bar{b}$, $b\bar{b}$, and QCD ($2 \to 2$) processes.

As was mentioned above, we consider only the classical signature $(n \geq 2)jets + E_T^{\rm miss}$ for squark and gluino detection. We considered three different kinematical regions:

(A) $m_{\tilde{g}} \gg m_{\tilde{q}}$,

(B) $m_{\tilde{q}} \gg m_{\tilde{g}}$,

(C) $m_{\tilde{q}} \sim m_{\tilde{g}}$, $m_{\tilde{q}} > m_{\tilde{g}}$.

We also considered the case where all sparticles are heavy, with the exception of the third-generation sfermions and LSP [11]. For case A, squark production through the process $pp \to \tilde{q}\tilde{q}$ dominates at LHC. Squark decays into quarks and LSPs, $\tilde{q} \to q\tilde{\chi}_1^0$, lead to the signature $2jets + E_T^{\rm miss}$. For case B, gluino pair production $pp \to \tilde{g}\tilde{g}$ is dominant. The gluino decays $\tilde{g} \to q\bar{q}\tilde{\chi}_1^0$ lead to the $(n \geq 3)jets + E_T^{\rm miss}$ signature. For case C, both squarks and gluinos are produced, $pp \to \tilde{q}\tilde{q}, \tilde{g}\tilde{g}, \tilde{q}\tilde{g}$, at a similar rate. Their decays give events featuring either two jets or $(n \geq 3)$ jets. We considered two types of cuts:

Cuts (a). $(n \geq 2)$ jets with $E_{T\rm jet1} \geq E_{T1}$, $E_{T\rm jet2} \geq E_{T2}$, and $E_T^{\rm miss} \geq E_{T0}$.

Cuts (b). $(n \geq 3)$ jets with $E_{T\rm jet1} \geq E_{T1}$, $E_{T\rm jet2} \geq E_{T2}$, $E_{T\rm jet3} \geq E_{T3}$, and $E_T^{\rm miss} \geq E_{T0}$.

Cuts (a) and (b) are appropriate for investigating the kinematical points A and B, respectively; for the point C, cuts (a) and (b) are both useful. We have calculated the SM backgrounds for various values of $E_{T\rm jet1}$, $E_{T\rm jet2}$, $E_{T\rm jet3}$, and E_{T0} of the cut parameters. Our results are presented in Tables 1 and 2 for a given total luminosity L.

In this article, we have considered the case where all squarks have the same mass and $m_{\tilde{\chi}_2^0}, m_{\tilde{\chi}_1^\pm} > \min(m_{\tilde{g}}, m_{\tilde{q}})$. The last requirement leads to the suppression of events featuring leptons, only the classical signature with $(n \geq 2)jets + E_T^{\rm miss}$ being essential. The shape of the squark and gluino differential decay width depends rather strongly on the relation

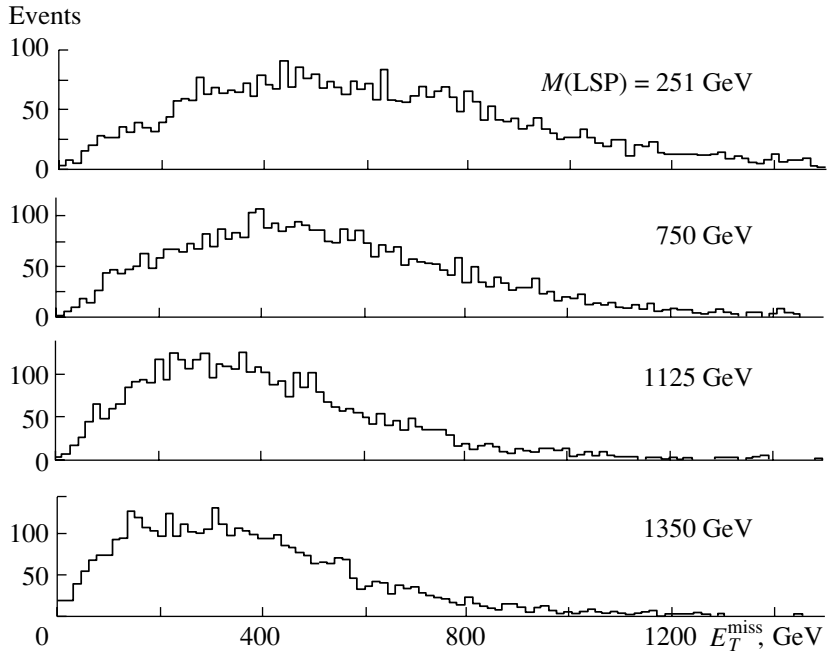

Fig. 1. E_T^{miss} distribution for various LSP masses ($m_{\tilde{g}} = 1500$ GeV, $m_{\tilde{q}} = 1950$ GeV): case B.

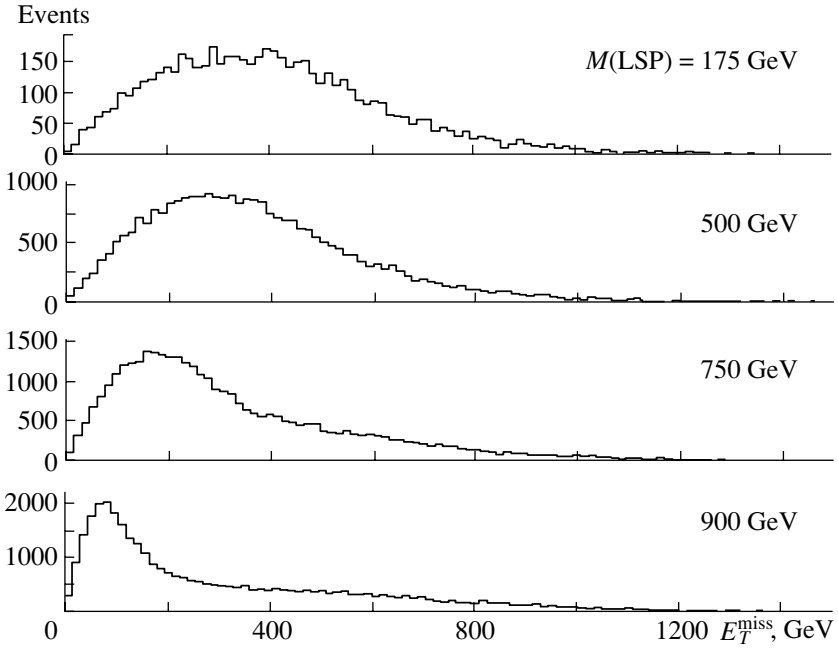

Fig. 2. E_T^{miss} distribution for various LSP masses ($m_{\tilde{g}} = 1000$ GeV, $m_{\tilde{q}} = 1950$ GeV): case B.

between the squark, gluino, and LSP masses. We have considered various values of the squark and gluino masses. We set the LSP mass to $m_{\tilde{\chi}_1^0} = k \times \min(m_{\tilde{g}}, m_{\tilde{q}})$ with $k = 1/6, 0.5, 0.75$, and 0.9. The value of $k = 1/6$ corresponds approximately to the standard case with universal gaugino masses.

4. RESULTS

The results of our calculations are presented in Tables 3–6 and in Fig. 1–6. In assessing the LHC (CMS) potential for gaugino discovery, we have used the significance defined as $S_{12} = \sqrt{N_s + N_b} - \sqrt{N_b}$, which is appropriate for estimating discovery potential in the case of future experiments [12]. We also

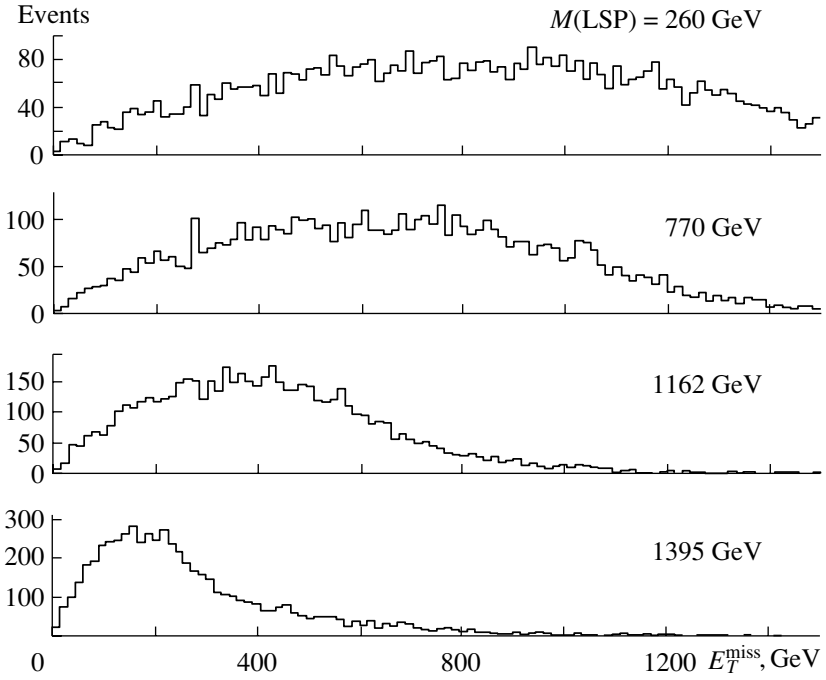

Fig. 3. E_T^{miss} distribution for various LSP masses ($m_{\tilde{g}} = 2000$ GeV, $m_{\tilde{q}} = 1550$ GeV): case A.

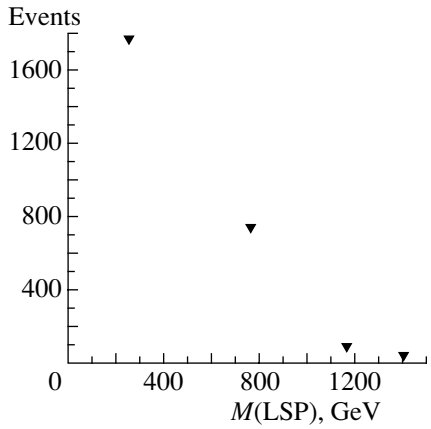

Fig. 4. Signal events versus the LSP mass ($m_{\tilde{g}} = 2000$ GeV, $m_{\tilde{q}} = 1550$ GeV): case A, cut 16a.

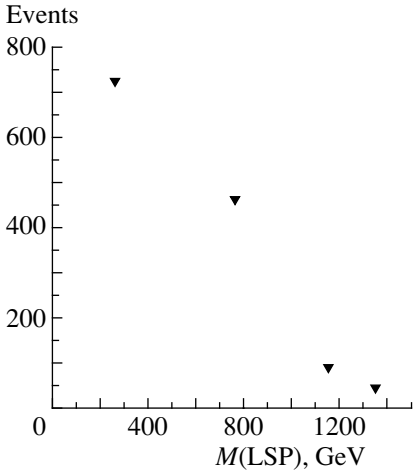

Fig. 5. Signal events versus the LSP mass ($m_{\tilde{g}} = 1500$ GeV, $m_{\tilde{q}} = 1950$ GeV): case B, cut 16b.

imposed the additional requirement that the signal-to-background ratio be larger than 0.5 ($S/B > 0.5$). For the sake of comparison, we also give the values of the frequently used significance [1] defined as $S_2 = N_s/\sqrt{N_s + N_b}$ and the 5σ discovery probability [12] for two values of the background, N_{back}. Here, $N_s = \sigma_s L$ is the average number of signal events and $N_b = \sigma_b L$ is the average number of background events for a given total luminosity L.

From our results, it follows that, for fixed values of the squark and gluino masses, the visibility of signal decreases with increasing LSP mass. This fact has a trivial explanation. In the squark or gluino rest frame, the jet spectrum does indeed become softer with increasing LSP mass. In addition, product squark pairs and gluinos have total transverse momenta close to zero in the parton model. For high LSP masses, there is a partial cancellation of missing transverse momenta from two LSP particles. The fact that, with increasing LSP mass, the E_T^{miss} spectrum becomes softer is explicitly seen in Fig. 1–3.

Figures 4–6 demonstrate that, within a well-defined cut, the number of signal events decreases with increasing LSP masses; for this reason, the

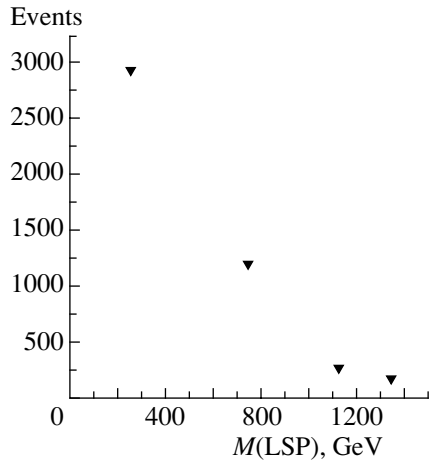

Fig. 6. Signal events versus the LSP mass ($m_{\tilde{g}} = 1500$ GeV, $m_{\tilde{q}} = 1550$ GeV): case C, cut 14b.

detection of supersymmetry is complicated for LSP masses close to the gluino or squark masses.

5. CONCLUSION

We have presented the results of the calculations for the production of squark and gluino pairs at LHC (CMS) with their subsequent decays into jets for the case of nonuniversal gaugino masses. We have found that the visibility of the signal by an excess over the SM background in $(n \geq 2)jets + E_T^{\text{miss}}$ events depends rather strongly on the relation between the mass of the LSP $\tilde{\chi}_1^0$ and the $\tilde{q}, \tilde{g}$ masses. The visibility of the signal for fixed values of the squark and gluino masses decreases with increasing the LSP mass. For a relatively large LSP mass close to the gluino or the squark masses and for $m_{\tilde{g}}, m_{\tilde{q}} \geq 1.5$ TeV, the signal is too small to be observable.

ACKNOWLEDGMENTS

We are indebted to the participants of the Daniel Denegri working group on physics simulations at LHC for enlightening comments. This work was supported by the Russian Foundation for Basic Research (project no. 99-02-16956) and by the INTAS–CERN grant no. 377.

REFERENCES

1. S. Abdullin *et al.,* CMS NOTE 1998/006.
2. R. Barbieri *et al.,* Nucl. Phys. B **367**, 28 (1991); H. Baer, C. Chen, F. Paige, and X. Tata, Phys. Rev. D **50**, 2148 (1994); **52**, 2746 (1995); **53** (6241 (1996).
3. For a review see, for instance, R. Barbieri, Riv. Nuovo Cimento **11**, 1 (1998); A. B. Lahanas and D. V. Nanopoulos, Phys. Rep. **145**, 1 (1987); H. E. Haber and G. L. Kane, Phys. Rep. **117**, 75 (1985); H. P. Nilles, Phys. Rep. **110**, 1 (1984); N. V. Krasnikov and V. A. Matveev, Fiz. Élem. Chastits At. Yadra **28**, 1125 (1997) [Phys. Part. Nucl. **28**, 441 (1997)].
4. V. S. Kaplunovsky and J. Louis, Phys. Lett. B **306**, 269 (1993).
5. N. Polonsky and A. Pomarol, Phys. Rev. Lett. **73**, 2292 (1994).
6. N. V. Krasnikov and V. V. Popov, Preprint No. 976TH/96, INR (Institute for Nuclear Research, Moscow, 1996).
7. C. Kolda and J. March-Russell, Phys. Rev. D **55**, 4252 (1997).
8. S. I. Bityukov and N. V. Krasnikov, Nuovo Cimento A **112**, 913 (1999).
9. S. Abdullin, A. Khanov, and N. Stepanov, CMS NOTE TN/94-180.
10. H. Baer, F. Paige, S. Protopopesku, and X. Tata, Preprint No. EP-930329 (Florida State Univ., 1993).
11. See, for instance, J. Bagger, J. L. Feng, and N. Polonsky, hep-ph/9905292.
12. S. I. Bityukov and N. V. Krasnikov, Mod. Phys. Lett. A **13**, 3235 (1998); Nucl. Instrum. Methods Phys. Res. A **452**, 518 (2000).

Physics of Atomic Nuclei, Vol. 64, No. 7, 2001, pp. 1323–1325. Translated from Yadernaya Fizika, Vol. 64, No. 7, 2001, pp. 1399–1401.

ELEMENTARY PARTICLES AND FIELDS
Theory

Pole Contributions in Semileptonic Decays of *D* Mesons

K. R. Nasriddinov, B. N. Kuranov, G. G. Takhtamyshev, and T. A. Merkulova

Institute of Nuclear Physics, Uzbek Academy of Sciences, pos. Ulughbek, Tashkent, 702132 Republic of Uzbekistan

Received April 7, 2000

Abstract—The contributions of the axial-vector and vector resonance states to $D \to P(V)l\bar{\nu}_l$ decays are investigated on the basis of phenomenological chiral Lagrangians. It is shown that inclusion of such intermediate states improves agreement with experimental data. © *2001 MAIK "Nauka/Interperiodica".*

In [1], semileptonic $D \to P(V)l\bar{\nu}_l$ decays were investigated on the basis of the method of phenomenological chiral Lagrangians [2]. However, no account of pole resonance states was taken there in these decays. The present study is devoted to exploring the contributions of such states to the probabilities of $D \to P(V)l\bar{\nu}_l$ decays.

Within this method, the weak-interaction Lagrangian has the form

$$L_W = \frac{G_\mathrm{F}}{\sqrt{2}}(J_\mu^{11-i12}\sin\theta_\mathrm{C} + J_\mu^{13-i14}\cos\theta_\mathrm{C})l_\mu^+,$$

where $G_\mathrm{F} \simeq 10^{-5}/m_p^2$ is the Fermi constant, θ_C is the Cabibbo angle, $l_\mu = \bar{u}_l\gamma_\mu(1+\gamma_5)u_{\nu_l}$ is the leptonic current, and J_μ^{11-i12} and J_μ^{13-i14} are the hadronic currents.

The axial-vector and vector meson currents are defined as

$$J_\mu^i = \frac{m_v^2}{g}v_\mu^i + \frac{m_a^2}{g}a_\mu^i,$$

where m_v and m_a are the masses of, respectively, the vector and the axial-vector mesons; g is the universal coupling constant; and v_μ^i and a_μ^i are the fields of, respectively, the 1^- and the 1^+ mesons ($i = 1, ..., 15$).

The Lagrangians that describe the strong interaction of pseudoscalar mesons with vector mesons and of axial-vector mesons with vector and pseudoscalar mesons can be written [3, 4], respectively, as

$$L_S(1^-, 0^-) = gf_{klm}\varphi^l\partial_\mu\varphi^k v_\mu^m \qquad (1)$$

and as

$$L_S(1^+, 1^-, 0^-) = -F_\pi g^2 f_{klm}a_\mu^k v_\mu^l\varphi^m, \qquad (2)$$

where $F_\pi = 93$ MeV, f_{klm} are the structure constants of the $SU(4)$ group ($k, l, m = 1, ..., 15$), and φ^l are the fields of 0^- mesons.

Within the method of phenomenological chiral Lagrangians, the Lagrangian that describes the strong interaction of vector mesons with vector and pseudoscalar mesons has the form [5]

$$L_S(vv\varphi) = -g_{vv\varphi}\varepsilon_{\mu\nu\alpha\beta}\mathrm{tr}(\partial_\mu\hat{V}_\nu\partial_\alpha\hat{V}_\beta\hat{\varphi}), \qquad (3)$$

where $g_{vv\varphi} = 3g^2/16\pi^2F_\pi$ is the coupling constant, $\hat{V}_\mu = \frac{1}{2i}\lambda_i v_\mu^i$, and $\hat{\varphi} = \frac{1}{2}\lambda_i\varphi^i$.

The amplitudes of these decays can be represented as [6]

$$lM\,(D(p) \to P(p_1)l(k_l)\nu(k_v))$$
$$= G_\mathrm{F}\bar{u}(k_v)[f_1 + g_1\gamma_5 + \hat{p}\,(f_2 + g_2\gamma_5)$$
$$+\hat{p}_1\,(f_3 + g_3\gamma_5)]u(k_l),$$
$$M\,(D(p) \to V(p_1)l(k_l)\nu(k_v))$$
$$= G_\mathrm{F}\epsilon_\mu^\lambda(p_1)\bar{u}(k_v)\gamma_\mu[f_1 + g_1\gamma_5 + \hat{p}\,(f_2 + g_2\gamma_5)$$
$$+\hat{p}_1\,(f_3 + g_3\gamma_5)]u(k_l),$$

where $\epsilon_\mu^\lambda(p_1)$ is the polarization vector of the 1^- mesons, f_i and g_i are form factors ($i = 1, 2, 3$) depending on the momenta of outgoing particles, $q = p - p_1$, and k_l and k_v are the 4-momenta of the leptons ($\hat{p}_i \equiv p_{i\mu}\gamma^\mu$).

Table 1. Probabilities $\Gamma(10^{10}\ \mathrm{s}^{-1})$ of semileptonic $D \to Pl\bar{\nu}_l$ decays

Decays	I [1]	II	Experimental data from [8]
$D^- \to K^0\mu^-\bar{\nu}_\mu$	10.3	5.2	$6.62^{+2.84}_{-1.89}$
$D^- \to \pi^0\mu^-\bar{\nu}_\mu$	0.47	0.24	—
$\bar{D}^0 \to K^+\mu^-\bar{\nu}_\mu$	10.2	5.2	8 ± 1
$\bar{D}^0 \to \pi^+\mu^-\bar{\nu}_\mu$	0.94	0.48	—
$D_s^- \to \bar{K}^0\mu^-\bar{\nu}_\mu$	0.81	0.41	—
$D^- \to K^0e^-\bar{\nu}_e$	11.0	5.6	6.24 ± 0.85
$D^- \to \pi^0e^-\bar{\nu}_e$	1.0	0.5	—
$\bar{D}^0 \to K^+e^-\bar{\nu}_e$	11.0	5.6	9.16 ± 0.53
$\bar{D}^0 \to \pi^+e^-\bar{\nu}_e$	1.0	0.51	$0.94^{+0.29}_{-0.24}$
$D_s^- \to \bar{K}^0e^-\bar{\nu}_e$	0.84	0.43	—

1063-7788/01/6407-1323$21.00

Table 2. Probabilities $\Gamma(10^{10}\ \mathrm{s}^{-1})$ of semileptonic $D \to Vl\bar{\nu}_l$ decays

Decays	I [1]	II	Experimental data from [8]
$D^- \to K^{*0}\mu^-\bar{\nu}_\mu$	2.47	3.38	4.26 ± 0.57
$D^- \to \rho^0\mu^-\bar{\nu}_\mu$	0.93×10^{-1}	2.1×10^{-1}	$(1.89^{+1.42}_{-1.23}) \times 10^{-1}$
			$0.22 \pm 0.07 \pm 0.05$ [11]
$\bar{D}^0 \to K^{*+}\mu^-\bar{\nu}_\mu$	2.48	3.37	—
$\bar{D}^0 \to \rho^+\mu^-\bar{\nu}_\mu$	1.85×10^{-1}	4.19×10^{-1}	—
$D_s^- \to \bar{K}^{*0}\mu^-\bar{\nu}_\mu$	1.89×10^{-1}	4.02×10^{-1}	—
$D^- \to K^{*0}e^-\bar{\nu}_e$	2.73	3.59	4.54 ± 0.47
$D^- \to \rho^0 e^-\bar{\nu}_e$	1.01×10^{-1}	2.26×10^{-1}	$< (3.5 \pm 0.1) \times 10^{-1}$
			$0.20 \pm 0.07 \pm 0.05$ [11]
$\bar{D}^0 \to K^{*+}e^-\bar{\nu}_e$	2.76	3.72	4.84 ± 0.79
$\bar{D}^0 \to \rho^+ e^-\bar{\nu}_e$	2.02×10^{-1}	4.36×10^{-1}	—
$D_s^- \to \bar{K}^{*0}e^-\bar{\nu}_e$	2.05×10^{-1}	4.19×10^{-1}	—

With the aid of these Lagrangians, we have calculated the probabilities of semileptonic $D \to P(V)l\bar{\nu}_l$ decays with allowance for the axial-vector and vector pole contributions by using the BETA package (see Tables 1 and 2). The pole contributions of the vector mesons D^{*-} and D_s^{*-} and of the axial-vector mesons D_A^- and D_{s1}^- were included in the calculations acording to Lagrangians (1)–(3) (use was also made of the approximation $m_{D_A^-} \simeq m_{D_{s1}^-}$ for a unknown D_A^--meson mass). The relevant probabilities calculated without taking into account the pole contributions of the $1^\pm$ mesons [1] are additionally included in Tables 1 and 2 for the sake of comparison.

The diagrams representing these decays are displayed in Fig. 1. It should be noted that the diagram in Fig. 1*c* contributes about 7% to the partial widths with respect to $D \to Vl\bar{\nu}_l$ decays.

It can be seen that, upon the inclusion of the contributions of the pole $1^\pm$ mesons, the calculated probabilities of $D \to Pl\bar{\nu}_l$ decays are nearly one-half as great as the probabilities without these contributions and are in good agreement with available experimental data [8] within the experimental error. This is not so only for $\bar{D}^0 \to K^+l^-\bar{\nu}_l$ channels. At the same time, our results for these decays agree well with the predictions from [9] and with the experimental data from [10].

The calculated probabilities of $D \to Vl\bar{\nu}_l$ decays (see Table 2) are also in good agreement with available experimental data [8, 11] within the experimental error. It can be seen that, for $D \to K^*l^-\bar{\nu}_l$ channels, these probabilities taking into account the pole contributions agree better with experimental data; for $D \to \rho l^-\bar{\nu}_l$ channels, the probabilities calculated with allowance for the pole contributions better correlate with the predictions of heavy-quark effective theory [12] and of lattice QCD [13–16] than those without these contributions [1].

A comparison of the relative probabilities (the notation used here is identical to that in [1]) with the experimental data from [8, 11] yields

$$R_3 \equiv \frac{\Gamma(D^- \to K^0\mu^-\bar{\nu}_\mu)}{\Gamma(D^- \to K^0e^-\bar{\nu}_e)} = 0.94,$$
$$R_3^{\mathrm{expt}} = 1.06^{+0.48}_{-0.34};$$
$$R_4 \equiv \frac{\Gamma(\bar{D}^0 \to K^+\mu^-\bar{\nu}_\mu)}{\Gamma(\bar{D}^0 \to K^+e^-\bar{\nu}_e)} = 0.93,$$
$$R_4^{\mathrm{expt}} = 0.84 \pm 0.12;$$
$$R_5 \equiv \frac{\Gamma(D^- \to \rho^0e^-\bar{\nu}_e)}{\Gamma(D^- \to K^{*0}e^-\bar{\nu}_e)} = 0.064,$$
$$R_5^{\mathrm{expt}} = 0.045 \pm 0.014 \pm 0.009;$$
$$R_6 \equiv \frac{\Gamma(D^- \to \rho^0\mu^-\bar{\nu}_\mu)}{\Gamma(D^- \to K^{*0}\mu^-\bar{\nu}_\mu)} = 0.061,$$
$$R_6^{\mathrm{expt}} = 0.051 \pm 0.015 \pm 0.009;$$
$$R_7 \equiv \frac{\Gamma(D^- \to \rho^0l^-\bar{\nu}_l)}{\Gamma(D^- \to K^{*0}l^-\bar{\nu}_l)} = 0.061,$$
$$R_7^{\mathrm{expt}} = 0.047 \pm 0.013;$$
$$R_8 \equiv \frac{\Gamma(\bar{D}^0 \to K^{*+}e^-\bar{\nu}_e)}{\Gamma(\bar{D}^0 \to K^+e^-\bar{\nu}_e)} = 0.66,$$
$$R_8^{\mathrm{expt}} = 0.51 \pm 0.18 \pm 0.06;$$

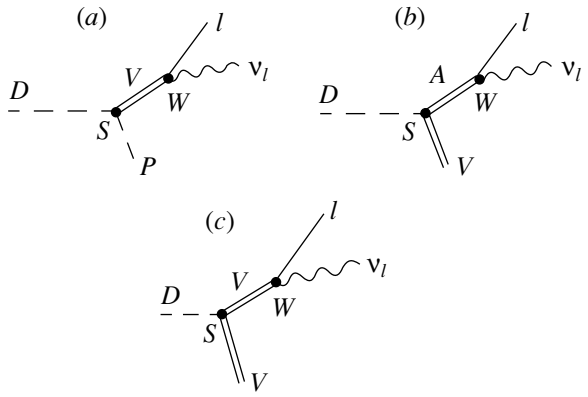

Diagrams representing $D \to P(V)l\bar{\nu}_l$ decays with allowance for pole contributions, W and S being, respectively, the weak and the strong-interaction vertex.

$$R_9 \equiv \frac{\Gamma(D^- \to K^{*0}e^-\bar{\nu}_e)}{\Gamma(D^- \to K^0 e^-\bar{\nu}_e)} = 0.64,$$

$$R_9^{\text{expt}} = 0.65 \pm 0.09 \pm 0.10;$$

$$R_{10} \equiv \frac{\Gamma(D^- \to K^{*0}\mu^-\bar{\nu}_\mu)}{\Gamma(\bar{D}^0 \to K^+\mu^-\bar{\nu}_\mu)} = 0.67,$$

$$R_{10}^{\text{expt}} = 0.43 \pm 0.09 \pm 0.09.$$

It can be seen that, for $D \to P(V)l\bar{\nu}_l$ decays, the theoretical and experimental ratios of the decay probabilities comply well. We note that the method of phenomenological chiral Lagrangians that allows for the pole contributions from intermediate axial-vector and vector mesons makes it possible to reproduce better the relative probabilities R_8, R_9, and R_{10} than other theoretical approaches [8].

In summary, the method of phenomenological chiral Lagrangians describes well $D \to P(V)l\bar{\nu}_l$ decays.

ACKNOWLEDGMENTS

We are grateful to A.M. Rakhimov for stimulating discussions.

REFERENCES

1. K. R. Nasriddinov and G. G. Takhtamyshev, Yad. Fiz. **61**, 368 (1998) [Phys. At. Nucl. **61**, 315 (1998)].
2. S. Weinberg, Phys. Rev. Lett. **18**, 188 (1967); S. Coleman, I. Wess, and B. Zumino, Phys. Rev. **177**, 2239 (1969); S. Gasiorowics and D. A. Geffen, Rev. Mod. Phys. **41**, 531 (1969); M. K. Volkov and V. N. Pervushin, *Essentially Nonlinear Quantum Theory, Dynamical Symmetries, and Meson Physics* (Atomizdat, Moscow, 1978).
3. Yu. L. Kalinovskiĭ, V. N. Pervushin, G. G. Takhtamyshev, and N. A. Sarikov, Fiz. Élem. Chastits At. Yadra **19**, 111 (1988) [Sov. J. Part. Nucl. **19**, 47 (1988)].
4. K. R. Nasriddinov, Yad. Fiz. **57**, 1141 (1994) [Phys. At. Nucl. **57**, 1077 (1994)].
5. I. Wess and B. Zumino, Phys. Lett. B **37B**, 95 (1971); Yu. L. Kalinovskiĭ, V. N. Pervushin, and N. A. Sarikov, Soobshch. Ob'edin. Inst. Yad. Issled., Dubna, No. R2-86-307 (1987); K. R. Nasriddinov, Yad. Fiz. **58**, 314 (1995) [Phys. At. Nucl. **58**, 267 (1995)].
6. Yu. L. Kalinovsky, K. R. Nasriddinov, *et al.,* Phys. Lett. B **211**, 350 (1988).
7. G. G. Takhtamyshev and T. A. Merkulova, Soobshch. Ob'edin. Inst. Yad. Issled., Dubna, No. E11-97-182 (1997).
8. Particle Data Group, Phys. Rev. D **54**, 444 (1996).
9. V. O. Galkin, A. Yu. Mishurov, and R. N. Faustov, Yad. Fiz. **55**, 1080 (1992) [Sov. J. Nucl. Phys. **55**, 608 (1992)].
10. J. C. Anjos *et al.,* Phys. Rev. Lett. **62**, 1587 (1989); J. Adler *et al.,* Phys. Rev. Lett. **62**, 1821 (1989).
11. E. M. Aitala *et al.,* FERMILAB Pub-96/399-E (Batavia, 1996).
12. B. Bajc, S. Fajfer, and R. J. Oakes, Phys. Rev. D **53**, 4957 (1996).
13. V. Lubicz, G. Martinelli, M. S. McCarthy, and C. T. Sachrajda, Phys. Lett. B **274**, 415 (1992).
14. A. Abada *et al.,* Nucl. Phys. B **416**, 675 (1994).
15. C. R. Allton *et al.,* Phys. Lett. B **345**, 513 (1995).
16. K. C. Bowler *et al.,* Phys. Rev. D **51**, 4905 (1995).

Translated by A. Isaakyan

Physics of Atomic Nuclei, Vol. 64, No. 7, 2001, pp. 1326–1328. Translated from Yadernaya Fizika, Vol. 64, No. 7, 2001, pp. 1402–1404.

ELEMENTARY PARTICLES AND FIELDS
Theory

Decay $\tau^- \to \phi\pi^-\nu_\tau$ and ω–ϕ Mixing

K. R. Nasriddinov, B. N. Kuranov, G. G. Takhtamyshev, and T. A. Merkulova

Institute of Nuclear Physics, Uzbek Academy of Sciences, pos. Ulughbek, Tashkent, 702132 Republic of Uzbekistan

Received April 7, 2000

Abstract—The decay process $\tau^- \to \phi\pi^-\nu_\tau$ is investigated on the basis of the method of chiral phenomenological Lagrangians. It is shown that the calculated value of the decay probability is very sensitive to variations in the angle of ω–ϕ mixing. The resulting value of this probability is compared with available experimental data and with the results of other theoretical calculations. © *2001 MAIK "Nauka/Interperiodica".*

Presently, much attention is being given to the decay processes $\tau^- \to (\omega, \phi)\pi^-\nu_\tau$. Investigations of various channels of these decays would provide a clue to solving the problem of the existence of second-class currents [1] and the problem of ω–ϕ mixing in these decays. Previously, the decay channels $\tau^- \to (\omega, \phi)\pi^-\nu_\tau$ were studied within the conserved-vector-current (CVC) hypothesis [2] and the vector-dominance model [3]. Here, we consider the decay channel $\tau^- \to \phi\pi^-\nu_\tau$ on the basis of the method of phenomenological chiral Lagrangians [4]. Within this method, $\tau \to VP\nu_\tau$ τ-lepton decay channels were investigated in [5]. In order to study these decays, it was found there that the weak hadronic currents between pseudoscalar and vector meson states are given by

$$J^i_\mu = F_\pi g v^a_\mu \varphi^b f_{abi}, \tag{1}$$

where $F_\pi = 93$ MeV; $g \simeq \sqrt{12.8\pi}$ is a universal coupling constant; v^i_μ and φ^i are the fields of, respectively, 1^- and 0^- mesons; and f_{abi} are the structure constants of the $SU(3)$ group $(a, b, i = 1, ..., 8)$.

From expression (1) for the currents, it follows, however, that the probabilities of the decay processes $\tau^- \to (\omega, \phi)\pi^-\nu_\tau$ vanish, so that these decays can occur only owing to second-order effects. In [6], the decay channel $\tau^- \to \omega\pi^-\nu_\tau$ was therefore investigated on the basis of the Lagrangian for anomalously strong interaction. The present study is devoted to an analysis of the decay channel $\tau^- \to \phi\pi^-\nu_\tau$ within the method of phenomenological chiral Lagrangians. With the aid of this method, the hadronic decays of the τ lepton into final states containing up to three pseudoscalar mesons were investigated in [7, 8].

Within the formalism of phenomenological chiral Lagrangians, the Lagrangian of anomalously strong interaction has the form [4]

$$L_S(vv\varphi) = -g_{vv\varphi}\varepsilon_{\mu\nu\alpha\beta}\mathrm{tr}(\partial_\mu \hat{V}_\nu \partial_\alpha \hat{V}_\beta \hat{\varphi}), \tag{2}$$

where $\hat{V}_\mu = \frac{1}{2i}\lambda_i v^i_\mu$, $\hat{\varphi} = \frac{1}{2}\lambda_i \varphi^i$, and $g_{vv\varphi} = 3g^2/16\pi^2 F_\pi$ is the coupling constant. According to (2), the Lagrangian describing ρ^--meson interaction with ϕ and π^- mesons has the form

$$L_S(\rho^- \to \phi\pi^-) = -0.0016 i g_{vv\varphi}\varepsilon_{\mu\nu\alpha\beta}\partial_\mu\phi_\nu\partial_\alpha\rho^+_\beta\pi^-, \tag{3}$$

where it is assumed that the angle of ω–ϕ mixing is 39°.

The weak-interaction Lagrangian has the form

$$L_W = \frac{G_\mathrm{F}}{\sqrt{2}} J^h_\mu l^+_\mu + \mathrm{h.c.} \tag{4}$$

Here, $G_\mathrm{F} \simeq 10^{-5}/m_p^2$ is the Fermi constant; l_μ is the leptonic current, $l_\mu = \bar{u}_l\gamma_\mu(1+\gamma_5)u_{\nu_l}$; and the hadronic currents are given by

$$J^h_\mu = J^{1+i2}_\mu \cos\theta_\mathrm{C} + J^{4-i5}_\mu \sin\theta_\mathrm{C},$$

where θ_C is the Cabibbo angle. In the case being considered, the ρ-meson current has the form

$$J^{1+i2}_\mu = \frac{m^2_\rho}{g}\rho_\mu.$$

In accordance with the Lagrangians in (3) and (4), we define the amplitude for the decay process $\tau^- \to \phi\pi^-\nu_\tau$ as

$$M = \frac{0.0016 G_\mathrm{F} m^2_\rho g_{vv\varphi}\cos\theta_\mathrm{C}}{\sqrt{2}g[S_1 - m^2_\rho - i(m_\rho\Gamma_\rho)]} \times \varepsilon_{\mu\nu\alpha\beta}P^\phi_\alpha K^\rho_\mu \epsilon^\phi_\beta \bar{u}_{\nu_l}\gamma_\nu(1+\gamma_5)u_\tau, \tag{5}$$

where ϵ^ϕ_β is the ϕ-meson polarization vector; P^ϕ_α and K^ρ_μ are the 4-momenta of the ϕ and the ρ meson,

1063-7788/01/6407-1326$21.00

respectively; Γ_ρ is the decay width of the ρ meson; and m_ρ is its mass. It follows that the decay amplitude squared has the form

$$\begin{aligned}
|\,M\,|^2 = -K[m_\phi^2 m_\pi^2(0.5(S_2 - m_\pi^2)\\
+0.5(S_3 - m_\phi^2)) - m_\phi^2(0.5(S_2 - m_\pi^2))^2\\
-m_\pi^2(0.5(S_3 - m_\phi^2))^2 + 0.25(S_2 - m_\pi^2)\\
\times(S_3 - m_\phi^2)(S_1 - m_\pi^2 - m_\phi^2)\\
-(0.5(S_1 - m_\pi^2 - m_\phi^2))^2\\
\times(0.5(S_2 - m_\pi^2) + 0.5(S_3 - m_\phi^2))],
\end{aligned}$$

where

$$K = \frac{2.4 \times 10^{-5} G_F^2 m_\rho^4 (g\cos\theta_C)^2}{(16\pi^2 F_\pi)^2[(S_1 - m_\rho^2)^2 + (m_\rho\Gamma_\rho)^2]}.$$

Here, $S_1 = (k_\tau - k_\nu)^2$, $S_2 = (k_\tau - P_\phi)^2$, and $S_3 = (k_\tau - P_{\pi^-})^2$ are the Mandelstam variables.

The diagram describing the decay process in question is depicted in the figure. The $\tau^- \to \phi\pi^-\nu_\tau$ decay diagram was calculated with the aid of the BETA subroutine [9]. In these calculations, we used ω–ϕ mixing [10] in the form

$$\omega = V_8 \sin\theta_V + V_0 \cos\theta_V,$$
$$\phi = V_8 \cos\theta_V - V_0 \sin\theta_V.$$

At $\theta_V = 39°$, the result for the rate of the decay process $\tau^- \to \phi\pi^-\nu_\tau$ is

$$\Gamma(\tau^- \to \phi\pi^-\nu_\tau) = 0.38 \times 10^6 \mathrm{s}^{-1}.$$

This result complies well with the experimental value of $\Gamma(\tau^- \to \phi\pi^-\nu_\tau) < (12.04 \pm 0.07) \times 10^8 \mathrm{s}^{-1}$ from [10], but it is below the predictions of the vector-dominance model [3], $\Gamma(\tau^- \to \phi\pi^-\nu_\tau) = (0.41 \pm 0.17) \times 10^8\ \mathrm{s}^{-1}$, and is four orders of magnitude less than the upper limit on this quantity within the CVC hypothesis [2], $\Gamma(\tau^- \to \phi\pi^-\nu_\tau) < 0.31 \times 10^{10}\mathrm{s}^{-1}$. But in the case of ideal mixing, $\theta_V = 35.3°$, we obtain, for this channel, the value of $\Gamma(\tau^- \to \phi\pi^-\nu_\tau) = 1.27 \times 10^8\ \mathrm{s}^{-1}$, which is above the prediction from [3]. It should be noted that the value that we found here for the rate of the decay process $\tau^- \to \phi\pi^-\nu_\tau$ is very sensitive to the choice of the mixing angle, varying with it in proportion to

$$\frac{1}{2\sqrt{3}}\cos\theta_V - \frac{1}{2\sqrt{2}}\sin\theta_V.$$

As to the decay process $\tau^- \to \omega\pi^-\nu_\tau$, its rate is proportional to

$$\frac{1}{2\sqrt{3}}\sin\theta_V + \frac{1}{2\sqrt{2}}\cos\theta_V;$$

that is, the decay rate is virtually independent here of the mixing angle [6]. Hence, the decay channel being studied can serve as an ideal source of information about ω–ϕ mixing. A more accurate measurement of the decay process $\tau^- \to \phi\pi^-\nu_\tau$ at $c\tau$ factories in the future would permit a precise determination of the angle of ω–ϕ mixing. It is worth noting that the result obtained in [3] differs from ours in that, there, the sensitivity of the relative probability $R_{\omega\phi}$ of the $\omega\pi$ and $\phi\pi$ channels to variations in the mixing angle was demonstrated only at specific values of the parameter r characterizing the approach adopted in that study.

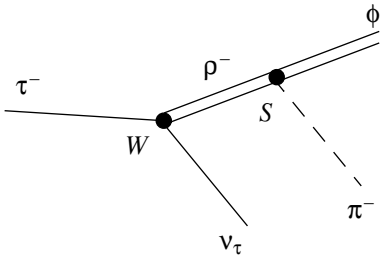

Diagram representing the decay channel $\tau^- \to \phi\pi^-\nu_\tau$, W and S being, respectively, the weak- and the strong-interaction vertex.

In our calculations for the probability of the decay process $\tau^- \to \phi\pi^-\nu_\tau$, we took into account the contributions from the $\rho(770)$, $\rho(1450)$, and $\rho(1700)$ mesons, whose widths are 151, 310, and 235 MeV, respectively. Here, in just the same way as in case of the decay mode $\tau^- \to \omega\pi^-\nu_\tau$ [6], the contributions of the vector intermediate states $\rho(1450)$ and $\rho(1700)$ are dominant, exceeding considerably the $\rho(770)$ contribution. We note that, in [3], this decay channel was studied with allowance for only a ρ' meson in addition to a ρ meson.

In summary, the method of phenomenological chiral Lagrangians makes it possible to describe accurately the decay channel $\tau^- \to \phi\pi^-\nu_\tau$, which is of interest, in particular, as an ideal source of information for precisely determining the angle of ω–ϕ mixing.

ACKNOWLEDGMENTS

We are grateful to M.M. Musakhanov and A.M. Rakhimov for interest in this study and stimulating discussions.

REFERENCES

1. S. Weinberg, Phys. Rev. **112**, 1375 (1958); C. Leroy and J. Pestieau, Phys. Lett. B **72B**, 398 (1978).
2. S. I. Eidelman and V. N. Ivanchenko, Phys. Lett. B **257**, 437 (1991).
3. G. Lopez Castro and D. A. Lopez Falcon, Phys. Rev. D **54**, 4400 (1996).

4. S. Weinberg, Phys. Rev. Lett. **18**, 188 (1967); S. Coleman, I. Wess, and B. Zumino, Phys. Rev. **177**, 2239 (1969); S. Gasiorowics and D. A. Geffen, Rev. Mod. Phys. **41**, 531 (1969); M. K. Volkov and V. N. Pervushin, *Essentially Nonlinear Quantum Theory, Dynamical Symmetries, and Meson Physics* (Atomizdat, Moscow, 1978).
5. K. R. Nasriddinov and T. A. Merkulova, Yad. Fiz. **61**, 1661 (1998) [Phys. At. Nucl. **61**, 1549 (1998)]; Phys. Rev. D **57**, 6860 (1998).
6. K. R. Nasriddinov, B. N. Kuranov, and T. A. Merkulova, hep-ph/9901414.
7. K. R. Nasriddinov, Yad. Fiz. **57**, 1141 (1994) [Phys. At. Nucl. **57**, 1077 (1994)].
8. K. R. Nasriddinov and Sh. Kh. Dzhuraev, Ukr. Fiz. Zh. **41**, 143 (1996).
9. G. G. Takhtamyshev and T. A. Merkulova, Soobshch. Ob'edin. Inst. Yad. Issled. (Dubna), No. E11-97-182 (1997).
10. Particle Data Group, Phys. Rev. D **54**, 99 (1996).

Translated by A. Isaakyan

Physics of Atomic Nuclei, Vol. 64, No. 7, 2001, pp. 1329–1336. From Yadernaya Fizika, Vol. 64, No. 7, 2001, pp. 1405–1412.

ELEMENTARY PARTICLES AND FIELDS
Theory

Pion-Distribution Amplitude within the Instanton Model*

I. V. Anikin, A. E. Dorokhov, and L. Tomio[1)]

Joint Institute for Nuclear Research, Dubna, Moscow oblast, 141980 Russia

Received February 2, 2000

Abstract—The leading-twist pion-distribution amplitude is obtained at a low normalization scale of order ρ_c (inverse average size of an instanton). Pion dynamics, consistent with gauge invariance and low-energy theorems, is considered within the instanton vacuum model. The results are QCD-evolved to higher momentum-transfer values and are in agreement with recent data from CLEO on the pion transition form factor. It is also shown that some previous calculations violate the axial Ward–Takahashi identity.

1. INTRODUCTION

At high momentum transfers, the amplitudes of exclusive hadron processes due to factorization of large- and short-distance dynamics [1–3] are expressed, in the leading logarithmic approximation, as the convolution of hard and soft scattering amplitudes. The first ones are calculable in perturbative QCD; they are dominated by hard one-gluon-exchange diagrams. The second ones describe the soft transition of initial and final hadron states into quarks; they are determined in terms of hadron distribution amplitudes (DA) [1]. These phenomenological functions have the meaning of the amplitude of hadron decay (in the infinite-momentum frame, $p_h \to \infty$) into a quark–antiquark pair (in the meson case), with momentum fractions xp_h and $\bar{x}p_h (\bar{x} = 1 - x)$ and a virtuality μ^2. Since DAs depend on dynamics at large distances, they can be calculated only by a nonperturbative technique.

The first attempt at calculating hadron DAs was made in [4]. It resulted in a two-humped shape for the pion DA. However, the applicability of this form of DA to exclusive processes at high momentum transfers was questioned some time ago [5]. It was shown that, in the collinear approximation, soft one-gluon exchange, which corresponds to large values of the strong coupling constant, is dominant at momentum-transfer values far from the asymptotic region. Moreover, the prediction based on this DA overshoots large Q^2 data on the pion transition form factor published recently by the CLEO collaboration [6] (for discussions, see, e.g., [7]).

By using a refined technique to extract hadronic DAs based on QCD sum rules with nonlocal condensates [9], it was shown later on [8] that the pion DA at a low-energy scale is closer in form to the asymptotic one. It was also found that the form of hadron DAs is very sensitive to the structure of the nonperturbative vacuum in terms of nonlocal condensates. In [10, 11], nonlocal condensates were modeled within the instanton model.

In this article, quark–pion dynamics developed on the basis of the instanton vacuum model (for a recent review, see, e.g., [12]) is used to calculate the leading-twist pion DA at a low normalization point of order ρ_c (inverse effective size of an instanton). The instanton model of the QCD vacuum gives a dynamical mechanism of chiral symmetry breaking, provides a solution to the $U_A(1)$ problem, and leads to understanding the physics of light pseudoscalar mesons. Moreover, it dynamically generates the momentum-dependent effective quark mass M_q and quark–pion vertex $g_{\pi qq}$ and, as a consequence, provides inherently a natural ultraviolet cutoff parameter in quark-loop integrals through the effective instanton size ρ_c.

The instanton-model parameters are naturally related to basic quantities of low-energy physics. The inverse effective instanton size ρ_c^{-1} directly measures the average virtuality of quarks that flow through the vacuum with a momentum k_q, where $\langle k_q^2 \rangle \equiv \lambda_q^2 \approx 2\rho_c^{-2}$ [10] ≈ 0.5 GeV^2 [13]. The quark-mass parameter M_q is given by the Goldberger–Treiman relation $M_q = g_{\pi qq} f_\pi$, with the quark–pion coupling constant being fixed by the compositeness condition. Finally, the effective instanton density n_c is determined via the gap equation.

Earlier attempts [14] (see also [15]) at calculating the pion DA were made within the model developed

*This article was submitted by the authors in English.

[1)]Instituto de Física Teórica, Univ. Estadial Paulista (UNESP), Rua Pamplona 145, BR-01405-900 São Paulo, SP, Brazil.

in [16], which was further improved. The effective action proposed in [16] is valid only in the chiral limit and was modified consistently in [17]. The effective quark Lagrangian involving contributions of nonzero quark modes was considered in [18]. In [11], it was shown that the kernel of the effective instanton-induced four-quark interaction can be expressed in terms of a gauge-invariant quantity, nonlocal quark condensate, whereby nonperturbative effects of the instanton field are effectively resummed. What is important in the context of the present study is that, within nonlocal models, the form of conserved currents is generally different from that of usual local currents (see, e.g., [19]). These points lead to the conclusion that the approach of [16] is not fully consistent with low-energy theorems. In view of these facts, it is necessary to revise some of the previous calculations. In particular, the approach of [16] fails to satisfy the axial Ward–Takahashi identity (WTI). As was shown in [19], the local part of the axial current is modified by a nonlocal term. Physically, this means that usual local currents are defined via (free) current quarks and that a modification by nonlocal terms occurs owing to the transition from current- to constituent-quark description in effective models. These additional terms are not suppressed by a small instanton-density parameter and lead to a correction on the order of 30% to the pion decay constant F_π. Since the pion decay constant is an integral measure of the pion DA, the main motivation of the present study is to estimate the effect of such terms on the leading term of the wave function.

This article is organized as follows. In Section 2, we define the pion DA. In Section 3, we write the effective instanton-induced action in terms of quark fields gauged by P-ordered exponential phase factors. The gauge fields in the phase factor (vector, axial-vector, etc.) are in general unphysical; however, their introduction is convenient for generating conserved currents of the model. The results and main conclusions are presented in the last section. In the Appendix, we show how the axial WTI is satisfied within the nonlocal four-quark model.

2. PION-DISTRIBUTION AMPLITUDE AT A LOW-ENERGY SCALE

The axial projection of the pion light-cone DA $\varphi_A(x)$ defines the leading asymptotic behavior of the pion form factor. It parameterizes the structure of the matrix element

$$\langle 0|J_\mu^A(z,-z)|\pi^+(p)\rangle = ip_\mu F_\pi \int_0^1 dx e^{i(2x-1)p\cdot z}\,\varphi_A(x) \tag{1}$$

of the bilocal operator

$$J_\mu^A(z,-z) = \bar d(z)\gamma_\mu\gamma_5 P\exp\left(i\int_{-z}^{z} A_\mu(z)dz^\mu\right)u(-z), \tag{2}$$

where the light-cone limit is considered; $z^\mu = \lambda n^\mu$, n^μ being the lightlike vector, $n^2 = 0$, normalized by the condition $p\cdot n = 1$; $F_\pi = 130$ MeV is the weak pion decay constant; and the leading-twist pion light-cone DA is normalized by the condition

$$\int_0^1 dx\varphi_A(x) = 1. \tag{3}$$

The path-ordered Schwinger phase factor is required for gauge invariance, and the integration is performed along the lightlike direction z. This factor will be neglected in the following, since the possible contribution of a classical field (instanton) produces higher twist corrections to the DA and that of a quantum field gives corrections in a small instanton-density parameter.

The bilocal current (2) is defined in terms of current quarks, and the effective low-energy model that we are going to use is described in terms of constituent quarks U and D. In order to derive the matrix element (2), we therefore consider the vertex $\langle 0|J_\mu^A(z,-z)|U(k)\bar D(k)\rangle$, which, after the extraction of the pion pole, takes the form

$$\langle 0|J_\mu^A(z,-z)|U(k)\bar D(p-k)\rangle = \langle 0|J_\mu^A(z,-z)|\pi^+(p)\rangle\frac{1}{m_\pi^2-p^2}\Gamma^a_{\pi q}(k,p), \tag{4}$$

where

$$\Gamma^a_{\pi q}(k,p) = \langle \pi^+(p)|U(k)\bar D(p-k)\rangle.$$

Expressing the matrix element

$$\langle 0|J_\mu^A(z,-z)|U(k)\bar D(p-k)\rangle$$

in terms of a loop integral, taking into account constituent-quark rescattering, and selecting the pion pole, we can then reduce the expression for the DA to the form[2)]

$$p^\mu F_\pi\varphi_A(x) = 2N_c\int\frac{d^4k}{(2\pi)^4 i}\delta(x-k\cdot n) \times \mathrm{tr}\{\Gamma^a_{\pi q}(k,p)\,S(k)^A\Gamma^{\mu a}(k,p)S(k-p)\}, \tag{5}$$

where x is the pion-momentum (p) fraction carried by a quark. The delta function in (2) accumulates

[2)] This expression generalizes that which was given previously in [14] (and also in [15]). In those studies, the local-axial-current vertex $\gamma_\mu\gamma_5$ was used instead of the dressed one, $\Gamma^\mu(k,q)$. As will be seen below, this approximation is inconsistent with the axial WTI.

information about all the moments of the DA and is related to them by the Mellin transformation.

In the above expression, $S(k)$, ${}^{A}\Gamma^{\mu a}(k,p)$, and $\Gamma^{a}_{\pi q}(k,p)$ are the dressed quark propagator, the quark-axial-current vertex, and the quark–pion vertex, respectively. The main subject of the rest of this article is to specify these functions. To this end, we use a covariant effective low-energy model with a separable nonlocal four-quark interaction. Moreover, the actual calculations will be done within a model where interquark interaction is induced by instanton exchange. The advantages of the instanton model are the following:

(i) The form of the nonlocal interaction is given by quark zero modes.

(ii) The parameters of the model are directly related to the fundamental low-energy constants.

One can verify that the numerical dependence of the results on the pion mass and current quark mass is negligible and can be ignored within the following considerations: $m_\pi = 0$ and $m_{\rm curr} = 0$. However, the interplay of the effective quark mass M_q and the scale of nonlocality of the vacuum field, λ_q^2, has an important effect on the form of the DA.

3. GAUGED NONLOCAL FOUR-FERMION MODEL AND CONSERVED CURRENTS

1. Let us consider the nonlocal chirally invariant action given by

$$S = S_0 + S_{4q} \tag{6}$$

with

$$S_0 = \int d^4x d^4y\, \delta(x-y)\, \bar{Q}(x,X) i\widehat{\partial}_y Q(X,y), \tag{7}$$

$$S_{4q} = \frac{1}{2} G_I \int d^4X \int \prod_{n=1}^{4} d^4x_n\, K_I(x_1,x_2,x_3,x_4) \tag{8}$$

$$\times \left\{ \sum_i \left[\bar{Q}_R(X-x_1,X)\Gamma_i Q_L(X,X+x_3)\right] \right.$$

$$\left. \times \left[\bar{Q}_R(X-x_2,X)\Gamma_i Q_L(X,X+x_4)\right] + (R \leftrightarrow L) \right\},$$

where $Q_{R(L)}(x,y) = \dfrac{1\pm\gamma_5}{2} Q(x,y)$ are gauged quark fields of definite chirality and the matrix combinations $\Gamma_i \otimes \Gamma_i$ are given by

$$1\otimes 1 - \tau^a \otimes \tau^a, \tag{9}$$

$$\frac{1}{2(2N_c-1)} (\sigma_{\mu\nu}\otimes\sigma_{\mu\nu} - \tau^a\sigma_{\mu\nu}\otimes\tau^a\sigma_{\mu\nu}).$$

Here, τ^a are the Pauli matrices for the flavor space, and $N_c = 3$ is the number of colors. The form of the action is motivated by the instanton vacuum model; in the local limit, it reduces into the 't Hooft vertex. In the following, we neglect the terms induced by tensor interaction in (9) since they do not contribute to scalar channels. The action in (6) effectively describes the instanton-exchange-induced interaction between quarks and is a nonlocal generalization of the Nambu–Jona-Lasinio (NJL) model. We assume that the nonlocal kernel $K_I(x_1,x_2,x_3,x_4)$ has the separable form

$$K_I(x_1,x_2,x_3,x_4) = f(x_1)f(x_2)f(x_3)f(x_4) \tag{10}$$

and relate, in what follows, the function $f(x)$ to the profile function for the quark zero mode in the instanton field.

In order to render the nonlocal action (6)–(8) gauge-invariant with respect to external fields, the quarks are coupled by path-ordered phase factors:

$$Q(x,y) \equiv P\exp\left\{ -i \int_x^y dz^\mu\, \Lambda^a_\mu(z) \frac{\tau^a}{2} \right\} q(y),$$

$$\Lambda^a_\mu(z) = V^a_\mu(z) + A^a_\mu(z)\gamma_5.$$

We use a formalism based on the path-independent definition of the derivative of the line path integral [20],

$$\frac{\partial}{\partial y^\mu} \int_x^y dz^\nu\, \Lambda_\nu(z) = \Lambda_\mu(y). \tag{11}$$

This means that the terms induced by nonminimal couplings are ignored. This formalism was used in [21] (see also [22, 23]) for gauging nonlocal interactions. The incorporation of a gauge-invariant interaction with gauge fields is very relevant to correctly treating the hadron characteristics probed by external sources, such as hadron form factors [19] and parton distribution functions [11].

2. Conserved currents are given by the derivatives of the action with respect to the external fields at zero. In the presence of a nonlocal interaction, the currents involve both local and nonlocal terms. For our purpose, it is sufficient to regard a vertex featuring one external isovector axial-vector current. It is given by[3)]

$${}^{A}\Gamma^{\mu a}_{4q}(k_1,k_2,k_3,k_4,q) \tag{12}$$

$$= \gamma^\mu\gamma_5\tau^a/2 + G_I f(k_1)f(k_2)f(k_3)f(k_4)$$

[3)] Here, we follow spin–isospin classification of currents that was given in [19]. Our definitions and those from that study differ in the definition of the path integral. This difference is displayed in the form of (momentum) space nonlocal form factors $F_\mu(k',k)$. Still, the longitudinal components of the currents are identical in the two approaches, as this must be.

$$\times \sum_{j=\mathrm{I}}^{\mathrm{III}} \sum_{i} \left[(\Gamma_i^\alpha)_{13}\ (\Omega_{i\alpha}\ )_{24}\right]_j^a H_j^\mu\ (k_1,k_2,k_3,k_4,q)\,,$$

where k_i are the quark in(out)-going momenta and q is the momentum flowing through the current. The usual local piece of the vertex is obtained by gauging the kinetic term (7), which is equivalent to the application of a covariant derivative, $i\widehat{D}_y = i\widehat{\partial}_y + \widehat{V}(y) + \widehat{A}(y)\gamma_5$.

The nonlocal four-quark part of the current is generated from the interaction term (8). In order to expand the path-ordered exponentials entering into the interaction, we use the technique described in [21] (see also [24]). This method consists, first, in obtaining the Fourier transform and constructing the Taylor expansion of the kernel $K_I(x_1,x_2,x_3,x_4)$; after that, it is necessary to convert the powers of momenta into derivatives acting on the path-ordered exponentials and quark fields, to make the inverse Fourier transformation, and then to perform resummation.

There are two types of nonlocal vertices that are generated from (8) and which contribute to the isovector axial current: type I and type III. A type-I vertex is given by

$$H_{\mathrm{I}}^\mu\ (k_1,k_2,k_3,k_4,q) \tag{13}$$
$$= F^\mu\ (k_1+q,k_1) + F^\mu\ (k_3-q,k_3)\,,$$

with the corresponding matrix combinations

$$\left[(\Gamma_i^\alpha)_{13}\ (\Omega_{i\alpha}\ )_{24}\right]_{\mathrm{I}}^a\,, \tag{14}$$

$$\epsilon^{abc}(\tau^c\otimes i\gamma_5\tau^b), \qquad -\epsilon^{abc}(i\gamma_5\tau^b\otimes\tau^c);$$

a type-III vertex is given by

$$H_{\mathrm{III}}^\mu\ (k_1,k_2,k_3,k_4,q) \tag{15}$$
$$= F^\mu\ (k_2+q,k_2) + F^\mu\ (k_3-q,k_3)$$
$$-F^\mu\ (k_1+q,k_1) - F^\mu\ (k_4-q,k_4)\,,$$

with the matrix terms

$$(i\gamma_5\tau^a\otimes 1), \qquad -(i\gamma_5\otimes\tau^a). \tag{16}$$

In the above expressions, the nonlocal vertex function $F^\mu\ (k\pm q,k)$ is defined as

$$F^\mu\ (k\pm q,k) = (2k\pm q)^\mu\ \frac{\left[f\ (k\pm q)\,/f\ (k)-1\right]^2}{(k\pm q)^2-k^2}$$

and we use the same notation for the function f and its Fourier transform. The law of energy–momentum conservation is implicitly given by the factor $(2\pi)^4\,\delta(k_1+k_2+q-k_3-k_4)$.

3. The vertices given in the preceding subsection are bare ones. It is now necessary to "dress" the model by taking into account rescattering processes. The first step is to construct the dressed quark propagator by means of the Schwinger–Dyson equation. We treat it in the ladder approximation, which is equivalent to retaining only the leading order in the $1/N_c$ expansion. In the chiral limit, this equation is given by

$$M(p) = i2N_cG_If^2(p) \tag{17}$$
$$\times\int\frac{d^4k}{(2\pi)^4}\,\frac{\mathrm{tr}\left[\widehat{k}+M(k)\right]}{k^2-M^2(k)}f^2(k),$$

where a momentum-dependent quark mass $M(p) = M_q\tilde{Q}(p)$ ($\tilde{Q}(0)=1$) is defined by the dressed quark propagator

$$S_F^{-1}(p) = \widehat{p} - M_q\tilde{Q}(p). \tag{18}$$

A solution to Eq. (3) can be written simply as $M(p) = M_qf^2(p)$. On the other hand, the momentum dependence of the nonperturbative part of the quark propagator in the nonperturbative vacuum, $\tilde{Q}(p)$, describes the nonlocal properties of the quark condensate and is given by

$$\tilde{Q}(p) = p^2N_Q\int\frac{d^4x}{(2\pi)^4}\exp(-ip\cdot x)Q(x^2), \tag{19}$$
$$Q(x) = \langle :\bar{q}(0)E_g(0,x)q(x):\rangle/\langle :\bar{q}(0)q(0):\rangle,$$

where the Schwinger factor $E_g(0,x) = P\times\exp\left(i\int_0^x A_\mu(z)dz^\mu\right)$ in terms of the vacuum gluon field $A_\mu(z)$ guarantees gauge invariance and N_Q gives normalization. Through a solution to the gap equation (17), the function $f(p)$ is therefore related to the nonperturbative scalar propagator (19) as

$$f(p) = \sqrt{\tilde{Q}(p)}. \tag{20}$$

We now specify the QCD vacuum model as given by the instanton-induced interaction. In this case, the scalar part of the quark propagator is[4)]

$$Q_{\mathrm{I}}(x) = \frac{8\rho_c^2}{\pi}\int\limits_0^\infty drr^2\int\limits_{-\infty}^{\infty}dt \tag{21}$$
$$\times\frac{\cos\left[(r/R)\left(\arctan(t+|x|/R)-\arctan(t/R)\right)\right]}{[R^2+t^2]^{3/2}[R^2+(t+|x|)^2]^{3/2}},$$

where $R^2=\rho_c^2+r^2$ and the $\cos[...]$ factor, which comes from the Schwinger factor, effectively sums an infinite set of quark–instanton interaction terms. The normalization factor in (19) is $N_{Q_I} = 2\pi^2\rho_c^{-2}$. The explicit expressions for the instanton field and quark zero mode were used [10, 25] to obtain the above equation. Equation (3), which is obtained

[4)]The nonlocal condensate $Q(x)$ and the form factor $f(k)$ are naturally defined in the Euclidean region, where they decrease fast. All loop integrals, like that in (3), are evaluated in Euclidean space ($k^2\to -k_{\mathrm{E}}^2$, $d^4k\to id^4k_{\mathrm{E}}$). Physical results are then obtained by means of an analytic continuation back to Minkowski space.

in the chiral limit, determines the parameter G_I as $G_I = M_q^2/(N_f n_c)$, where n_c is the effective instanton density, and coincides with the result presented in [16].

The pion mass[5)] and the quark–pion vertex are obtained by using the Bethe–Salpeter equation for the quark–antiquark scattering amplitude. The pion state is manifested as a pole in the amplitude, and, in the ladder approximation with a separable kernel, the quark–pion vertex near the pole is given by

$$\Gamma^a_{\pi q}(k,p) = g_{\pi q} f(p-k) f(k) i\gamma_5 T^a, \qquad (22)$$

where the quark–pion coupling is defined by the compositeness condition

$$\frac{1}{g^2_{\pi q}} = \left.\frac{dJ_{PP}(p)}{dp^2}\right|_{p^2=m_\pi^2} \qquad (23)$$

and

$$J_{PP}(p) = i2N_c \int \frac{d^4k}{(2\pi)^4} f^2(k_+) f^2(k_-) \qquad (24)$$
$$\times \mathrm{tr}\left[i\gamma_5 S_F(k_-) i\gamma_5 S_F(k_+)\right]$$

is the pion-field-polarization operator. In Eq. (3), we have used the dressed quark propagator and introduced the notation $k^\mu_\pm = k^\mu \pm p^\mu/2$. Explicitly, the quark–pion coupling constant is given by [16]

$$\left(\frac{1}{g_{\pi qq}}\right)^2 = \frac{N_c}{4\pi^2}\int \frac{d^4k}{\pi^2 i} f^2(k) \qquad (25)$$
$$\times \frac{\left[f^2(k) - 2k^2 f(k) f'(k) + 4k^4 (f'(k))^2\right]}{\left(k^2 - M_q^2(k)\right)^2},$$

where $f'(k) \equiv \partial f(k)/\partial k^2$.

4. The nonlocal four-quark vertices Γ_{4q} induce the two-quark dressed vertices Γ_{2q} if one quark line is closed into a loop. The longitudinal part of the dressed two-quark axial-vector vertex resulting from (3) is given by [19]

$${}^A\Gamma^{\mu a}_{2q}(k,q) = \gamma^\mu\gamma_5 \frac{\tau^a}{2} - \gamma_5 \frac{q_\mu}{q^2}\frac{\tau^a}{2} \qquad (26)$$
$$\times \left\{ \left[M(k+q) + M(k)\right] - i4N_c N_f G_I f(k+q) f(k) \right.$$
$$\left. \times \int \frac{d^4l}{(2\pi)^4} \frac{M(l^2)}{l^2 - M(l^2)} f(l) \left[f(l-q) + f(l+q)\right] \right\},$$

where the gap equation (3) is used to obtain the first term in the braces. This vertex is a bare one—in particular, it is free from singularities. To obtain the full axial-vector vertex, we must take into account the transition of the current into the constituent quarks through their rescattering in the channel with pion quantum numbers. In the Appendix, we explicitly demonstrate that the full axial-vector current is given by

$${}^A\Gamma^{\mu a}_{\mathrm{full}}(k,q) \qquad (27)$$
$$= \left[\gamma^\mu - \frac{M(k+q) + M(k)}{q^2} q^\mu\right] \gamma_5 \frac{\tau^a}{2}.$$

It has a physical singularity corresponding to the pion and obviously satisfies the axial WTI:

$$q^\mu {}^A\Gamma_\mu(k,q) = S_F^{-1}(k+q)\gamma_5 + \gamma_5 S_F^{-1}(k).$$

The WTI and the requirement that the vertices contain no unphysical singularities uniquely define the longitudinal part of the vector and axial-vector vertices. The transverse part is model-dependent and, within the present approach, depends on the definition of the path integral.

4. RESULTS AND CONCLUSIONS

The pion DA is computed from (5) by using the dressed quark propagator (18), the quark–pion vertex (22), and the quark-axial-vector-current vertex (27). The momentum dependence of the dressed quantities is defined by the nonlocality of the quark condensate (19), which, in the present approach, is specified by the instanton model (3). The parameter values used in the present calculations are the following [11]: $\rho_c = 1.7\ \mathrm{GeV}^{-1}$, $M_q = 230$ MeV, and $n_c = 0.7\ \mathrm{fm}^{-4}$. They are consistent with the low-energy observables as discussed in the Introduction. In the calculation of the integral in (2), we use the Laplace transform technique described in [11]. In the present study, we do not use the constant-mass approximation.

The graph of $\varphi_A(x)$ is presented in Fig. 1 (solid curve), where we can see that its shape is similar to that of the asymptotic expression DA $\varphi_A^{\mathrm{asympt}}(x) = 6x\bar{x}$. The main contribution comes from the local part of the vertex (dash-dotted curve), and the contribution of the nonlocal part (dashed curve) is flat. The flat shape of the nonlocal contribution results from a summation of various nonlocal terms, which have a more complicated shape.

The pion DA that we found is defined at a low-energy scale $\mu_0 \sim \rho_c^{-1}$, where the application of the instanton model is expected to be justified. It serves as input data for the QCD evolution to the higher momentum-transfer scales $\mu_F^2 = Q^2$. To obtain this relation, it is convenient to expand the DA in Gegenbauer polynomials $C_n^{3/2}(x)$, which are the eigenfunctions of the kernel of the QCD evolution equations:

$$\varphi_A(x,\mu_F) = \varphi_A^{\mathrm{asympt}}(x) \qquad (28)$$

[5)] In the chiral limit, which is used in the present study, the pion mass is zero in accordance with Goldstone theorem; at finite current quark masses, it is deduced from the Gell-Mann–Oakes–Renner relation.

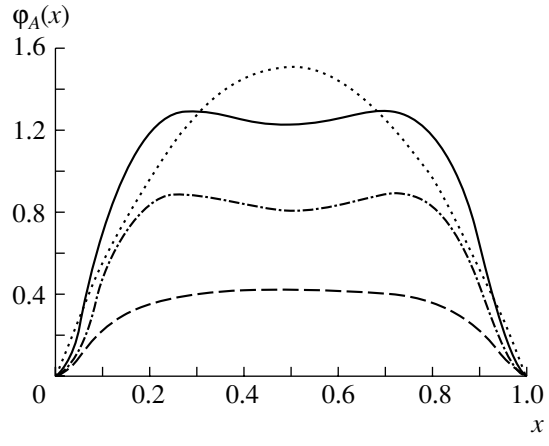

Fig. 1. Axial projection of the pion-distribution amplitude (solid curve) at the low-energy scale of $\mu_0^2 = 0.5$ GeV^2: (dash-dotted curve) contribution of the local part of the vertex, (dashed curve) contribution of the nonlocal part, and (dotted curve) asymptotic distribution amplitude.

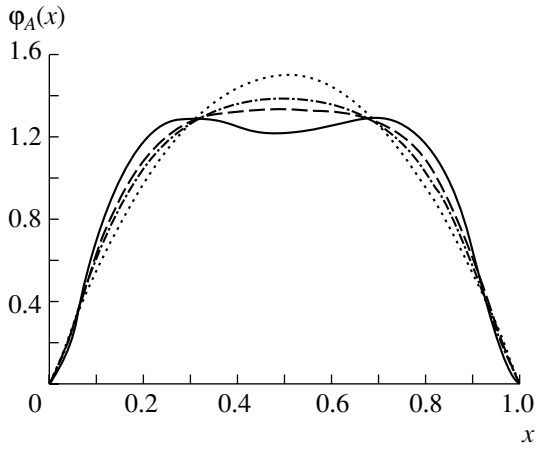

Fig. 2. Axial projection of the pion-distribution amplitude (solid curve) at the low-energy scale of $\mu_0^2 = 0.5$ GeV^2 and its evolution to higher momentum transfers squared of $Q^2 =$ (dashed curve) 1 and (dash-dotted curve) 10 GeV^2. The asymptotic distribution amplitude is shown by the dotted curve.

$$\times \left[1 + \sum_{n=2,4,\ldots}^{\infty} B_n(\mu_0) \left(\frac{\alpha_s(\mu_F)}{\alpha_s(\mu_0)}\right)^{\gamma_n} C_n^{3/2}(2x-1)\right].$$

Here, γ_n are the anomalous dimensions calculated in the leading order in the coupling constant $\alpha_s(\mu)$ and $B_n(\mu_0)$ are the coefficients in the Gegenbauer polynomial expansion. The model DA is well reproduced by the above expansion with only the first few nonzero coefficients:

$$B_2(\mu_0) = 0.069, \qquad B_4(\mu_0) = -0.061, \qquad (29)$$
$$B_6(\mu_0) = -0.017, \qquad B_{n\geq 8}(\mu_0) = 0.$$

The resulting distribution is extrapolated to higher experimentally accessible momentum scales by using perturbative QCD, so that a comparison with experimental data could be performed. For the QCD scale parameter, we choose the value of $\Lambda^3_{\overline{\rm MS}} = 250$ MeV. The pion DA evolved to the scales of 1 and 10 GeV^2 is shown in Fig. 2, along with the initial distribution at the scale of $\mu_0^2 = \lambda_q^2 = 0.5$ GeV^2.

New data on the pion transition form factor at rather high Q^2 are available from [6]. For the high-Q^2 behavior of the form factor, perturbative QCD predicts [3]

$$F_{\pi\gamma\gamma}\left(Q^2\right) = \frac{J}{\sqrt{2}}\frac{F_\pi}{Q^2}, \qquad (30)$$

with the constant J being defined in terms of the pion DA as

$$J = \frac{2}{3}\int_0^1 \frac{dx}{x}\varphi_A(x).$$

At asymptotically high Q^2, the DA evolves to $\varphi_A^{\rm asympt}(x)$ with $J^{\rm asympt} = 2$. At the highest presently available momenta of $Q^2 \approx 10$ GeV^2, this prediction is reduced by the lowest order QCD radiative corrections [26] to $J^{\rm asympt}(10\ {\rm GeV}^2) = 1.6$ and fits CLEO data well. Our predictions for noncorrected J is very stable with respect to Q^2 evolution—$J^{\rm model}\left(\mu_0^2\right) = 1.98$ and $J^{\rm model}\left(10\,{\rm GeV}^2\right) = 2.01$—and is thus indistinguishable from the predictions of perturbative QCD.

In summary, we have presented here some theoretical predictions for the pion-distribution amplitude. The nonperturbative formalism is based on the instanton model of the QCD vacuum, expressing hadron observables in terms of fundamental characteristics of the vacuum state. The effective instanton size ρ_c and the quark mass M_q appear to be the parameters of the model. The first one is given by the average virtuality of the vacuum quarks, while the second one is related to the pion decay constant by the Goldberger–Treiman relation. It has been shown that a correct normalization of the DA is obtained by using the compositeness condition and the strict implementation of PCAC, which improves some previous calculations given in [14, 15].

Our calculations are restricted to the instanton vacuum model. In the extended nonlocal NJL, where other spin–flavor terms in the interaction are possible, the pion DA can receive a contribution from the vertex with a vector insertion. The contribution of this piece to F_π is small and is estimated at -10% [19]. However, it would be interesting to consider its

effect on the form of the DA. We must also be aware that the nonlocality in this model is not fixed by any microscopic principle.

The extracted pion DA corresponds to a low normalization scale, where the effective instanton approach is justified. We have obtained the pion DA via a standard perturbative evolution to higher momentum values that are accessible by experiment. Reasonable agreement with the CLEO data on the pion transition form factor at high momentum transfer has been found. The formalism used to derive the above results constitutes a complementary approach to lattice simulations, QCD sum rules, and phenomenological fits to experimental data.

ACKNOWLEDGMENTS

The authors are grateful to S.B. Gerasimov, N.I. Kochelev, A.E. Maximov, S.V. Mikhailov, and M.K. Volkov for enlightening discussions on the results presented in this article. A.E. Dorokhov thanks colleagues from Instituto de Física Teórica, UNESP (São Paulo), for their hospitality and interest in this study. The work of A.E. Dorokhov was supported in part by St. Petersburg Center for Fundamental Research (grant no. 97-0-6.2-28). L. Tomio is grateful for partial support from Conselho Nacional de Desenvolvimento Científico e Tecnológico do Brasil (CNPq) and, in particular, thanks the Fundação de Amparo à Pesquisa do Estado de São Paulo (FAPESP) for essential support of this collaboration.

APPENDIX

For the sake of completeness, we present an explicit derivation of the full axial-vector vertex and demonstration of the axial WTI. After allowing for constituent-quark rescattering in the channel with pion quantum numbers, the full vertex becomes

$$ {}^{A}\Gamma^{\mu a}_{\text{full}}(k,p) = {}^{A}\Gamma^{\mu a}(k,p) + {}^{A}\Gamma^{\mu a}_{\text{rescat}}(k,p), \quad \text{(A.1)} $$

where ${}^{A}\Gamma^{\mu a}(k,p)$ is the bare vertex given by Eq. (26) and

$$ {}^{A}\Gamma^{\mu a}_{\text{rescat}}(k,p) \quad \text{(A.2)} $$
$$ = \frac{p^\mu p_\nu}{p^2} J^\nu_{PA}(p) \frac{G_I}{1 - G_I J_{PP}(p)} \frac{1}{g^2_{\pi q}} \Gamma^a_{\pi q}(k,p), $$

with $\Gamma^a_{\pi q}(k,p)$ and $J_{PP}(p)$ being defined by (22) and (24), respectively, and $J^\mu_{PA}(p)$ being given by

$$ J^\mu_{PA}(p) = i2N_c \int \frac{d^4k}{(2\pi)^4} f(k) f(k') \quad \text{(A.3)} $$
$$ \times \text{tr}\left\{ {}^{A}\Gamma^{\mu a}(k,p) \left[\widehat{k} + M(k)\right]^{-1} \right. $$
$$ \left. \times i\gamma_5 \left[\widehat{k'} + M(k')\right]^{-1} \right\} $$

with $k' = k + p$. By virtue of the gap Eq. (17), the vertex in (A.2) has a pole at $p^2 = m^2_\pi$. Comparing the residues at the poles in Eqs. (27) and (4) at $z = 0$, one obtains an expression for the pion decay constant. The integral in (A.3) reduces to the integral defining $g^{-2}_{\pi q}$ in (23) on the pion mass shell, and Eq. (A.3) can be written as $J^\mu_{PA}(p) = 2i\frac{M_q}{g_{\pi q}} p^\mu$. On the other hand, this matrix element defines the decay constant $J^\mu_{PA}(p) = 2F_\pi i p^\mu$. Thus, the pion decay constant F_π is reproduced as given by the Goldberger–Treiman relation [19], $F_\pi = \sqrt{2} M_q / g_{\pi q}$. In a similar way, one derives Eq. (5) by substituting, into the integral in (A.3), the factor $\exp[-i(p - 2k)z]$ projecting the quark with momentum k along lightlike direction z.

The full vertex can be rewritten in a form that explicitly satisfies the WTI. The first two terms on the right-hand side of Eq. (26) clearly satisfy the WTI. In order to compensate the third term of this equation, the rescattering term ${}^{A}\Gamma^{\mu a}_{\text{rescat}}(k,p)$ can be reduced, by using Eq. (26), to the form

$$ -i\frac{p^\mu}{p^2} \frac{G_I N_c N_f}{1 - G_I J_{PP}(p)} f(k') f(k) \left[G_I J_{PP}(p) \int \frac{d^4l}{(2\pi)^4} \frac{M(l^2)}{l^2 - M^2(l^2)} f(l) \left[f(l+p) + f(l-p) \right] \right. \quad \text{(A.4)} $$
$$ \left. - \int \frac{d^4l}{(2\pi)^4} \frac{\text{tr}\left\{ \left[\widehat{p} - M(l^2) - M(l'^2)\right] \left[\widehat{l'} + M(l'^2)\right] \gamma_5 \left[\widehat{l} + M(l^2)\right] \gamma_5 \right\}}{(l'^2 - M^2(l'^2))(l^2 - M^2(l^2))} \times f(l') f(l) \right], $$

where $l' = l + p$. By canceling one of the factors $l^2 - M^2(l^2)$ in the denominator of the integral with the term from the Dirac trace in the numerator and by properly shifting the variables of integration, the first term in the bracketed expression on the right-hand side of (A.4) can be rewritten in the same form as the second one. This demonstrates the required cancellation, and the full vertex is given by (27).

REFERENCES

1. V. L. Chernyak and A. R. Zhitnitsky, Pis'ma Zh. Éksp. Teor. Fiz. **25**, 544 (1977) [JETP Lett. **25**, 510 (1977)].

2. A. V. Radyushkin, Preprint No. R2-10717, OIYaI (Joint Institute for Nuclear Research, Dubna, 1977); A. V. Efremov and A. V. Radyushkin, Teor. Mat. Fiz. **42**, 97 (1980); Phys. Lett. B **94B**, 45 (1980).
3. S. J. Brodsky and G. P. Lepage, Phys. Lett. B **87B**, 359 (1979); Phys. Rev. D **22**, 2157 (1980).
4. V. L. Chernyak and A. R. Zhitnitsky, Phys. Rep. **112**, 173 (1984); Nucl. Phys. B **201**, 492 (1982).
5. N. Isgur and C. H. Llewellyn-Smith, Nucl. Phys. B **317**, 526 (1989); Phys. Rev. Lett. **52**, 1080 (1984); A. V. Radyushkin, Nucl. Phys. A **532**, 141 (1991).
6. CLEO Collab. (J. Gronberg *et al.*), Phys. Rev. D **57**, 33 (1998).
7. P. Kroll and M. Raulfs, Phys. Lett. B **387**, 848 (1996).
8. S. V. Mikhailov and A. V. Radyushkin, Pis'ma Zh. Éksp. Teor. Fiz. **43**, 551 (1986) [JETP Lett. **43**, 712 (1986)]; A. P. Bakulev and S. V. Mikhailov, Z. Phys. C **68**, 451 (1995).
9. S. V. Mikhailov and A. V. Radyushkin, Yad. Fiz. **49**, 794 (1989) [Sov. J. Nucl. Phys. **49**, 494 (1989)]; Phys. Rev. D **45**, 1754 (1992).
10. A. E. Dorokhov, S. V. Esaibegyan, and S. V. Mikhailov, Phys. Rev. D **56**, 4062 (1997); A. E. Dorokhov, S. V. Esaibegyan, A. E. Maximov, and S. V. Mikhailov, Eur. Phys. J. C **13**, 331 (2000); hep-ph/9903450.
11. A. E. Dorokhov and Lauro Tomio, Phys. Rev. D **62**, 014016 (2000); hep-ph/9803329.
12. T. Schäfer and E. V. Shuryak, Rev. Mod. Phys. **70**, 323 (1998) and references therein.
13. V. M. Belyaev and B. L. Ioffe, Zh. Éksp. Teor. Fiz. **83**, 876 (1982) [Sov. Phys. JETP **56**, 493 (1982)]; A. A. Ovchinnikov and A. A. Pivovarov, Yad. Fiz. **48**, 1135 (1988) [Sov. J. Nucl. Phys. **48**, 721 (1988)].
14. S. V. Esaibegyan and S. N. Tamarian, Yad. Fiz. **51**, 485 (1990) [Sov. J. Nucl. Phys. **51**, 310 (1990)].
15. V. Yu. Petrov and P.V. Pobylitsa, hep-ph/9712203; V. Yu. Petrov, M. V. Polyakov, R. Ruskov, *et al.,* Phys. Rev. D **59**, 114018 (1999).
16. D. I. Dyakonov and V. Yu. Petrov, Nucl. Phys. B **245**, 259 (1984).
17. M. Musakhanov, Eur. Phys. J. C **9**, 235 (1999).
18. Yu. A. Simonov, Phys. Lett. B **412**, 371 (1997).
19. R. D. Bowler and M. C. Birse, Nucl. Phys. A **582**, 655 (1995); R. S. Plant and M. C. Birse, Nucl. Phys. A **628**, 607 (1998).
20. S. Mandelstam, Ann. Phys. (N.Y.) **19**, 1 (1962).
21. J. Terning, Phys. Rev. D **44**, 887 (1991).
22. B. Holdom, Phys. Rev. D **45**, 2534 (1992); B. Holdom and R. Lewis, Phys. Rev. D **51**, 6318 (1995).
23. J. W. Bos, J. H. Koch, and H. W. L. Naus, Phys. Rev. C **44**, 485 (1991).
24. M. A. Ivanov, M. P. Locher, and V. E. Lyubovitskij, Few-Body Syst. **21**, 131 (1996).
25. E. V. Shuryak, Nucl. Phys. B **203**, 116 (1982); M. Hutter, Preprint LMU-95-03 (München, 1995); hep-ph/9502361.
26. E. Braaten, Phys. Rev. D **28**, 524 (1983).

Physics of Atomic Nuclei, Vol. 64, No. 7, 2001, pp. 1337–1346. Translated from Yadernaya Fizika, Vol. 64, No. 7, 2001, pp. 1413–1422.

ELEMENTARY PARTICLES AND FIELDS
Theory

Vacuum Energy and Casimir Force in the Presence of a Dimensional Parameter in the Boundary Condition

S. L. Lebedev*

Chuvash State Pedagogical University, ul. Karla Marksa 38, Cheboksary, 428000 Russia

Received December 23, 1999; in final form, April 24, 2000

Abstract—The Hamiltonian for a scalar field that satisfies the boundary condition $-\partial_n\varphi = (1/\delta)\varphi$ must include a surface potential energy. The corresponding term in the Casimir energy $\widetilde{E}_{\rm C}$ proves to be a leading one when the dimension of the region is $l \sim \delta$. The energy $\widetilde{E}_{\rm C}$ does not involve arbitrariness associated with regularization and is an unambiguously determined function of the field mass m, the size l, and the penetration depth δ. The inclusion of the surface term is of importance for ensuring that the derivative $-\partial\widetilde{E}_{\rm C}/\partial l$ is equal to the ll component of the vacuum energy–momentum tensor. The Casimir energy $\widetilde{E}_{\rm C}$ is related to its volume component $E_{\rm C}$ by a Legendre transformation where the quantity conjugate to $1/\delta$ is the product of the vacuum surface energy and δ. If δ is negative and if $\hbar/mc > \mid \delta \mid$, there exists a critical value $l = l_c(\delta)$ above which $(l > l_c)$ the vacuum is unstable; if a self-interaction of the form φ^4 is taken into account, this will lead to a phase transition accompanied by the formation of a condensate of the field φ. If $\delta = +0$ or ∞ and if the dimensionalities are even, it is possible to construct a vacuum energy–momentum tensor (not only energy) that is finite over the entire space. Specially chosen counterterms leave unchanged the analytic dependence of the vacuum energy on the dimensionality of space and the character of the coordinate dependence of the energy density for $x > \hbar/mc$. © *2001 MAIK "Nauka/Interperiodica".*

1. INTRODUCTION

Evaluation of the vacuum energy for fields that are defined in finite regions is a key point in calculating Casimir pressure in QED [1] and the properties of hadrons obtained in the QCD bag model [2]. At the same time, a finite and unambiguous expression for the vacuum energy as a function of the parameters of the region being considered can be derived only for a specific class of field models and for specific geometries of the boundaries. By way of example, we indicate that, in the case of a scalar model, the Casimir energy—and the Casimir pressure together with it—can be determined ambiguously, which is associated with the dependence of the counterterms on the dimensions of the finite-size region being considered [3, 4]. Specific calculations for the Dirichlet or Neumann boundary conditions and a spherical boundary were performed in [5–7]. General considerations that were put forth in [8] reveal that surface singularities in the vacuum energy–momentum tensor and, hence, the counterterms in the expression for the energy are independent of the dimensions of the region. The discovery of such a dependence in the aforementioned studies was due to the coincidence of the dimensional parameters that determine the local (curvature) and global (volume) properties of a sphere. This can be seen, for example, from the fact that the vacuum energy admits a geometric expansion, whose first few terms were found in [9, 10] for a massless scalar field and for an electromagnetic field.[1)] In connection with the aforesaid, it would be of interest to investigate the vacuum energy of a massive field for more general boundary conditions and also in the presence of a dimensional quantity that characterizes the boundary, but which is not associated with the volume.

Specifically, we consider a massive scalar field defined in a D-dimensional space $\Re_t \times [0, l] \times \Re^{D-2}$. In the absence of the curvature of the surface, we introduce a dimensional penetration depth in the boundary condition:[2)]

$$\partial_1\varphi(t, 0, \mathbf{x}_\perp) = \frac{1}{\delta}\varphi(t, 0, \mathbf{x}_\perp), \quad \varphi(l) = 0. \qquad (1)$$

*e-mail: lebedev@td.lpi.ac.ru;lsl@chuvsu.ru

[1)]For a flat space, the terms of the series are expressed in terms of surface integrals of (increasing) powers of curvatures, the integrals themselves being additionally multiplied by coefficients (which are in general divergent) whose form is determined only by the field type and the type of the boundary conditions, but not by the geometry of the boundary.

[2)]Here, we perform our calculations in the system of units where $\hbar = c = 1$ and use the notation $x^\mu = (t, x_1, \mathbf{x}_\perp)$ and a metric of signature $(+, -, -, \ldots)$. For the sake of simplicity, we consider a nonsymmetric boundary condition.

The characteristic length δ in Eq. (1) should be treated as a macroscopic parameter that determines the strength of the boundary interaction

$$\frac{1}{2\delta}\int d^{D-2}\mathbf{x}_\perp\,\varphi^2(t,0,\mathbf{x}_\perp). \tag{2}$$

The surface interaction in (2) is associated with the divergence-operator term in the (symmetrized) energy–momentum tensor [11]

$$\widetilde{T}_{\mu\nu}=\frac{1}{2}\left[\partial_\mu\varphi,\partial_\nu\varphi\right]_+-\frac{1}{2}g_{\mu\nu}(\partial\varphi)^2 \tag{3}$$

$$+\frac{1}{2}g_{\mu\nu}m^2\varphi^2+\xi\partial^\lambda(g_{\mu\nu}\left[\varphi,\partial_\lambda\varphi\right]_+-g_{\mu\lambda}\left[\varphi,\partial_\nu\varphi\right]_+)$$

with a fixed coefficient ξ, which takes the same value of $1/4$ for all dimensionalities of space. Only at this value of ξ is the energy of the system (that is, the integral of $\widetilde{T}_{00}$) conserved and can its vacuum expectation value be represented in the form of the sum of the half-frequencies.

The presence of a dimensional parameter in the boundary condition drastically changes the character of the dependence of the Casimir energy in a region on the dimensions of this region—for example, we obtain, at $m=0$, a van der Waals curve with an equilibrium point at $l\simeq 1.8\delta$ (see Fig. 1) instead of the monotonic behavior $E_\mathrm{C}\sim l^{-3}$ [1]. The contribution of the surface energy (2) to the Casimir energy is especially pronounced at $\delta\sim l$. It also turned out that the inclusion of the surface energy (2) is of crucial importance for fulfillment of the adiabatic condition

$$-\frac{\partial\widetilde{E}_\mathrm{C}}{\partial l}=\langle\widetilde{T}_{11}\rangle_{\delta,l}, \tag{4}$$

which relates two known methods for calculating the Casimir force (the meaning of the notation used is explained below). The finite vacuum energy $\widetilde{E}_\mathrm{C}$ in Eq. (4) is defined unambiguously despite the fact that the singular behavior of the vacuum energy–momentum tensor at the boundary becomes much more complicated for $0<\delta<\infty$ [11].

Of considerable interest is also the case of negative values of δ. For $m|\delta|c/\hbar<1$, there exists a critical dimension $l_c(\delta)\gtrsim|\delta|$ above which the vacuum becomes unstable, with the result that modes of imaginary frequencies appear in the system; however, the vacuum is stable for $0<l<l_c$. In order to define unambiguously the Casimir energy $\widetilde{E}_\mathrm{C}$ for $l<l_c$, one can no longer use the requirement that this energy vanish for $l\to\infty$ (see [1].) For this purpose, we propose invoking the relation $\widetilde{E}_\mathrm{C}|_{\delta\to-\infty}=\widetilde{E}_\mathrm{C}|_{\delta\to+\infty}$, which stems from the coincidence of the sets of resonator modes for $\delta=+\infty$ and for $\delta=-\infty$. In the last section, the problem of the boundary divergences is solved by the dimensional-regularization method for the case of $\delta=0$ or $\delta=\infty$. As a result, finite expressions are also obtained for local densities and not only for energy, as in the ζ-regularization method. The result admits a generalization to the case of any even dimensionality of space. Similar points from other studies—in particular, the physical meaning of the wall vacuum energy $Sm^3c^4/48\pi\hbar^2$ (S is the wall area), which was found previously in [6, 11, 12]—are discussed in the Conclusion.

2. ENERGY–MOMENTUM TENSOR AND VACUUM ENERGY

Normalized solutions to the Klein–Gordon equation are given by

$$\widetilde{\varphi}_k(x)=(2\omega)^{-1/2}(2\pi)^{1-D/2} \tag{5}$$
$$\times\exp\left[-i\omega t+i\mathbf{q}\cdot\mathbf{x}_\perp\right]\psi_k(x_1),$$

where $\omega=\sqrt{m^2+\mathbf{q}^2+k^2}$ and the discrete set of functions

$$\psi_k(x)=N_k\sin k(x-l), \tag{6}$$
$$N_k=\left[\frac{l}{2}\left(1-\frac{\sin 2kl}{2kl}\right)\right]^{-1/2}$$

describes resonator modes. The wave number $k=z/\delta$ ($\widetilde{l}\equiv l/\delta$) is found from the spectral equation

$$\Delta(z)\equiv z^{-1}\tan z\widetilde{l}+1=0, \tag{7}$$

which follows from the boundary conditions in (1). Equation (7) has only the real-valued solutions $z=z_{n\delta}$; by virtue of invariance under the substitution $(k\to-k)$, it is sufficient here to take into account only the positive branch $z_{n\delta}>0$. The poles of $\Delta(z)$ at the points

$$z_{n\infty}\widetilde{l}=\frac{\pi}{2}+n\pi,\quad n=0,1,..., \tag{7a}$$

correspond to the Neumann boundary conditions ($\delta=\infty$). Further calculations rely on the expansion of the field $\varphi(x)$ in the basis of the functions in (5) and employ a conventional definition for creation and annihilation operators and for the vacuum state.[3)]

Using the argument principle for the function $\Delta(z)$, one can transform the sums over the transcendental roots in Eq. (7) into corresponding integrals (see Appendix), whereby the renormalized vacuum energy–momentum tensor can eventually be defined as

$$\langle\widetilde{T}_{\mu\nu}\rangle_{\delta,l}=\frac{\mathrm{K}_D}{\delta}\int\limits_\mu^\infty dt(t^2-\mu^2)^{\frac{D-1}{2}} \tag{8}$$

[3)]It should be borne in mind that a canonical quantization of the system specified by Eq. (3) must take into account its degeneracy since it is a system featuring higher (second) derivatives (see [11]).

$$\times\left\{\frac{(1-t)e^{-t\widetilde{l}}}{\sinh t\widetilde{l}+t\cosh t\widetilde{l}}\ \mathrm{diag}\begin{bmatrix}\cosh 2tx'-1\\ \dfrac{t^2(1-D)}{t^2-\mu^2}\\ (1-\cosh 2tx')I\end{bmatrix}\right.$$
$$\left.+\,e^{-2tx'}\,\mathrm{diag}\begin{bmatrix}1\\0\\-I\end{bmatrix}\right\},$$

where

$$\mathrm{K}_D=\frac{\delta^{1-D}}{2(4\pi)^{\frac{D-1}{2}}\Gamma\left(\dfrac{1+D}{2}\right)},\qquad(9)$$
$$\mu=m\delta,\ x'=(l-x_1)/\delta,$$

and where expressions of the same type appear on the $(D-2)$-dimensional diagonal corresponding to $\mathbf{x}_\perp$.

The vacuum energy can also be defined directly as the sum of half-frequencies that is interpreted, for example, via ζ-function regularization [3, 13]. At the same time, evaluation of the same quantity by the Green's function method [1, 13] must rely on the modified tensor $\widetilde{T}_{\mu\nu}$ rather than on its first three terms [11] [we denote by $T_{\mu\nu}$ their sum on the right-hand side of Eq. (3)].

The 11 component of the tensor in (8) determines the Casimir pressure $P=\langle\widetilde{T}_{11}\rangle_{\delta,l}$, which, by virtue of translational invariance, coincides with $\langle T_{11}\rangle_{\delta,l}$; that is, the additional term that involves the divergence operator does not affect the pressure. The role of such a term on the right-hand side of Eq. (3) is that the value of $\xi=1/4$ is the only one at which the adiabatic relation (4) is satisfied. A point that is of importance for proving this relation is that the vacuum energy per unit area has the form

$$\widetilde{E}_{\mathrm{vac}}=\int\limits_{x_0}^{l-y_0}dx_1\,\langle\widetilde{T}_{00}\rangle_{\delta,l}=\widetilde{E}_{\mathrm{C}}(l,\delta)\qquad(10)$$
$$+\,\widetilde{E}_{w1}(x_0,\delta)+\widetilde{E}_{w2}(y_0,0)+\ldots,$$

where the ellipsis stands for terms that vanish both in the limit $x_0,y_0\to 0$ and in the limit $l\to\infty$. Thus, we conclude that, in the limit $x_0,y_0\to 0$, only the finite part (Casimir energy)

$$\widetilde{E}_{\mathrm{C}}(l,\delta)=\mathrm{K}_D\int\limits_{\mu}^{\infty}dt\,\frac{(t^2-\mu^2)^{\frac{D-1}{2}}e^{-t\widetilde{l}}}{\sinh t\widetilde{l}+t\cosh t\widetilde{l}}\qquad(11)$$
$$\times\left[\widetilde{l}(t-1)-\frac{1}{t+1}\right],$$

which vanishes for $l\to\infty$, is dependent on the dimension of the region. The boundary divergences are present in (10) in the form of isolated-wall energies $\widetilde{E}_{w1,2}$; for example,

$$\widetilde{E}_{w1}(x_0,\delta)=\mathrm{K}_D\mu^{D-1}\qquad(12)$$
$$\times\int\limits_1^{\infty}\frac{d\xi}{2\xi}\,(\xi^2-1)^{\frac{D-1}{2}}\,\frac{1-\mu\xi}{1+\mu\xi}\,e^{-2mx_0\xi}.$$

A specific representation of $\widetilde{E}_{w1,2}$ depends on the regularization method. At the same time, the Casimir energy $\widetilde{E}_{\mathrm{C}}$ is defined unambiguously. By analogy with the energy $\widetilde{E}_{\mathrm{vac}}$ (10), we can determine its volume (E_{vac}) and surface ($\Pi_{\mathrm{vac}}=\widetilde{E}_{\mathrm{vac}}-E_{\mathrm{vac}}$) terms, the term E_{vac} being calculated in terms of T_{00} [the first three terms in expression (3)]. For the volume and the surface contribution, we then have expansions of the form (10), which lead to $E_{\mathrm{C}}(l,\delta)$ and $\Pi_{\mathrm{C}}(l,\delta)$, respectively; for example,

$$\Pi_{\mathrm{C}}(l,\delta)=\mathrm{K}_D(1-D)\qquad(13)$$
$$\times\int\limits_{\mu}^{\infty}dt\,\frac{t^2(t^2-\mu^2)^{\frac{D-3}{2}}e^{-t\widetilde{l}}}{(t+1)(\sinh t\widetilde{l}+t\cosh t\widetilde{l})}$$

and $E_{\mathrm{C}}=\widetilde{E}_{\mathrm{C}}-\Pi_{\mathrm{C}}$.

From Eq. (4), it follows that the volume term E_{C} cannot be used to calculate the Casimir force if the parameter δ is considered as a quantity that is independent of l. On the other hand, differentiation with respect to the parameter yields

$$\delta\frac{\partial\widetilde{E}_{\mathrm{C}}}{\partial\delta}=-\Pi_{\mathrm{C}}.\qquad(14)$$

Introducing the notation $\lambda=\delta^{-1}$ and $f=\Pi_{\mathrm{C}}/\lambda$, we then find that $\widetilde{E}_{\mathrm{C}}$ and E_{C} are related by the Legendre transformation

$$\widetilde{E}_{\mathrm{C}}(l,\lambda)=E_{\mathrm{C}}(l,f(l,\lambda))+\lambda f(l,\lambda),$$

so that

$$\left(\frac{\partial E_{\mathrm{C}}}{\partial l}\right)_f=\left(\frac{\partial\widetilde{E}_{\mathrm{C}}}{\partial l}\right)_\lambda.\qquad(15)$$

Expression (15) provides a means for calculating the Casimir force in the case where the product $f=\Pi_{\mathrm{C}}\delta$ is constant and where the parameter δ is treated as a function of f and l:

$$\left(\frac{\partial E_{\mathrm{C}}}{\partial f}\right)_l=-1/\delta.\qquad(15a)$$

The parameter f corresponds to one-half of the Casimir part of the expectation value $\langle\varphi^2(0)\rangle$ [see Eq. (2)].

Asymptotic properties. The behavior of the integral on the right-hand side of Eq. (11) in the Dirichlet

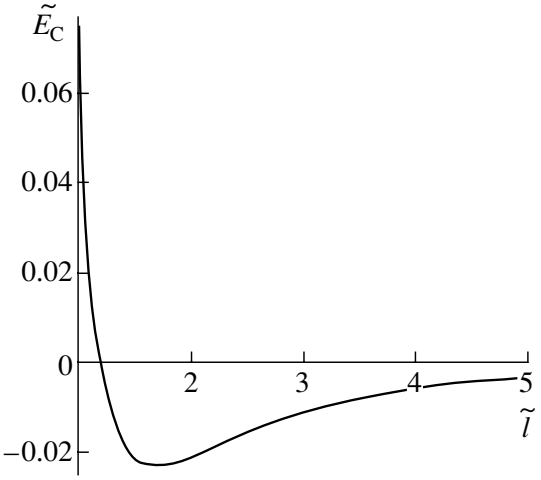

Fig. 1. Wall-interaction energy $\widetilde{E}_C(l,\delta)$ (11) in units of K_D [see Eq. (9)] as a function of $\widetilde{l} = l/\delta$ (the dimension is $D = 4$, and the mass is $m = 0$).

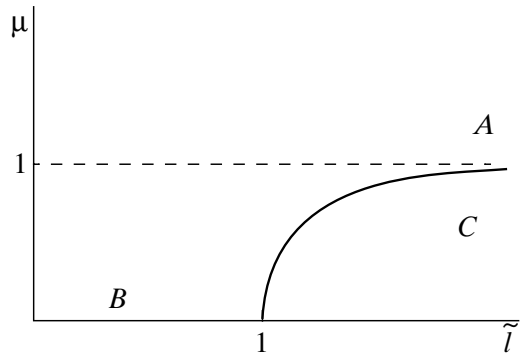

Fig. 2.

($\delta \ll l$) and the Neumann ($\delta \gg l$) regime is especially clear in the massless case ($m = 0$):

$$\widetilde{E}_C(\delta,l) = K_D \frac{\zeta(D)\Gamma(D)}{(2\widetilde{l})^{D-1}} \times \left[-1 + C^1_{D-1}\,\widetilde{l}^{-1} - C^2_D\,\widetilde{l}^{-2} + C^3_{D+1}\left(1 + \frac{\zeta(D+2)}{2\zeta(D)}\right)\widetilde{l}^{-3}\right], \quad (16)$$

$$\widetilde{E}_C(l,\delta) = K_D \widetilde{l}^{-D+1} \times \begin{cases} A_D - (D-1)A_{D-2}\widetilde{l}, & D = 3,4,\ldots, \\ A_2 + \widetilde{l}\ln(4\gamma_E\widetilde{l}/\pi) - \widetilde{l}, & D = 2. \end{cases} \quad (17)$$

Here, C^m_n are binomial coefficients, $A_D = 2^{1-D}(1 - 2^{1-D})\Gamma(D)\zeta(D)$, and $\ln\gamma_E = 0.577$; in expression (17), we have retained only the leading corrections.

For the pressure, the expansion that corresponds to Eq. (16) has the form ($\delta \ll l$)

$$\langle\widetilde{T}_{11}\rangle_{\delta,l} = \frac{(D-1)\Gamma(D)\zeta(D)}{(4\pi)^{\frac{D-1}{2}}\Gamma\left(\frac{1+D}{2}\right)}(2l)^{-D} \times \left[-1 + C^1_D\widetilde{l}^{-1} - C^2_{D+1}\widetilde{l}^{-2} + C^3_{D+2}\left(1 + \frac{\zeta(D+2)}{2\zeta(D)}\right)\widetilde{l}^{-3} + \ldots\right]. \quad (18)$$

With the exception of the anomalous term involving the ratio of ζ functions, the remaining four terms in the bracketed expression on the right-hand side of Eq. (18) can be obtained by expanding $(l+\delta)^{-D}$ in powers of $\widetilde{l}^{-1}$. Thus, Eq. (18) confirms the interpretation of δ as a penetration depth [14].

It is interesting to compare the expansion in (18) at $D = 4$ with the analogous expression for an electromagnetic field in a region bounded by impedance walls. We have

$$\langle\widetilde{T}_{11}\rangle_{\delta,l} = \frac{\pi^2}{480l^4}\left[-1 + 4\frac{\delta}{l} - 10\frac{\delta^2}{l^2} + 20\left(1 + \frac{9\pi^2}{185}\right)\frac{\delta^3}{l^3} + \cdots\right], \quad (19)$$

$$P = \frac{\pi^2}{240l^4}\left[-1 + \frac{16}{3}\frac{\delta}{l} - 24\frac{\delta^2}{l^2} + \frac{640}{7}\left(1 + \frac{9\pi^2}{740}\right)\frac{\delta^3}{l^3} + \ldots\right]. \quad (20)$$

Here, expression (20) (the last term apart) was borrowed from [1, 14], while δ is the depth of the skin layer. The growing distinction between the corresponding expansion coefficients in expressions (19) and (20) is likely to be associated with spin effects, whose role must become more pronounced with increasing depth of field interaction with the boundary.

Numerical calculations. The gross behavior of the energy $\widetilde{E}_C$ as a function of $\widetilde{l} = l/\delta$ (at $m = 0$) is illustrated in Fig. 1. The calculations also reveal that, in the region $l = (1{-}5)\delta$, the contribution of the surface energy Π_C exceeds in absolute value the contribution of the energy E_C by a factor of 3 to 5. That the signs of $\Pi_C(l,\delta)$ and $E_C(l,\delta)$ are opposite in this region shifts the point of minimum from $l \simeq 4.5\delta$ for E_C to the point $l \simeq 1.8\delta$ for $\widetilde{E}_C$.

3. NEGATIVE δ

For $\delta \equiv -\delta_1 < 0$, solutions to the equations of motion have the former form specified by (5) and (6), but the spectral equation changes to become ($z = k\delta_1, \widetilde{l} = l/\delta_1$)

$$\Delta_1(z) \equiv z^{-1}\tan z\widetilde{l} - 1 = 0. \qquad (21)$$

Along with the real-valued roots $z_{n\delta}$, it now has the imaginary roots $z = \pm i\kappa\delta_1$. In view of this, the total set of states includes the surface Tamm modes (see also [9])

$$\widetilde{\varphi}_b(x) = (2\omega_b)^{-1/2}(2\pi)^{(1-D)/2} \qquad (22)$$
$$\times \exp\left[-i\omega_b\, t + i\mathbf{q}\cdot\mathbf{x}_\perp\right]\psi_b(x_1),$$

where

$$\psi_b(x) = N_b \sinh\kappa(x-l), \qquad (23)$$

$$N_b = \left[\frac{l}{2}\left(\frac{\sinh 2\kappa l}{2\kappa l} - 1\right)\right]^{-1/2},$$

$$\omega_b = \sqrt{m^2 + \mathbf{q}^2 - \kappa^2}. \qquad (24)$$

The parameter κ is the only (positive) solution to the equation

$$\kappa\delta_1 = \tanh\kappa l\ . \qquad (25)$$

It exists under the condition $l > \delta_1$ and is of order δ_1^{-1} if $l \gg \delta_1$. When $\delta_1 \to l - 0$, we have $\kappa \sim \sqrt{3(l-\delta_1)/l^3} \to 0$.

For $m > \kappa$, expression (24) specifies real-valued frequencies of surface modes. If $m < \kappa$, the spectrum develops imaginary frequencies (see also [1, 11]). The reason behind the emergence of time-dependent solutions in the set of functions specified by (22) is that it is impossible to localize a particle in a region of dimensions κ^{-1}, which are less than the Compton length. The regions A and B of the parameters $\mu = m\delta_1$ and $\widetilde{l} = l/\delta_1$ in Fig. 2 represent the case of $m > \kappa$. The region C in this figure corresponds to an unstable vacuum. In this region of parameter values, a consistent description is possible if the Lagrangian of the model is supplemented with terms that describe the self-interaction of the field φ (for example, of the form $(\lambda/4)\varphi^4$). By using the arguments presented in [1, 15], it can be shown that the presence of a tachyon surface mode will result in the decay of an unstable vacuum with the formation of the condensate $\varphi(x) = Q_{\min}\psi_b(x)$, where $\psi_b(x)$ is the surface mode (23) and

$$Q_{\min} = \sqrt{\frac{\kappa^2 - m^2}{\bar{\lambda}}},$$

$$\bar{\lambda} = \frac{\lambda}{4\delta_1}\,\frac{\sinh^2(2\kappa l) + 6(\widetilde{l} - \cosh^2(\kappa l))}{(\widetilde{l} - \cosh^2(\kappa l))^2}.$$

For the sake of simplicity, we have considered here a two-dimensional case. In the following, we disregard self-interaction and assume that $m > \kappa$.

The boundary of the region C is the graph of $\widetilde{l} = l/\delta_1 = \widetilde{l}_c(\kappa\delta_1)$ of the implicit function in (25). From the figure, we can see that, for $\mu < 1$, only the values in the range $0 < \widetilde{l} < \widetilde{l}_c$ are admissible; that is, the limit $\widetilde{l} \to \infty$ cannot be used to define unambiguously the Casimir energy [in a way similar to that adopted in Eq. (10) for $\delta > 0$]. In view of this, we will give a brief account of the procedure for calculating the vacuum energy–momentum tensor and the Casimir energy for the case where the parameters μ and $\widetilde{l}$ lie in the region A or B (see Fig. 2).

The contributions of surface and resonator modes appear additively in the unrenormalized expectation value $\langle\widetilde{T}_{\mu\nu}\rangle = \langle\widetilde{T}_{\mu\nu}\rangle^{(b)} + \langle\widetilde{T}_{\mu\nu}\rangle^{(\mathrm{res})}$. The regularized sums that are taken over the transcendental roots of Eq. (21) and which appear in $\langle\widetilde{T}_{\mu\nu}\rangle^{(\mathrm{res})}$ transform into integrals with the aid of the function Δ_1'/Δ_1 taking the place of Δ'/Δ in (A.4). Upon deforming the contour of integration in such a way that it circumvents the positive imaginary semiaxis $k = it/\delta_1$ ($t \geq 0$) [see Eqs. (A.4)–(A.7)], the integral receives a contribution not only from the cut $(im, i\infty)$ but also from the pole at $k = i\kappa$, which lies below the branch point im. It turns out that the contribution of the pole to the eventual expression for the renormalized energy–momentum tensor [see Eq. (9), where δ must be replaced by δ_1]

$$\langle\widetilde{T}_{\mu\nu}\rangle_{\delta,l} = \mathrm{K}_D\delta_1^{-1}\int\limits_{\mu}^{\infty} dt(t^2-\mu^2)^{\frac{D-1}{2}} \qquad (26)$$

$$\times\left\{\frac{(1+t)e^{-t\widetilde{l}}}{\sinh t\widetilde{l} - t\cosh t\widetilde{l}}\ \mathrm{diag}\begin{bmatrix}\cosh 2tx' - 1\\ \dfrac{t^2(1-D)}{t^2-\mu^2}\\ 1-\cosh 2tx'\end{bmatrix}\right.$$
$$\left. + e^{-2tx'}\,\mathrm{diag}\begin{bmatrix}1\\0\\-I\end{bmatrix}\right\}$$

is exactly canceled by the contribution of the surface modes, $\langle\widetilde{T}_{\mu\nu}\rangle^{(b)}$. The renormalization in (26) reduces to the subtraction of the contribution from Minkowski space [see Eq. (A.6)]. In passing, we note that $\langle\widetilde{T}_{\mu\nu}\rangle^{(b)}$ features the factor $\Gamma\left(\frac{1-D}{2}\right)$; therefore, it formally goes to infinity at odd D ($D = 3, 5, \ldots$). Of course, the total vacuum energy–momentum tensor (26) is finite for any $D \geq 2$.

The definition of the Casimir energy for $\mu = m\delta_1 > 1$ is identical to that in the case of $\delta > 0$, since the passage to the limit $\widetilde{l} \to \infty$ (along with the passage to the limit $x_0, y_0 \to 0$) is possible. In accordance with Eq. (10), we therefore obtain

$$\widetilde{E}_{\rm C}(l,\delta_1) = {\rm K}_D \int\limits_{\mu}^{\infty} dt\, \frac{(t^2-\mu^2)^{\frac{D-1}{2}} e^{-t\widetilde{l}}}{\sinh t\widetilde{l} - t\cosh t\widetilde{l}} \qquad (27)$$
$$\times \left[\frac{1}{1-t} - \widetilde{l}(t+1)\right].$$

We also have

$$\widetilde{E}_{w1}(x_0,\delta_1) \qquad (28)$$
$$= {\rm K}_D \int\limits_{\mu}^{\infty} \frac{dt}{2t}\, (t^2-\mu^2)^{\frac{D-1}{2}}\, \frac{1+t}{1-t}\, e^{-2t\widetilde{x}_0},$$

where

$$\widetilde{x}_0 = x_0/\delta_1.$$

Algebraic transformations that involve discarding terms of order x_0 and y_0 and which lead (for $\delta < 0$ as well) to the right-hand side of Eq. (10) can be repeated, without any changes, for the case of $\mu < 1$.[4)] However, the wall contributions $\widetilde{E}_{w1}$ and $\widetilde{E}_{w2}$ involve ambiguities, since it is impossible to use the limiting transition $\widetilde{l} \to \infty$. This comes as no surprise since $\widetilde{E}_{w1}$ cannot be defined for a half-space in view of the emergence of imaginary frequencies [11]. The partition of the energy $\widetilde{E}_{\rm vac}$ [see Eq. (10)] into three terms must be interpreted in the sense that all $\widetilde{l}$-independent terms of its asymptotic expansion for $\widetilde{x}_0, \widetilde{y}_0 \to 0$ are contained in the expressions for $\widetilde{E}_{w1}$ and $\widetilde{E}_{w2}$ (the first of these involves δ); of terms of this asymptotic expansion that depend on $\widetilde{l}$, it is necessary to discard only those that vanish in the limit $\widetilde{x}_0, \widetilde{y}_0 \to 0$. Since there are no terms on the right-hand side of (10) that are dependent on l and which are singular in this limit, $\widetilde{E}_{\rm C}$ is defined apart from an additive constant independent of l. For $\delta > 0$, this arbitrariness is removed by the condition $\widetilde{E}_{\rm C}(\infty,\delta) = 0$ [1]. We now require that two Neumann limits be coincident (see Introduction):

$$\widetilde{E}_{\rm C}\Big|_{\delta\to-\infty} = \widetilde{E}_{\rm C}\Big|_{\delta\to+\infty}. \qquad (29)$$

The eventual expressions for the energies $\widetilde{E}_{\rm C}(l,\delta_1)$ and $\widetilde{E}_{w1}(x_0,\delta_1)$ for $\mu < 1$ and $l < l_c$ are obtained from (27) and (28) by applying the principal-value prescription to the integrals appearing there. This rule of circumvention of the pole at $t = 1$ is chosen in order to ensure that the result is real-valued. However, any other prescription for the circumvention of the pole, while leading to the emergence of an imaginary part, would produce, in the sum of expressions (27) and (28), a contribution of order $\widetilde{x}_0$, which must be discarded. The last circumstance stems from the fact that the residue of the integrand in (27) at the point $t = 1$ is independent of $\widetilde{l}$.

To conclude this section, we present, for reference, the Neumann asymptotic expansion of the Casimir pressure for the massless case. With the aid of Eqs. (8) [or (4) and (17)] and (26), it is obtained in the form

$$\langle \widetilde{T}_{11}\rangle_{\delta,l} = \frac{\Gamma(D)\, l^{-D}}{2(4\pi)^{\frac{D-1}{2}}\Gamma\left(\frac{D+1}{2}\right)} \qquad (30)$$
$$\times \left[B_{D-1}(D-1)\zeta(D) \mp B_{D-3}\zeta(D-2)\,\widetilde{l} + \ldots\right],$$

where $\widetilde{l} = l/|\delta| \ll 1$, $B_D = 2^{-D}(1-2^{-D})$, and the upper (lower) sign corresponds to the case of $\delta > 0$ ($\delta < 0$). The emergence of the correction term in brackets on the right-hand side of (30) is entirely due to the surface contribution $\Pi_{\rm C}$ (13) to the Casimir energy, and this is the point where the Neumann regime differs from the Dirichlet regime (that at positive δ). Finally, it should be noted that relations (4) and (14) hold for negative values of δ as well, which correspond to the stability regions A and B in Fig. 2.

4. INTERPRETATION OF BOUNDARY DIVERGENCES AT $\delta = 0$ OR ∞

The boundary singularities in the vacuum energy–momentum tensor[5)] is a stumbling block for any field theory where the local properties of the model used are related to observables.[6)] Analytic-regularization methods, which are extensively used at present [16], make it possible to assign finite values to quantities like $E_{\rm vac} = \sum_\nu \frac{1}{2}\omega_\nu$, infinite terms being included in the renormalization of bare constants (see, for example, [3, 6, 17]). However, there remains the problem of a singular behavior of renormalized $\langle T_{\mu\nu}(x)\rangle$ at the boundary [8]. For $\delta = +0$ or ∞ and even D, it will be shown below that, by changing somewhat the computational prescription, we can define a local, everywhere finite expression for renormalized $\langle T_{\mu\nu}(x)\rangle$. The vacuum energy obtained with the aid of this expression coincides with relevant results of alternative

[4)] The vacuum tensor in (26) is defined in the region B in Fig. 2, and the corresponding integrand for $m > \kappa$ does not have poles here.

[5)] The expansion of the tensor in (8) for $x \to 0$ involves $x^{-D}, \delta^{-1}x^{1-D}, mx^{1-D}$, etc., terms [11].

[6)] The history of the problem can be traced in [8, 10, 13, 19]; see also [16, p. 145].

calculations (for example, calculations based on the method of ζ-function regularization).

In (10), boundary singularities are represented by the wall energies; therefore, we consider the 00 component of expression (8) in the limit $l \to \infty,\ \delta = +0$ (the limit $\delta = \infty$ differs from the above limit only by the sign). We have

$$\langle \widetilde{T}_{00} \rangle_{0,\infty} = \left(\frac{m^2}{2\pi}\right)^{D/2} \begin{cases} \rho^{-D/2}\, K_{D/2}(\rho), & 0 < \rho \lesssim 1,\ x/l \to 0, \quad (31a) \\ (\rho')^{-D/2}\, K_{D/2}(\rho'), & 0 < \rho' \lesssim 1,\ x'/l \to 0, \quad (31b) \end{cases}$$

where $\rho = 2mx$ and $\rho' = 2mx' = 2m(l-x)$. By using recursion relations between Macdonald functions [18], we transform the energy density (31a) of the left wall as

$$\langle \widetilde{T}_{00} \rangle_{0,\infty} = \langle \widetilde{T}_{00} \rangle_{0,\infty} - \frac{d}{d\rho} f_D(\rho) \qquad (32)$$

$$= \left(\frac{m^2}{2\pi}\right)^{D/2} \frac{\rho^{1-\epsilon}\, K_{\epsilon-1}(\rho)}{(1-D)(3-D)\cdots(1-2\epsilon)}.$$

Here, $\epsilon \equiv D/2 - n \to 0$; $n = 1, 2, \ldots$; and the function

$$f_D(\rho) = \left(\frac{m^2}{2\pi}\right)^{D/2} \qquad (33)$$

$$\times \left[\frac{\rho^{1-D/2} K_{D/2}(\rho)}{1-D} + \frac{\rho^{2-D/2} K_{D/2-1}(\rho)}{(1-D)(3-D)} + \cdots + \frac{\rho^{1-\epsilon} K_{\epsilon}(\rho)}{(1-D)(3-D)\cdots(1-2\epsilon)}\right]$$

possesses the following properties:

(i) For the values D ($\mathrm{Re}\,\epsilon < -n$), which were continued to the left half-plane, we have

$$f_D(0) = f_D(\infty) = 0, \qquad (34)$$

so that the term in (32) that involves the divergence operator does not contribute to the wall energy,

$$\widetilde{E}_{w1}(0,0) = \left(\frac{m^2}{2\pi}\right)^{D/2} \qquad (35)$$

$$\times \int_0^\infty dx\ \rho^{-D/2}\, K_{D/2}(\rho) = \frac{m^{D-1}\Gamma\left(\frac{1-D}{2}\right)}{8(4\pi)^{\frac{D-1}{2}}}$$

(see [6, 11, 12]). We note that the energy of the Neumann wall is $\widetilde{E}_{w1}(0,\infty) = -\widetilde{E}_{w1}(0,0) = -E_{w1}(0,0)$.

(ii) At physical values of $D = 2, 4, 6 \ldots$, the term f'_D on the left-hand side of (32) plays the role of a counterterm that eliminates all nonintegrable singularities in the energy density (31a).

(iii) The counterterm does not change the exponential character of the asymptotic behavior of the energy density at large distances ($x \gg 1/m$) from the boundary. Thereby, the Compton length determines the distance beyond which the absence of translational symmetry does not have a noticeable effect on the local properties of the vacuum.

The energy density (32) is not defined unambiguously: any regular function that possesses the property specified in (34) can be added to $f_D(\rho)$ (see § 6.6 in [13]).

As a result, we conclude that, according to (10), the total vacuum energy at $\delta = +0$ involves the Casimir term

$$\widetilde{E}_{\mathrm{C}}(l,0) \qquad (36)$$

$$= -\frac{m^D l}{(4\pi)^{\frac{D-1}{2}}\Gamma(\frac{D+1}{2})} \int_1^\infty d\xi\, \frac{(\xi^2-1)^{\frac{D-1}{2}}}{e^{2\xi ml} - 1}$$

and the double wall energy (35). For $\delta = \infty$, $\widetilde{E}_{\mathrm{C}}(l,0)$ (36) is replaced by a similar integral differing from that in (36) by a plus sign in the denominator of the integrand and by the common factor (-1), the energies of the Neumann ($x_1 = 0$) and the Dirichlet ($x_1 = l$) wall being mutually canceled.

The dimensional-regularization method does not yield a satisfactory result for the wall energy when $0 < \delta < \infty$. From expression (12) ($x_0 = 0$), it can be seen that, at even D, finite values cannot be assigned to μ-dependent corrections of orders $\mu, \mu^2, \ldots$ to the energy in (35). At odd $D \geq 3$, the energy in (35) itself is indefinite; as to the aforementioned corrections, they are finite, but their sum leads to a logarithmic singularity in the Neumann limit $\mu \to \infty$. It should be noted that, in the massless case, the vacuum-energy density (32) of the Dirichlet wall [in contrast to that in (31)] vanishes, which is peculiar to conformally symmetric models as well [13, 19].

5. CONCLUSION

Here, it is advisable to dwell at some length on a few studies whose results have a direct bearing on the subject matter of the present article. A scalar massless model of dimensions $D = 2$ and 3 was considered in [14] and [20], respectively; the results obtained there for the vacuum energy or for the vacuum energy–momentum tensor are consistent with

our Eqs. (8) and (11) if we set there $m = 0$ and $D = 2$ or 3. The analysis in [20] employed the idea [21] of a nonlocal regularization of the interaction between the field φ and a concentrated potential that represents the boundary; as a matter of fact, this is equivalent to introducing the potential energy (2). In [14], a correct expression for $\widetilde{E}_{\rm C}$ was obtained by discarding an "inconvenient" term—this is also equivalent to taking into account the surface energy (2) (see [11]). The first term in (18) (its dependence on D is implied here) was obtained in [12] ($m = 0, \delta = 0$, and D is arbitrary). Upon correcting an obvious misprint, expression (2.18) from [12] is consistent with (36). The doubled energy (35) also appears in [12], but it is not associated there with the energy of a half-space (see below).

Our expression (8) for $\langle\widetilde{T}_{11}\rangle_{\delta,l}$ at $\delta = 0$,

$$\langle\widetilde{T}_{11}\rangle_{0,l} = \frac{m^D(1-D)}{(4\pi)^{\frac{D-1}{2}}\Gamma\left(\frac{1+D}{2}\right)} \times \int\limits_1^\infty \frac{\xi^2(\xi^2-1)^{\frac{D-3}{2}}}{e^{2ml\xi}-1}\,d\xi\Bigg|_{ml\gg 1} = -\frac{m^D}{(4\pi ml)^{\frac{D-1}{2}}}\,e^{-2ml}\left[1+\frac{(D-1)(D+5)}{16ml}+\cdots\right], \tag{37}$$

does not agree with the result presented by Albuquerque [22], whose expression (2.13) taken at zero temperature differs from (37) and involves the dependence of the pressure on an arbitrary renormalization parameter. This seems unphysical—the regularization independence of the pressure in our case follows from relation (10), which is associated with a simple geometry of the boundaries. It was indicated above that such a dependence is peculiar to curved surfaces, provided that the parameters determining the curvature of the boundary and the dimensions of the region being considered coincide.

Let us consider the problem of physically interpreting expression (35). In the absence of other dimensional parameters, the expression $m^{D-1}\,c^D/\hbar^{D-2}$ is the only energy characteristic of a hypersurface. In [6, 12, 23], it was proposed to apply the finite-renormalization principle to the energy in (35) ($\delta = 0$, $D = 4$); this is essentially equivalent to changing the reference point of the vacuum energy by $Sm^3/48\pi$, where S is the area of the boundary ($D = 4$). The basic argument of [6] in favor of the above shift of the reference point reduces to the requirement that the vacuum energy tend to zero as the region is indefinitely expanded. The energy $\widetilde{E}_{\rm C}(l,0) = E_{\rm C}(l,0)$ satisfies this condition [see Eq. (11)]. However, a transition to the limit $lm \to \infty$ (or $Rm \to \infty$ in the case of a sphere [6]) is ambiguous: an observer can be near one of the boundaries, or it can move away from any of them, remaining at the center of the resonator. In the first case, translational invariance remains violated and the vacuum-energy density must be nonzero in the surface layer of thickness about $1/m$. On the other hand, we recall that, for $m \to \infty$, the energy density (32) tends to zero everywhere, with the exception of the surface region indicated above, thereby satisfying the second requirement of suppression of vacuum effects for $m \to \infty$ [23], but only away from the boundary.

The expression

$$\int d\mathbf{x}_\perp \int\limits_0^{\sim\hbar/mc} dx_1\,\langle T_{00}(x)\rangle_{0,\infty}$$

corresponds to measuring the distinction between the vacuum energy in the bounded region $0 < x_1 \lesssim \hbar/mc$ and the same quantity in Minkowski space (because of the presence of the boundary, the coordinate x specifies not only the location but also the extension of the space interval). Such a measurement must lead to perturbations of about mc^2 in energy [24] that are multiplied by the statistical weight of the event, which is proportional to $S/(\hbar/mc)^2$, whence we obtain the required estimate $E_{\rm vac} \sim m^3c^4/\hbar^2$ for the vacuum energy divided by S. Thus, the signs of the vacuum energies of the Dirichlet and the Neumann wall seem to suggest that the perturbation depends on the dynamical properties of the boundary.

ACKNOWLEDGMENTS

I am grateful to A.I. Nikishov and V.I. Ritus for stimulating discussions.

This work was supported by the Russian Foundation for Basic Research (project nos. 95-02-04219-a, 96-15-96463, and 00-15-96566).

APPENDIX

The integrals with respect to the momentum $\mathbf{q}$ [see Eq. (5)] that were used to derive expressions (8) and (26) can be evaluated by means of the technique of D-dimensional integration:

$$\int \frac{d^{D-2}q}{\omega} = \pi^{\frac{D-3}{2}}M^{D-3}\Gamma\left(\tfrac{3-D}{2}\right), \tag{A.1}$$

$$\int \frac{d^{D-2}q}{\omega}q_i^2 = \tfrac{1}{2}\pi^{\frac{D-3}{2}}M^{D-1}\Gamma\left(\tfrac{1-D}{2}\right), \tag{A.2}$$

$$\int \frac{m_\perp^2}{\omega}\,d^{D-2}q = -\tfrac{1}{2}\pi^{\frac{D-3}{2}}M^{D-3}\Gamma\left(\tfrac{1-D}{2}\right) \times \left[m^2+(2-D)k^2\right] \tag{A.3}$$

{see Eq. (4.3.1) in [25]}. Here, we adopted the notation $\omega = \left(m_\perp^2 + k^2\right)^{1/2}$, $M = (m^2 + k^2)^{1/2}$, and $m_\perp^2 = m^2 + \mathbf{q}^2$; note also that there is no summation over i on the left-hand side of (A.2).

Summation over the transcendental roots of Eq. (7) can be performed with the aid of the Cauchy residue theorem. By using the argument principle [26], it can be shown that

$$\frac{1}{2\pi i}\int\limits_{\mathrm{D}} \frac{f(z)}{1-\sin 2z\widetilde{l}/2z\widetilde{l}}\frac{\Delta'(z)}{\Delta(z)}\,dz = \qquad (A.4)$$

$$= \sum_{z_{n\delta}>0} \frac{f(z_{n\delta})}{1-\sin 2z_{n\delta}\widetilde{l}/2z_{n\delta}\widetilde{l}} - \sum_{n=0}^{\infty} f(z_{n\infty}),$$

where $f(z)$ is a function that is analytic in the right half-plane. The roots $z_{n\delta}$ and the function $\Delta(z)$ are defined in (7), while $z_{n\infty}$ is specified in (7a). Equality (A.4) renders obvious the basic idea of choosing the function $\Delta(z)$: in addition to the poles $z_{n\infty}$ and $z_{n\delta}$, the expression Δ'/Δ also has zeros that coincide with the poles of the second factor in front of the integral. The positively oriented contour of integration goes along the axis $\mathrm{Im}\, z$ and is closed at infinity [it is schematically shown in Eq. (A.4)]. The requirements for $f(z)$ that are necessary for closing the contour in this way are satisfied in the case being considered. For $\delta > 0$, all roots $z_{n\delta}$, as well as $z_{n\infty}$, lie on the real axis and are embraced by this contour. The second term on the right-hand side of Eq. (A.4) is calculated with the aid of the Abel–Plana formula [1, 27]. Performing elementary transformations and discarding the integral along the circle in (A.4), we reduce the sum in question to the form

$$\sum_{z_{n\delta}>0} \frac{f(z_{n\delta})}{1-\sin 2z_{n\delta}\widetilde{l}/2z_{n\delta}\widetilde{l}} \qquad (A.5)$$

$$= \frac{\widetilde{l}}{\pi}\int\limits_0^\infty f(z)\,dz - \frac{\widetilde{l}}{2\pi i}$$

$$\times \int\limits_0^\infty \frac{(1-t)[f(it)-f(-it)]}{\sinh t\widetilde{l} + t\cosh t\widetilde{l}}\, e^{-t\widetilde{l}}\,dt.$$

Upon the substitution of the expressions corresponding to the unrenormalized expectation values $\langle \widetilde{T}_{\mu\nu}\rangle$ for $f(z)$, the first integral on the right-hand side of (A.5) develops terms that are removed by subtracting the quantity $\langle T_{\mu\nu}\rangle_M$ (contribution from Minkowski space):

$$\langle T_{\mu\nu}\rangle_M = \frac{\Gamma(\frac{1-D}{2})}{\sqrt{\pi}(4\pi)^{D/2}} \qquad (A.6)$$

$$\times \int\limits_0^\infty dk\, M^{D-3}\,\mathrm{diag}\begin{bmatrix} -M^2 \\ k^2(1-D) \\ M^2 \end{bmatrix}.$$

Thus, expressions (A.5) and (A.6) can be used to find the eventual integral representations of the renormalized tensors $\langle \widetilde{T}_{\mu\nu}\rangle_{\delta,l}$ or $\langle T_{\mu\nu}\rangle_{\delta,l}$.

The computational procedure described above is applicable to the case of negative δ as well if $m > \kappa$. Under this condition, the integrals with respect to the momentum $\mathbf{q}$ take the former values in (A.1)–(A.3) for the resonator modes; for the surface modes (22), the result is obtained from (A.1)–(A.3) by means of the substitution $k \to i\kappa$. The contribution of the surface modes to vacuum expectation values requires no renormalization. The aforementioned singular dependence on D disappears from the total expression (26). The mechanism of its cancellation can easily be understood by using the analog of Eq. (A.5) for the case of $\delta \equiv -\delta_1 < 0$:

$$\sum_{z_{n\delta}>0} \frac{f(z_{n\delta})}{1-\dfrac{\sin 2z_{n\delta}\widetilde{l}}{2z_{n\delta}\widetilde{l}}} - \frac{\widetilde{l}}{\pi}\int\limits_0^\infty f(z)\,dz \qquad (A.7)$$

$$= \frac{-\widetilde{l}}{2\pi i}\int\limits_0^\infty \frac{(1+t)[f(it)-f(-it)]}{\sinh t\widetilde{l} - t\cosh t\widetilde{l}}\, e^{-t\widetilde{l}}\,dt$$

$$+ \frac{f(z_*)}{\dfrac{\sin 2z_*\widetilde{l}}{2z_*\widetilde{l}} - 1}.$$

The principal-value prescription in the integral takes into account the presence of the pole at $t_* = -iz_* = \kappa\delta_1$, whose contribution is represented by the last term on the right-hand side of Eq. (A.7). In order to derive this equation, one can make use of the properties of the function Δ_1'/Δ_1 [see Eq. (21)]. Making the relevant substitutions for the function $f(z)$, one can verify that, each time, the contribution of the pole at z_* exactly cancels the contribution $\langle \widetilde{T}_{\mu\nu}\rangle^{(b)}$ of surface modes to the components of the renormalized tensor in (26).

REFERENCES

1. V. M. Mostepanenko and N. N. Trunov, *Casimir Effect and Its Applications* (Énergoatomizdat, Moscow, 1990).
2. P. Hasenfratz and J. Kuti, Phys. Rep. **40**, 75 (1978).
3. S. K. Blau, M. Visser, and A. Wipf, Nucl. Phys. B **310**, 163 (1988).
4. G. Cognola, L. Vanzo, and S. Zerbini, J. Math. Phys. **33**, 222 (1992).

5. S. Leseduarte and A. Romeo, Ann. Phys. (N.Y.) **250**, 448 (1996).
6. M. Bordag, E. Elizalde, K. Kirsten, and S. Leseduarte, Phys. Rev. D **56**, 4896 (1997); hep-th/9608071.
7. V. V. Nesterenko and I. G. Pirozhenko, Phys. Rev. D **57**, 1284 (1998).
8. D. Deutsch and P. Candelas, Phys. Rev. D **20**, 3063 (1979).
9. R. Balian and C. Bloch, Ann. Phys. (N.Y.) **60**, 401 (1970); **64**, 271 (1971).
10. P. Candelas, Ann. Phys. (N.Y.) **143**, 241 (1982).
11. S. L. Lebedev, Zh. Éksp. Teor. Fiz. **110**, 769 (1996) [JETP **83**, 423 (1996)].
12. J. Ambjorn and S. Wolfram, Ann. Phys. (N.Y.) **147**, 1 (1983).
13. N. D. Birrell and P. C. W. Davies, *Quantum Fields in Curved Space* (Cambridge Univ. Press, Cambridge, 1982; Mir, Moscow, 1984).
14. V. M. Mostepanenko and N. N. Trunov, Yad. Fiz. **42**, 1297 (1985) [Sov. J. Nucl. Phys. **42**, 818 (1985)].
15. A. B. Migdal, *Fermions and Bosons in Strong Fields* (Nauka, Moscow, 1978).
16. *Quantum Field Theory under the Influence of External Conditions,* Ed. by M. Bordag (B. G. Teubner, Stuttgart, 1998).
17. G. Kennedy, R. Critchley, and J. S. Dowker, Ann. Phys. (N.Y.) **125**, 346 (1980).
18. *Higher Transcendental Functions (Bateman Manuscript Project),* Ed. by A. Erdelyi (McGraw-Hill, New York, 1953; Nauka, Moscow, 1974), Vol. 2.
19. B. S. DeWitt, Phys. Rep. C **19**, 295 (1975).
20. A. Blasi, R. Collina, and J. Sassarini, Int. J. Mod. Phys. A **9**, 1677 (1994).
21. K. Symanzik, Nucl. Phys. B **190**, 1 (1981).
22. L. C. Albuquerque, Phys. Rev. D **55**, 7754 (1997).
23. M. Bordag, K. Kirsten, and D. V. Vassilevich, in *Quantum Field Theory under the Influence of External Conditions,* Ed. by M. Bordag (B. G. Teubner, Stuttgart, 1998), p. 50.
24. V. B. Berestetskiĭ, E. M. Lifshitz, and L. P. Pitaevskiĭ, *Quantum Electrodynamics* (Nauka, Moscow, 1989; Pergamon, Oxford, 1982).
25. J. C. Collins, *Renormalization: an Introduction to Renormalization, the Renormalization Group, and the Operator-Product Expansion* (Cambridge Univ. Press, Cambridge, 1984; Mir, Moscow, 1988).
26. A. I. Markushevich and L. A. Markushevich, *An Introduction to the Theory of Analytic Functions* (Prosveshchenie, Moscow, 1977).
27. G. Barton, J. Phys. A **14**, 1009 (1981).

Translated by A. Isaakyan

Physics of Atomic Nuclei, Vol. 64, No. 7, 2001, pp. 1347–1348. Translated from Yadernaya Fizika, Vol. 64, No. 7, 2001, pp. 1423–1424.

75th Anniversary of Boris Lazarevich Ioffe's Birthday

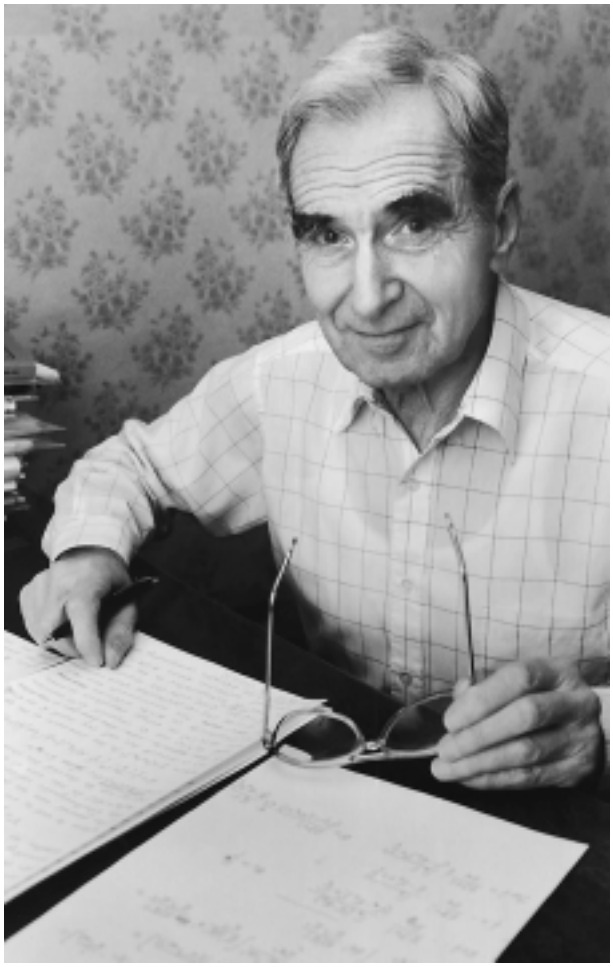

On July 6, 2001, Professor Boris Lazarevich Ioffe, eminent theoretical physicist, a corresponding member of the Russian Academy of Sciences, head of the Laboratory of Theoretical Physics at the Institute of Theoretical and Experimental Physics (ITEP, Moscow, Russia), celebrated his 75th birthday.

On December 31, 1949, Boris Lazarevich graduated from the Faculty of Physics at Moscow State University; immediately after that (on January 1, 1950), he joined the Laboratory of Theoretical Physics at Laboratory no. 3 (USSR Academy of Sciences), which was later named Thermal Physics Laboratory (TPL), currently known as the Institute of Theoretical and Experimental Physics. At that time, A.I. Alikhanov was the director of Laboratory no. 3 (TPL) and I.Ya. Pomeranchuk headed its Laboratory of Theoretical Physics. In addition to exams compulsory for all students of the Moscow State University, Ioffe was able to pass nine exams introduced by Landau (who was the examiner himself at that time) to select young talented theoretical physicists (so-called theoretical minimum) and was reckoned since then among representatives of Landau's scientific school. Thus, Ioffe had a privilege of being tutored by three renowned physicists, Alikhanov, Landau, and Pomeranchuk.

Throughout more than 50 years of creative activity, Ioffe greatly contributed to the development of the theory of elementary particles, high-energy physics, the theory of nuclear reactors, and applied nuclear physics. Listed below are only the most important of his results.

In an investigation that Ioffe performed with L.B. Okun and A.P. Rudik in 1956, it was established for the first time that parity violation must be accompanied by the violation of charge symmetry or symmetry with respect to time reversal and that an experimental observation of P-odd pair correlations of particle spins and momenta would imply charge-symmetry violation. This conclusion, which was of fundamental importance for the theory of elementary particles, was obtained prior to the discovery of parity nonconservation and served as a basis for Landau's hypothesis of CP conservation and for the two-component theory of neutrinos. This result of Ioffe, Okun, and Rudik was registered as a discovery and was quoted in the Nobel lectures of T.D. Lee and C.N. Yang.

Shortly after the emergence of the Gell-Mann–Feynman hypothesis of a conserved vector current (CVC) in weak interactions, Ioffe, together with V.G. Vaks, proved, in 1958, that, in such a theory, the structural part of the vector current in the amplitude for the pion radiative decay $\pi \to e + \nu + \gamma$ is determined by the neutral-pion lifetime. This relation is of paramount importance since it represents one of the few corollaries of the CVC hypothesis that were confirmed experimentally (this was done in 1963 by P. Depommier, J. Heintze, C. Rubbia, and W. Soergel).

In 1967, Ioffe, together with E.P. Shabalin, showed that the theory of weak interactions that involves only ordinary and strange hadrons becomes inappropriate

1063-7788/01/6407-1347$21.00

at energies of about a few GeV. These results are of fundamental importance—in particular, they served later on as a basis for the Glashow–Iliopoulos–Maiani hypothesis of the existence of charmed particles and of the form of the weak interaction of hadrons (GIM mechanism).

In 1969, Ioffe found that, in deep-inelastic lepton–hadron scattering, the interaction occurs in a space-time region near the light cone and is characterized by longitudinal distances linearly growing with time. In the literature on high-energy physics, times corresponding to such longitudinal distances are referred to as Ioffe times. These results, which were registered as a discovery, form a basis of a modern description of deep-inelastic processes that relies on the method of an operator-product expansion near the light cone; in particular, they are widely used in analyzing the interaction of virtual photons with nucleons and nuclei.

In 1976, Ioffe proposed an efficient method for seeking the Higgs boson in electron–positron annihilation, where it can be produced in association with a Z boson, $e^+e^- \to ZH$. It is in this way that the H boson is being sought presently at CERN.

Some results of prime importance were obtained by Ioffe in studying the properties of baryons within QCD. In particular, he showed that baryon masses emerge owing to the presence of a quark condensate. The equation that he derived and which relates the proton mass to the quark condensate is referred to as the Ioffe formula, while the quark current describing the proton is known as the Ioffe current. Ioffe introduced the concept of the magnetic susceptibility of a quark condensate and showed that it determines the magnetic moments of baryons. He calculated the magnetic moments of the proton, of the neutron, and of hyperons—that is, he solved the problem that Feynman thought to be the most important for proving that QCD is a true theory of strong interactions.

In studying the spin structure of the proton, Ioffe established an elegant relationship between the Gerasimov–Drell–Hearn sum rule for hadron production by polarized photons and the Bjorken and Ellis–Jaffe sum rules for spin-dependent structure functions for deep-inelastic scattering. He also developed a method for nonperturbatively computing quark distributions in the nucleons, mesons, and the photon. The resulting quark distributions in the pion and in the photon are in good agreement with experimental data and can be used as initial conditions for solving evolution equations. Ioffe's investigations of the properties of hadrons in nuclear matter at finite temperatures and densities also led to some interesting results.

Noteworthy are the results that Ioffe obtained in the theory of nuclear reactors and in applied nuclear physics. He developed the theory of a deep deterioration of a fuel material in nuclear reactors. This theory, which, according to Yu.B. Khariton, was highly appreciated by I.V. Kurchatov, is presently used as a basis in calculations underlying measurements of the reactivity and other physical properties of atomic power plants. Ioffe supervised the physical calculations of the power heavy-water reactor for the A-1 power station in the Czech and Slovak Republic (commissioned in 1973) and of research reactors in the Soviet Union (ITEP), China, and Yugoslavia.

Ioffe made an important contribution to the work on the hydrogen bomb in the Soviet Union (1951–1953): among other things, he calculated the thermal conductivity of a fully ionized gas containing relativistic electrons and determined the energy transfer to photons in such a gas with allowance for their anisotropy. Together with the group of researchers headed by Ya.B. Zeldovich, he proved the impossibility of implementing the "Tube" hydrogen-bomb project. In connection with this project, Ioffe studied the effect of polarization on the propagation of photons in a fully ionized gas. The results of this investigation are applied in analyses of some astrophysics problems.

Boris Lazarevich is the author of two discoveries, 290 scientific studies, and two monographs. In 1994, he was awarded an Alexander von Humboldt prize (Germany); in the same year, he was elected to fellowship in the American Physical Society. He is also a member of the Executive Committee of the United Physical Society of the Russian Federation. Apart from scientific articles, Ioffe wrote the historical narrative "A Top-Secret Task" (*Novyi Mir*, Nos. 5, 6, 1999).

The Bureau of the Editorial Board of the journal *Yadernaya Fizika* (known in the English-speaking word as *Physics of Atomic Nuclei*); the members of the ITEP staff; and his colleagues, friends, and disciples congratulate heartily Boris Lazarevich on the 75th anniversary of the his birth and wish him good health and many years of creative activity.

Editorial Board